

https://dspace.org/

Controls of sulphide mineralisation at the kamoa copper deposit, with an emphasis on structural controls

Banza, Franck Twite

2016

https://hdl.handle.net/10539/23734

Banza, Franck Twite. 2016. Controls of sulphide mineralisation at the Kamoa copper deposit, with an emphasis on structural controls, University of the Witwatersrand, https://hdl.handle.net/10539/23734

Downloaded from a DSpace repository. https://dspace.org/

Controls of sulphide mineralisation at the Kamoa copper deposit, with an emphasis on structural controls

Franck Twite Banza

A Dissertation submitted to the Faculty of Science, University of the Witwatersrand, Johannesburg, in fulfilment of the requirements for the degree of Master of Science.

December, 2016



IVANHOE MINES
NEW HORIZONS

DECLARATION

I declare that this dissertation is my own, unaided work. It is being submitted for the Degree of Master in Science at the University of the Witwatersrand, Johannesburg. It has not been submitted before for any degree or examination in any other University.



_____
Signature of Candidate

____1ST ____day of ____December____ 2016.

ABSTRACT

The Kamoa copper deposit, situated approximately 25 km west of the Kolwezi Cu-Co district of the Democratic Republic of Congo, is one of the largest high-grade undeveloped copper deposits in the world. Kamoa is a new discovery which occurs on the western edge of the Congolese portion of the Central African Copperbelt. Two main rock units are present at Kamoa, sandstone and conglomerate of the Mwashya Subgroup of the Roan Group, and overlying diamictite and interbedded siltstone-sandstone of the Grand Conglomérat unit of the Nguba Group. The deposit occurs along a stratigraphically controlled redox boundary at the base of the Grand Conglomérat. The Kamoa deposit occurs broadly within a NNE-trending structural high bound to the west by the West Scarp fault and to the east by the Kansoko trend. Within this area the host rocks dip gently away from two localized domes, which expose rocks of the Mwashya Subgroup.

Drill core data indicate that the Kamoa deposit includes areas of higher and lower grade, some of which appear at the deposit scale to be related to known or interpreted faults. The aim of this study was to determine the role of structure(s) in the genesis and distribution of hypogene copper sulphides, and to identify the nature of those structures and their timing relative to mineralisation. Detailed structural logging in drill core has focused on analysis of foliations, folds, mesoscopic faults, strain shadows and strain fringes. True thickness isopach maps were used to investigate spatial relationships of mineralisation with facies/thickness changes and faults throughout the deposit.

In the southern part of the Kamoa deposit, a linear NNW zone of abrupt change in stratal thickness named the “Mupaka Fault” is oblique to the localised domes and correlates well with higher copper grades. This fault may represent an important transport path for the hydrothermal fluids in the Kamoa deposit. Thickness variations, facies change, steep bedding and rotated mesoscopic faults demonstrate that the Mupaka Fault is a syn-sedimentary growth fault that occurs during the deposition of the Nguba Group rocks. The close relationship between copper mineralisation and structures demonstrates that structures played a significant role in the formation of ore at Kamoa. Zones of thickness variations of stratigraphic units may represent potential prospective areas for future exploration work.

The development of S_1 foliation, strain shadows and strain fringes is coeval and related to a NW shortening direction. The Kolwezian deformation event is believed to be responsible for the development of these structures. Strain fringes reveal a straight orientation of fibres during coaxial deformation; this supports the interpretation of a single phase of deformation within the Kamoa deposit. The non-deformed distal part of the fringe, the straight orientation of fibres, the lack of undulose extinction and recrystallisation features demonstrate the simple geometry of strain shadows and strain fringes. These characteristics suggest a new growth of

minerals under low temperature and high pressure fluid. The analysis of minerals within fringes suggests little potential for remobilisation of minerals in strain shadows and strain fringes because none of the mechanisms of recrystallisation (bulging, subgrain rotation and grain boundary migration) have been observed. A syn- or post-orogenic origin of copper sulphides, probably related to the Lufilian orogeny is proposed.

ACKNOLEDGEMENTS

I would like to thank my supervisors, Dr. Paul Nex and Prof. Judith Kinnaird who provided excellent guidance and support during all phases of this study. Their patience, motivation and continuous encouragement have allowed me to complete this dissertation. Also special thanks to Prof. Cees Passchier for the Microtectonics course provided at the Stellenbosch University, this was invaluable in helping me to understand micro-structures.

I gratefully acknowledge the assistance given by the management of Ivanhoe Mines in giving me a post-graduate grant and study leave. I thank Mr. Stephen Torr and Dr. David Broughton for providing the opportunity. A special note of thanks goes to Dr. David Broughton for guidance and for so many hours of fruitful discussions concerning this study, I am deeply grateful to you. Thank you also to Mr. George Gilchrist for support and guidance throughout this project, particularly for help on true thickness calculations of stratigraphic units which were crucial for this research; and to Mr. David Edwards for his patience, support and for sharing invaluable knowledge of the Kamoa geology.

Sincere thanks are due to all the staff at Kamoa Copper S.A., especially the geology team. I am grateful to the core shed staff including Francis, Peters, Gilbert, Daniel and Papy for the core boxes transportation. Special thanks go to Polydor Kakunde from the Kamoa mineralogy Lab for all the sample preparation. I owe gratitude to my colleagues at Kamoa: Mr. Mike Freer, Mr. Paul Arscott, Pontien Kalala, Christelle Nkulu, Christian Munyungu, Mr. David Mitchel, Fabrice Nkomba, Jacques Kayumba, Lydia Makong, Patrick Kasongo, Sean Wessels, Thierry Yangala, Micheline Kyenge, David Kabwe, Jean-Yves Davies, Paul Kazadi and Mr. Shiko Kebonte for their encouragement. Jacques Cremer, Christian Monene, Antoine Kimbasi and Ismael Kayembe were useful for computer matters and dataset information. A special thanks go to Nozimilo Sekete for the administrative assistance during my research. Big thanks are due to Dr. Wayne Barnett, Michael Kirschbaum, Innocent Mushobekwa, Andy Friese and Tim Brooks for valued discussions and advice regarding my studies.

In South Africa, I have met many people who assisted me during my research; I would like to thank Josia Shilunga, Despina Tshipala, Kevin Dalton, Siyanda, Luke Peters and Dr. Jeremie Lehmann who deserves a particular mention. I am grateful to Prof. Alexander Ziegler and Mr. Jacques Gerber for help with the Scanning electron microscope at MMU (University of the Witwatersrand). I would also like to thank Caiphus Majola who made my thin sections.

Last, but not least, I would like to thank my family for their love, and encouragement during the tough time; my mother Françoise Nday and my future wife Delvareine Kabwayi; thank you for believing in me.

TABLE OF CONTENTS

DECLARATION……..ii

ABSTRACT ……iii

ACKNOWLEDGEMENTS ……v

TABLE OF CONTENTS……vi

LIST OF FIGURES ……xii

LIST OF TABLES ……xix

CHAPTER 1 - Overview of the Central African Copperbelt……..1

1.1 Introduction……1

1.2 Regional Geology……2

1.2.1 Katangan Supergroup in the Zambian Copperbelt……4

1.2.2 Katangan Supergroup in the DRC Copperbelt……7

1.3 Tectonic setting of the Lufilian Arc……9

1.4 Aims of the thesis……12

1.5 Methodology……13

CHAPTER 2 - The Kamoa Copper Deposit……14

2.1 Introduction……14

2.2 Geological overview……15

2.3 Lithology and stratigraphy……17

2.4 Sedimentary environment……20

2.5 Structure……20

2.6 Metamorphism……21

2.7 Alteration……21

2.8 Mineralisation……23

2.9 Sulphur Isotopes……24

2.10 Fluid inclusions……25

2.11 Conclusion……25

CHAPTER 3 - Lithostratigraphical variation and features of the Nguba Group within the Kamoa area……26

3.1 Introduction……26

3.2 Mwashya Subgroup……26

3.3 Nguba Group……28

3.3.1 Basal diamictite (Ng 1.1.1) ……28

3.3.1.1 Lower basal diamictite (Ng 1.1.1.1)……38

3.3.1.2 Intercalated siltstone (Ng 1.1.1.2) ……38

3.3.1.3 Upper basal diamictite (Ng 1.1.1.3) ……39

3.3.2 Lower laminated pyritic siltstone/sandstone (Ng 1.1.2)……40

3.3.3 Middle diamictite package (Ng 1.1.3) ……43

3.3.4 Upper laminated pyritic siltstone/sandstone (Ng 1.1.4) ……45

3.3.5 Upper diamictite unit (Ng 1.1.5) ……47

3.3.6 Uppermost diamictite unit (Ng 1.1.6) ……47

3.4 Mafic igneous rocks……48

3. 5 Petrography of the Mwashya Subgroup and Nguba Group rocks……49

3.5.1 Mwashya Subgroup……49

3.5.2 Nguba Group……50

3.6 Discussion……52

3.7 Conclusion……53

CHAPTER 4 - Structural features of the Kamoa deposit……54

4.1 Introduction……54

4.1.1 Local structural setting……57

4.2 Bedding (S_0)……58

4.3 Zone of abrupt change in stratal thickness of the Basal diamictite: "Mupaka Fault" ……59

4.3.1 Steep bedding……61

4.3.2 Soft-sediment deformation structures……65

4.3.3 Mesoscopic faults……67

4.3.4 Timing of features within the steep bedding……67

4.4 Secondary foliation S_1……73

4.4.1 Introduction……73

4.4.2 Foliation within borehole core……73

4.4.3 The Rf-ϕ method……74

4.4.4 Foliation microstructures……82

4.4.4.1 Mechanisms of foliation development……82

4.4.4.2 Morphological classification of foliation microstructure……84

4.4.4.3 Microanalysis of foliation within the Kamoa deposit……85

4.4.4.3.1 Introduction……85

4.4.4.3.2 Secondary foliation within diamictites……86

4.4.4.3.3 Secondary foliation in siltstones……91

4.4.4.3.4 Secondary foliation in the Mwashya Subgroup rocks……93

4.4.4.4 Microstructural description of minerals in the foliated rocks……93

4.5 Strain fringes and strain shadows……97

4.5.1 Introduction……97

4.5.2 Mesoscopic analysis of strain shadows and strain fringes……97

4.5.3 Microstructural observations of strain shadows and fringes……103

4.5.3.1 Introduction……103

4.5.3.2 Description of strain fringes and strain shadows……103

4.6 Veins……112

4.7 Mesoscopic folds……115

4.8 Faults……120

4.8.1 Macro faults……120

4.8.1.1 Fault type 1 (FA1) ……121

4.8.1.2 Fault type 2 (FA2) ……121

4.8.1.3 Fault type 3 (FA3) ……122

4.8.2 Mesoscopic faults……124

4.9 Discussion……128

4.10 Conclusion……129

CHAPTER 5 - Mineralisation and associated structural features of the Kamoa deposit……132

5.1 Mineralisation……132

5.2 Mineral zonation……139

5.3 Supergene mineralisation……139

5.4 Stratigraphic position of the ore mineralisation……143

5.5 Structural features relative to copper mineralisation……146

5.6 Discussion……152

5.7 Conclusion……154

CHAPTER 6 - Discussion and conclusions……155

6.1 Discussion……155

6.1.1 Introduction……155

6.1.2 Lithostratigraphical variation and features of the Nguba Group……156

6.1.3 Deformation history……158

6.1.4 Mineralisation……159

6.1.5 Timing of copper mineralisation relative to deformation……162

6.1.6 Mineral alteration……165

6.1.7 Microthermometry……165

6.2 Conclusions……165

6.2.1 Implications for future exploration……166

6.2.2 Recommendations for further work……167

References……168

Appendix A……174

Appendix B……232

Appendix C……241

LIST OF FIGURES

Fig. 1.1: Geological map of the CACB showing distinct tectonic domains……**2**

Fig. 1.2: Sketch map of the Pan African system in central and Southern Africa ……..…..…..**3**

Fig. 1.3: Lithostratigraphy of the Katangan Supergroup, Zambian Copperbelt……..**5**

Fig. 1.4: Stratigraphic column of the Katangan Supergroup in the DRC Copperbelt……..……**8**

Fig. 1.5: Map showing the tectonic zoning in the Lufilian fold belt and distribution of copper deposits in the Zambian and Congolese Copperbelt……**10**

Fig. 2.1: Project geological setting of the Kamoa copper deposit……..……**15**

Fig. 2.2: Geologic map of the Kamoa area……**16**

Fig. 2.3: Magnetic image map showing structural interpretation ……..**22**

Fig. 2.4: Simplified geology section showing the zonation of ore minerals……**23**

Fig. 3.1: Photo illustrating the Mwashya Subgroup rocks……..…..**26**

Fig. 3.2: Elevation contour map of the contact between the Grand Conglomérat and the Mwashya Subgroup……..**27**

Fig. 3.3: Detailed stratigraphy of the Grand Conglomérat (Ng 1.1) within the Kamoa Copper deposit……..**29**

Fig. 3.4: Map showing the location of cross-sections presented in the study……..**30**

Fig. 3.5: Section line A-A’ (lithostratigraphical variation)……**31**

Fig 3.6: Section line B-B’ (lithostratigraphical variation)……..**32**

Fig. 3.7: Section line C – C’ (lithostratigraphical variation)……..**33**

Fig. 3.8: Section line D – D’ (lithostratigraphical variation)……**34**

Fig. 3.9: Section line E – E’ (lithostratigraphical variation)……..**35**

Fig. 3.10: Section line F – F’ (lithostratigraphical variation)……**36**

Fig. 3.11: Isopach map of the Basal diamictite (Ng 1.1.1)……..**37**

Fig. 3.12: Photo illustrating the Lower basal diamictite (Ng 1.1.1.1)……..**38**

Fig. 3.13: Photo illustrating the Intercalated siltstone (Ng 1.1.1.2)……..**39**

Fig. 3.14: Photo illustrating the Upper basal diamictite (Ng 1.1.1.3)……**39**

Fig. 3.15: Photo illustrating the Lower laminated pyritic siltstone/sandstone (Ng 1.1.2)…….**40**

Fig. 3.16: Hand sample photographs of some of the features of the Lower laminated pyritic siltstone/sandstone (Ng 1.1.2)……..**41**

Fig. 3.17: Photo illustrating the clast-poor diamictite within the Lower laminated pyritic siltstone/sandstone (Ng 1.1.2)……..**41**

Fig. 3.18: Isopach map of the Lower laminated pyritic siltstone/sandstone (Ng 1.1.2)……..**42**

Fig. 3.19: Photo illustrating the Middle diamictite unit (Ng 1.1.3)……..**43**

Fig. 3.20: Isopach map of the Middle diamictite unit (Ng 1.1.3)……..**44**

Fig. 3.21: Photo illustrating the Upper laminated pyritic siltstone/sandstone (Ng 1.1.4)……..**45**

Fig. 3.22: Isopach map of the Upper pyritic siltstone/sandstone unit (Ng 1.1.4)……..**46**

Fig. 3.23: Photo illustrating the Upper diamictite (Ng 1.1.5)……..**47**

Fig. 3.24: Photo illustrating the conglomerate of the Ng 1.1.6……..**48**

Fig. 3.25: Photo illustrating the mafic igneous rocks……..**49**

Fig. 3.26: Photomicrographs of the Mwashya Subgroup……..**50**

Fig. 3.27: Photomicrographs of the lithologies commonly seen within the Grand Conglomérat Subgroup……..**51**

Fig. 3.28: Cross section showing the thickness of different stratigraphic units of the Grand Conglomérat that overlie the Mwashya subgroup ……..**52**

Fig. 4.1: Map showing the studied borehole locations……..**55**

Fig 4.2: Map showing the location of boreholes with hand samples or thin sections presented in chapter 4……..**56**

Fig. 4.3: (A). Geological and lineament map showing the NE-trending mega-folds (in yellow) and the strong NS cross-cutting fault network pattern west of Kamoa, with NE linking fault structures (in purple). The geological map is draped on an aeromagnetic image of the Kamoa project area. 1= Makalu dome. 2= Kamoa dome. (Mvondo, 2012). (B). North-northeast and east-trending, folds developed in the deposit area (Gilchrist, 2014)……**57**

Fig. 4.4: Map showing the distribution of boreholes with bedding measurements……**58**

Fig. 4.5: Lower hemisphere equal area stereographic projection of poles to bedding measured in the Lower and Upper laminated siltstone/sandstone……**59**

Fig. 4.6: Grade Profiles and structural features for boreholes DMAK_RD030 and DD860……**60**

Fig. 4.7: Photographs of hand samples illustrating sub-vertical bedding containing high-grade copper mineralisation……**62**

Fig. 4.8: Relationship between foliation (S_1) and steep bedding……**63**

Fig. 4.9: SEM images for the steep bedding……**64**

Fig. 4.10: Orientation of structural features from the Basal diamictite (Ng 1.1.1) of the borehole DMAK_RD034……**65**

Fig. 4.11: Detailed investigation of the zone in the vicinity of the steep bedding……**66**

Fig. 4.12: Hand samples illustrating S_0 bedding and mesoscopic faults both in steep and shallow dipping beds for the borehole DD860……**68**

Fig. 4.13: Features of mesoscopic faults within the steep bedding……**69**

Fig. 4.14: Map showing the distribution of boreholes with mesoscopic fault measurements…..**70**

Fig. 4.15: Lower hemisphere equal area stereographic projection of poles to mesoscopic faults recorded in the Nguba Subgroup rocks……**71**

Fig. 4.16: Photograph of core box showing steep bedding associated with mesoscopic faults for the potential growth fault located in the northern part of the deposit……**71**

Fig. 4.17: Map showing the true thickness isopach map of the Basal diamictite and interpreted growth faults……**72**

Fig. 4.18: S_1 foliation defined by the alignment of clasts seen in photographs of borehole core……**75**

Fig. 4.19: Photos of borehole core showing S_1 foliation defined by alignment of sulphides…….**76**

Fig. 4.20: Map showing the orientation of S_1 foliation in different areas of the Kamoa deposit……..**77**

Fig. 4.21: Photographs of borehole core showing a strong foliation……**78**

Fig. 4.22: Median intensity of S_1 foliation superimposed on a magnetic map……..**79**

Fig. 4.23: Orientation of S_1 foliation at different depths in borehole DD912……..**80**

Fig. 4.24: Evaluation of strain in diamictite……**81**

Fig. 4.25: Development of foliation by progressive simple shear and pure shear (Passchier and Trouw, 2005)……..**82**

Fig. 4.26: Schematic diagram of some important mechanisms contributing to development of secondary foliation in rocks (Passchier and Trouw, 2005)……**83**

Fig. 4.27: Morphological classification of foliations using an optical microscope (Passchier and Trouw, 2005)……**84**

Fig. 4.28: Map showing the distribution of boreholes with thin sections displaying S_1 foliation……..**85**

Fig. 4.29: Schematic diagram of the S_1 foliation and L_1 lineation showing the orientation of thin sections cut to investigate the intensity of the foliation in different orientations ……**86**

Fig. 4.30: Scanned photos of thin sections illustrating S_1 within diamictite……..……**88**

Fig. 4.31: Photomicrographs and SEM images of S_1 foliation within the diamictite……..…..**89**

Fig. 4.32: Photomicrographs and SEM images of S_1 foliation within the diamictite……**90**

Fig. 4.33: Photomicrographs of the strong foliation observed in the borehole located on the fold.....**91**

Fig. 4.34: Illustration of S_1 foliation in siltstone……**92**

Fig. 4.35: Microphotographs showing S_1 foliation in the Mwashya Subgroup sandstones…….**93**

Fig. 4.36: Photomicrographs illustrating the morphology of quartz, muscovite and chlorite in the different types of foliations (S_1)……**95**

Fig. 4.37: Illustration of the morphology of minerals within strain fringes……**96**

Fig. 4.38: Illustration of development of strain shadows and strain fringes……**97**

Fig. 4.39: Morphology of strain shadows/fringes……**98**

Fig. 4.40: Morphology of strain shadows and strain fringes in the borehole DD793……**99**

Fig. 4.41: Morphology of strain shadows and strain fringes in the borehole DD084……**100**

Fig. 4.42: Morphology of the strain shadows and strain fringes in borehole DD595……**101**

Fig. 4.43: Strain shadows/fringes zonation in the boreholes DD793, DD084 and DD595……**102**

Fig. 4.44: Scanned thin sections illustrating strain fringes in diamictite……**105**

Fig. 4.45: Photomicrographs of strain fringes in diamictite……**106**

Fig. 4.46: SEM images showing strain fringes and their composition……**107**

Fig. 4.47: Scanned thin sections illustrating strain shadows in diamictite……**108**

Fig. 4.48: Photomicrographs illustrating strain shadows in diamictite……**109**

Fig. 4.49: SEM images showing strain shadows and their composition……**110**

Fig. 4.50: Illustration of strain shadows and strain fringes in siltstone……**111**

Fig. 4.51: Theoretical model for the development of strain fringes in coaxial progressive deformation around cubic and spherical core objects in the case of displacement controlled and face-controlled fibres (Passchier and Trouw, 2005)……**112**

Fig. 4.52: Orientation of veins and bedding in the Kamoa deposit……**113**

Fig. 4.53: Images of veins in the Kamoa deposit……**114**

Fig. 4.54: Map showing the distribution of veins in the Kamoa deposit superimposed on a magnetic map ……**115**

Fig. 4.55: Photographs of hand samples illustrating mesoscopic folds within the Kamoa deposit……**116**

Fig. 4.56: Relationship between bedding and the axial planes of mesoscopic folds……..**117**

Fig. 4.57: Photomicrographs of mesoscopic folds……**118**

Fig. 4.58: Photomicrographs of mesoscopic folds……**119**

Fig. 4.59: SEM images of mesoscopic folds……**120**

Fig. 4.60: Photo showing fault type 1……**121**

Fig. 4.61: Photo showing fault type 2……**122**

Fig. 4.62: Photo showing fault type 3……**122**

Fig. 4.63: Lower hemisphere equal area stereographic projection of poles to fault planes. (Mvondo, 2012)……..**124**

Fig. 4.64: Map showing the predominant or median sense of movement of mesoscopic faults within boreholes in the studied area……**125**

Fig. 4.65: Photographs of mesoscopic faults observed in boreholes cores within the studied area…… **126**

Fig. 4.66: Photomicrographs of mesoscopic faults in thin section……..**127**

Fig. 5.1: Photograph of borehole core showing the redox boundary located at the contact between the Mwashya Subgroup and the Grand Conglomérat unit……**132**

Fig. 5.2: Schematic stratigraphic diagram of the Kamoa deposit……**133**

Fig. 5.3: Photomicrographs showing the mineralogy of the Mwashya subgroup rocks……**134**

Fig. 5.4: Copper sulphide textures at the Kamoa copper deposit……**136**

Fig. 5.5: Reflected light photomicrographs showing the mineralogy of the ore zone in the borehole DD963.... ……**137**

Fig. 5.6: Schematic diagram illustrating the mineral zonation, the copper grade and sulphur profile together with the plot of copper-sulphur ratio versus depth for the borehole DD963……**140**

Fig. 5.7: Plot of copper-sulphur ratio versus depth for the borehole DD963……..**141**

Fig. 5.8: Map showing the lateral zonation of sulphides in the Kamoa deposit……**142**

Fig. 5.9: Map showing borehole locations and the variation in stratigraphic position of copper mineralisation. The location of fence diagrams presented in chapter 5 is also shown……**144**

Fig. 5.10: Section line B-B' (including copper content and structural features) ……..**145**

Fig. 5.11: Section line C – C' (including copper content and structural features) ……..**147**

Fig. 5.12: Section line D – D' (including copper content and structural features)……..**148**

Fig. 5.13: Section line E – E' (including copper content and structural features)……..**149**

Fig. 5.14: Section line F – F' (including copper content and structural features) ……..**150**

Fig. 5.15: Isopach map of the Basal diamictite (Ng 1.1.1) with superimposed copper grade information from boreholes……..**151**

Fig. 5.16: Simplified schematic of mineral zonation in the Kamoa deposit……**152**

Fig. 5.17: Plot of Cu+/H+ versus Fe+/H+ activity ratios showing the standard zoning and paragenetic sequence that is commonly observed in sedimentary-hosted stratiform copper deposits when a copper-bearing fluid reacts with a pyritic shale (after Ripley *et al.,* 1985 in Robb, 2005)……**153**

Fig. 6.1: Geological map of the CACB showing the location of deposits and cities ……..**156**

Fig. 6.2: Simplified stratigraphic model of the Kamoa deposit……..**157**

Fig. 6.3: Proposed schematic diagram showing the current genetic model and the precipitation mechanism that occurred in the Kamoa deposit……**160**

Fig. 6.4: Schematic diagram illustrating the model for ore formation in the Kamoa deposit……..**161**

LIST OF TABLES

Table 1.1: Lithostratigraphy of the Katangan Supergroup (Cailteux, 1994)……..**6**

Table 1.2: Katangan stratigraphic column and dates of major tectonism in southern Katanga……**12**

Table 2.1: Stratigraphic column of the Grand Conglomérat within the Kamoa copper deposit……**19**

Table 4.1: Illustration of the orientation of S_1 foliation in different areas of the Kamoa deposit……**74**

Table 5.1: Stratigraphic position of copper mineralisation in the boreholes investigated……..**143**

CHAPTER 1

Overview of the Central African Copperbelt

1.1 Introduction

The Kamoa copper deposit is situated approximately 25 km west of the Kolwezi Cu-Co deposits in the Democratic Republic of Congo (DRC). The deposit is located on the western edge of the Congolese portion of the Central African Copperbelt (CACB) (Fig. 1.1) (Broughton and Rogers, 2010; Parker *et al.,* 2013; Schmandt *et al*., 2013). The deposit is hosted within the Grand Conglomérat unit of the Nguba Group, stratigraphically above rocks that host most of the major deposits in the DRC portion of the CACB (Broughton and Rogers, 2010). The borehole core data indicates that the deposit extends at least 5 km east-west and 23 km north-south. The deposit occurs along a stratigraphically-controlled redox boundary at the base of the Grand Conglomérat. Kamoa is unusual in that it is not hosted within the Mines Subgroup, which is the typical host for many of the deposits in other DRC Mines (Broughton and Rogers, 2010). In the majority of the DRC copper mines, orebodies occur within mega-breccia fragments where main stage mineralisation probably pre-dated later folding and brecciation (Cailteux 1994; Cailteux *et al.,* 2005a). Unlike most of the DRC deposits, Kamoa is hosted in a recognisable and continuous stratigraphy above the Mines Group and shares more common characteristics with some of the Zambian deposits in the CACB, as well as the Polish Kupferschiefer deposits.

Previous research on Kamoa has yielded valuable information about the stratigraphy and mineralisation of the deposit (Broughton and Rogers, 2010; Parker *et al.,* 2013; Schmandt *et al*., 2013). However, there is a lack of understanding of the controls on the distribution of the sulphide mineralisation at Kamoa. The purpose of this study is to understand the controls on the type, distribution and abundance of copper minerals and associated alteration minerals at Kamoa, at scales ranging from regional to microscopic. The focus will be primarily on hypogene copper mineralisation, but part of the study will also characterise the effects of later processes such as leaching and supergene mineralisation.

1.2 Regional Geology

The CACB is the world's largest sedimentary rock-hosted stratiform copper province (Fig. 1.1). It is hosted in metasedimentary rocks of the Neoproterozoic Katangan Supergroup, within the Pan-African (ca. 580–530 Ma) Lufilian arc, a regional fold-and-thrust belt (Fig. 1.2) (Kampunzu and Cailteux, 1999; Cailteux *et al.,* 2005a). The northern part of the CACB forms a northward convex belt, encompassing deposits in the classical Zambian and DRC Copperbelt. More recently, developed mines in the Domes Region of NW Zambia are also included in this province (Selley *et al.,* 2005).

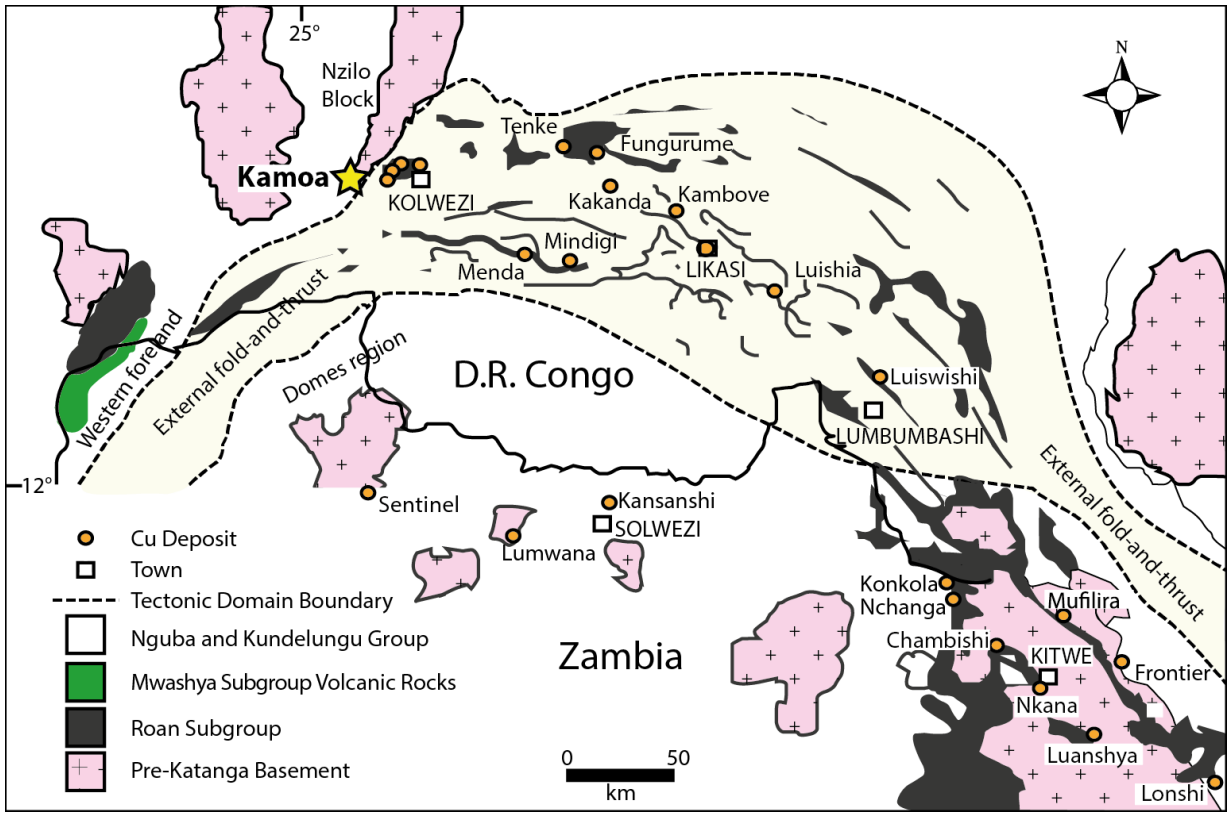

Fig. 1.1: Geological map of the CACB showing distinct tectonic domains. The Zambian Copperbelt in the southeast portion is proximal to basement, with autochthonous deposits in the Domes region. The Congolese Copperbelt extends in an arc from Lubumbashi in the east northward to Tenke Fungurume and then west to Kolwezi: this area is characterised by basement-detached, allochthonous deposits of the External Fold and Thrust Belt. The Kamoa deposit lies on the western edge of the Katangan basin, the host rocks are relatively undisturbed (autochthonous). Modified after Cailteux (1994).

The Pan-African belts, extending across southern Africa between the Congo Craton in the north and the Kalahari Craton in the south, form a curved zone linking the Damara Orogen of Namibia and Botswana with the Lufilian Arc of southern DRC and central-northern Zambia (Fig. 1.2) (Unrug, 1983; Cosi *et al* 1992).

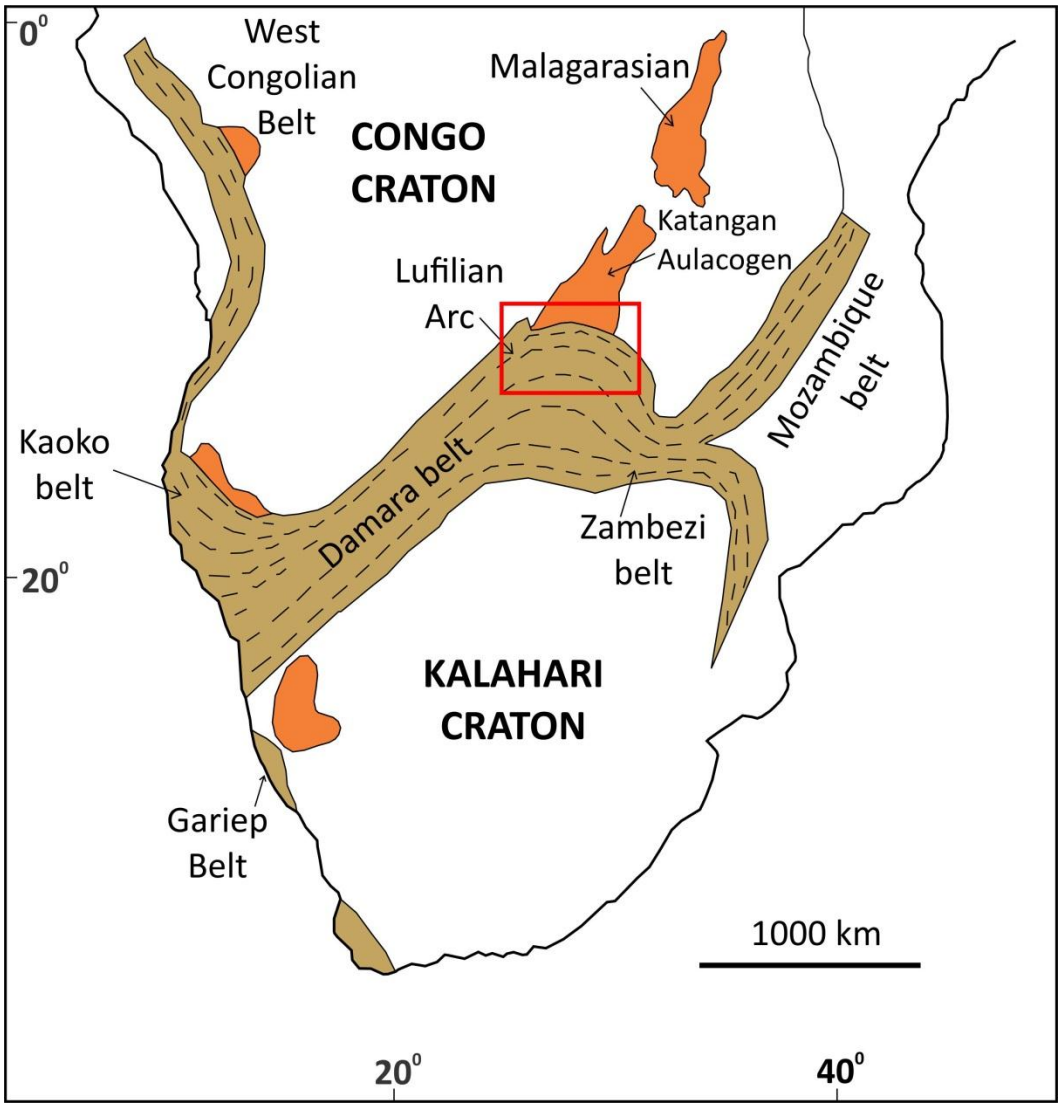

Fig. 1.2: Sketch map of the Pan African system in central and Southern Africa. The red rectangle shows the location of the Lufilian Arc (Modified after Kampunzu and Cailteux, 1999).

1.2.1 Katangan Supergroup in the Zambian Copperbelt

In the Zambian Copperbelt, deposits are hosted by the Neoproterozoic Katangan Supergroup, a ~5 km thick basinal succession of predominantly marginal marine and terrestrial metasedimentary rocks that lack significant volumes of igneous rocks (Selley *et al.,* 2005). The Katangan Supergroup in the Zambian Copperbelt has been subdivided into the Roan Group including the Lower Roan Subgroup, Upper Roan Subgroup, Mwashya Subgroup; the Nguba Group; and the Kundelungu Group (Fig. 1.3 and Table 1.1).

The Mindola Subgroup contains a basal siliclastic sequence with locally abundant conglomerates, a middle section of intercalated pelites and carbonates, and upper sequence of carbonates and occasionally thin horizons of evaporites. Pelitic and sandstone horizons located in the upper and middle portions of the Lower Roan form the Copperbelt Orebody Member, and generally host copper and cobalt mineralisation (Barron, 2003; Selley *et al*., 2005)(Fig. 1.3).

The Kitwe and Bancroft Subgroups are carbonate-rich composed predominantly of dolomite and dolomitic siltstone (Fig. 1.3). The Mwashya Subgroup is composed of carbonaceous shale, and siltstone with dolomite, quartzite and gabbro. The basal portion of the Nguba Group is represented by the Grand Conglomérat. In the Zambian Copperbelt, the Grand Conglomérat is generally less than a hundred metres thick and contains intercalated sandstones, iron formation, and small mafic igneous bodies. It is overlain by the Kakontwe Limestone, a massive limestone to dolostone unit, which varies in thickness from <50 m to 500 m. The Kundelungu Group is not generally exposed in the Zambian Copperbelt. The Petit Conglomérat is the base of this unit (Barron, 2003).

The majority of ore deposits in the Zambian Copperbelt occur within a 200 m stratigraphic interval centred on the rocks of the Copperbelt Orebody Member. The deposits are broadly stratiform and are grouped into argillite- (70% of ore) and arenite-hosted (30% of ore) types (Selley *et al*., 2005). The distribution, geometry, and size of deposits are fundamentally controlled by early sub-basin fault architecture and the availability of both in situ and mobile reductants, the distribution of which is linked to basin structures (Selley *et al*., 2005).

Two mineralisation assemblages occur in the Zambian Copperbelt. The volumetrically dominant type consists of pre-folding disseminated Cu-Co sulphides. Lesser vein-hosted Cu-Co sulphides also occur. The most typical sulphide assemblage in the deposits is chalcopyrite-bornite with subsidiary chalcocite and pyrite (Selley *et al*., 2005). The Zambian Copperbelt also contains ubiquitous, but volumetrically minor, Cu-U-Mo-(Au) mineralisation in post-folding veins which locally may form deposits (Kansanshi) (Selley *et al*., 2005).

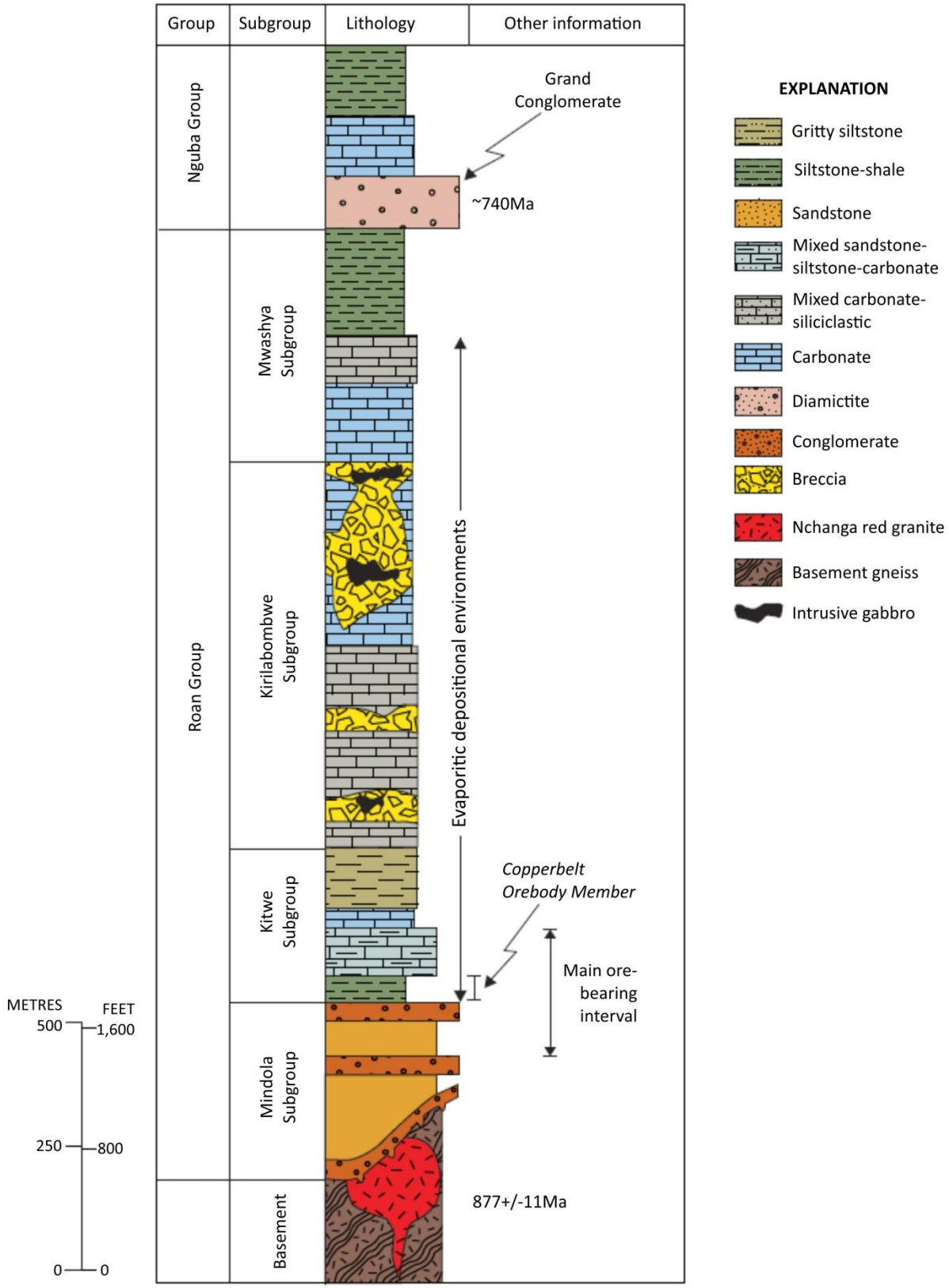

Fig. 1.3: Lithostratigraphy of the Katangan Supergroup, Zambian Copperbelt, showing approximate average thicknesses of strata. USGS (2013) after Selley and others (2005).

Table 1.1: Lithostratigraphy of the Katangan Supergroup (Cailteux, 1994)

CONGO					ZAMBIA		
		GROUP	SUB-GROUP	LITHOLOGIES			
		Kundelungu (prev. Upper Kundelungu. Ks) K	Plateaux K-3	Arkoses, conglomerates, sandstones, shales			
			Kiubo K-2	Sandstones carbonated, siltstones or shales, limestones			
			Kalule K-1	K-1.3 Carbonated silstones and shales: grey to pink Oolitic limestones at base (calcaire rose oolithique)			
				K-1.2 Carbonated silstones and shales; pink to Grey dolomite at base (calcaire rose)			
				K-1.1 "Petit conglomérat"glacial diamictite			
		N'Guba (perv. Lower Kundelungu. Ki) G	Monwezi G-2	Dolomitic sandstones, silstones or shales			
			Likasi G-1	G-1.3 Carbonated silstones and shales			
				G-1.2 Dolomited limestones, dolomitic shales and Silstoness			
				G-1.1 "Grand conglomérat": glacial dolomictite			
GROUP	SUB-GROUP	FORMATION	LITHOLOGIES	LITHOLOGIES	FORMATON	SUB- GROUP	GROUP
Roan	Mwashya R-4	Upper R-4.2	Shales, carbonaceous shales or sandstones	Black shales		Mwashya	Mwashya
		Lower R-4.1	Dolomites, jasper beds, pyroclastics and hematite; local Stratiform Cu-Co mineralisations	Dolomite interbedded with dolomitic shales; gabbro bodies	Kanwangungu	Bancroft RU1-RU2	Upper Roan
	Dipeta R-3	R.3.4	Dolomite interbedded with argillaceous to dolomitic Silstones and feldspathic sandstones; intrusive basic bodies				
		R-3.3		Shales			
		R-3.2		Dolomites or argillaceous dolomites; local stratiform Cu mineralisation			
		R.G.S. R-3.1	Dolomitic silstones	Arenites, argillites and dolomitic argillites; occasional Dolomites at the base; main stratiform Cu-Co Mineralisation in the lower part (ore Shale)	Kibalongo	Kitwe RL3-RL6	Lower Roan
	Mines R-2	Kambove R-2.3	Laminitic, stromatolitic, talcose dolomites and dolomitic Siltstones; local stratiform Cu-Co mineralisation		Chingola		
		Dolomitic shale R-2.2	Dlomitic shales, carbonaceous shales, dolomities and occasional sandstones or arkoses		Pelito-arkosic		
			Dolomitic shales, sandy dolomite at top; stratiform Cu-Co (upper Orebody)		Ore Shale		
		Kamoto R-2.1	R-2.1.3"roches siliceuses cellulaire" (R.S.C): stromatolitic dolomite with interbedded siltstones; Cu-Co at top base				
			R-2.1.2: "R.S.F./D.Strat". Bedded dolomities with siltstones; silty dolomite in the lower part; stratiform Cu-Co (Lower Orebody)				
			R-2.1.1"Grey RAT"; dolomitic siltstone; Cu-Co at top				
<900Ma	RAT R-1	R-1.3	"Red RAT": Pink-lilac, hematitic, chloritico-dolomitic massive siltstones	Conglomerates, course arkoses and argillaceous siltstones; occasional Cu-Co mineralisation	Mutonda	Mindola (Footwall) RL7	
		R-1.2	Pink to purple-grey, hematitic, chloritic siltstones; sandstones in the lower part; stromatolitic dolomite at top				
		R-1.1	Purple-red, hematitic, slighty dolomitic bedded siltstones				
	Basal conglomerate	Base of the RAT sequence unknown		Quartzites	Kafufya		
				Pebble and coble conglomerate	Chimfunsi		

1.2.2 Katangan Supergroup in the DRC Copperbelt

The Katangan Supergroup in the DRC also encompasses the Roan, Nguba and Kundelungu Groups (Fig. 1.4 and Table 1.1) (Cailteux, 1994).

In DRC the Roan Group has been subdivided into the basal R.A.T. (Roche Argillo Talqueuse) Subgroup, Mines Subgroup, Dipeta Subgroup, and Mwashya Subgroup (Cailteux, 1994; Cailteux *et al.,* 2005b) (Fig. 1.4 and Table 1.1). The R.A.T Subgroup is a sedimentary sequence composed of red massive to irregularly bedded terrigenous-dolomitic rocks (Cailteux *et al.,* 2005b). Tectonic breccias generally occur at the contact with the Mines Group. However, in a number of thrust sheets, Red R.A.T. is in conformable sedimentary contact with Grey R.A.T which forms the base of the Mines Subgroup (Cailteux, 2005b). Apart from the colour difference reflecting distinct depositional redox conditions, lithological, petrographical and geochemical features of Red and Grey R.A.T. are similar (Cailteux *et al.,* 2005b). Based on the observation that Grey R.A.T and Red R.A.T interfinger with each other instead of having a stratigraphic contact, Broughton *et al.,* (2007) and other geologists suggested that the Grey R.A.T and the Red R.A.T are part of the same stratigraphic unit.

Above the grey R.A.T is the Mines Subgroup (R 2) which is composed of intercalations of argillaceous-silty dolomite and dolomitic shales. Above the Mines Subgroup is the Dipeta Subgroup (Fig. 1.4 and Table 1.1). It is characterised predominantly by argillaceous and siliciclastic beds at the base and by carbonate at the top (Cailteux, 1994). This stratigraphic unit attains at least 600 m in thickness (Cailteux, 1994). Above the Dipeta Subgroup is the Mwashya Subgroup (Fig. 1.4). In the DRC Copperbelt the Mwashya is generally dolomitic. The lower Mwashya consists dominantly of fine-grained, bedded dolomite with minor siliceous beds and commonly two or more pyroclastic horizons and acid and basic lava flows. The upper Mwashya is composed of dolomitic to calcareous shale [with interbeds of glacial diamictite in the upper portion]. Usually the presence of diamictite results in the rocks being assigned to the Nguba Group. More recent subdivision assigns “lower Mwashya” to Dipeta/upper Roan and upper Mwashya as Mwashya (Cailteux *et al.,* 2007; Bull *et al.,* 2011).

The Nguba Group succeeds the Roan Group, it is subdivided into two Subgroups which are the Likasi (Ng 1) and the Monwezi (Ng 2) Subgroup (François, 1973 in Cailteux, 1994). The basal portion of the Nguba Group is the Grand Conglomérat unit (Ng 1.1). It is generally a massive, matrix-supported pebbly and cobbly diamictite. The Grand Conglomérat is overlain by the Kakontwe Limestone (Ng 1.2), which can be <50-500 m thick. Above the Kakontwe Limestone is the Nguba Shales (Ng 1.3) that can be up to 5000 m thick. The Nguba shales (Ng 1.3) are overlain by the Monwezi Subgroup (Ng 2) which is composed of dolomitic sandstones, siltstones or shales (Ng 2).

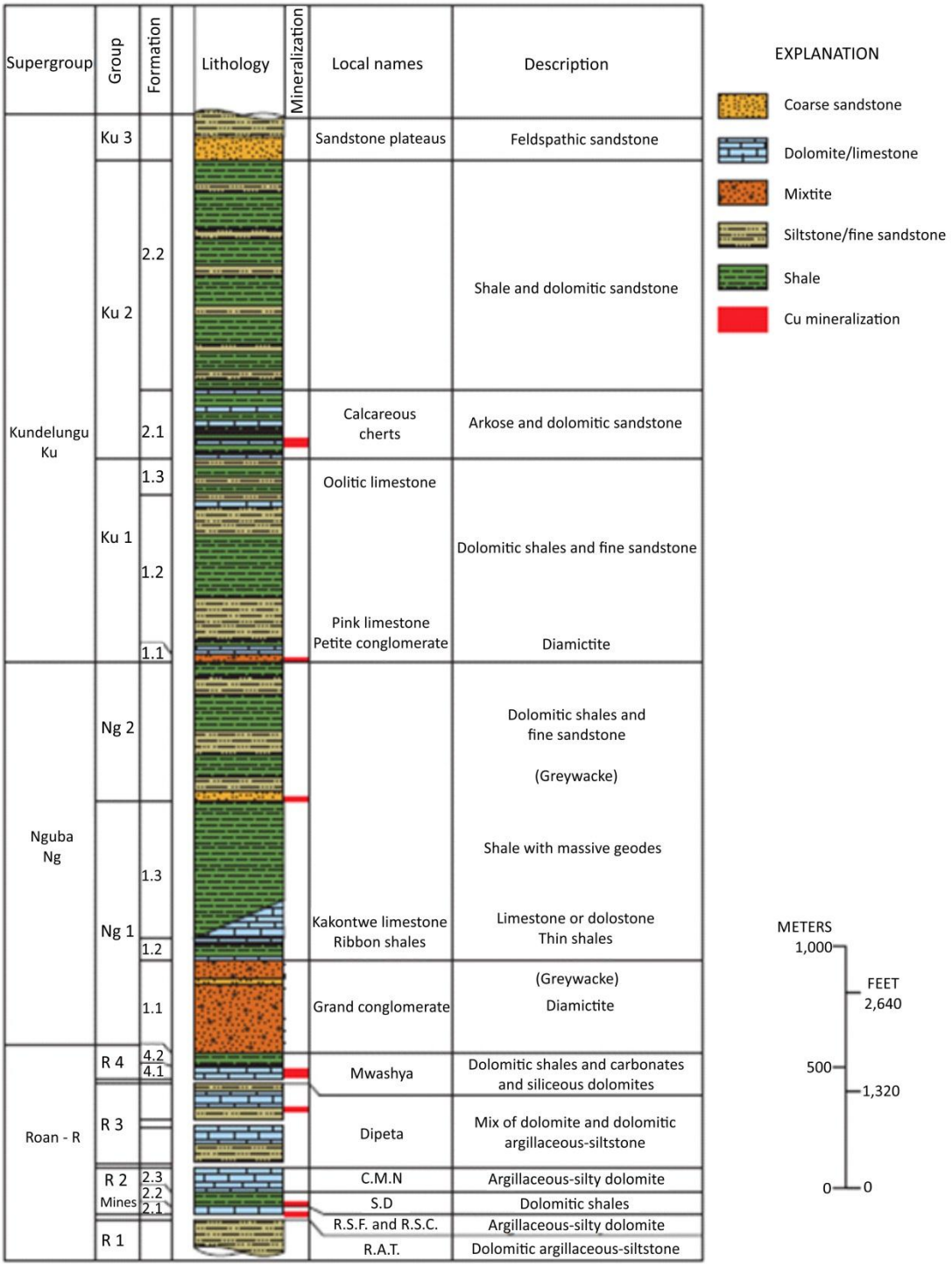

Fig. 1.4: Stratigraphic column of the Katangan SuperGroup in the DRC Copperbelt, showing the location of mineralised strata. C.M.N.:“Calcaire á minerais noirs” (black limestone ore); S.D.:“Schistes Dolomitiques” (dolomitic shales); R.S.F.:“roches siliceuses feuilletées“(laminated siliceous rocks), and R.S.C.:“Roches Siliceuses Cellulaires“ (cellular siliceous rocks), and R.A.T. “roches argilo-talqueuses” (clayey talcose rocks). USGS (2013) after François (2006).

The Kundelungu Group succeeds the Nguba group. The Petite Conglomérat, which forms the base of this unit, can be up to 50 m thick and contains fragments of the underlying Kakontwe Limestone. Above the Petit Conglomérat, the Kundelungu Group consists of several thousands of metres of sandstone, siltstone, and dolomitic shale. Capping this sequence is 600-700 m of sandstone, arkose and sandy schists (Cailteux, 1994).

In the D.R.C. Copperbelt, the mineralisation is hosted primarily in the basal part of the Mines Subgroup, a transgressive supratidal to subtidal sedimentary sequence deposited under quiet, shallow-water conditions (Cailteux, 1994; Cailteux *et al.,* 2005a). The Congo-type stratiform deposits are generally characterised by two major Cu–Co orebodies, the ‘‘lower’’ and ‘‘upper’’ orebodies, totalling 15–55 m cumulative thickness (average: 20–25 m).

The lower orebody host-rocks include: a massive chloritic–dolomitic siltite known as Grey R.A.T. (‘‘Roches Argilo-Talqueuses’’); a fine-grained stratified dolostone (D.Strat. ‘‘Dolomie Stratifiée’’); silicified stromatolitic-dolomites forming laminites alternating with thin chloritic–dolomitic silty beds (R.S.F. ‘‘Roches Siliceuses Feuilletées’’). The Upper Orebody host-rocks include the Dolomitic Shales (S.D.). A generally ‘‘barren’’ reef-type stromatolitic dolomite (R.S.C., ‘‘Roches Siliceuses Cellulaires’’) occurs between the two orebodies (Table 1.1) (Cailteux *et al.,* 2005a).

1.3 Tectonic setting of the Lufilian Arc

The depositional history of the Lufilian Arc was controlled by continental rifting leading to formation of a passive continental margin on the southern side of the Congo craton (Porada and Berhorst, 2000). The Lufilian Orogeny is reported to have occurred between 560 and 550 Ma, during the collision of the 'Angola-Kalahari Plate' and the 'Congo-Tanzania Plate' with accompanying northeast directed thrusting (Kampunzu and Cailteux, 1999; Porada and Berhorst, 2000).

The Lufilian arc comprises a succession of folds and faults and thrust structures which is convex northwards (Daly, 1986; François, 1973; Jackson *et al.,* 2003; Selley *et al.,* 2005). The current tectonic architecture of the Lufilian Arc was formed under a compressive regime during inversion from extensional to compressional tectonics in the Katangan basin (François, 1973; Kampunzu and Cailteux, 1999; Key *et al.,* 2001; Selley *et al.,* 2005).

The Lufilian belt is divided into four different domains from north to south: the External fold and thrust belt, the Domes region, the Synclinorial belt, and the Katanga high (Porada and Berhorst, 2000; Key *et al.,* 2001; Selley *et al.,* 2005) (Fig. 1.5).

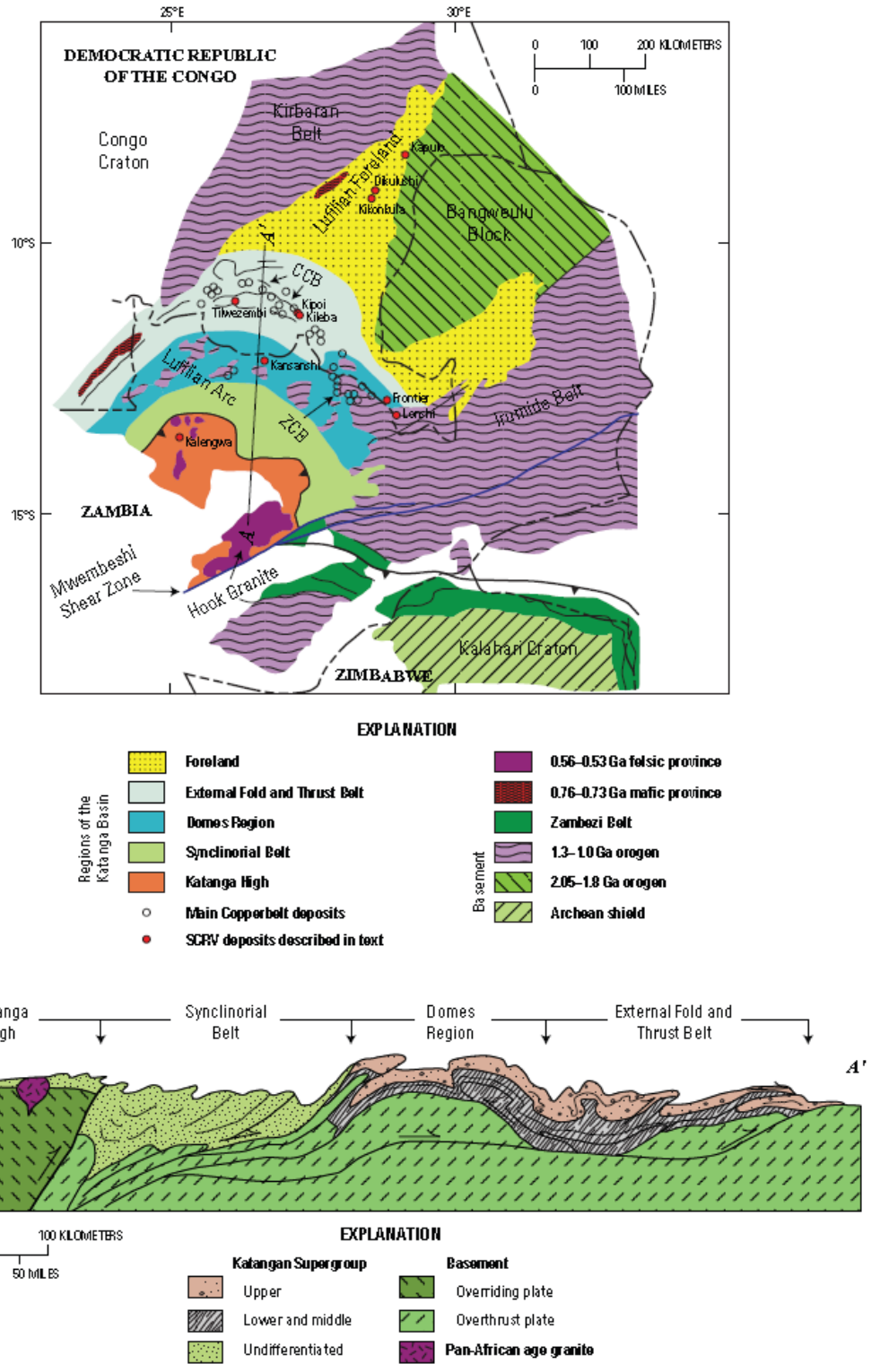

Fig. 1.5: Map showing the tectonic zoning in the Lufilian fold belt and distribution of copper deposits in the Zambian and Congolese Copperbelt (ZC and CCB respectively). The schematic cross section of the Lufilian Arc (S-N section in the map) shows the variation in structural style between tectonic zones. (USGS, 2013 after Selley *et al.,* 2005).

Kampunzu and Cailteux (1999) proposed the following model for major events of the Lufilian orogeny:

The first stage (D1 or Kolwezian) corresponded to major folding and thrusting with a northwards transport direction (François, 1973; Cailteux and Kampunzu, 1995). It gave the Lufilian belt the structure of a thin-skinned fault-and-thrust belt. Low-angle thrust faults formed in the R.A.T. and Dipeta Subgroups, detaching the Roan from the basement.

The second stage (D2 or Monwezian) affected the folded and thrusted terranes by E-W sinistral strike-slip faulting in the western part of the CACB (Monwezi fault system). The bending of the arc is interpreted as related to strike-slip tectonics of stage D2 due to the action of an indentor similar to that envisaged for the India-Asia collision.

The stage D3 (Chilatembo) is represented by a NE-SW regional scale transverse structure, suggesting a NW-SE compression (Kipata *et al*., 2013).

Jackson *et al.,* (2003) proposed that during the Lufilian orogeny, the Katangan basin was transformed first by extrusion of allochthonous evaporites (De Magnée and François, 1988), then by orogenic shortening. They considered that salt tectonics may explain spectacular breccias extending over an area of 25,000 km^2. They proposed that salt tectonics began during deposition of the Roan Supergroup. In the mid-Roan period, small walls and extrusions of evaporite gigabreccia began to be emplaced. In early Kundelungu time, evaporitic diapirs enlarged. Also, they suggested that Lufilian deformation began between 850 and 650 Ma when diapirs were laterally squeezed and formed salt welds, followed by 65 km northward extrusion of a large sheet of co-mingled Roan evaporite and carbonate-dominated sedimentary rocks. The extrusion must have been emplaced rapidly enough to cover the top of a single preorogenic stratigraphic unit without overriding any synorogenic deposit. Jackson *et al.,* (2003) proposed that by the continuation of shortening, large thrust sheets were emplaced lubricated by the preexisting salt-sediment extrusive sheet. They conclude that the shape of the Outer Lufilian Arc may have been controlled by the former northern edge of the evaporitic basin. Table 1.2 summarises the stratigraphy and major tectonic events suggested by Jackson *et al.,* (2003) after restoring the thickness of evaporites layers.

Regarding small scale structures, two kinematic phases have been identified in the Lufilian Arc: an early east-northeast directed phase and a later northerly directed phase. The northerly phase developed throughout the DRC Copperbelt and in the northwest of Zambia; with the east-northeast phase well developed in the Zambian Copperbelt (Daly, 1986). The two kinematic phases are poorly understood, their development in different areas does not establish whether they occurred sequentially or whether they reflect the same deformation event (Daly, 1986).

Table 1.2: Katangan stratigraphic column and dates of major tectonism in southern Katanga. Stratigraphy and symbols after François (1973) and De Magnée and François (1988); ages based on Cahen *et al.,* (1984). The side column shows qualitatively restored evaporite thicknesses inferred in the original Roan Supergroup. This restored column is similarly scaled but is twice as thick because of the inferred evaporites, whose actual thicknesses are conjectural. Basal units below R.1 are unknown in Katanga and are based on the Zambian Copperbelt. (Note that the data on age are taken from Jackson *et al.,* 2003 and are no longer considered acceptable).

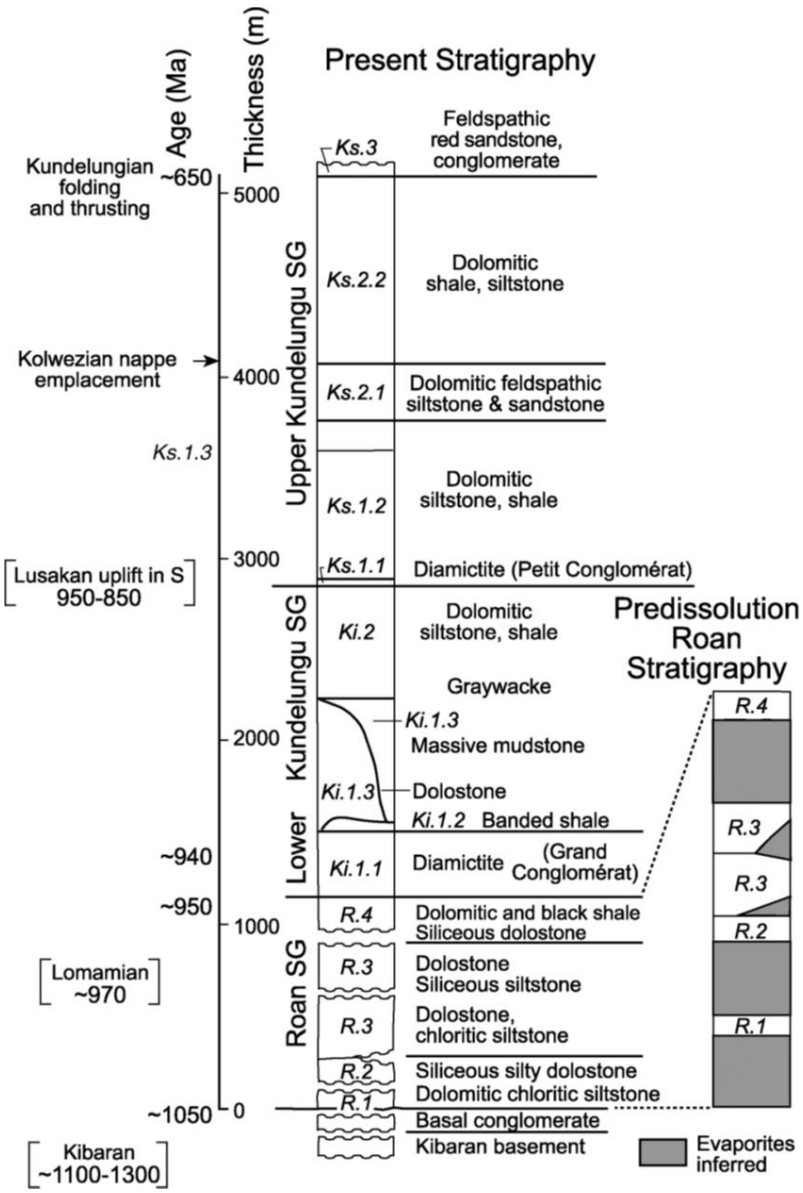

1.4 Aims of the thesis

The principal aim of the study was to determine the role of structures in the genesis and distribution of hypogene mineralisation, and to identify the nature of those structures and their

timing relative to mineralisation. Borehole core data indicates that the Kamoa deposit includes areas of higher and lower grade, some of which appear at the deposit scale to be related to known or interpreted faults. Most of the work of this study is focused on high-grade zones as they display the location of important mineralisation possibly related to structure.

1.5 Methodology

For the completion of the above aims, the following work was performed, wherever possible on oriented cores:

- Detailed description and measurement of fault zones, both large scale (zones of fracturing etc.) and small scale (mesoscopic faults commonly observed in Ng 1.1.2);
- Description and measurement of foliation, symmetric and asymmetric sulphide and gangue mineral growth around clasts, veins, and other mesoscopic structural elements. The micro-tectonic deformation structures are described in thin sections and related to the timing of the sulphide mineralisation;
- Description and orientation of folds, including mesoscopic folds observable in bedded rocks (Roan sandstones, Ng 1.1.1.2 siltstone-sandstone, Ng 1.1.2 and Ng 1.1.4 siltstone in the Table 2.1) and larger folds determined from variation in bedding angles;
- Oriented polished thin sections were used to supplement observations for the above work, and to investigate possible differences in permeability between mineralised and un-mineralised rock;
- Detailed geological cross sections were constructed to better understand the distribution of the mineralisation from small (wedge holes) to large (2-400 m spaced) scale in the Kamoa deposit;
- Structural contour and isopach maps of all the Ng 1.1 units have been made to help to understand the controls on the high grade and low grade portions;
- Structural mapping of outcrops in the Kamoa area have been conducted to help constrain geometries of structural elements observed in core;
- Available geophysical data (currently magnetics) was used to constrain the tectonic/ geologic model.

CHAPTER 2

The Kamoa Copper Deposit

2.1 Introduction

The Kamoa Copper deposit was discovered more than 100 years after the initial period of Belgian exploration in the CACB, just west of Kolwezi in an area thought to be unprospective (Broughton and Rogers, 2010). Exploration was undertaken in the studied area by the Tenke Fungurume Consortium in the period 1971 to 1975, and some regional stream-sediment sampling may have occurred in the current project area, although no information on sample locations is available for any sampling that may have occurred within the confines of the Kamoa Project (Parker *et al.,* 2013). The lack of typical copperbelt indicators such as vegetation anomalies and Mines Subgroup mega-fragments caused explorers to lose interest in this area.

The discovery history of the deposit has been described by Broughton and Rogers (2010). Ivanhoe's work program started in January 2004 and African Mining Consultants were contracted to conduct the exploration activities in the Kamoa area. In May 2004, regional stream sediment samples were taken and an airborne magnetic and radiometric survey was flown over the Ivanhoe license areas, using a line spacing of 250 m. From the end of 2004 through 2008, the exploration team used a systematic ranking approach developed by Douglas Haynes Discovery Ltd. for identification, prioritisation, and refinement of numerous exploration targets, including Kamoa, within the Ivanhoe licenses. The potential for copper mineralisation was defined in mid-2004 by strongly anomalous stream-sediment catchments, with a maximum value of 3,679 ppm Cu. Subsequently, soil sampling surveys located copper in soil anomalies to the NNW of Kamoa and the magnetic lows were eventually recognised as gentle domes.

A reverse-circulation drilling program was initiated in May 2006, targeting anomalies at both the Makalu and Kamoa domes. Many holes were drilled on the domes as they displayed good copper anomalies, however, they returned poor results. The first hole that returned a good intercept was one that reached the diamictite and the intercalated siltstone of the Grand Conglomérat before terminating in feldspathic sandstone of the Mwashya.

A diamond drilling program started in mid-2008 to follow up the 2006 drilling, based on the recognition that mineralisation occurred at the redox boundary between the reduced Grand Conglomérat and the underlying oxidised footwall hematitic Mwashya Subgroup sandstone. The initial drill section oriented east-west intersected copper mineralisation at the base of the Grand Conglomérat along a distance of about 4.5 km.

2.2 Geological overview

The Kamoa deposit is located approximately 25 km west of the world-class Kolwezi Cu-Co deposits (Fig. 2.1). The Kamoa project lies in a broadly-folded terrane centred on the Kamoa and Makalu domes between the West Scarp Fault and Kansoko Trend (Fig. 2.2). The domes form erosional windows exposing the redox boundary between the underlying hematitic Roan sandstones, and the overlying carbonaceous and sulphidic (reduced) Grand Conglomérat diamictite. Unlike most of the deposits of the Katangan Copperbelt, the host rocks at Kamoa are intact and relatively undisturbed (Broughton and Rogers, 2010; Parker *et al.,* 2013). Figure 2.1 summarises the project geological setting of the Kamoa area.

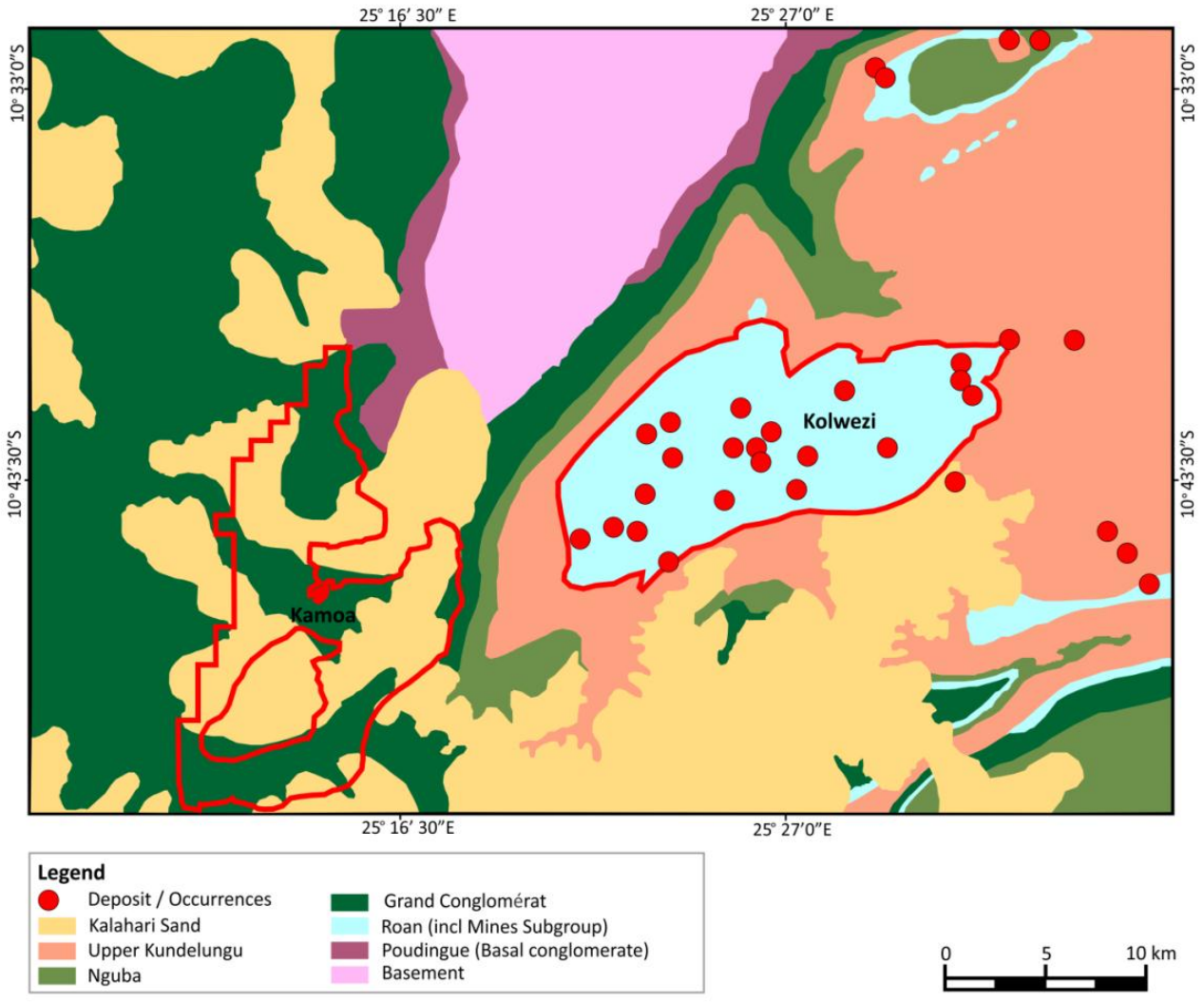

Fig. 2.1: Project geological setting of the Kamoa copper deposit, outlined in red, showing the location in relation to the Kolwezi deposit. The Kolwezi district comprises mega-fragments of the Mines Subgroup emplaced above the Upper Kundelungu.

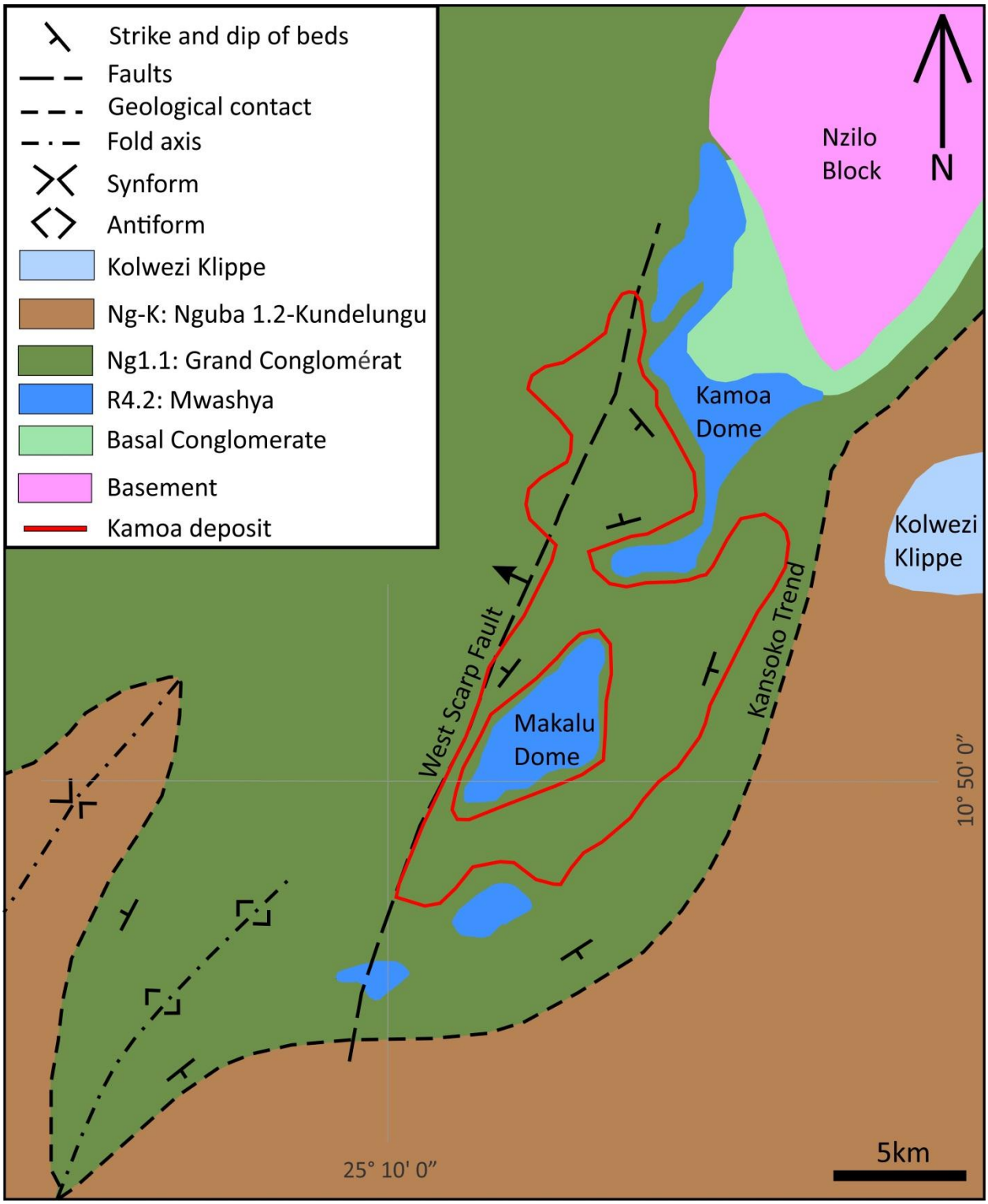

Fig. 2.2: Geologic map of the Kamoa area. The Mwashya Subgroup and overlying Nguba Group host rocks dip gently ~ 5 to 20° away from the domes. East of the Kamoa deposit is a major regional north northeast trending structure (the Kansoko trend) interpreted as the western structural edge of the main Katangan basin. The map is based on geophysics and field data. Modified after Broughton and Rogers (2010).

Basement rocks exposed to the north of Kamoa within the Nzilo block consist of Kibaran quartzite, weakly metamorphosed ferruginous siltstone and sandstone, mafic rocks, carbonaceous phyllite and dolomite (Fig. 2.2). The Kibaran Belt (Fig. 1.5.) is a Mesoproterozoic fold-and-thrust belt composed of meta-sedimentary and meta-igneous rocks that trends NE over some 1300 km from the Katanga region in the DRC up to the Ankole region in SW Uganda (Kokonyangi *et al.,* 2007; Tack *et al.,* 2010). The belt consists of a variety of metasedimentary rocks, including metapelites, quartzites, metaconglomerates, and subordinate meta-graywackes, meta-cherts, calc-silicates, and volcanosedimentary rocks intruded by important masses of mafic and felsic bodies (Kokonyangi *et al.,* 2007). The Kibaran Supergroup extends to the NW of the Lufilian arc where it consists of the Kibaride belt. It consists of a 110 km thick metasedimentary succession, including paragneisses, slates, quartzites, meta-cherts, meta-conglomerates, and subordinate calc-silicates and volcanosedimentary sequences. The metasedimentary rocks of the Kibaride Belt were generally affected by low- to medium-grade metamorphism, with amphibolite facies grade documented locally (Kokonyangi *et al.,* 2007).

2.3 Lithology and stratigraphy

In the Kamoa deposit, six main lithostratigraphic units are identified: Kibaran basement rocks, basal conglomerate ("Poudingue"), haematitic feldspathic sandstones of the Mwashya Subgroup, diamictite, siltstone-sandstone, and locally intercalated by mafic volcanic rocks within the Grand Conglomérat (Broughton and Rogers, 2010).

Basement rocks exposed to the north of Kamoa within the Nzilo block (Fig. 2.2) consist of Kibaran-age quartzite, weakly metamorphosed ferruginous siltstone and sandstone, sandstones, mafic rocks, carbonaceous phyllite and dolomite and minor mafic rocks (Schmandt, 2012).

The basal conglomerate ("Poudingue") rests unconformably on Kibaran (basement) quartzite. This lithostratigraphic unit includes thin to >10 m thick conglomerate bands within pebbly, and sandstone beds. The sedimentary rocks are typically immature and poorly sorted except for some of the conglomerate bands that have a weak feldspathic cement (Parker *et al.,* 2013).

The Mwashya Subgroup is sharply overlain by the Grand Conglomérat of the Nguba Group (Ng 1.1). The deposit area contains sub-cropping Grand Conglomérat rocks around the margins of several gentle domes exposing Roan Group haematitic sandstones and siltstones that form the footwall for the Kamoa deposit (Fig. 2.2). There are lithological similarities between the Lower Roan Subgroup siliciclastic rocks of the Zambian Copperbelt and the pre-Nguba rocks observed

at Kamoa; however the stratigraphic positioning suggests correlation with the Mwashya Subgroup (Schmandt *et al*., 2013).

At Kamoa, there are two main stratigraphic sequences: the Mwashya Subgroup and the Grand Conglomérat Subgroup (Table 2.1 and Fig. 2.2). The Mwashya Subgroup at Kamoa has been assigned a stratigraphic code of R 4.2 (Table 2.1). It constitutes the footwall to the deposit. In the north of the Kamoa area, this unit unconformably overlies basement metasedimentary rocks (Fig. 2.2). Most drilling in the deposit area has only intersected the upper 5 to 15 m of the footwall. This unit is pink to grey, massive to coarsely-bedded feldspathic sandstone with conglomeratic layers, interbedded with lesser maroon-coloured fine-grained sandstone and siltstone. Carbonate cement, disseminated carbonate (dolomite), potassium feldspar are present; disseminated specular haematite is common to ubiquitous (Broughton and Rogers, 2010; Schmandt *et al.,* 2013).

The Grand Conglomérat at Kamoa comprises 4 lithofacies: diamictite, laminated pyritic siltstone/sandstone, rhythmite, and turbiditic lenses (Schmandt *et al.,* 2013). Diamictite (SDT) and siltstone (SSL) are the most important volumetrically and create the five main stratigraphic units. Turbiditic lenses and rhythmite are volumetrically minor (Schmandt, 2012).
There are five stratigraphic units of the Grand Conglomérat at Kamoa (Table 2.1), from the bottom to the top: the Basal diamictite, (Ng 1.1.1) composed of clast-poor and clast-rich diamictite with occasional intercalated siltstone; the Lower laminated pyritic siltstone/sandstone, (Ng 1.1.2) composed of mudstone, siltstone and sandstone with abundant pyrite; the Middle diamictite package, (Ng 1.1.3) which comprises clast-rich diamictite with increase of pyrite at the base; the Upper laminated pyritic siltstone/sandstone, (Ng 1.1.4); and the Upper diamictite unit, (Ng 1.1.5) (Schmandt, 2012). The project geology team recognises six lithostratigraphic units based on subdivision of the Upper diamictite unit into two distinct units: Ng 1.1.5 and the Ng 1.1.6 which consists dominantly of diamictite with minor sandstone and conglomerates (Table 2.1). In chapter 3, more details are presented on the description and lithostrastigraphical variations of the Nguba Group.

Thicknesses of as much as 10 m of superficial Kalahari sands occur mostly west of the West Scarp Fault and in the southern part of the Project area (Parker *et al.,* 2013).

Table 2.1: Stratigraphic column of the Grand Conglomérat within the Kamoa Copper deposit. The Mwashya Subgroup constitutes the footwall to the deposit.

Stratigraphic Codes			Description	Thickness
Grand Conglomérat (Ng 1.1)	**Uppermost diamictite Ng 1.1.6**		Thick generally chloritic clast poor, slightly sandy diamictites containing 7-15% clasts; occasionally up to 20%. Occasionally contains thin sandstone beds +/- thin siltstone and reworked diamictite intercalated with clast to matrix supported conglomerate, sandstone beds and thin siltstone.	100-350 m
	Upper diamictite Ng 1.1.5		Diamictite with 7 to 15% clasts, quartzite +argillites (>locally mafics to the north) with frequent rim replacement by pyrite >pyrrhotite>>chalcopyrite. 1-4% sulphides. Contains zones of reworking. Matrix-supported conglomerates near top at Kansoko.	<200->550 m
	Upper laminated pyritic siltstone Ng 1.1.4		Pyritic sandy siltstone, bedded, laminated with planar >>irregular bedding. Minor pebbly bands. Soft sediment slumping. 1-12% mostly bedded pyrite. Gradational upper and lower contacts, often reworked at the base.	+/- 20 m
	Middle diamictite package Ng 1.1.3		Typical diamictite. Often weakly carbonaceous and generally clast rich ranging from 20-40% pebbles>>cobbles. General clast assemblage quartzite > argillite > mafic with occasional exotics (mica schist, dolomite, shale) in argillaceous matrix. Often contains weak minor reworked zones. Thin weakly pyritic siltstone. ± pyrrhotite + trace chalcopyrite. Sandy pebbly siltstone with thin zones of reworked diamictite. 0.5-1% replacement pyrite increasing to 5% in bottom +/- 5m. Often contains weakly reworked zones.	100-200m
	Lower laminated pyritic siltstone Ng 1.1.2		Laminated pyritic siltstone containing 15-30% pyrite occurring in bedding or as blebs and disseminations in sandy areas. Kamoa Pyritic Siltstone (KPS). Normally with slightly sandy graded beds towards base with shale rip-up clasts. Always decrease in pyrite over the basal 3-5m.	20-46 m
	Basal diamictite Ng 1.1.1	***Ng 1.1.1.3***	Argillaceous >> sandy and often chloritised. Diamictite generally clast poor but not in all cases. <20% clasts of quartzite > mafics>argillite >> quartz < 100mm. Significant copper mineralisation occurs. Gradational base.	40->100 m
		Ng 1.1.1.2	Siltstone, massive to weakly bedded. Can be preferentially mineralised. Often more than one band 1-11m thick intercalated with "reduced > "oxidised" facies diamictite.	Up to +50 m
		Ng 1.1.1.1	Maroon to light grey diamictite >20-35% subangular-subrounded clasts < 70mm of sandstone + quartzites + quartz with occasional large mafic pebbles. Frequently matrix & replacement hematite alteration. Sandy irregular base. Normally oxide copper + chalcocite mineralisation	<10-25 m
Mwashya Subgroup (R.4)	**R.4.2**		Feldspathic sandstone, fine- to coarse-grained with minor intercalations of hematite rich siltstone bands. Occasionally slightly pyritic but generally containing detrital specularite grains in the matrix. Varies from grey when fresh to pink when weathered.	30-300 m +

2.4 Sedimentary environment

There are different opinions on the genesis of the Grand Conglomérat. Binda and Van Eden (1972) regard the Grand Conglomérat in Zambia as a glacio-marine facies of the Precambrian continental glaciation based on borehole core from the Ndola area. Selley and others (2005) regard the Grand Conglomérat as "a sequence of debris flows and diamictites containing beds of intercalated siltstone and coarse lithic sandstone" while Wendorff and Key (2009) worked mainly on the Zambian part and concludes that the Grand Conglomérat has a glacio-marine origin. Recent research by Master and Wendorff (2011) concludes that the Grand Conglomérat is glaciogenic. However, based on borehole core from the Kamoa area, Eyles and Kennedy (pers. comm 2013) suggest that the diamictites are not tillites, but genetically related to subaqueous mass flow deposits typical of tectonically active, steep-sided rift basins. They suggest that diamictites may be re-sedimented glacially derived debris and that while ice may have delivered sedimentary rocks to basin margins, it played no direct role in the deposition of the diamictites.

2.5 Structure

The western edge of the Kamoa deposit is offset by the west-side down West Scarp Fault (Fig. 2.2). Across this fault, thicknesses of stratigraphic units and facies variations suggest that the fault was not active during the deposition of the upper Mwashya Subgroup and lower Nguba Group (Broughton and Rogers, 2010; Schmandt, 2012). Other mapped faults, do not show tectonic geomorphic indicators such as steep scarps, offset drainage, vegetation lineaments or other features suggestive of late Quaternary-or Holocene-age surface structure (Hull, 2013).

East of the Kamoa deposit is the Kansoko trend, a major regional north-northeast trending structure identified on the aeromagnetic data. There are no geomorphic exposures of this structure but the geophysical data combined with regional geology suggest it represents a major, east-side down normal fault that is now marked by an east-dipping monocline (Schmandt *et al.,* 2013) (Fig. 2.2). This structural zone appears to mark the western structural edge of the main Katangan basin and contains highly folded rocks. To the east of this structure the Katangan basin contained the Roan Group, whereas to the west of the structure in the Kamoa area the Roan Group appears to be absent or highly condensed (Broughton and Rogers, 2010; Schmandt, 2012).

In the mineral resource area, approximately 44 minor structures have been identified by SRK based on geophysical data, drilling and oriented structural information. Their model suggests that the most persistent faults are oriented roughly north-south; smaller scale faults have a

mostly east-west orientation and a smaller population of structures have an interconnecting northeast-southwest orientation (Barnett, 2013). The project geology team proposed a revised structural model based on topography, geophysical data, and lithological discontinuities interpreted from the borehole data (Fig. 2.3). It is important to note that this model is a subset of the fault interpretation proposed by SRK.

2.6 Metamorphism

The rocks in the Kamoa area contain biotite, chlorite, and are weakly metamorphosed to lower greenschist facies (Parker *et al.,* 2013).

2.7 Alteration

Detailed logging of borehole core suggests that the alteration minerals include chlorite, sericite, hematite, carbonate, potassium feldspar and biotite. Based on the mineral assemblages, Schmandt *et al.,* (2013) suggested three sequential types of hydrothermal alteration which occur in the Kamoa area: potassic, silicic, and magnesian alteration.

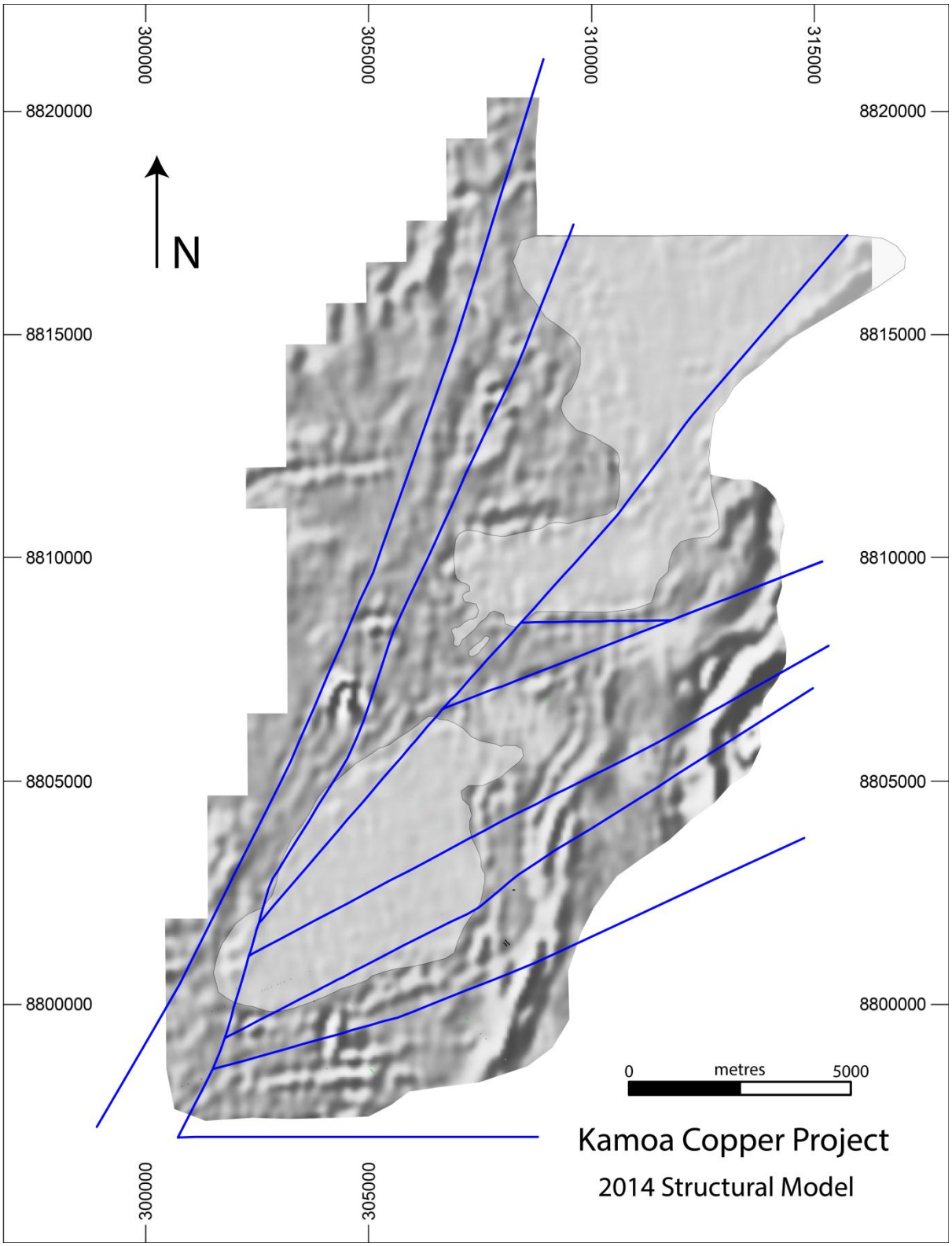

Fig. 2.3: Magnetic image map showing structural interpretation. The blue lines represent the interpreted faults. Modified after Gilchrist (2014).

2.8 Mineralisation

At Kamoa the Grand Conglomérat appears to be relatively reduced compared to the immediately underlying haematitic Mwashya Subgroup sandstone. The redox boundary at the contact between these units is a fundamental control on copper sulphide precipitation at Kamoa (Broughton and Rogers, 2010; Parker *et al.,* 2013). Copper sulphide mineralogy at Kamoa is vertically zoned with respect to this redox boundary. The sulphide mineral zonation from the bottom to the top is as follows: chalcocite and/or bornite, chalcopyrite, pyrite and minor sphalerite and or galena. This zonation is typical of sedimentary rock-hosted stratiform copper deposits (White and Wright 1966; Brown 1992; Brown 1997). Near the surface, the diamictites have been leached, resulting in localised zones of copper oxides and secondary copper sulphide enrichment (Fig. 2.4).

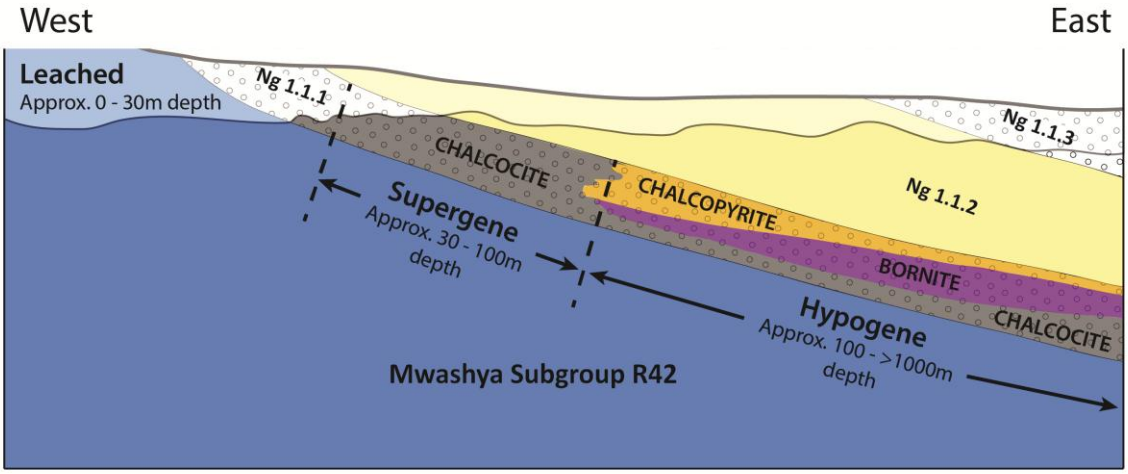

Fig. 2.4: Simplified geology section showing the zonation of ore minerals (Peters *et al.,* 2016). The Mwashya Subgroup and overlying Nguba Group host rocks dip gently (~ 5°) away from the domes. Copper mineralisation comprises distinct styles: hypogene (chalcocite, bornite and chalcopyrite) and supergene mineralisation (secondary chalcocite, with minor native copper and cuprite). Near the surface, the mineralisation has been removed by weathering (Broughton and Rogers 2010).

Mineralisation at Kamoa has to date been intersected down dip to depths of more than 1500 m. The mineralised zone ranges up to 17 m thickness, averaging approximately 6 m. The mineralised sequence at the base of the diamictite consists of several interbedded units which appear to control copper mineralisation. These units are, from bottom upward, the Lower basal diamictite (Ng 1.1.1.1), the Intercalated siltstone (Ng 1.1.1.2), and the Upper basal diamictite (Ng 1.1.1.3). Chalcocite and bornite zones are not always well developed. The Lower basal diamictite (Ng 1.1.1.1) unit generally hosts lower-grade (<0.5% Cu) mineralisation. Most of the

higher-grade mineralisation occurs within the siltstone and sandstone of the Intercalated siltstone (Ng 1.1.1.2) or in the clast-poor of the Upper basal diamictite (Ng 1.1.1.3) (Table 2.1).

The Kamoa deposit also contains leached and supergene zones, and local oxide mineralisation, which define a typical, leached capping-supergene-hypogene profile (Broughton and Rogers, 2010). Secondary chalcocite, with minor native copper and cuprite, defines a supergene zone, particularly within local fracture zones and along the Basal diamictite-Mwashya sandstone contact, which shows preferential weathering. Grades of >5 percent Cu are common within supergene zones. Malachite and chrysocolla occur locally, generally after chalcocite, but do not form a significant zone (Broughton and Rogers, 2010).

At Kamoa, copper sulphides occur as both very fine-grained, disseminations in the matrix and as coarse-grained rims to clasts or, especially with the mafic clasts, as partially to completely replaced clasts. Fine-grained sulphides are usually anhedral and generally equi-dimensional (Schmandt, 2012). Vein-hosted sulphide minerals are minor or absent at Kamoa. Fine-grained copper sulphides are disseminated in the matrix, they represent an average approximately 90% of the total sulphide content of the rocks while the coarse-grained represent less than 10%. The coarse-grained copper sulphides are visible by naked eye. The rim sulphides are generally anhedral, massive, and may form grains up to 5 cm in length (Schmandt *et al.,* 2013).

The Kamoa deposit shares a common redox architecture with all other major sedimentary rock-hosted stratiform copper deposits of the CACB (such as Konkola, Nkana, Nchanga, Mufulira, Tenke Fungurume, and Kolwezi) as the copper mineralisation occurs at the stratigraphically lowest major redox boundary in the Katangan basin (Broughton and Rogers, 2010; Parker *et al.,* 2013).

2.9 Sulphur Isotopes

Schmandt (2012) investigated the sulphur isotope compositions of sulphides and sulphates to better constrain sources of sulphur in the Kamoa deposit. The sulphur isotope data from Kamoa suggest that most of the reduced sulphur in the rocks was formed during early bacterial sulphate reduction and recycled during copper mineralisation. It appears that minor amounts of isotopically heavier, reduced sulphur from thermochemical reduction of both evaporitic anhydrite and seawater sulphate were fixed in sulphides in the upper Mwashya Subgroup rocks and in volcanic rocks. This sulphur forms a minor component of Kamoa sulphides. These isotopic data were interpreted by Schmandt *et al.,* (2013) as indicating that, unlike most other deposits of the CACB, Kamoa appears to represent a single pulse of intense copper

mineralisation and lacks a heterogeneous sulphur isotope pattern typical of a multistage mineralisation process (Schmandt *et al.,* 2013).

2.10 Fluid inclusions

Schmandt (2012) analysed primary fluid inclusions in coarse-grained ankerite intergrown with chalcopyrite, quartz, potassium feldspar, chlorite, and biotite in rims of clasts to determine the temperature and salinity of their parental fluids. Mineral textures in the samples analysed suggest that copper sulphides and gangue minerals were precipitated from the same fluid so the fluid inclusion data from the ankerite was assumed to be representative of the rim-mineralising fluids. The fluid inclusion data suggests that the fluids responsible for precipitation of sulphide and silicate minerals in diamictite clast rims were saline ranging from ~23 to 26 wt % NaCl wt equiv, and had homogenisation temperatures varying from 210° to 240°C; beyond what would be expected for shallow burial (Schmandt, 2012; Schmandt *et al.,* 2013).

2.11 Conclusion

Kamoa is located in the Grand Conglomérat of the Nguba Group; it differs from the other DRC deposits in that it is not located within the Mines Subgroup, which is the typical host for many of the deposits. The Kamoa deposit shares lithological similarities with the siliciclastic-hosted deposits of the Zambian Copperbelt.

CHAPTER 3

Lithostratigraphical variation and features of the Nguba Group within the Kamoa area

3.1 Introduction

The overall stratigraphy and lithological variations within the Kamoa area have been well established. Two main rock units are present at Kamoa, the Mwashya Subgroup and the overlying Grand Conglomérat unit of the Nguba Group. An overview of the various lithologic and stratigraphic units is presented with a particular focus on thickness variations as this will contribute to a greater understanding of the sedimentary and tectonic framework. The Kamoa deposit area is weathered in outcrop and covered by overburden composed of Kalahari sands, residual soil and saprolite. Rock types at Kamoa have been described utilising data from borehole cores. Note that the common prefix "DKMC_DD" of Kamoa boreholes is abbreviated as follows "DD" (i.e. DKMC_DD641 will be DD641). However the prefixes "DMAK_DD", "DMAK_RD" and "DKMC_GD" are not abbreviated (i.e. DMAK_RD030 remains DMAK_RD030).

3.2 Mwashya Subgroup

The Mwashya Subgroup at Kamoa constitutes the footwall to the deposit. This unit consists of texturally immature, feldspathic sandstone showing a massive and thickly-bedded texture (20 cm to 1 m) (Fig. 3.1).

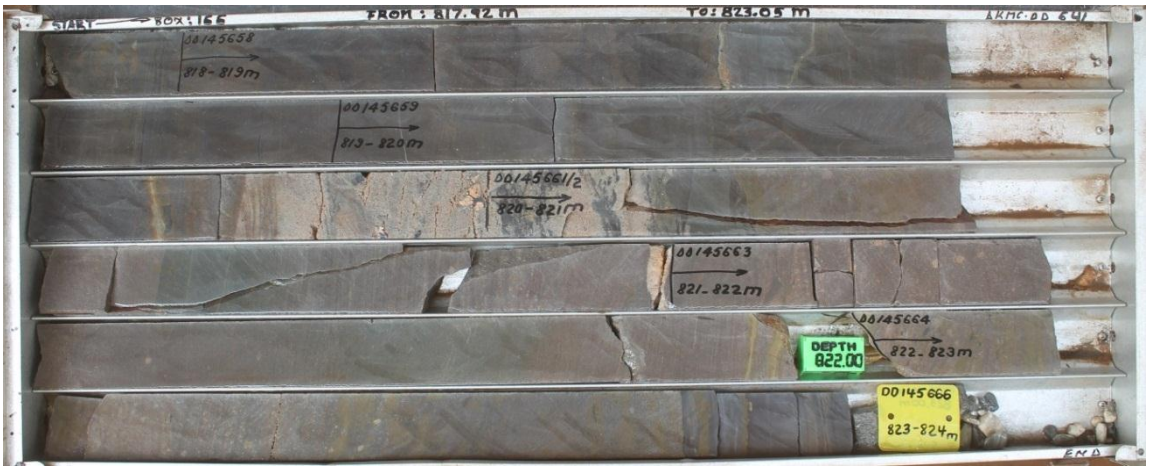

Fig. 3.1: Pinkish to maroon, light-grey to medium grey, laminated and massive feldspathic sandstone with intercalations of thin layers of siltstone. DD641, 817.92 – 823.05 m.

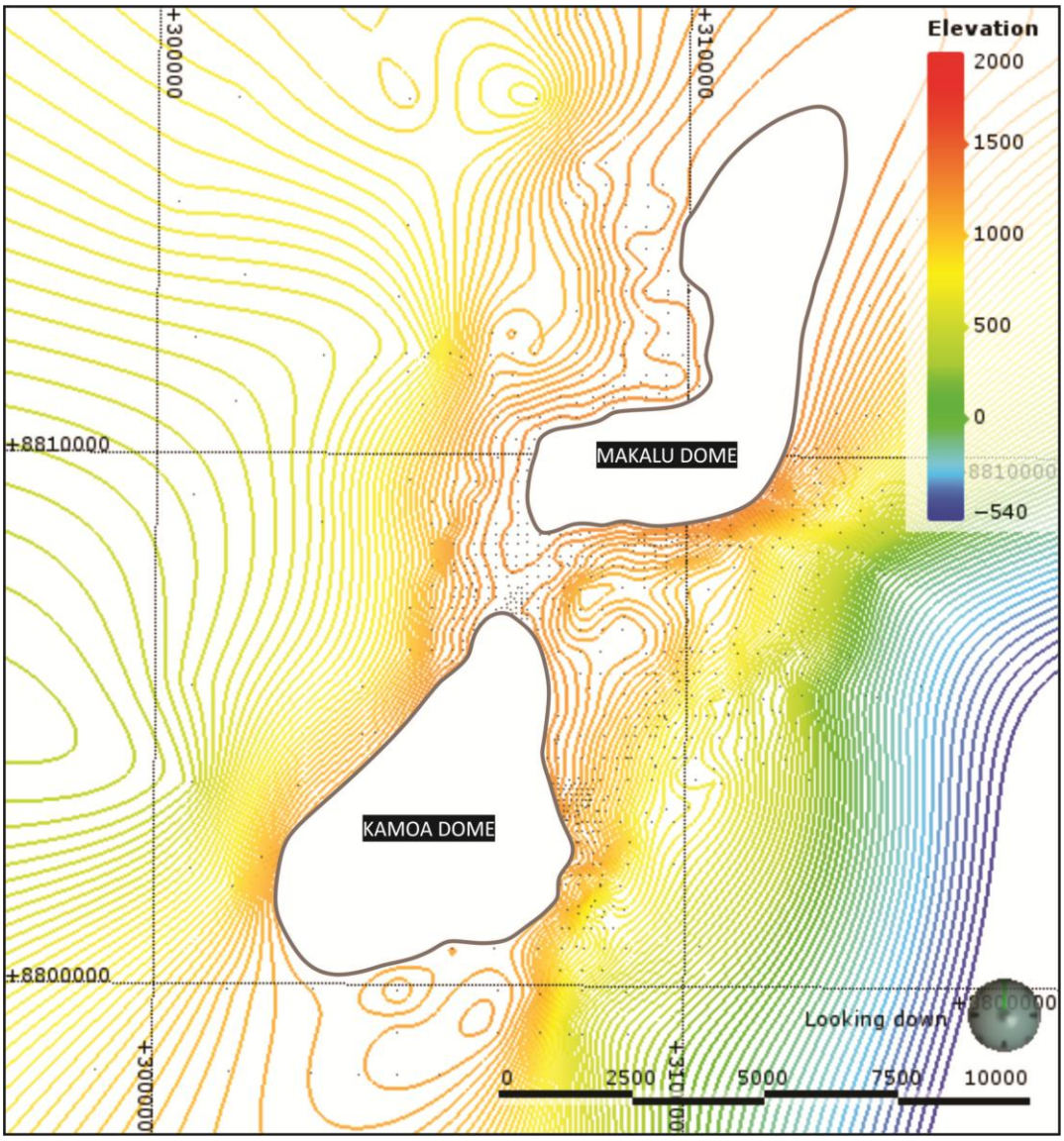

Fig. 3.2: Elevation contour map of the contact between the Grand Conglomérat and the Mwashya Subgroup unit which crops out in series of domes (dark brown lines). The value "0" in the elevation scale represents sea level.

The Mwashya Subgroup dips gently (~5-10°) away from the domes (Fig. 3.2). Most boreholes within the deposit were stopped after drilling a few metres of this unit as it is unmineralised. However, the deepest holes have shown that the thickness of this unit ranges from several tens to several hundreds of metres. In the north of the Kamoa area, this unit unconformably overlies basement metasedimentary rocks (above a basal conglomerate unit known locally as the Poudingue). Minor intercalations of haematite-rich siltstone bands are present in this unit (0.1 to 20 cm). The thickness of beds within this unit ranges from centimetres to several metres.

Occasional pebbles of sandstone and siltstone that rarely exceed a centimetre can be observed within the unit. The rock varies from grey or beige when fresh to pink when weathered.

The compositional immaturity, high and low energy sedimentary structures and occasional pebble conglomerates suggest the Mwashya Subgroup sedimentary rocks at Kamoa were deposited in a marginal marine or subaerial fluvial environment. The contact between the Mwashya Subgroup and the overlying Nguba subgroup is gradational and occasionally sharp. The lowermost diamictite is generally sandy, suggesting erosion of the underlying, poorly lithified Mwashya Subgroup sedimentary rocks (Schmandt *et al*., 2013).

3.3 Nguba Group

The Grand Conglomérat unit is the basal portion of the Nguba Group. In the Kamoa area the Grand Conglomérat subgroup is composed of diamictites, laminated pyritic siltstones/ sandstones and feldspathic sandstones. Volumetrically the diamictites and siltstones are the most important lithologies and constitute the main stratigraphic units underlying the greater Kamoa area. Copper mineralisation is situated in the Basal diamictite (Ng 1.1.1) and occasionally at the base of the Lower laminated pyritic siltstone/sandstone (Fig. 3.3). Brief lithologic and stratigraphic descriptions combined with cross sections and pictures of the rock types in typical core are presented in this chapter.

An overview of the various stratigraphic and lithologic units of the Grand Conglomérat is presented with a particular focus on lateral thickness variations within the Kamoa deposit. More than 800 boreholes were used from the Kamoa database to construct isopach maps and examine the stratigraphic and lithological variations within the Kamoa deposit. Figure 3.4 shows the location of borehole cross-sections that are presented in this study (Figs. 3.5 to 3.10). Isopach maps of different stratigraphic units (Ng 1.1.1, Ng 1.1.2, Ng 1.1.3 and Ng 1.1.4) of the Nguba subgroup were established based on the true thickness.

As with the Mwashya Subgroup, the six stratigraphic units of the Nguba Group dip gently away from the dome (Fig. 3.5).

3.3.1 Basal diamictite (Ng 1.1.1)

The Basal diamictite is composed of three lithologies which constitute minor stratigraphic units: the Upper basal diamictite (Ng 1.1.1.3), the Intercalated siltstone (Ng 1.1.1.2) and the Lower basal diamictite (Ng 1.1.1.1) (Fig. 3.3). The Basal diamictite shows an abrupt change of thickness

oriented NNW-SSE between the southwest and the northeast areas, this structure is named the "Mupaka Fault" (Fig. 3.11). The thickness of the Basal diamictite ranges from 3 to 35 m in the east part of the Mupaka Fault, and from 40 to 120 m to the west of this structure (Figs. 3.6 to 3.10). This stratigraphic unit pinches out in some areas of the northeast part of the Kamoa deposit (Fig. 3.9).

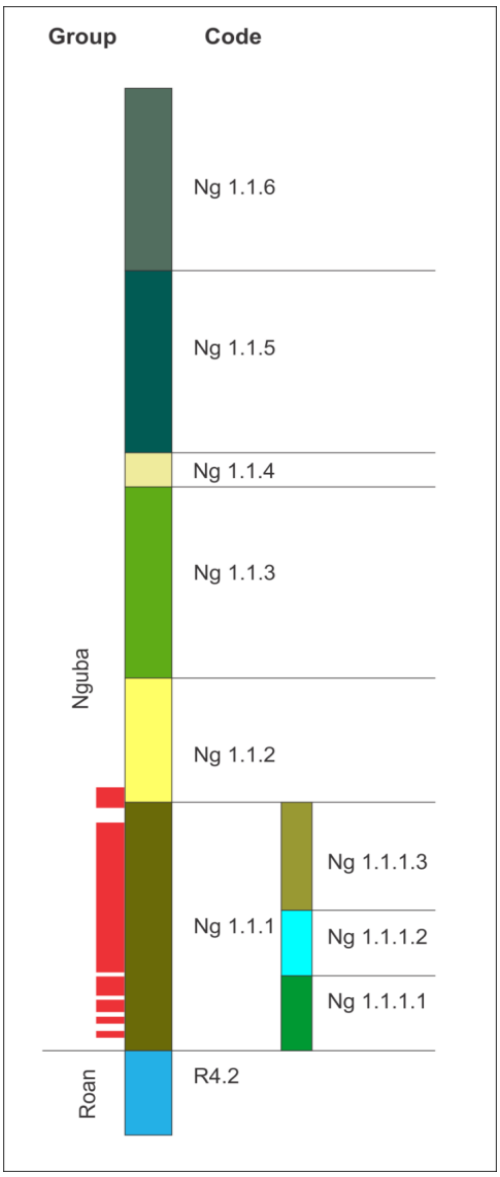

Fig. 3.3: Detailed stratigraphy of the Grand Conglomérat (Ng 1.1) within the Kamoa Copper deposit. The Grand Conglomérat unconformably overlies sandstone assigned to the Mwashya Subgroup. Copper mineralisation (in red) is hosted in the Basal diamictite unit of the Grand Conglomérat (Ng 1.1.1).

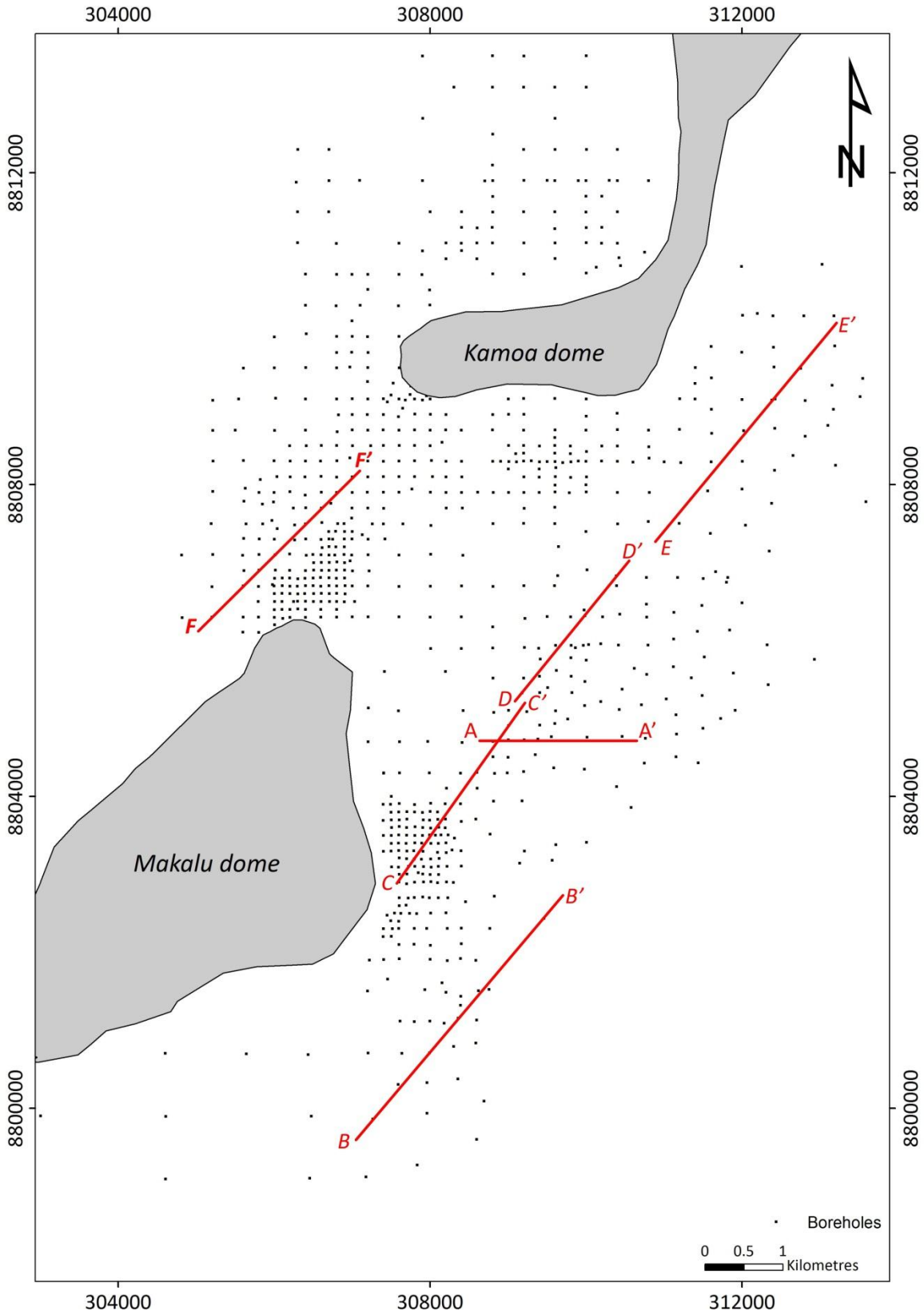

Fig. 3.4: Map showing the location of cross-sections presented in the study.

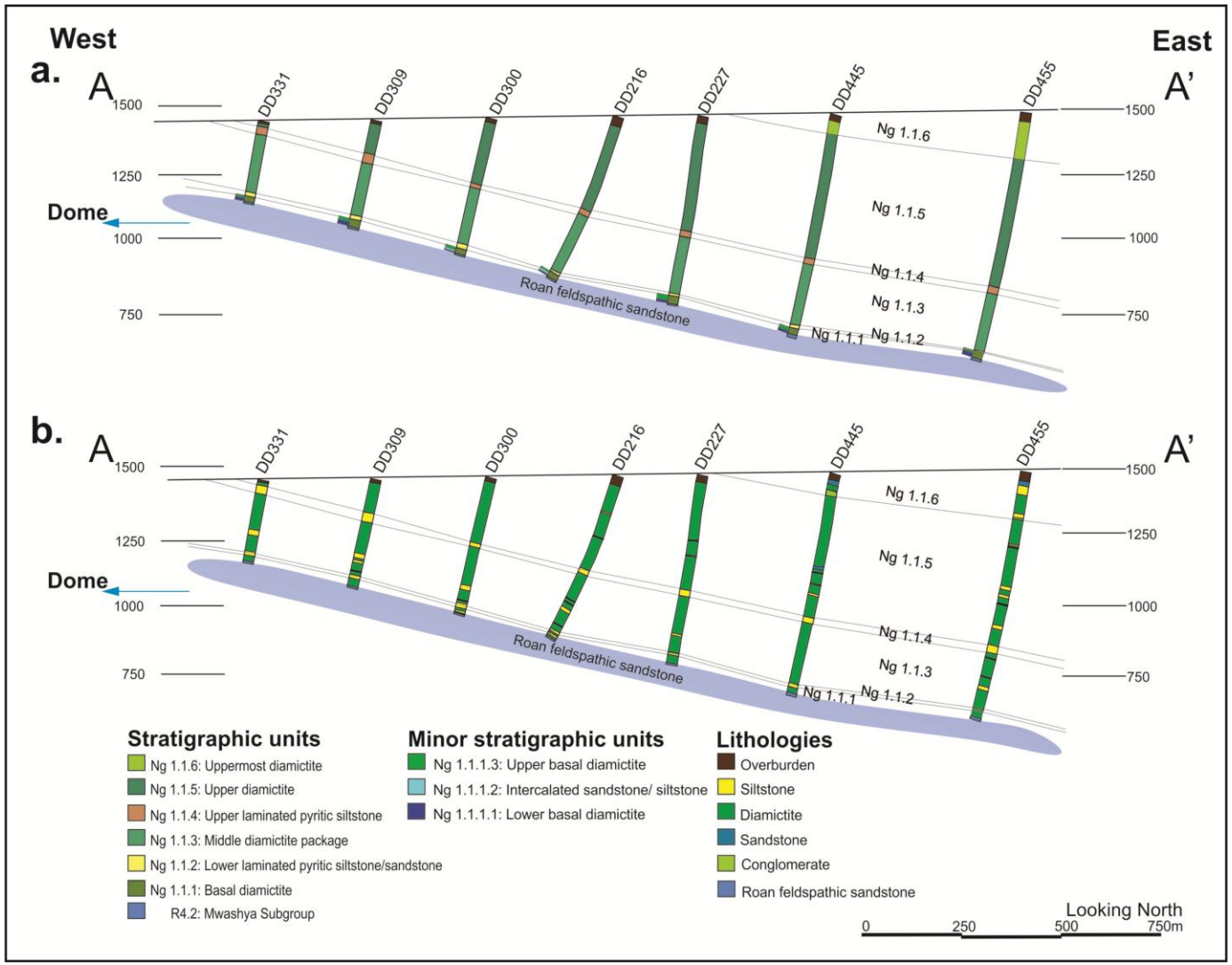

Fig. 3.5: Section line A-A' located in the central area of the Kamoa deposit (8804713N) showing the Mwashya Subgroup and the overlying Nguba Group host rocks that dip gently (~ 5°) away from the domes. (a). Cross section showing major and minor stratigraphic units. (b). Cross section showing the distribution of different lithological units. Views looking north. Location of the line of section is shown in Fig 3.4.

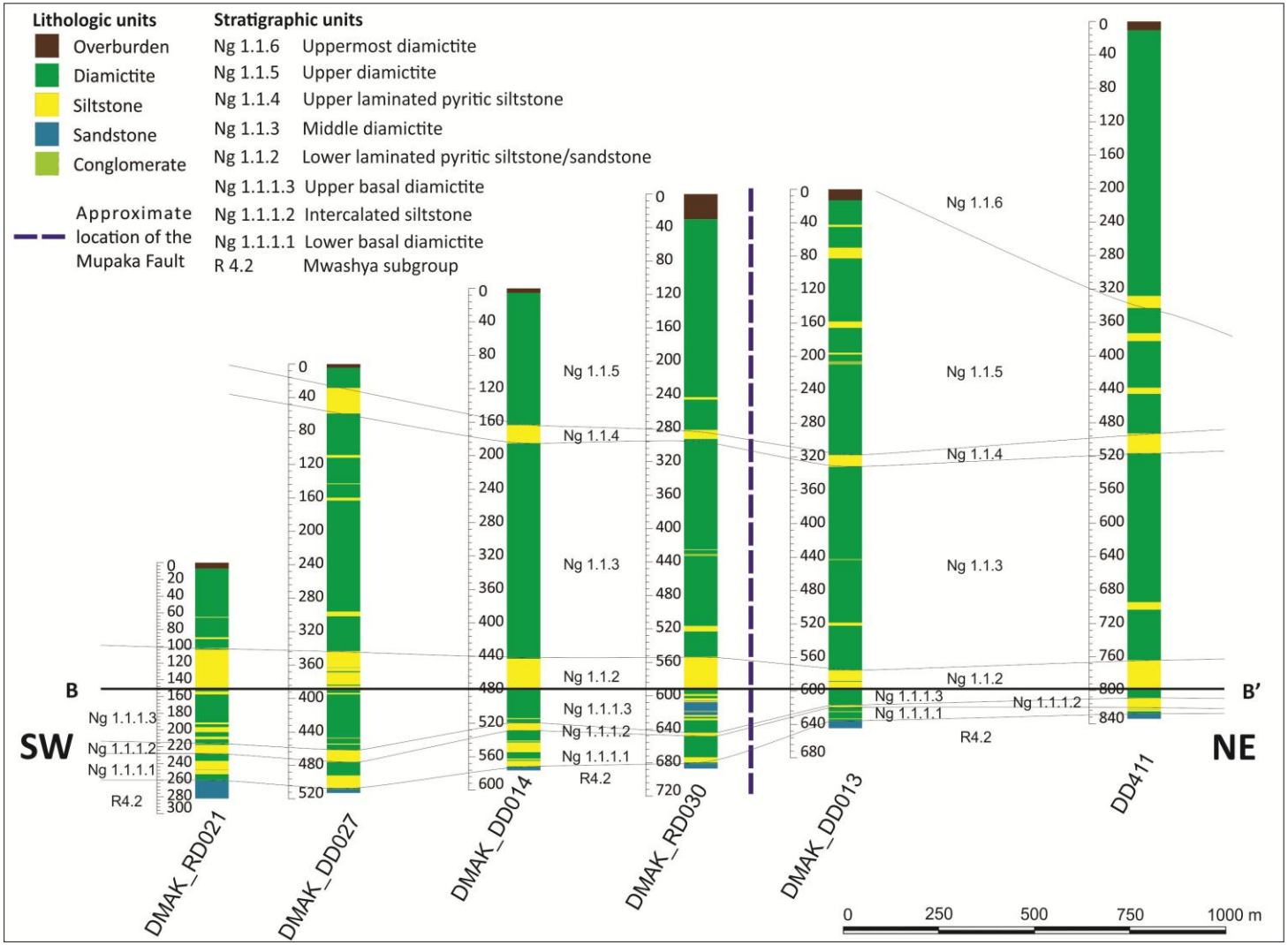

Fig. 3.6: Section line B-B'. Cross section drilled in the southwest part of the deposit. From the Mupaka Fault, an increase of siltstone and sandstone layers is observed. The cross section is hung from the base of the Lower laminated pyritic siltstone/sandstone (Ng 1.1.2). The hanging wall of borehole core DMAK_RD021 has been eroded as it is close to the dome. Location of the line of section is shown in Fig. 3.4.

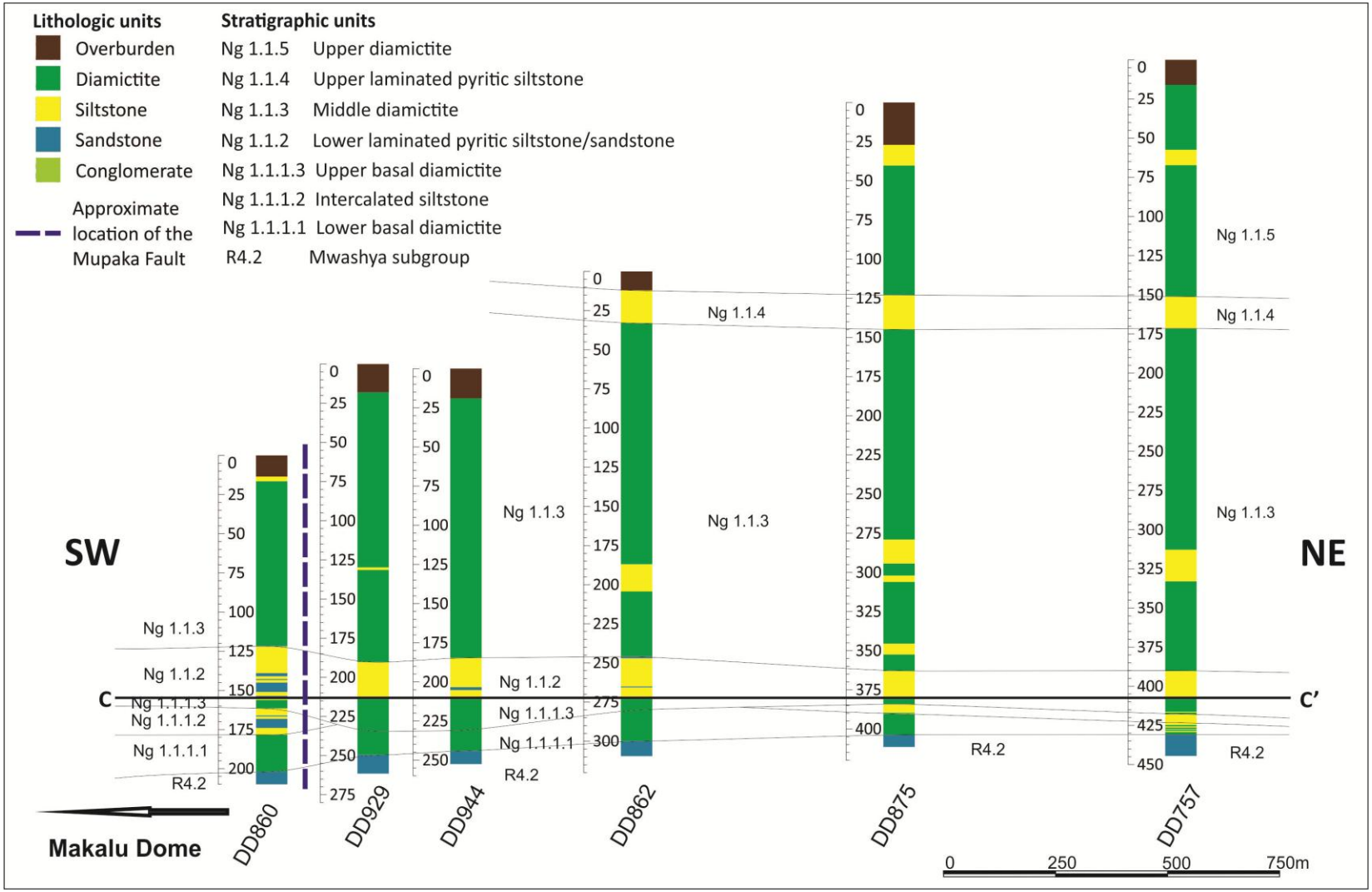

Fig. 3.7: Section line C – C' drilled in the east of the Makalu dome. The hanging wall of boreholes DD860, DD929, DD944 has been eroded because of the proximity to the domes. The cross section is hung from the base of the Lower laminated pyritic siltstone/sandstone (Ng 1.1.2). Location of the line of section is shown in Fig. 3.4.

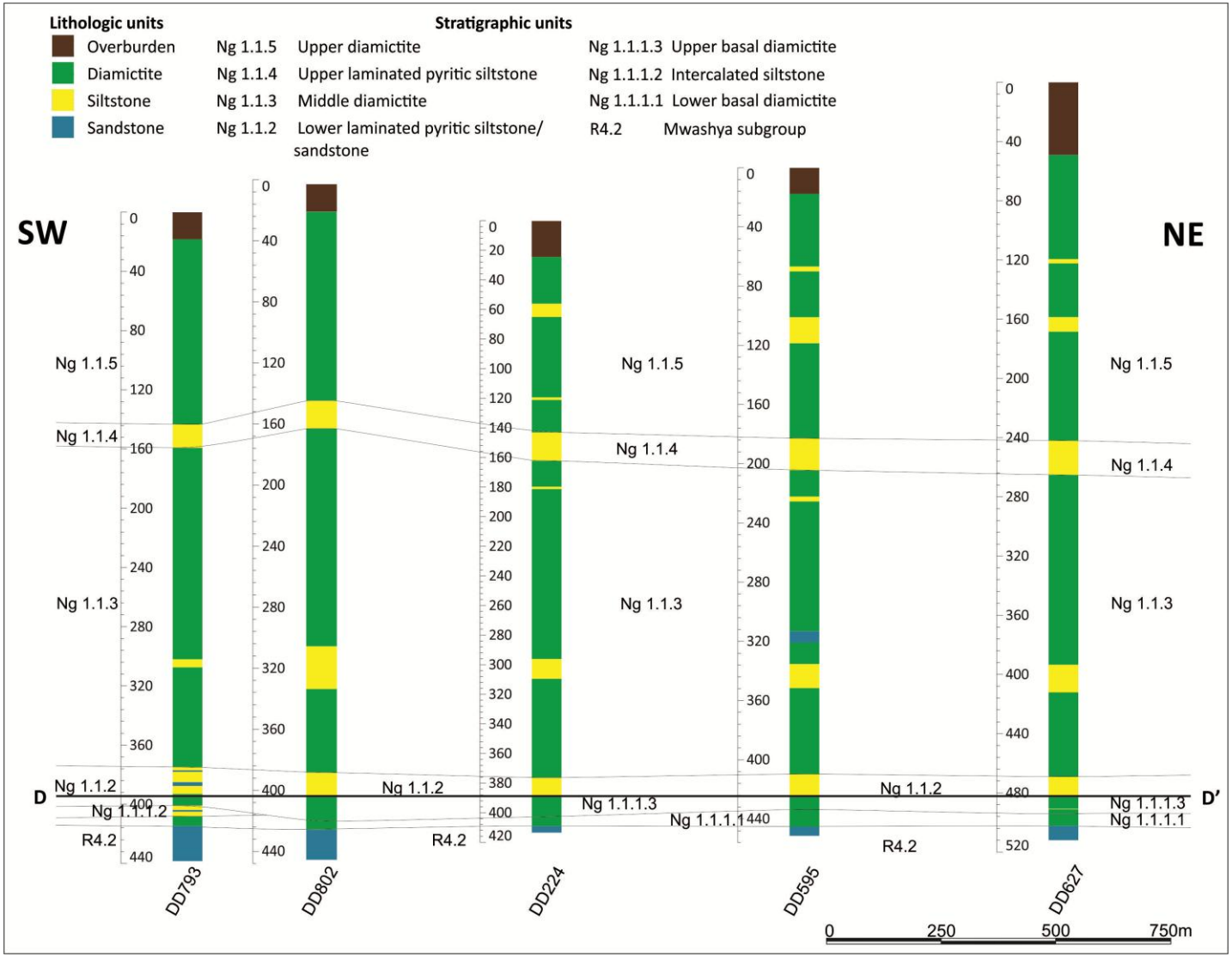

Fig. 3.8: Section line D – D'. The intercalated siltstone (Ng 1.1.1.2) pinches out in the central area of the Kamoa deposit, in the borehole DD793. The cross section is hung from the base of the Lower laminated pyritic siltstone/sandstone (Ng 1.1.2). Location of the line of section is shown in Fig. 3.4.

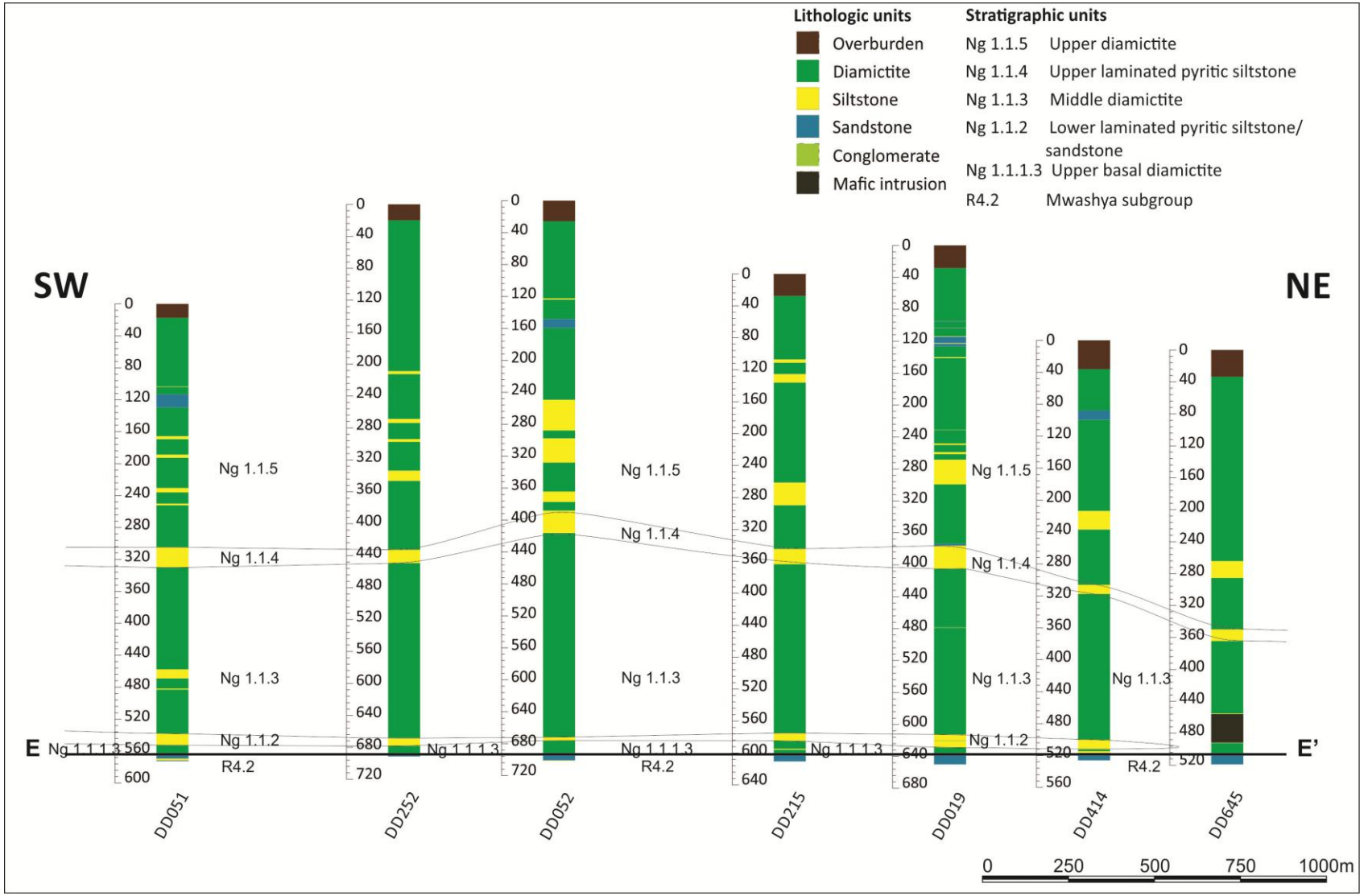

Fig. 3.9: Section line E – E' drilled in the east part of the Kamoa Dome. In the borehole DD645, mafic igneous rocks appear at the base of the Nguba Group. Therefore the Kamoa pyritic siltstone doesn't appear and the stratigraphy is difficult to establish. The cross section is hung from the top of the Roan feldspathic sandstone (R4.2). Location of the line of section is shown in Fig. 3.4.

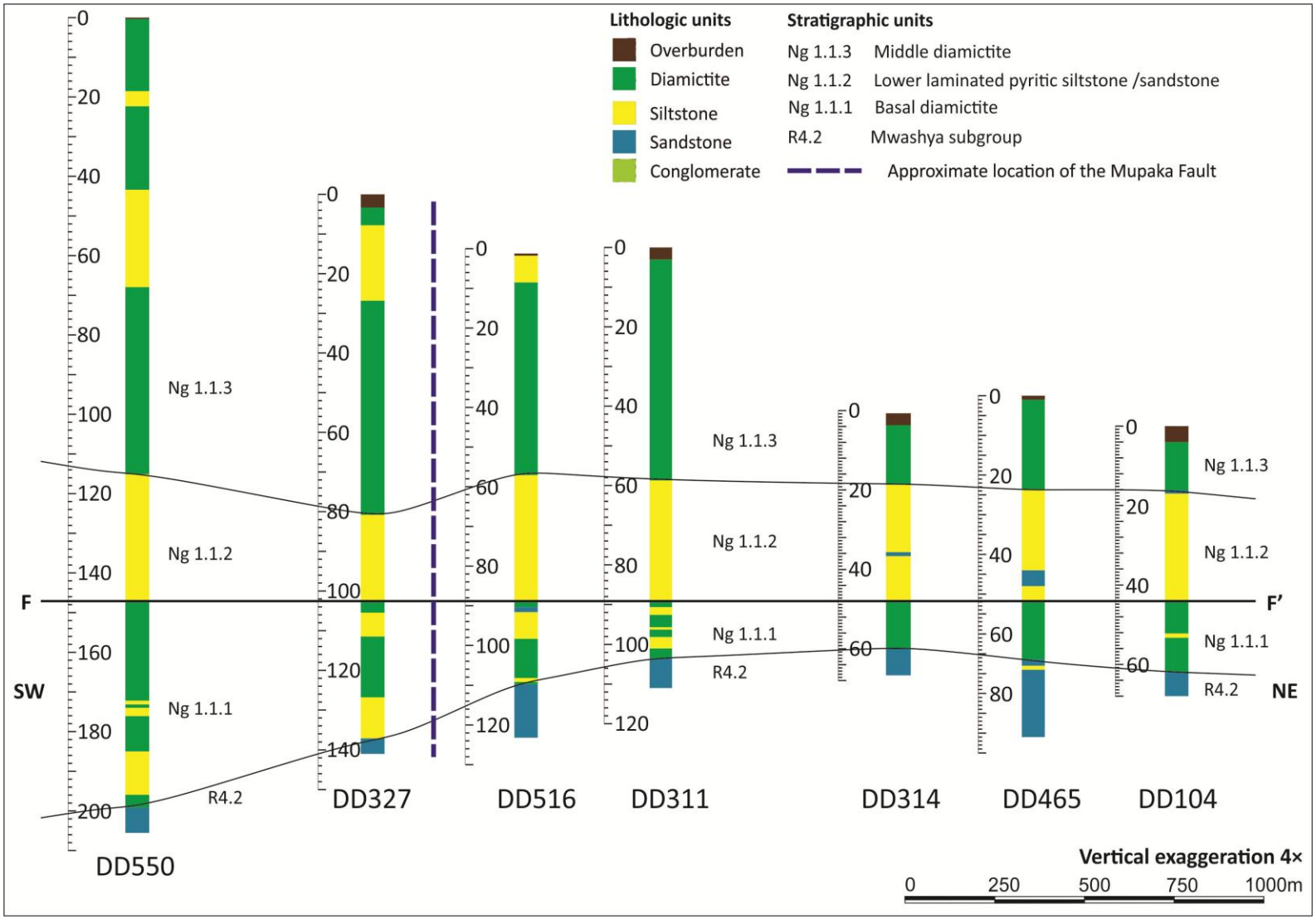

Fig. 3.10: Section line F – F'. The section is hung from the base of the Lower laminated pyritic siltstone/sandstone. Vertical exaggeration (4×) has been applied to improve the view of the section line, otherwise lithological units will not be visible as the boreholes are shallow. Location of the line of section is shown in Fig. 3.4.

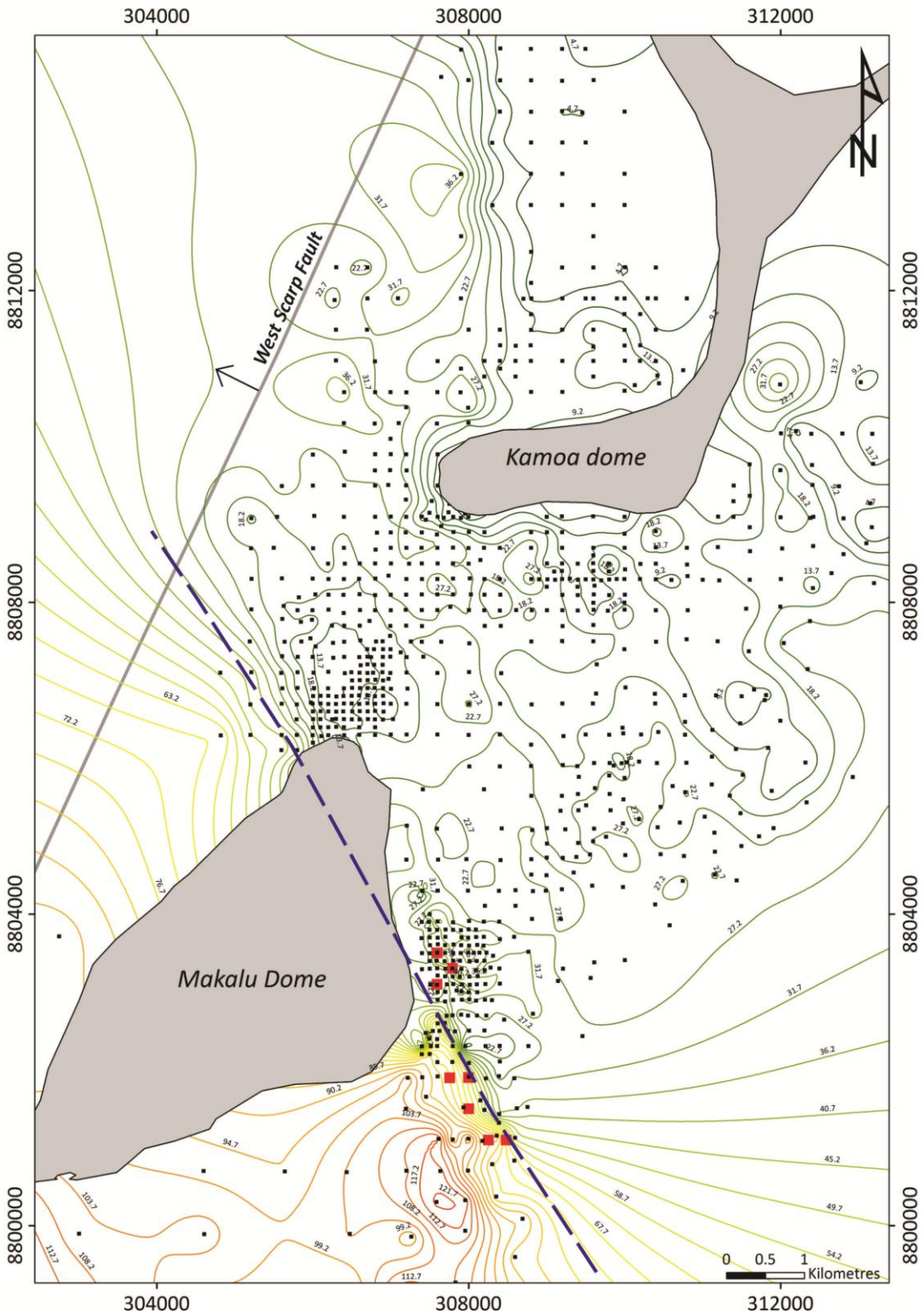

Fig. 3.11: Isopach map of the Basal diamictite (Ng 1.1.1). The blue dashed line shows the approximate location of the Mupaka Fault. The red points are boreholes with locally subvertical bedding in the Basal diamictite. Note that the map is based on true thickness. Contour lines in the bottom right and top left corner of the map are incorrect because they are not based on borehole information and are an artefact of data processing.

3.3.1.1 Lower basal diamictite (Ng 1.1.1.1)

This unit is composed of olive, maroon to light grey diamictite which contains an average of 20 to 35% of clasts (Fig. 3.12). The Lower basal diamictite is poorly mineralised and sandy at the base. Generally 5 to 25 m thick, this unit thins or pinches out east of the Mupaka Fault and increases in the west part of this interpreted growth fault (40 – 80 m) (Fig. 3.6 and Fig. 3.10). In the northeast part of the Kamoa area the Ng 1.1.1.1 varies from 1 to 5 m, in the eastern central part this unit is absent or thinner while in central part of the deposit this sequence varies from 5 to 20 m. The clasts are sub-angular to sub-rounded and the overall size is less than 100 mm, excluding large mafic igneous clasts which can be up to 0.5 m. The clasts are poorly sorted and composed of quartzites, quartz, mafic igneous rocks and sandstone with occasional large mafic clasts (Fig. 3.12). Haematite alteration just above the contact between the Nguba Group and the Roan footwall give rises to a maroon-coloured “oxide facies”. The percentage of clasts and their sizes within this unit decreases in the west of the Mupaka Fault and increases in the east of this structure.

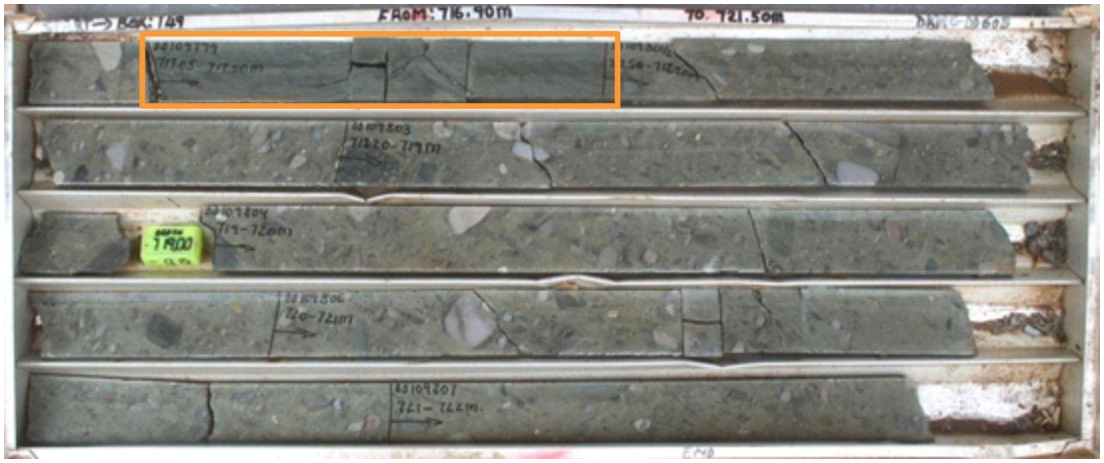

Fig. 3.12: Lower basal diamictite (Ng 1.1.1.1). Olive to greenish grey, clast-rich diamictite with quartz, quartzite and mafic igneous clasts which are rounded to subangular and sized from 5 to 100 mm. Note the presence of a large mafic clast in the orange rectangle. DD608, 716.90 - 721.50 m.

3.3.1.2 Intercalated siltstone (Ng 1.1.1.2)

This unit is composed primarily of interbedded olive, grey to dark grey siltstone and sandstone, massive to bedded with occasional bands of fine pebbles (Fig. 3.13). The unit is discontinuous within the deposit area, and absent or less than 2 m thick in the north-east part of the deposit area (Fig. 3.6 and 3.9). The Ng 1.1.1.2 increases abruptly in thickness to the west of the Mupaka Fault, varying from 5 to 20 m (Fig. 3.6 and 3.7).

The locally Intercalated siltstone (Ng 1.1.1.2) contains a reduced facies of diamictite, when present this lithology is preferentially mineralised.



Fig. 3.13: Intercalated siltstone (Ng 1.1.1.2) composed of medium and light grey laminated siltstone on top, with massive and weakly laminated sandstone at the base. Fine- and coarse-grained chalcopyrite occurs disseminated in the matrix and in the bedding. The dashed red line shows the contact between siltstone and sandstone. DD891, 220.55 - 225.66 m.

3.3.1.3 Upper basal diamictite (Ng 1.1.1.3)

This sequence is composed of medium to dark grey, olive diamictite with a argillaceous, silty and chloritised matrix.

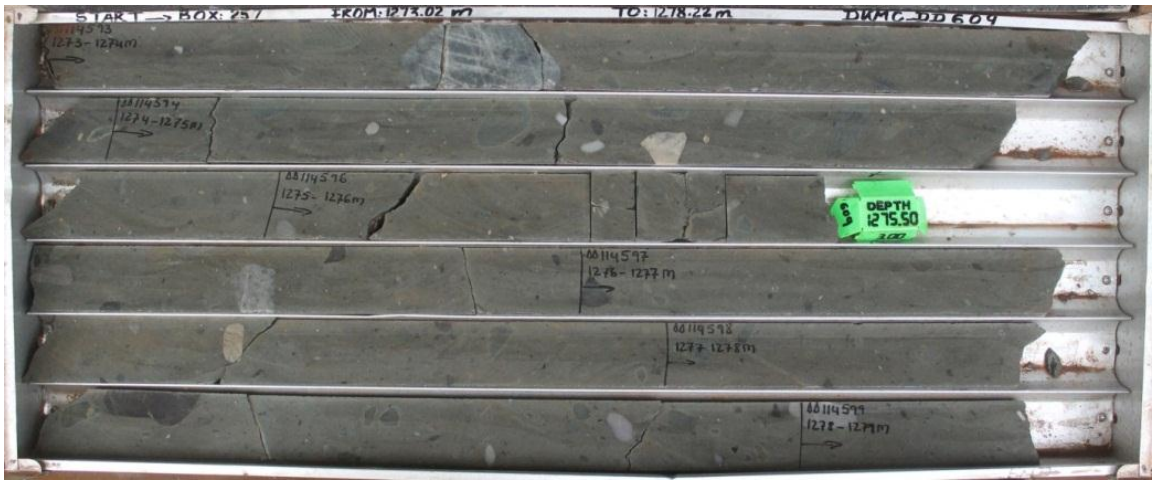

Fig. 3.14: Upper basal diamictite (Ng 1.1.1.3) composed of medium to light grey, clast-poor diamictite. Clasts are composed of argillite, quartzite and mafic igneous rocks. Their size ranges from 50 to 100 mm with occasional large pebbles up to 200 mm. DD609, 1273.02 - 1278.22 m.

The thickness of Ng 1.1.1.3 varies within the deposit area from 3 to 15 m east of the Mupaka Fault and from 30 - 60 m west of this structure (Fig. 3.6 and Fig. 3.9). In the west of the Mupaka Fault, this unit is intercalated with siltstone and sandstone layers. The diamictite is generally clast-poor with 10 to 20% quartzite, argillite and mafic clasts. The clasts are poorly sorted and range from 20 to 100 mm (Fig. 3.14).

3.3.2 Lower laminated pyritic siltstone/sandstone (Ng 1.1.2)

This unit, also called the "Kamoa Pyritic Siltstone" (KPS), comprises light to medium grey, greenish black, laminated to bedded mudstone/siltstone (Fig. 3.15 and 3.16) with occasional clasts, dropstones and intercalated sandstone layers with a mixture of massive, thickly bedded and pebbly sandstone bands. The Ng 1.1.2 can contain clast-poor diamictite; this is occasionally seen in the northeast area (Fig. 3.17). The thickness of the KPS changes abruptly across the Mupaka Fault (Fig. 3.6, 3.7 and 3.18). To the east of this fault the Ng 1.1.2 varies from 3 to 15 m in thickness and is occasionally absent to the east of the Kamoa dome (Fig. 3.9). To the west of the Mupaka Fault, the Ng 1.1.2 increases up to 40 m in thickness (Fig. 3.7). The Ng 1.1.2 is predominantly well stratified, and laminated with 15% to 30% bedded, coarse-grained and disseminated pyrite (Fig. 3.15). Soft-sediment deformation textures (Fig. 3.16a), syn-sedimentary faults (Fig. 3.16a), folds and reworked features are commonly observed within this unit. The contact between the Ng 1.1.2 and the Basal diamictite is sharp and marked clearly by 30 to 50 mm of varves (Fig. 3.16c).

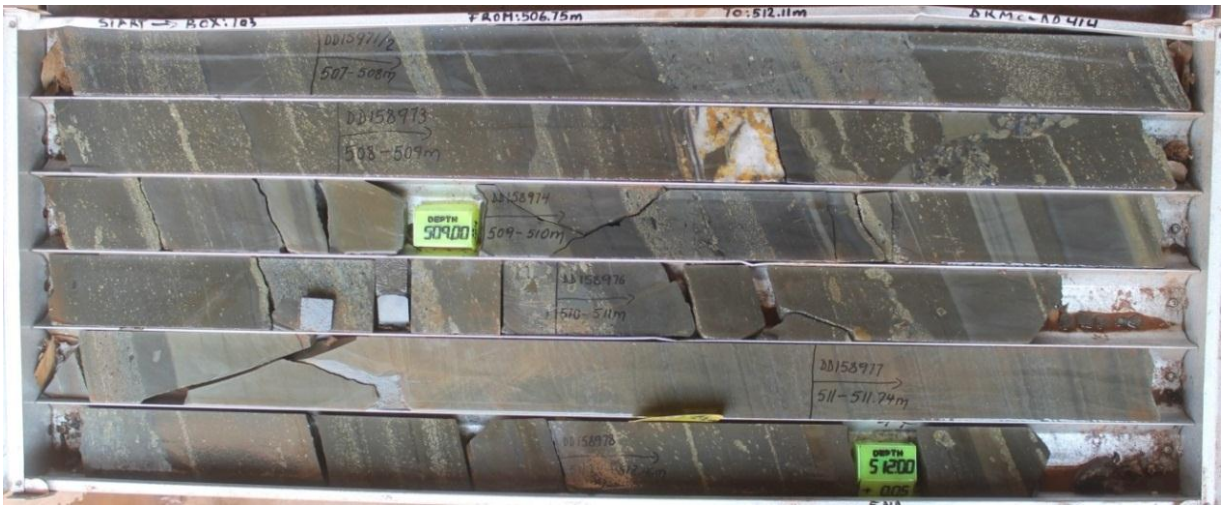

Fig. 3.15: Lower laminated pyritic siltstone/sandstone (Ng 1.1.2). Light to medium grey, bedded to laminated pyritic siltstone with intercalations of poorly laminated sandstone and small pebbly layers (right corner on the top row of the core box). Occasional dropstones are also present. DD414, 506.75 – 512.11 m.

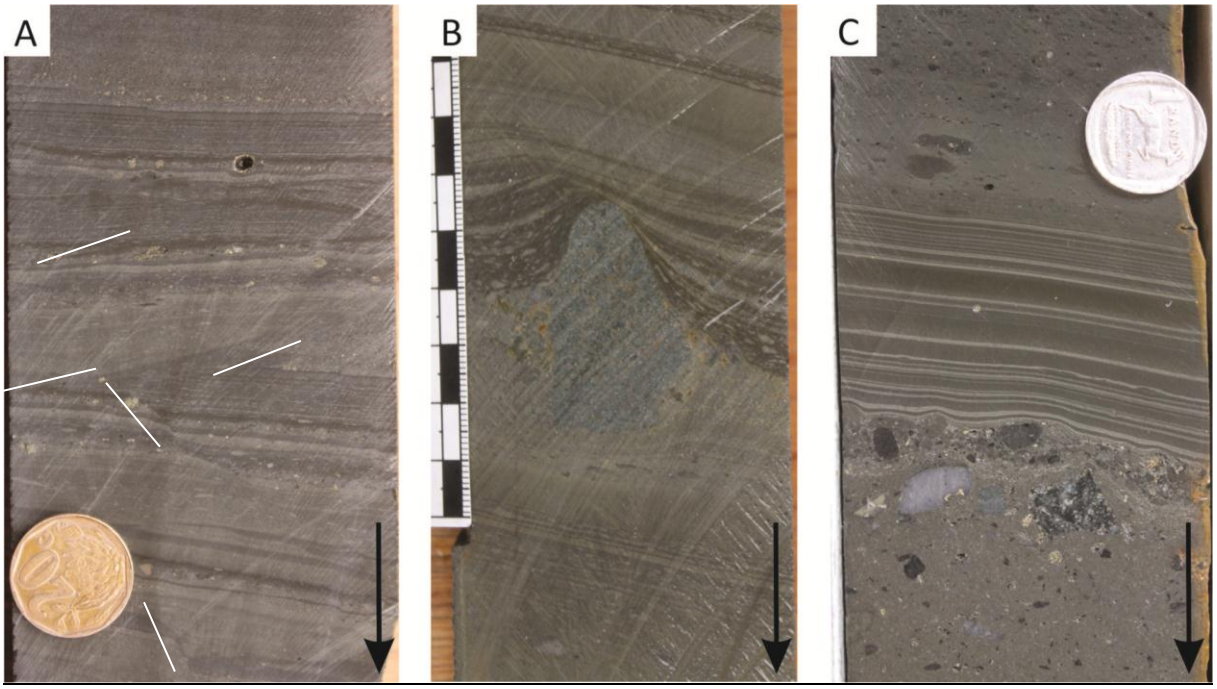

Fig. 3.16: Hand sample photographs of some of the features of the Lower laminated pyritic siltstone/sandstone (Ng 1.1.2). (A). Syn-sedimentary mesoscopic faults show both normal and reverse sense of movement (highlighted by white lines). Pyrite in fine- and coarse-grained disseminations. DD912, 478.79 m. (B). The clast deforms beds. The texture suggests this is a dropstone that was deposited from melting ice. DD912, 469 m. (C). Varves at the base of the Kamoa Pyritic Siltstone (Ng 1.1.2) overlying the basal diamictite (Ng 1.1.1). DD757, 407.71 m. The arrows show the downhole direction.

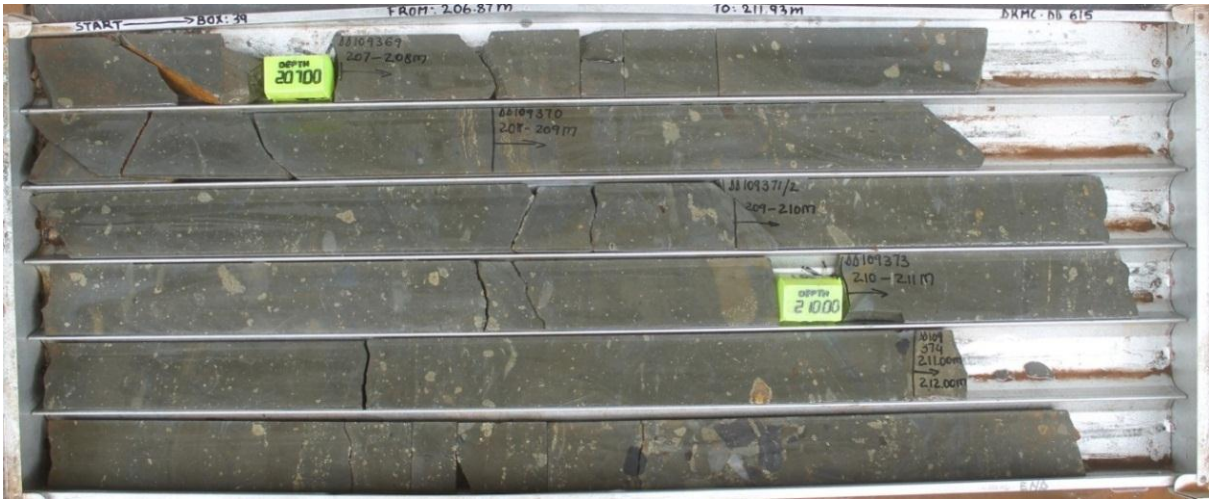

Fig. 3.17: Greenish grey to olive, clast-poor diamictite with abundant pyrite as replacements of clasts and disseminations. This rock represents the Kamoa Pyritic Siltstone in the east of the Kamoa Dome. DD615, 206.87 – 211.93 m.

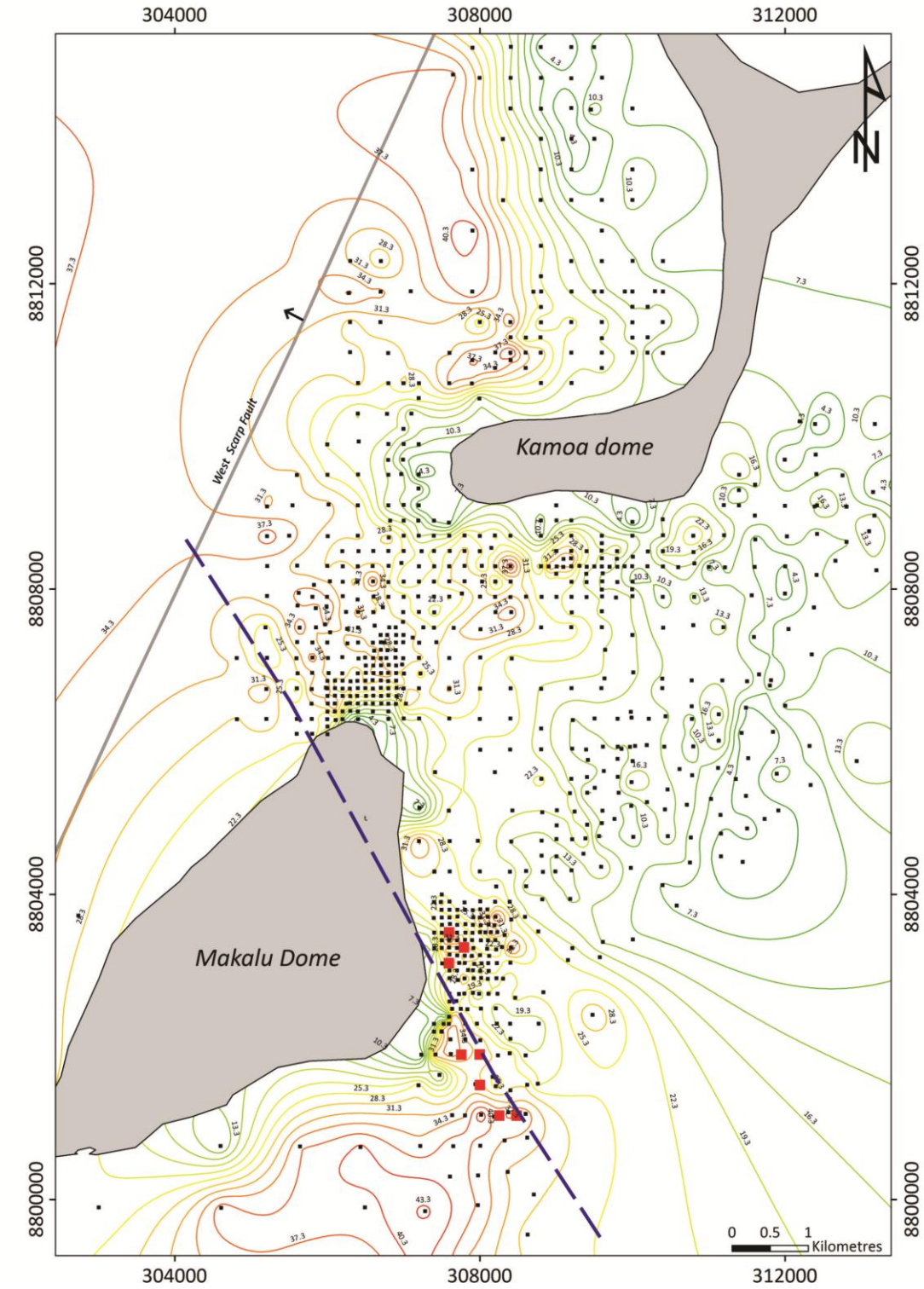

Fig. 3.18: Isopach map of the Lower laminated pyritic siltstone/sandstone (Ng 1.1.2). The map shows that the thickness of the KPS increases from the northeast to the southwest. The blue dashed line shows the approximate location of the Mupaka Fault. The red points are boreholes with locally subvertical bedding in the Basal diamictite. Note that the isopach map is based on true thickness. Contours lines in the bottom right and top left corner of the map are incorrect because they are not based on borehole information and are an artefact of data processing.

3.3.3 Middle diamictite package (Ng 1.1.3)

This unit is generally a medium to dark grey, clast-rich diamictite with 20 to 40% clasts, sized from 50 mm to 1 m (Fig. 3.19). The thickness of the Ng 1.1.3 is relatively consistent across the Kamoa deposit varying from 150 to 250 m. The isopach map of this unit does not show an abrupt change of stratal thickness (Fig. 3.20).

The clast assemblage is composed of quartzite, quartz, argillite, mafic igneous rocks with occasional exotics (mica schist, dolomite, shale) in an argillaceous silty and muddy matrix. The Ng 1.1.3 often contains thin layers of pyritic siltstone, sandy pebbly siltstone and reworked diamictite. The unit contains 0.5 - 1% fine-grained pyrite increasing up to 5% near the contact with the Lower laminated pyritic siltstone/sandstone (Ng 1.1.2).

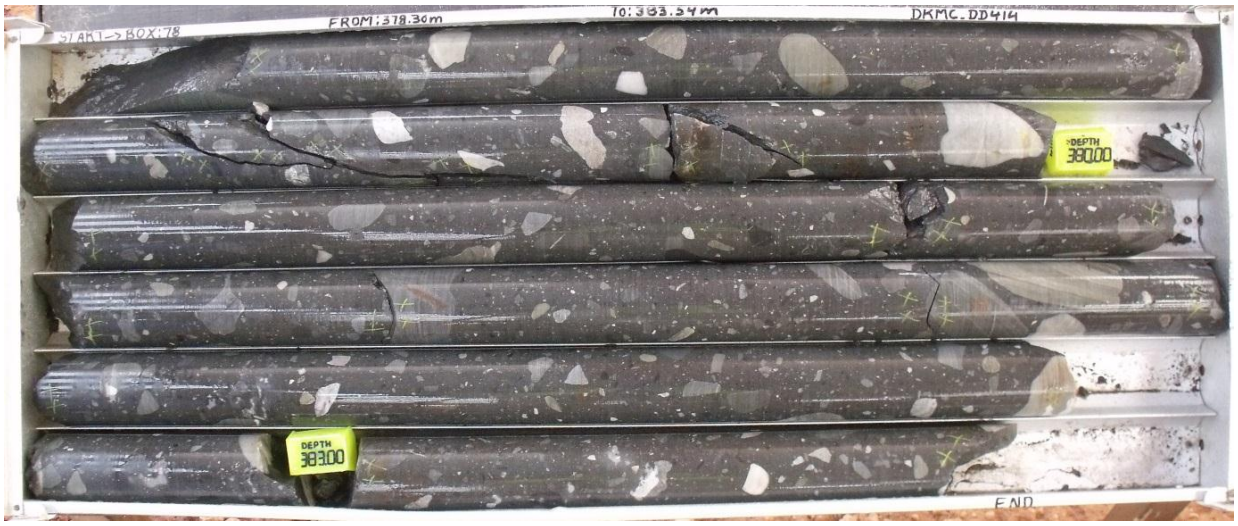

Fig. 3.19: Middle diamictite unit (Ng 1.1.3). Dark to medium grey, clast-rich diamictite with dominantly quartzite, quartz and argillite clasts. Clasts represent about 40% of the total volume of the rock. DD414, 378.30 – 383.54 m.

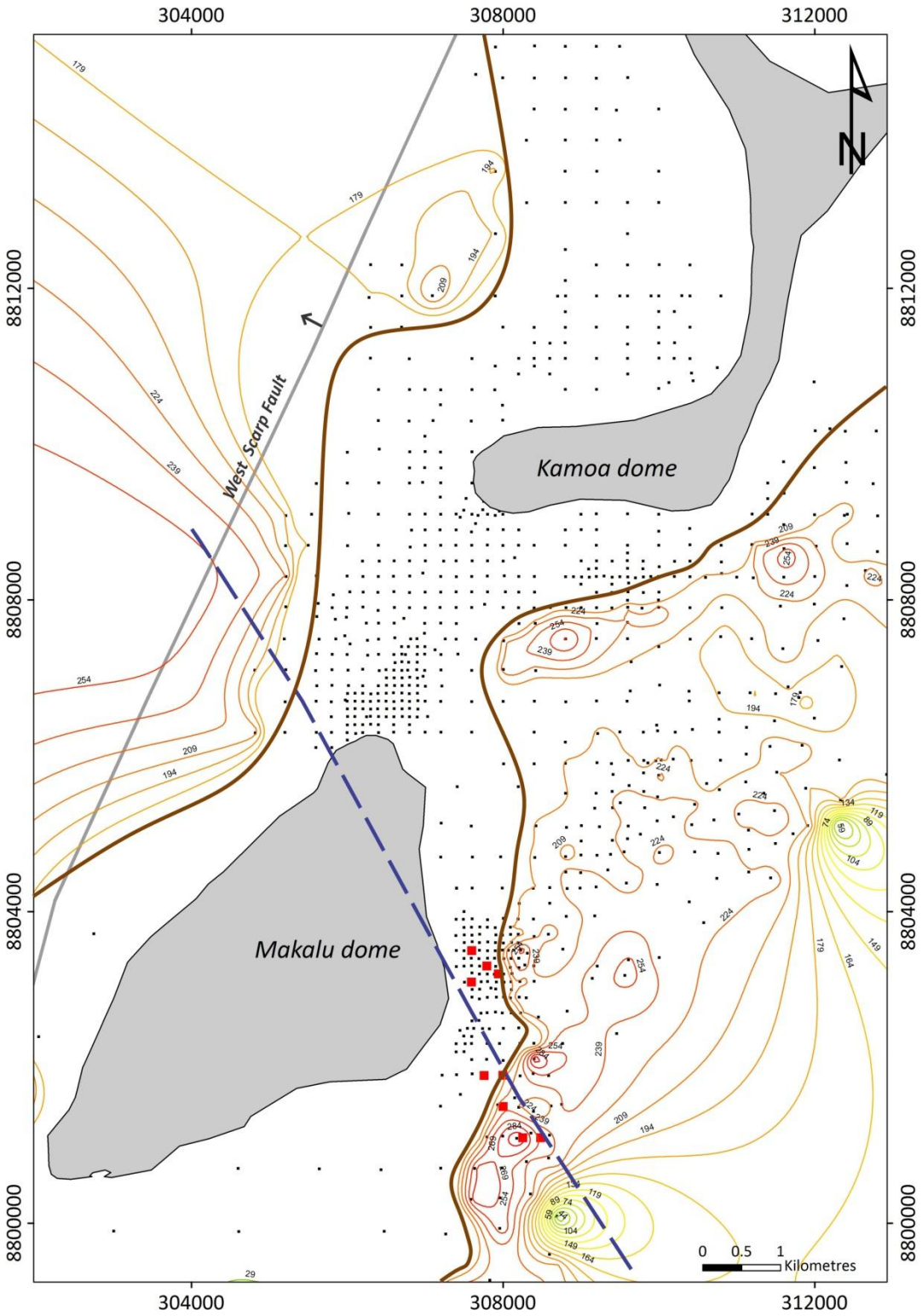

Fig. 3.20: Isopach map of the middle diamictite unit (Ng 1.1.3). The blue dashed line shows the approximate location of the Mupaka Fault. The Middle diamictite (Ng 1.1.3) is partially or completely eroded between the two brown lines. Note that the map is based on true thickness. Contour lines in the bottom right and top left corner of the map are incorrect because they are not based on borehole information and are an artefact of data processing.

3.3.4 Upper laminated pyritic siltstone/sandstone (Ng 1.1.4)

This unit contains light, medium to greenish grey bedded to laminated pyritic siltstone with intercalations of light grey sandstone and minor pebbles (Fig. 3.21). The thickness of the Ng 1.1.4 varies from 5 to 25 m (Fig. 3.6, 3.7, 3.8 and 3.9). The isopach map of the true thickness of the Upper laminated pyritic siltstone/sandstone (Ng 1.1.4) shows a weak change in stratal thickness (Fig. 3.22). Syn-sedimentary faults, syn-sedimentary folds and reworked textures are commonly observed within this unit. Dropstones are common at the base of this unit.



Fig. 3.21: Upper laminated pyritic siltstone/sandstone (Ng 1.1.4) composed of light to medium grey, bedded to laminated siltstone. There is an abundance of disseminated and coarse-grained pyrite in the matrix and along the bedding planes. DD455, 670.06 - 675.28 m.

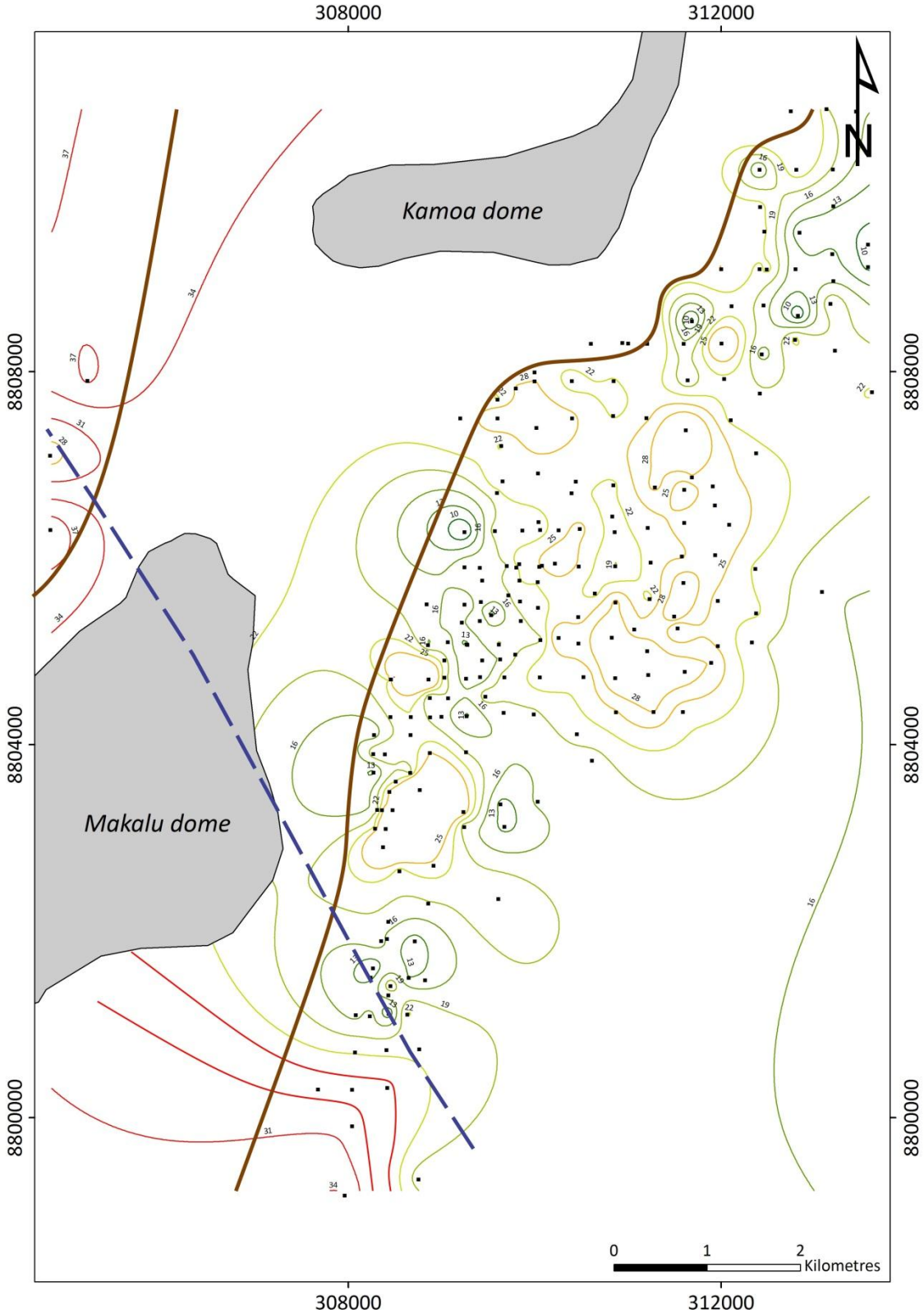

Fig. 3.22: Isopach map of the Upper pyritic siltstone/sandstone unit (Ng 1.1.4). The blue dashed line shows the approximate location of the Mupaka Fault. The Upper laminated pyritic siltstone/sandstone (Ng 1.1.4) is partially or completely eroded between the two brown lines. Note that the map is based on true thickness.

3.3.5 Upper diamictite unit (Ng 1.1.5)

This unit is composed of light to greenish grey, clast-poor diamictite with 7 to 15% clasts. The clasts consist of quartzite, mafics and argillites and range from 5 to 50 mm in size (Fig. 3.23). The thickness of this sequence ranges from 200 to 350 m. The Ng 1.1.5 is intercalated with occasional thin to thick layers of sandstone, siltstone and reworked diamictite. Minor pyrite is disseminated within the matrix and frequently in the rims of clasts. Occasional pyrrhotite is associated with chalcopyrite in rims of clasts. Calcite veins are common in this unit.



Fig. 3.23: Upper diamictite (Ng 1.1.5) composed of light to greenish grey clast-poor diamictite. The composition of clasts consists of mafic igneous rocks, quartzite and quartz. DD904, 390.68 – 396.12 m.

3.3.6 Uppermost diamictite unit (Ng 1.1.6)

The Uppermost diamictite unit Ng 1.1.6 is composed of light to greenish grey, clast-poor diamictite with 7 to 15% of clasts, occasionally up to 20%. The clasts consist of quartzite, mafics and argillites. The Ng 1.1.6 is intercalated with thick conglomerate, sandstone and siltstone beds. This unit has been eroded within 1.5 to 2 km of the domes, therefore it is present only in the deepest holes within the central, eastern and northern area of the deposit. The maximum thickness of this unit is 350 m. A 0.5 to 15 m thick conglomerate horizon separates the Nguba 1.1.6 and the Nguba 1.1.5 (Fig. 3.24). This horizon is composed of rounded to sub-angular, small to medium clasts in carbonate and chlorite altered matrix. The clasts are dominantly composed of quartzite, quartz, mafic igneous rocks and their size ranges from 5 to 20 mm with occasional larger clasts up to 150 mm. The conglomerate layers are commonly associated with coarse-

grained sandstone bands. Minor pyrite is disseminated within the matrix. The composition of the diamictite of the Ng 1.1.6 is similar to that observed in the Ng 1.1.5.



Fig. 3.24: Conglomerate composed of rounded to sub-angular, small to medium sized clasts in carbonate and chlorite altered matrix. This lithological unit constitutes the stratigraphic marker between the Ng 1.1.6 and Ng 1.1.5. DD553, 532.60 – 537.89 m.

3.4 Mafic igneous rocks

In the eastern area of the Kamoa dome, mafic igneous rocks occur as flows near the base of the Grand Conglomérat and here the Lower laminated pyritic siltstone/sandstone is thin or absent (Fig. 3.9 and 3.25). The mafic rocks include massive basalt, local basaltic hyaloclastite, gabbroic-dioritic–textured rocks, and dolerite (Broughton and Rogers, 2010). Pebbles of these mafic lithologic units occur in most of the diamictite packages. Mafic igneous rocks occur as clasts in some Mwashya Subgroup conglomerates and Grand Conglomerate diamictites but the clasts may also be derived from lithologically similar mafic basement rocks (Schmandt *et al.,* 2013).



Fig. 3.25: Mafic igneous rocks in the eastern part of the Kamoa dome. DD623, 393.17 – 398.24 m.

3. 5 Petrography of the Mwashya Subgroup and Nguba Group rocks

Samples were collected during core logging for transmitted and reflected light microscopy. Comprehensive illustrations are shown in Appendix A.

3.5.1 Mwashya Subgroup

The mineralogy of the feldspathic sandstone is composed of quartz, micas (muscovite, biotite), plagioclase, microcline and chlorite (Fig. 3.26a). The overall grain size ranges from 25 to 200 µm. The greywacke is commonly intercalated with thin layers of laminated to diffusely laminated siltstones (5 – 25 µm) which are dominantly composed of biotite and specular haematite. The thickness of laminations varies from 0.1 to 1 mm. Trace pyrite and rare chalcopyrite can be observed as fine- and coarse-grained material disseminated in the matrix (50 µm to 3 mm) (Fig. 3.26b).

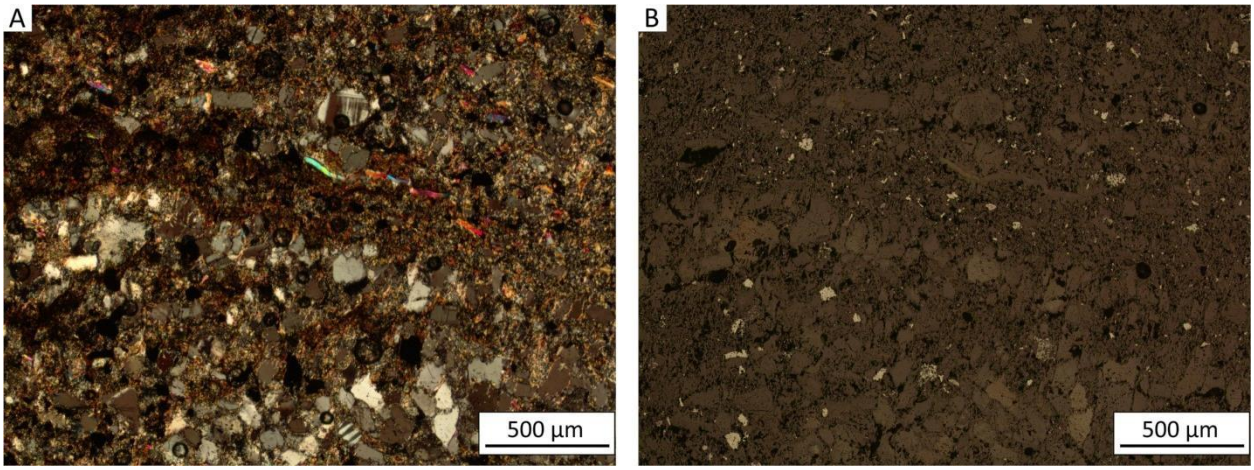

Fig. 3.26: Photomicrographs of the Mwashya Subgroup. (A). Transmitted light, cross-polarised photomicrograph of the feldspathic sandstone composed of quartz, muscovite, biotite, plagioclases and microcline. A fine-grained siltstone containing biotite and specular haematite is observed in the middle of the photomicrograph (sub horizontal layer). DD915, 581.67 m. (B). Reflected light, cross polarised photomicrograph of (A) showing disseminated pyrite.

3.5.2 Nguba Group

The diamictites are composed of quartz, chlorite, plagioclase, microcline, muscovite, biotite, carbonate minerals (calcite) and lesser pyrite (Fig. 3.27a, b). The laminated pyritic siltstones are composed of quartz, chlorite, microcline, carbonate, muscovite, biotite and abundant pyrite (Fig. 3.27c, d). The greywacke layers are dominated by quartz with minor feldspar, carbonate minerals (calcite) and pyrite (Fig. 3.27e, f).

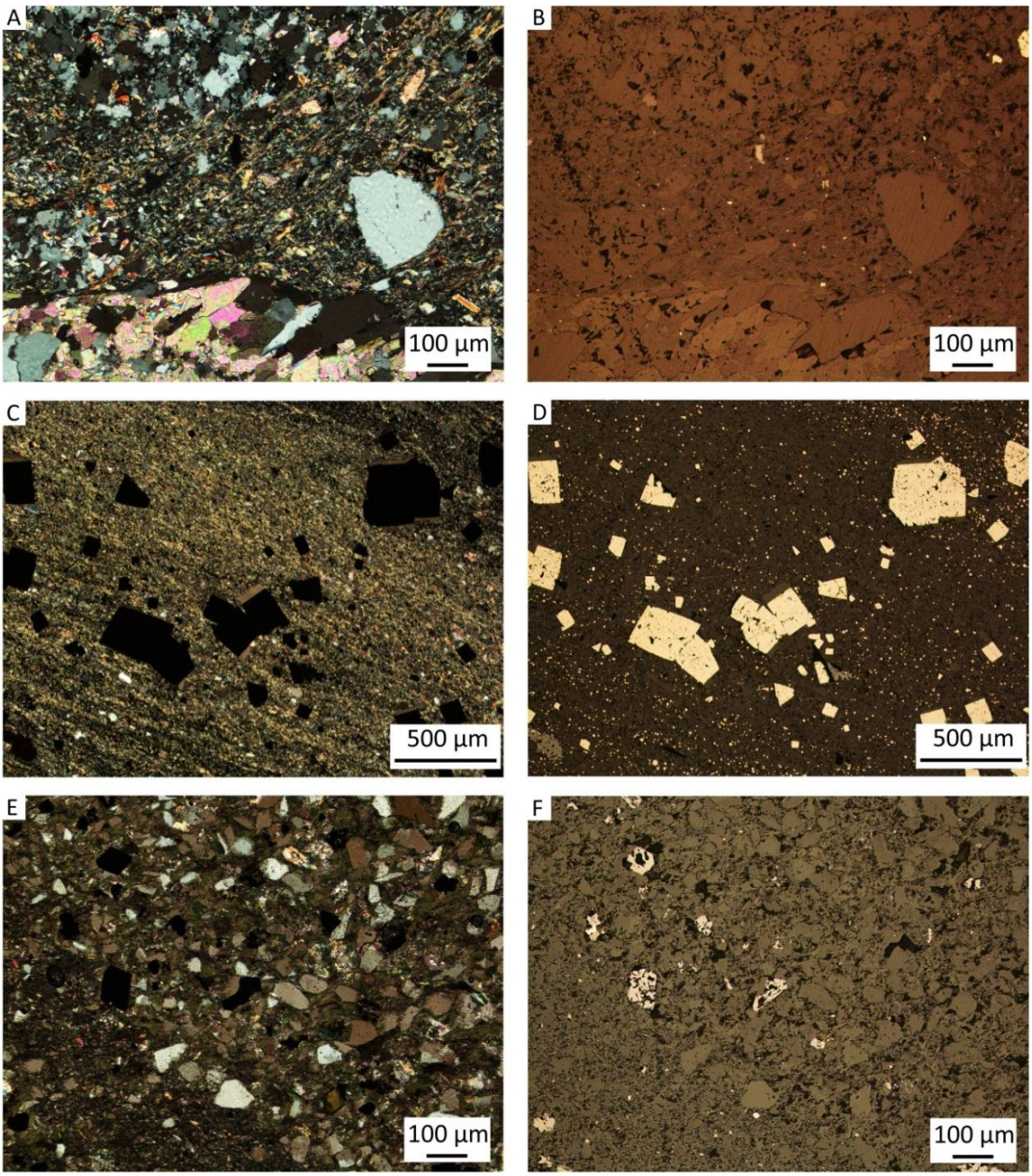

Fig. 3.27: Photomicrographs of the lithologies commonly seen within the Grand Conglomérat Subgroup. (A). The middle diamictite (Ng 1.1.3) composed of clast-rich diamictite. The mineralogy of the matrix is composed of quartz, micas, chlorite and minor carbonate; the clasts are sub-rounded and composed of quartz, micas, carbonate and chlorite with some muscovite. DD904 at 823.66 m. Cross polars. (B). Photomicrograph of (A) showing fine-grained pyrite. Reflected light, plane polarised light. (C). Transmitted light, cross polarised photomicrograph of the Upper laminated pyritic siltstone/sandstone (Ng 1.1.4) composed of quartz, chlorite and biotite with rare muscovite. Thin laminations spaced with 10 to 50 µm are observed. Chlorite is present in strain shadows of euhedral pyrite. DD904 at 789.08 m. (D) Reflected light, cross polarised photomicrograph of (C) showing framboidal and euhedral pyrite in siltstone. (E). Transmitted light, cross polarised photomicrograph of the intermediate sandstone (Ng 1.1.5) dominantly composed of quartz associated with minor biotite, chlorite and occasional muscovite. The overall size of grains ranges from 5 to 60 µm. DD904, at 149.50 m. (F) Reflected light, plane polarised photomicrograph of (E) showing fine and coarse grained pyrite.

3.6 Discussion

Within the Kamoa deposit, the Makalu and Kamoa domes expose the Mwashya Subgroup which forms the footwall to the deposit. The thickness of different stratigraphic units does not change significantly across the domes (Fig. 3.28). Therefore, in the absence of any other evidence it is suggested that the domes are a result of deformation during the Lufilian orogeny.

The facies of the Basal diamictite is not the same throughout the deposit. In the west of the Mupaka Fault (south and south west part of the Makalu dome), the amount of clasts is generally low (7-15 %) while in the east of this fault clasts are abundant (25-35 %). Also, in the west of the Mupaka Fault, the amount of intermediate siltstone/sandstone layers increases significantly. All these features suggest that there were syn-sedimentary faults during the deposition of the Nguba Group rocks.

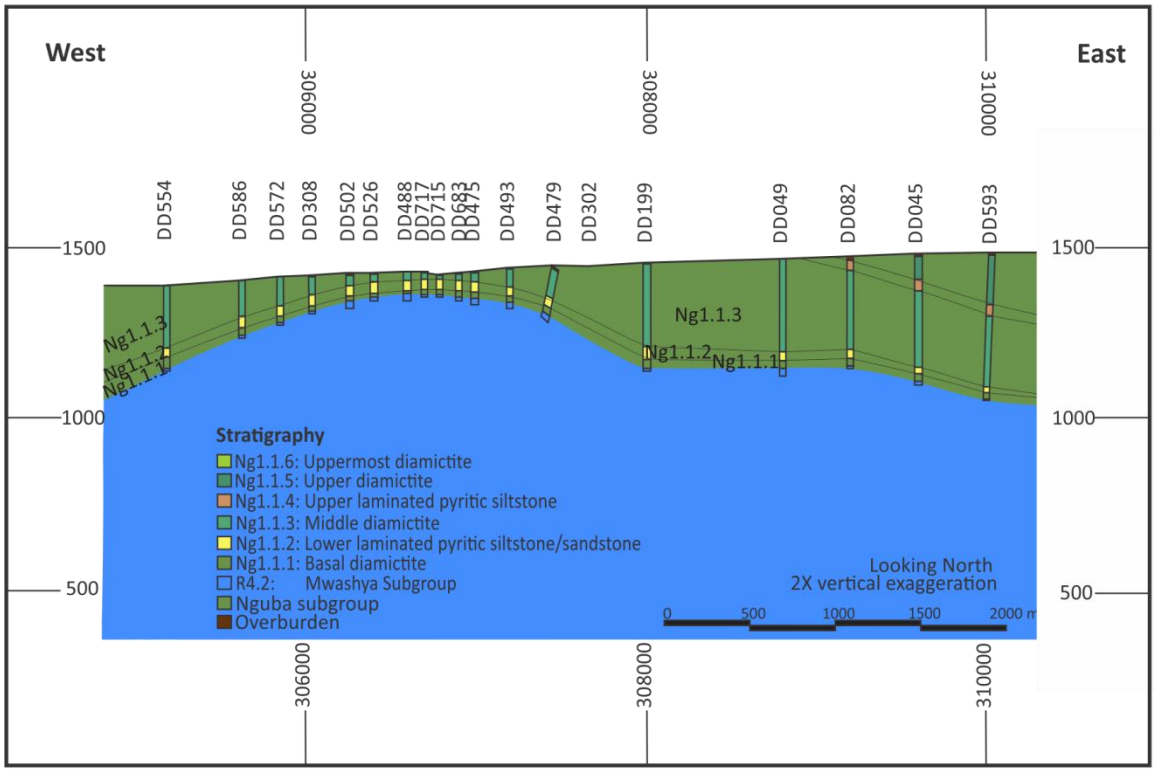

Fig. 3.28: Cross section showing the thickness of different stratigraphic units of the Grand Conglomérat that overlie the Mwashya subgroup which forms the domes in the deposit area.

3.7 Conclusion

Work completed within the Kamoa deposit has revealed that the thickness of the Basal diamictite (Ng 1.1.1), the Lower laminated pyritic siltstone/sandstone (Ng 1.1.2) and the Upper laminated pyritic siltstone/sandstone (Ng 1.1.4) change abruptly across the Mupaka Fault. Isopach maps of the Middle diamictite, the Upper diamictite and the Uppermost diamictite units do not show an abrupt change in stratal thickness, this may be explained by the fact that these units are eroded.

Understanding the genesis of the zone showing the abrupt change of thickness associated with high grade copper mineralisation can aid in the development of future exploration techniques. The next chapter will illustrate in detail the structural features of the Kamoa deposit with an emphasis on the Mupaka Fault.

CHAPTER 4

Structural features of the Kamoa deposit

4.1 Introduction

Structural features are an important source of information to provide a greater understanding of the Kamoa copper deposit and the role of tectonism in its formation and deformation. An understanding of the tectonic stresses acting on the Kamoa deposit during and after the deposition of the Grand Conglomérat sedimentary rocks is essential for the establishment of the relationship between the local and the regional tectonic stress. The study of structural features in thin section, including the interpretation of the metamorphic and deformational conditions during their formation, is an important tool to unravel the tectonic and metamorphic evolution of an area (Passchier and Trouw, 2005). Faults are commonly, but not always, marked by the macroscopic development of a variety of tectonites commonly termed fault rocks (Killick, 2003). The recording of the presence and distribution of fault rock can be a useful guide to unravelling the brittle geological structures.

In order to gain adequate information, 122 boreholes were investigated in detail, to gain a better understanding of the structural features of the Kamoa deposit (Fig. 4.1). Complete details of borehole cores logged and sampled are contained in Appendix B. Core logging focused on the two stratigraphic units hosting copper mineralisation, the Basal diamictite (Ng 1.1.1) and the Lower laminated pyritic siltstone/sandstone (Ng 1.1.2) of the Grand Conglomérat. Detailed structural logging of borehole core has focused on analysis of the characteristics and distribution of foliations, folds, mesoscopic faults, strain-shadows, and strain-fringes. Also, the nature of a zone of abrupt change of thickness of the Basal diamictite and the Lower laminated pyritic siltstone/sandstone has been investigated in detail (Figs. 3.11 and 3.18). Structural measurements of these features are presented in Appendix C. In addition, 170 polished thin sections have been carefully described to unravel the tectonic evolution of the studied area (Fig. 4.1). To better constrain the fine-grained mineralogy, textures and structures; 18 polished thin sections were investigated using the scanning electron microscope FEI Quanta 200 ESEM from the University of the Witwatersrand (SEM) (Appendix A). Unless stated, all structural measurements are displayed in strike/dip convention. Figure 4.2 displays the location of Kamoa boreholes with hand samples or thin sections presented in this chapter.

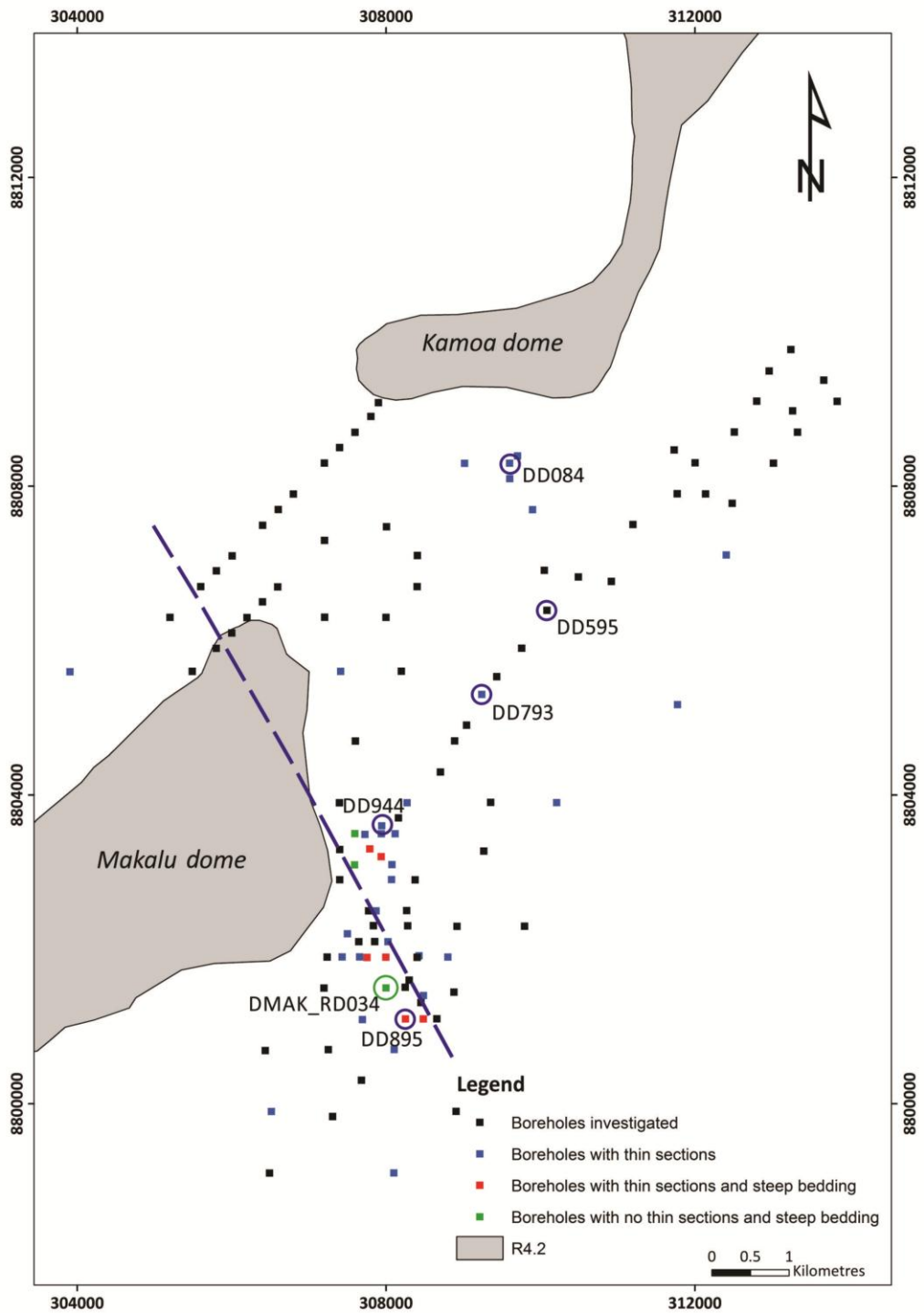

Fig. 4.1: Map showing the studied borehole locations. The green points are boreholes with steep bedding (> 70°), in the Basal diamictite. The red points are boreholes with steep bedding where thin sections were collected, the blue points are the boreholes with thin sections and the black points are other boreholes investigated. The steep bedding in the Intercalated siltstone of the borehole DMAK_RD034 (in a green circle) has an orientation of 349/75E. Boreholes within blue circles were investigated to better understand the morphologies of strain shadows and strain fringes in the Kamoa deposit. The blue dashed line shows the approximate location of the Mupaka Fault.

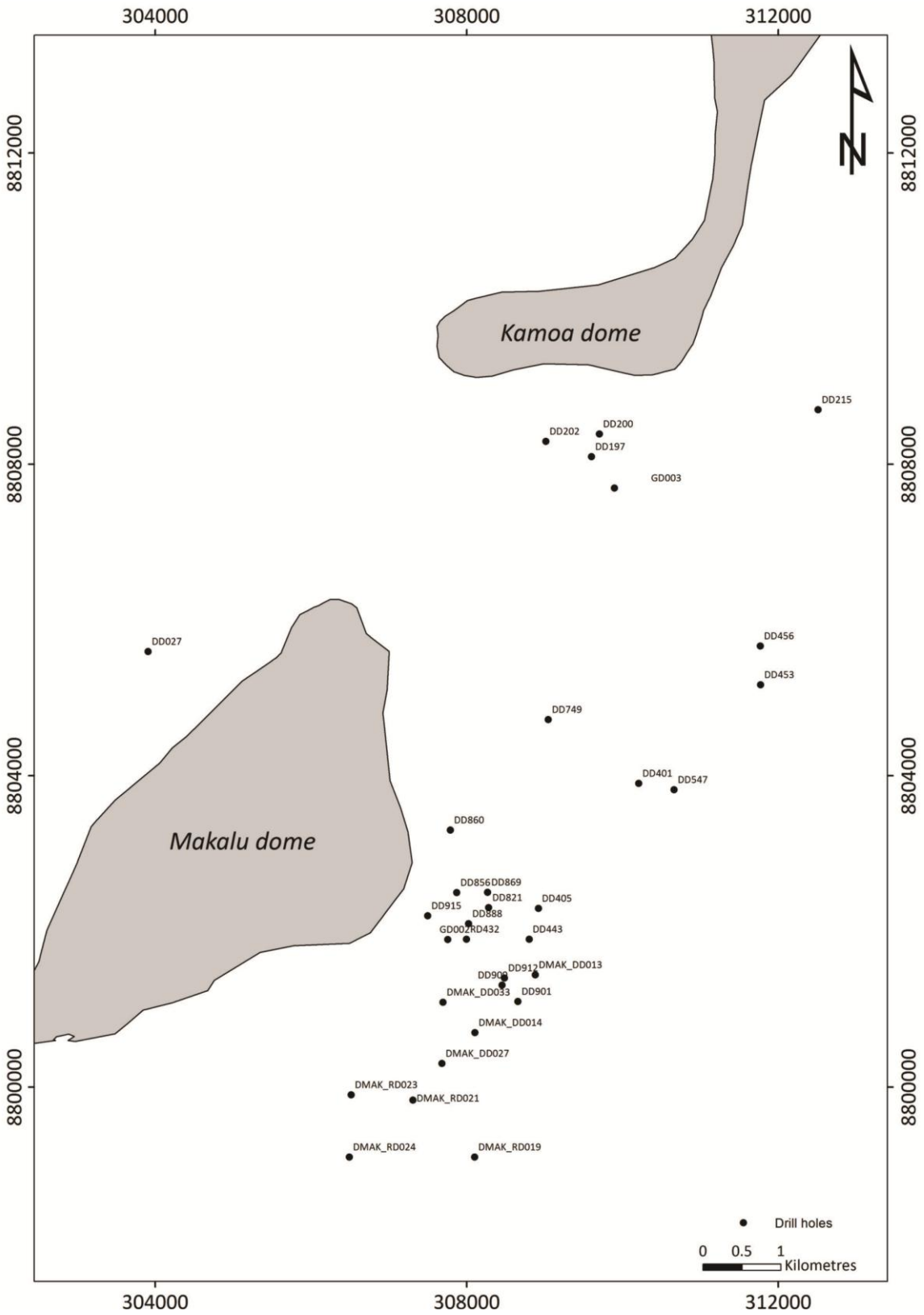

Fig. 4.2: Map showing the location of boreholes with hand samples or thin sections presented in this chapter.

4.1.1 Local structural setting

Within the project area regional folds strike northeast and the Makalu and Kamoa domes lie along a NNE trend (Broughton and Rogers, 2010; Mvondo, 2012; Gilchrist, 2014) (Fig. 4.3). Research by Gilchrist (2014) based on the Kamoa borehole database suggested that the project area is folded in two different orientations: a dominant folding aligns with the domes and has fold hinges trending NNE; and a set of more subtle folds with a wavelength approximately 4 km, trends west-east (Fig. 4.3b).

The majority of the Kamoa area lies on a broad, gentle plateau between two major north-northeast trending structures (Parker *et al.,* 2013). East of the Kamoa deposit is the Kansoko trend, a major regional north-northeast trending structure identified on the aeromagnetic data (Fig. 4.3a). The Kansoko trend structure is the interpreted as a boundary of the External Fold and Thrust Belt, its geology is currently poorly defined. To the west is a prominent escarpment and magnetic feature named the West Scarp Fault.

Unlike the tectonically-dismembered deposits of the Katangan Copperbelt, and the External Fold and Thrust Belt, the host rocks at Kamoa are intact and relatively undisturbed (Parker *et al.,* 2013).

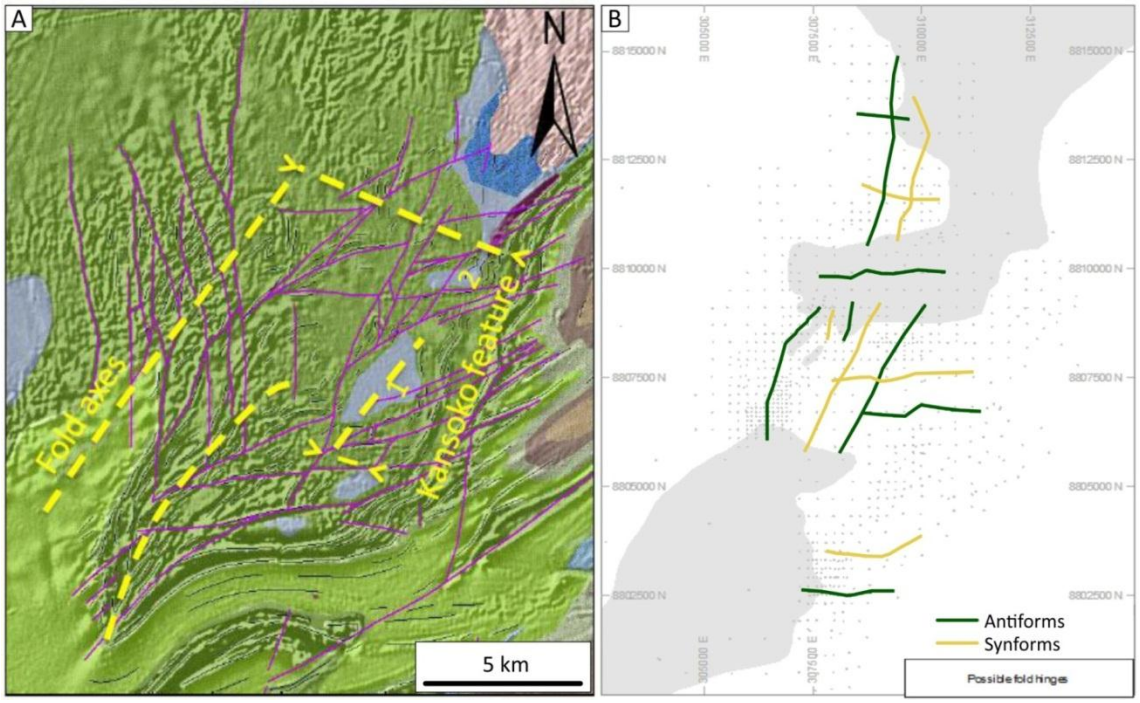

Fig. 4.3: (A). Geological and lineament map showing the NE-trending mega-folds (in yellow) and the strong NS cross-cutting fault network pattern west of Kamoa, with NE linking fault structures (in purple). The geological map is draped on an aeromagnetic image of the Kamoa project area. 1= Makalu dome. 2= Kamoa dome. (Mvondo, 2012). (B). North-northeast and east-trending, folds developed in the deposit area (Gilchrist, 2014).

4.2 Bedding (S_0)

Bedding is a primary layering related to the original rock-forming process. At Kamoa, bedding is commonly observed in siltstone and sandstone layers whereas the diamictites commonly lack bedding because of their massive texture. Where present, the thickness of bedding varies from a centimetre to several metres (Fig. 3.21). Bedding (S_0) has been studied in 142 oriented boreholes that are widespread across the studied area (Fig. 4.4). On the east side of the domes, bedding dips gently towards the southeast at angles of 8-20 degrees while on the west side of the domes it dips to the west (Fig. 4.5a).

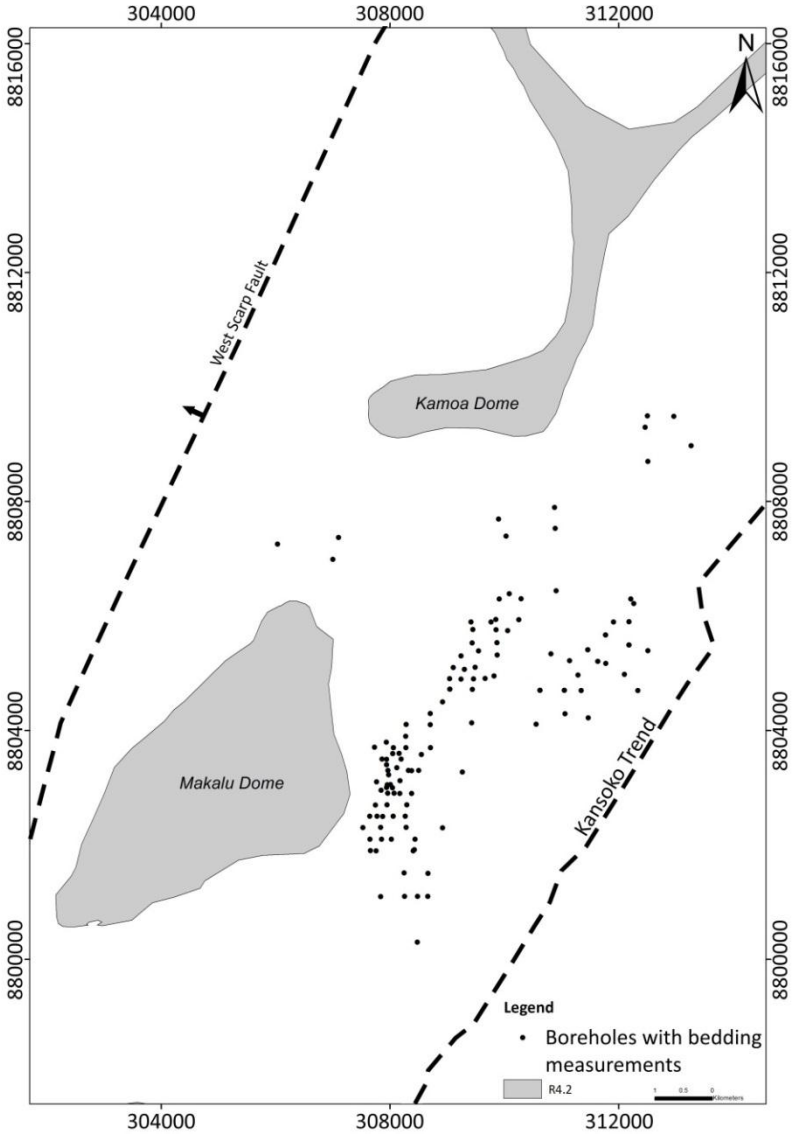

Fig. 4.4: Map showing the distribution of boreholes with bedding measurements.

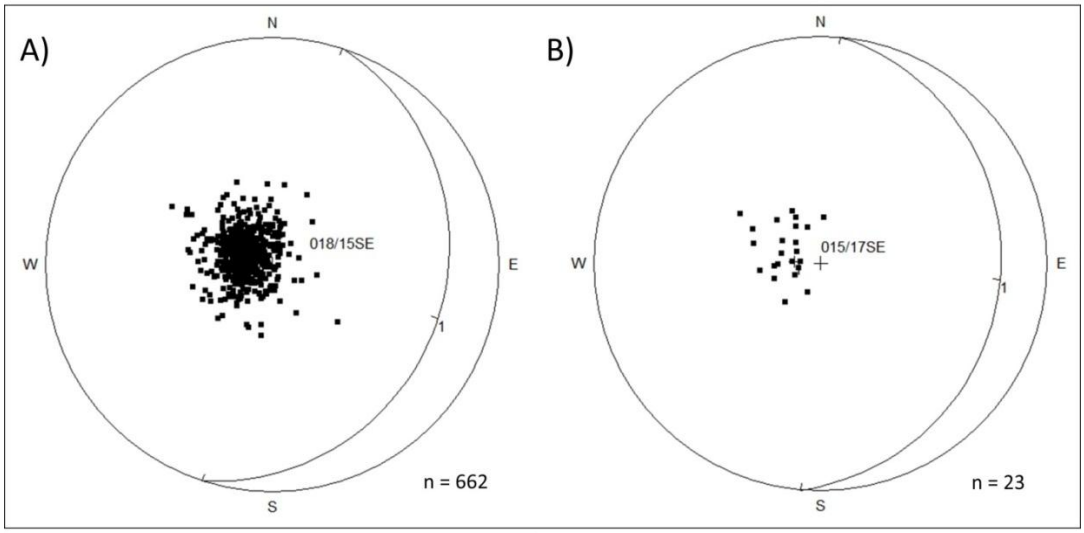

Fig. 4.5: (A). Lower hemisphere equal area stereographic projection of poles to bedding measured in the Lower and Upper laminated siltstone/sandstone in 142 oriented boreholes, from the Kamoa geological dataset. (B). Lower hemisphere equal area stereographic projection of poles to bedding measured in the boreholes located across the approximate location of the Mupaka Fault (8 oriented boreholes).

4.3 Zone of abrupt change in stratal thickness of the Basal diamictite: "Mupaka Fault"

In the southern part of the Kamoa deposit, an abrupt change in stratigraphic thickness of the Basal diamictite (Ng 1.1.1) is interpreted as due to a growth fault (Fig. 3.11). This change ranges from 40 – 60 m in true thickness (Fig. 3.11). A minor change in the stratal thickness of the Lower and Upper laminated pyritic siltstone/sandstone also is observed along the Mupaka Fault, ranging from 10 to 15 m of true thickness (Figs. 3.18 and 3.22).

The Mupaka Fault is oblique to the localised domes and, coincides with an area of higher copper grades. Intersections of the highest copper grade mineralisation (grade copper ranges from 6 to 20%) coincide with steeply dipping bedding (> 70°), and occasional thin mineralised veins (Fig. 4.6). The steep bedding suggests the presence of a growth fault formed during the deposition of the Grand Conglomérat.

Steeply dipping bedding, soft-sediment deformation, slump features and syn-sedimentary mesoscopic faults occur throughout the Kamoa area in the Lower laminated pyritic siltstone/sandstone and in the Intercalated siltstone. This suggests that there were probably multiple growth faults of varying size distributed throughout the Kamoa deposit (Broughton, D., pers. comm. 2016).

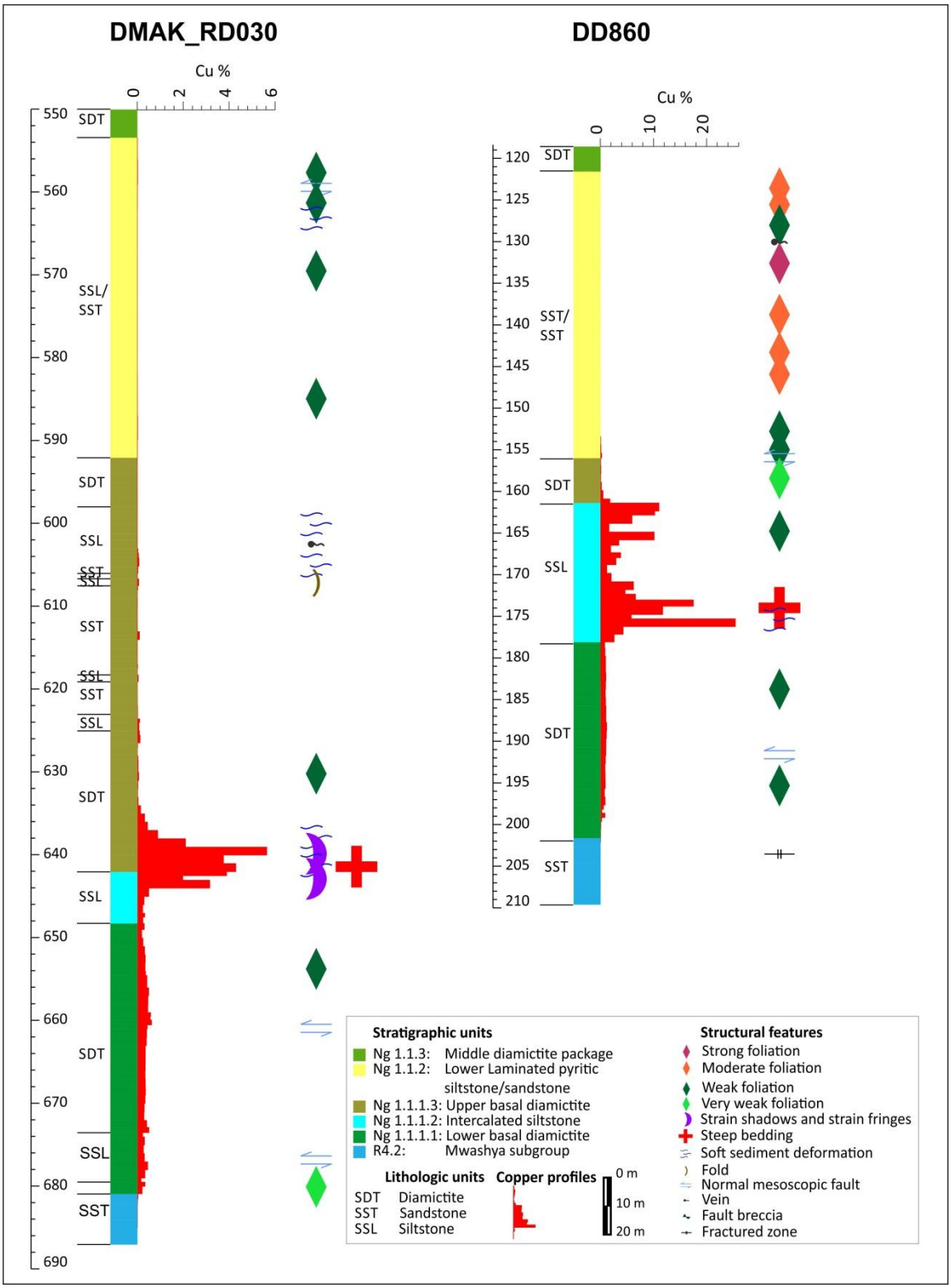

Fig. 4.6: Grade profiles and structural features for boreholes DMAK_RD030 and DD860. The highest copper grade coincides with steeply dipping bedding. The interval of steep bedding in borehole DD860 has a drilled thickness of approximately two metres.

4.3.1 Steep bedding

Steep bedding is observed in boreholes with thicker Basal diamictite located adjacent to the Mupaka Fault (Fig. 4.1). It is generally observed in the Intercalated siltstone (Ng 1.1.1.2), where it is composed of siltstones and mudstones which comprise mainly quartz, feldspar, muscovite and biotite (Figs. 4.7, 4.8 and 4.9). Occasional dropstones are present, they are composed of quartz, biotite, plagioclase and rare carbonate; and their size ranges from 0.5 to 1.5 cm. Bedding (S_0) is spaced from 1 mm to 1 cm. The S_1 foliation is defined by alignment of minerals within the rocks (mostly muscovite and quartz), alignment of fine- and coarse-grained sulphides (chalcopyrite, bornite and chalcocite), occasional alignment of clasts and alignment of occasional strain fringes/shadows around dropstones. The angle between the steep beds and the S_1 foliation is about 30° (Fig. 4.7a, c and Fig. 4.8). Mesoscopic faults within the steep bedding are defined by the displacement of beds. In addition, they contain copper sulphides. These mesoscopic structures are interpreted as a result of soft sediment deformation during the deposition of sedimentary rocks (Fig. 4.7a, b). Clasts disrupt and deform the laminations and suggest that this occurred when the sedimentary were unconsolidated (Fig. 4.7 c).

The highest copper grade is coincident with steeply dipping bedding in nine boreholes with thicker Basal diamictite located adjacent to the Mupaka Fault. This steep bedding appears to be a local control for copper mineralisation (Fig. 4.6). The drilled thickness of the zone with steep bedding varies from 20 cm to 2 m. Mesoscopic faults are common features seen within the steeply bedded zone, they generally show a normal sense of movement (Fig. 4.7). The steep bedding strikes NNW/SSE (349/75E), this orientation is parallel to the orientation of the growth fault and perpendicular to the trend of S_1 foliation (Fig. 4.10). In the same borehole, macroscopic observations and structural measurements reveal that S_1 within the steep bedding shows a similar NE strike compared to the core with gently-dipping beds (Fig. 4.10). Also the minerals that define S_1 foliation in steep bedding are similar to the minerals defining S_1 in gently-dipping beds.

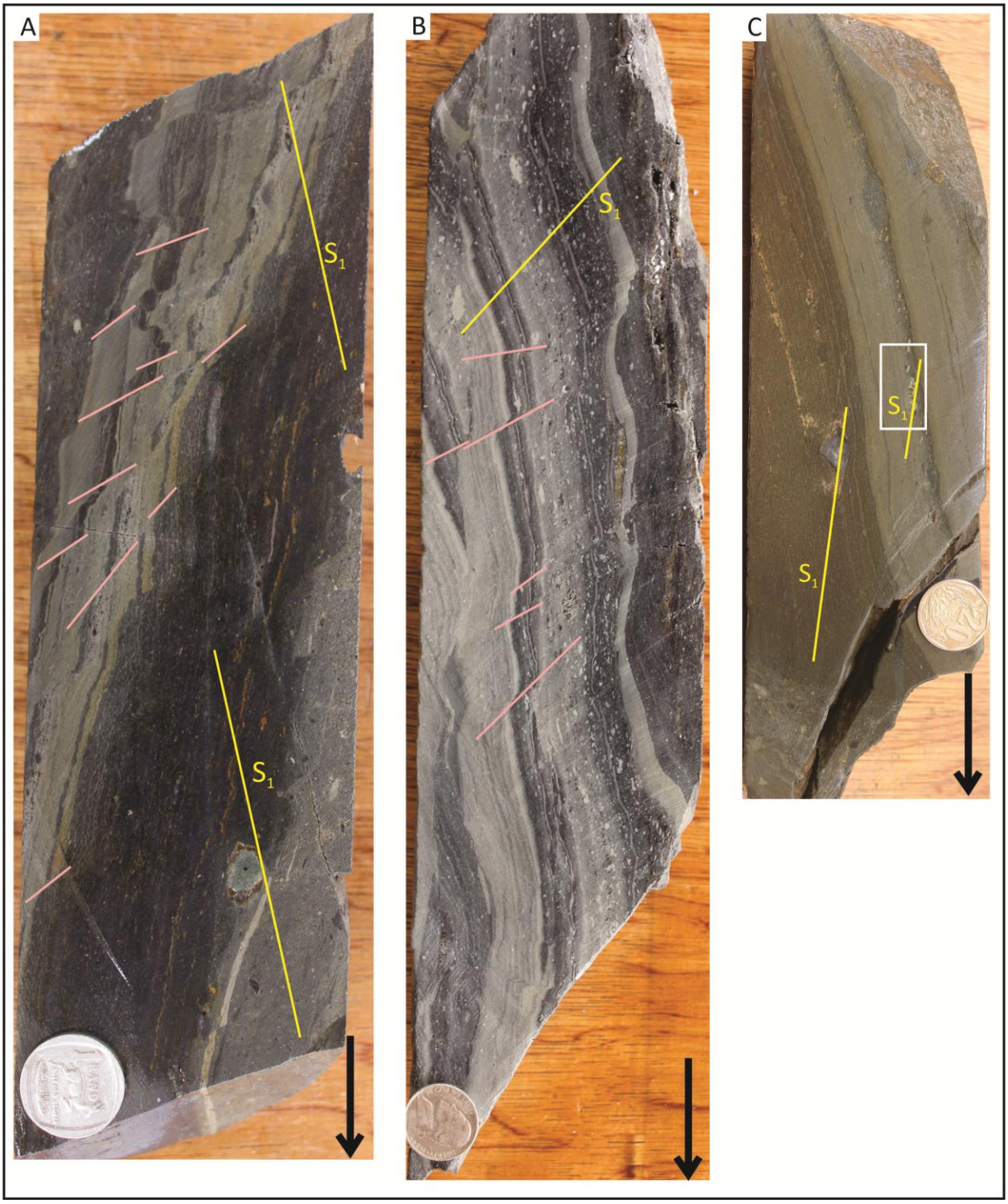

Fig. 4.7: Photographs of hand samples illustrating sub-vertical bedding containing high-grade copper mineralisation. The pink lines show mesoscopic faults. The width of the borehole core is 6.4 cm (HQ core). (A). Siltstone/mudstone displaying steep bedding with abundant fine-grained bornite and traces of chalcopyrite. Bornite is present in strain fringes to the clast (bottom right). An S_1 foliation is defined by alignment of coarse-grained bornite (yellow line). Mesoscopic faults are gently dipping and show a normal sense of movement. DKMC_RD432, 300.14 - 300.31 m. The azimuth of the borehole is 360° and its inclination is -90°. (B). Steep bedding

associated with fine- to coarse-grained bornite and traces of chalcopyrite in siltstone/mudstone. Mesoscopic faults show dominantly a normal sense of movement relative to steep bedding. The bedding shows soft sediment deformation. DD860, 173.20 m - 174 m. The azimuth of the borehole is 270° and its inclination is -90°. (C). Steep bedding overprinted by an S_1 foliation defined by alignment of fine- and coarse-grained chalcopyrite. Chalcopyrite occurs also in strain fringes around the occasional clast (middle of the sample). The fringe structure is elongate and parallel to the foliation (S_1). DMAK_RD030, 641.80 - 642.03 m. The azimuth of the borehole is 270° and its inclination is -80°. The black arrows show downhole direction.

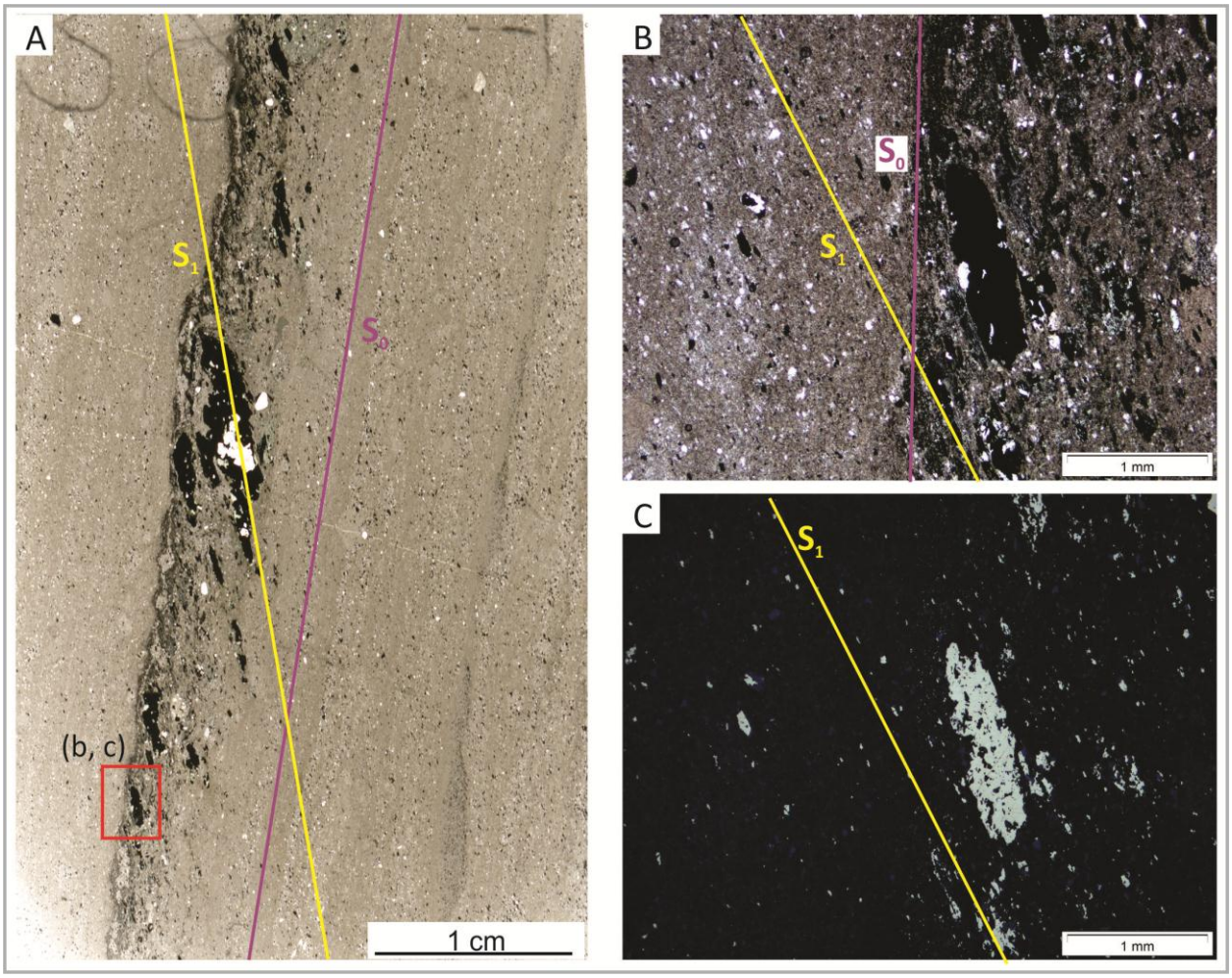

Fig. 4.8: Relationship between foliation (S_1) and steep bedding. DMAK_RD030, 641.86 – 641.90 m (white square in Fig. 4.7c). (A). Scanned thin section showing steep bedding and foliation (S_1). The alignment of coarse-grained chalcopyrite (black areas) defines a foliation (S_1) which occurs at an angle of about 30˚ to the steep bedding. The beds are spaced from 1 to 5 mm apart. (B). Transmitted light, plane polarised photomicrograph showing detail of A. The rock is composed of a fine-grained matrix which comprises quartz, biotite and minor chlorite. Chlorite and quartz are present in the rims of clasts. Some minerals within the rocks are aligned and form S_1 foliation. (C). Reflected light, plane polarised photomicrograph of (B) showing a strong foliation (S_1) defined by the alignment of fine- and coarse-grained chalcopyrite.

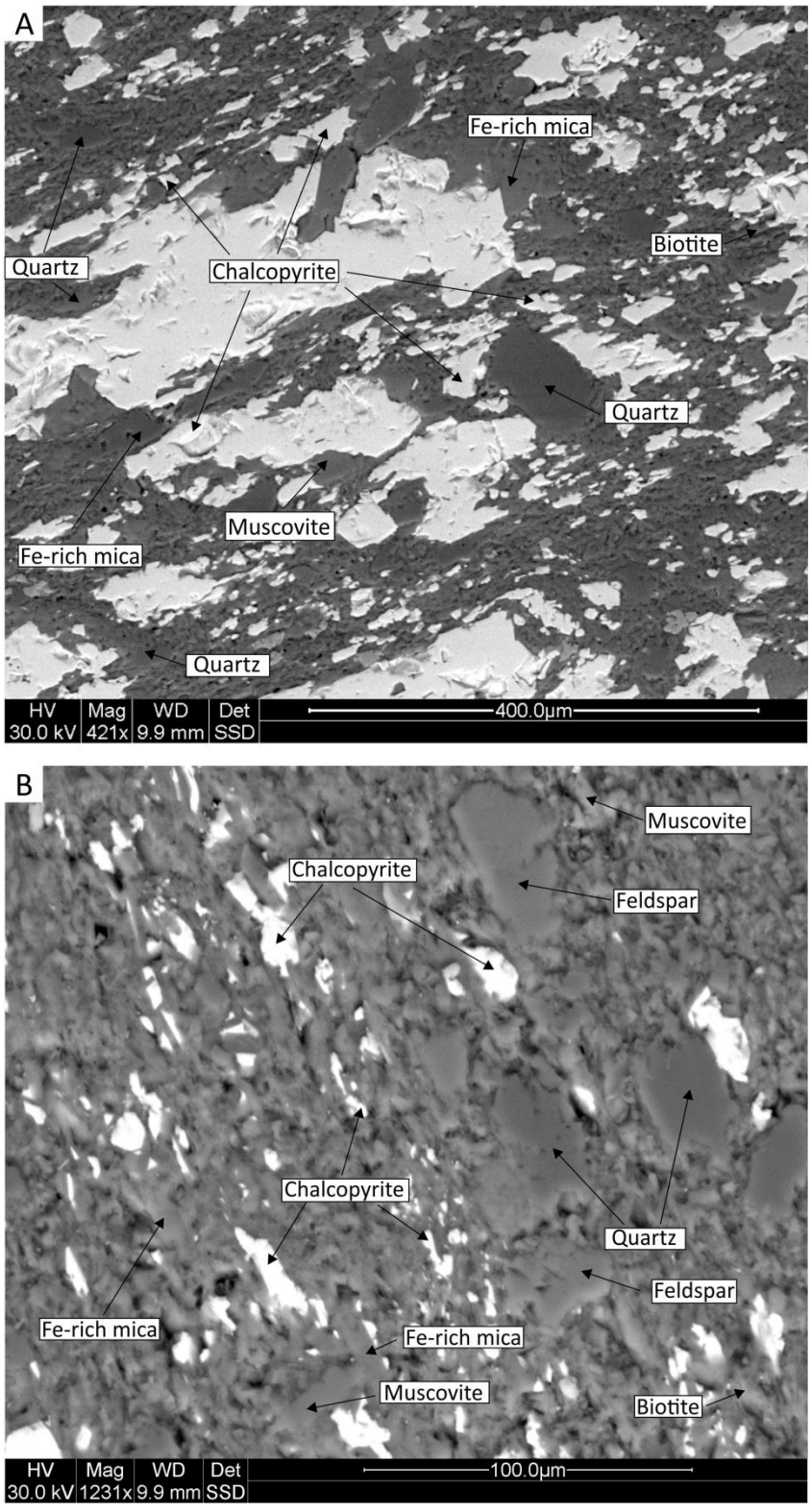

Fig. 4.9: SEM images for the steep bedding. (A). S_1 foliation defined by the alignment of chalcopyrite, quartz, muscovite, biotite and iron-rich mica. Chalcopyrite occurs as elongated and aligned grains defining an S_1 foliation. From DMAK_RD030 at 641.86 m. (B). S_1 foliation defined by the alignment of quartz, feldspar, chalcopyrite, biotite and muscovite. From DKMC_GD002 at 379.58 m.

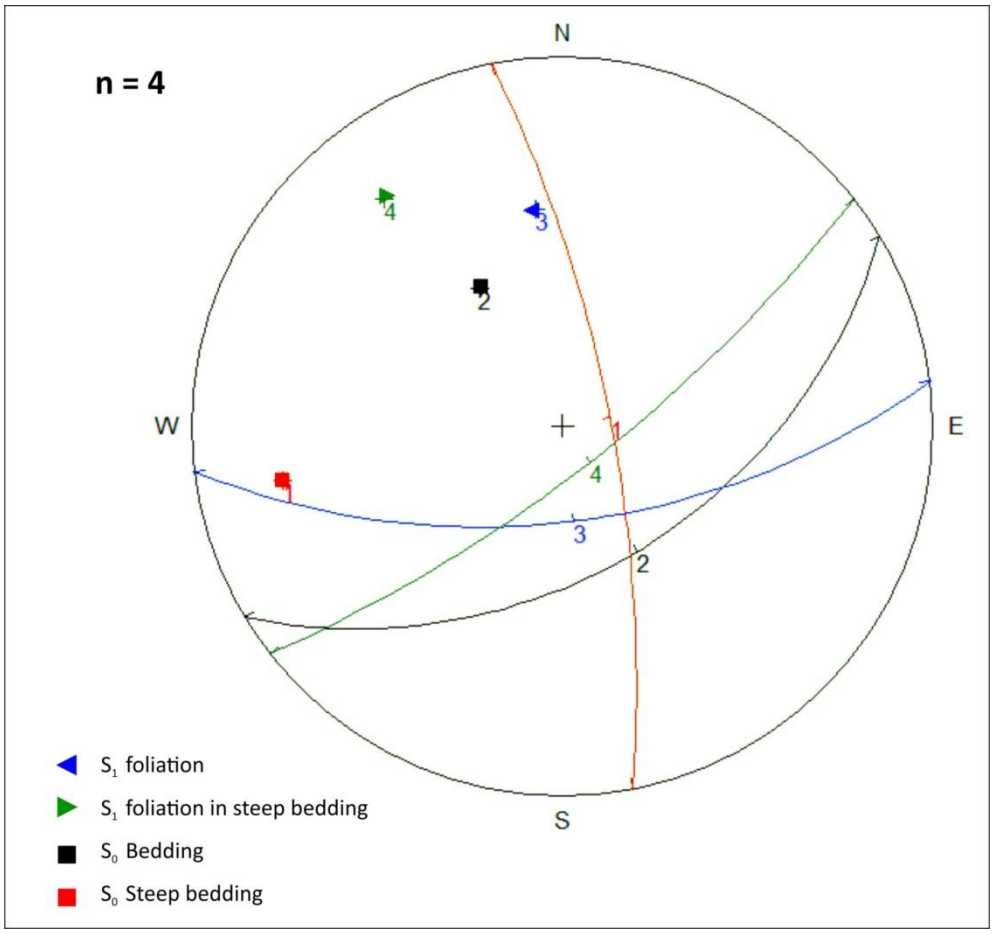

Fig. 4.10: Orientation of structural features from the Basal diamictite (Ng 1.1.1) of the borehole DMAK_RD034. S_0 in the steep bedding is striking NNW/SSE whereas S_0 in the adjacent beds is striking ENE/WSW. The orientation of S_1 foliation in steep bedding is similar to that in the gently dipping beds of the neighbouring core.

4.3.2 Soft-sediment deformation structures

Soft-sediment deformation structures occur in sediments that are not yet lithified, they may include load casts, flame structures, slump structures, dish structures, sole markings and seismites (Van Loon, 2009).

Soft-sediment deformation structures are common features observed in the Kamoa deposit. Within the Basal diamictite of boreholes located adjacent to the Mupaka Fault, they are generally observed in and around the steep bedding with high-grade copper mineralisation (Fig. 4.6 and Fig. 4.11). The down-hole length of soft-sediment deformation structures varies from 0.5 cm to 7 m; they include slump folds, load casts, and syn-sedimentary mesoscopic faults.

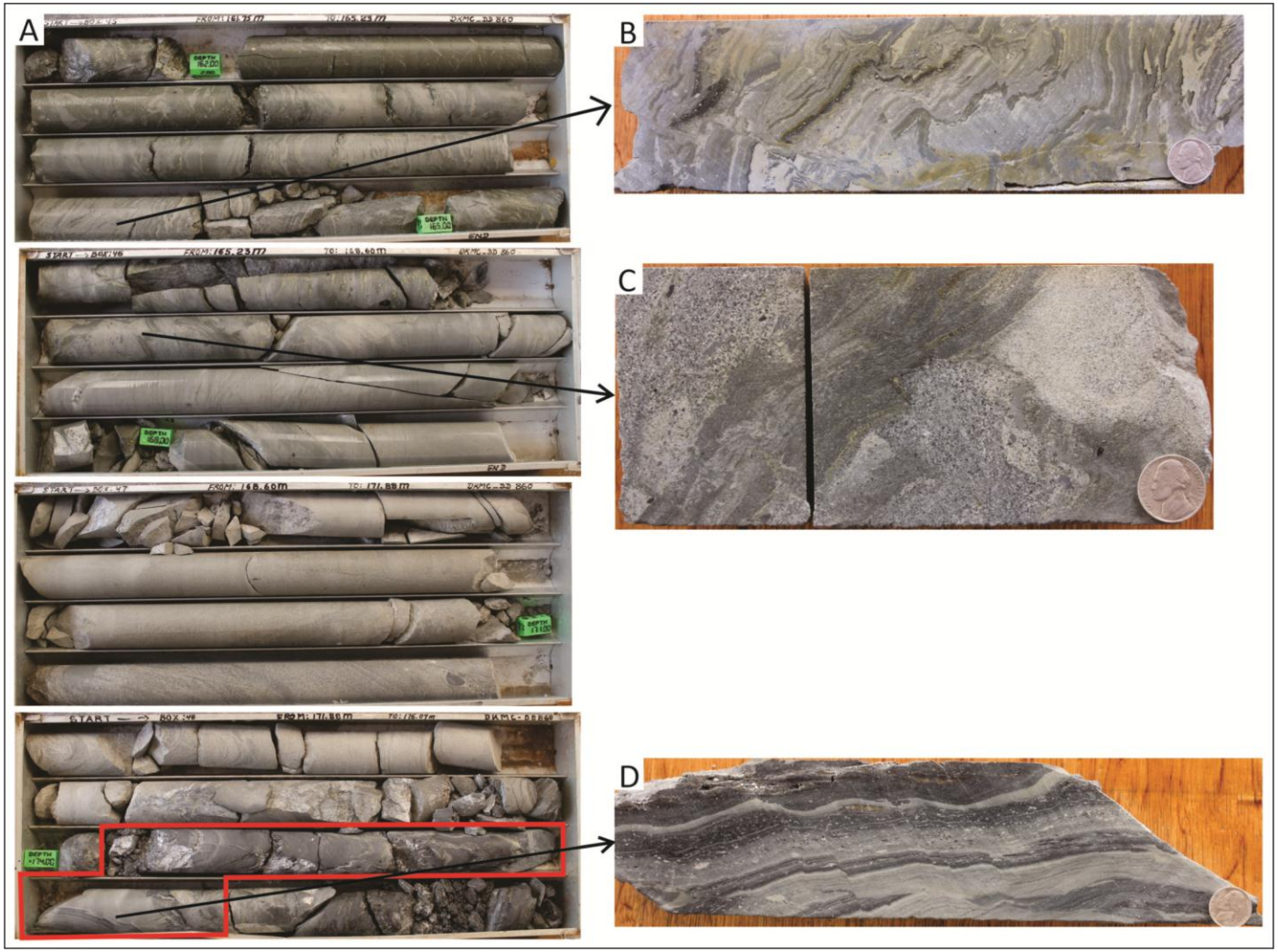

Fig. 4.11: Detailed investigation of the zone in the vicinity of the steep bedding. (A). Soft-sediment deformation and slumping textures commonly observed around the steep bedding (red rectangle). The rock is composed of siltstone and sandstone. D860, 161.75 - 176.09 m. (B). Slump folds and mesoscopic faults in siltstone layer. (C). Sample illustrating a soft-sediment deformation structure in siltstone and sandstone layers. (D). Zone of steep bedding which contains abundant fine- and coarse-grained bornite. Normal mesoscopic faults are also observed.

4.3.3 Mesoscopic faults

Mesoscopic faults are faults observed in hand specimens and outcrop, they are widespread in the Kamoa deposit, where they occur generally as steep features showing a normal sense of movement (Fig. 4.12).

Mesoscopic faults truncating steep bedding are commonly horizontal and show a normal sense of movement relative to bedding; they appear spatially associated with soft-sediment deformation features (Figs. 4.7 and 4.11). Within steep bedding, at different depths, mesoscopic faults generally show a similar orientation relative to the downhole direction, their dip varies between 1 and 20 degrees (Fig. 4.7a, b). Mesoscopic faults are commonly sub-vertical in gently-dipping beds adjacent to the steep beddings while they are gently-dipping in steep bedding.

The orientation of S_1 foliation within the mesoscopic faulted steep bedding is similar to the orientation of S_1 foliation in the neighboring rocks (Figs. 4.10 and 4.12). S_1 foliation is oblique to the mesoscopic faults and forms an angle of about 30° with the S_0 bedding (Figs. 4.7a, b and 4.13).

The orientation of mesoscopic faults was studied using the Kamoa geological dataset (Fig. 4.14). It is important to highlight that the structural measurements were not collected as part of the routine data collection of the thesis because most boreholes had been already cut for geochemical analysis. As a result of the study, it appears most of the mesoscopic faults are steeply dipping and minor gently dipping (Fig. 4.15). The stereographic projection of poles to mesoscopic faults shows a large scatter of data and a preferred orientation cannot be deducted. However, some of the mesoscopic faults appear similar to the trend of the Mupaka Fault (Fig. 4.15).

4.3.4 Timing of features within the steep bedding

Bedding was originally formed horizontally during the rock-forming process. Gently-dipping mesoscopic normal faults are commonly associated with the steep bedding while steeply-dipping normal faults occur in boreholes further from the zone of steep bedding. These mesoscopic faults are all interpreted as syn-sedimentary features formed prior to lithification of sedimentary rocks. Therefore within the steep bedding, the mesoscopic faults have been rotated with the bedding from steep to gently dipping during the development of the growth fault.

Isopach maps and structural features from borehole core suggest that growth faults of varying size (small to large scale) may form a network system within the deposit area. Steep bedding is observed in four boreholes adjacent to the potential growth fault located in the south of the Kamoa dome (Figs. 4.16 and 4.17).

Growth faults may form during extension and early rifting of the basin. Similar structures have been described in the Zambian Copperbelt (Selley *et al.,* 2005; Broughton, 2014).

S_1 foliation is the youngest major event within the steep bedding zone, it is not related to the rotation of beds. S_1 is weakly developed and does not deform early structural features such as mesoscopic faults.

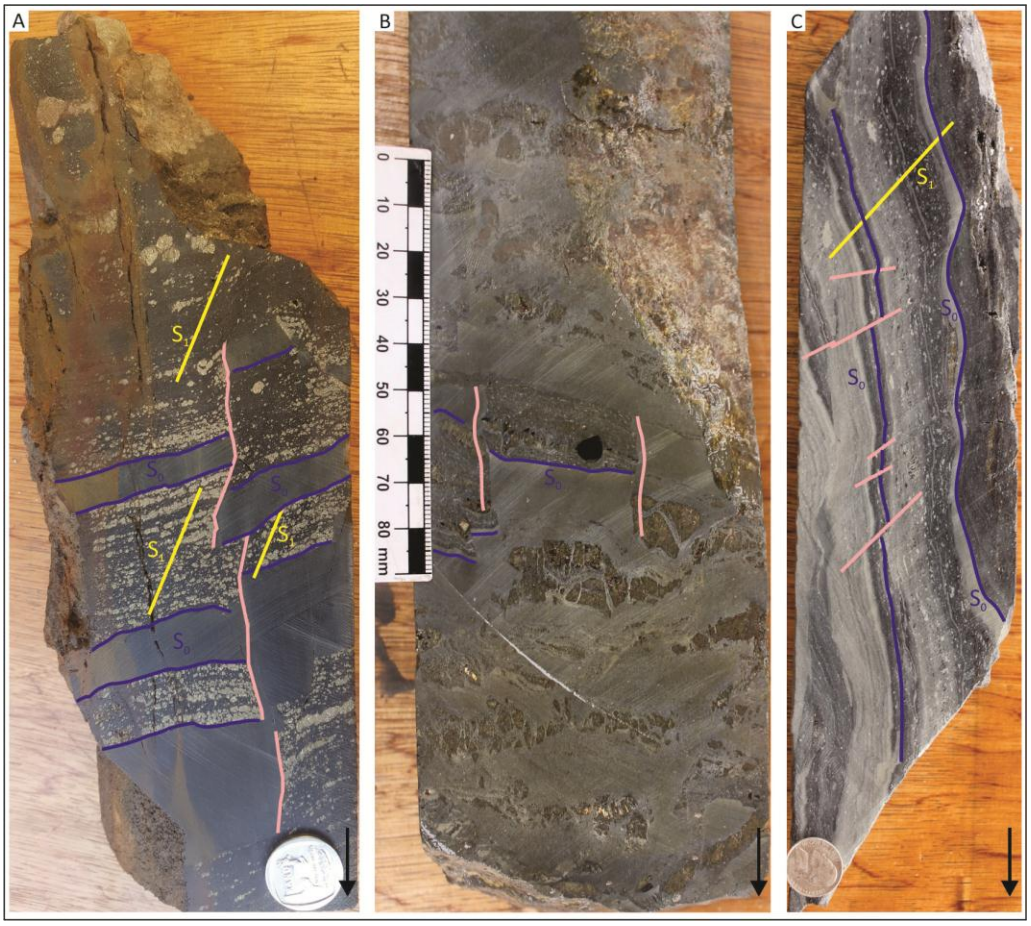

Fig. 4.12: Hand samples illustrating S_0 bedding and mesoscopic faults both in steep and gently dipping beds for the borehole DD860. Mesoscopic faults are shown by pink lines. (A). Sub-vertical mesoscopic faults in gently dipping beds. S_1 foliation is defined by the alignment of coarse-grained pyrite. Depth at 125.02 - 125.14 m. (B). Steep mesoscopic faults defined by the offset of beds. Depth at 165.75 – 165.90 m. (C). Abundant mesoscopic faults showing dominantly a normal sense of movement defined by the offset of beds. S_1 foliation is defined by the alignment of fine-grained bornite. Depth at 173.20 - 174 m.

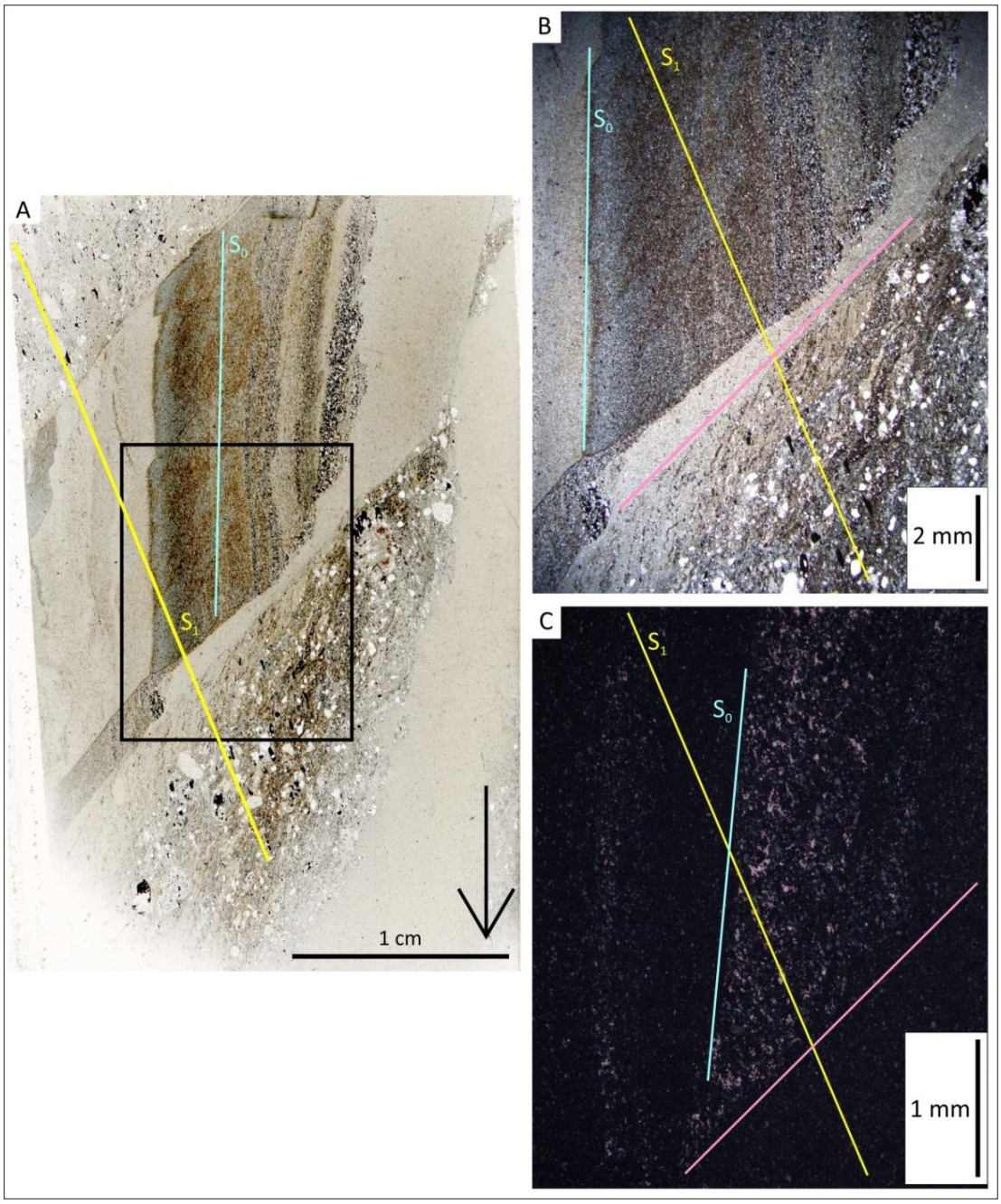

Fig. 4.13: Features of mesoscopic faults within the steep bedding. (A). Thin section including mesoscopic faults showing a normal sense of movement identified by the displacement of siltstones and mudstones beds. A weak S_1 foliation defined by the alignment of sulphides is observed (black areas). S_1 foliation is oblique to the mesoscopic fault and forms an angle of about 30° with the steep bedding. This indicates that S_1 postdates the mesoscopic fault. (B). Detail of A. Plane-polarised photomicrograph showing the mineralogy of the rock which is mainly composed of quartz, biotite and muscovite. Abundant quartz fragments are observed in siltstone/mudstone (right corner, 0.5 to 50 mm), they seem parallel to S_0. The mesoscopic fault is defined by the displacement of siltstone beds. (C). Reflected light, cross-polarised photomicrograph of B showing a weak foliation defined by the alignment of fine- and coarse-grained bornite. FT_82 from borehole DKMC_RD432 at 333 m depth. The black arrow shows the downhole direction.

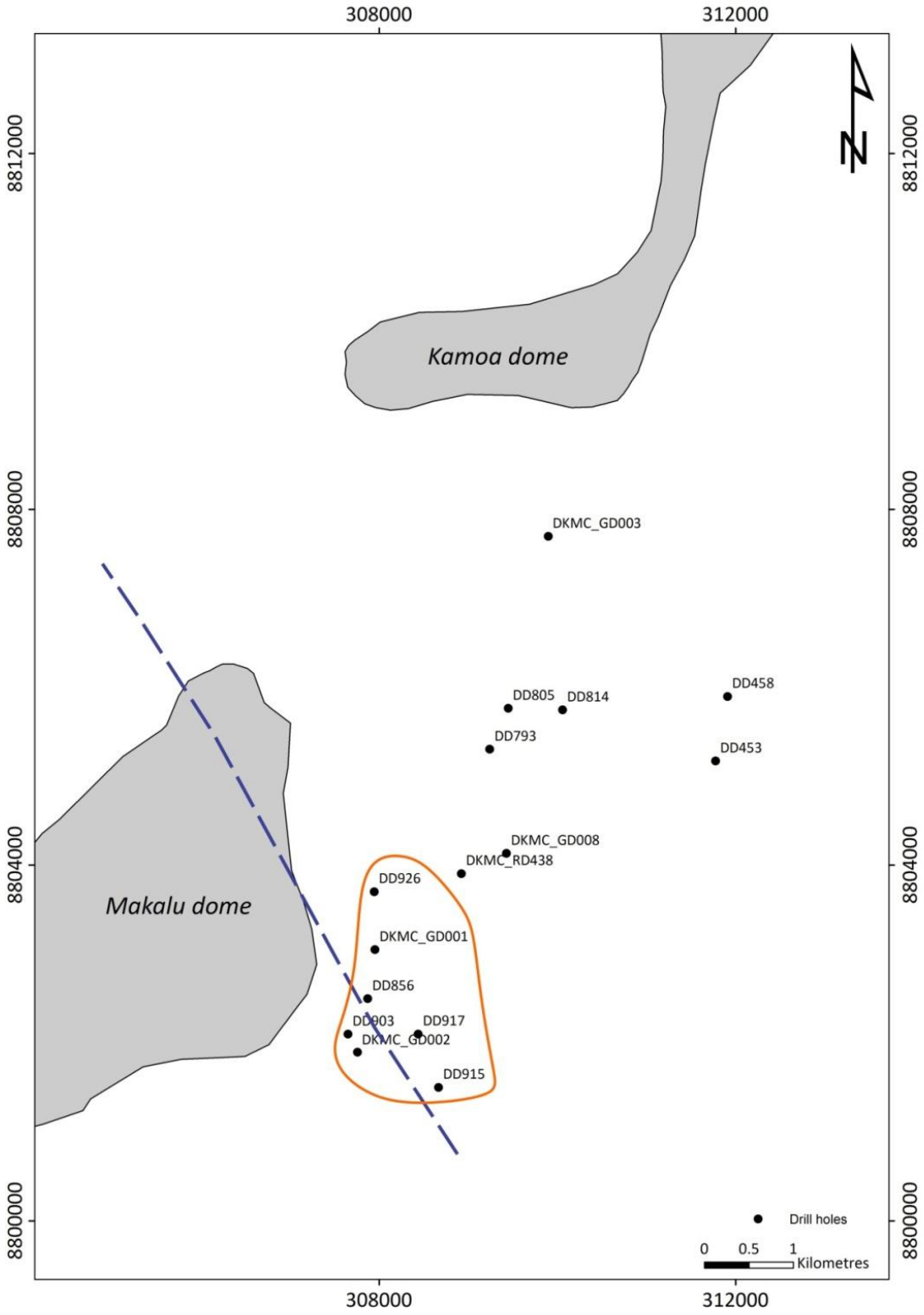

Fig. 4.14: Map showing the distribution of boreholes with mesoscopic fault measurements. The blue dashed line shows the approximate location of the Mupaka Fault. The orange polygon encircles the boreholes located adjacent to the Mupaka Fault.

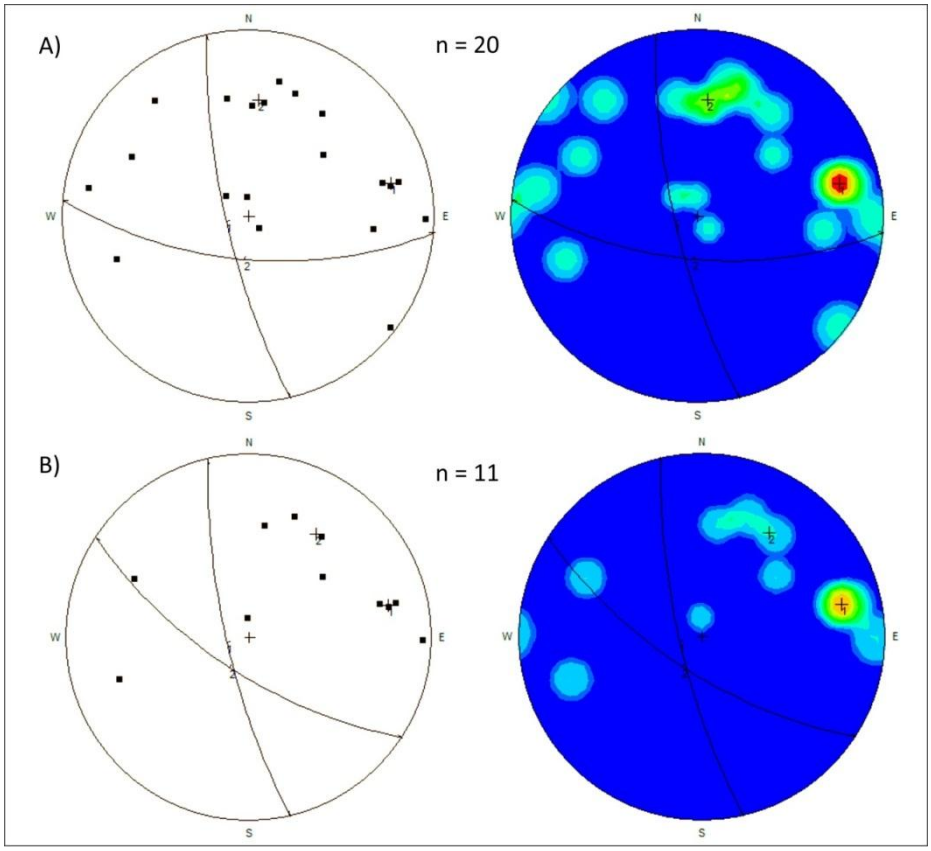

Fig. 4.15: Lower hemisphere equal area stereographic projection of poles to mesoscopic faults recorded in the Nguba Subgroup rocks. (A). All measurements recorded (15 boreholes). (B). Measurements within boreholes adjacent to the Mupaka Fault (7 boreholes).

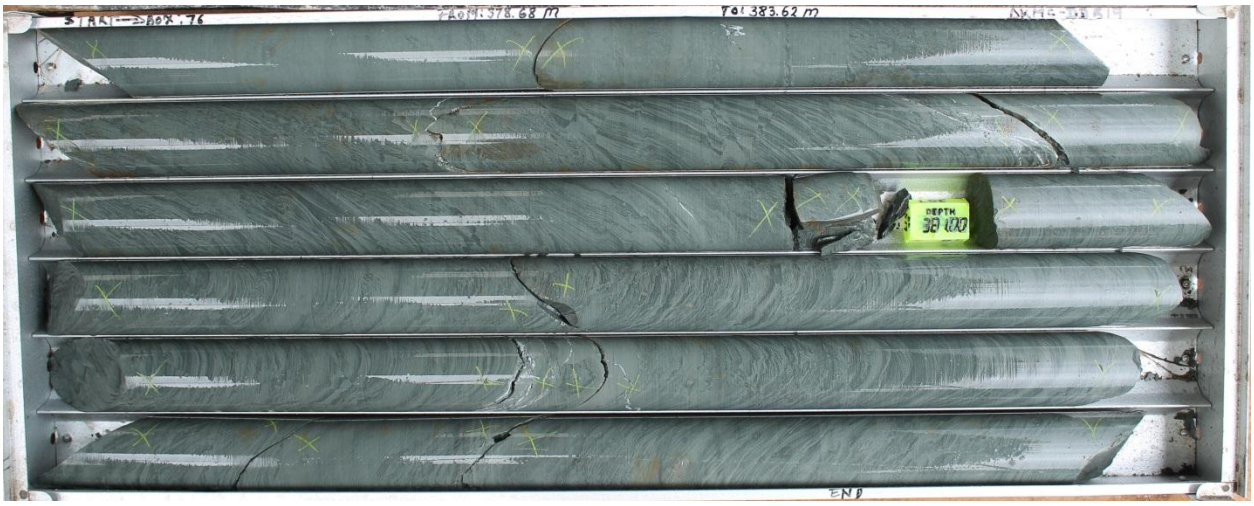

Fig. 4.16: Photograph of core box showing steep bedding associated with mesoscopic faults. The steep bedding looks similar to that adjacent to the Mupaka Fault but located higher in the stratigraphy (Ng 1.1.6). DD519, 378.68 – 383.62 m. The azimuth of the borehole is 270° and its inclination is 85°.

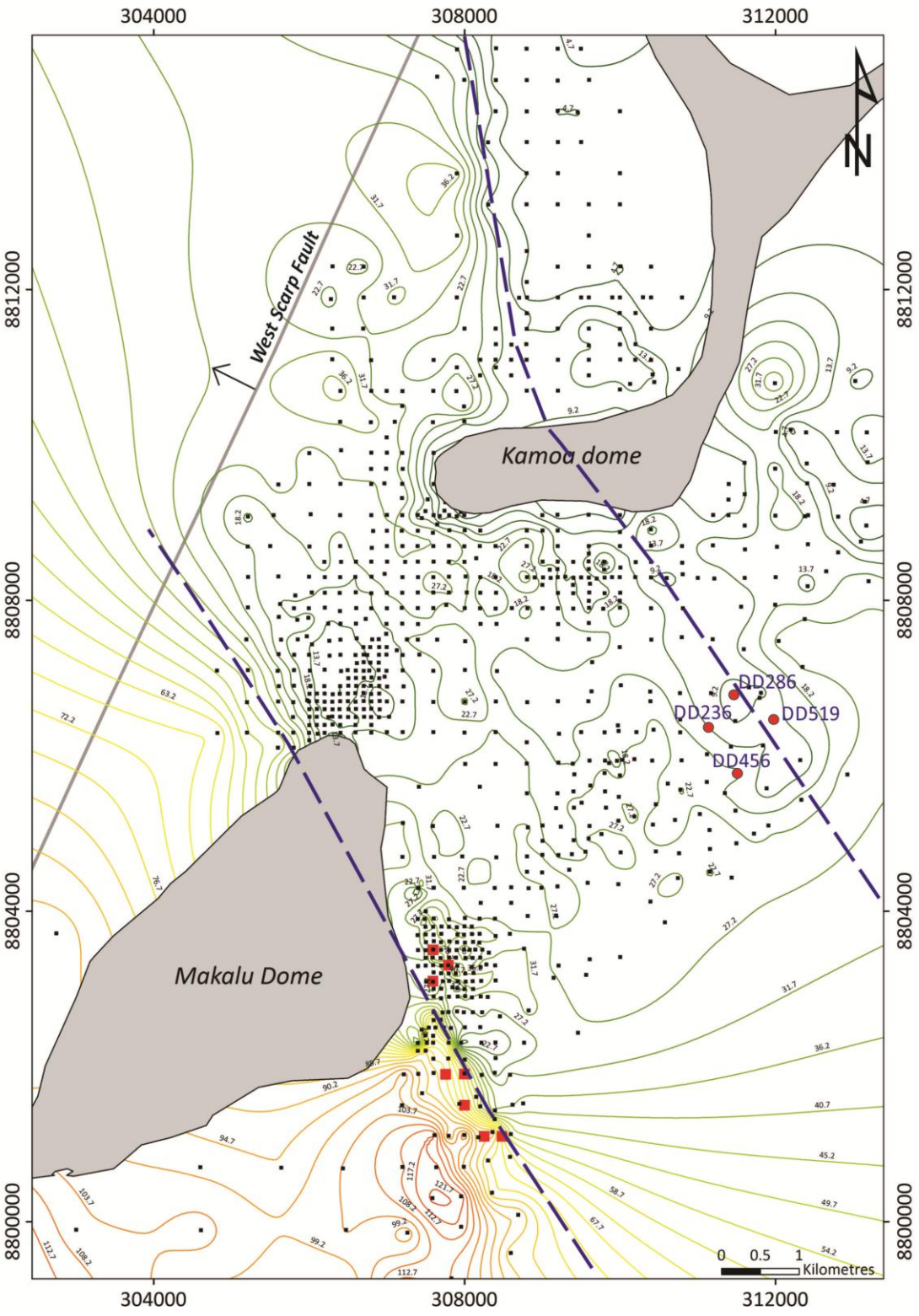

Fig. 4.17: True thickness isopach map of the Basal diamictite and interpreted growth faults. The blue dashed lines show the approximate location of interpreted growth faults which commonly trend NNW-SSE. In the north of the Kamoa dome the growth fault trends N-S. The boreholes with steep bedding around the Mupaka Fault are labelled.

4.4 Secondary foliation S_1

4.4.1 Introduction

Foliation is a general term used to describe any planar feature that occurs penetratively in a body of rock (Marshak and Mitra, 1988; Passchier and Trouw, 2005). Foliations are subdivided into primary and secondary, the first being of sedimentary or igneous origin and the second formed by deformational processes (Marshak and Mitra, 1988; Passchier and Trouw, 2005). Their study in thin section and their interpretation is an important tool to unravel the tectonic and metamorphic evolution of an area. Foliations are also used as reference structures to establish the relative growth periods of metamorphic minerals, especially porphyroblasts (Passchier and Trouw, 2005).

4.4.2 Foliation within borehole core

Within the Kamoa deposit, the gently dipping host rocks of the lower Nguba Group locally contain a steep to vertical foliation. This foliation is commonly defined by the alignment of fine- and coarse-grained sulphides, alignment of minerals within the matrix and locally by the heterogeneous alignment of clasts (Figs. 4.18 and 4.19).

The alignment of clasts is very weak to inconsistent and defines generally a weak foliation (Fig. 4.18 a-c). Sulphides including bornite, chalcopyrite, pyrite, pyrrhotite and chalcocite, most of which consistently define a variably weak to strong foliation within the Kamoa rocks (Fig. 4.19).

In this study, the intensity of the S_1 foliation has been classified in 4 categories: very weak, weak, moderate and strong (Figs. 4.18 and 4.19). The average orientation of S_1 appears to be heterogeneous, its variation is shown in map view (Fig. 4.20) and also tabulated (Table 4.1). In most areas S_1 dips steeply to the southeast, however in three boreholes between the Kamoa and Makalu domes the foliation dips to the northwest. It is important to note that the S_1 foliation does not change attitude in the zone with steep bedding.

In the boreholes located close to the fold axial traces of both sets of folds (Fig. 4.3.B) the foliation is strong and defined by the alignment and elongation of clasts (Fig. 4.21). S_1 foliation seems intensely developed along folds and less developed away from these features, this suggests a relationship between foliation and folding. It is not possible to distinguish between the two sets of folds.

Table 4.1: Illustration of the orientation of S_1 foliation in different areas of the Kamoa deposit.

Areas	**Strike/dip**
East and south east of the Kamoa dome	044/78SE
Central area of the Kamoa deposit	089/85S; 012/74E
East of the Makalu dome	057/71SE
South east of the Makalu dome	072/60SE
South of the Kamoa dome	064/71NW

The variability, distribution, intensity and geometry of the S_1 foliation has been investigated in detail from several single boreholes to better understand the huge scatter of foliation measurements (Fig. 4.23). As a result of the study, it appears that the orientation of S_1 is similar at different depths within the same borehole (Fig. 4.23c). However, the dip of S_1 foliation varies according to the rock or mineral defining the foliation; chalcopyrite commonly show a steeply dipping foliation compared to pyrite (Fig. 4.23b). Also, the intensity of S_1 varies between lithological units; it appears more developed in siltstone and diamictite layers while it is weak in Nguba sandstone (Fig. 4.23a). The heterogeneity of foliation may be due to the core orientation as well as to the ductility of minerals defining the foliation.

4.4.3 The Rf-ϕ method

The clasts in the diamictites tend to have their long axes in various orientations, thus the Rf-ϕ method is the appropriate method used to estimate the strain on elliptical objects (Ramsay and Huber, 1983; Twiss and Moores, 1992, Fossen, 2010).

In the study area, the Rf-ϕ method has been used to evaluate the strain in the diamictite assuming that clasts reflect the finite strain in the rock (Rf). Strain measurements include the following parameters: the long axis (X); the short axis (Y) and the angle between the long axis and the reference line (Phi) (Fig. 4.24). Two boxes of core illustrating respectively a non-foliated and a moderately-foliated rock have been investigated in detail and the strain measurements described above were obtained from the clasts, then graphs showing a plot of the ellipticity (X/Y) against phi were analysed. As a result of the study, it appears that the rock with a moderate foliation displays a cluster of points whereas the non-foliated rock shows no obvious pattern to the point distribution (Fig. 4.24). This result suggests that elongation of the clasts occurred during the foliation development.

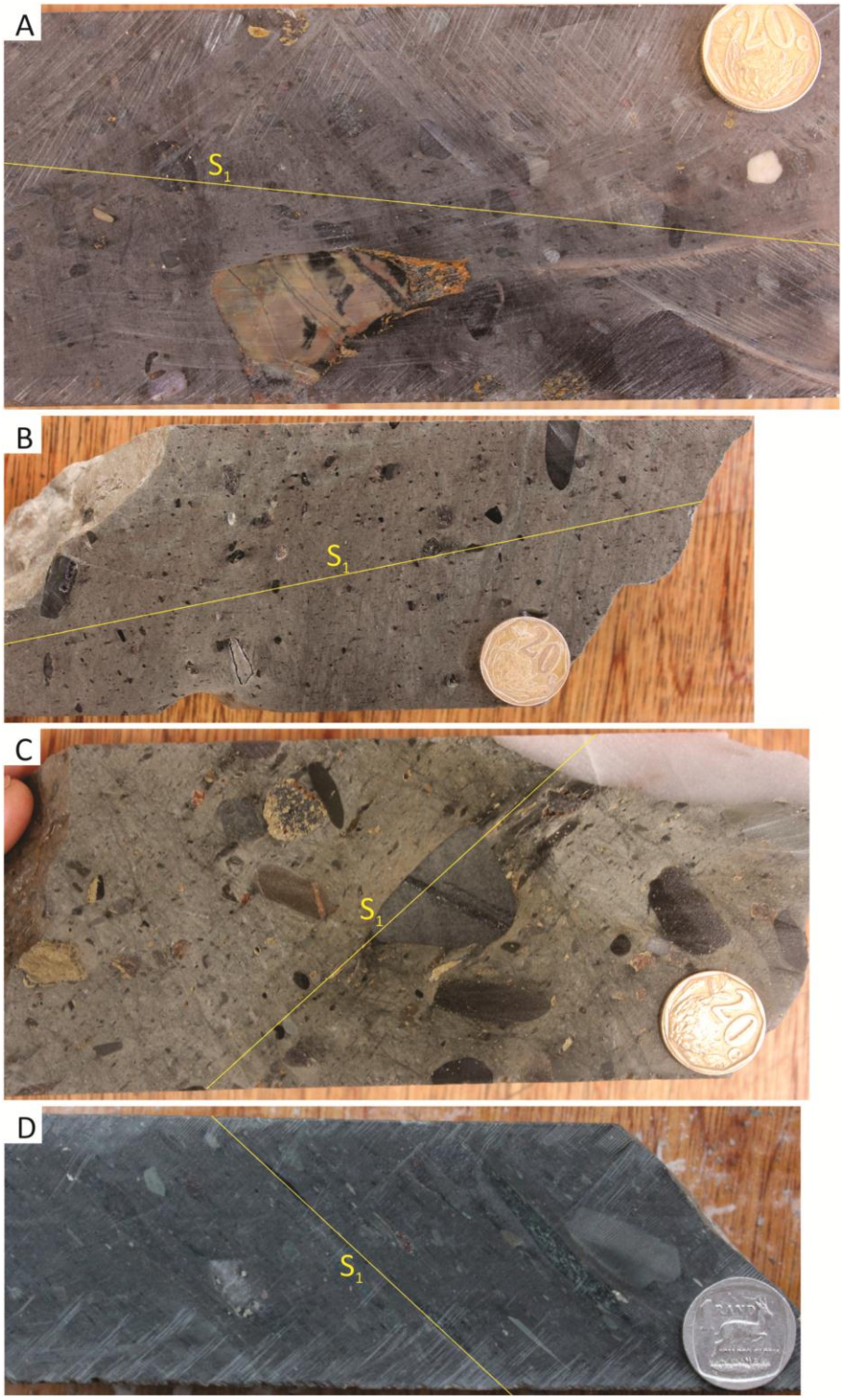

Fig. 4.18: S_1 foliation defined by the alignment of clasts seen in photographs of borehole core. (A). A very weak foliation defined by very poor alignment of clasts. DMAK_DD014, 528.48 - 540.77 m. (B). A weak foliation defined by poor alignment of clasts. DD888, 274.66 – 279 m. (C). Moderate foliation defined by alignment of clasts and coarse-grained chalcopyrite. Most large clasts are not aligned with S_1. DD453, 1147.61 - 1150.29 m. (D). A strong foliation defined by alignment and elongation of clasts. DTJI_DD001, 398.61 – 398.82m.

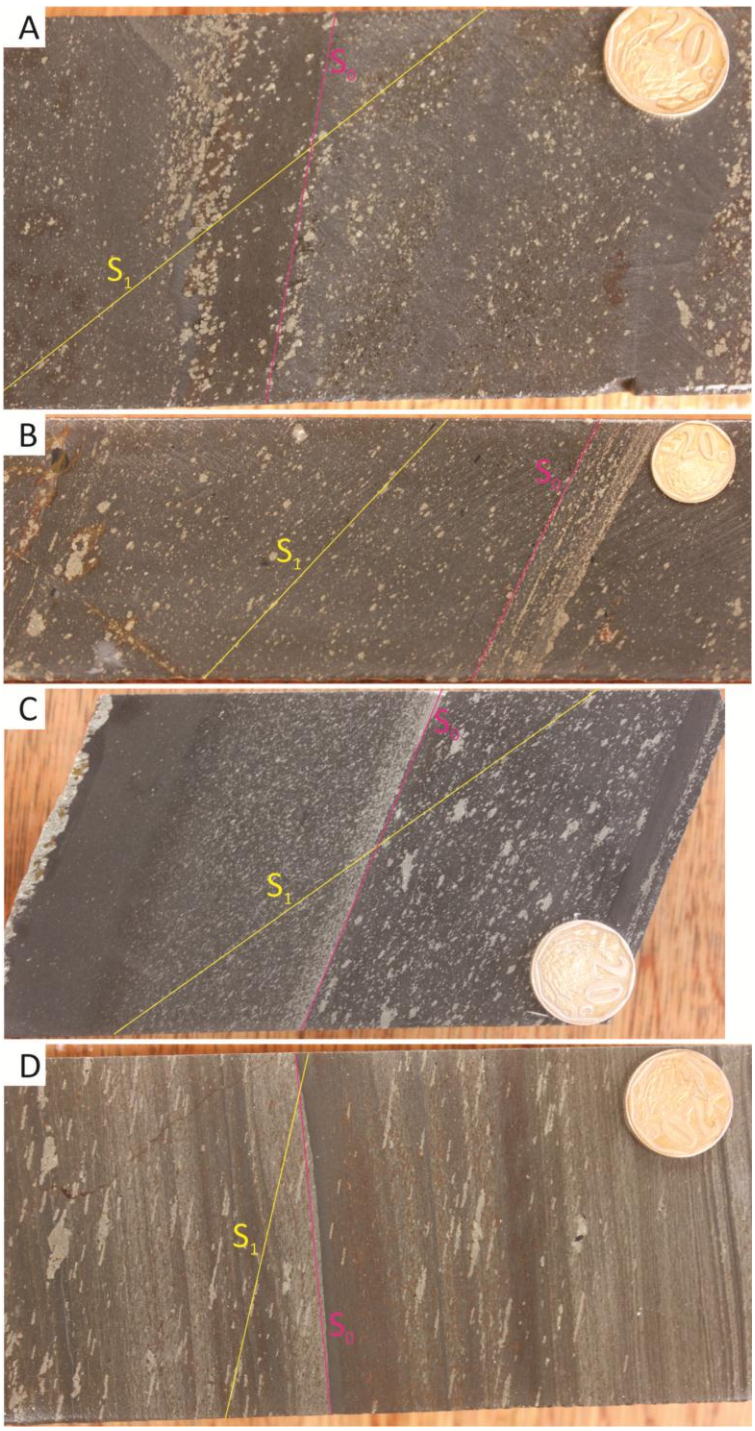

Fig. 4.19: Photos of borehole core showing S_1 foliation defined by alignment of sulphides. (A). A very weak foliation defined by alignment of coarse-grained pyrite. DD869, 209.50 – 216 m. (B). A weak foliation defined by alignment of coarse-grained pyrite. DD405, 499.03 – 503 m. (C). A moderate foliation defined by alignment of coarse-grained pyrite. DD888, 196.18 – 216.70 m. (D). A strong foliation defined by the alignment of coarse-grained pyrite. DMAK_DD013, 589 – 595.24 m. S_0 bedding is also observed in the core photos, it forms an angle of about 30° with the S_1 foliation.

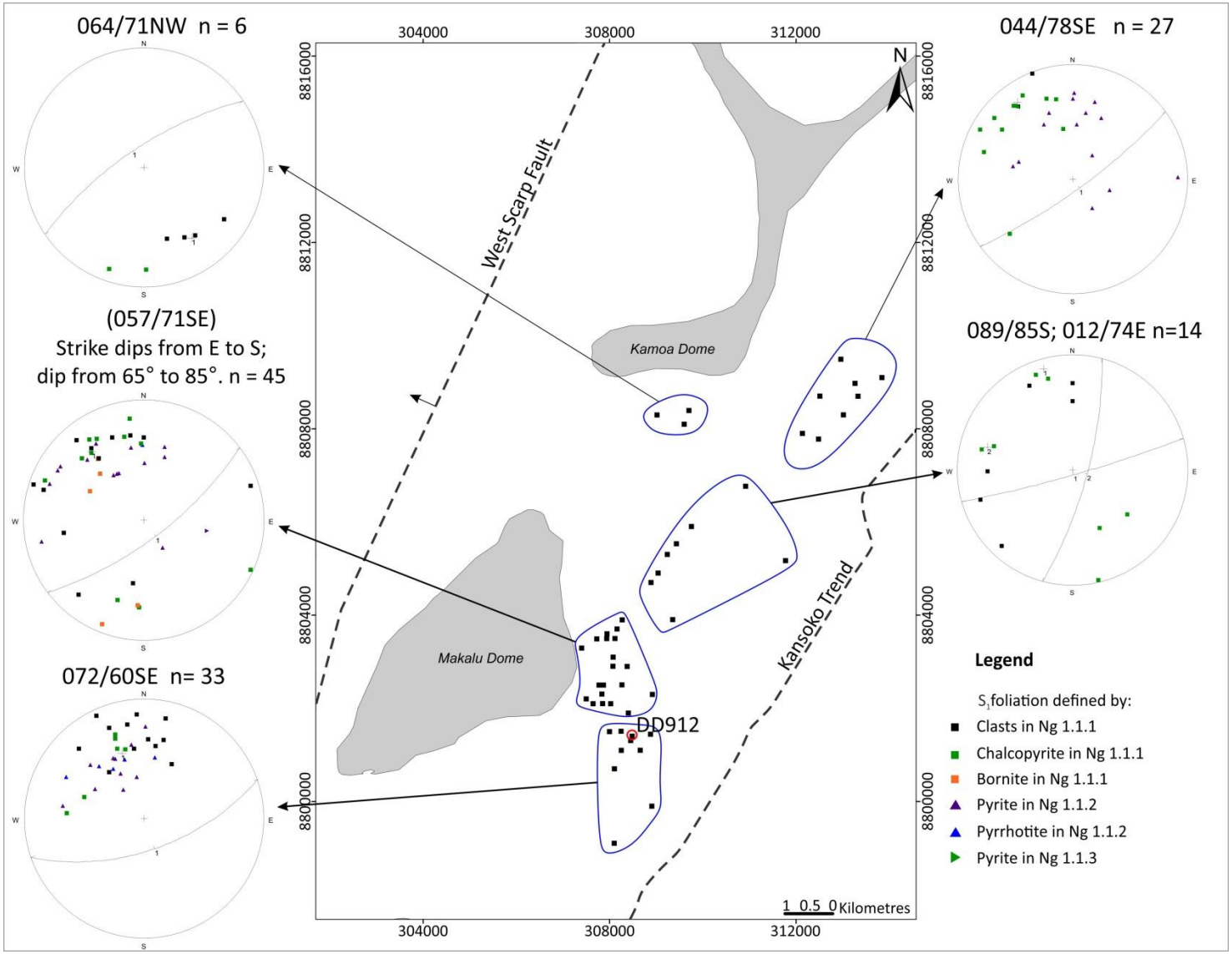

Fig. 4.20: Map showing the orientation of S_1 foliation in different areas of the Kamoa deposit. Lower hemisphere equal area stereographic projection of poles to foliations.

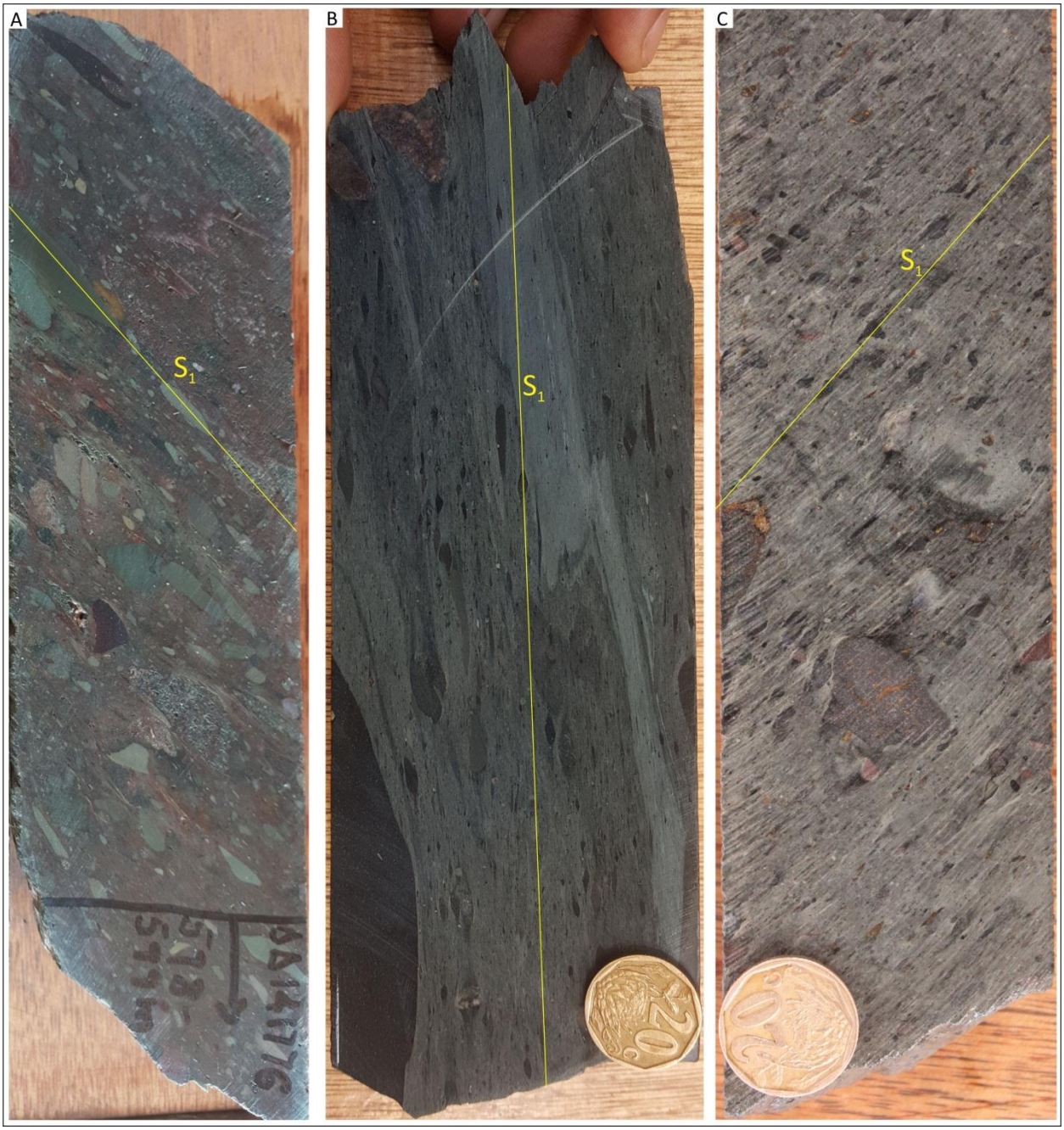

Fig. 4.21: Photographs of borehole core showing a strong foliation. Core photographs are from the boreholes located on the folds. (A). Strong foliation defined by the alignment and elongation of clasts. DTJI_DD001, 597.80 - 598 m. (B). Strong foliation defined by the alignment and elongation of clasts. DD071, 101.73 - 101.89 m. (C). Strong foliation defined by the alignment of clasts. DD037, 1050 – 1050.15 m.

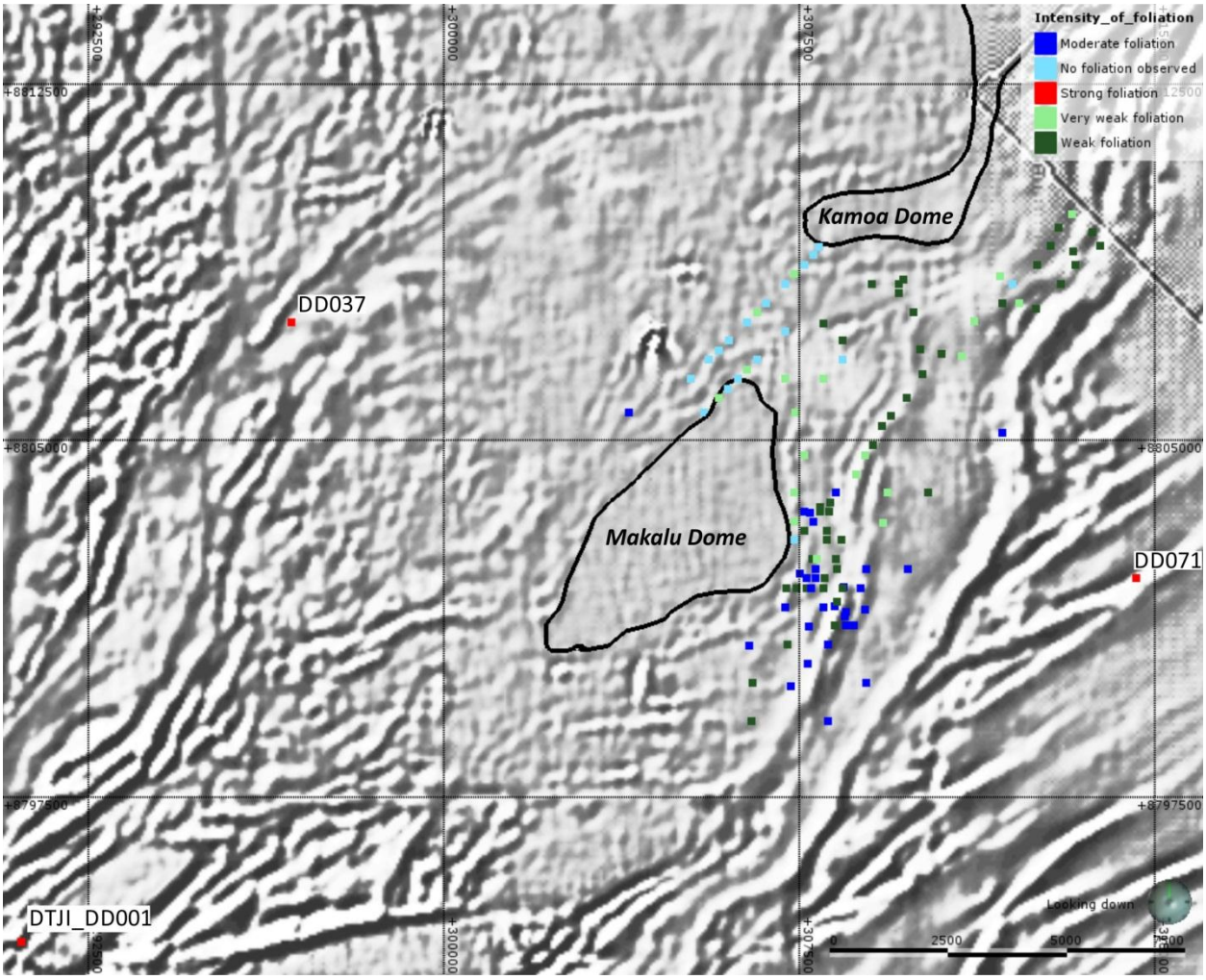

Fig. 4.22: Median intensity of S_1 foliation superimposed on a magnetic map. S_1 appears more developed along the folds (labelled boreholes). The intensity of foliation was assessed in the Lower laminated pyritic siltstone/sandstone (Ng 1.1.2) and in the Basal diamictite (Ng 1.1.1). Note that for the two boreholes located in west and southwest part of the deposit (left side of the map), the intensity was assessed in the Upper diamictite unit (Ng 1.1.3).

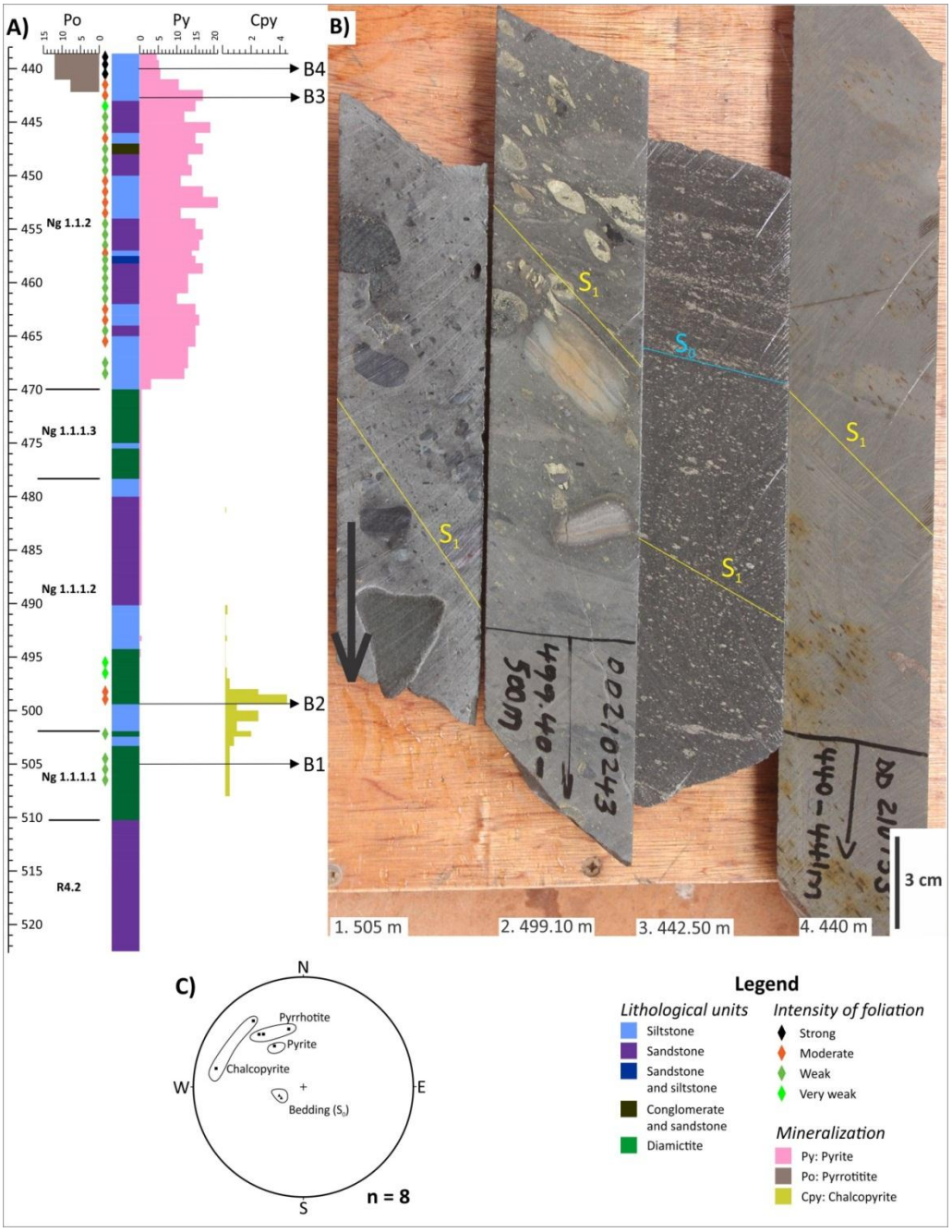

Fig. 4.23: Orientation of S_1 foliation at different depths in borehole DD912. (A). The intensity of S_1 appears moderate and strong in siltstone while it is weak in sandstone. S_1 is defined by sulphides and alignment of clasts. (B). 1. Very weak foliation defined by poor alignment of small clasts at 505 m depth. 2. Weak to moderate foliation defined by alignment of coarse-grained chalcopyrite and aligned strain-shadows at 499.10 m depth. 3. Moderate foliation defined by alignment of coarse-grained pyrite. At 442.50 m depth. 4. Moderate foliation defined by alignment of coarse-grained pyrrhotite and pyrite. At 440 m depth. (C). Lower hemisphere equal area stereonet projection of poles to S_1 foliation in the borehole DD912. S_1 as defined by chalcopyrite and pyrrhotite dips steeply compared to the foliation defined by pyrite. The average orientation of S_1 foliation in the borehole DD912 is striking NE/SW. The azimuth of the borehole is 320° and its inclination is 80°. The black arrow shows the downhole direction.



Fig. 4.24: Evaluation of strain in diamictite. (A). Hand sample showing a non-foliated diamictite, clasts are randomly oriented. Strain parameters are also illustrated. X/Y represents the Ellipticity and phi the angle between the long axis and the reference line. Hand sample from DD749, 452.24 - 452.67 m. (B). Plot of strain measurements recorded in DD749, 447.02 – 452.32 m. A random distribution of points is observed. (C). Diamictite showing a moderate foliation defined by the alignment of clasts. Hand sample from DMAK_DD027, 449.45 – 449.68 m. (D). Plot of strain measurements recorded in DMAK_DD027, 445.20 to 450.19 m. A concentration of points is observed in the upper left part of the diagram.

4.4.4 Foliation microstructures

4.4.4.1 Mechanisms of foliation development

Secondary foliations develop in response to permanent rock deformation (Passchier and Trouw, 2005). The main controlling factors on their development are the composition of the rocks, stress orientation and magnitude, metamorphic conditions including temperature, lithostatic and fluid pressure, and also fluid composition.

Passchier and Trouw (2005) summarised the main processes that are thought to play a role during formation of secondary foliations as follows:

- Mechanical rotation of tabular or elongate grains;
- Solution transfer;
- Crystalplastic deformation;
- Dynamic recrystallisation and the orientation of new grains and subgrains;
- Static recrystallisation and mimetic growth;
- Oriented growth in a differential stress field and
- Microfolding.

Figure 4.25 illustrates the development of foliation by progressive simple and pure shear.

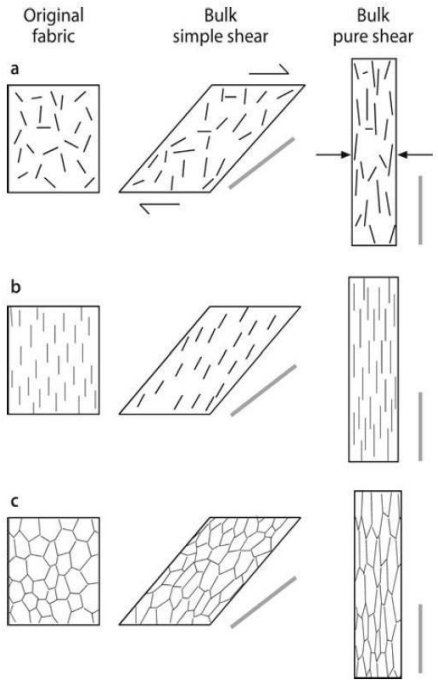

Fig. 4.25: Development of foliation by progressive simple shear and pure shear (Passchier and Trouw, 2005). (a). A random initial orientation of isolated elongate or planar minerals; (b). An initial preferred orientation of isolated elongate or planar minerals; (c). Originally equidimensional grains. In c a grain shape preferred orientation is formed. Grey bars indicate the direction of the *XY*-plane of finite strain for the deformation shown.

During homogeneous ductile deformation, a set of randomly oriented planes will tend to rotate in such a way that their mean orientation will trace the direction of the XY plane of finite strain (Fig. 4.26).

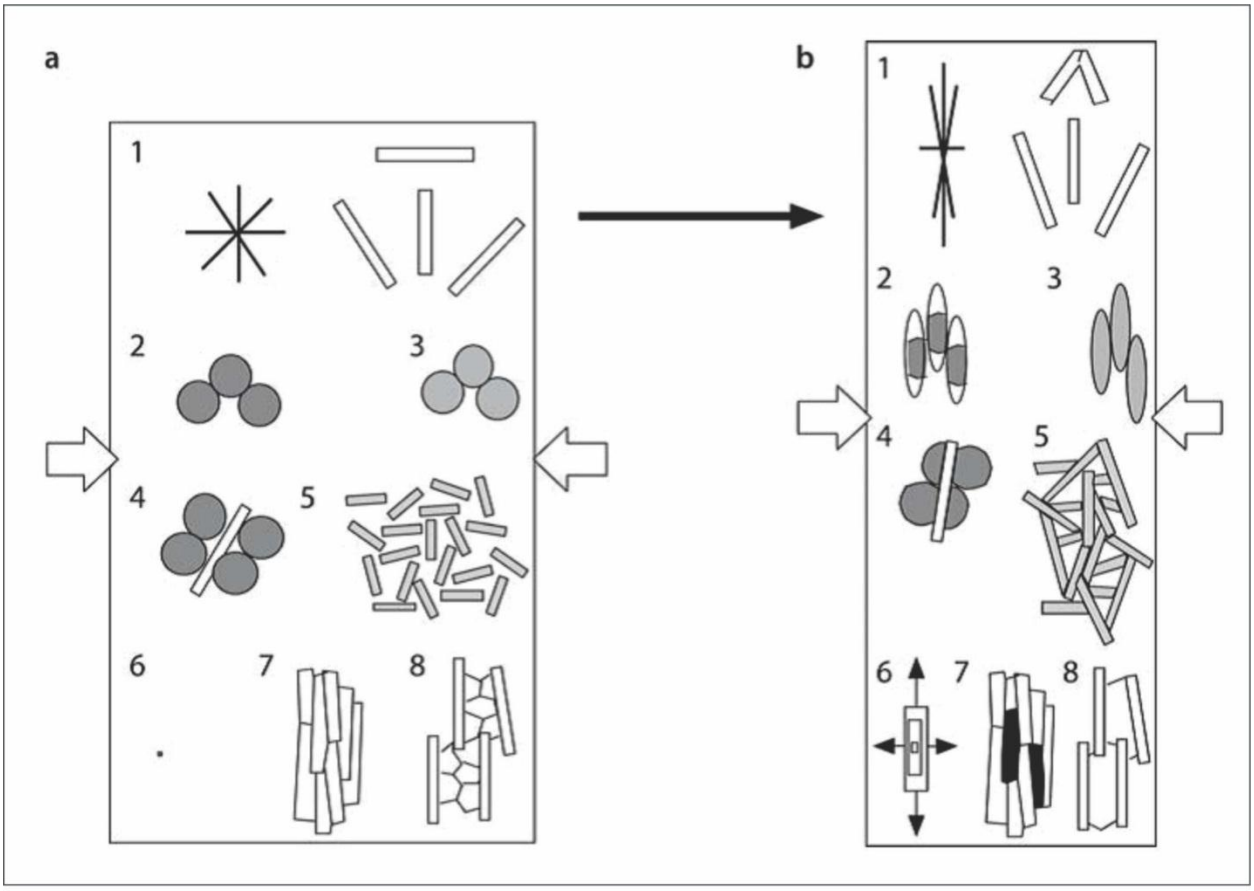

Fig. 4.26: Schematic diagram of some important mechanisms contributing to development of secondary foliation in rocks. a Fabrics at the onset of deformation. b Fabric elements after deformation. 1 Elongate crystals (open rectangles) rotate in response to deformation in a way similar to theoretical passive markers (solid lines) but there are differences; minerals may fold when normal to the shortening direction and thus strengthen a preferred orientation, or rotate at slower rate than material lines when highly oblique to the shortening direction. 2 Mineral grains change shape by stress-induced solution transfer; grey is original material, white are overgrowths. 3 Mineral grains change shape by crystalplastic deformation such as dislocation creep or solid-state volume diffusion. 4 Polymineralic aggregates develop foliations by processes 1 + 2 when assisted by stress-induced solution transfer. 5 Grain growth of micas parallel to (001) during or after shortening leads to an increase of foliation intensity because grains oriented in the direction of the foliation can grow to greater length than those in oblique orientations. 6 Oriented nucleation and growth of a mineral in a stress field. 7 Mimetic growth of elongate grains due to restrictions in growth direction imposed by an existing foliation. 8 Restricted growth parallel to platy minerals. (Passchier and Trouw, 2005).

4.4.4.2 Morphological classification of foliation microstructure

Foliations are useful for the establishment of overprinting relations of successive deformation phases. The classification of foliation used in this study follows Passchier and Trouw (2005) (Fig. 4.27). This classification is based on the fabric elements that define the foliation including elongate or platy grains, compositional layers or lenses, or planar discontinuities. The distribution of these fabric elements in the rock defines whether the foliation is spaced or continuous. In the first case, the fabric elements are not homogeneously distributed and the rock is divided into lenses or layers of different composition. Continuous foliation is used for rocks in which the fabric elements are homogeneously distributed, normally down to the scale of the individual minerals (Passchier and Trouw, 2005). The continuous foliation or cleavage is subdivided in two categories based on the size of grains defining the foliation: if defined by fine-grained it is called "slaty cleavage"; if defined by coarse-grained (visible with naked eye) it is called "continuous schistosity".

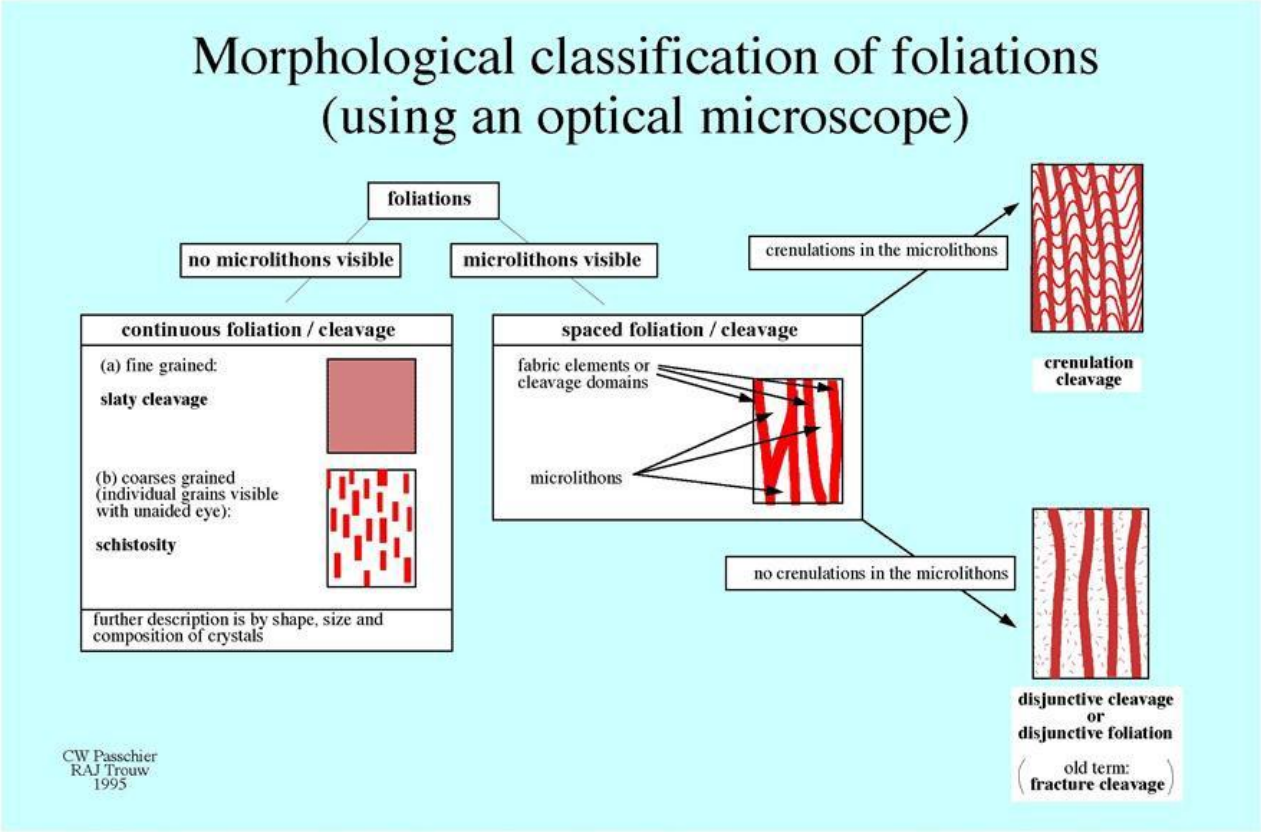

Fig. 4.27: Morphological classification of foliations using an optical microscope. The main criterion in the classification of foliations is the presence of microlithons. From: Microtectonics training course by Cees Passchier at the Geological Society of South Africa, Stellenbosch 2015.

4.4.4.3 Microanalysis of foliation within the Kamoa deposit

4.4.4.3.1 Introduction

In the project area, 97 thin sections which contained an S_1 foliation were studied in detail to better understand the structural history of the deposit (Fig. 4.28).

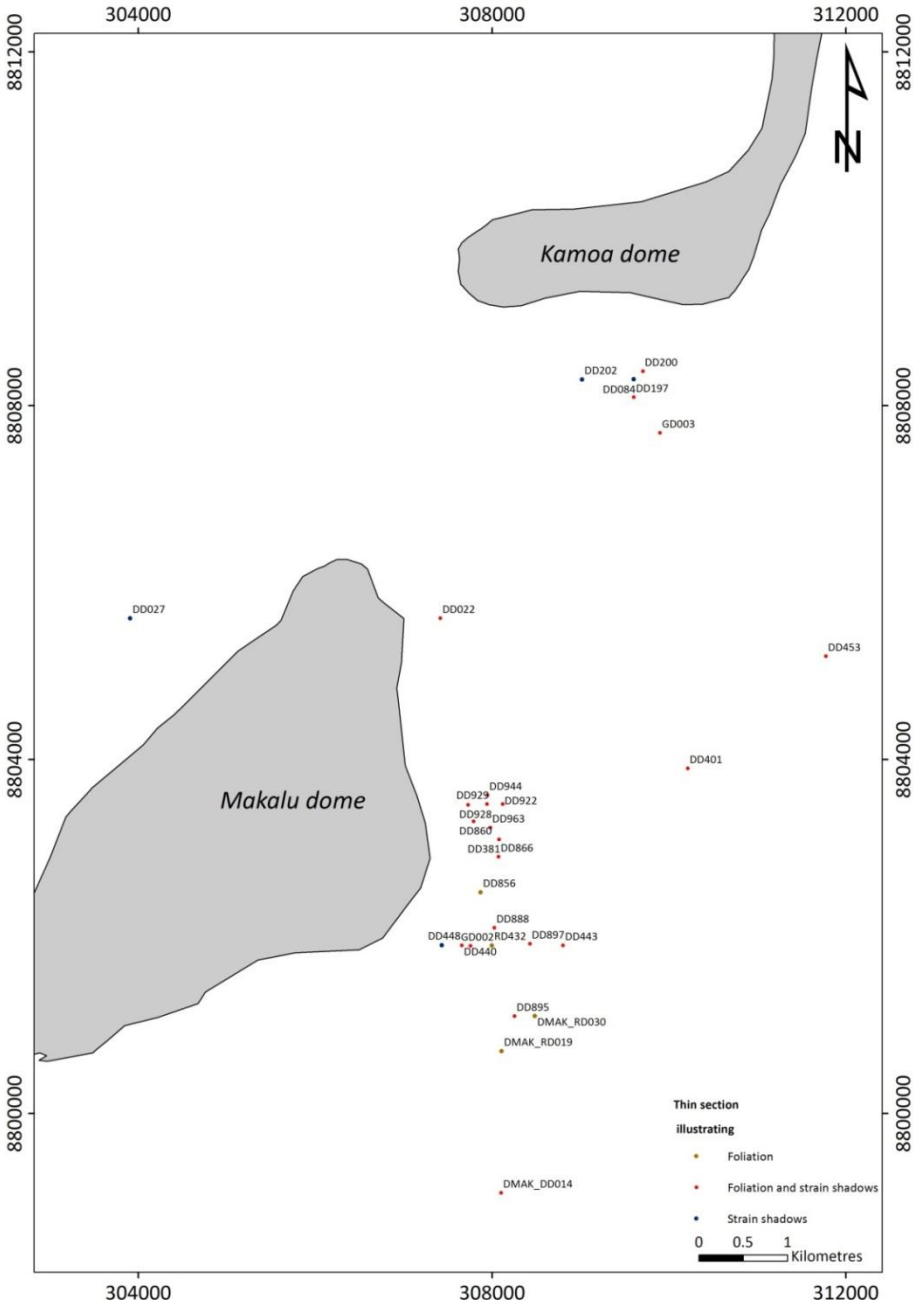

Fig. 4.28: Map showing the distribution of boreholes with thin sections displaying S_1 foliation.

Most of the thin sections were cut parallel to the orientation of foliation and lineation (XZ); however some thin sections (13) were cut perpendicular to the lineation and parallel to the foliation (XY) to better investigate the morphology of the foliation. Thin section analyses reveal that the intensity of foliation is not homogeneously distributed; S_1 appears more developed in sections cut parallel to the orientation of foliation (XZ) than in sections cut perpendicular to the lineation (XY) (Fig. 4.29).

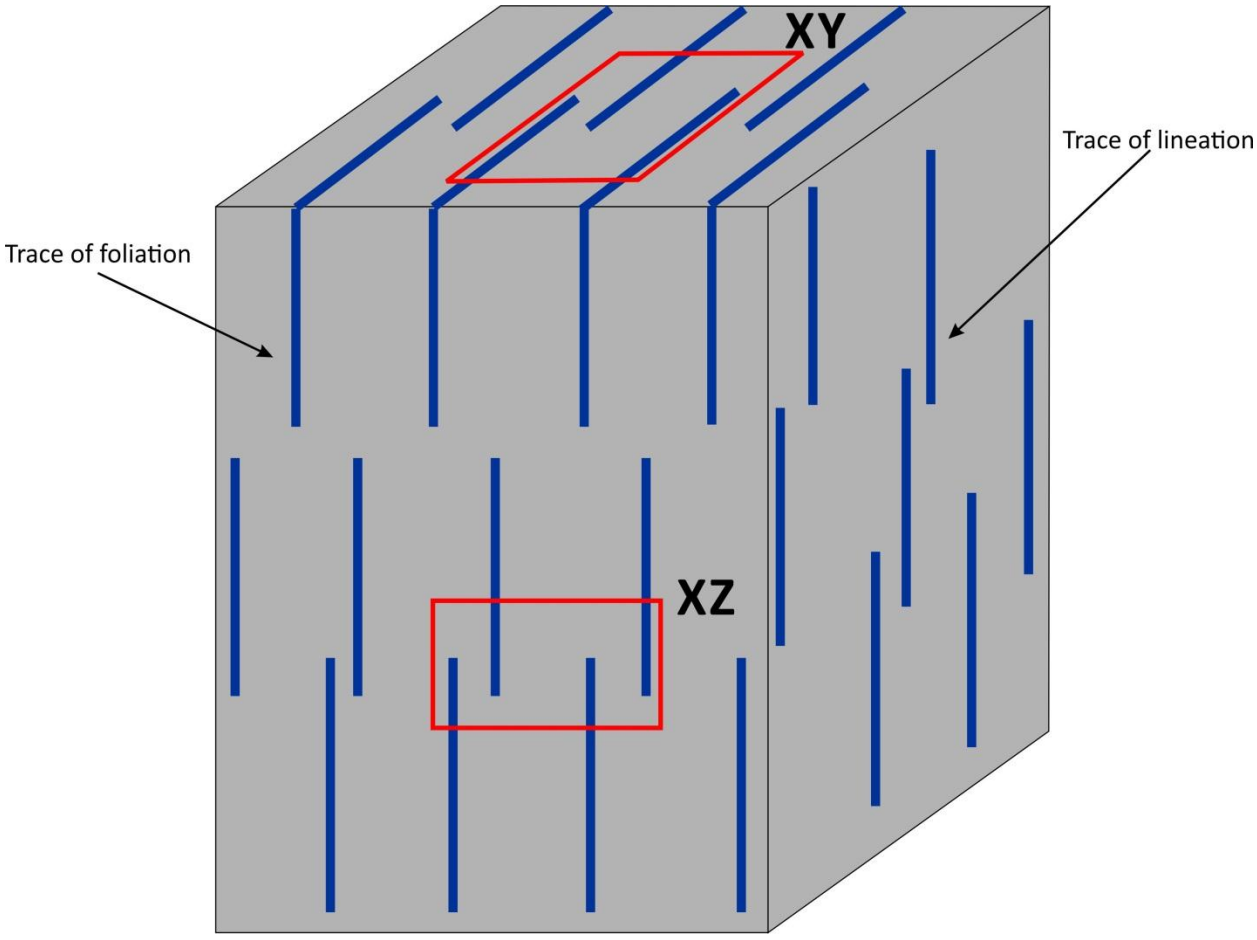

Fig. 4.29 Schematic diagram of the S_1 foliation and L_1 lineation showing the orientation of thin sections cut to investigate the intensity of the foliation in different orientations.

4.4.4.3.2 Secondary foliation within diamictites

In the diamictite, S_1 is defined by an alignment of clasts, the alignment of minerals within the matrix, the alignment of fine- and coarse-grained sulphides within the matrix or in the replacement of clasts (Fig. 4.30). The morphology of foliation observed in thin sections within

diamictite is a continuous foliation defined by the alignment of fine- and coarse-grained disseminated sulphides, the alignment of strain shadows/fringes and the alignment of sulphides replacing clasts (Figs. 4.30; 4.31a, b and 4.32a, b). S_1 defined by the alignment of clasts is weak, very weak or absent in the diamictite unit (Figs. 4.30; 4.31a, b and 4.32a, b). Small argillite and volcanic (basalt) clasts tend to be aligned parallel to S_1 foliation. However, quartz and quartzite clasts do not show an alignment or elongation of clasts. This may be due to the low intensity of deformation which seems to have deformed soft and small clasts within the diamictite. Therefore, S_1 in the diamictite seems to be closely related to the competence of the clasts (i.e. mafic clasts can be deformed easily compared to quartz and quartzite clasts) (Fig. 4.18b, c).

In the matrix of diamictite, S_1 is difficult to observe under an optical microscope because the matrix is composed of fine- to very fine-grained mineral grains (Figs. 4.31a and 4.32a). However incipient foliations defined by quartz and micas are commonly observed.

Because of the limited magnification of the optical microscope, 12 thin sections showing different intensities of foliation (very weak, weak and moderate foliation) were investigated using the scanning electron microscope (SEM) (Appendix A). As a result of the investigation, it appears that the minerals within the matrix of foliated diamictite show an S_1 foliation defined commonly by the alignment of micas, quartz, magnetite, and copper sulphides (Figs. 4.31 and 4.32).

Observations of thin sections from the boreholes located along macroscopic folds show a strong foliation defined both by the elongation of clasts and by the alignment of minerals in the matrix (Fig. 4.33). This helps to confirm that the deformation intensity is higher along the folds (Fig. 4.22).

In the deposit area, clasts within diamictite are randomly oriented and define a very weak, or weak to moderate foliation, this may suggest that the S_1 foliation may have been developed from a random fabric by pure shear deformation (Figs. 4.18a – c; 4.25, 4.30 and 4.32a).

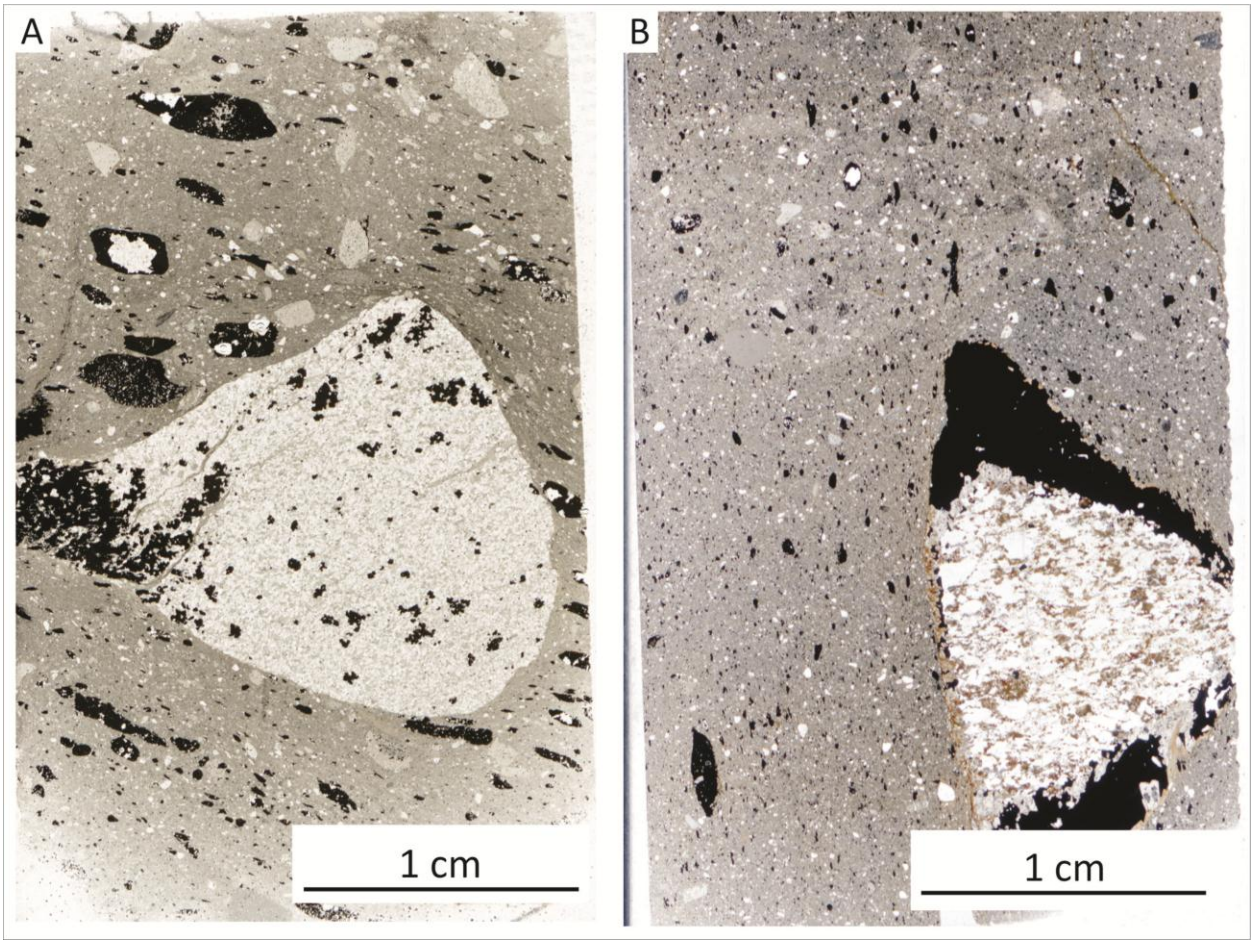

Fig. 4.30: Scanned photos of thin sections illustrating S_1 within diamictite. (A). Continuous schistosity defined by a combination of elongate sulphides and some aligned clasts. Sulphides within the clasts do not show a clear S_1, they are preserved by the clasts. Sample FT_36 from borehole DD895 at 580.46 m depth. (B). Continuous schistosity defined by alignment of fine- and coarse-grained sulphides. A strain shadow is observed in the bottom right corner, this structure is parallel to S_1 foliation. Sample FT_66 from borehole DD944 at 227.31 m depth.

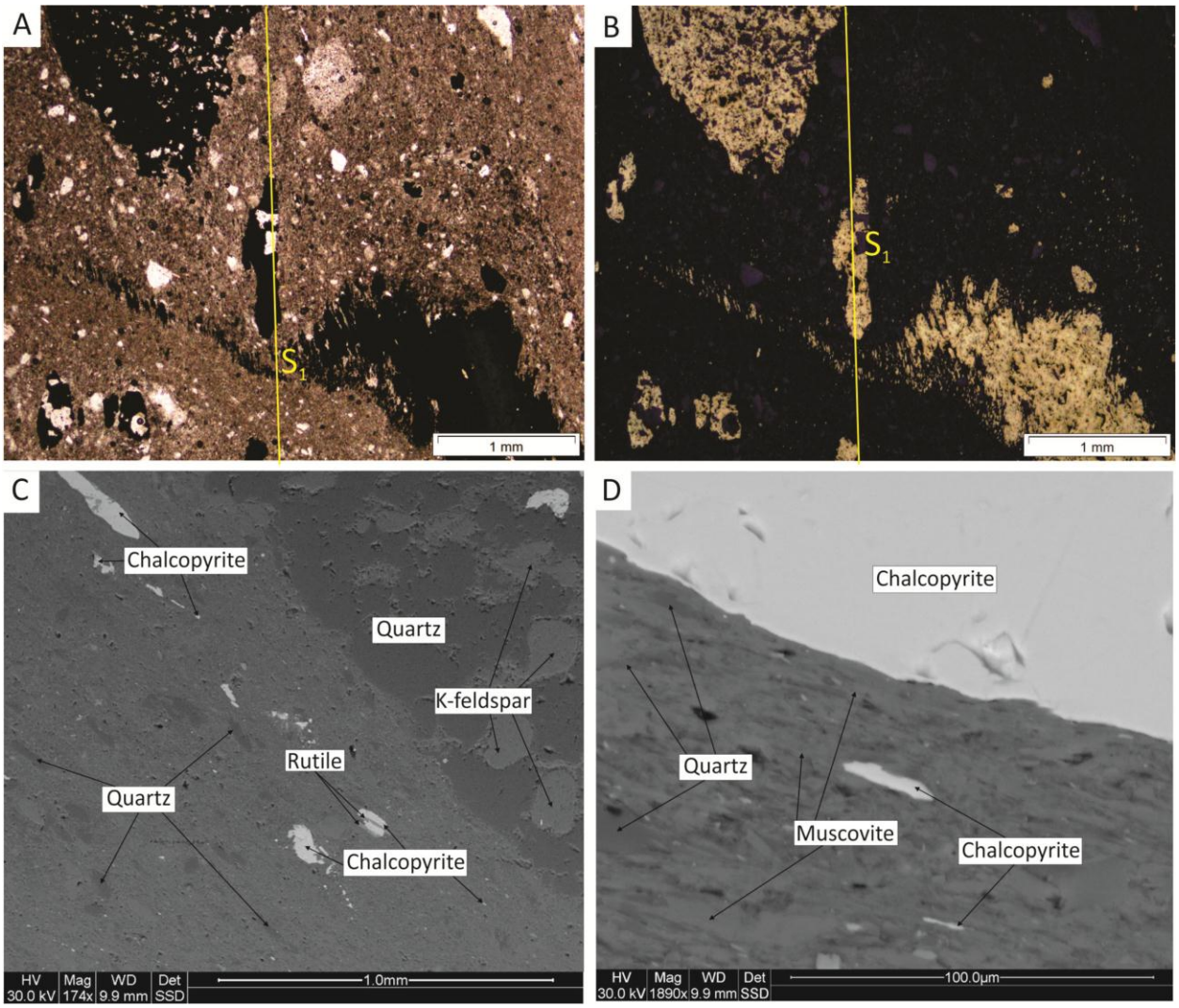

Fig. 4.31: Photomicrographs and SEM images of S_1 foliation within the diamictite. (A). Continuous schistosity to slaty cleavage defined by the alignment of sulphides. A very weak foliation defined by the alignment of quartz and composite clasts is observed in the fine- grained matrix. Not all clasts are aligned. FT_36 from borehole DD895 at 580.46 m depth (PPL). (B). Reflected light image of A. showing a continuous schistosity and slaty cleavage defined by aligned and elongated fine- and coarse-grained chalcopyrite (PPL). (C). SEM image illustrating an S_1 foliation defined by the alignment of quartz and chalcopyrite. This alignment of quartz has not been identified by optical microscopy. Image captured on FT_36 presented on Figure 4.30. (D). SEM image showing an S_1 foliation defined by the alignment of muscovite, chalcopyrite and quartz. It is important to note that the alignment of muscovite has not been identified by optical microscopy. Image captured on FT_36 presented on Figure 4.30.

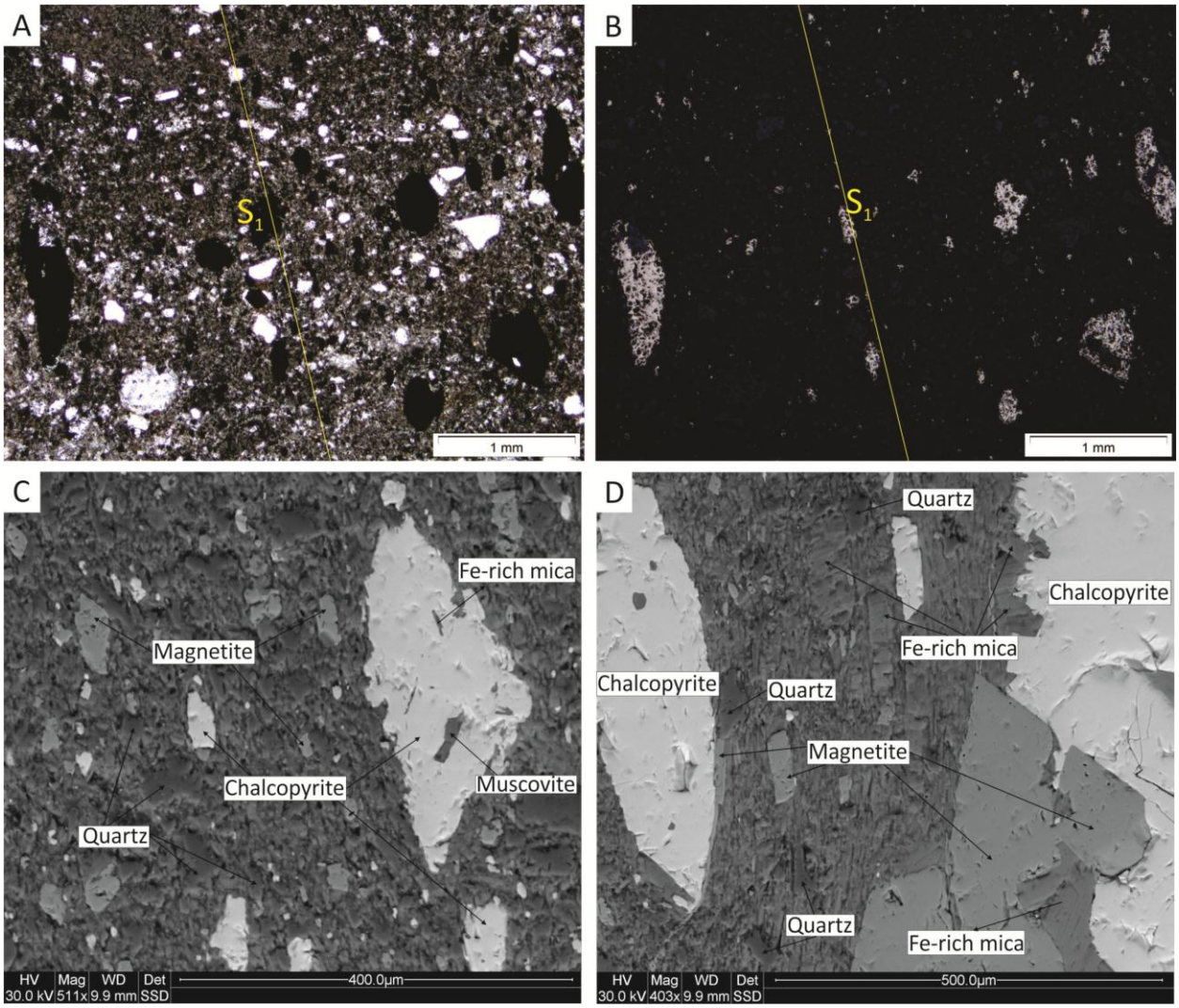

Fig. 4.32: Photomicrographs and SEM images of S_1 foliation within the diamictite. (A). Weak foliation defined by the alignment of sulphides (black areas). Clasts seem randomly oriented. Thin section FT_66 from borehole DD944 at 227.31 m depth. (PPL). (B). Reflected light image of C showing a continuous foliation defined by the alignment of coarse- and fine-grained chalcopyrite. Reflected light. (C). SEM image displaying an S_1 foliation defined by the alignment of minerals in the fine-grained matrix (magnetite, some quartz, and chalcopyrite). Under optical microscopy, there was no identification of any foliation defined by the alignment of minerals in the matrix. Image captured on FT_66 presented in Figure 4.30. (D). Foliation defined by the alignment of quartz, magnetite, iron-rich micas and chalcopyrite. SEM image captured on FT_66 illustrated on Figure 4.30.

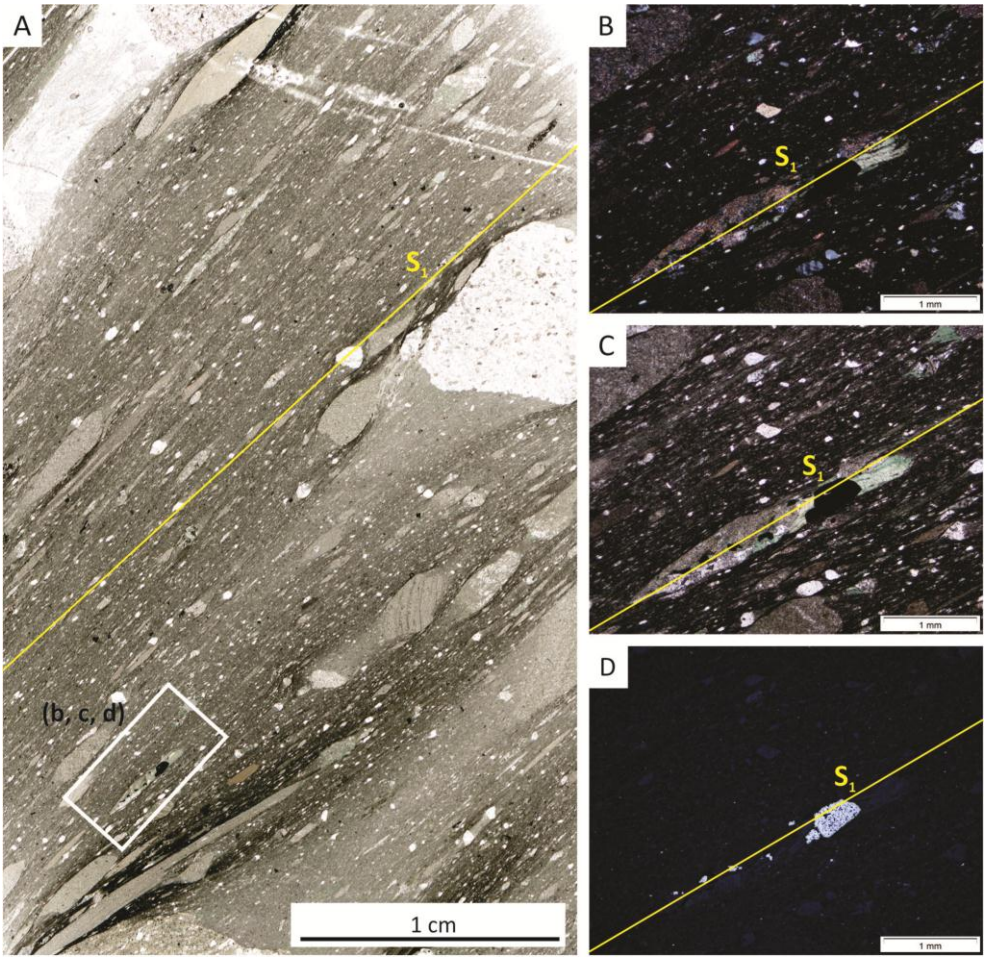

Fig. 4.33: Photomicrographs of the strong foliation observed in the borehole located on the fold. (A). Scanned thin section showing a strong foliation defined by clast elongation, minerals and strain shadows. (B). Photomicrograph showing a continuous schistosity defined by the elongation and alignment of minerals in the matrix and by the alignment of clasts. (XPL). The clasts are composed of quartz, plagioclase, carbonate, biotite and chlorite. Chlorite and quartz form the fringes to a euhedral pyrite grain (middle of field of view). The matrix is fine-grained and mainly comprises quartz and chlorite (C). Photomicrograph of B in plane light. (D). Reflected light image of C. illustrating euhedral pyrite as a rigid object to the strain fringe structure. Sample FT_16 from borehole DTJI_DD001 at 567 m depth. DTJI_DD001 is located about 13 km SW of the Makalu dome (out of the studied area).

4.4.4.3.3 Secondary foliation in siltstones

In siltstones (Ng 1.1.2 and Ng 1.1.1.2), the S_1 foliation is commonly defined by an alignment of sulphides and minerals within the matrix. In the studied area (including the boreholes in Fig. 4.22), the matrix within the siltstones hosts a secondary foliation commonly when sulphides are present in the rock. The morphology of the secondary foliation varies from a slaty cleavage to continuous schistosity (Fig. 4.34).

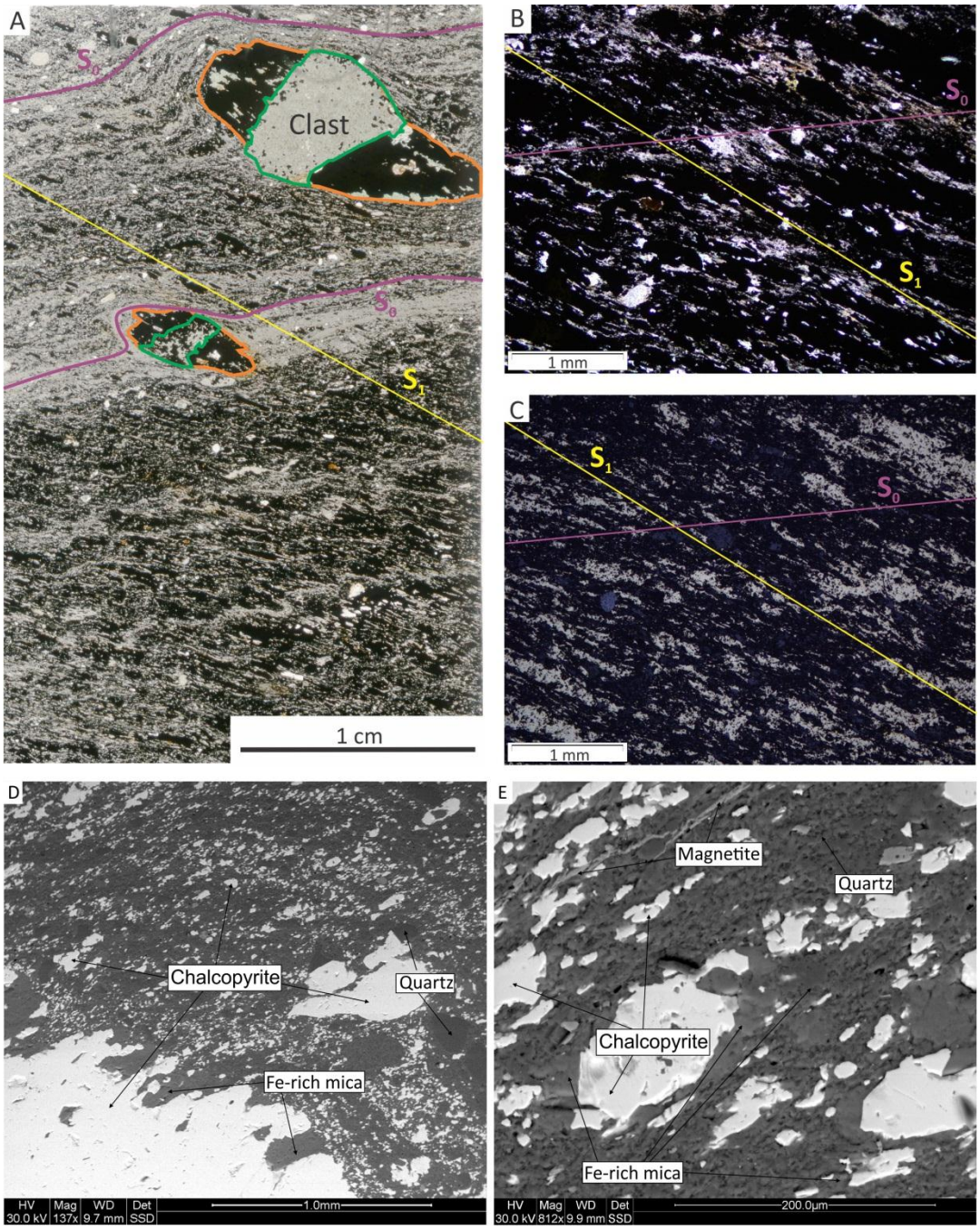

Fig. 4.34: Illustration of S_1 foliation in siltstone. (A). Scanned thin section image illustrating a strong foliation (S_1) defined by the alignment of minerals in the matrix and alignment of fine- and coarse-grained sulphides (black areas). Bedding (S_0) forms an angle of about 40° with S_1. Fringes (in orange) around major clasts (in green) appear to deform the bedding (in purple). Thin section FT_78 from borehole DKMC_GD002, at 379.58 m depth. (B). Image showing the detail of A. Continuous schistosity and slaty cleavage defined by the alignment of quartz and micas. S_0 is also observed. (PPL). (C). Reflected light image of (B) showing a continuous schistosity and slaty cleavage defined by elongation and alignment of fine- and coarse-grained chalcopyrite. (D). SEM image showing a detail of A. Strong foliation defined by chalcopyrite. Iron rich-mica is observed in the strain shadow to chalcopyrite. (E). Strong foliation defined by the alignment of chalcopyrite, magnetite and iron rich-mica in the fine-grained matrix. SEM image captured on Figure 4.34 A.

4.4.4.3.4 Secondary foliation in the Mwashya Subgroup rocks

Within the Kamoa deposit S_1 is generally not identified in the Mwashya Subgroup sandstone, however, it has been observed in the borehole DTJI_DD001 located approximately 13 km SW of the Makalu dome (Fig. 4.22). This borehole is situated on a macro-fold and contains rocks displaying a strong foliation. The S_1 foliation is defined by the alignment of muscovite, quartz, chlorite and occasionally by plagioclase and framboidal pyrite (Fig. 4.35).

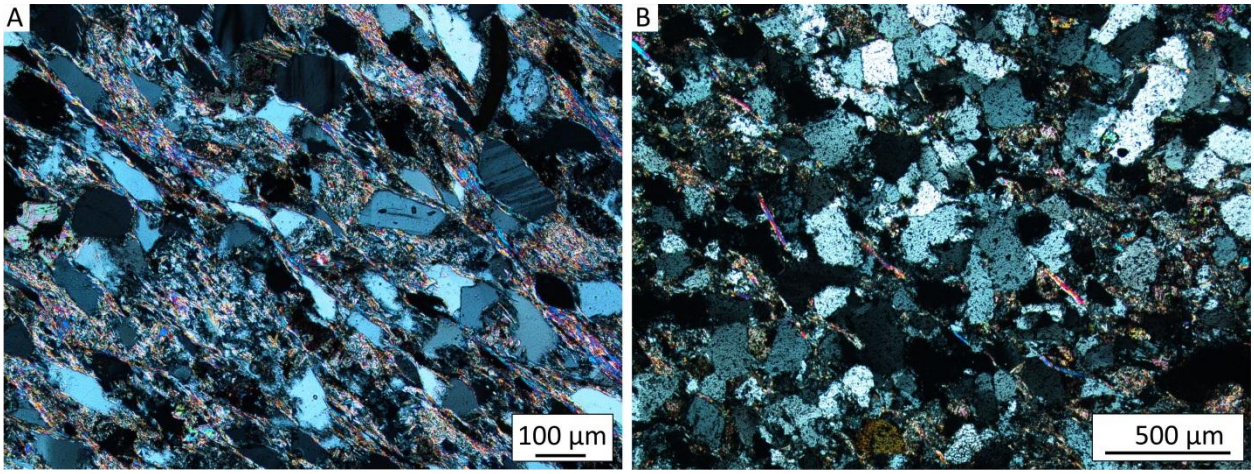

Fig. 4.35: Microphotographs showing S_1 foliation in the Mwashya Subgroup sandstones. (A). Slaty cleavage defined by the alignment of muscovite, quartz and plagioclases. Thin section from DTJI_DD001 at 615.58 m depth. (XPL). (B). Foliation defined by muscovite. Thin section from DTJI_DD0001 at 611.90 m depth. (XPL).

4.4.4.4 Microstructural description of minerals in the foliated rocks

The behaviour of minerals during deformation within the matrix of the foliated rocks is very difficult to study due to their very fine-grain size. The use of the SEM has facilitated the examination of fine-grained minerals which are not otherwise visible using a petrological microscope.

In the Basal diamictite (Ng 1.1.1), the matrix is composed mainly of quartz, muscovite and chlorite (Fig. 4.36). The morphology of these minerals has been the subject of detailed investigation in weak, moderate and strongly foliated rocks, as described below.

Coarse-grained quartz (40 - 500 µm) is generally anhedral and sub-rounded; single grains are oriented and parallel to the S_1 foliation. Fine-grained quartz (5 - 40 µm) is aligned and defines an S_1 foliation (Fig. 4.36 b-f). Most muscovite grains (3 - 50 µm) help to define the S_1 foliation but other grains are randomly oriented (Fig. 4.36 b-c). Coarse- and fine-grained chlorite (50–500 µm) is generally aligned and helps to define the S_1 foliation (Fig. 4.36 c).

Non-sulphide (gangue) minerals within strain fringes and strain shadows include quartz, carbonate, muscovite, chlorite and occasional plagioclase. The grains of quartz in these structures are coarse-grained (50 - 500 μm) and form grain aggregates showing an equigranular to inequigranular shape (Fig. 4.37). These aggregates are aligned and define a preferred orientation. The boundaries between polygonal quartz grains are regular (Fig. 4.37). Undulose extinction is generally absent in these quartz grains. Muscovite commonly overgrows quartz grains (Fig. 4.37).

Secondary mineral assemblages at Kamoa suggest that three sequential types of hydrothermal alteration (potassic, silicific, and magnesian alteration) have affected the rocks (Schmandt *et al.,* 2013).

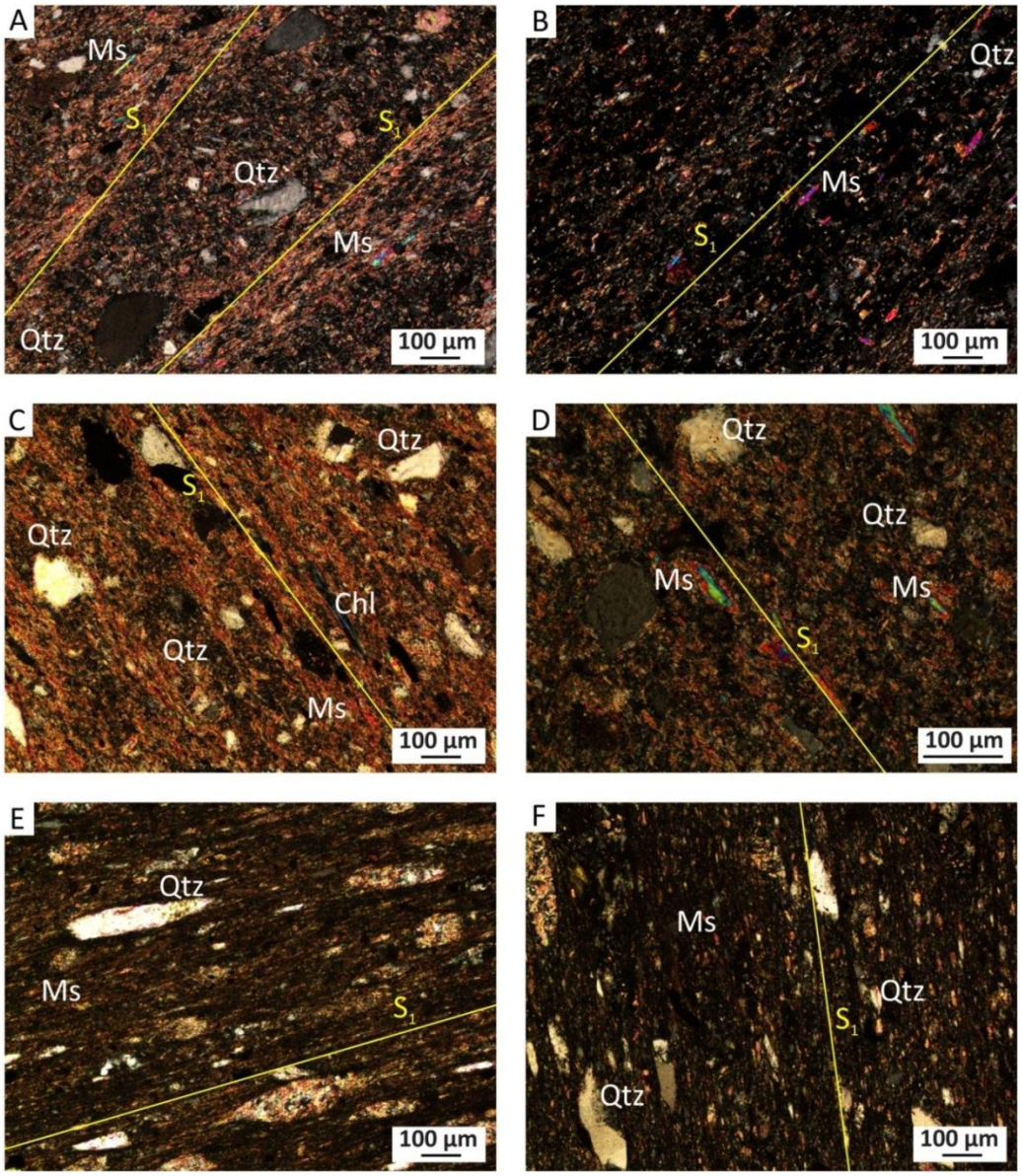

Fig. 4.36: Photomicrographs illustrating the morphology of quartz, muscovite and chlorite (XPL) in the different types of foliations (S_1). Quartz grains do not form aggregates, they occur as isolated single grains. (A). Weak foliation defined by alignment of fine-grained muscovite + quartz within the matrix (5 - 40 µm). Muscovite grains are also randomly oriented in the matrix. Coarse-grained quartz (40 - 100 µm) is sub-angular to sub-rounded, un-oriented and does not define an S_1 foliation. FT_036, from borehole DD895 at 580.46 m depth. (B). Weak to moderate foliation defined by alignment of fine-grained muscovite and quartz (3 - 40 µm). The black areas represent sulphides. FT_082, from borehole DKMC_RD432 at 333 m. (C). Moderate foliation defined by alignment of muscovite and quartz grains within the fine-grained matrix (3 - 40 µm). Quartz grains (50 - 100 µm) are sub-angular to sub- rounded and define a weak foliation. FT_067, from borehole DD944 at 230.28 m. (D). Moderate foliation defined by the alignment of muscovite and quartz grains (3 - 40 µm). FT_042, from borehole DD200 at 188.97 m. (E). Strong foliation defined by alignment of quartz, muscovite and chlorite in the matrix (3 - 25 µm). Quartz clasts (up to 300 µm) are also aligned and define an S_1 foliation. FT_017, from borehole DTJI_DD001 at 568.38 m. (F). Strong foliation defined by alignment of fine-grained minerals composed of quartz, muscovite and chlorite. The quartz clasts are sub-angular and define an S_1 foliation. FT_017, from borehole DTJI_DD001 at 569.88 m.

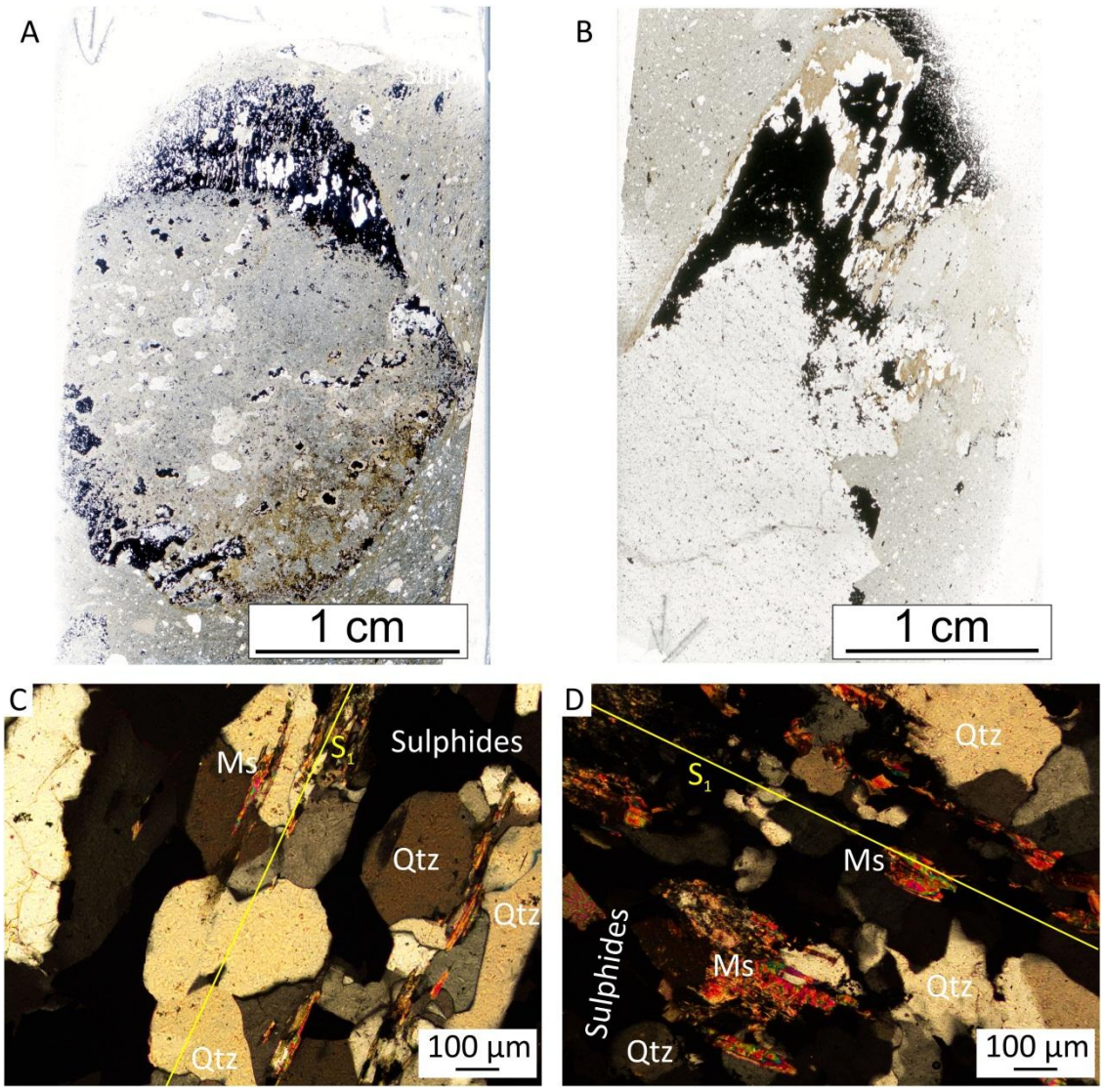

Fig. 4.37: Illustration of the morphology of minerals within strain fringes. (A). Scanned thin section including a large clast with a fringe. FT_029, from borehole DD888 at 265.72 m. (B). Scanned thin section illustrating a strain fringe. FT_051, from borehole DD401 at 784.63 m. (C). Detailed photomicrograph of the fringe in A. Aggregates of quartz grains showing a preferred orientation (S_1). The grain aggregates show equigranular shape and the boundaries between the polygonal grains are regular. Muscovite grains overgrow the quartz grains and define an S_1 foliation. The areas in black are sulphides. (XPL). (D). Detailed photomicrograph of the fringe in B. Aggregates of quartz grains showing a preferred orientation (S_1). The shape of aggregates is inequigranular and the boundaries between the grains are regular. Muscovite grains form overgrowths on the quartz grains and define an S_1 foliation. The opaque areas are sulphides. (XPL).

4.5 Strain fringes and strain shadows

4.5.1 Introduction

Dilation sites are voids in a rock filled with fluid, in which material may be deposited during deformation (Passchier and Trouw, 2005). They include veins, strain shadows and fringes and microboudins (Bons *et al.,* 2012). Voids can form in rocks at sites of high rheology contrast and/or where fluid pressure is high.

A strain shadow is a cone-shaped domain adjacent to a rigid object (e.g. clasts or euhedral pyrite in the direction of foliation (S_1) and is usually composed of a different mineral to that of the rigid object. A strain shadow is commonly massive, if it contains fibres it is called a "strain fringe" (Fig. 4.38) (Passchier and Trouw, 2005). Fibres within a strain fringe can help to evaluate the tectonic history of an area (Etchecopar and Malavielle, 1987; Koehn *et al.,* 2000, Bons *et al.,* 2012; Chatalov, 2014).

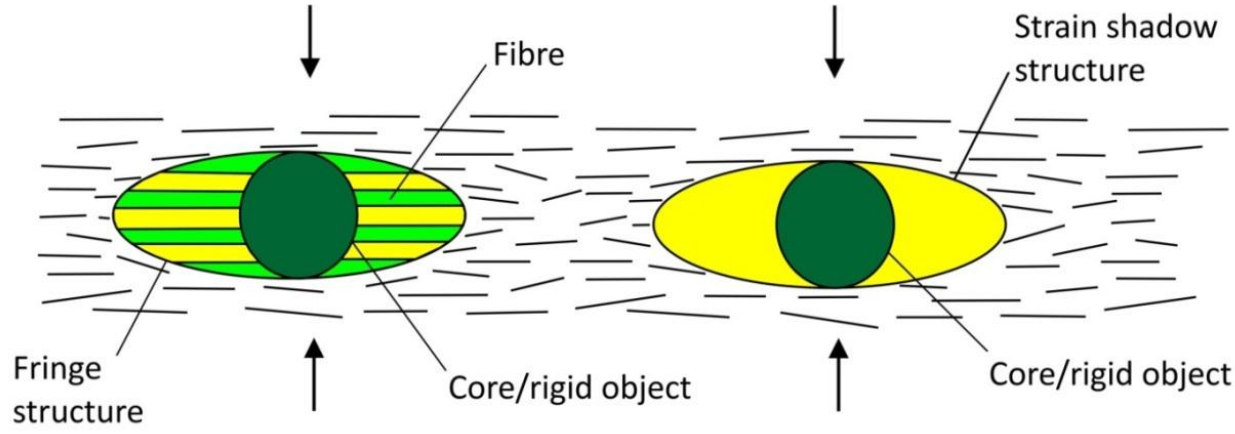

Fig. 4.38: Illustration of development of strain shadows and strain fringes. Modified after Passchier and Trouw (2005).

4.5.2 Mesoscopic analysis of strain shadows and strain fringes

To study strain shadows and strain fringes, 5 boreholes were investigated in detail within the project area, with details from 3 of them presented here with the rest in Appendix C (Blue ringed symbols in Fig. 4.1).

Strain shadows and strain fringes are common features observed in the Kamoa mineralised zone, in the Lower laminated pyritic siltstone/sandstone and rarely in the upper diamictite units. Three morphological types of strain shadows/fringes are distinguished by the location of the growths on the rigid object: asymmetric upwards; asymmetric downwards and symmetric.

Clasts with growth all the way around are fairly common in the Nguba Subgroup rocks. It is not known if these growths developed during the stress field or formed by the replacement of clast (Fig. 4.39).

The overall orientation of strain shadows and strain fringes is closely similar to the orientation of S_1 throughout the borehole core. Strain shadows/fringes are well developed in the clast-poor diamictite of the Upper basal diamictite and poorly developed in the clast-rich Lower basal diamictite (Figs. 4.40, 4.41 and 4.42).

Strain shadows and strain fringes locally display a vertical zonation from the base to the top of the mineralised zone as follows: symmetric strain shadows are dominant at the base, whereas asymmetric upwards strain shadows are dominant in the centre and top (Figs. 4.40 and 4.42). There is not an abrupt change in this zonation, and an overlap between the two types is commonly observed (Fig. 4.43). Asymmetric downwards strain shadows/fringes are uncommon (Fig. 4.43). Strain shadows/fringes are commonly formed around quartz and mafic igneous clasts and are less common around quartzite clasts (Figs. 4.41 and 4.42). Strain fringes vary in length from a centimetre to several centimetres (up to 15 cm). In the Basal diamictite of boreholes DD793, DD084 and DD595; strain shadows/fringes were counted one by one in intervals of ≤ 1m length, the result is presented in the Figure 4.43.

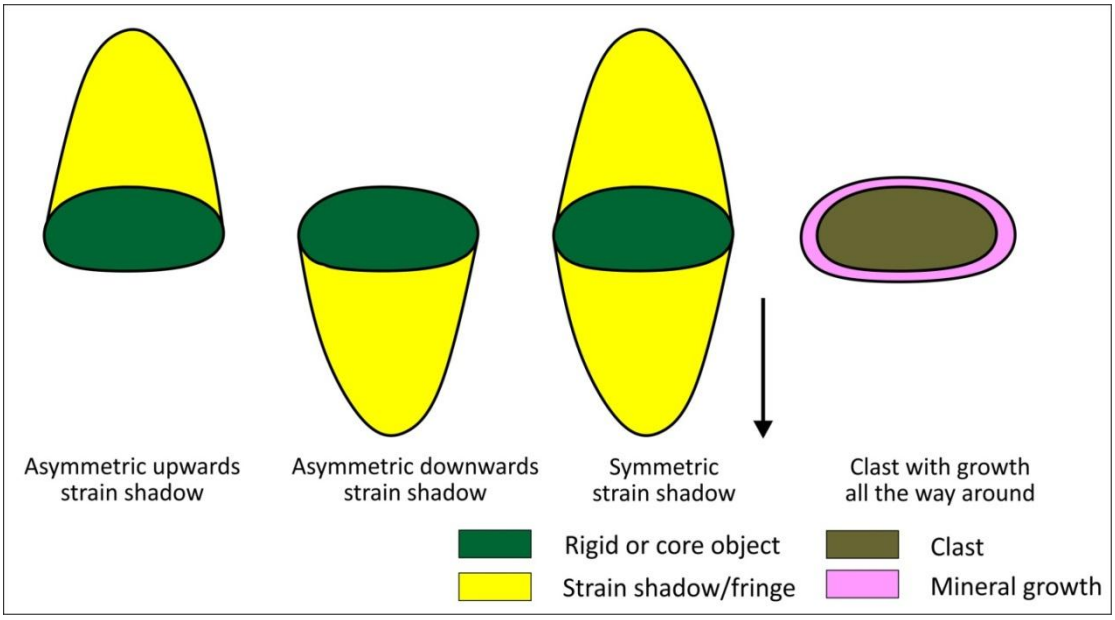

Fig. 4.39: Morphology of strain shadows/fringes. The arrow shows the down-hole direction.

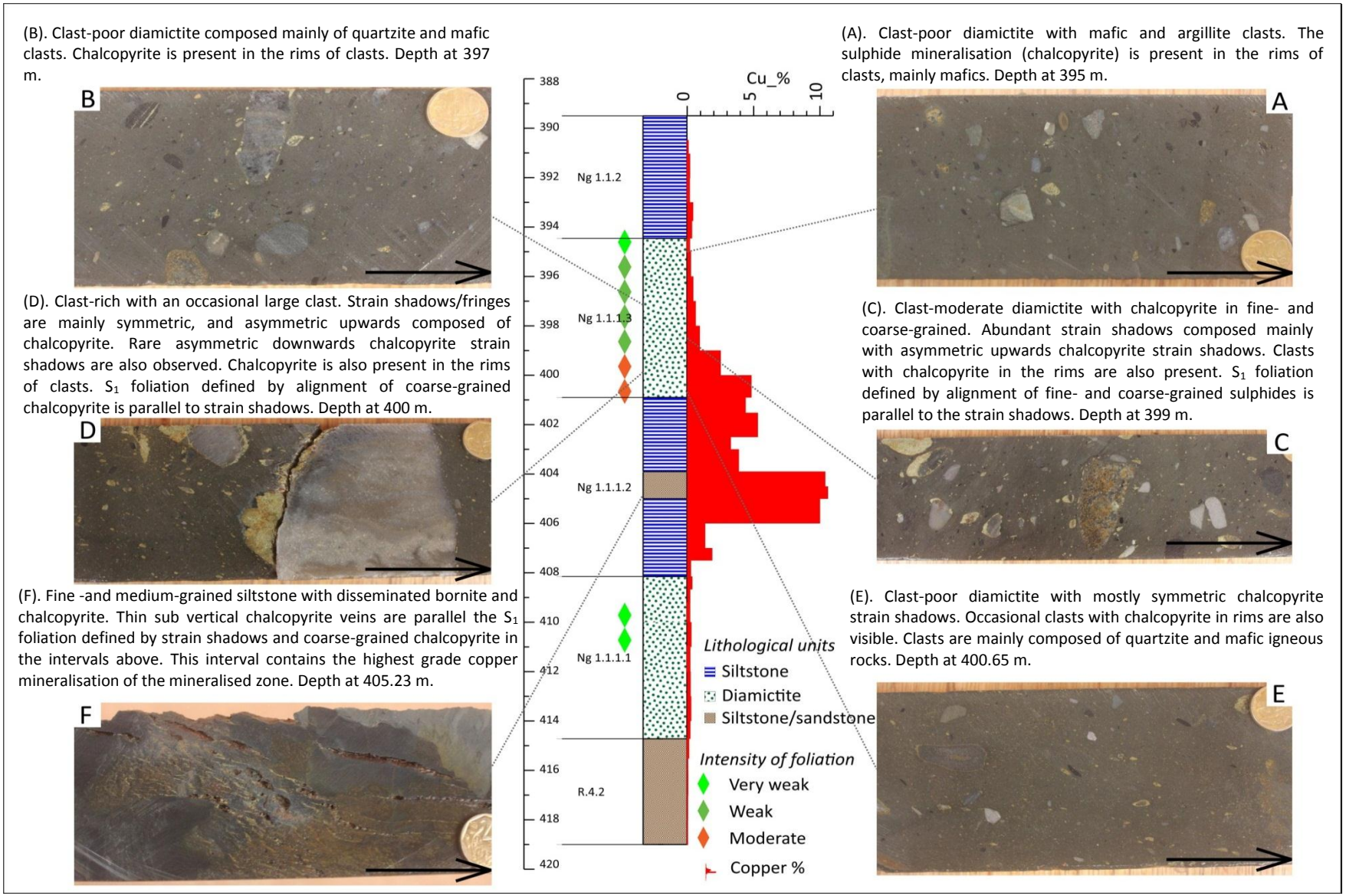

Fig. 4.40: Morphology of strain shadows and strain fringes in the borehole DD793. The black arrows show the downhole direction. There is a correlation between strain shadows/fringes with copper grade. The intercalated siltstone contains the ore mineralised zone (5 m at 1% Cu cut-off). In the Upper basal diamictite S_1 is well defined when copper grade increases.

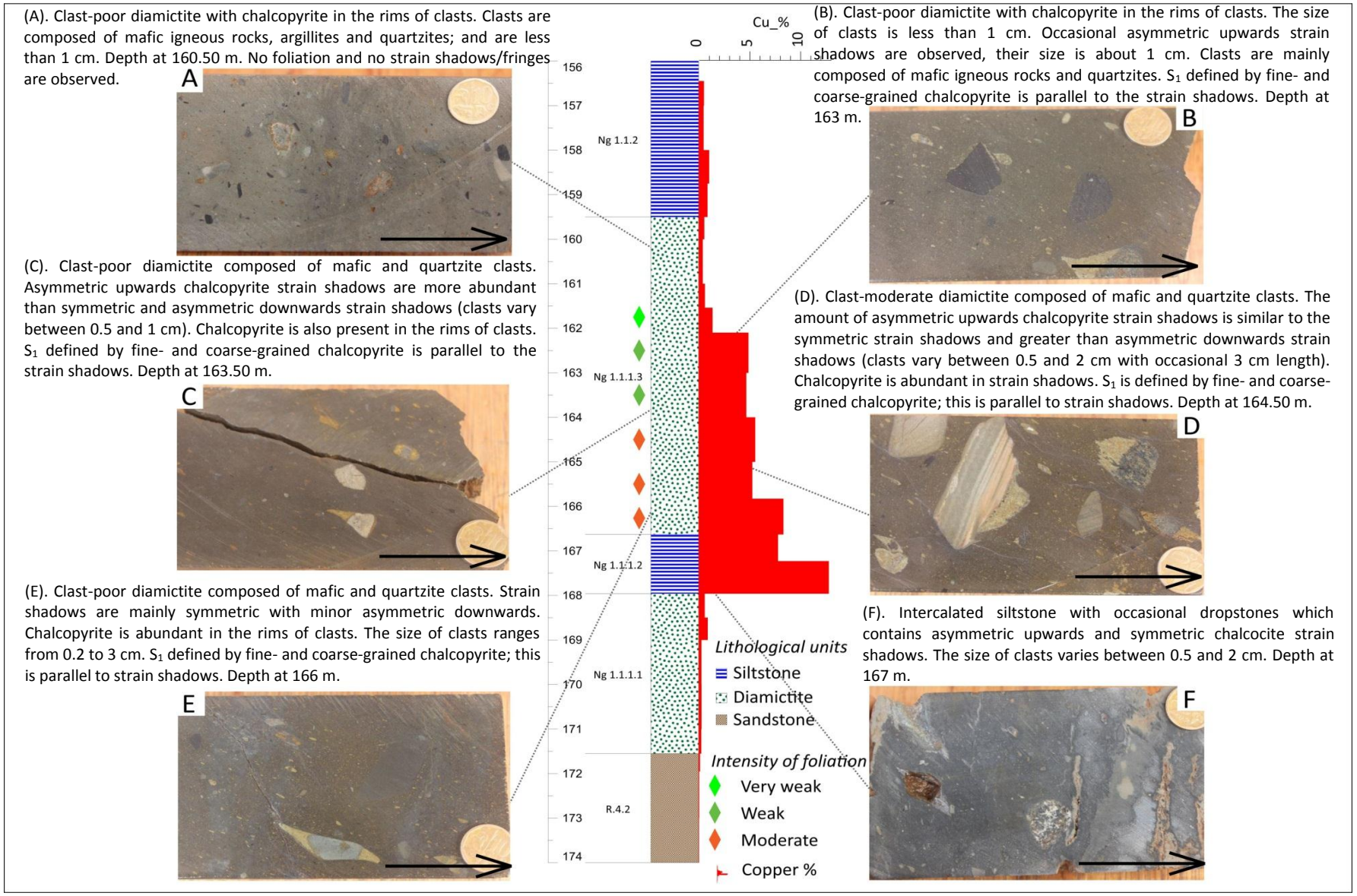

Fig. 4.41: Morphology of strain shadows and strain fringes in the borehole DD084. Strain shadows are absent or rare below the Intercalated siltstone. In the Upper basal diamictite (Ng 1.1.1.3), the intensity of foliation correlates well with the increase of copper grade. Also, copper grade correlates well with the occurrence of strain shadows/fringes. The highest grade is contained in the Intercalated siltstone (Ng 1.1.1.2).

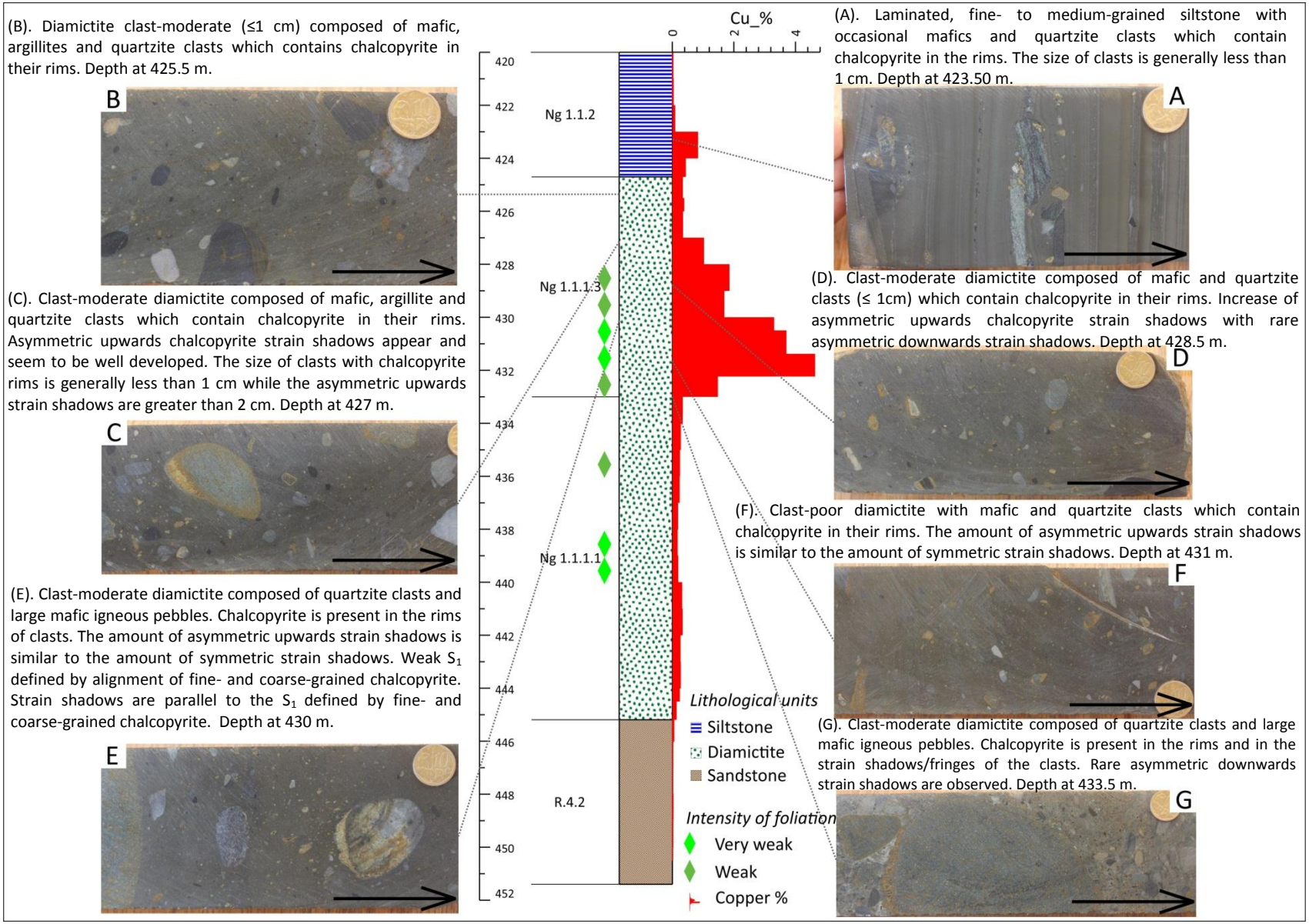

Fig. 4.42: Morphology of the strain shadows and strain fringes in borehole DD595. Below the depth 433.5 m, strain shadows are absent or rare and the copper mineralisation is not significant. Very weak to weak foliation defined by chalcopyrite. S_1 is consistent in the high copper grade zone.

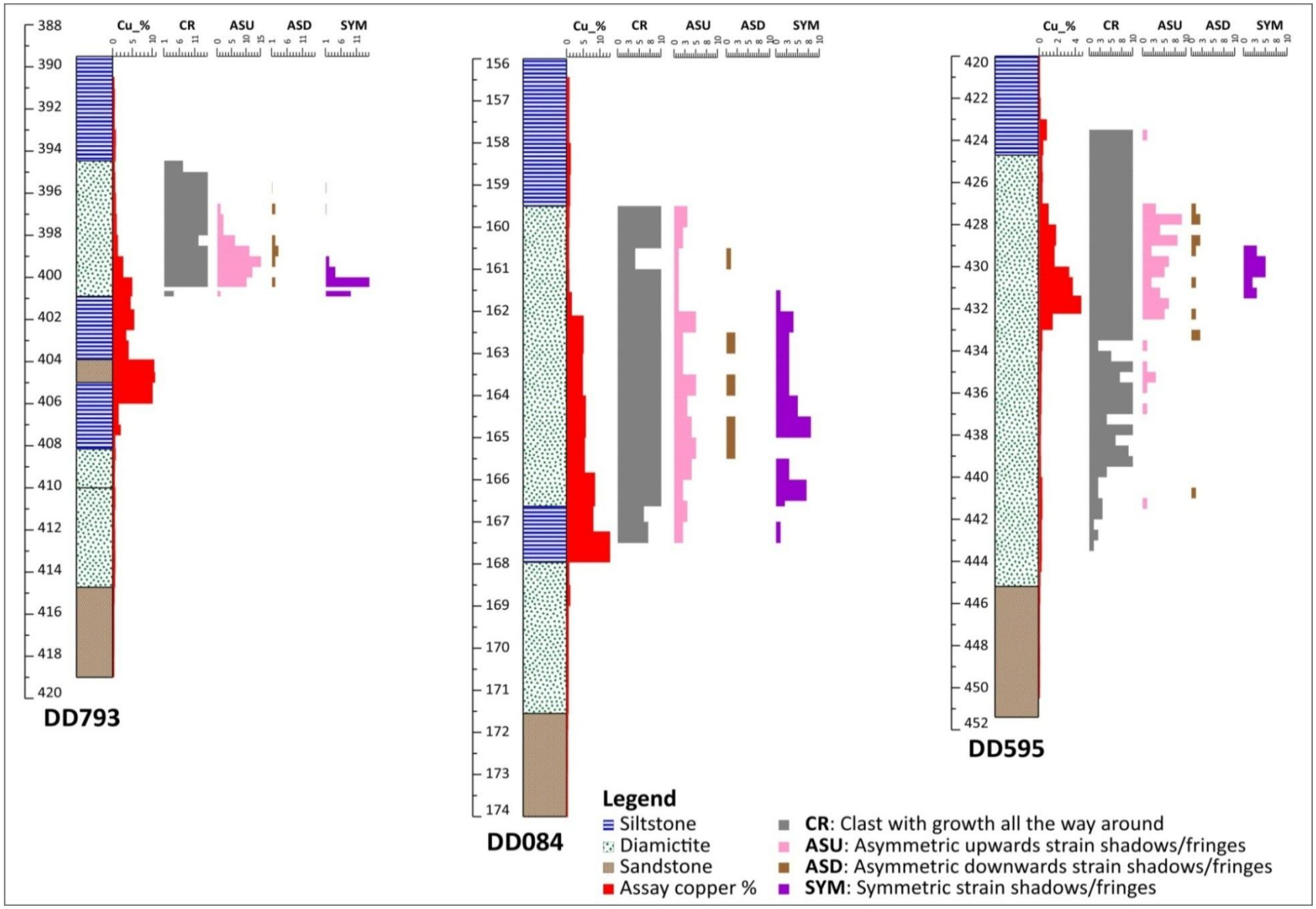

Fig. 4.43: Strain shadows/fringes zonation in the boreholes DD793, DD084 and DD595. Crude vertical distribution from symmetric at the base to asymmetric up-hole at the top of the mineralised zone. There is not an abrupt change in this zonation, an overlap is generally observed. Asymmetric down-hole growths are rare or absent in the Basal diamictite of the Grand Conglomérat. Note that data are truncated at the maximum number of the scale bar.

4.5.3 Microstructural observations of strain shadows and fringes

4.5.3.1 Introduction

Rigid objects in a ductile deforming rock cause local perturbations of the stress field and flow pattern. In the case of low temperature deformation and high fluid pressure, increased pressure solution may occur adjacent to the rigid object on the side of the shortening, while extensional gashes may open on the contact of the object and the matrix on the extensional side. New crystalline material may grow in these gashes and form strain shadows on both sides of the rigid core object (Fig. 4.38) (Passchier and Trouw, 2005). Pressure shadows are the low-normal stress sides facing the least compressive stress (σ_3). If the crystals in such strain shadows are elongate or fibrous, these are known as strain fringes (Fig. 4.38). The combination of core object and fringes is called a fringe structure. Fringe structures carry information on flow and deformation history in both their internal and external shape, and are therefore useful as kinematic indicators (Passchier and Trouw, 2005; Bons *et al.,* 2012).

Within the Kamoa deposit, strain fringes and strain shadows have been studied in detail in 61 thin sections that are well distributed throughout the project area (Fig. 4.28). In addition, six thin sections were studied under the scanning electron microscope. The study includes the shape, the size and the mineral composition of rigid objects in strain shadows/fringes. The composition of minerals in strain shadows and in fringes has also been investigated. Because of the importance of fringes, their morphologies have been described in detail.

4.5.3.2 Description of strain fringes and strain shadows

Within the Basal diamictite and the Lower laminated pyritic siltstone/sandstone, strain shadows and strain fringes have been observed in all lithological units. They are commonly asymmetric (on one side of the rigid object) and symmetric (on two sides of the rigid object), however in some cases they overgrow all faces of the core object (Passchier and Trouw, 2005; Bons *et al.,* 2012). In strain shadows and fringes, copper sulphides are generally more abundant than gangue minerals (Figs. 4.44 to 4.49).

In the diamictite unit, the rigid object to the strain shadows/fringes is generally formed by mafic igneous clasts, quartz clasts and quartzite clasts. Clasts are commonly sub rounded to sub angular and their size varies from 0.5 cm to 3 cm with occasional large clasts or boulders which can measure up to 15 cm (Fig. 4.44). The length of fringes and strain shadows within the diamictite varies from several tens of microns to 1.5 cm, occasionally up to 3 cm. Euhedral pyrite locally forms the rigid object on which strain fringes/shadows developed; pyrite grains

range in size from 20 µm to 4 mm, with occasional large grains up to 1 cm (Figs. 4.47d and 4.48c, d). In diamictite, strain shadows/fringes are commonly enriched with abundant copper sulphides, quartz, iron-rich micas, carbonate, chlorite, ankerite, plagioclase and albite (Figs. 4.44 to 4.49).

In siltstone and sandstone layers, rigid objects within strain fringes/shadows are commonly composed of euhedral pyrite, coarse-grained pyrite with minor sphalerite and occasional clasts (Fig. 4.50). Euhedral pyrite as a rigid object varies in size from 20 µm to 4 mm with occasional large euhedral grains that can measure up to a centimetre in diametre. Strain shadows/fringes are composed of quartz and chlorite with occasional muscovite and biotite (Fig. 4.50). In siltstone and sandstone units, copper sulphides such as chalcopyrite, bornite and chalcocite are only present in strain shadows/fringes when the rigid object is a clast (Fig. 4.34a). The length of strain shadows and fringes in these lithological units varies from 20 µm to 0.1 mm when the rigid object is composed of euhedral pyrite and from few tens of microns to 1.5 cm when the rigid object is a clast.

In a strain shadow and strain fringe, the size of the rigid object appears to control the size of the fringe and the strain shadow. Therefore, small rigid objects have obviously thinner overgrowths while large rigid objects contain thicker overgrowths (Figs. 4.44 and 4.47). The boundary between strain shadows/fringes and the adjacent matrix is commonly sharp (Figs. 4.44 and 4.47).

Fibres within strain fringes have generally a straight orientation, however a weak curvature in the distal part of the fringes is commonly observed. The slightly curved shape of fibres may be due to the heterogeneity in the local deformation (Chatalov, 2014). The distal parts of the core object in the fringes are undeformed and fibres lack undulose extinction and grain boundary structures (Figs. 4.44, 4.45 and 4.46). Fibres within strain fringes are undeformed and show a displacement-control (clasts and euhedral pyrite), they are simply parallel to the long dimension of the fringe (Fig. 4. 44 and Fig. 4.51). The straight fringes show that the long axis of the fringes represents the X-direction of finite strain (Fig. 4.44) (Passchier and Trouw, 2005).

Fibre growth in fringes occurs as antitaxial at the boundary between the rigid object and the fringe or as syntaxial at the boundary between the matrix and the fringe (Koehn *et al.,* 2000; Passchier and Trouw, 2005; Bons *et al.,* 2012). The observation of strain fringes shows that the fibre growth occurs between the rigid object and the fringe, therefore they are classified as antitaxial strain fringes (Fig. 4.44).

The presence of coarse-grained albite in strain fringes/shadows intergrown with copper sulphides suggests an albitic alteration coeval with copper mineralisation (Fig. 4.46c, d).

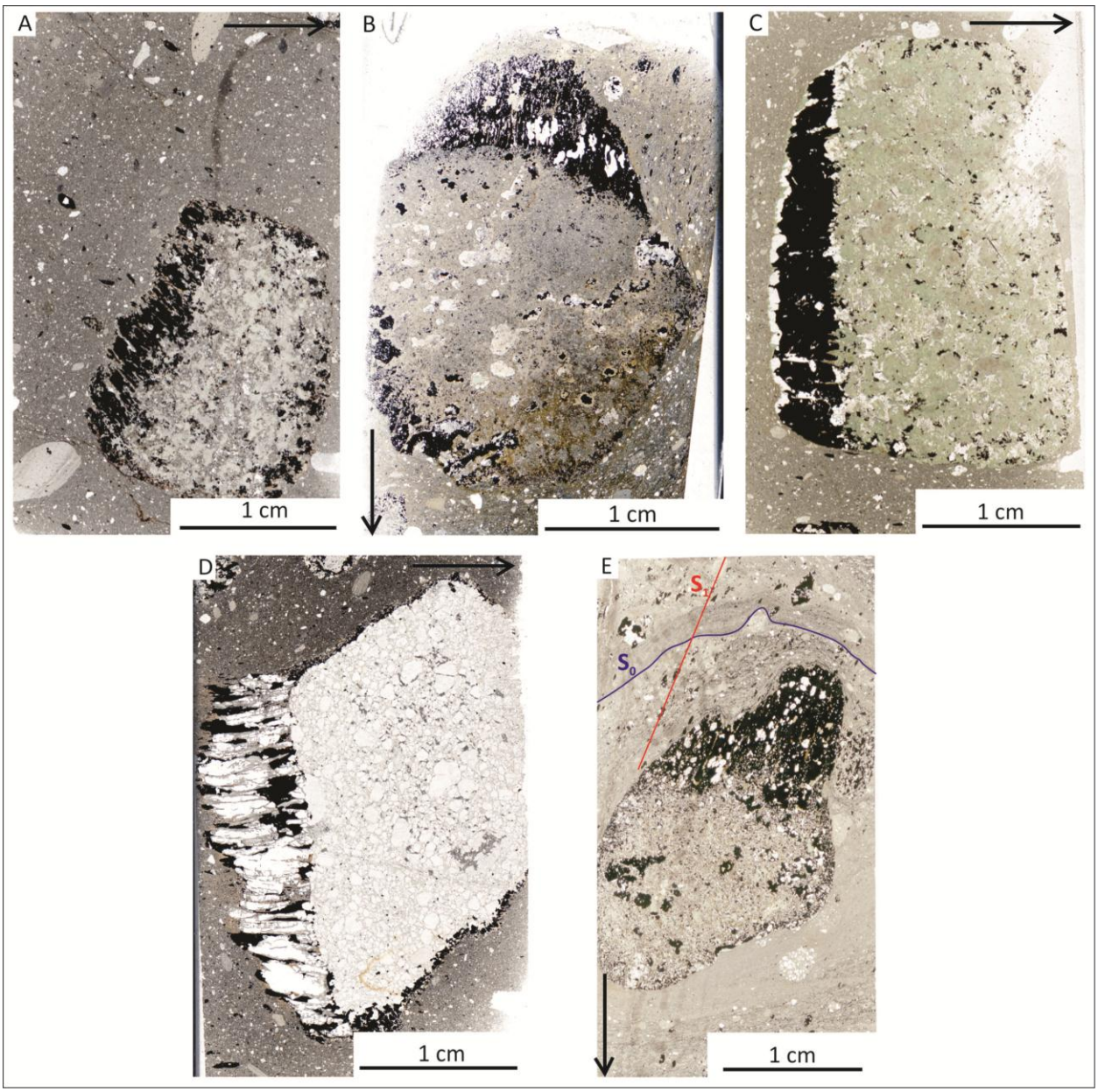

Fig. 4.44: Scanned thin sections illustrating strain fringes in diamictite. The rigid object to the fringes is composed of large clasts. The fibres in the fringes are straight and suggest a coaxial deformation. Strain fringes show a preferential growth on the top of the clast. (A). A replacement of clast by sulphides is observed on the right side of the clast. FT_044, from borehole DD197, at 211.85 m depth. (B). Sulphide is partially replacing the clast (base of the clast). FT_029, from borehole DD888, at 265.72 m depth. (C). Fringe composed mostly of sulphides. FT_038A, from borehole DD453, at 1148.94 m depth. (D). Fringes are slightly curved. FT_032A, from DD944 at 227.89 m depth. (E). The fringe seems to deflect the bedding (S_0). S_1 is sub-perpendicular to S_0. A partial replacement of the clast by sulphide is observed. FT_031, from DMAK_DD014 at 522.46 m. Black areas are copper sulphides. The black arrows show the downhole direction. Details regarding the composition of clasts and strain fringes are presented in Fi. 4.44 and 4.45).

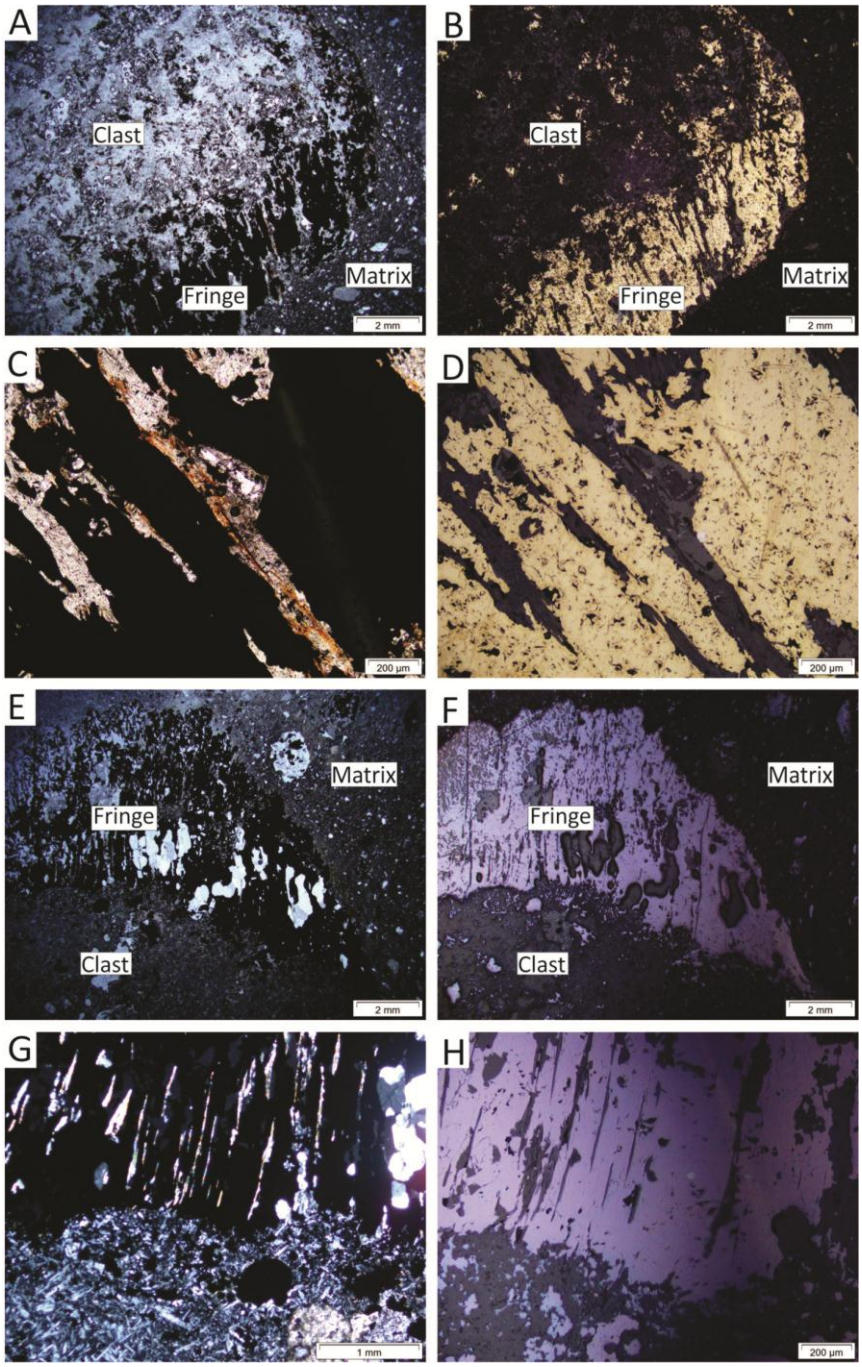

Fig. 4.45: Photomicrographs of strain fringes in diamictite (from Figure 4.44). (A). Fibres of quartz, chlorite and carbonate in strain fringe around a clast. The mineralogical composition of the fibres is similar to the composition of the clast. (XPL). From borehole DD197, at 211.85 m depth. (B). Reflected light photomicrograph of A showing chalcopyrite fibres in the fringe and in partial replacement of the clast. (C). Detailed photomicrograph of A showing the straight fibres composed of quartz, chlorite and carbonates. (PPL). (D). Detailed photomicrograph of B showing straight chalcopyrite fibres. (E). Fibres of quartz, chlorite, muscovite and carbonates in a strain fringe around a large clast. This large clast is composed of plagioclase, quartz, chlorite and biotite with minor muscovite. (XPL) (F). Reflected light photomicrograph of E showing bornite in the fringe of the large clast. (G). Detailed photomicrograph of E illustrating straight fibres composed of muscovite and quartz. (H). Photomicrograph detail of F showing straight fibres of bornite.

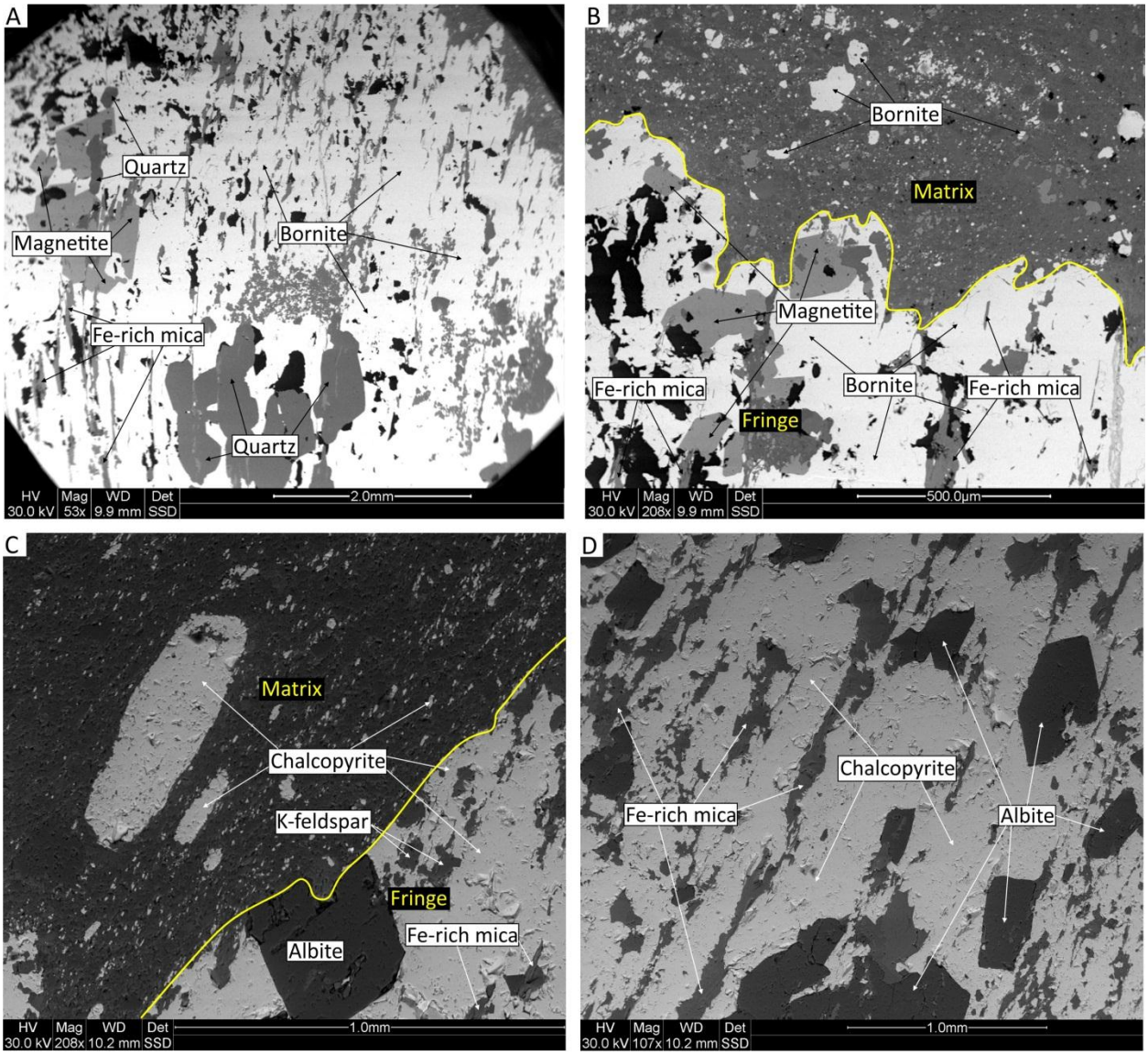

Fig. 4.46: SEM images showing strain fringes and their composition. (A). Fringe composed of bornite, iron-rich mica, quartz and magnetite. Fibres are straight and undeformed. (B). Photo illustrating a sharp contact between the fringe and the matrix. Image A and B were captured from FT_29 as shown in Figure 4.44b. Note that dark areas are holes. (C). Image illustrating the edge of fringe composed of chalcopyrite, iron-rich mica, K-feldspar and albite. An S_1 foliation defined by the alignment of chalcopyrite is also observed. The straight fibres within the fringe are parallel to S_1. (D). Fibres of chalcopyrite, iron-rich mica within the fringe are undeformed and straight. Image C and D were captured on FT_31 presented in Figure 4.44e.

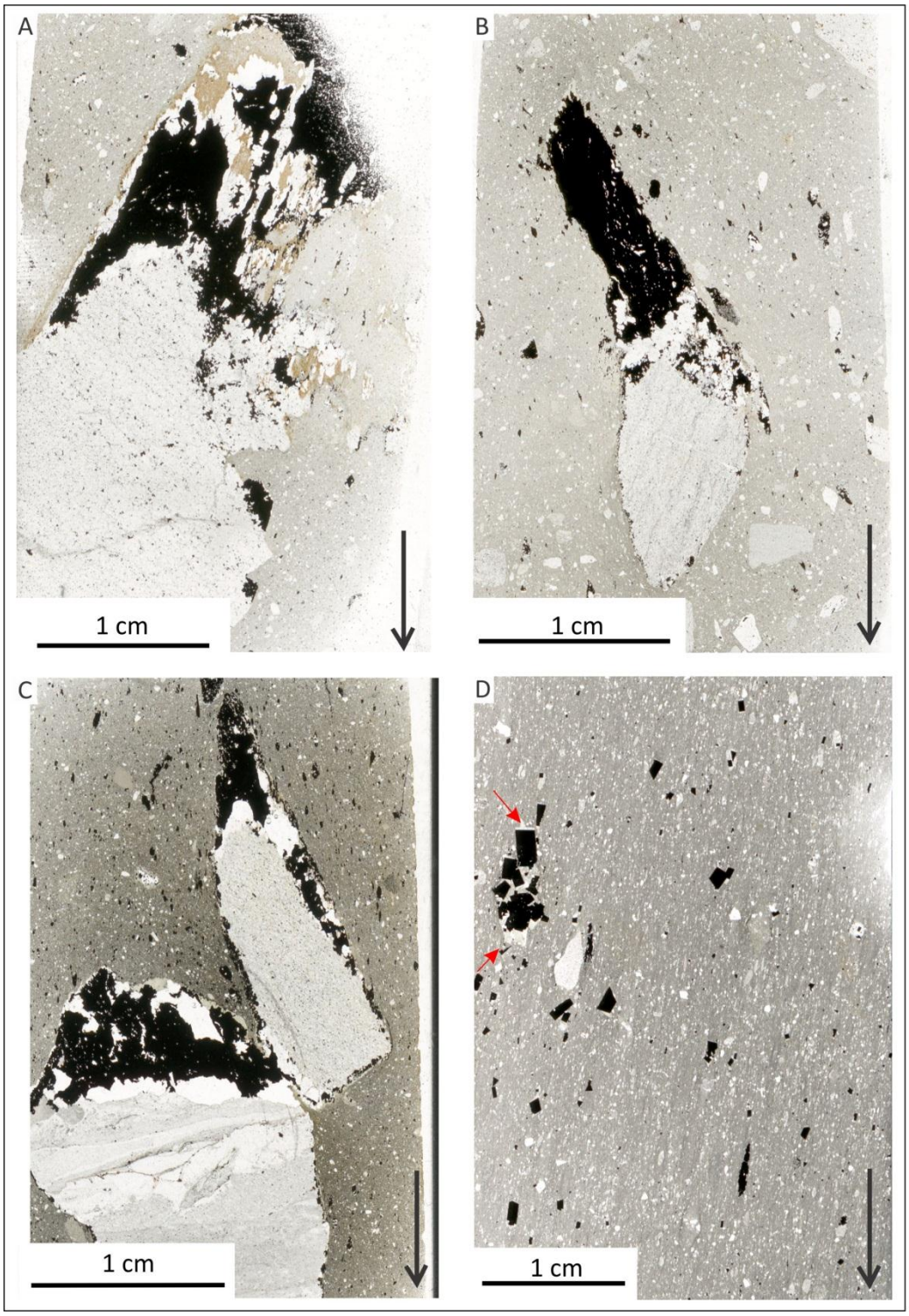

Fig. 4.47: Scanned thin sections illustrating strain shadows in diamictite. The rigid object of the strain shadow is composed of clasts in (A), (B) and (C). In (D), euhedral pyrite forms the rigid object to the strain shadow (red arrows). The composition of clasts and strain shadows for each image is presented in Fig. 4.48 and 4.49. (A). FT_51 from borehole DD401, at 784.63 m depth. (B). FT_50 from borehole DD401 at 783.29 m depth. (C). FT_39 from borehole DD381, at 240.16 m. (D). FT_19 from borehole DTJI_DD001 at 100.51 m. The black arrows show the downhole direction.

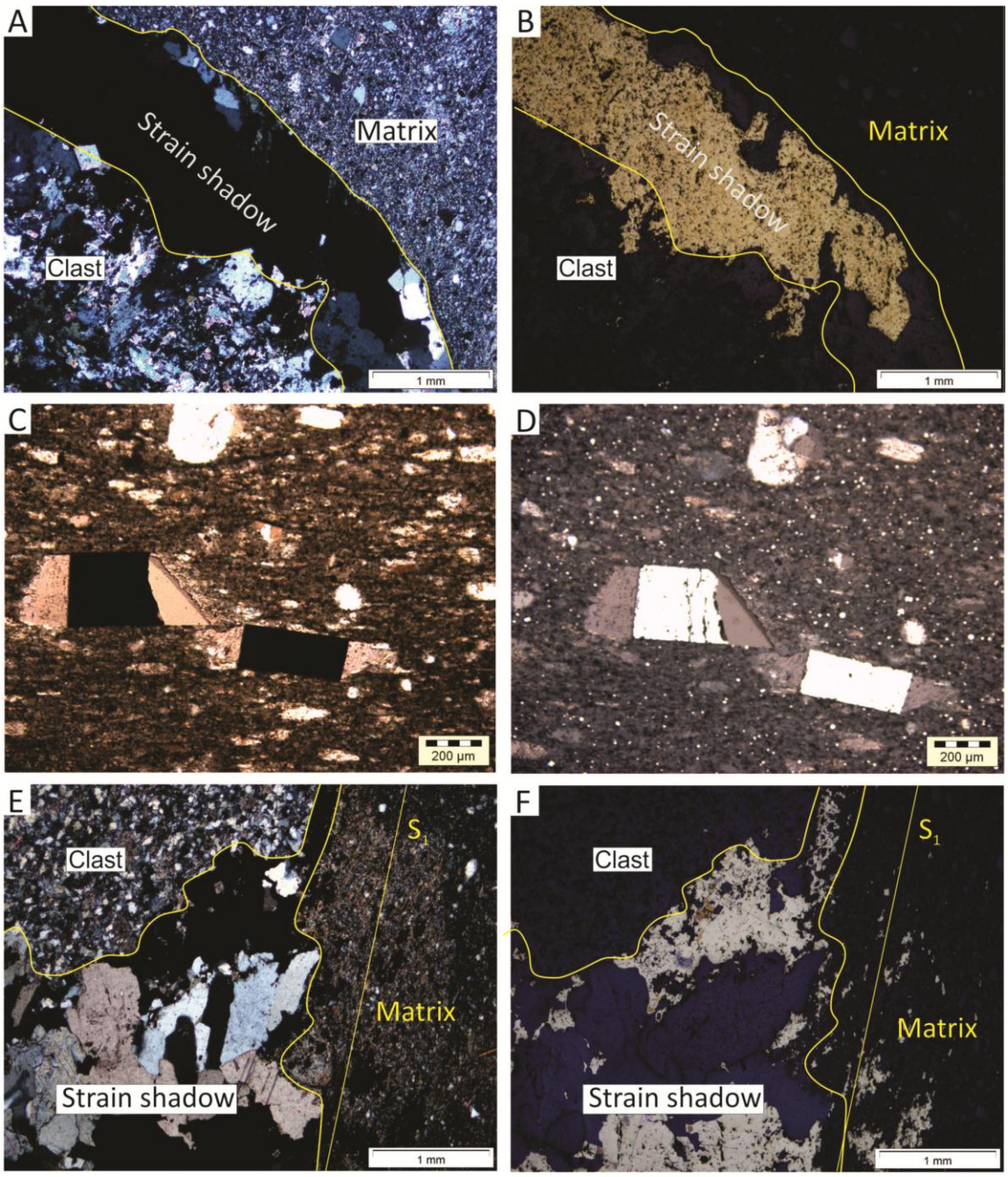

Fig. 4.48: Photomicrographs illustrating strain shadows in diamictite. (A). Chalcopyrite (black area), quartz and carbonate in a strain shadow to a mafic igneous clast with a few chlorite fibres around chalcopyrite. The mineralogical composition of the clast is similar to the mineralogical composition of the strain shadow structure (XPL). From borehole DD453, at 1148.94 m depth. (B). Reflected light photomicrograph of A showing chalcopyrite in strain shadow. (C). Quartz in strain shadow to euhedral pyrite. The slaty cleavage defined by the alignment of clasts is parallel to the strain shadows. From borehole DTJI_DD001, at 100.51 m depth. (PPL) (D). Reflected light photomicrograph of C illustrating euhedral pyrites as rigid objects to the strain shadows, this may suggest that pyrite predates the foliation. (E). Carbonate, quartz and chalcopyrite in strain shadow to a quartz clast (top left). From borehole DD401, at 783.29 m depth. (F). Reflected light photomicrograph of E showing non fibrous chalcopyrite within the strain shadow around the quartz clast. Disseminated coarse-grained chalcopyrite forms a slaty cleavage (S_1) which is sub parallel to the strain shadow.

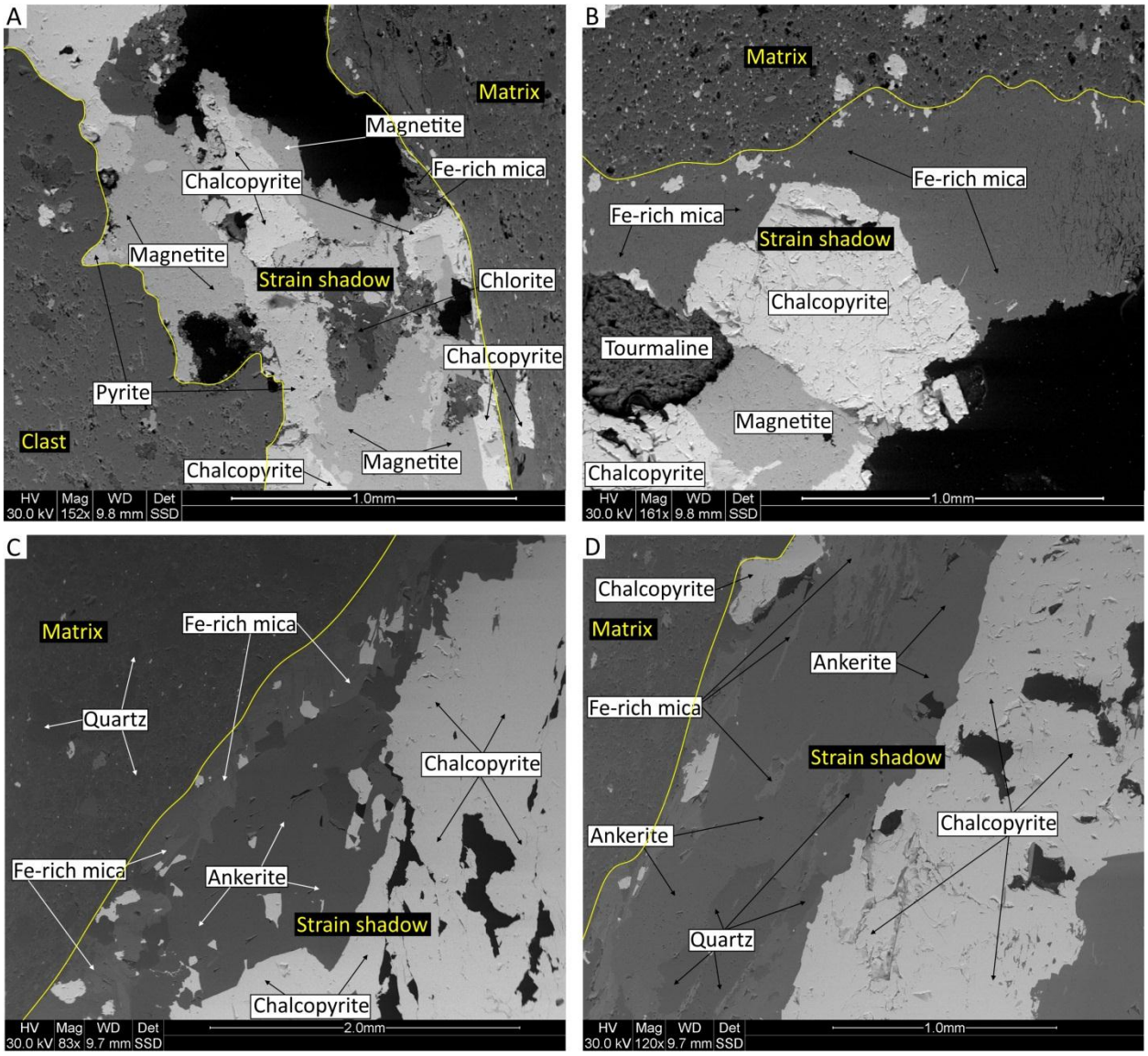

Fig. 4.49: SEM images showing strain shadows and their composition. (A). Chalcopyrite, magnetite, iron-rich mica, pyrite and occasional chlorite are identified in the strain shadow. (B). Strain shadow composed of iron-rich mica, chalcopyrite, magnetite and tourmaline. A sharp contact separates the strain shadow and the matrix. Image A and B were captured on FT_39 presented on Figure 4.47c. (C). Chalcopyrite, iron-rich mica and ankerite form the strain shadow to the clast. The contact between the strain shadow and the matrix is sharp. (D). Strain shadow enriched with chalcopyrite, ankerite, iron rich mica and quartz. Image C and D were captured on FT_51 presented in Figure 4.47a. Dark areas are holes.

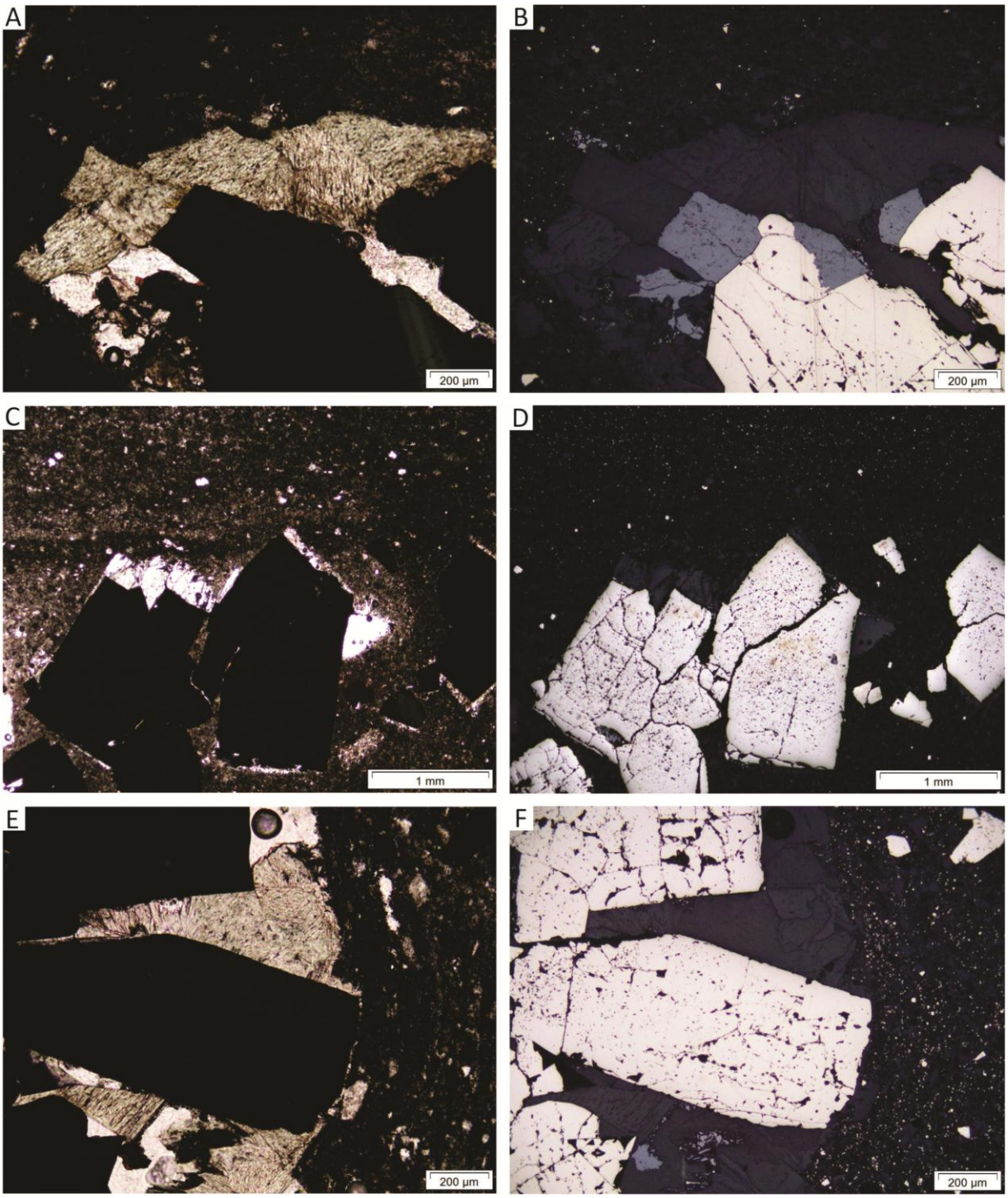

Fig. 4.50: Illustration of strain shadows and strain fringes in siltstone. (A). Chlorite and quartz in strain shadows. From DD202, at 165.75 m depth. (PPL) (B). Reflected light photomicrograph of A showing sphalerite and euhedral pyrite as rigid objects of the strain shadows. (C). Chlorite and quartz fibres to euhedral pyrite. Euhedral pyrite seems to overgrow the syn-sedimentary mesoscopic fold. From DD027 at 77.65 m. (PPL). (D). Reflected light photomicrograph of C showing euhedral pyrites as rigid objects of the strain fringes. (E). Chlorite and quartz strain shadows. From DD202, at 165.75 m. (PPL). (F). Reflected light image of E illustrating euhedral pyrite as rigid objects to the strain shadows. Traces of sphalerite are observed in the strain shadow.

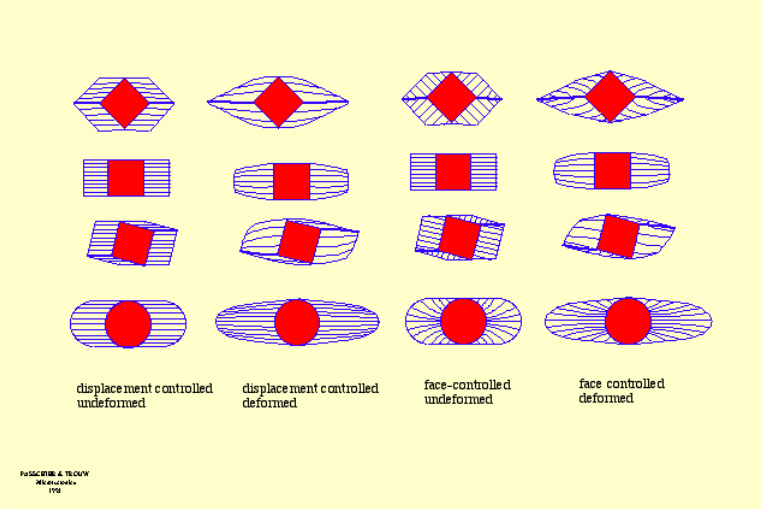

Fig. 4.51: Theoretical model for the development of strain fringes in coaxial progressive deformation around cubic and spherical core objects in the case of displacement controlled and face-controlled fibres. Rigid and deforming fringes are shown. In the case of cubic core objects, the shape of the fringe strongly depends on the original orientation of the core object with respect to the opening direction of the fringe. From Microtectonics short course GSSA Stellenbosch, 2015.

4.6 Veins

Veins are dilation sites that are voids in a rock filled with fluid, in which material is deposited from solution (Passchier and Trouw, 2005; Bons *et al.,* 2012). Veins are generally uncommon in the Kamoa deposit and rare in the mineralised zone. Most veins appear to follow the trend of bedding (Fig. 4.52), their thicknesses varies from a centimetre to several metres (<3 m).

The composition of veins varies; they can contain a single or several of these minerals: quartz, haematite, dolomite, carbonates, iron oxides, pyrite, chlorite and copper sulphides (Fig. 4.53). In the Kamoa deposit, quartz veins are most significant (in term of thickness) and appear parallel to bedding (Fig. 4.53a, b and c). Calcite veins are narrow (< 1 cm) and most abundant in the upper stratigraphic units (Ng 1.1.3, Ng 1.1.4, Ng 1.1.5 and Ng 1.1.6).

Veins with copper minerals are rare (less than 0.1% of the mineralisation), they show two orientations: steeply dipping to the northwest and gently dipping to the southwest (Fig. 4.52b). Narrow chalcopyrite veins can be observed in the Basal diamictite. In the Lower laminated pyritic siltstone/sandstone (Ng 1.1.2), pyrite occurs in bedding-parallel layers where the beds are folded (syn-sedimentary folding); this may suggest that pyrite formed in soft beds possibly early during lithification (Fig. 4.53c).

Within the deposit area, the density of veins is higher in the eastern part (east of Kamoa and Makalu domes), and lower in the western part (west of Makalu and Kamoa domes) (Fig. 4.54).

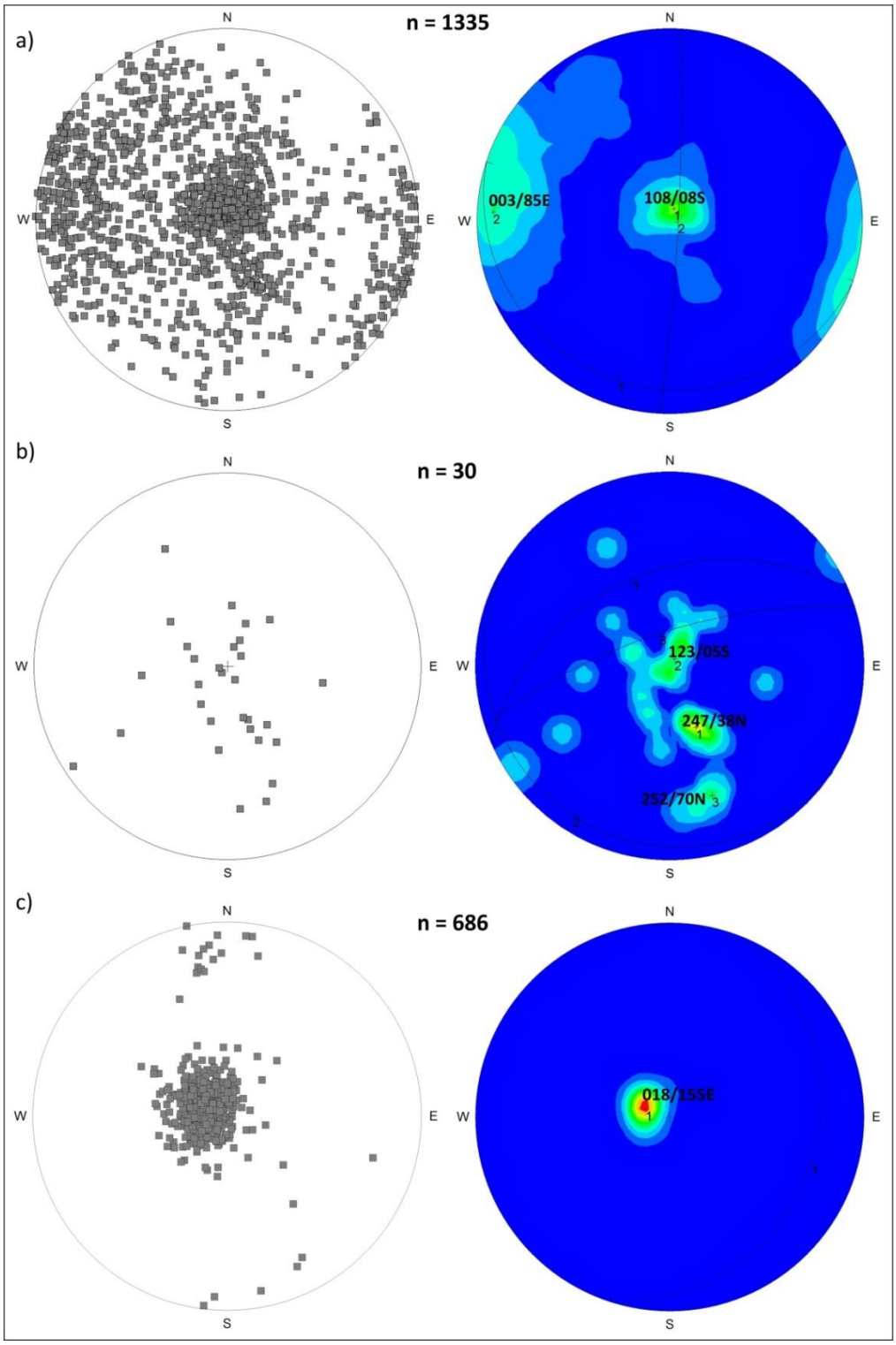

Fig. 4.52: Orientation of veins and bedding in the Kamoa deposit. Lower hemisphere equal area stereographic projection. (A). Poles to veins (all types including mineralised and non-mineralised). (B). Poles to veins with copper sulphides. (C). Poles to bedding.



Fig. 4.53: Images of veins in the Kamoa deposit. (A). Bedding- parallel quartz vein associated with trace chlorite. DD037, 1298.73 - 1298.78 m. (B). Bedding-parallel quartz and pyrite vein in the Lower laminated pyritic siltstone/sandstone (Ng 1.1.2). DD401, 766.6 - 766.68 m. (C). Folded pyrite vein in a fibrous carbonate layer within the Lower laminated pyritic siltstone/sandstone. This feature suggests that pyrite formed in soft beds, possibly early during lithification. DD895, 515.42 – 515.43 m. (D). Quartz, pyrite and iron oxide vein showing a slightly brecciated texture. DMAK_DD027, 353 - 353.29 m. (E). Quartz vein with trace chalcopyrite and bornite in the Basal diamictite. Non-planar vein parallel to the very weak foliation defined by alignment of clasts. DMAK_DD014, 560.20 - 560.21 m. (F). Quartz vein in the diamictite. DMAK_RD024, 89.42 - 89.45 m.

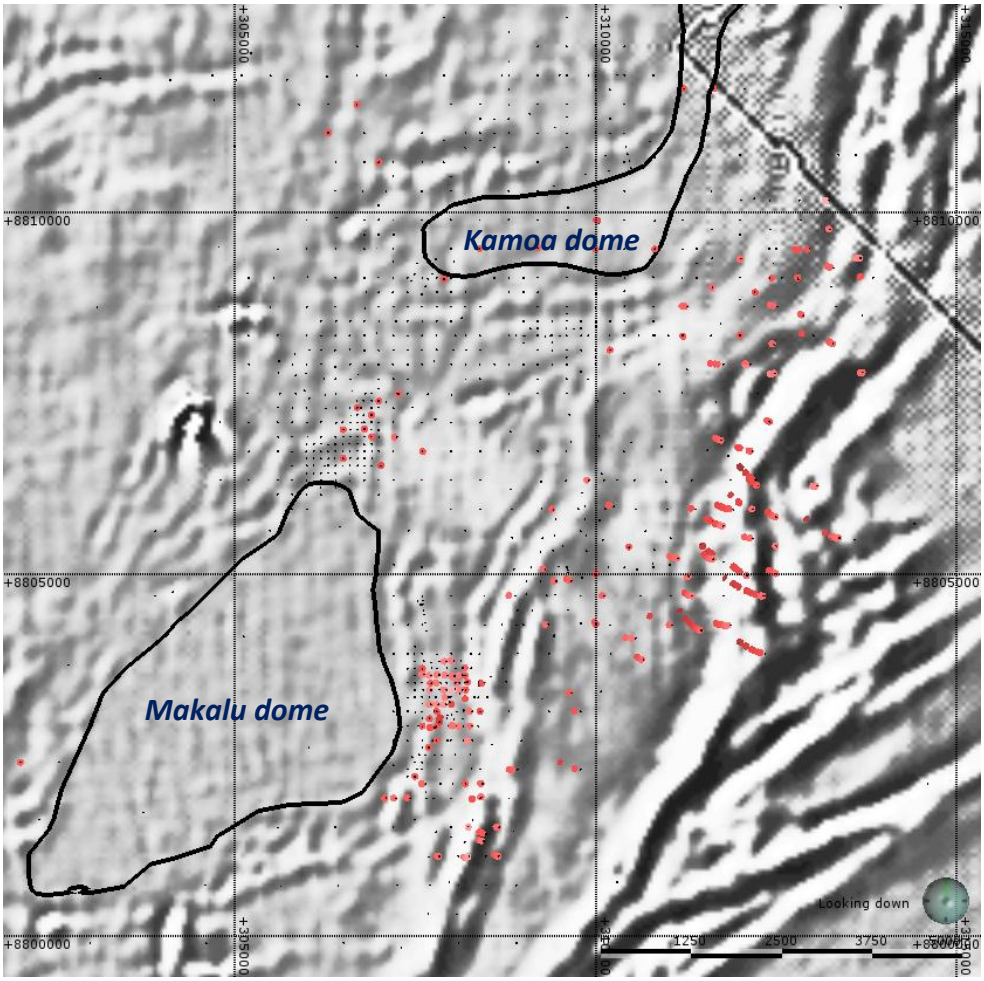

Fig. 4.54: Map showing the distribution of veins in the Kamoa deposit superimposed on a magnetic map. The intensity of veins is higher in the east and lower in the centre and west part of the deposit. The red points represent veins that have been collected in different stratigraphic units in the Kamoa boreholes. Data from the Kamoa geological dataset.

4.7 Mesoscopic folds

In the Kamoa borehole core, mesoscopic folds are fairly common structural features that can be observed. They are generally tight to isoclinal, asymmetric and recumbent (Fig. 4.55). These features are observed in siltstones, sandstones and mudstones (especially in the Ng 1.1.2, Ng 1.1.4 and Ng 1.1.1.2). In the boreholes, the fold axial plane of mesoscopic folds appears to be generally parallel to bedding (Figs. 4.55 and 4.56), however the fold trends have not been defined because of the poor or lack of orientation within cores with folds.

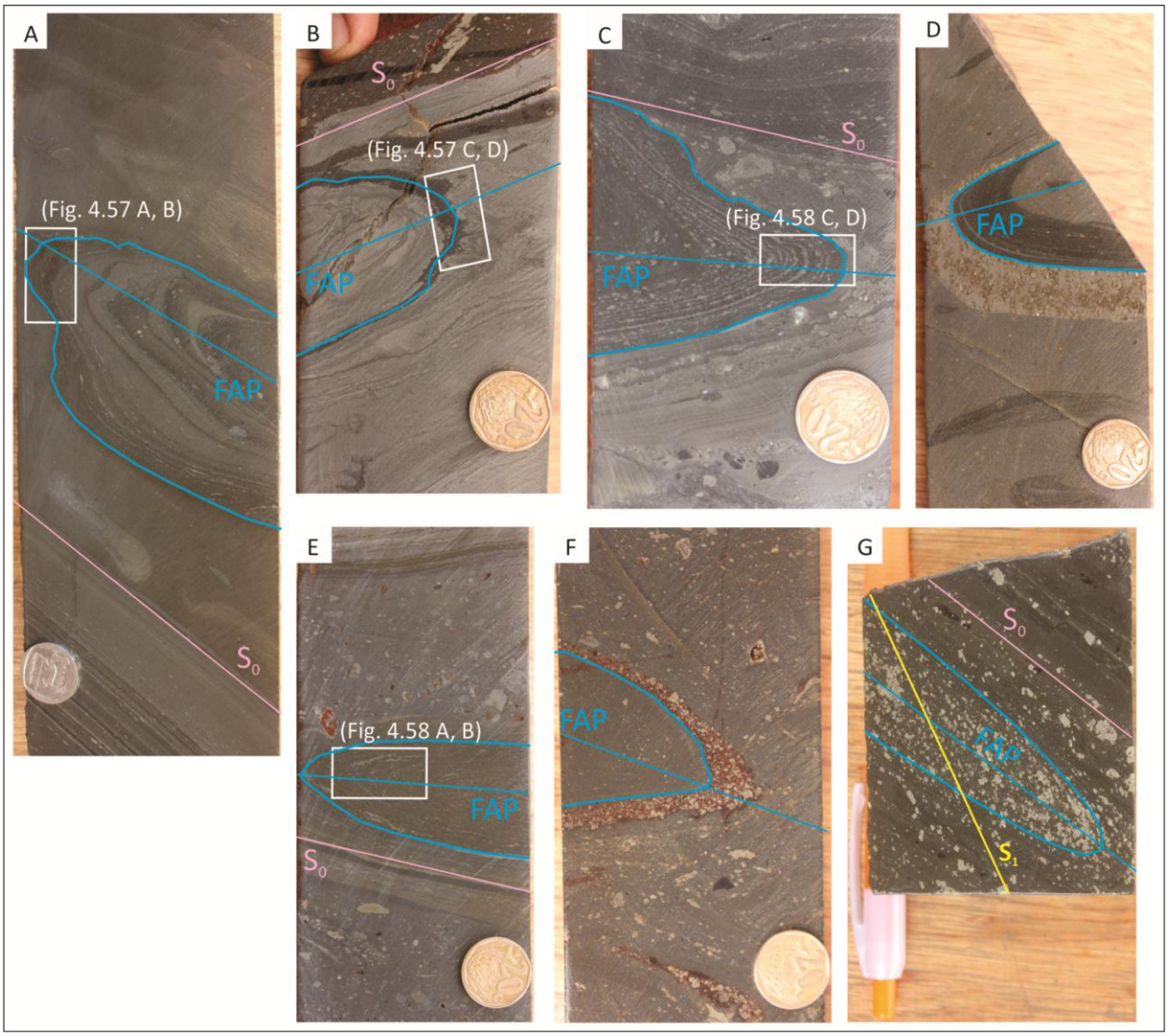

Fig. 4.55: Photographs of hand samples illustrating mesoscopic folds within the Kamoa deposit. (A). Asymmetric, tight and recumbent fold observed in the Lower Laminated pyritic siltstone/sandstone with a fold axial plane parallel to bedding. Sample from borehole DKMC_GD003 at 515.32 m depth. (B). Asymmetric, tight and recumbent fold in sandstone with a fold axial plane parallel to bedding (S_0). Core sample from borehole DD197 at 205.04 m depth. (C). Asymmetric, tight and recumbent fold developed in siltstone with a fold axial plane parallel to bedding. Core sample from borehole DMAK_DD033 at 234.79 m depth. (D). Asymmetric, tight and recumbent fold in sandstone and siltstone layers with abundant coarse-grained pyrite in the layers. Core sample from borehole DD027 at 77.60 m depth. (E). Tight and recumbent mesoscopic fold developed in Intercalated siltstone. The axial plane of the fold is parallel to the bedding. Sample from the borehole DMAK_RD023 at 96.37m depth. (F). Asymmetric, tight and recumbent fold in diamictite. Layering shown by abundant coarse-grained pyrite and iron oxides. Sample from borehole DD084 at 149.82 m depth. (G). Tight and asymmetric fold within siltstone. Euhedral pyrite defines a weak S_1 which is oblique to the fold axial plane and bedding, this suggests that folds are prior to the development of foliation. Core sample from borehole DD215 at 580 m depth. Bedding is shown in pink and the fold axial plane in blue in all images.

Thin section observations have revealed that mesoscopic folds contain framboidal and euhedral pyrite. Framboidal pyrite within the Kamoa mesoscopic folds is completely undeformed and no fabric can be observed (Figs. 4.57, 4.58 and 4.59).

In three boreholes, the orientation of the fold axial plane was compared to the orientation of bedding, it does appear that these features display a similar orientation (Fig. 4.56). In addition, the slumping texture and the presence of framboidal pyrite disseminated within the mesoscopic folds suggest that they may be syn-sedimentary slump folds of non-tectonic origin. Euhedral pyrite overgrows the sedimentary lamination and contains strain fringes/shadows; this indicates that euhedral pyrites are later than the lamination (Fig. 4.50c, d). The rock within the fold hinges does not exhibit an axial planar foliation, however some of the samples display a weak alignment of sedimentary rocks and framboidal pyrites (Fig. 4.58).

The mineralogy of folded layers is composed of quartz, biotite, and chlorite with rare muscovite. Layering is shown by grain size variation and alternating dark and light coloured layers (Figs. 4.57a, c; and 4.58a, c). This corresponds to a variation in grain size with the darker layers being more fine-grained and possibly containing more sheet silicates. The grain size is overall less than 5 µm with frequent slightly larger (up to 10 µm) angular quartz fragments. Within the darker layers disseminated rounded framboidal pyrite grains are common, they constitute up to 40%. Euhedral pyrite appears to overgrow the mesoscopic folded layers and is associated with strain shadows/fringes which are parallel to S_1 foliation. Strain fringes around euhedral pyrite are composed mainly of quartz and chlorite with minor muscovite. Strain shadows around euhedral pyrite are dominantly composed of quartz (Fig. 4.50c, e).

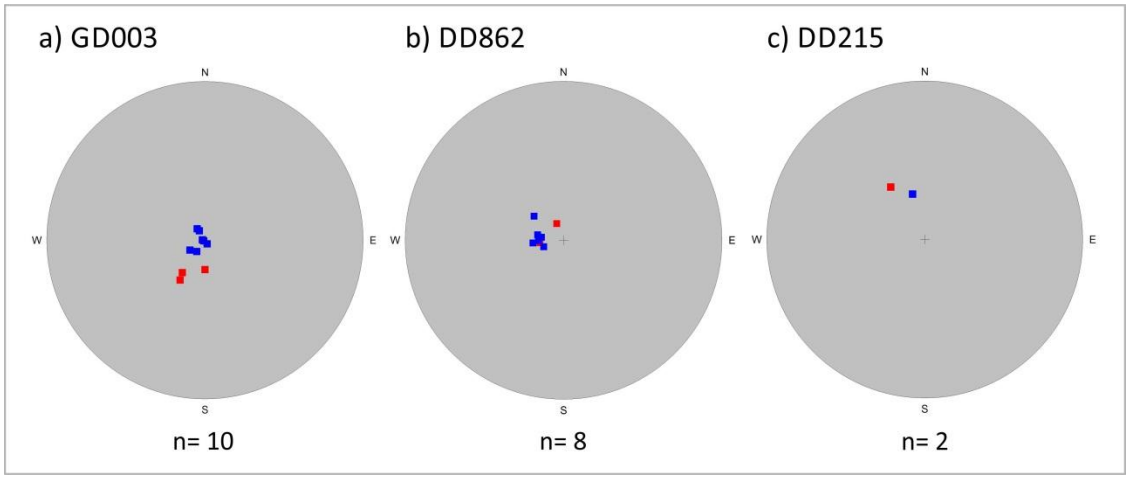

Fig. 4.56: Relationship between bedding and the axial planes of mesoscopic folds. The orientation of the fold axial planes is similar to the orientation of the beds. Lower hemisphere equal area stereographic projections.

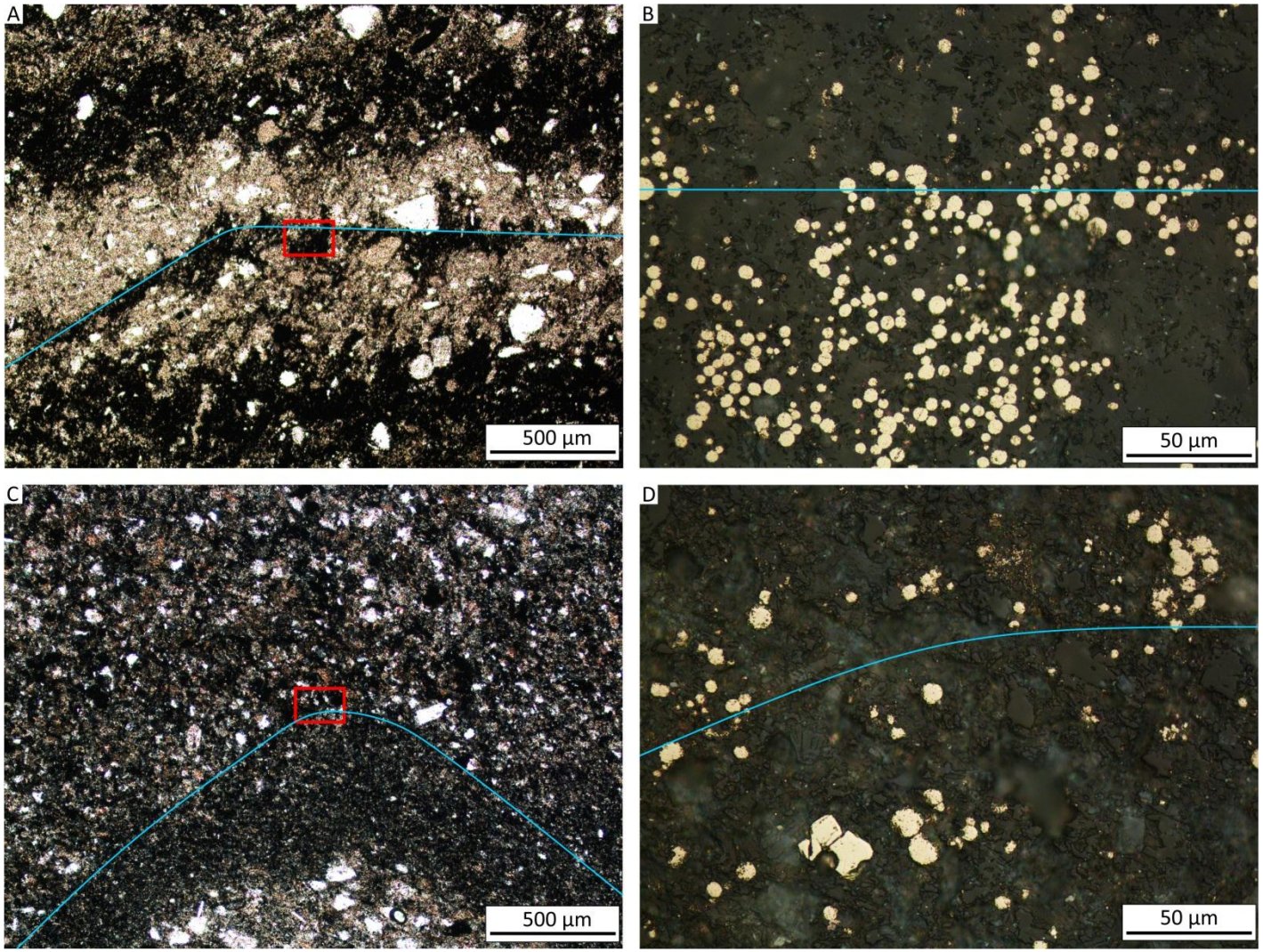

Fig. 4.57: Photomicrographs of mesoscopic folds. (A). Fine-grained matrix composed of quartz and micas. The secondary foliation is not observed (PPL). (B). Detail of A (red square), Reflected light photomicrograph showing abundant framboidal pyrite disseminated in the fold. Sample FT_21B, shown in Fig. 4.55a. (C). Sedimentary fold with no foliation observed. (PPL) (D). Detail of C (red square). Reflected light photomicrograph illustrating the presence of framboidal pyrite disseminated in the fold. The blue lines show trace of folded bedding. Sample FT_43, shown in Fig. 4.55b.

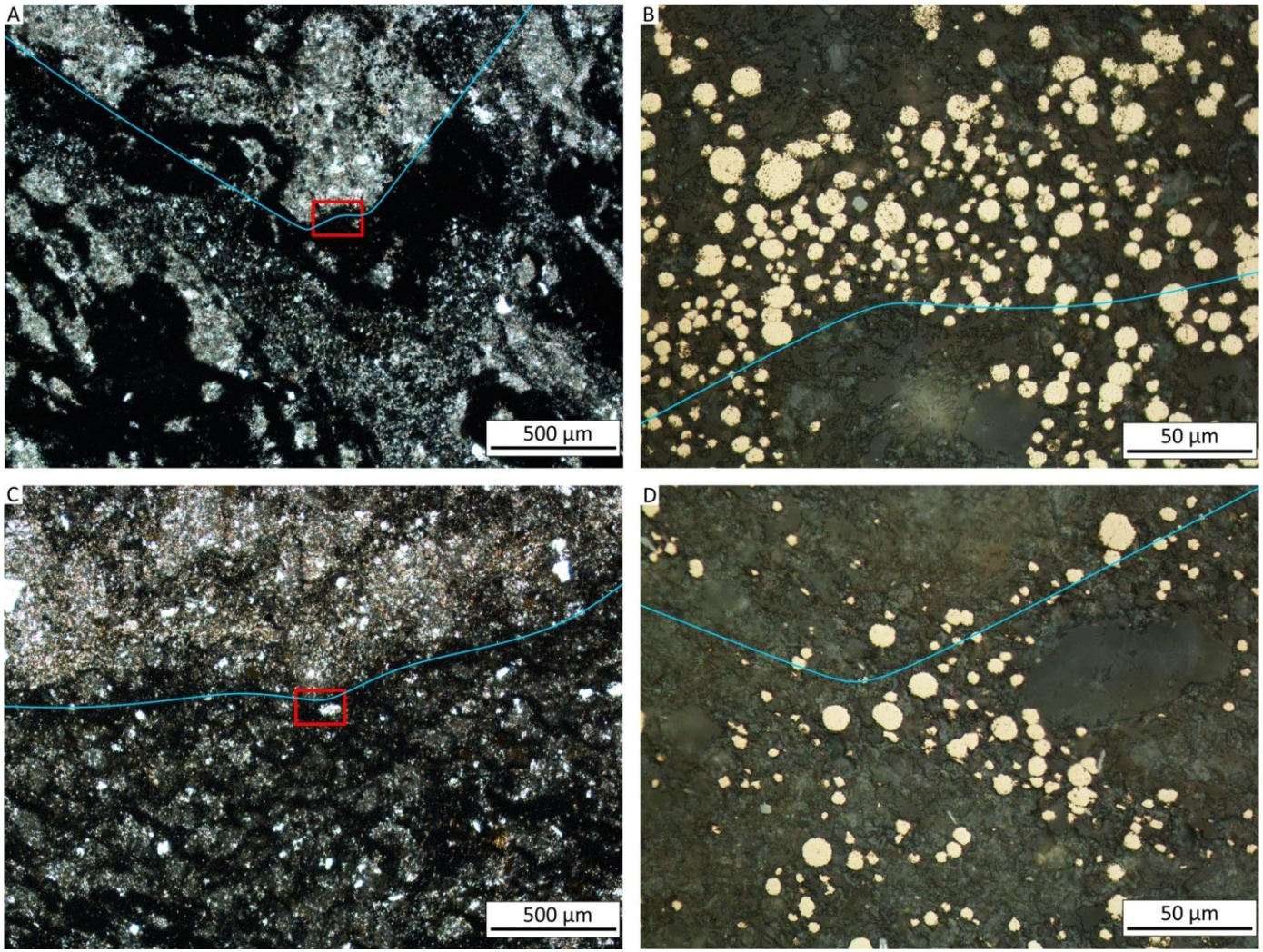

Fig. 4.58: Photomicrographs of mesoscopic folds. (A). Sedimentary mesoscopic fold showing a weak alignment of minerals. The rock is composed of quartz and micas. (PPL). (B). Detail of A (red square). Reflected light photomicrograph showing abundant framboidal pyrite disseminated in the folds. Sample FT_49, shown in Fig. 4.55e. (C). Mesoscopic fold composed of quartz and micas. (PPL) (D). Detail of C (red square) showing a slight fabric defined by framboidal pyrite. This fabric is oblique to the folded bedding. Reflected photomicrograph. The blue lines show trace of folded bedding. Sample FT_48, shown in Fig. 4.55c.

Studies under the scanning electron microscope (SEM) help to confirm that the minerals within the mesoscopic folds do not define a secondary foliation (S_1) suggesting that these folds with sub-horizontal axial planes are due to soft-sediment deformation rather than tectonic deformation (Fig. 4.59).

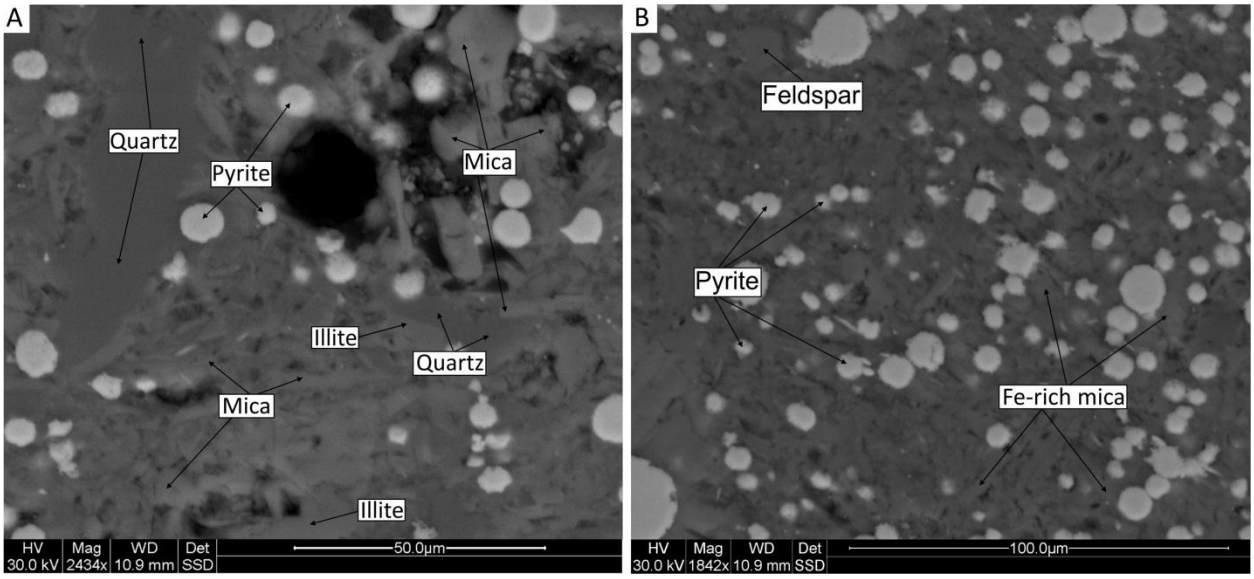

Fig. 4.59: SEM images of mesoscopic folds. (A). Mica, quartz and illitte are randomly oriented and framboidal pyrite is completely undeformed. Image captured on FT_49 from Figure 4.55e. (B). Mica in the mesoscopic fold does not show a preferred orientation however a weak alignment of some framboidal pyrite is observed. Image captured on FT_48 from Figure 4.55c. Dark areas are holes.

4.8 Faults

4.8.1 Macro faults

At Kamoa, the classification of faults within borehole core is based in the cohesiveness of the rock and proportion of matrix to clasts. A geometrical classification of fault breccia is used to qualitatively describe the increasing degree of disaggregation of initially intact rock (Mort and Woodcock, 2008).

Crackle breccia has >75% clasts, mosaic breccia 60-75% clasts, and chaotic breccia has <60% clasts. Within the project area, faults are subdivided in three broad categories: faults type 1, type 2 and type 3 (Twite *et al.,* 2012). Structural measurements of these features have been collected.

The mineralogy along the fault related fractures are mainly comprised of clay, haematite, dolomite, kaolinite, pyrrhotite, pyrite, and sericite.

4.8.1.1 Fault type 1 (FA1)

The fault type 1 suggests the high probability of a significant structure. This feature includes gouge zones with slickensides (Fig. 4.60), clast-supported tectonic breccia containing two lithologies, clast-supported breccia containing abundant slickensides and any obvious discontinuity that separates two lithologies or zones with extremely different alteration/mineralisation intensity (Twite *et al.,* 2012).



Fig. 4.60: Fault type 1. Gouge, mosaic to chaotic breccia. Slickensides are present in the edge of the fault zone. A fractured zone is observed around the significant fault. DKMC_GD003, 147.80 – 148 m.

4.8.1.2 Fault type 2 (FA2)

This fault type suggests a moderate probability of a significant structure. The feature includes any clast-supported tectonic breccia not defined as fault type 1 (Fig. 4.61), gouge not defined as fault type 1, zone of poor recovery containing some indication that the poor recovery was related to the faulting, slickensided fragments, different rock types present compared to adjacent lithologies, very broken to rubbly zones containing slickensides or characterised by alteration/mineralisation that is extremely different compared to adjacent rock. These zones containing abundant slickensides (Twite *et al.,* 2012).



Fig. 4.61: Fault type 2. Crackle breccia with slickensides. Thin gouges are observed associated with crackle breccias. No significant fractures occur around the fault. DD547, 96.75 – 99 m.

4.8.1.3 Fault type 3 (FA3)

This feature suggests a possible geologically significant structure. It includes clast-supported breccia where clasts are still articulated, suggesting minimal displacement. These may represent the edges of influence of more significant faults. They are characterised by badly broken to rubbly zones not classified as fault type 2 or fault type 1 (Fig. 4.62). This feature consists of zones containing multiple slickensides not classified as fault type 2 or fault type 1, single slickensides associated with some type of thin fill, especially if containing clay or fault gouge. When thicker, such structures should be classified as fault type 2 or fault type 1 (Twite *et al.,* 2012).



Fig. 4.62: Fault type 3. Badly broken to rubble zone. This feature may possibly represent a geological structure. DD456, 338.15 – 339.08 m.

SRK Consulting (Canada) assisted the Kamoa geology team in interpretation of structural and geotechnical data from borehole core (Barnett, 2012; Mvondo, 2012; Barnett, 2013 and Barnett, 2014). A summary of their interpretation includes the identification of faults which are commonly illustrated by steep dipping angle (typically <50 degrees) intersections, fault gouges, breccias, fracture and slickensides. The steps and slickensides on fault planes most commonly indicate a reverse-sinistral type of movement, but reverse faulting and normal faulting is also indicated locally (Barnett, 2012). A stereographic analysis of fault plane orientation data measured along the borehole cores indicates two main trends of north- and north-northeast-trending faults occurring with subordinate east-striking faults (Mvondo, 2012). The north-striking fault set dips steeply (>70 degrees) either eastward or westward. Similarly, the north-northeast trending set dips steeply (> 70 degrees) toward either west-northwest or east-southeast (Fig. 4.63). In contrast, some east-striking faults dip steeply to the north (> 60 degrees), whereas others dipping gently (< 30 degrees) between the south and southeast directions suggesting the presence of discrete thrust faults in the project area (Mvondo, 2012). The stereographic analysis of faults suggests that faults are parallel to the basement trend (Fig. 4.63).

SRK proposed a structural model which consists of a total of 31 faults divided into 6 sets of differing orientations (Barnett, 2014). The model was based on the geological and geotechnical information (faults, fractures and joints), oriented core information, surface geophysics, and topographic surfaces. This model is based on boreholes separated by 100 to 800 m, therefore stratigraphic offset is difficult to characterise.

AMEC suggested a simplistic structural model which assumed that faults are single vertical planes (Parker *et al.,* 2013) (Fig. 2.3). This model includes 9 faults showing two main orientations: a dominant north-northeast and a west-east orientation.

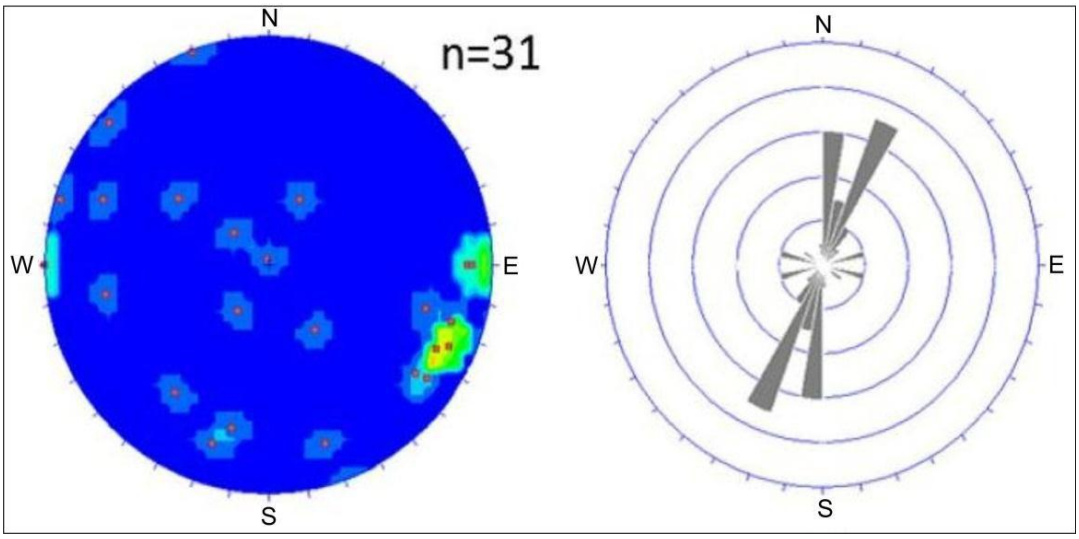

Fig. 4.63: Lower hemisphere equal area stereographic projection of poles to fault planes. (Mvondo, 2012). Two main trends of north- and north-northeast-trending faults are observed. Faults appear parallel to the NNE trend of the Nzilo basement.

4.8.2 Mesoscopic faults

Mesoscopic faults are small-scale faults with offsets that are less than the core diameter. They are not significant structures, but can usually demonstrate a sense of movement. It is possible that they could be related to larger structures, and mineralisation.

Within the investigated boreholes, about 75% of mesoscopic faults recorded show a normal sense of movement, 20% show reverse sense of movement and 5% do not show a clear sense of movement. The predominant sense of movement of mesoscopic faults within the studied boreholes is normal with minor reverse (Fig. 4.64).

Mesoscopic faults are commonly observed in siltstone and sandstone layers. They generally contain framboidal pyrite, euhedral pyrite in the fault planes (Fig. 4.65). In the mineralised zone, they generally contain copper sulphides along the fault planes. Mesoscopic faults appear to be syn-sedimentary, post or synchronous with the deposition of framboidal pyrite (Fig. 4.65). Copper minerals appear to postdate the formation of mesoscopic faults, this has been observed in thin sections where S_1 defined by copper sulphides cut the mesoscopic faults (Fig. 4.66).

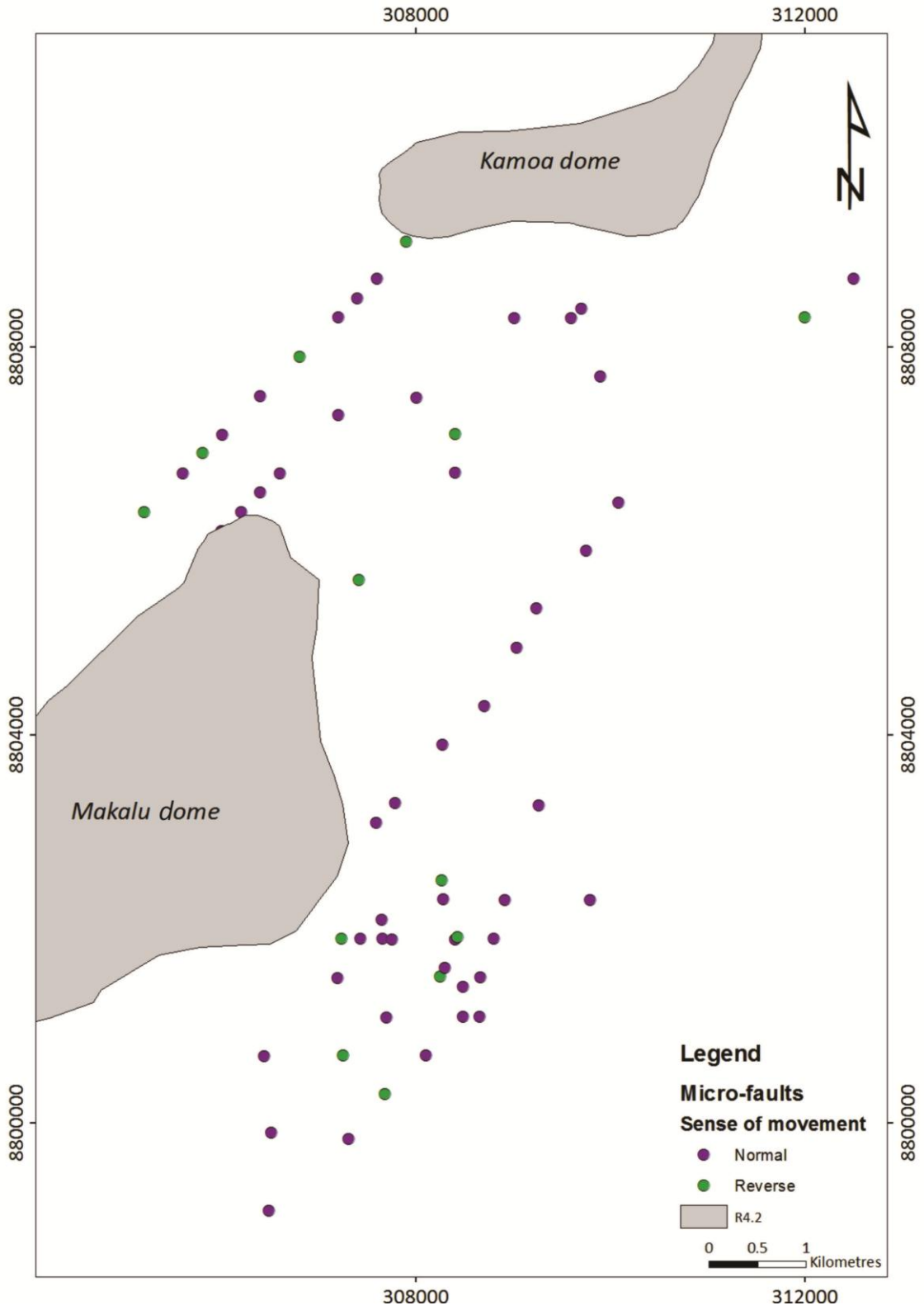

Fig. 4.64: Map showing the predominant or median sense of movement of mesoscopic faults within boreholes in the studied area.

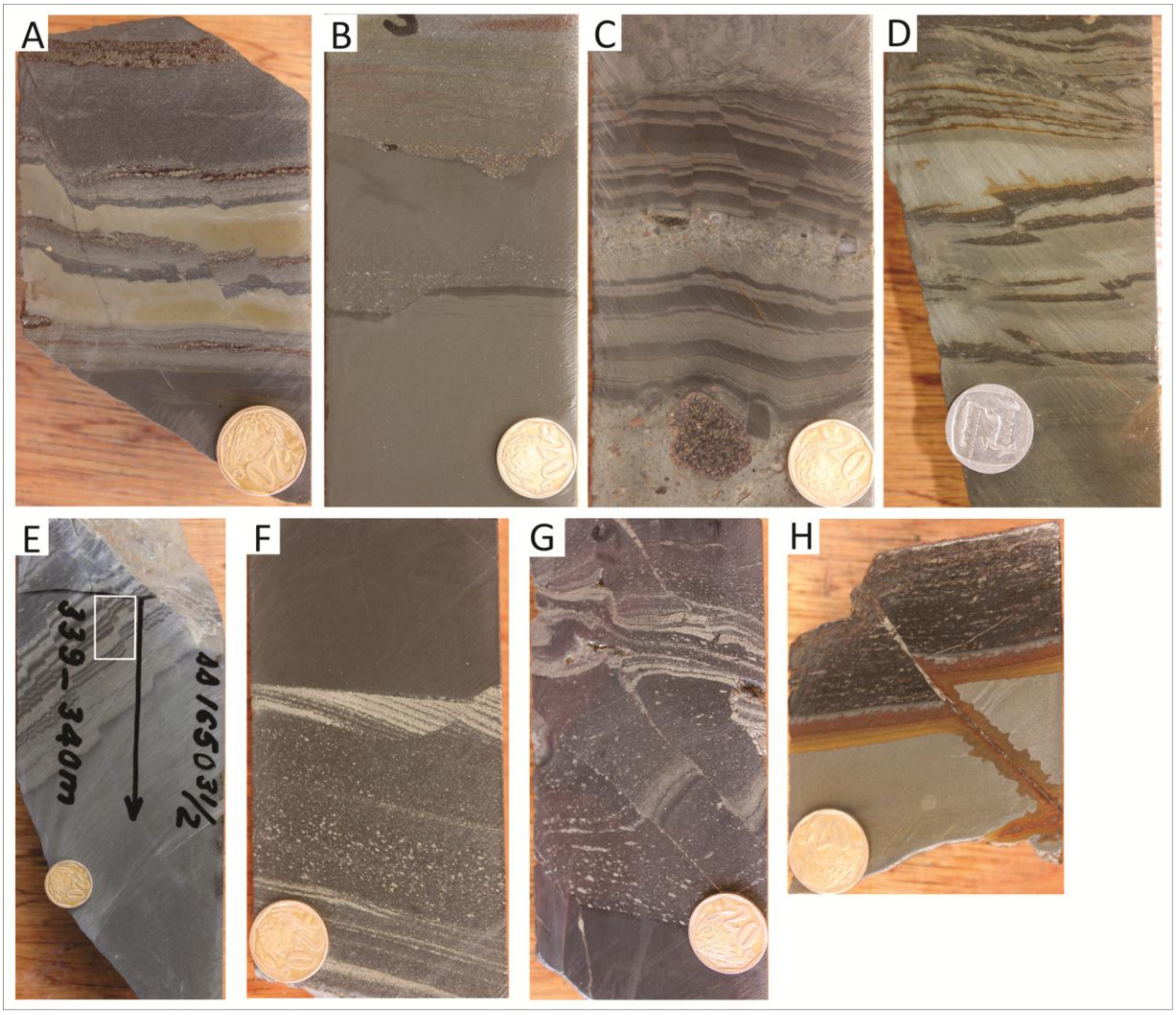

Fig. 4.65: Mesoscopic faults observed in boreholes cores within the studied area. (A). Normal mesoscopic faults cut the sedimentary rocks which contain sulphide mineralisation. Possible syn-sedimentary faults. DMAK_RD021 at 121.85 - 121.91 m. (B). Syn-sedimentary normal mesoscopic fault defined by displacement of beds. DD821, 234 – 234.50 m. (C). Abundant normal mesoscopic faults which appears to be syn-sedimentary. DMAK_RD030, 660.86 - 660.94 m. (D). Mesoscopic faults showing a reverse sense of movement. DD443, 525.10 - 525.15 m. (E). Reverse mesoscopic faults define by the offset of beds. DKMC_GD002, 342.15 - 342.20 m. (F). Pyrite beds disrupted by a syn-sedimentary normal mesoscopic fault. DD901, 608.82 - 608.84 m. (G). Growth structures mineralised by pyrite. Fine and coarse pyrite in thin beds disrupted by normal mesoscopic faults defined by displacement of beds. DD915, 517 - 517.09 m. (H). Reverse mesoscopic fault defined by the offset of beds. The fault with overgrowth minerals may have formed at the same time or after the deposition of the mineralisation. DD405, 498.73 - 498.76 m.

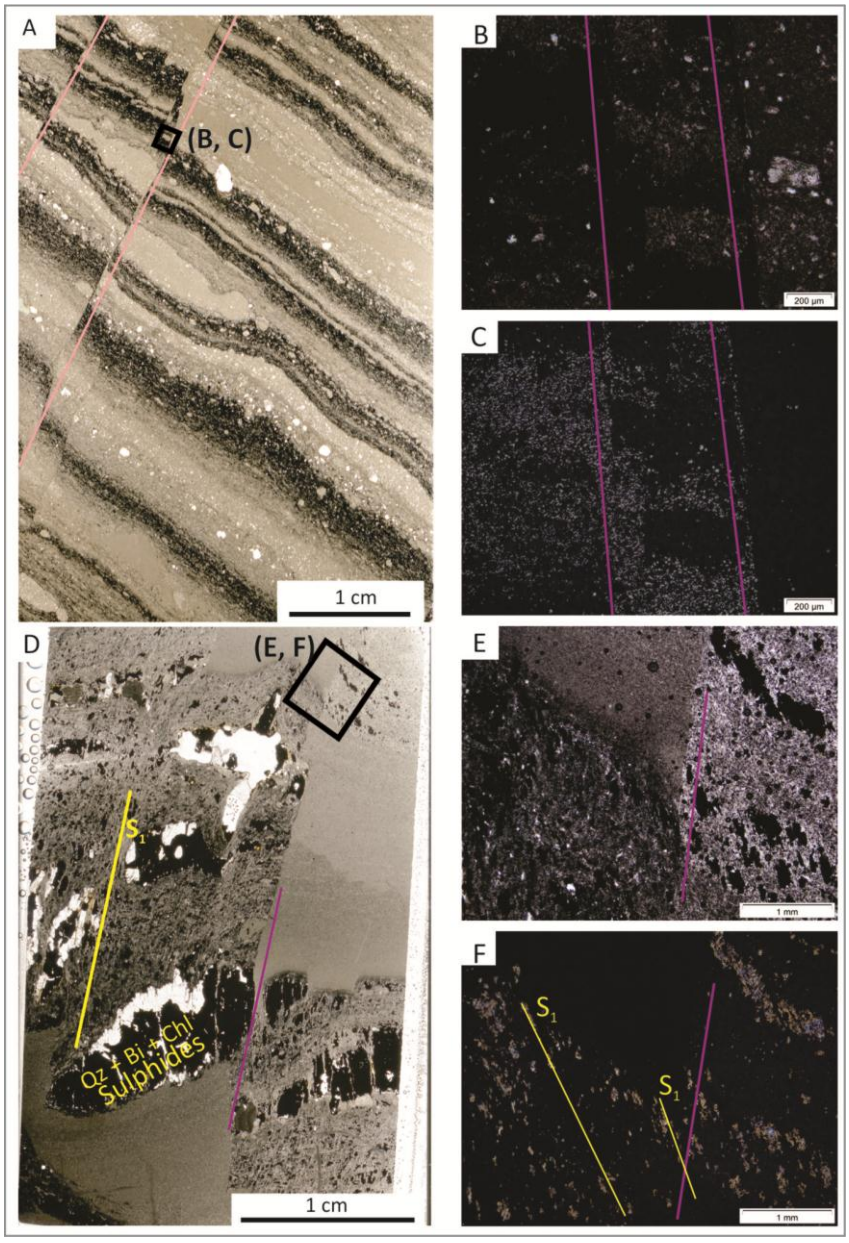

Fig. 4.66: Photomicrographs of mesoscopic faults in thin section. (A). Scanned thin section showing reverse mesoscopic faults defined by offset of mudstone beds. The beds are spaced at less than 1 mm. Occasional clasts are also observed. Sample from borehole DKMC_GD002, 339 – 339.10 m illustrated in Figure 4.65e. (B). Cross-polarised photomicrograph showing detail of A. (C). Same view as B, reflected light. Abundant framboidal pyrite disseminated in the layers and in the mesoscopic fault. (D). Scanned thin section showing a mesoscopic fault defined by displacement of siltstone and mudstone beds. Continuous schistosity defined by alignment of coarse-grained chalcopyrite and trace bornite (black areas). Quartz, biotite and chlorite are present in the strain fringe of coarse-grained chalcopyrite. Sample from the borehole DD860, at 165.86 m depth. (E). Detail of D. Mesoscopic fault defined by the displacement of siltstone beds. (F). Reflected light, cross-polarised photomicrograph of E showing a continuous schistosity defined by the alignment of fine- and coarse-grained chalcopyrite associated with traces of bornite. The photomicrograph shows that S_1 defined by chalcopyrite and trace bornite cuts the mesoscopic fault, thus S_1 is later compared to the mesoscopic faults. The purple lines indicate the mesoscopic fault planes. The yellow lines represent S_1 foliation.

4.9 Discussion

The linear NNW-SSE zone of abrupt change in stratal thickness named the "Mupaka Fault" shows soft-sediment deformation, steep bedding, syn-sedimentary mesoscopic faults, and slump folds. These characteristics indicate that this linear feature is a growth fault that was active during the deposition of the Nguba subgroup rocks. The orientation of steep bedding within the linear zone in one borehole strikes NNW/SSE, whereas the typical regional bedding strikes NNE/SSW. The Mupaka Fault may have formed during a NE/SW extension of the sedimentary basin. Growth faults (in rift basins) tend to form conjugate arrays, such that individual faults may not be perpendicular to regional extension (Broughton, D., pers. comm. 2016).

Mesoscopic faults are commonly sub-vertical in gently-dipping beds adjacent to the steep bedding while they are gently-dipping in steep bedding; this suggests that they have been rotated from steep to gently-dipping along the bedding by the same event that rotated S_0. Copper sulphides within the steep bedding occur as aligned and elongated grains that define an S_1 foliation. This suggests that the foliation played a significant role and was synchronous with the development of copper sulphides in the steep bedding zone.

The S_1 foliation defined by clasts in the diamictite unit seems to be closely related to the competence of the clasts (i.e. mafic igneous clasts can be deformed easily compared to quartz and quartzite clasts). Copper sulphides within the clasts of foliated rocks are randomly aligned and S_1 foliation is not observed. This observation suggests that these sulphides may form before or during the development of S_1 (Nex pers. comm., 2016). Clasts as rigid objects may preserve copper sulphides from deformation.

Clasts in the Kamoa rocks are randomly oriented and define a very weak, weak to moderate foliation, this may suggest that the S_1 foliation may have been developed from a random fabric by pure shear deformation (Fig. 4.25a).

The steep foliation (S_1) striking NE/SW may be related to a NW directed compression event during the Lufilian orogeny (590-550 Ma). However, this steep foliation S_1 does not seem to be related to the two orientations of folds identified within the project area.

Strain shadows and strain fringes are in places crudely vertically zoned from the base to the top of the mineralised zone as follows: symmetric strain shadows/fringes at the base followed by asymmetric upwards strain shadows/fringes. There is no abrupt change in this zonation, and a gradational overlap is generally observed. Asymmetric downwards strain shadows/fringes are rare or absent in the Basal diamictite of the Grand Conglomérat.

The fibres in the strain fringes are straight and lack undulose extinction and grain boundary structure. In addition, the distal parts of the core object in the fringes are undeformed. As the fringes are straight, the long axis of the fringes represents the X-direction of finite strain. Strain shadows and strain fringes formed during pure shear deformation, probably at the same time as the development of the S_1 foliation in the deposit area. The possibility of using quartz-fringes to determine strain rate in the host rock for dating purposes using isotope geochronology should be considered (Passchier and Trouw, 2005).

Mesoscopic folds generally lack axial planar foliation and are associated with soft-sediment deformation textures. In addition, their fold axial planes are generally parallel to bedding (S_0). Framboidal pyrites are abundant in the mesoscopic folds, they are completely undeformed and no significant fabric can be observed. Studies under the scanning electron microscope (SEM) help to confirm that the minerals within the mesoscopic folds do not define a secondary foliation (S_1) suggesting that these folds with sub-horizontal axial planes are due to soft-sediment deformation rather than tectonic deformation.

Folded pyrite veins within the Lower laminated pyritic siltstone/sandstone suggest that pyrite formed in soft beds, possibly early during lithification.

Faults are commonly illustrated by a steep dipping angle and the offset between stratigraphic units across interpreted faults is generally less than 10 m except for the West Scarp Fault, which is up to 400 m. In the project area, the spacing between boreholes varies from 50 to 800 m, which makes it difficult to identify the nature of any offset in the stratigraphy and its origin. Apparent offset could be due to the tectonic activity or to the folding of the sedimentary basin. Tectonic faults are interpreted to post-date the deposition of the sulphide mineralisation.

4.10 Conclusion

In this chapter structural features of the Kamoa project area have been investigated in detail and interpretations have been proposed. A summary regarding the main features discussed is as follows:

- A linear NNW-SSE zone of abrupt change in stratal thickness named the "Mupaka Fault" was a growth fault active during the deposition of the Nguba subgroup rocks.

- Most of the mesoscopic faults observed in the project area show a normal sense of

movement. They are commonly associated with soft-sediment deformation features. Mesoscopic faults appear to be syn-sedimentary, post or synchronous with framboidal pyrite. Copper sulphides appear to postdate the formation of mesoscopic faults.

- A secondary foliation (S_1) has been recognised in the studied area. It is defined by the alignment of fine- and coarse-grained sulphides within the matrix or in the replacement of clasts, the alignment or elongation of clasts and the alignment of minerals within a matrix. S_1 foliation has been studied in borehole core and also in thin section. In addition, the orientation of S_1 was recorded in different areas of the deposit (Fig. 4.20). In most areas S_1 foliation dips steeply to the southeast, however in three boreholes between the Kamoa and Makalu domes the S_1 foliation dips to the northwest. The steep foliation (S_1) striking NE/SW may be related to a NW directed compression event during the Lufilian orogeny (590-550 Ma).

  Thin section observations show that the most common morphology of S_1 is a continuous foliation defined by the alignment of fine- and coarse-grained sulphides disseminated in the matrix.

- Strain fringes and strain shadows are common features observed in the Basal diamictite of the Grand Conglomérat. The overall orientation of strain shadows and strain fringes is closely similar to the orientation of the S_1 foliation. Strain fringes/shadows are indicators showing that the deformation occurred at a low temperature and at high fluid pressure (Passchier and Trouw, 2005). Quartz clasts, quartzite clasts, mafic igneous clasts and euhedral pyrites constitute the rigid objects to the strain fringes and strain shadows. Strain fringes are composed of copper minerals, chlorite and quartz with minor muscovite and biotite whereas strain shadows contain abundant sulphides (including chalcopyrite, bornite, chalcocite, pyrite and sphalerite), quartz, carbonate and chlorite with occasional plagioclase. In the Kamoa deposit, strain fringes are interpreted as structures caused by a progressive coaxial deformation.

- Mesoscopic folds are structural features commonly observed in siltstone and sandstone layers, they are generally tight to isoclinal, asymmetric and recumbent. Their studies suggest that they may be syn-sedimentary slump folds of non-tectonic origin.

- Veins are generally uncommon in the Kamoa deposit, they appear to follow the orientation of bedding (S_0). Mineralised veins are rare and show two main orientations:

steeply-dipping to the northwest and gently-dipping to the southeast following the orientation of bedding.

The next chapter will focus on the timing of the mineralisation relative to sedimentary rocks deposition, diagenesis and structural features. The importance of structural features will be discussed and fence diagrams illustrating the distribution of these features will be presented combined with copper grades.

CHAPTER 5

Mineralisation and associated structural features of the Kamoa deposit

5.1 Mineralisation

The current model of mineralisation for the Kamoa deposit is that of a redox-controlled sedimentary rock-hosted stratiform copper deposit. At Kamoa, the contact between the Mwashya Subgroup and the Grand Conglomérat unit of the Nguba Subgroup constitutes the controlling redox boundary (Fig. 5.1). A schematic stratigraphic diagram showing the nomenclature for the Roan and Nguba Groups used in this chapter is shown in Figure 5.2. Copper sulphides are contained in the Basal diamictite of the Grand Conglomérat unit above the redox boundary (Ng 1.1.1) (Fig. 5.2). The Lower basal diamictite (Ng 1.1.1.1) generally hosts only minor copper sulphides (<1% Cu); however in the boreholes located in the south of the Kamoa dome, this unit may contain significant copper mineralisation. Abundant copper sulphides are generally observed in the Upper basal diamictite (Ng 1.1.1.3) and in the locally Intercalated siltstone unit (Ng 1.1.1.2) that overlies the Lower basal diamictite. The lowermost 3 m to 5 m of the Lower laminated pyritic siltstone/sandstone (Ng 1.1.2) generally contains fine-grained pyrite, but it may also locally host copper mineralisation.

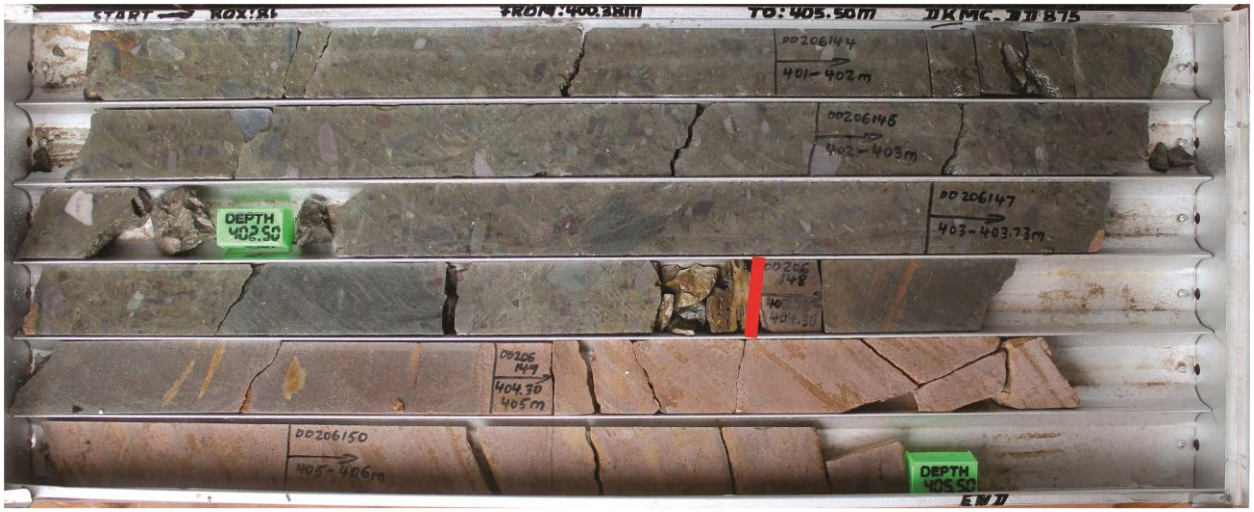

Fig. 5.1: Photograph of borehole core showing the redox boundary located at the contact between the Mwashya Subgroup (red beds) and the Grand Conglomérat unit (grey beds). The red line indicates the boundary between the two stratigraphic units.

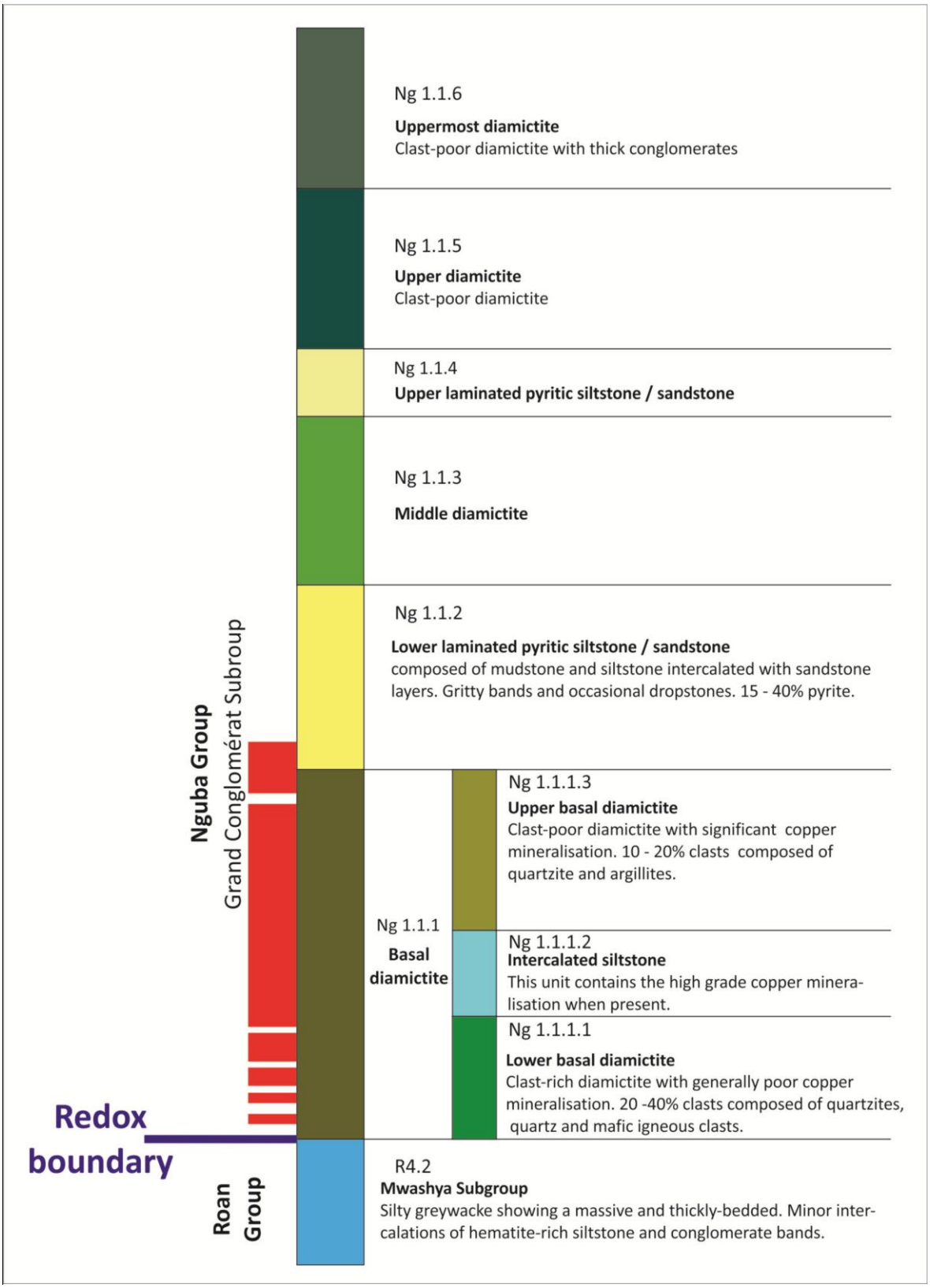

Fig. 5.2: Schematic stratigraphic diagram of the Kamoa deposit. The general location of copper mineralisation is shown by the red bars to the left of the stratigraphic column.

Within the Kamoa deposit, mineral resources are reported using a cut-off grade of 1% and a minimum thickness of 3 metres. A 1% Cu cut-off grade is typical of deposits in Zambia where a similar style of mineralisation has been identified (Parker *et al.,* 2013). The mineralisation in each stratigraphic unit within the Kamoa deposit is characterised below. Note that the term "fine-grained" includes particles with an average diameter less than 0.2 mm and "coarse-grained" are particles greater than 0.2 mm.

The Mwashya Subgroup (R4.2) greywacke contains mainly specular haematite. Occasional fine- and coarse-grained bornite/chalcocite associated with rare native copper is observed in the top three metres immediately below the redox boundary (Fig. 5.3). In addition traces of cuprite, malachite and chrysocolla can be observed in this zone. Fresh Mwashya Subgroup rocks also host euhedral pyrite and chalcopyrite. No significant copper mineralisation has been observed in this unit.

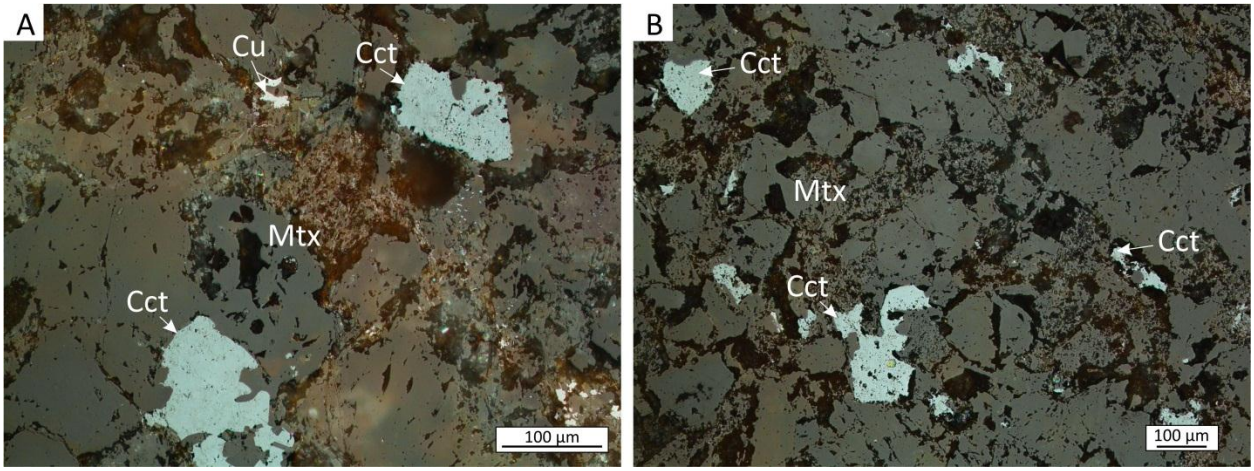

Fig. 5.3: Photomicrographs showing the mineralogy of the Mwashya subgroup rocks. (A). Chalcocite is disseminated in sandstone. A trace of native copper is also observed. (B). Fine- and coarse-grained chalcocite disseminated in sandstone. A and B photomicrographs are from TS_34, from DD963 at 249.90 m. Abbreviations: Cct = chalcocite; Cu = native copper and Mtx = Matrix.

The mineralised zone contained in the Basal diamictite and locally in the Lower laminated pyritic siltstone/sandstone (Ng 1.1.1 and Ng 1.1.2), has a thickness ranging from 0.5 to 7 m in the northeast part of the deposit (east and south of the Kamoa dome; north of the Makalu dome) and from 5 to 17 m in the southeast part (south and southeast of the Makalu dome). The copper content within the mineralised zone varies from 1 to 8%, occasionally up to 15%. For most boreholes, the grade profile shows a sharp transition from less than 0.5% Cu to over 1% Cu at the bottom of the continuous zone grading over 1% Cu.

Within the Basal diamictite (Ng 1.1.1), chalcopyrite is the most abundant copper sulphide (~50%) followed by bornite (~30%) and then by chalcocite (~20%) (Figs. 5.4 and 5.5). Traces of native copper are also observed at the base of this unit (Fig. 5.5a).

Chalcocite occurs mainly as elongate and fine-grained disseminations in the matrix, with a grain size from 5 to 200 µm (Fig. 5.5c). The fine-grained chalcocite may represent 90% of the total amount of chalcocite in the rock. Coarse-grained chalcocite occurs as elongate grains, it is observed in disseminations as well as in the rims of clasts (Fig. 5.5a, b). It may represent 8 – 12% of the total amount of chalcocite in the rock. Fine-grained chalcocite is well developed in the Intercalated siltstone (Ng 1.1.1.2).

Bornite occurs commonly as elongate and anhedral fine grains ranging in size from 3 – 200 µm disseminated in the matrix, comprising 70 – 80% of the total volume (Fig. 5.5c, d). Coarse-grained bornite is elongate and represents about 8 - 15% while bornite in the rim of clasts represents about 2 – 5% of the total amount of bornite in the rock (Figs. 5.4b, 5.5c and d). In the Intercalated siltstone, the amount of bornite is up to 20% and locally more; this may change the colour of the rock from light grey to darkish blue.

Chalcopyrite occurs as elongate grains in a variety of grain sizes (Figs. 5.4a, 5.5c, d and e). The finest fraction occurs as anhedral grains ranging from 5 - 200 µm comprising 40 – 60% of the total chalcopyrite volume. Coarse-grained chalcopyrite ranging from 200 µm – 3 mm is disseminated in the fine-grained matrix of the diamictite. Within the diamictite, chalcopyrite occurs also as elongate grains up to 5 mm in length and as a rim to clasts or fragments, their amount ranges from 5 – 10% of the total chalcopyrite volume. When the Intercalated siltstone (Ng 1.1.1.2) is present, abundant fine-grained chalcopyrite can be observed. This represents up to 20% of the total volume of the rock.

Minor pyrite is observed in the Basal diamictite (Ng 1.1.1), especially in the Upper basal diamictite (Ng 1.1.1.3) where it occurs as framboidal pyrite (3 µm - 25 µm) as well as coarse-grained euhedral pyrite (200 µm to 1 mm) (Fig. 5.5f). Framboidal and euhedral pyrite are replaced by chalcopyrite (Fig. 5.5f). The amount of pyrite in the Basal diamictite is generally less than 0.5% of the total volume of the rock. Observations from thin sections show that framboidal pyrite is commonly more abundant than coarse-grained and euhedral pyrite in this unit.

Traces of sphalerite are rarely observed at the top of the Basal diamictite (Ng 1.1.1) in association with pyrite and chalcopyrite. In the west of the Makalu dome, sphalerite is commonly observed. This mineral occurs generally as fine-grained anhedral grains and its size varies from 5 to 100 µm, occasionally up to 150 µm. Euhedral sphalerite is very rare but can be seen in few intersections within the borehole cores.

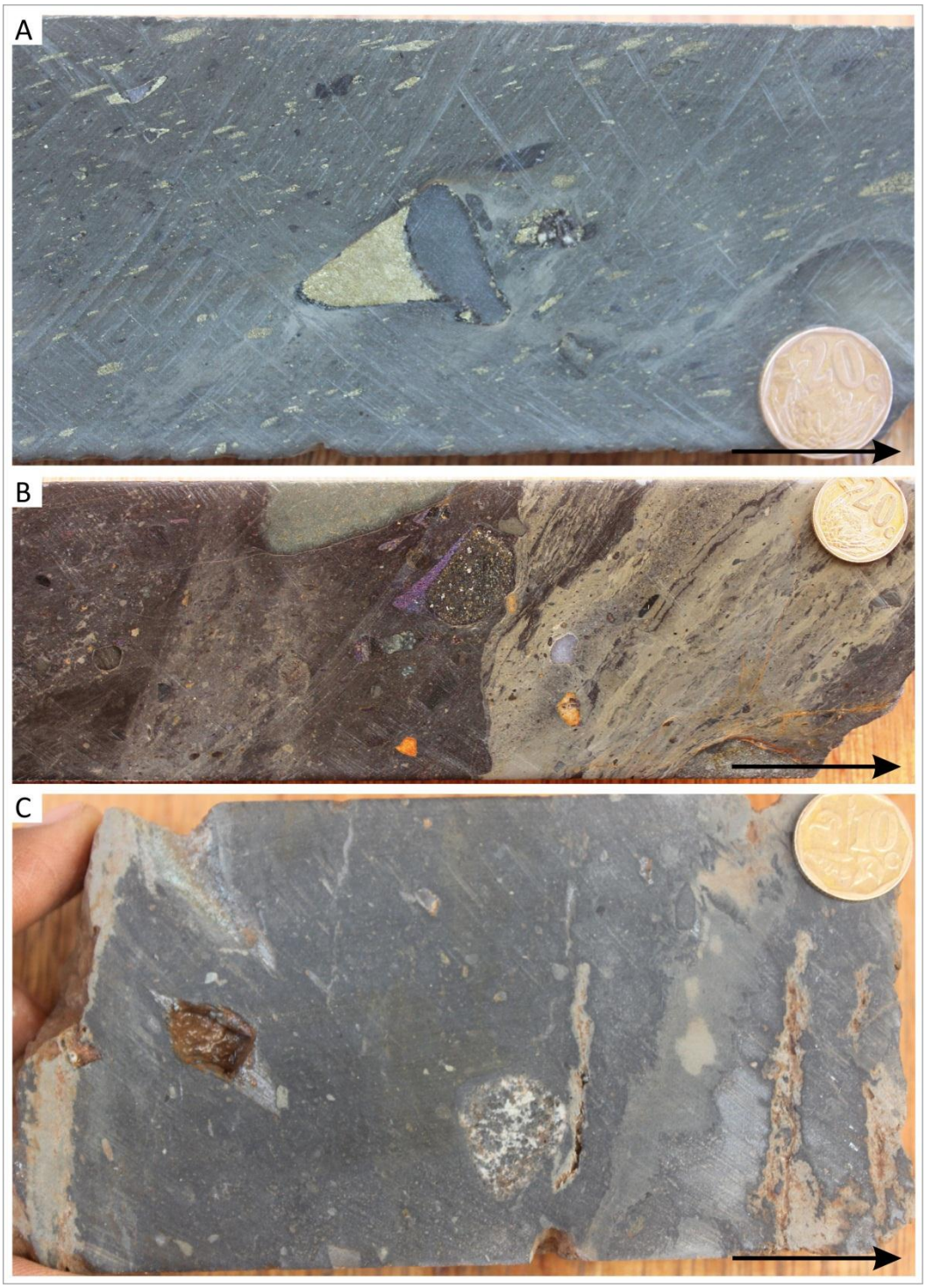

Fig. 5.4: Copper sulphide textures at the Kamoa copper deposit. (A). Chalcopyrite occurs as aligned and elongate fine- and coarse-grained disseminations in the diamictite. S_1 foliation is defined by the alignment of chalcopyrite. A well-developed asymmetric upward strain shadow is visible in the middle of the sample. DD909, 552.40 - 558.09 m. (B). Fine-grained bornite is disseminated in the diamictite. Asymmetric upward bornite strain shadow is observed in the middle of the sample. DD888, 265 – 265.25 m. (C). Chalcocite occurs as fine- grained material disseminated in the diamictite. An asymmetric downward strain shadow is observed on the left side of the sample. DD084, 167 – 167.10 m.

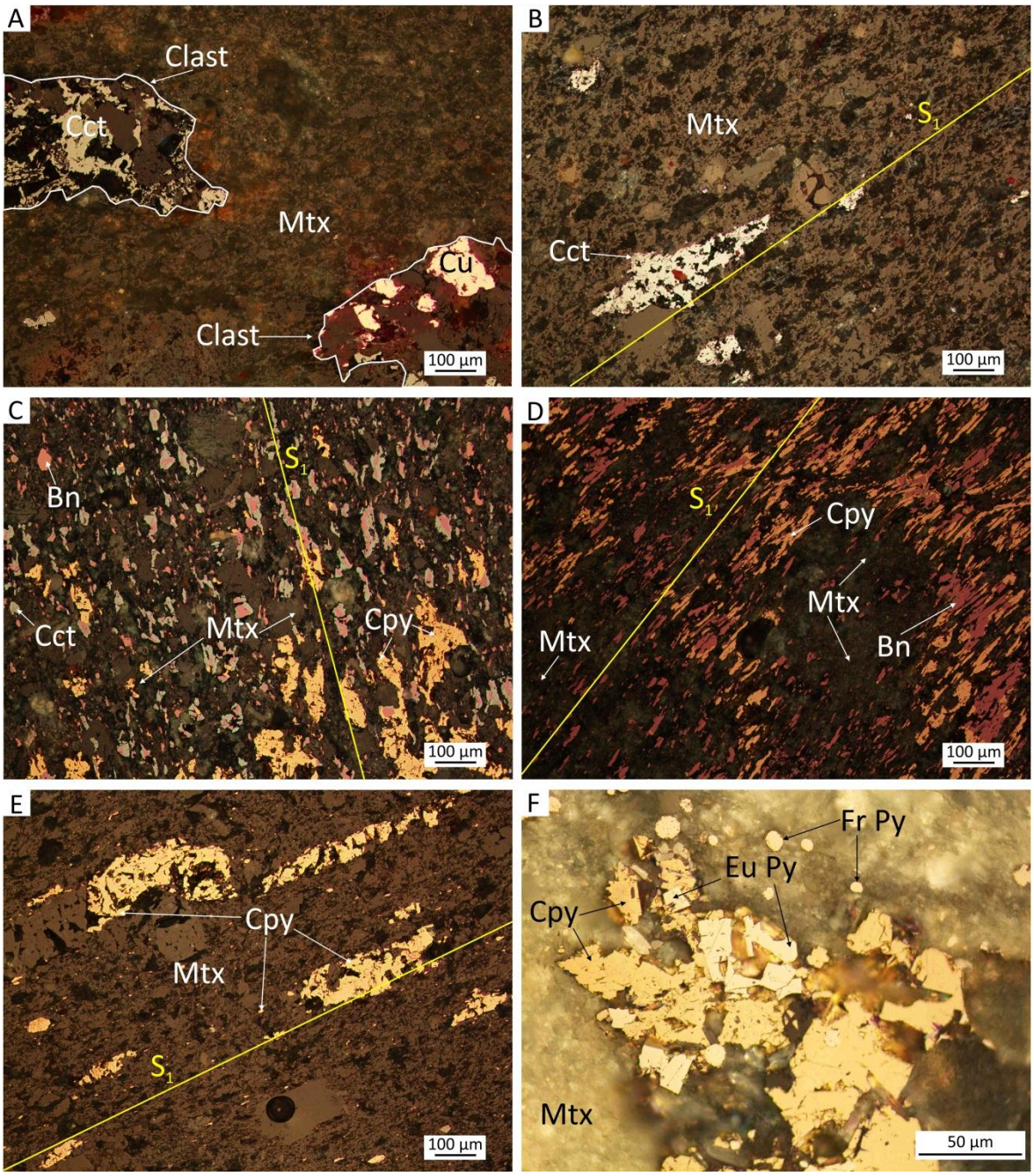

Fig. 5.5: Reflected light photomicrographs showing the mineralogy of the ore zone in the borehole DD963. (A). Chalcocite associated with native copper replacing the clast. TS_30 at 238.56 m. (B). Coarse- and fine-grained chalcocite defining an S_1 foliation. S_1 is defined by alignment of chalcocite. TS_22 at 225.35 m depth. (C). Fine-grained bornite, chalcopyrite and chalcocite disseminated in a matrix of sandstone. The slaty cleavage is defined by the sulphides. TS_18 at 221.71 m. (D). Fine-grained disseminated bornite associated with fine- grained chalcopyrite. The mineralisation forms a slaty cleavage. TS_14 at 219.28 m depth. (E). Fine- and coarse-grained chalcopyrite disseminated in the matrix. Slaty cleavage defined by the alignment of fine- and coarse-grained chalcopyrite. TS_7 at 211.88 m. (F). Framboidal pyrite replaced by euhedral pyrite and anhedral chalcopyrite. TS_1 at 200.15 m depth. The abbreviations on the photomicrographs represent: Cct = chalcocite; Bn = bornite; Cpy = chalcopyrite; Eu Py = euhedral pyrite; Fr Py = framboidal pyrite, and Mtx = matrix.

The Lower laminated pyritic siltstone/sandstone (Ng 1.1.2) contains abundant pyrite ranging from 20 to 30% of the total volume of the rock. Pyrite occurs as framboidal and euhedral grains in the rock. The size of framboids varies from 3 to 40 μm while the size of the euhedral pyrite ranges from 25 μm to 1 mm, and occasionally up to 4 mm in size. Framboidal pyrite represents 70% of the total amount of pyrite in the rock while euhedral pyrite constitutes 30%. Framboidal pyrite is disseminated in the fine-grained matrix, especially in mudstones; its abundance in the rock may change the colour of the rock from light grey to greenish or brownish grey. Euhedral pyrite occurs as disseminations in the rock, along the bedding/laminations, and in the rim of clasts. Coarse-grained pyrite occurs as euhedral and elongated grains up to 5 mm in length.

In the lower 3 – 5 m of the Lower laminated pyritic siltstone/sandstone (Ng 1.1.2), pyrite abundance decreases significantly while copper sulphides start to appear. Rare coarse-grained chalcopyrite is observed in the rim of occasional clasts as well as in the pebbly bands located at the base of the unit. The total copper grade in this unit is generally less than 0.5%, however in the area located in the north and northwest of the Makalu dome; this unit may contain significant copper mineralisation as high as 5%. Traces of pyrrhotite are also observed in this unit, with a grain size varying from 0.1 to 1 mm and occasionally up to 5 mm.

The sulphides in the middle diamictite (Ng 1.1.3) comprise pyrite with trace pyrrhotite and rare chalcopyrite. With a total volume of 2 – 3.5%, pyrite occurs as fine- and coarse-grained euhedral pyrite. Minor framboidal grains are observed in the fine-grained matrix. Coarse-grained pyrite is also observed in the rim of clasts. Trace chalcopyrite occurs as fine grains associated with trace pyrrhotite. As in the Basal diamictite, chalcopyrite tends to replace euhedral and framboidal pyrite. At the bottom of this unit (3 – 5 metres above the Lower laminated pyritic siltstone/sandstone), the amount of pyrite increases up to 6 % in volume.

Sulphides in the Upper laminated pyritic siltstone/sandstone (Ng 1.1.4) occur as framboidal and euhedral grains similar to those in the Lower laminated pyritic siltstone/sandstone (Ng 1.1.2). However, the upper unit contains only 12 to 15% pyrite, and copper sulphides are absent.

The Upper diamictite (Ng 1.1.5) and the Uppermost diamictite (Ng 1.1.6) display similar sulphide assemblages which are composed of fine-grained pyrite with less coarse-grained pyrite. The percentage estimation of pyrite in the unit ranges from 0.2 – 0.5%. Traces of fine-grained chalcopyrite are associated with trace pyrrhotite around the rims of clasts.

5.2 Mineral zonation

Vertical ore sulphide zonation is generally observed within the Kamoa deposit (Fig. 5.6); this correlates well with an overall decrease in Cu/S ratio from the bottom to the top of the mineralised zone (Fig. 5.7). The lateral zonation is also observed, this is defined by the dominant sulphide species within the mineralised zone (Fig. 5.8).

From the contact between the Mwashya Subgroup and the Grand Conglomérat unit of the Nguba Subgroup upward, the mineral zonation sequence typically consists of haematite (Fe_2O_3) associated with occasional native copper, chalcocite (Cu_2S), bornite (Cu_5FeS_4), chalcopyrite ($CuFeS_2$) and pyrite (FeS_2). Sphalerite ((Zn, Fe) S) mineralisation is weakly developed, above zones with well-developed copper sulphides.

There is no abrupt change in the mineral zonation; an overlap between sulphides is generally observed (Fig. 5.6). The lower more copper-rich sulphides partially replace the overlying, more copper-poor sulphides. A plot of copper/sulphur ratio (total copper divided by total sulphur) versus the depth indicates a persistent vertical zonation which is not affected by the decrease or change of copper grade in the rock (Fig. 5.7). Figure 5.6 illustrates the relationship between the mineral zonation, the copper grade and the copper-sulphur ratio versus depth in the borehole DD963. To better understand the sulphide zonation in the Basal diamictite (Ng 1.1.1), 34 thin sections from the borehole DD963 have been described in detail, and 6 representative images of them are presented here (Fig. 5.5) with the remainder shown in Appendix A. The location of the thin sections presented in the Figure 5.5 is shown in Figure 5.6.

5.3 Supergene mineralisation

Copper oxide and secondary sulphides are observed at shallow depths, commonly in the boreholes drilled adjacent to the edges of the domes. Chalcocite occurs as both hypogene and supergene mineralisation. As supergene mineralisation, chalcocite is commonly associated with native copper, occasional cuprite and rare malachite in contrast to the classical paragenetic sequence. Supergene copper minerals occur out of sequence with respect to the vertical zoning; these minerals include chalcocite, native copper, chrysocolla, cuprite and malachite that generally occur along fractures, joints and as replacement minerals. The contact between the Basal diamictite (Ng 1.1.1) and the Mwashya Subgroup (R4.2) is commonly weathered and secondary chalcocite is commonly observed in this interval.

When the rock is weathered, iron oxides are disseminated in the matrix, in the fractures as well as in the veins which range from 10 µm to 1 mm thick.

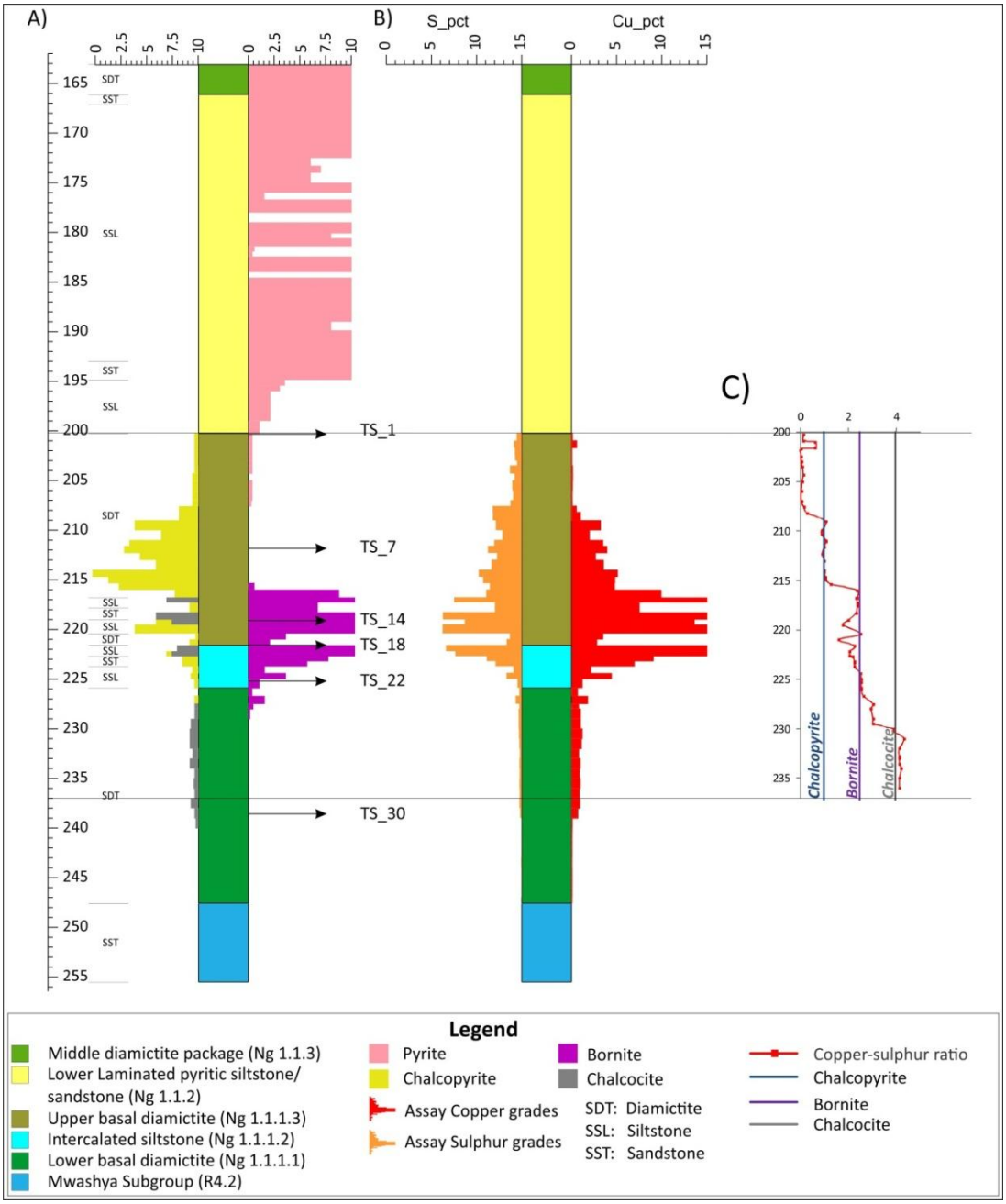

Fig. 5.6: Schematic diagram illustrating the mineral zonation, the copper grade and sulphur profile together with the plot of copper-sulphur ratio versus depth for the borehole DD963. (A). The typical sulphide zonation is defined by an upward sequence of chalcocite-bornite-chalcopyrite-pyrite. An overlap between the copper sulphide zones is shown. The lithological log is shown on the right of the depth log. The length of the bars on the left and right side of the log represents the estimated amount of sulphides in different intervals. (B). Copper grade profile showing a sharp transition between low and high copper grades at the bottom contact. A gradational transition is observed at the top contact. Copper sulphides are mainly contained in the Upper basal diamictite (Ng 1.1.1.3) and in the Intercalated siltstone (Ng 1.1.1.2). The Lower basal diamictite (Ng 1.1.1.1) does not contain significant copper mineralisation (< 0.5% Cu). The assay copper and sulphur grades are truncated at 15%. The sulphur grade correlates well with the copper grade. (C). Plot of copper-sulphur ratio versus depth illustrating the vertical zonation of sulphides; an overlap between copper sulphides can be observed. Downhole depth represents metres.

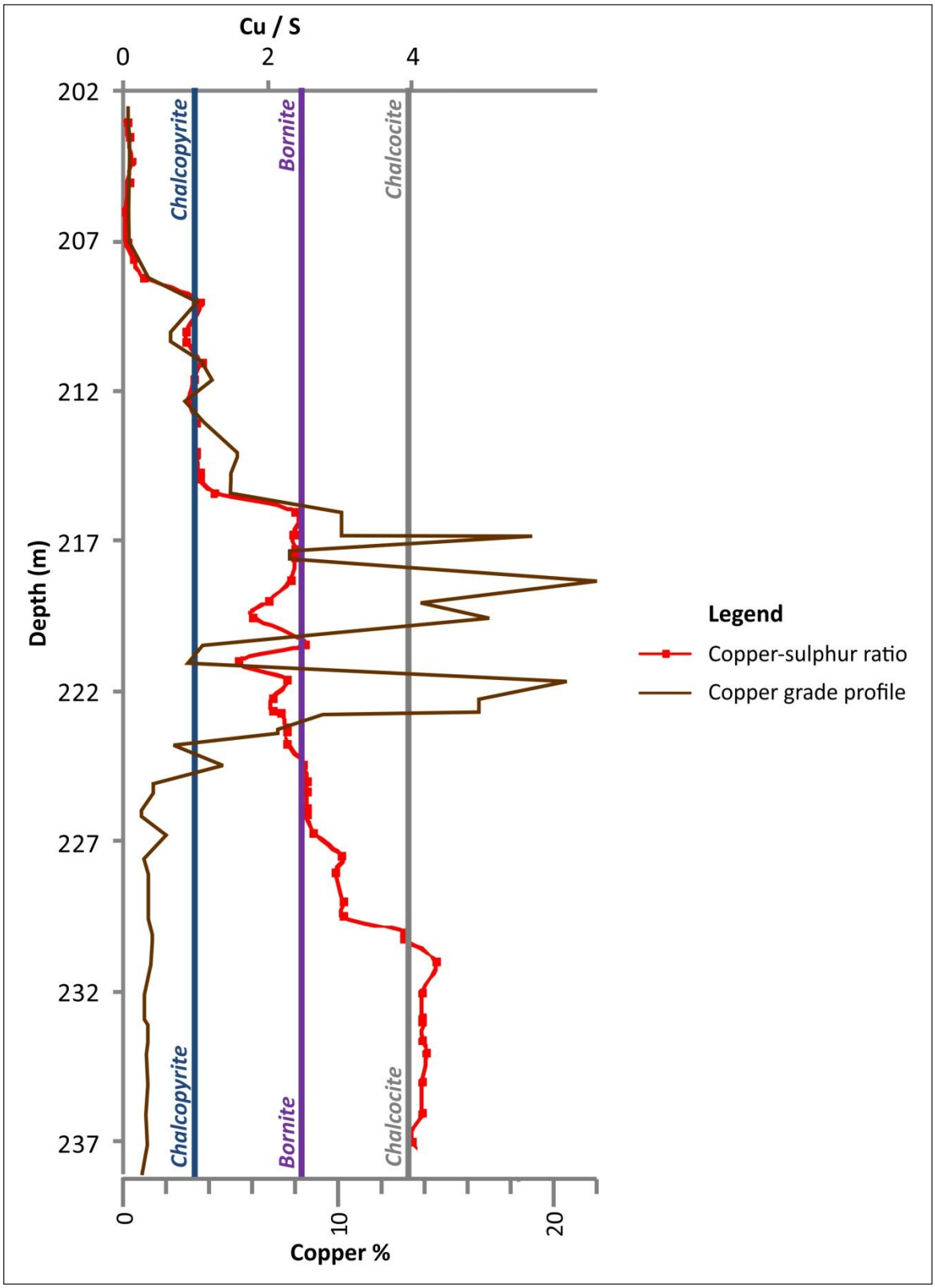

Fig. 5.7: Plot of copper-sulphur ratio versus depth for the borehole DD963. The vertical zonation of copper sulphides is shown by the plot of copper sulphur ratio.

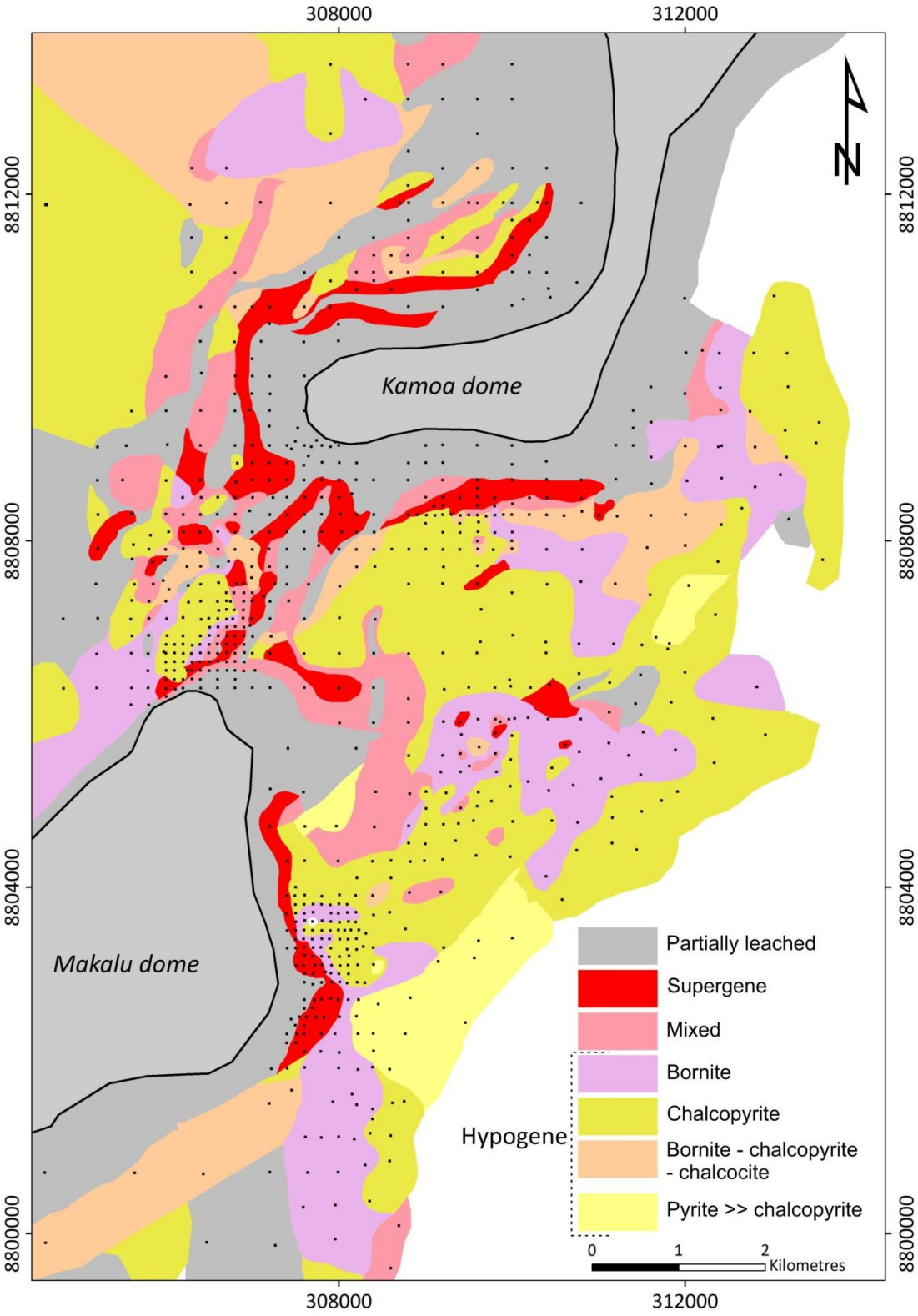

Fig. 5.8: Map showing the lateral zonation of sulphides in the Kamoa deposit. The zonation is defined by the dominant sulphide species within the mineralised zone (Peters *et al.,* 2016).

5.4 Stratigraphic position of the ore mineralisation

In the deposit area, two completely distinct ore mineralised zones have been identified. In the north part of the deposit (east and south of the Kamoa dome; north and east of the Makalu dome), the ore mineralised zone is defined by chalcopyrite, bornite and chalcocite. It occurs commonly between the top of the Lower basal diamictite (Ng. 1.1.1.1) and the base of the Upper basal diamictite (Ng 1.1.1.3), however the presence or absence of different minor stratigraphic units (Ng 1.1.1.1; Ng 1.1.1.2 and Ng 1.1.1.3) may affect the location of the ore mineralised zone. For instance in the east and south of the Kamoa dome where the Intercalated siltstone and the Lower basal diamictite are absent; copper mineralisation occurs in the Upper basal diamictite overlying the Mwashya Subgroup rocks (Fig. 5.9). In the west part of the deposit (south and southeast of the Makalu dome), copper mineralisation is generally located in the Lower basal diamictite, on top of the Mwashya Subgroup rocks (Figs. 5.9 and 5.10).

The boreholes investigated show varying stratigraphic positions of continuous mineralised zones grading over 1% Cu (Fig. 5.9). These have been divided into 8 types shown in map view (Fig. 5.9) and tabulated (Table 5.1). In most of the boreholes located in the north of the Makalu dome, in the east and south of the Kamoa dome, copper mineralisation appears in the Upper basal diamictite and locally in the Lower laminated pyritic siltstone/sandstone. To the east and south-east part of the Makalu dome, copper mineralisation occurs commonly in the Intercalated siltstone. However, to the south of the Makalu dome, copper mineralisation occurs in the Lower basal diamictite. Figure 5.9 illustrates this spatial variation.

Table 5.1: Stratigraphic position of copper mineralisation in the boreholes investigated. The number of boreholes corresponding to each stratigraphic position of the ore mineralised zone is illustrated. The spatial variation of each stratigraphic position of copper mineralisation is also provided. Note that 5 investigated boreholes do not have significant copper mineralisation, therefore they have not been taken into account.

Stratigraphic position of the ore mineralisation	**Number of boreholes**	**Area(s)**
Lower laminated pyritic siltstone/sandstone (Ng 1.1.2)	2	Not defined
Lower laminated pyritic siltstone/sandstone and the Upper basal diamictite (Ng 1.1.2 and Ng 1.1.1.3)	11	North and Northwest of the Makalu dome
Upper basal diamictite (Ng 1.1.1.3)	42	Central and northeast part of the deposit
Upper basal diamictite and the Intercalated siltstone (Ng 1.1.1.3 and Ng 1.1.1.2)	16	Central part of the deposit
Upper basal diamictite and the Lower basal diamictite (Ng 1.1.1.3 and Ng 1.1.1.1)	6	Not defined
Intercalated siltstone (Ng 1.1.1.2)	17	East of the Makalu dome
Intercalated siltstone and the Lower basal diamictite (Ng 1.1.1.2 and Ng 1.1.1.1)	2	Not defined
Lower basal diamictite(Ng 1.1.1.1)	19	South and southeast of the Makalu dome.

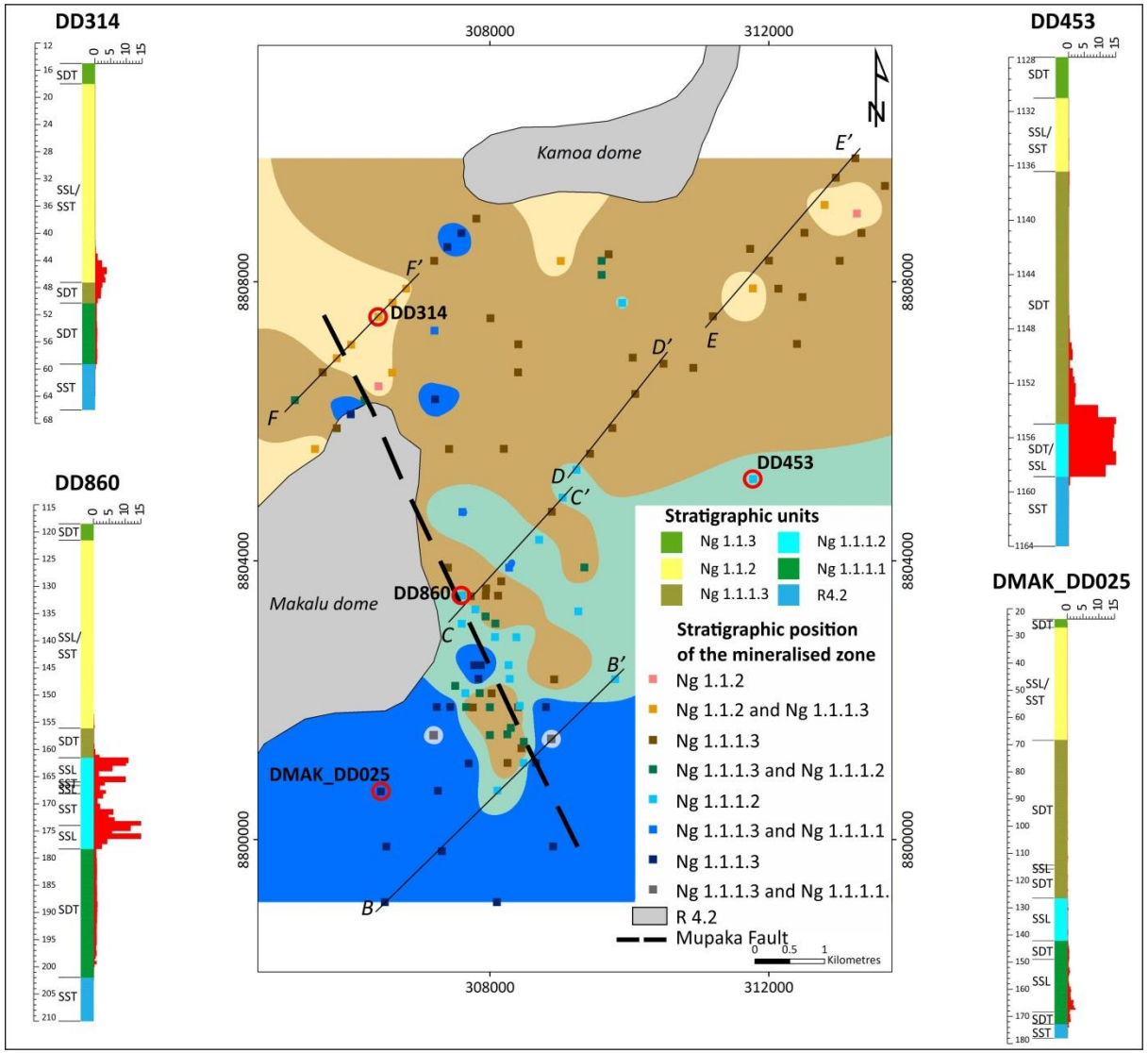

Fig. 5.9: Map showing borehole locations and the variation in stratigraphic position of copper mineralisation shown in borehole logs. B – B'; C – C'; D – D'; E – E' and F - F' show the location of fence diagrams presented in this chapter which contain lithostratigraphic data, copper content and structural features. The dashed dark line represents the approximate location of the Mupaka Fault, this feature seems to be the boundary between the two ore mineralised zones.

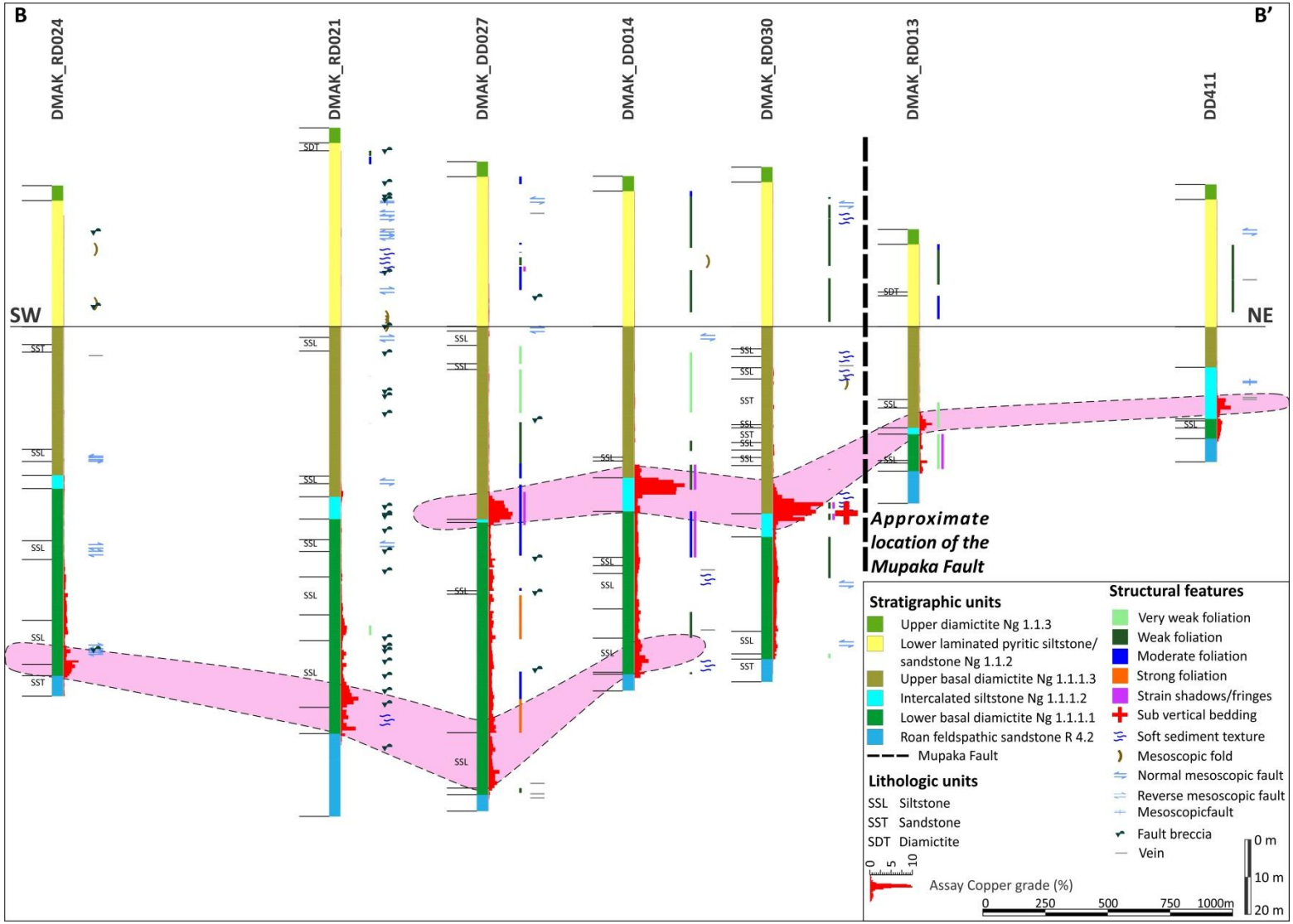

Fig. 5.10: Section line B-B'. Two distinct mineralised parts are shown (pink layers surrounded by dashed lines). In some of the boreholes, strain shadows/fringes structures correspond with the increase of copper content. Cross section hung from the base of the Lower laminated pyritic siltstone/sandstone (Ng 1.1.2).

5.5 Structural features relative to copper mineralisation

Strain shadows, strain fringes and secondary foliations (described in detail in Chapter 4) are the most common structures observed in the Basal diamictite (Ng 1.1.1) and in the Lower laminated pyritic siltstone/sandstone (Ng 1.1.2) (Fig. 5.10 to 5.14). In these stratigraphic units, sulphides such as pyrite (euhedral), chalcopyrite, bornite and chalcocite are commonly aligned and define the S_1 foliation (Fig. 5.5b to e).

Fence diagrams of the 5 cross sections illustrated in Chapter 3 are presented here (Fig. 5.10 to 5.15), and their locations are shown in Figure 5.9. These fence diagrams show 3 stratigraphic units which are the Basal diamictite (Ng 1.1.1), the Lower laminated pyritic siltstone/sandstone (Ng 1.1.2) and the Mwashya Subgroup (R4.2). Copper content and structural features such as strain shadows/fringes, sub-vertical bedding, S_1 foliation, mesoscopic faults, fractures, veins, breccias, soft-sediment deformation, mesoscopic folds are indicated on the right side of borehole logs. Note that the structural information presented in Figure 5.10 to 5.14 shows only data recorded in logging, obviously it does not include structural features observed in thin sections.

The results of the investigation of structural features combined with copper content using fence diagrams show a correlation between high copper grades and strain shadow/fringe structures in the diamictite (Fig. 5.10; 5.11; 5.12 and 5.13).

The Mupaka Fault interpreted as a growth fault (described in detail in Chapter 4) correlates well with higher copper grades (Fig. 5.15). This highest grade copper mineralisation is located in the Intercalated siltstone (Ng 1.1.1.2). The thickness of the ore zone varies from 4 to 12 m, locally up to 17 m.

In the mineralised zone, structural features such as the S_1 foliation, strain shadows and strain fringes are commonly observed when sulphides are present (Fig. 5.10 to 5.14). The intensity of foliation depends on the abundance of copper sulphides in the ore zone. When there are abundant copper sulphides the rocks show a well-defined foliation while where there are minor copper sulphides the rocks display a weak foliation; therefore sulphides help to emphasise the S_1 foliation. Visually copper sulphides in siltstone and sandstone layers do not show a clear secondary foliation (S_1), possibly due to the fine-grained size of minerals; however a well-defined foliation is commonly observed in thin sections. Strain shadows and strain fringes are commonly observed in the diamictites and locally in siltstones and sandstones layers where the rigid object is composed of pyrite and rare clasts (detailed described in Chapter 4).

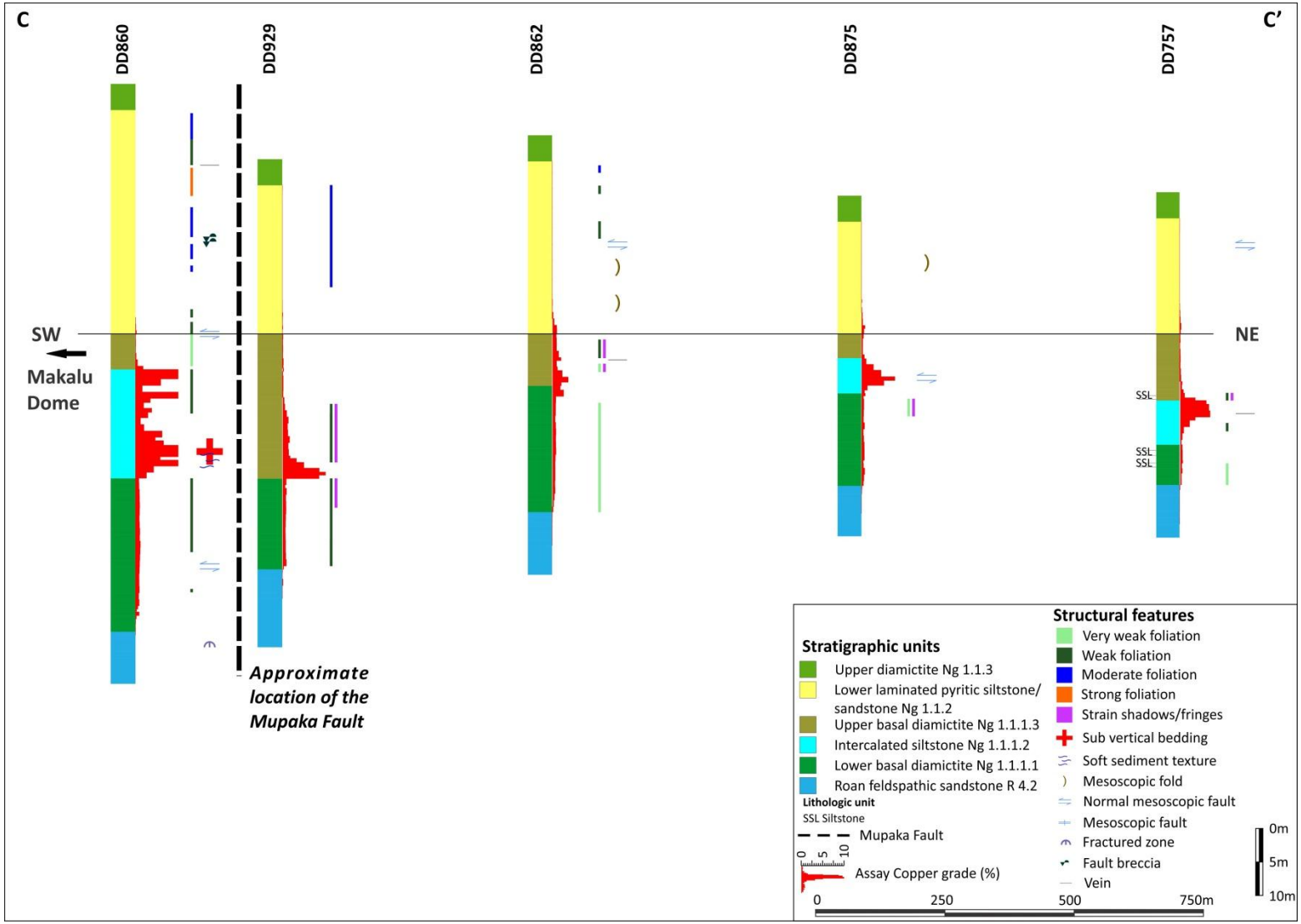

Fig. 5.11: Section line C – C'. Section indicates that when the Intercalated siltstone is present in the borehole, it contains the ore zone (cut-off grade over 1% Cu). The Upper basal diamictite may contain the ore zone when the Intercalated silstone is absent. Strain shadow/fringe structures correlate well with the highest grade copper mineralisation. Cross section hung from the base of the Lower laminated pyritic siltstone/sandstone (Ng 1.1.2).

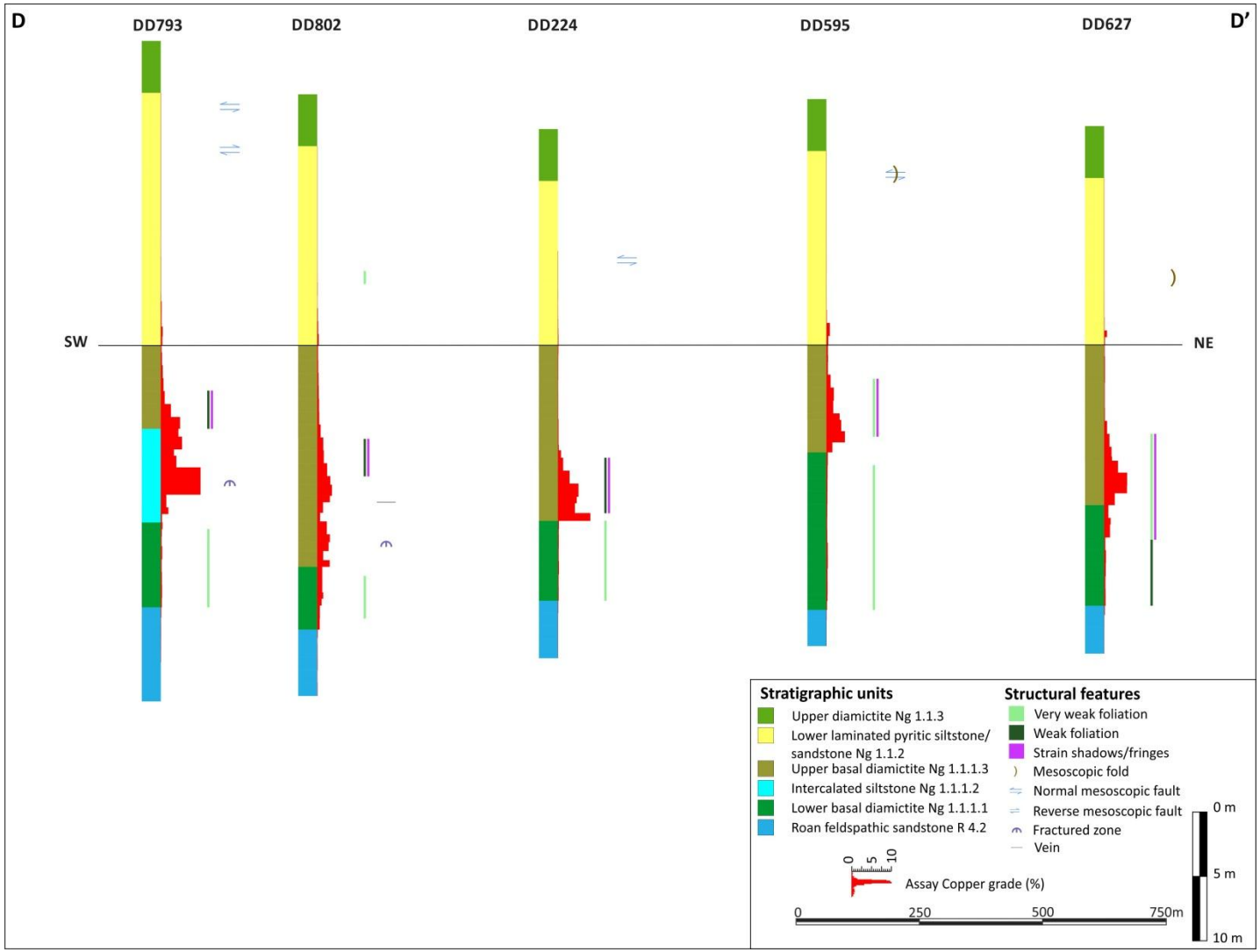

Fig. 5.12: Section line D – D'. Copper mineralisation occurs in the Intercalated siltstone in the borehole DD793, then this unit pinches out and the mineralisation appears in the Upper basal diamictite (Ng 1.1.1.3). Strain shadow/fringe structures correlate well with the highest copper mineralisation. A weak S_1 foliation is observed within boreholes on this section. Cross section hung from the base of the Lower laminated pyritic siltstone/sandstone (Ng 1.1.2).

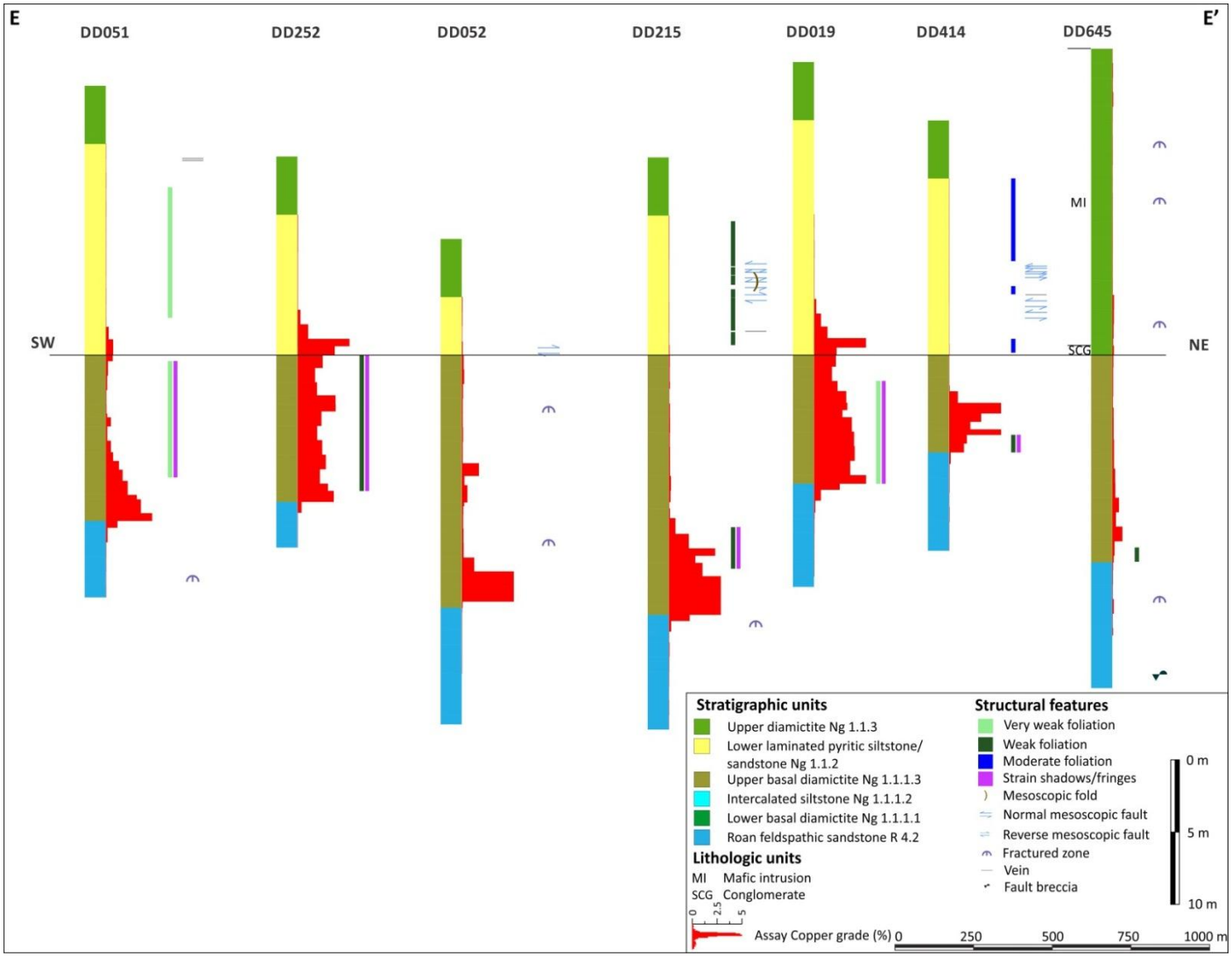

Fig. 5.13: Section line E – E'. The Intercalated siltstone and the Lower basal diamictite units are absent. Copper mineralisation appears at the contact between the Upper basal diamictite and the Mwashya Subgroup. In some boreholes, strain shadows/fringes correlate well with the highest grade copper mineralisation. The Lower laminated pyritic siltstone/sandstone is absent in borehole DD645. Cross section hung from the base of the Lower laminated pyritic siltstone/sandstone (Ng 1.1.2).

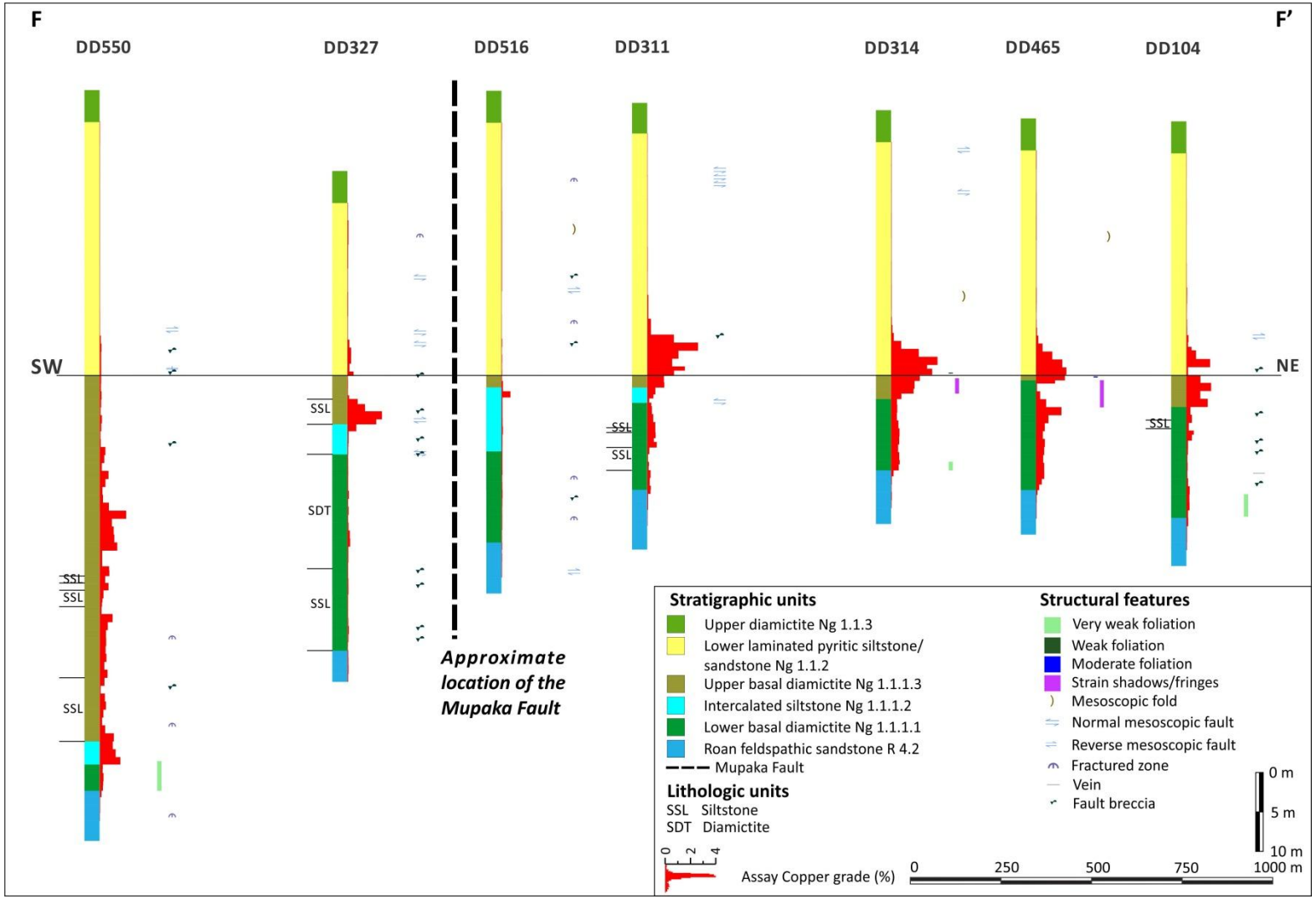

Fig. 5.14: Section line F – F'. In the NE of the section line, copper mineralisation is hosted at the base of the Lower laminated pyritic siltstone/sandstone whereas in the SW; it is located in the Upper basal diamictite and in the Intercalated siltstone. Some strain shadows/fringes are observed in the Upper basal diamictite. Cross section hung from the base of the Lower laminated pyritic siltstone/sandstone (Ng 1.1.2).

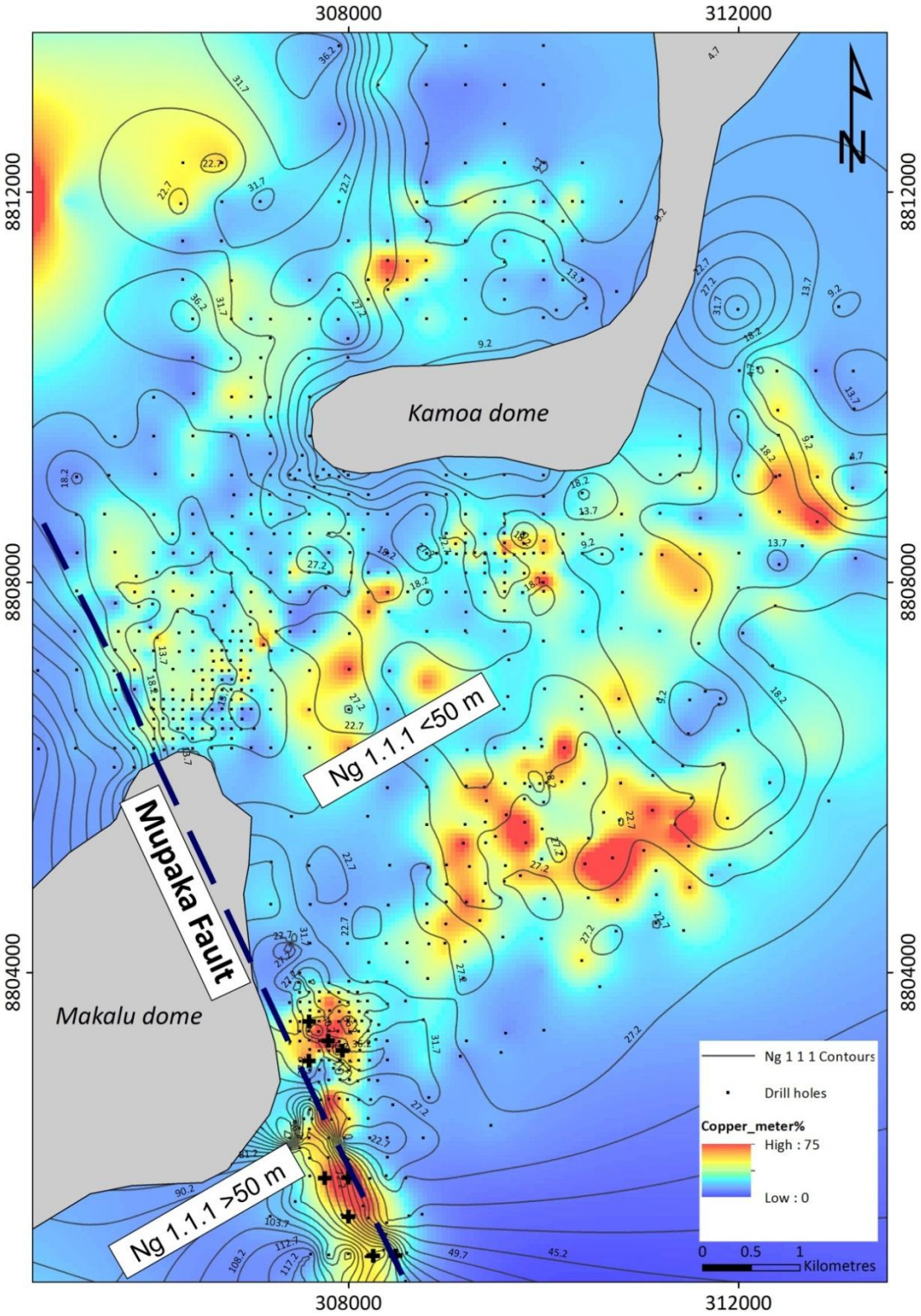

Fig. 5.15: Isopach map of the Basal diamictite (Ng 1.1.1) with superimposed copper grade information from boreholes. The blue dashed line ("Mupaka Fault") shows the approximate location of the zone of abrupt change in stratal thickness of the Basal diamictite. There is a general NNW trend structures from isopachs and copper grade information. Black crosses represent boreholes with steep bedding. Contours lines in the bottom right corner of the map are incorrect because they are not based on borehole information and are an artefact of data processing.

5.6 Discussion

Near the surface, mineralisation within diamictites, siltstones and sandstones has been leached. Supergene zone ranges from 30 to 100 m depth from surface (Fig. 5.16). Chalcocite occurs as hypogene mineralisation in most of the boreholes; however, in shallow boreholes around the domes or in leached areas, chalcocite occurs as supergene mineralisation that locally extends up to 250 m depth.

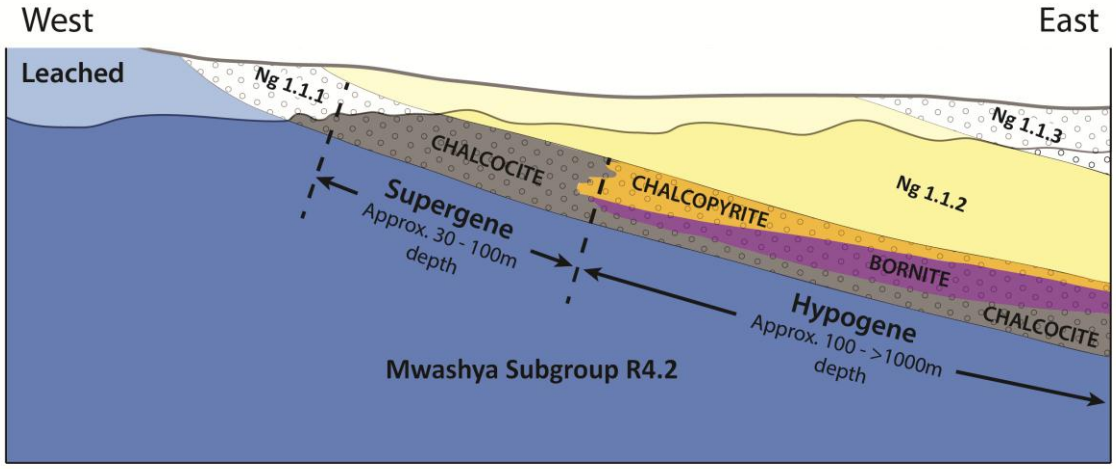

Fig. 5.16: Simplified schematic of mineral zonation in the Kamoa deposit. Note that the figure is not to scale (Peters *et al.,* 2016).

Within the Kamoa deposit, chalcopyrite is the most abundant copper sulphide followed by bornite and then by chalcocite. The mineral zonation sequence consists of haematite associated with occasional native copper, chalcocite, bornite, chalcopyrite and pyrite with minor sphalerite. Pyrite has been partially to fully replaced in sequence by chalcopyrite, bornite, and then chalcocite. Ripley *et al.,* (1985) proposed a plot of Fe^{2+} versus Cu^{+} activity to explain the mineral zoning and paragenetic sequence that is often observed in sedimentary rock-hosted copper deposits (Fig. 5.17). The vertical sulphide zonation observed in the study area may be explained by the fact that fluid with a high initial copper content became progressively more dilute with respect to Cu as copper sulphides precipitated (Fig. 5.17) (Ripley *et al.,* 1985 and Robb, 2005).

The clast-rich diamictite from the Lower basal diamictite is a porous lithological unit, however it does not contains significant copper sulphides. The less porous lithological units such as mudstones, siltstones, sandstones and clast-poor diamictite within the Upper basal diamictite contain significant copper sulphides (Figs. 5. 11 and 5.12). In addition, in the mineralised zone, mudstones and siltstones contain significant copper minerals compared to sandstones. This suggests a relationship between the increase of copper grade and the grain size.

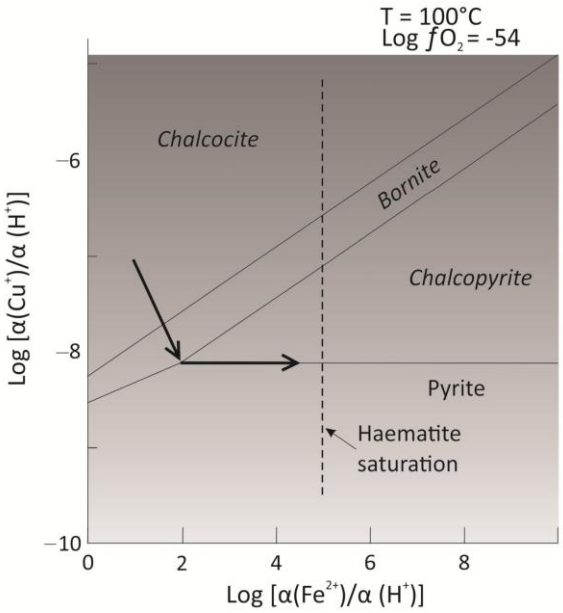

Fig. 5.17: Plot of Cu^+/H^+ versus Fe^+/H^+ activity ratios showing the standard zoning and paragenetic sequence that is commonly observed in sedimentary rock-hosted stratiform copper (SSC) deposits when a copper-bearing fluid reacts with a pyritic shale. In this case the original copper content of the fluid is high and then decreases as a function of copper-sulphide precipitation to form the paragenetic sequence of chalcocite–bornite–chalcopyrite–pyrite (after Ripley *et al.*, 1985 in Robb, 2005).

Within the Basal diamictite of the Grand Conglomérat (Ng 1.1.1), copper sulphides commonly appear aligned and define the S_1 foliation. Visually copper sulphides in siltstone and sandstone layers do not show a clear secondary foliation (S_1), possibly due to the fine-grained size of minerals; however a well-defined foliation is commonly observed in thin sections.

Recently Schmandt *et al.,* (2013) and Broughton (2014) suggested that the formation of copper sulphides at Kamoa took place relatively early, prior to the lithification of the host rocks. This interpretation discounted structural features such as strain fringes, strain shadows which are important tools to outline the deformation history of a deposit (Etchecopar and Malavielle, 1987; Koehn *et al.,* 2000, Bons *et al.,* 2012; Chatalov, 2014). These structures are interpreted to have been developed during or post a deformation event (Passchier and Trouw, 2005). Strain shadows and strain fringes structures are common features observed in the mineralised zone, they contain copper sulphides such as chalcopyrite, bornite and chalcocite. At any particular depth of the mineralised zone, the mineral assemblage of copper sulphide is generally similar in fine-grained disseminated, in coarse-grained, in the rim of clasts and in strain shadows/fringes structures suggesting that these copper sulphides in the different textures were precipitated at the same time. In addition, strain shadows and strain fringes commonly correlate well with high grade copper values (Fig. 5.10, 5.11, 5.12 and 5.13). The presence of copper sulphides in strain

shadows and strain fringes suggests a significant role of deformation in the development of copper mineralisation. This suggests that copper mineralisation in the Kamoa deposit is syn- to post- deformation age related to the Lufilian orogeny. Alternatively, the initial copper mineralisation within the Kamoa deposit maybe remobilised during the Lufilian orogeny, sulphides such as chalcopyrite, bornite and chalcocite may recrystallise and redistribute in the rock forming a steep dipping S_1 foliation, strain shadows and strain fringes.

Three sequential types of hydrothermal alteration are recognised in the Kamoa deposit: potassic, silicic and magnesian alteration (Schmandt *et al.,* 2013). The presence of coarse-grained albite in strain fringes/shadows intergrown with copper sulphides suggests an albitic alteration coeval with copper mineralisation.

In the deposit area, the interpreted growth fault termed the "Mupaka Fault" correlates well with the high-grade copper zone (Fig. 5.15). Several deposits in the CACB appear to have formed adjacent to early, syn-sedimentary growth faults (Selley *et al.,* 2005; Broughton, 2014).

5.7 Conclusion

Within the Kamoa deposit copper mineralisation is largely stratiform, confined and restricted in the Basal diamictite (0.5 – 17 m) of the Grand Conglomérat and locally in the Lower laminated pyritic siltstone/sandstone. Two distinct ore zones are observed: one in the east of the approximate location of the Mupaka Fault where copper mineralisation is located in the Intercalated siltstone, in the Upper basal diamictite and locally in the Lower laminated pyritic siltstone/sandstone. The other ore zone is observed in the south and southwest of the Mupaka Fault where copper mineralisation is located at the base of the Lower basal diamictite. The Mupaka Fault appears to be the boundary between the two separate ore zones. Also, it appears that there is a relationship between high-grade copper zones and the Mupaka Fault.

Copper sulphides commonly appear aligned and define the S_1 foliation, this suggests a significant role of deformation in the development of copper mineralisation. Strain shadows and strain fringes are common features observed in the mineralised zone, they contain copper sulphides such as chalcopyrite, bornite and chalcocite. The fact that strain shadows and strain fringes contain copper sulphides indicates a new growth or remobilisation and recrystallisation of minerals during or post a deformation event.

The next chapter will discuss the structural controls, the sulphide mineralisation and the lithostrastigraphical variations of the Kamoa deposit in a regional scale within the CACB.

CHAPTER 6

Discussion and conclusions

6.1 Discussion

6.1.1 Introduction

The Kamoa copper deposit is a recent stratiform copper discovery located on the western edge of the Congolese portion of the CACB in lithologies previously not expected to host copper. As such it is important to understand its geological setting and the controls on mineralisation. Understanding which of the geological controls were critical to the formation of the Kamoa deposit is important for continued mineral exploration. Previous research on Kamoa has yielded valuable information about the stratigraphy and mineralisation, however there is a lack in the understanding of the controls on distribution of the hypogene sulphide mineralisation (Broughton and Rogers, 2010; Parker *et al.,* 2013; Schmandt *et al.,* 2013).

The main discussion points regarding the data presented in this study for the Kamoa deposit are: the lithostratigraphical variation and features of the Nguba Group, the structural history and the timing of copper mineralisation with respect to deformation.

The Kamoa deposit occurs along a stratigraphically-controlled redox boundary at the base of the Grand Conglomérat. Kamoa is unusual in that it is not hosted within the Mines Subgroup, which is the typical host for many of the deposits in other DRC Mines (Broughton and Rogers, 2010). In the majority of the DRC copper mines, ore bodies occur within mega-breccia fragments where main stage mineralisation probably pre-dated later folding and brecciation (Cailteux, 1994; Cailteux *et al.,* 2005a). Unlike most of the DRC deposits, Kamoa is hosted in a recognisable and continuous stratigraphy above the Mines Group and shares more common characteristics with some of the Zambian deposits in the CACB, as well as the Polish Kupferschiefer deposits. To set the Kamoa deposit into a regional context, it has been compared to some deposits in the Zambian Copperbelt based on their stratigraphic architecture and mineralisation styles (Fig. 6.1).

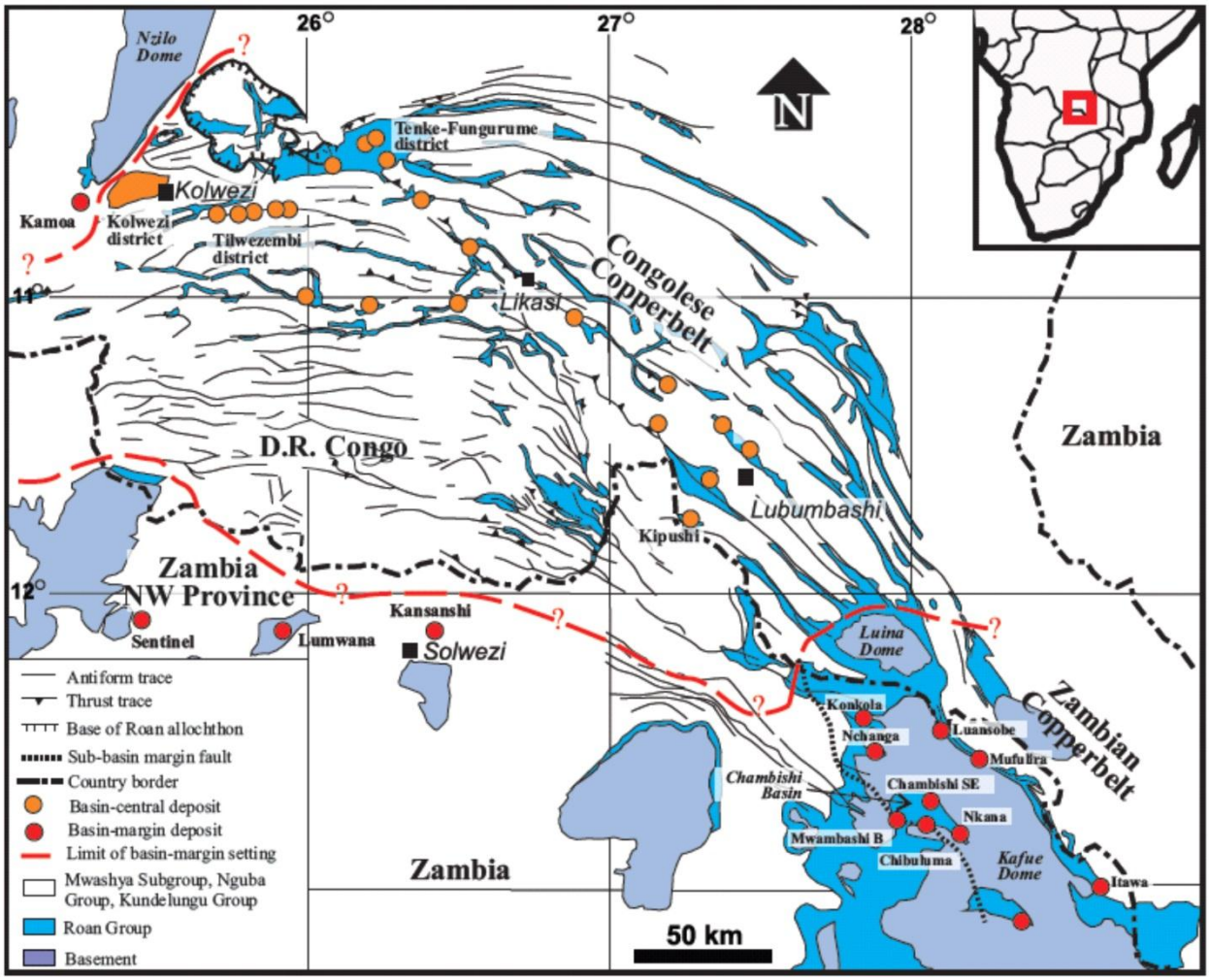

Fig. 6.1: Geological map of the CACB showing the location of deposits and cities (Broughton, 2014).

6.1.2 Lithostratigraphical variation and features of the Nguba Group

The interpreted growth fault named the “Mupaka Fault”, described in Chapter 3, 4 and 5, represents a significant interpretation in this thesis (Fig. 6.2). The Mupaka Fault strikes NNW/SSE, whereas the typical regional bedding strikes NNE/SSW. The stratal thicknesses of units in the Kamoa deposit vary from 40 to 60 m in true thickness. The stratigraphic units thicken towards the WSW, suggesting that the depositional trend is oriented ENE to WSW and that the source of sedimentary rocks is located to the north-east part of the deposit.

The facies of the Basal diamictite is not the same throughout the deposit. In the west of the Mupaka Fault (south and south west part of the Makalu dome), the amount of clasts is generally low (7-15 %) while in the east of this fault clasts are abundant (25-35 %). Also, in the

west of the Mupaka Fault, the amount of intermediate siltstone/sandstone layers increases significantly. All these features suggest that there were syn-sedimentary faults during the deposition of the Nguba Group rocks at Kamoa.

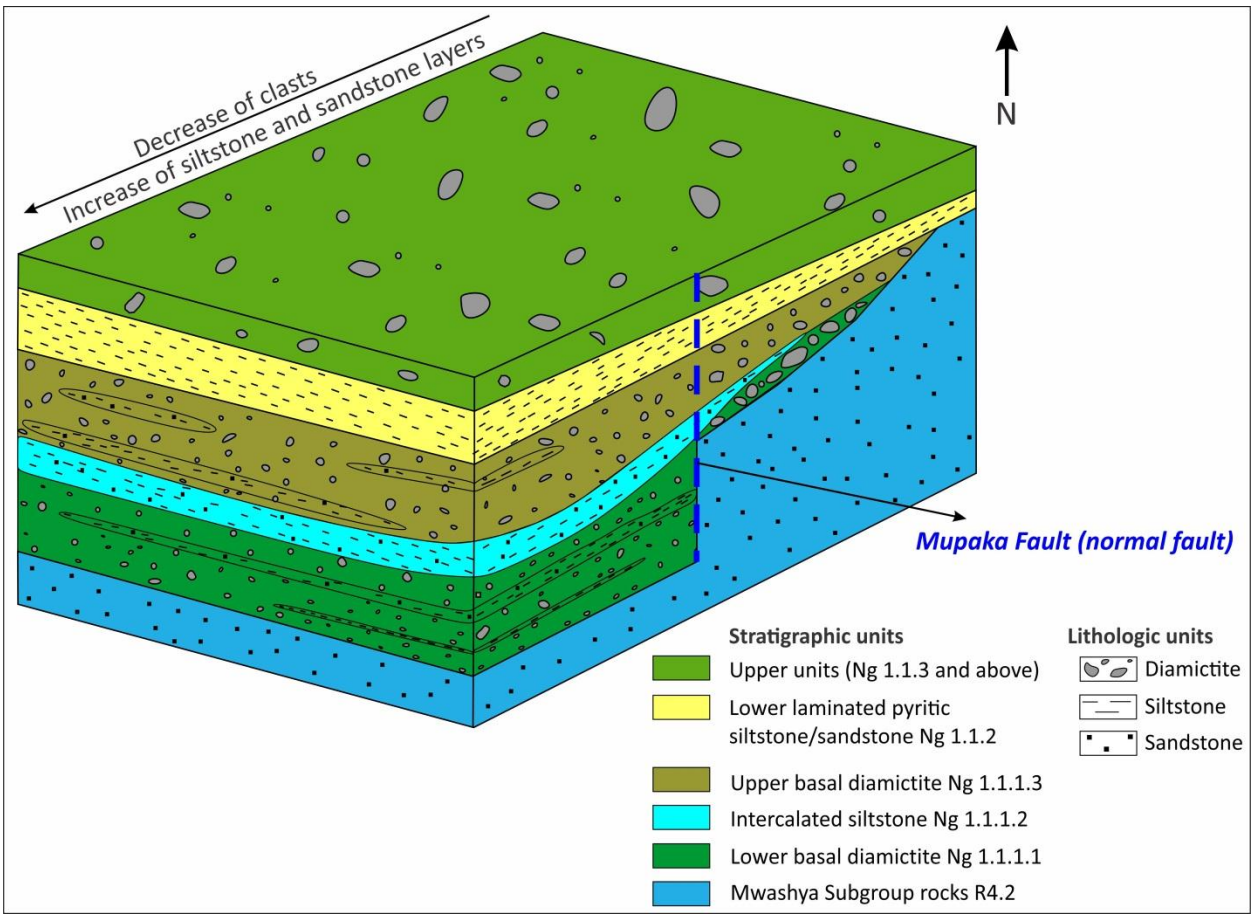

Fig. 6.2: Simplified stratigraphic model of the Kamoa deposit. The abundance and size of clasts decreases from the north-east to the south-west. Siltstone and sandstone layers increase in thickness to the WSW. Steep bedding occurs within 50 m of the Mupaka Fault.

The Grand Conglomérat correlates with the glacial diamictites of the global Sturtian glacial event; this has been dated between ~ 765 Ma and 735 Ma (Key *et al.,* 2001). In the Kamoa area the Grand Conglomérat has a thickness of approximately one kilometre and has a strike length of several kilometres. The accommodation space for the thousand metre thickness of the Grand Conglomérat is better explained by a gradual regional subsidence. The thickness variations, the facies change, the steep bedding and the rotated mesoscopic faults within the deposit are better explained by syndepositional growth faults (Broughton, D., pers. comm. 2016).

In the Zambian Copperbelt, extension associated with early rifting led to the development of syn-sedimentary faults in the basins and the connection of these basins along master faults at the time of the Copperbelt Orebody Member deposition (Selley *et al.,* 2005; Hitzman *et al.,* 2012). Syn-sedimentary growth faults have been observed in several deposits in the Zambian Copperbelt such as Mwambashi, Chambishi, Konkola, Musoshi (Selley *et al.,* 2005) and Fishtie (Hendrickson *et al.,* 2013). Unlike most of the deposits in the Zambian Copperbelt where the presence of basement rocks helps to better identify growth faults, the Mwashya Subgroup constitutes the footwall to the Kamoa deposit.

The tectonic-stratigraphic models of the Lower Roan Group in the Zambian Copperbelt is similar to that developed from studies of the Phanerozoic intracontinental rifts where rift evolution generally progressed from small isolated subbassins bounded by a complex array of discontinuous faults, to a system of broader, interconnected depocenters controlled by master faults (Selley *et al*., 2005).

Within the Kamoa deposit, the Makalu and Kamoa domes expose the Mwashya Subgroup which forms the footwall to the deposit. The thickness of different stratigraphic units does not change significantly across the domes. Therefore it is suggested that the domes are a result of deformation during the Lufilian orogeny.

6.1.3 Deformation history

Kampunzu and Cailteux (1999) divided the Lufilian Orogeny into the Kolwezian (D1); Monwezian (D2) and Chilatembo (D3) deformation events. Of these deformation events, only the Kolwezian stage has been identified in the deposit area based on the data presented here. The timing of deformation in the CACB is related to the Pan-African Lufilian Orogeny dated between ~590 and 500 Ma (Hitzman *et al.,* 2012).

Kolwezian deformation event in the Kamoa deposit (D_1)

The Kolwezian event is characterised by major folding and thrusting with a northern transport direction of the Katangan Supergroup rocks (François, 1973; Kampunzu and Cailteux, 1999).

In the Kamoa deposit, S_1 foliation is illustrated by the alignment of fine- and coarse-grained sulphides (euhedral pyrite, chalcopyrite, bornite and chalcocite), the alignment of strain shadows/fringes and locally by the heterogeneous alignment of clasts. Petrographic and SEM studies show an S_1 delineated by micas, elongated quartz grains and sulphides. In some thin sections two preferred orientations of mica are observed.

The S_1 foliation is not homogeneously distributed in all dimensions; it appears more developed on thin sections cut parallel to the orientation of foliation and less developed on thin sections cut perpendicular to the lineation. The heterogeneity of foliation may be explained by the strength of sulphides and clasts. The low-strength sulphide shows a steep foliation compared to the high-strength sulphide relative to the shortening direction. For instance, the strength of pyrite is high compared to other sulphides such as pyrrhotite, chalcopyrite, bornite and chalcocite, therefore pyrite shows a relatively low intensity of foliation compared to other sulphides. On the other hand, clasts in the diamictite are randomly oriented and define a very weak, weak to moderate foliation, this supports the idea that the S_1 foliation has been developed from random oriented material by pure shear deformation. Unlike other sulphides, framboidal pyrites are not deformed; this observation suggests a low intensity of deformation in the Kamoa deposit.

Strain shadows and strain fringes are generally parallel to the S_1 foliation. In addition, similar copper sulphide assemblages are observed in these features at any particular location. These observations suggest that the development of S_1 foliation is coeval with strain shadows and strain fringes. The analysis of strain fringes reveals a straight orientation of fibres during a coaxial deformation, this fact strongly supports the idea that a single phase of deformation occurs in the Kamoa deposit (Passchier and Trouw, 2005).

The average orientation of S_1 foliation is NE/SW strike with variations between NNE-SSW to E-W. This orientation points to a NW shortening direction during D_1 leading to the development of S_1 foliation. The orientation of foliation is consistent with the ENE-trending folds described in the Kolwezi district and interpreted to have formed during the thrusting of sedimentary rocks (François, 1973). These observations support that the Kolwezian stage is responsible for the development of the S_1 foliation in the Kamoa deposit.

In the Kamoa area, mesoscopic folds generally lack axial planar foliation and are associated with soft-sediment deformation textures. In addition, their fold axial planes are generally parallel to bedding (S_0). Framboidal pyrites are abundant in the mesoscopic folds, they are completely undeformed and no significant fabric can be observed. Studies under the scanning electron microscope (SEM) help to confirm that the minerals within the mesoscopic folds do not define a secondary foliation (S_1) suggesting that these folds with sub-horizontal axial planes are due to soft-sediment deformation rather than tectonic deformation.

6.1.4 Mineralisation

The current model of mineralisation within the Kamoa deposit is typical of sedimentary rock-hosted stratiform copper deposits (Fig. 6.3) (Broughton and Rogers, 2010; Schmandt *et al.,*

2013). This genetic model correlates with the interpretations of formation of mineralisation in the CACB (Hitzman *et al.,* 2005; Robb, 2005; Hitzman *et al.,* 2012). Oxidising saline brines migrated up-dip through Roan Supergroup rocks and leached copper. The brines encountered a redox boundary at the base of the Grand Conglomérat unit. This caused the precipitation of copper sulphide minerals in the Basal diamictite (Ng 1.1.1) below a hanging wall composed of pyritic siltstone-sandstone and upper diamictite units (Fig. 6.3) (Schmandt *et al.,* 2013; Broughton, 2014). The footwall composed of Mwashya Subgroup rocks could have behaved as an acquifer for the circulation of cupriferous fluids to the base of the greybeds.

The mineralisation at Kamoa is stratabound; it is confined in the Basal diamictite and locally in the Lower laminated pyritic siltstone/sandstone unit located above the redox boundary. The thickness of the mineralised zone ranges from 0.5 to 10 m in the northeast part of the deposit and from 5 to 20 m in the southwest part.

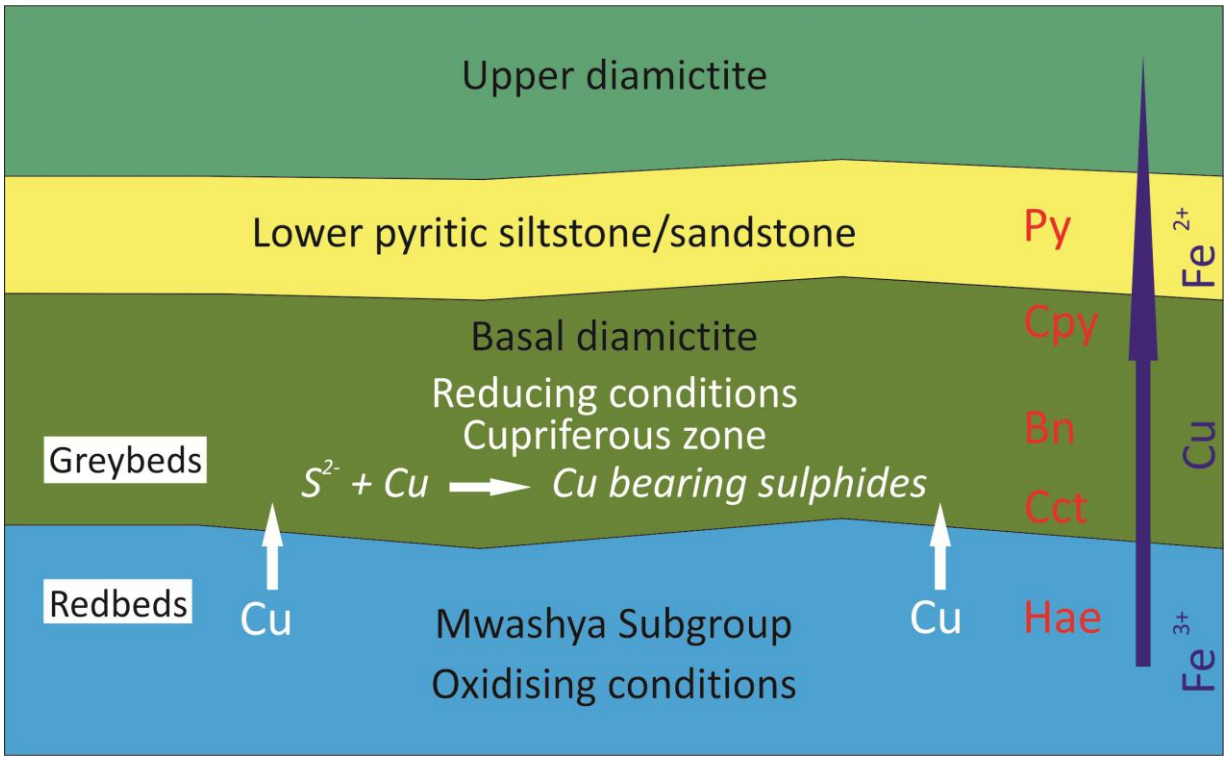

Fig. 6.3: Proposed schematic diagram showing the current genetic model and the precipitation mechanism that occurred in the Kamoa deposit. Copper mineralisation occurs where ore fluid has encountered a reducant unit which is the Basal diamictite of the Grand Conglomérat. The Lower laminated pyritic siltstone/sandstone and the upper diamictite units constitute the unmineralised host rocks (Ng 1.1.2 and above units). Hae, haematite; Cct, chalcocite; Bn, bornite; Cpy, chalcopyrite and Py, pyrite.

The copper grade map of the Kamoa deposit illustrates a strong structural control on the grade distribution, the highest-grade copper mineralisation is oriented north-northwest, and it is coincident with the north-northwest trending interpreted syn-sedimentary growth fault. This suggests that the NNW-trending growth fault was probably an important transport path for the hydrothermal fluids, and is therefore considered as a primary mineralising structure in the Kamoa deposit (Fig. 6.4). The importance of syn-sedimentary growth faults in the ore distribution has also been reported in the Zambian Copperbelt (Selley *et al.,* 2005; Hitzman *et al.,* 2012).

In the mineralised zone, copper sulphides occur as fine- and coarse-grained disseminations in the matrix; they are commonly aligned and locally elongated defining an S_1 foliation. Copper sulphides within the clasts of foliated rocks are randomly oriented and lack S_1 foliation. Strain shadows and strain fringes are common mesoscopic structures, they contain copper sulphides and their amount ranges from 5 – 10% volume. The fact that copper sulphides define an S_1 foliation and occur in strain shadows/fringes demonstrates the important role for deformation in the development of copper mineralisation.

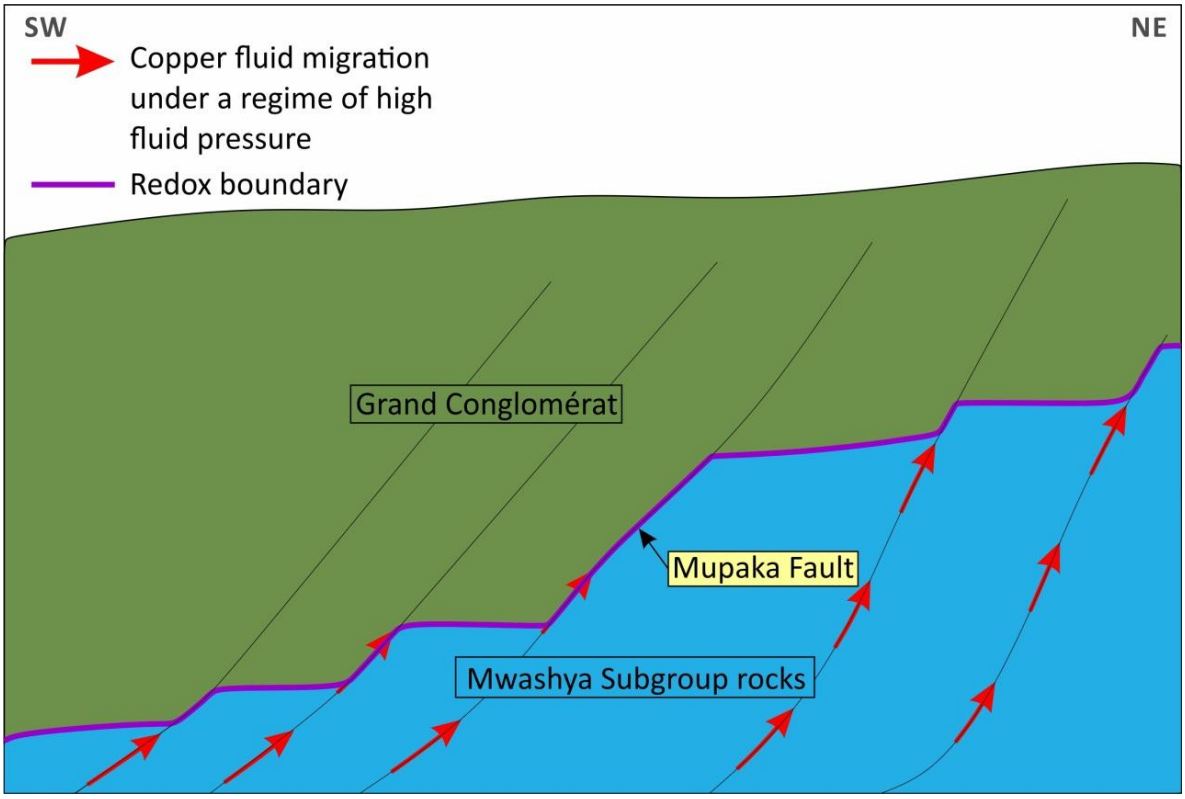

Fig. 6.4: Schematic diagram illustrating the model for ore formation in the Kamoa deposit. Syn-sedimentary faults may represent the conduits of copper mineralising fluids under a regime of high fluid pressure. The redox boundary causes the precipitation of copper sulphides.

The clast-rich diamictite of the Lower basal diamictite unit is a porous lithological unit, however it does not contains significant copper sulphides. The less porous lithological units such as mudstones, siltstones, sandstones and clast-poor diamictite of the Upper basal diamictite unit contain significant copper sulphides. A possible explanation for this relationship is that the low permeability rocks may serve as lithological traps for mineralising fluids, therefore providing a suitable environment for development of high fluid pressure domains above the porous unit represented by the Lower basal diamictite (Marshall and Gilligan, 1993). This interpretation is supported by the presence of high fluid pressure and low temperature structures such as strain shadows and strain fringes that contain a significant amount of copper sulphides (Passchier and Trouw, 2005; Bon *et al.,* 2012).

6.1.5 Timing of copper mineralisation relative to deformation

The Cu-Co mineralisation of the CACB was deposited in several stages that include syn- and diagenetic mineralisation (Unrug *et al.,* 1988; Selley *et al.,* 2005, Cailteux *et al.,* 2005a, Hitzman *et al.,* 2012); syn- and post-orogenic mineralisation (Torrealday *et al.,* 2000; McGowan *et al.,* 2005; Selley *et al.,* 2005; El Desouky *et al.,* 2009) and a syn-orogenic remobilisation stage (Torremans *et al.,* 2013; Turlin *et al.,* 2015). This multistage origin of copper mineralisation has also been recognised for the Kupferschiefer mineralisation (Alderton *et al.,* 2015). The source of Cu-Co metals is a subject of debate in the CACB (Cailteux *et al.,* 2005a; Hitzman *et al.,* 2005; Selley *et al.,* 2005). Some authors proposed that the metal sources are pre-Katangan continental rocks (Cailteux *et al.,* 2005a); whilst others proposed the dewatering of red-bed sedimentary rocks containing iron oxyhydroxides (Hitzman *et al.,* 2005).

Schmandt *et al*., (2013) identified two stages of sulphide mineralisation at Kamoa, the first generation occurred early during diagenesis and formed framboidal and cubic pyrite. Framboidal pyrite has a light sulphur isotopic signature varying between -11 and -5‰, suggesting that it precipitated from solutions or bacterial reduction of seawater sulphates. The second, later generation of sulphide mineralisation is characterised by copper sulphides and secondary pyrite. Copper sulphides display similar sulphur isotopic values to that of diagenetic pyrite suggesting that they derived some sulphur from framboidal pyrite (Schmandt *et al.,* 2013).

Within the Kamoa deposit, a diagenetic origin of the copper mineralisation is suggested based on the non-fracture controlled distribution of copper sulphides and the replacive textures of diagenetic framboidal pyrite by copper sulphides (Hitzman *et al.,* 2012; Schmandt *et al.,* 2013). Similar observations have been used to support the diagenetic origin of the Cu-Co mineralisation in the CACB (Cailteux *et al.,* 2005a). The fact that copper sulphides within the

clasts of foliated rocks are randomly oriented and lack an S_1 foliation does not support either a diagenetic or the syn-orogenic origin of copper mineralisation because clasts as rigid objects may preserve copper sulphides (Nex. P., pers. comm., 2016).

In the mineralised zone, copper sulphides are commonly aligned and locally elongated defining an S_1 foliation. Strain shadows and strain fringes are enriched with copper sulphides, quartz, carbonate, ankerite, chlorite, plagioclases and albite. The rigid objects to strain shadows and strain fringes consist mainly of clasts. The mineral growth within strain shadows and strain fringes is generally similar to that of the host rock matrix implying that their formation occurs in a geochemical closed system (Chatalov, 2014). The fact that strain shadows and strain fringes contain copper sulphides indicates a new growth or remobilisation and recrystallisation of minerals during or post a deformation event (Marshall and Gilligan, 1993; Passchier and Trouw, 2005).

In a case where copper mineralisation was formed early (i.e. during diagenesis) and remobilised during a deformation event; initial copper minerals may be remobilised in veins, foliations, strain shadows and strain fringes. In most of the deposits of the CACB, remobilisation has been identified based on massive Cu-Co sulphides veins (Tillberg, 2012). However, in the mineralised zone of the Kamoa deposit, veins with copper sulphides are rare or absent. Thus, the analysis of strain shadows and strain fringes that contain copper sulphides may provide useful information on the formation of copper mineralisation. Strain fringes have been recognised as important tools to unravel the deformation history of a deposit (Etchecopar and Malavielle, 1987; Koehn *et al.,* 2000, Passchier and Trouw, 2005; Bons *et al.,* 2012; Chatalov, 2014). The non-deformed distal part of the fringe, the straight orientation and the displacement control of fibres, the lack of undulose extinction and recrystallisation features demonstrate the simple geometry of strain fringes in the Kamoa deposit. These characteristics suggest a low temperature growth and high fluid pressure (Passchier and Trouw, 2005; Chatalov, 2014).

The sulphur isotopic data for all the copper mineralisation is homogeneous suggesting a single mineralising event and lacks a heterogeneous sulphur isotope pattern typical of a multistage mineralisation process (Schmandt *et al.,* 2013). The observation and the analysis of strain fringes suggest that these structures were not a product of recrystallisation; they are new growths related to a deformation event. Furthermore, the ductile remobilisation is most effective in temperatures ranging from 350° to 500° C during metamorphism (Marshal and Gilligan, 1993). Dolomite intergrown with sulphide in clast rims (interpreted in this study as strain shadows and strain fringes) contains primary fluid inclusions that yield homogenisation temperatures ranging from 210° to 240°C (Schmandt *et al.,* 2013); these temperatures are under the effective temperatures for recrystallisation.

Within the Kamoa deposit, copper sulphides display a vertical and lateral mineral zonation. The mineral zoning consists of chalcocite-bornite-chalcopyrite and pyrite. This simple paragenetic sequence contrasts with the complex paragenetic sequence that may result from remobilisation as this process may modify the zonation (Marshall and Gilligan, 1993).

At any particular location within the mineralised zone, identical copper sulphide assemblages are observed in fine- and coarse-grained disseminations as well as in strain shadows and strain fringes. This observation suggests that copper sulphides in different textures are coeval and therefore were introduced at the same time. The diamictite must have been quite competent for strain shadows and strain fringes to be formed; this implies that the formation of copper mineralisation occurs after the deposition and lithification of the host rocks. In addition, it would be difficult to reproduce the identical assemblage of copper sulphides in strain shadows and strain fringes, fine- and coarse-grained disseminations at any particular depth of the mineralised zone after a remobilisation event relative to a deformation phase (Sillitoe *et al.,* 2010). Sillitoe *et al.,* (2010) suggested a massive fluid expulsion event to explain the generation of copper sulphides in different textures throughout enormous rock volumes over several kilometres of strike. The asymmetric upwards common morphology of strain shadows and strain fringes (85 – 90%) is better explained by an ascendant movement of fluid during a deformation event. This explanation doesn't work for the uncommon downwards strain shadows/fringes. The other possibility to explain the deposition of copper mineralisation is a closed system that maintains the hydrothermal fluids within the basin (Hitzman *et al.,* 2005). The fluid movement in the basin may be induced initially by early rifting or basin inversion during a deformation event. It would be difficult to have extension-related heat at the same time as the development of the S_1 foliation.

Based on the study completed on micro- and mesoscopic structures associated with copper mineralisation; it is proposed that there was a syn- or post-orogenic origin for the copper mineralisation within the Kamoa deposit.

6.1.6 Mineral alteration

Three sequential types of hydrothermal alteration are recognised in the Kamoa deposit: potassic, silicic and magnesian alteration (Schmandt *et al.,* 2013). SEM work performed in this study reveals the presence of coarse-grained albite in strain fringes/shadows intergrown with copper sulphides. This observation may suggest an albitic alteration coeval with copper mineralisation. It is possible that this alteration event may correspond with the postpeak metamorphism of the Lufilian Orogeny that occurred at approximately 512 to 500 Ma (Torrealday *et al.,* 2000; Hitzman *et al.,* 2012).

6.1.7 Microthermometry

Homogenisation temperatures for mineral growths (here interpreted as strain shadows/ fringes) range from 210° to 240° C and salinities varying from 23 to 26 wt % NaCl wt equiv (Schmandt *et al.,* 2013). These temperatures and salinities contrast with most of the Cu-Co deposits in the CACB that contain homogenisation temperatures varying between 115° to 220° C and salinities ranging from 11.3 to 20.9 wt.% NaCl equiv for the early diagenetic stratiform phase (El Desouky *et al.,* 2009). The second hypogene Cu-Co phase recognised as having produced syn-orogenic sulphides in veins and tectonic breccia is related to hydrothermal fluid with high temperatures ranging between 270° to 385° C and salinity between 35 to 45.5 wt.% NaCl equiv (El Desouky *et al.,* 2009).

6.2 Conclusions

The objective of this thesis was to investigate the structural controls of sulphide mineralisation within the Kamoa deposit. The research combined borehole core logging, true thickness isopach maps of stratigraphic units, copper grade maps, fence diagrams, petrographic and SEM work. The result of the study documents the importance of macro and mesoscopic structures in the formation of copper mineralisation at Kamoa.

The interpreted growth fault named “Mupaka Fault” has been characterised by thickness variations, facies change, steep bedding and the rotated mesoscopic faults. This growth fault appears to control the location of the highest copper grade mineralisation and may represent an important transport path for the hydrothermal fluids. The precipitation of copper sulphides is caused by the redox boundary located between the oxidising Mwashya Subgroup below and the reducing Grand Conglomérat unit above.

The development of S_1 foliation, strain shadows and strain fringes is coeval and related to a NW shortening direction. The Kolwezian deformation event is believed to be responsible for the development of these structures. Strain fringes reveal a straight orientation of fibres during coaxial deformation; this supports the interpretation of a single phase of deformation within the Kamoa deposit.

At any particular depth in the mineralised zone, copper sulphide assemblages in strain shadows and strain fringes and fine- and coarse-grained disseminations are similar suggesting that copper sulphides were introduced at the same time. The occurrence of copper sulphides in strain shadows and strain fringes indicates a new growth or remobilisation and recrystallisation of minerals during or post a deformation event. The non-deformed distal part of the fringe, the straight orientation and the displacement control of fibres, the lack of undulose extinction and recrystallisation features demonstrate the simple geometry of strain shadows and strain fringes. These characteristics suggest a new growth of minerals under low temperature and high pressure fluid. There is little potential for remobilisation of minerals in strain shadows and strain fringes because none of the mechanisms of recrystallisation (bulging, subgrain rotation and grain boundary migration) have been observed. In addition, the lateral and vertical zonation contrasts with the complex paragenetic sequence that may result from remobilisation.

A massive fluid expulsion event may explain the generation of copper sulphides in different textures throughout the Kamoa deposit. The asymmetric upwards common morphology of strain shadows and strain fringes suggests an ascendant movement of fluid during a deformation event. However, this explanation doesn't work for the uncommon downwards strain shadows and strain fringes.

The close relationship between copper mineralisation and structures (macro and mesoscopic) demonstrates that structures played a significant role in the formation of ore. Based on core logging, petrologic and microstructural evidences, it is proposed that there was a syn- or post-orogenic origin of copper sulphides, probably related to the Pan-African orogeny.

6.2.1 Implications for future exploration

The NW trends in highest-grade copper mineralisation are evident across the Kamoa deposit and thus NW extensions to these trends form priority exploration targets. The use of the seismic method could help to constrain zones of thickness variations of stratigraphic units that may represent potential prospective areas for future exploration work. The NW structures are not necessarily evident in magnetics or through observed offsets of layers, they can be recognised from thickening of stratigraphic units.

6.2.2 Recommendations for further work

The research that has been conducted for this thesis has not provided all the answers, however it has highlighted some topics on which further work would be useful. The following recommendations for future work are suggested:

- More fluid inclusion work to determine temperatures, pressures and chemical environment at which strain shadows and strain fringes were generated;
- A sulphur isotope study of sulphides from the matrix and from strain fringes/shadows would indicate whether they have different sulphur isotope signatures;
- Microcomputer tomography would be helpful to indicate the 3D distribution of sulphides in strain fringes and strain shadows and compare it to the distribution of sulphides in the matrix.

References

Alderton D.H.M, Selby D., Kucha, H., Blundell D.J., 2016. A multistage origin for Kupferschiefer mineralization. *Ore Geology Reviews,* **79**, 535 – 543.

Barnett, W., 2012. Kamoa Structural Interpretation. *Unpublished SRK Consulting (Canada) Inc. technical report, 31 slides.*

Barnett, W., 2013. Kamoa Structural Interpretation. *Unpublished SRK Consulting (Canada) Inc. technical report, 8 slides.*

Barnett, W., 2014. Kamoa Structural Interpretation. *Unpublished SRK Consulting (Canada) Inc. technical report, 21 slides.*

Barron, J. W., 2003. *The stratigraphy, metamorphism, and tectonic history of the Solwezi area, Northwest province, Zambia: Integrating geological field observations and airborne geophysics in the interpretation of regional geology*: PhD thesis, Golden, Colorado School of Mines, 233pp.

Binda, P., & Van Eden, J., 1972. Sedimentological evidence on the origin of the Precambrian Great Conglomerate (Kundelungu tillite), Zambia; *Palaeogeography, Paleoclimatology, Palaeoecology*, **12**, 151-168.

Bons, P.D., Elburg, M.A., Gomez-Rivas, E., 2012. A review of the formation of tectonic veins and their microstructures. *Journal of Structural Geology,* **43**, 33-62.

Broughton, D., 2013. Kamoa Copper Project, DRC: Power Point Presentations, African Metallogeny, 2nd SGA-SEG-UNESCO- IUGS short course. Kitwe, Zambia June 17-21st, 2013.

Broughton, D., 2014. *Geology and ore deposits of the Central African Copperbelt*: PhD thesis, Golden, Colorado School of Mines, 189pp.

Broughton, D. and Rogers, T., 2010. Discovery of the Kamoa copper deposit, Central Africa Copperbelt, D.R.C. *Society of Economic Geologists Special Publication,* **15**, 287-298.

Broughton, D., Hitzman, M., Selley, D., Scott, R., Bull, S., Large, R., McGoldrick, P., Croacker, M., Pollington, N., 2007. Geology and ore deposits of the Zambian Copperbelt. In Andrew, C.J. *et al.,* eds., *Digging Deeper – Proceedings of the 9th Biennial SGA Meeting:* Irish Association for Economic Geology, Dublin, 203-207.

Brown A. C. 1992. Sediment-hosted stratiform copper deposits. *Geoscience Canada* 19(3), 125-141. (reprinted in Sheahan P. A. & Cherry M. E. eds. *Ore Deposit Models,* **2***,* 99-115. Geological Association of Canada Reprint Series 6 1993).

Brown A. C., 1997. World-class sediment-hosted stratiform copper deposits: characteristics, genetic concepts and metallotects. *Australian Journal of Earth Sciences* **44**, 317 - 328.

Bull, S., Selley, D., Broughton, D., Hitzman, M., Cailteux, J., Large, R., and McGoldrick, P., 2011. Sequence and carbon isotopic stratigraphy of the Neoproterozoic Roan Group strata of the Zambian copperbelt: Precambrian Research, **190**, 70-89.

Cailteux, J., 1994. Lithostratigraphy of the Neoproterozoic Shaba-type (Zaire) Roan Supergroup and metallogenesis of associated stratiform mineralization. *Journal of African Earth Sciences,* **19,** 279-301.

Cailteux, J. and Kampunzu, H.A.B., 1995. The Katangan tectonic breccias in the Shaba province (Zaire) and their genetic significance. *Annales des Sciences Géologiques, Musée Royal de l'Afrique Centrale, Tervuren, Belgium,* **101**, 63-76.

Cailteux, J.L.H., Kampunzu A.B., Lerouge, C., Kaputo, A.K., Milesi, J.P., 2005a. Genesis of sediment-hosted stratiform copper-cobalt deposits, Central African Copperbelt. *Journal of African Earth Sciences,* **42**, 134-158.

Cailteux, J.L.H., Kampunzu, A.B.H., Batumike, M.J., 2005b. Lithostratigraphic position and petrographic characteristics of R.A.T. (''Roches Argilo-Talqueuses'') Subgroup, Neoproterozoic Katangan Belt (Congo). *Journal of African Earth Sciences,* **42**, 82-94.

Cailteux, J., Kampunzu, A., Lerouge, C., 2007. The Neoproterozoic Mwashya-Kansuki sedimentary rock succession in the central African Copperbelt, its Cu-Co mineralization, and regional correlations: Gondwana Research, **11**, 414-431.

Chatalov, A. 2014. Development of strain fringes in sedimentary rocks: evidence for deformation of Upper Ordovician glacial diamictites in the western Srednogorie Zone. *Geologica Balcanica,* 43 (1 – 3), 51-62.

Cosi, M., De Bonis, A., Gosso, G., Hunziker, J., Martinotti, G., Moratto, S., Robert, J.P., Ruhlman, F., 1992. Late Proterozoic thrust tectonics, high-pressure metamorphism and uranium mineralization in the Domes Area, Lufilian Arc, northwestern Zambia. *Precambrian Research,* **58**, 215-240.

Daly, M.C., 1986. Crustal shear zones and thrust belts; their geometry and continuity in Central Africa. *Philosophical Transactions. Royal Society of London* A, **317**, 111-128.

De Magnée, I., and François, A., 1988. The origin of the Kipushi (Cu, Zn, Pb) deposit in direct relation with a Proterozoic salt diapir, Copperbelt of Central Africa, Shaba, Republic of Zaire, in Friedrich, G.H., *et al.,* (eds.), Base metal sulfide deposits: Berlin, Springer-Verlag, p. 74–93.

El Desouky, H.A., Muchez, P., and Cailteux, J., 2009. Two Cu-Co sulphides phases and contrasting fluid systems in the Katanga Copperbelt, Democratic Republic of Congo: *Ore Geology Reviews*, **36**, 315 – 332.

Etchecopar, A., and Malavieille, J., 1987. Computer models of pressure shadows: a method for strain measurements and shear sense determination. *Journal of Structural Geology,* **9**, 667 - 677.

François, A., 1973. L'extrémité occidentale de l'arc cuprifère Shabien. Etude géologique, Gécamines, Likasi (Shaba-Zaïre), 65pp.

François, A., 2006. La partie centrale de l'Arc cuprifère du Katanga: étude géologique. Musée Royal de l'Afrique Centrale, **109**, 70 pp.

Fossen, H., 2010. Structural geology. Cambridge University Press.

Gilchrist, G., 2014. Kamoa structural model: some thoughts. *Unpublished Ivanhoe Mines technical presentation, 30 slides.*

Hendrickson, M.D., Hitzman, M.W., Wood, D., Humphrey, J.D., Wendlandt, R.F., 2013. Geology of the Fishtie deposit, Central Province, Zambia: iron oxide and copper mineralization in Nguba Group metasedimentary rocks: *Mineralium Deposita,* **50**, 717 – 737.

Hitzman, M., Kirkahm, R., Broughton, D., Thorson, J., Selley, D., 2005. The sediment-hosted stratiform copper ore system: *Economic Geology 100th Anniversary Volume*, 609 - 642.

Hitzman, M.W., Broughton D., Selley, D., Woodhead J., Wood D., Bull, S., 2012. The Central African Copperbelt: diverse stratigraphic, structural, and temporal settings in the world's largest sedimentary copper district: *Society of Economic Geologists, Special Publication,* **16**, 487 – 514.

Hull A., 2013. Evaluation of surface fault rupture hazard to tailings storage facility options. Kamoa Copper Project, Katanga, DRC, 48pp.

Jackson, M., Warin, O., Woad, G., Hudec, M., 2003. Neoproterozoic allochthonous salt tectonics during the Lufilian orogeny in the Katangan Copperbelt, central Africa. *Geological Society of America Bulletin,* **115**, 314-330.

Kampunzu, A.B. and Cailteux, J., 1999. Tectonic Evolution of the Lufilian Arc (Central Africa Copper Belt) During Neoproterozoic Pan African Orogenesis: *Gondwana Research,* **2**, 401-421.

Key, R.M., Liyungu, A.K., Njamu, F.M., Somwe, V., Banda, J., Mosley, P.M., Armstrong, R.A., 2001. The western end of the Lufilian arc in NW Zambia and its potential for copper deposits: *Journal of African Earth Sciences,* **33**, 503-508.

Killick. A.M., 2003. Fault rock Classification: An aid to structural interpretation in mine and exploration geology: *South African Journal of Geology,* **106**, 395-402.

Kipata, M.L., Delvaux, D., Sebagenzi, M.N., Cailteux, J. and Sintubin, M., 2013. Brittle tectonic and stress field evolution in the Pan-African Lufilian arc and its foreland (Katanga, DRC): from

orogenic compression to extensional collapse, transpressional inversion and transition to rifting: *Geologica belgica,* **16(1-2)**, 1-17.

Koehn, D., Hilgers, C., Bons, P.D., Passchier, C.W. 2000. Numerical simulation of fibre growth in antitaxial strain fringes: *Journal of Structural Geology,* **22**, 1311-1324.

Kokonyangi, J.W., Kampunzu, A.B., Armstrong, R., Makoto, A. Yashida, M., and Okudaira, T., 2007. U-Pb SHRIMP Dating of Detrital Zircons from the Nzilo Group (Kibaran Belt): Implications for the Source of Sediments and Mesoproterozoic Evolution of Central Africa: *Journal of Geology*, **115**, 99 – 113.

Marshak S, and Mitra G., 1988. Basic methods of structural geology. Prentice Hall, Englewood Cliffs, New Jersey.

Marshall, B., and Gilligan, L.B., 1993. Remobilization, syn-tectonic processes and massive sulphides deposits. *Ore Geology Reviews,* **8**, 39 – 64.

Master, S., Wendorff, M., 2011. Neoproterozoic glaciogenic diamictites of the Katanga Supergroup, Central Africa: *Geological Society, London, Memoirs*, **36**, 173-184.

McGowan, R.R., Roberts, S., Boyce, A.J., 2005. Origin of the Nchanga copper-cobalt deposits of the Zambian Copperbelt: *Mineralium Deposita,* **40**, 617 – 638.

Mort. K and Woodcock N.H., 2008. Quantifying fault breccia geometry: Dent Fault, NW England: *Journal of Structural Geology:* **30,** 701-709.

Mvondo, H., 2012. Structural Analysis and domain definition of the Kamoa project area, Democratic Republic of Congo (DRC). *Unpublished SRK Consulting (Canada) Inc. technical memorandum for Project 2CA029.000, 31 pp.*

Parker, H.M. Seibel, G. David, D. Peters, B. Jakubec, J. and Lawson, M., 2013. NI 43-101. Technical report of Kamoa Copper Project, Democratic Republic of Congo (DRC). *AMEC. NI 43-101 Technical report and 172449. Katanga, 371pp.*

Passchier, C.W., Trouw, R.A.J., 2005. Microtectonics, second edition Springer Verlag, Berlin.

Passchier, C.W., 2015. Microtectonics lectures. *GSSA short course, university of Stellenbosch, May 2015.*

Peters, B.F., Parker, H.M., Seibel, G., Joughin, W., David, D., 2016. NI 43-101. Kamoa 2016 Prefeasibilty Study. *Orewin Technical report, Jon No. 15003. Lualaba province, 445 pp.*

Porada, H. and Berhorst, V., 2000. Towards a new understanding of the Neoproterozoic-Early Palaeozoic Lufilian and northern Zambezi Belts in Zambia and Democratic Republic of Congo. *Journal of African Earth Sciences,* **30**, 727-771.

Ramsay, J.G. and Huber, M.I., 1983. The Techniques of Modern Structural Geology. Vol. **1**: Strain Analysis. London: Academic Press.

Ripley, E.M., Merino, E., Moore, C. and Ortoleva, P. 1985. Mineral zoning in sediment-hosted copper deposits. In K.H. Wolf (ed.), *Handbook of Stratabound and Stratiform Ore Deposits,* Elsevier, **6**, 237 – 360.

Robb, L.J. 2005. Introduction to ore-forming processes. Blackwell Publishing.

Schmandt, D., Broughton, D., Hitzman, M.W., Plink-Bjorklund, P., Edwards, D., and Humphrey, J., 2013. The Kamoa Copper Deposit, Democratic Republic of Congo: Stratigraphy, diagenetic and hydrothermal alteration, and mineralization. *Economic Geology,* **108**, 1301 - 1324.

Schmandt, D., 2012. *Stratigraphy and mineralization of the Kamoa Copper Deposit, Katanga, Democratic Republic of Congo.* Unpublished. Msc thesis, Golden, Colorado School of Mines, 122pp.

Selley, D., Broughton, D., Scott, R., Hitzman, M., Bull, S., Large, R., McGoldrick, P., Croaker, M., Pollington, N., 2005. A New Look at the Geology of the Zambia Copperbelt: *Economic Geology 100th Anniversary Volume* 965 - 1000.

Sillitoe, R.H., Perello, J., and Garcia, A., 2010. Sulfide-bearing veinlets throughout the stratiform mineralization of the Central African Copperbelt: Temporal and genetic implications. *Economic Geology*, **105**, 1361 – 1368.

Tack, L., Wingate, M.T.D., De Waeled, B., Meert, J., Belousova, E., Griffin, B., Tahon, A., Fernandez-Alonso M., 2010. The 1375 Ma "Kibaran event" in Central Africa: Prominent emplacement of bimodal magmatism under extensional regime. Precambrian Research, **180**, 63 – 84.

Taylor, C.D., Causey, J.D., Denning, P.D., Hammarstrom, J.M., Hayes, T.S., Horton, J.D., Kirschbaum, M.J., Parks, H.L., Wilson, A.B., Wintzer, N.E., and Zientek, M.L., 2013. Global Mineral Resource Assessment. Descriptive Models, Grade-Tonnage Relations, and Databases for the Assessment of Sediment-Hosted Copper Deposits—With Emphasis on Deposits in the Central African Copperbelt, Democratic Republic of the Congo and Zambia Scientific Investigations Report 2010–5090–J, 172pp.

Tillberg, M., 2012. Ore-forming processes and tectonic control of the sediment-hosted Cu-Co deposits in the Central African Copperbelt. Department of Earth Sciences, University of Gothenburg, ISSN 1400 - 3821.

Torrealday, H.I., Hitzman, M.W., Stein, H.J., Armstrong, R., and Broughton, D., 2000. Re-Os and U-Pb dating of the vein-hosted mineralisation at the Kansanshi copper deposit, northern Zambia: *Economic Geology,* **95**, 1165 – 1170.

Turlin, F., Eglinger, A., Vanderhaeghe, O., André-Mayer, A.-S., Poujol, M., Mercadier, J., Bartlett, R., 2015. Synmetamorphic Cu remobilization during the Pan-African orogeny: Microstructural, petrological and geochronological data on the kyanite-micaschists hosting the Cu(-U) Lumwana deposit in the Western Zambian Copperbelt of the Lufilian belt. *Ore Geology Reviews,* **75**, 52 – 75.

Twiss, R.J. and Moore, E.M., 1992. Structural geology. H.W. Freeman and Company.

Twite, F.B., Kirschbaum, M.J, Mushobekwa, I.M., 2012. Major structure logging. *Unpublished Kamoa technical presentation, 24 slides.*

Unrug, R., 1983. The Lufilian Arc: a microplate in the Pan-African collision zone of the Congo and the Kalahari cratons. *Precambrian Research,* **21**, 181-196.

Unrug, R., 1988. Mineralization controls and source of Metals in the Lufilian Fold Belt, Shaba (Zaire), Zambia, and Angola. *Economic Geology,* **83**, 1247-1258.

Van Loon, A.J. 2009. Soft-sediment deformation structures in siliciclastic sediments: an overview. *Geologos,* 2009, **15** (1), 3 – 55.

Wendorff, M. & Key, R. M. 2009. The relevance of the sedimentary history of the Grand Conglomérat Formation (Central Africa) to the interpretation of the climate during a major Cryogenian glacial event. *Precambrian Research*, **172**, 127–142.

White, W.S., and Wright, J.C., 1966. Sulfide zoning in the basal Nonesuch Shale, northern Michigan: *Economic Geology*, **61**, 1171–1190.

Appendix A

Petrographic descriptions and SEM images

170 Samples were collected during core logging for transmitted and reflected light microscopy. Comprehensive illustrations and descriptions are presented below.

To better constrain the fine-grained mineralogy, textures and structures; 18 polished thin sections were investigated using the scan electron microscope FEI Quanta 200 ESEM from the University of the Witwatersrand (SEM). This microscope is equipped with analytical systems, such as energy dispersive spectrometer, wavelength dispersive x-ray spectroscopy and electron backscatter diffraction.

Below is the list of abbreviations used in this section.

Table A.1. List of abbreviations.

CATEGORY	Code	Description
LITHOLOGY		
	SSL	Siltstone
	SST	Sandstone
	SDT	Diamictite
	SCG	Conglomerate
STRATIGRAPHY		
	Ng 1.1	Undifferentiated Nguba
	Ng 1.1.6	Uppermost diamictite
	Ng 1.1.5	Upper diamictite
	Ng 1.1.4	Upper laminated pyritic siltstone
	Ng 1.1.3	Middle diamictite package
	Ng 1.1.2	Lower laminated pyritic siltstone
	Ng 1.1.1	Basal diamictite
	Ng 1.1.1.3	Upper basal diamictite
	Ng 1.1.1.2	Intercalated siltstone
	Ng 1.1.1.1	Lower basal diamictite
	R4.2	Mwashya Subgroup
MINERALISATION		
	Py	Pyrite
	Cpy	Chalcopyrite
	Bn	Bornite
	Cct	Chalcocite
	Cu	Native copper
	Hae	Haematite

CATEGORY	Code	Description
STRUCTURE	**BD**	Bedding
	FLD	Fold
	FZ	Fractured zone
	LM	Lamination
	MFA	Mesoscopic fault
	SSD	Soft sediment deformation
	STB	Steep bedding
	STF	Strain fringe
	STS	Strain shadow
	VN	Vein
	VWFO	Very weak foliation
	WFO	Weak foliation
	MFO	Moderate foliation
	SFO	Strong foliation
	X	Breccia

Sample ID	Lithology	Feature	Description	Scanned TS	Transmitted light_Photomicrograph (XPL and PPL)	Reflected light_Photomicrograph
FT_01	SDT	VWFO	Thin section composed of a fine-grained matrix (60-70%), clasts (25%), iron oxides, some coarse-grained chalcocite and occasional chalcopyrite. This fine-grained matrix is constituted with quartz, micas, chlorite and iron oxides. Clasts are rounded to angular and composed of quartz (60%; 0.01-0.8 cm), micas (20%; 100 -300 µm) and chlorite (20%; 100-300 µm). Chalcocite and chalcopyrite occur in replacement of clasts (0.1%; up to 1 cm). Iron oxide occurs as fine- and coarse-grained (5 µm- 1 cm) dissemination within the fine-grained matrix and along fractures.	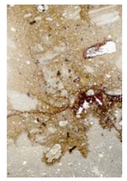	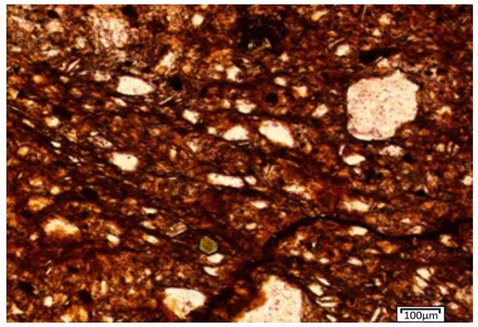	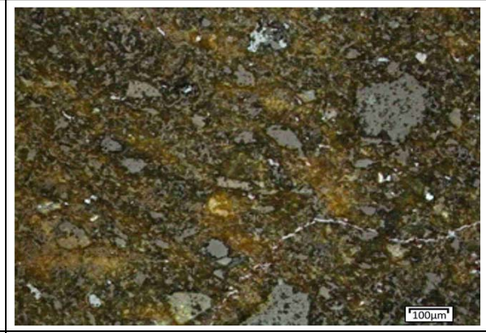
FT_02	SDT	VWFO	Clast-poor diamictite in a fine-grained matrix. This fine-grained matrix is constituted with quartz, chlorite, micas and the grain size varying from 5 µm to 10 µm. The matrix is aligned. Clasts are rounded to sub-angular and composed mainly of quartz (80%; up 0.5 cm) with minor chlorite (10%; 100-200 µm), micas (5%; 100-200 µm) and potassium feldspar (5%; 10-100 µm). Chalcopyrite occurs as fine- and coarse-grained dissemination within the matrix (0.3%) and in the replacement of clasts (0.1%). Chalcocite occurs as fine-grained (5-25 µm) dissemination in the matrix (0.3%). Trace native copper disseminated in the matrix. Very weak foliation defined by the alignment of minerals.	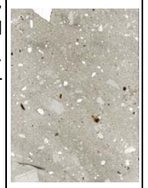	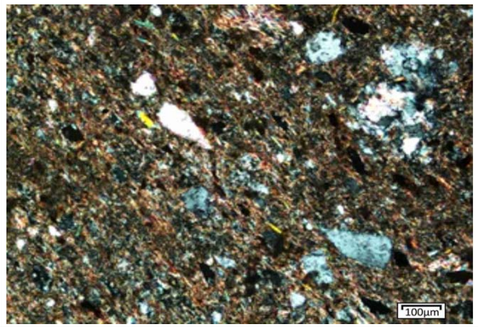	
FT_03B	SDT	WFO	Diamictite, clast-poor to moderate (10-20% clasts) in a fine-grained matrix (60-80%). This matrix is constituted of quartz, micas and chlorite. The grain size is overall - 5 µm to 10 µm. The matrix is not aligned. Clasts are rounded to sub-angular, they are not aligned. In addition, incipient Q and M domains occur insome areas of the section. Clasts are composed mainly of quartz (80%; up 0.4 cm) with minor chlorite (10%; 100-200 µm) and micas (10%; 100-200 µm). Chalcocite forms strain fringes around clasts. Coarse- grained native copper (0.1%; 100 - 250 µm) is observed within a quartz clasts; chalcocite occurs as fine- (0.4%; 5-25 µm) and coarse-grained (50-250 µm; up to 0.7%) in the fine-grained matrix.	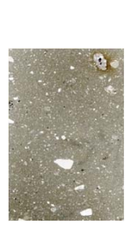	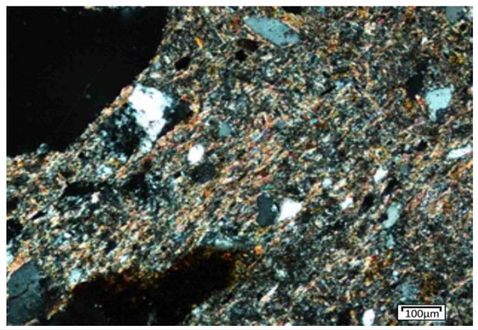	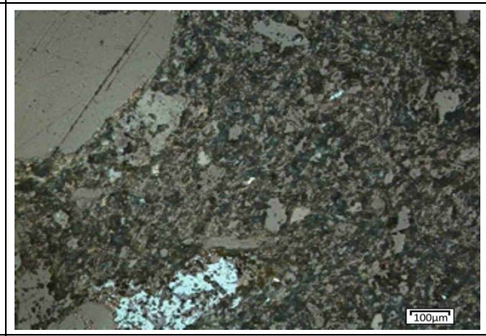
FT_04	SSL	FLD	Thin section including a tight fold shown by folding of the S0 sedimentary layering. This layering is shown by grain size variation and alternating dark- and light-coloured layers in PPL. The sedimentary layers are composed of iron oxides with micas and possible ilmenite. Beddings are showing a soft sedimentary deformation texture. No foliation observed within the fold, therefore the fold maybe syn-sedimentary. Presence of dropstones composed mainly of quartz in the beddings.	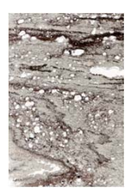	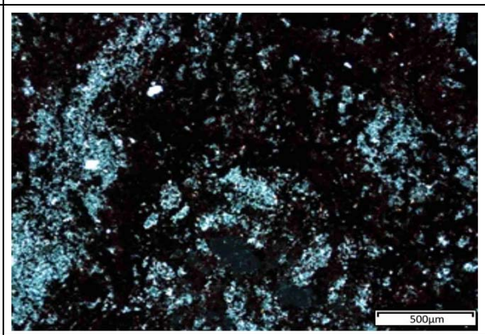	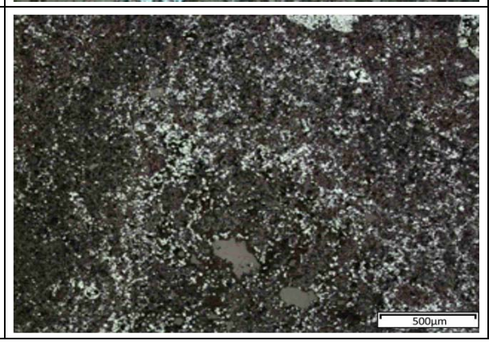

Sample ID	Lithology	Feature	Description	Scanned TS	Transmitted light_Photomicrograph (XPL and PPL)	Reflected light_Photomicrograph
FT_05	SSL	WFO	Laminated pyritic siltstone showing a foliation defined by alignment of pyrite. The matrix is fine- to coarse-grained, it is composed of quartz, biotite and minor muscovite. The grain size is overall sub-rounded -5 µm with frequent slightly larger angular quartz (up to 50µm). Laminations are spaced with 0.1 cm to 1 cm. Presence of rare quartz clasts which are possible dropstones. S1 foliation defined by the alignment of coarse-grained pyrite (50-300 µm) located around laminations. S1 is sub-perpendicular to the laminations. Abundant framboidal pyrite are observed in laminations (5-15 µm; up to 30%).		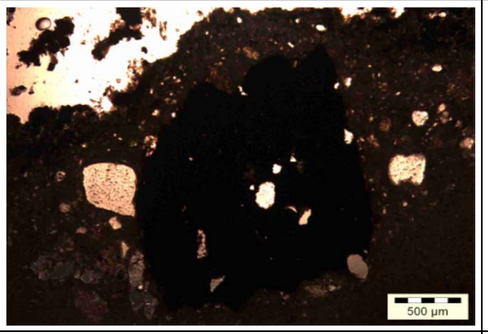	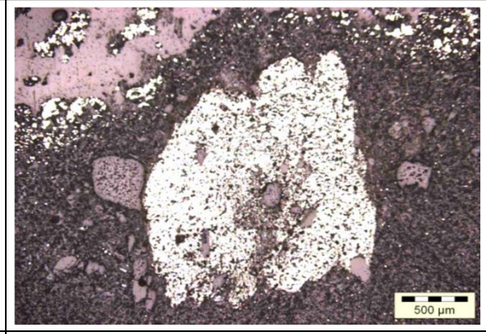
FT_06	SDT	VN	Thin section including a quartz vein (40%) within a mafic igneous clasts (60%). The mafic igneous clast is composed of chlorite, quartz, biotite with some muscovite. The grain size within the clast is 5 µm with some larger fragments up 0.5cm. The vein is composed of mainly quartz, chlorite, and pyrite with some chalcopyrite. Pyrite occurs as coarse-grained euhedral within the vein (30 µm- 1.5 mm; up 0.7%); chalcopyrite as coarse-grained (40 µm- 1.5 mm; up 0.1%).		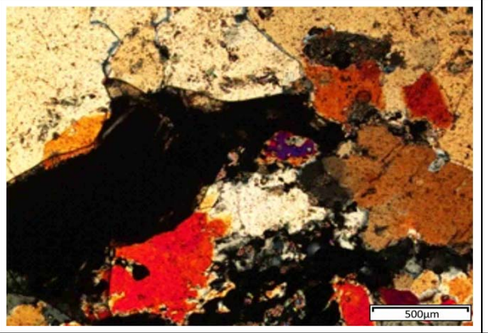	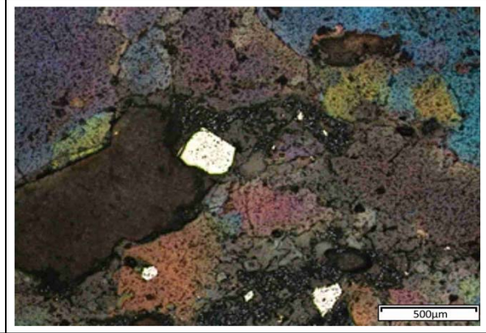
FT_07	SDT	MFO	Clast-poor diamictite(5%) in a fine-grained matrix (55%). Abundant chalcopyrite are observed, it is occured as fine- and coarse-grained material (40%). The fine-grained matrix is composed of quartz, silica, biotite and muscovite; the grain size is 5 µm with some fragments up 250 µm. The fine-grained matrix is not aligned everywhere, incipient Q and M domains occur in some areas of the thin section. Clasts (60 µm- 5mm) are composed mainly of quartz, chlorite, and micas. A soft sediment deformation texture is observed. S1 is defined by the alignment of fine- (2-50 µm; up to 25%) and coarse-grained (50 µm- 80 mm; up to 15%) chalcopyrite within the gangue.		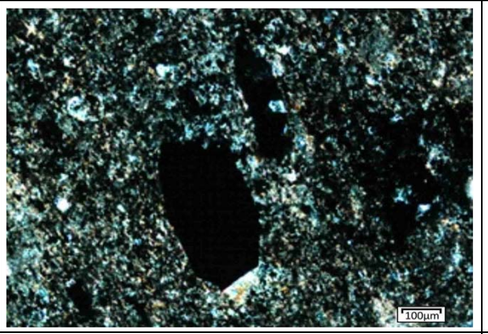	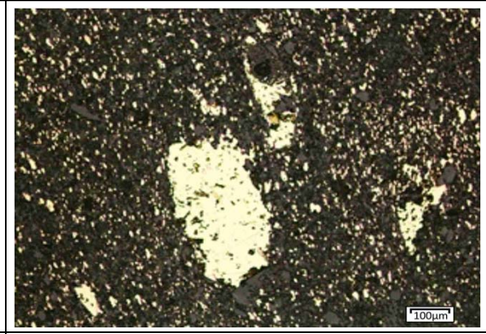
FT_07H	SDT	MFO	Thin section perpendicular to FT_07. Moderate foliation defined by the alignment of sulphides and minerals within the matrix. The intensity of foliation and the composition of the rock is similar to that of FT_07.		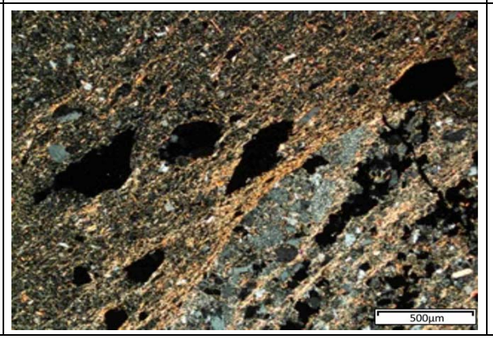	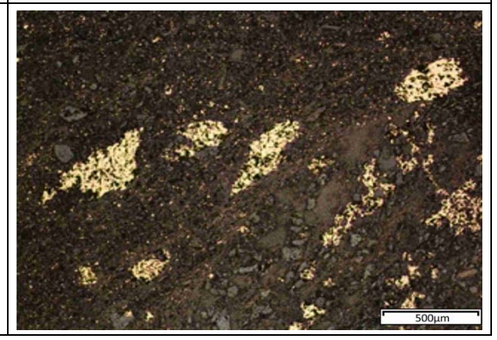

Sample ID	Lithology	Feature	Description	Scanned TS	Transmitted light_Photomicrograph (XPL and PPL)	Reflected light_Photomicrograph
FT_08A	SDT	MFO	Clasts poor diamictite (5- 15%) and fine to coarse grained chalcopyrite (20%) which is showing S1 in fine grained matrix (50-65%). This matrix is slightly aligned and composed of quartz, chlorite, biotite, and muscovite. The size of grains in the matrix is varying from 2 µm to 150 µm (for large fragments). The clasts are composed of quartz, chlorite, potassium feldspar, micas, and carbonate. All the clasts are not aligned but some of them are showing a weak alignment. Spaced foliation (S1) defined by alignment of fine and coarse grained chalcopyrite. The copper mineralization is mainly composed of chalcopyrite both in fine (2-50m; up 13%) and coarse-grained (50 µm – 5mm; up to 11%). Copper sulphides are partially to completely replace clasts.		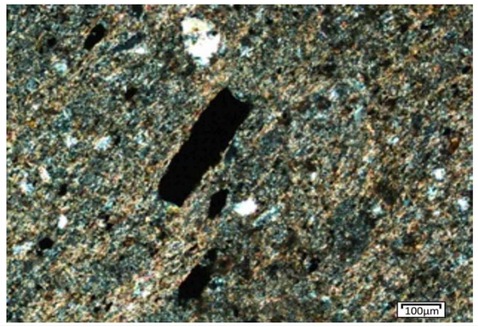	
FT_08AH	SDT	MFO	Thin section perpendicular to FT_08A. Moderate foliation defined by the alignment of sulphides and minerals within the matrix. The composition of the rock is similar to that of FT_09.		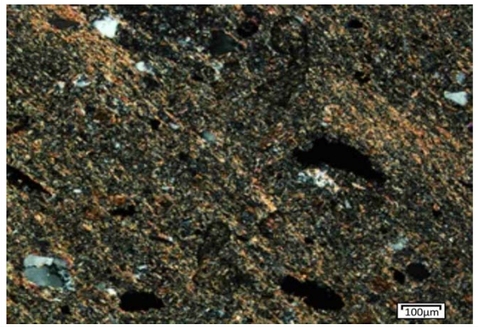	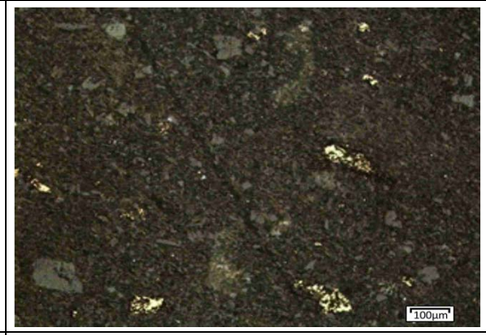
FT_08B	SDT	STS/MFO	Clast-poor diamictite intercalated with a fine-grained siltstone . The matrix is fine-grained matrix, slightly aligned and composed of quartz, chlorite, and micas. The size of grains wihtin the matrix varies from 2 to 150 µm (for large fragments). Clasts are composed of quartz, chlorite, K-feldspar, micas and carbonate. Most clasts are not aligned but minor amount shows a weak alignment. The intercalated siltstone is composed of quartz, chlorite, micas and minor K-feldspar. Continuous foliation (S1) defined by the alignment of fine- and coarse-grained chalcopyrite. The mineralisation is mainly composed of chalcopyrite which occurs as fine- (2-50 µm; up 18%) and coarse-grained (50 µm – 5 mm; up to 8%). Chalcopyrite tends to replace clasts (partially to completely).	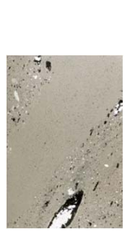	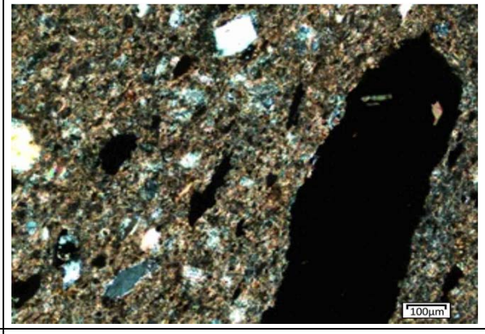	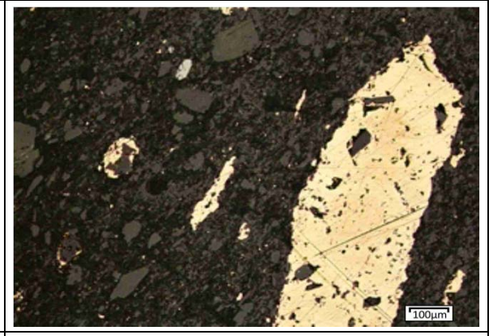
FT_09	SDT	MFO/STS	Clast-poor diamictite (70%) intercalated with a fine-grained and laminated siltstone (15%). The matrix within the clast-poor diamictite is composed of quartz, biotite, muscovite and minor chlorite. The matrix is fine-grained and aligned. Clasts are composed of quartz, carbonate, micas, and K-feldspar. The siltstone (2 µm to 15 µm) is composed of quartz and biotite. S1 foliation is defined by the alignment of fine- and coarse-grained chalcopyrite. Asymmetric strain shadows/fringes are observed. The mineralisation is mainly composed of chalcopyrite both in fine-grained (2-50m; up 14%), coarse-grained (50 µm – 5mm; up to 8%) and in replacements of clasts (0.5%). Clasts are partially to completely replaced by chalcopyrite.	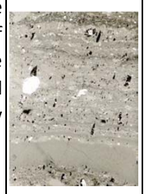	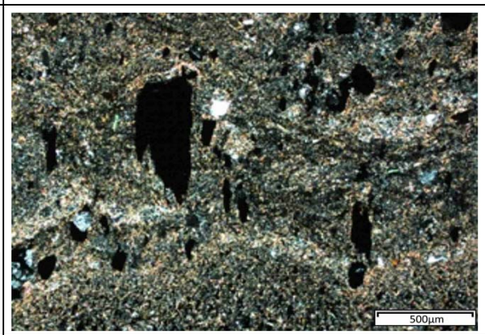	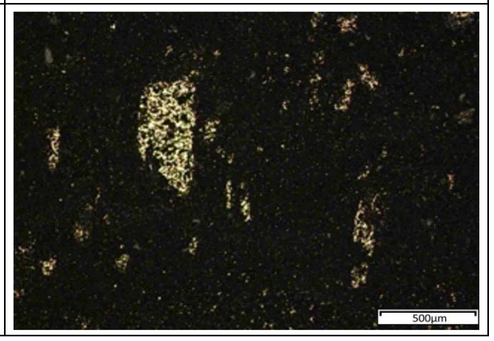

Sample ID	Lithology	Feature	Description	Scanned TS	Transmitted light_Photomicrograph (XPL and PPL)	Reflected light_Photomicrograph
FT_09H	SDT	MFO	Thin section perpendicular to FT_09. Moderate foliation defined by the alignment of sulphides and minerals within the matrix. The composition of the rock is similar to that of FT_09.		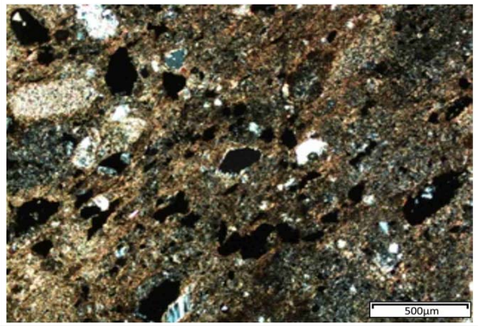	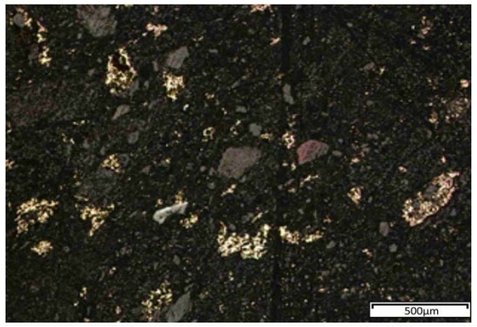
FT_10	SSL	X	Fine-grained siltstone showing a brecciated texture. The rock is fine-grained (0.2 µm to 20 µm) and mainly composed of quartz and micas. The texture of the breccia is a crackle breccia. It contains iron oxides and minor native copper. Clast doesn't touch each other and their size vary from 2 µm to 1cm. No rotation or dilation is observed in the thin section.		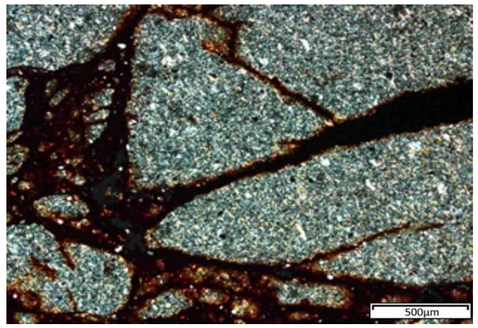	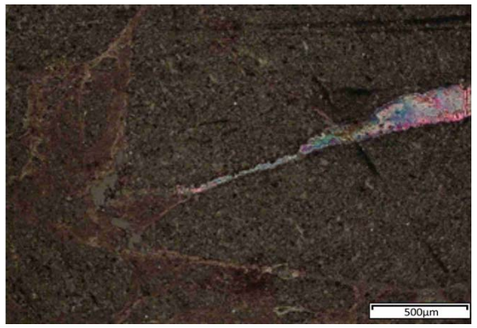
FT_11	SSL	MFO	Fine-grained siltstone (97%) with some pyrrhotite (2.5%) and rare chalcopyrite (0.5%). The rock is composed of quartz, micas and chlorite, the grain size is overall 5 µm to 10 µm. Minerals within the matrix are aligned. S1 foliation defined by alignment of coarse-grained pyrrhotite. Fine-grained chalcopyrite occurs in association with pyrrhotite. Possible euhedral pyrite within the matrix.		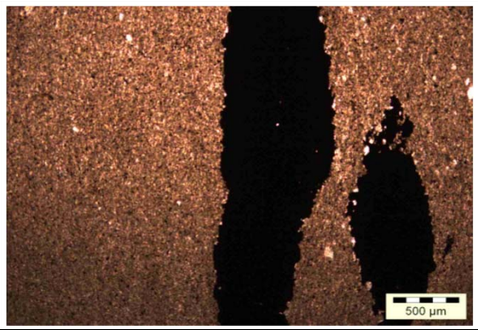	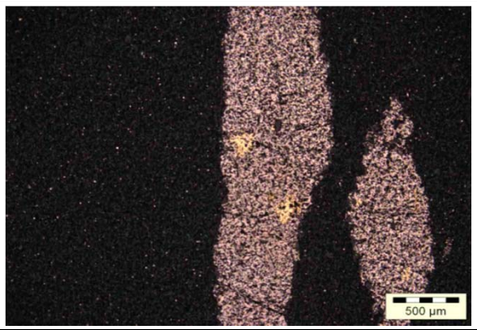
FT_12A	SDT	SFO/STS	Clast-poor diamictite showing a strong foliation defined by the alignment of coarse-grained pyrite and quartz clasts. The matrix is fine-grained and composed of quartz, chlorite and micas. Clasts are composed of quartz, micas, carbonate and potassium feldspar. Their size varies from 50 µm to 2 mm (up to 10%). Chlorite and quartz form strain shadows and strain fringes to euhedral pyrite. Clasts define a continuous schistosity. The euhedral pyrite overgrowth on the clasts and seems to be later than the rock. 25 - 40% pyrite occurs as coarse-(50 µm – 4mm; up to 30%) and fine-grained associated with framboidal grains (3 µm- 40 µm; up 10%).	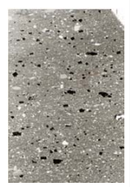	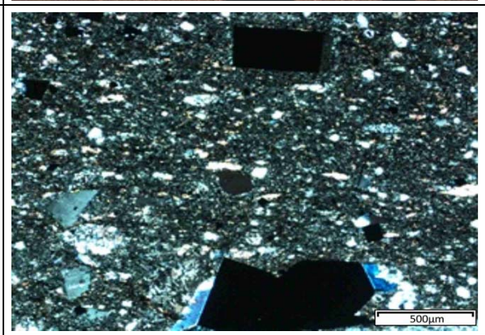	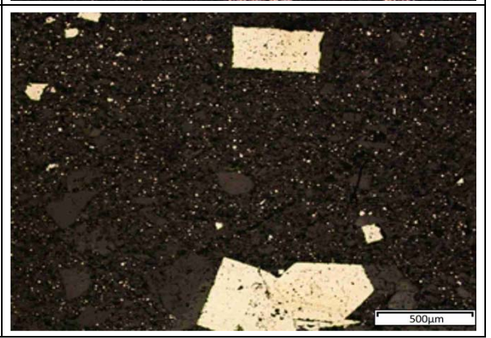

Sample ID	Lithology	Feature	Description	Scanned TS	Transmitted light_Photomicrograph (XPL and PPL)	Reflected light_Photomicrograph
FT_12B	SDT	SFO/STS	Moderate foliation defined by alignment of coarse grained pyrite and quartz clasts in a clasts poor diamictite. The matrix in the clasts poor diamictite is fine grained and composed of quartz, chlorite and micas. The grain size of the matrix is 5 µm - 50 µm; up to 50%. The clasts are composed of quartz, micas, carbonate, potassium feldspar, possible plagioclase and their size is varying from 50 µm to 2mm; 2cm for the large clast (up to 15% of the thin section). Chlorite, carbonate and quartz form the strain shadows and strain fringes around the euhedral pyrite. In addition the clasts are forming a continuous schistosity. The euhedral pyrite overgrowth on the clasts and seems to be later than the rock. 25 - 40% pyrite in coarse-grained (50 µm – 4mm; up to 35%) and fine grained associated with framboidal (3 µm- 40 µm; up 10%). Trace pyrrhotite around euhedral pyrite. Pyrite is replacing the clasts.	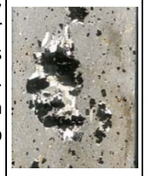	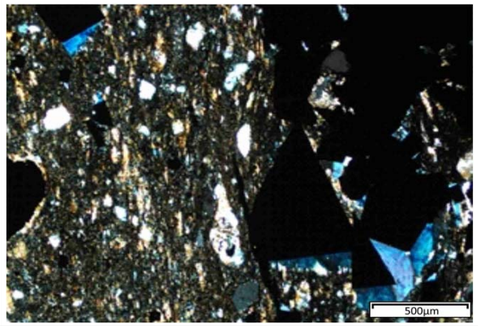	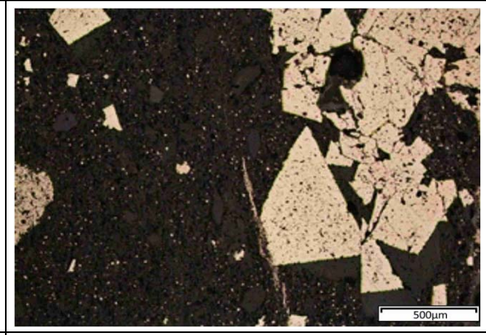
FT_12C	SDT	SFO/STS	Moderate foliation defined by alignment of coarse grained pyrite and quartz clasts in a clasts poor diamictite. The matrix in the clasts poor diamictite is fine grained and composed of quartz, chlorite and micas. The grain size of the matrix is 5 µm - 50 µm; up to 50%. The clasts are composed of quartz, micas, carbonate, potassium feldspar, plagioclase and their size is varying from 50 µm to 2mm; 2cm for the large clast (clasts up to 15% of the thin section). Chlorite, carbonate and quartz form the strain shadows and strain fringes around the euhedral pyrite. In addition the clasts are forming a continuous schistosity. The euhedral pyrite overgrowth on the clasts and seems to be later than the rock. 25 - 40% pyrite in coarse-grained (50 µm – 4mm; up to 35%) and fine grained associated with framboidal (3 µm- 40 µm; up 10%). Trace pyrrhotite around euhedral pyrite. Pyrite is replacing the clasts.	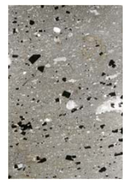	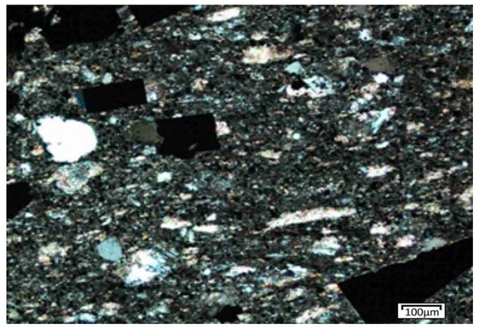	
FT_12CH	SDT	MFO	Thin section perpendicular to FT_12C. Moderate foliation defined by the alignment of sulphides and minerals within the matrix. The intensity of foliation decreases compared to adjacent thin section. The composition of the rock is similar to that of FT_12C.		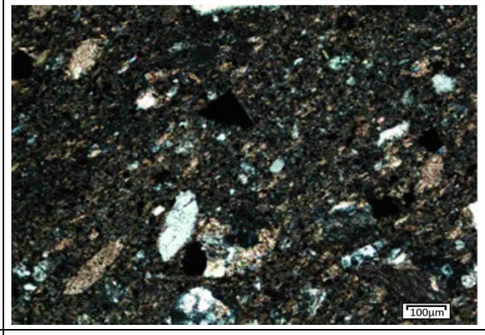	
FT_13	SDT	SFO/STS	Clast-moderate diamictite showing a strong foliation defined by the alignment and elongation of clasts. The matrix is fine-grained, it is composed of quartz, chlorite and micas. A slighty alignment of minerals is observed in the matrix. Clasts are composed of quartz, chlorite, muscovite, biotite, plagioclase and carbonate. The size of clasts vary between 50 µm and 1cm. Chlorite forms strain shadows and strain fringes to euhedral pyrite. Clasts are aligned and define a continous foliation. 2 - 6% pyrite in coarse-(50 µm- 2mm; 2%) and fine-grained associated with framboidal pyrite (2 -40 µm; up 4%).		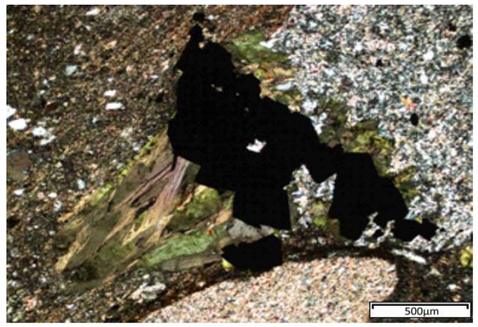	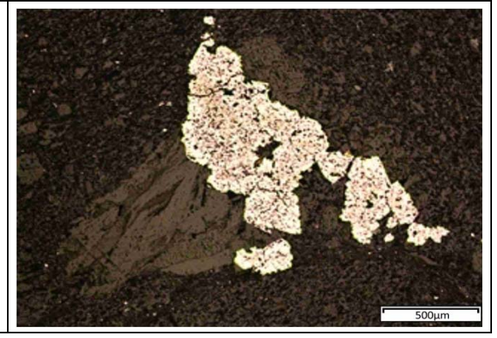

Sample ID	Lithology	Feature	Description	Scanned TS	Transmitted light_Photomicrograph (XPL and PPL)	Reflected light_Photomicrograph
FT_14	SDT	SFO/STS	Thin section showing a diamictite with strong foliation and strain shadows. The matrix is fine-grained and aligned, it is composed of quartz, chlorite and micas. Clasts are composed of quartz, chlorite, muscovite, biotite and carbonates. S1 foliation is defined by the alignment and elongation of clasts, alignment of minerals within the matrix and alignment of pyrite. Chlorite forms strain shadows and strain fringes to euhedral pyrites. 2 - 5% pyrite in coarse- and fine-grained associated with framboidal pyrite (2 - 40 µm; up 3%).		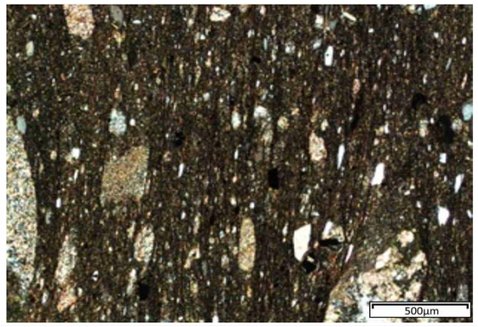	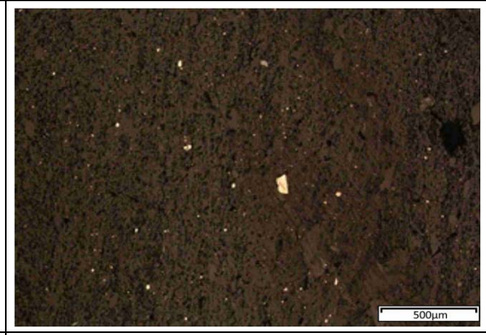
FT_15	SDT	SFO	Thin section including diamictite displaying a strong foliation. Clasts are composed of quartz, plagioclase, K-feldspar, biotite and chlorite. Strong foliation defined by the alignment of minerals within the matrix and the elongation of clasts. Possible crenulation defined by biotite. Strain fringes mostly defined by chlorite. Pyrite constitutes about 1.5 % of the thin section, it occurs as disseminations in the matrix. Rare coarse euhedral pyrite grains are visible.		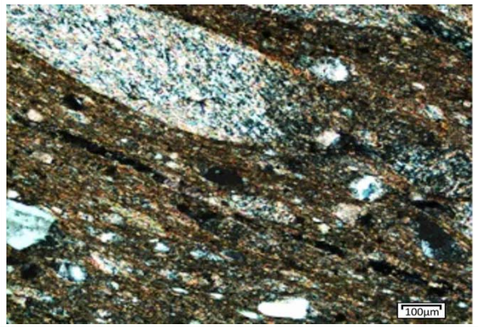	
FT_15H	SDT	SFO	Thin section perpendicular to FT_15. Strong foliation defined by the alignment of sulphides and minerals within the matrix. The intensity of foliation and the composition of the rock is similar to that of FT_15.		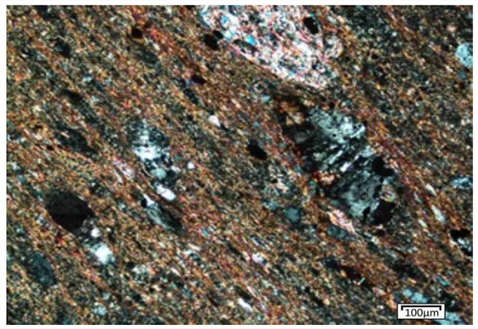	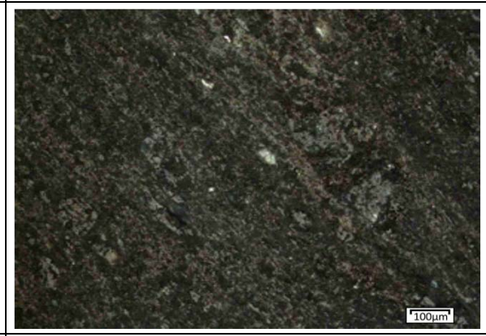
FT_16	SDT	SFO/STS	Thin section including a strong foliation in the diamictite. Clasts are composed of quartz, plagioclase, carbonate, biotite and chlorite. Clasts constitute about 75% and the matrix about 25% of the thin section. The matrix is fine-grained and comprises quartz and chlorite. Continuous schistosity defined by the alignment of minerals within the matrix and by the alignement/elongation of clasts. Chlorite and quartz are in strain fringes to clasts. Disseminated pyrite is observed in the matrix, it is associated with occasional coarse-grained euhedral pyrite. Trace chalcopyrite is observed, it seems to replace euhedral pyrite.		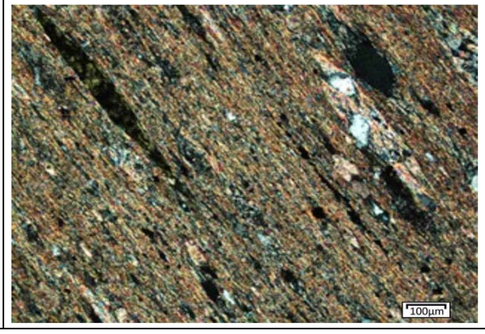	

Sample ID	Lithology	Feature	Description	Scanned TS	Transmitted light_Photomicrograph (XPL and PPL)	Reflected light_Photomicrograph
FT_16H	SDT	SFO	Thin section perpendicular to FT_16. Strong foliation defined by the alignment of sulphides and minerals within the matrix. The intensity of foliation and the composition of the rock is similar to that of FT_16.		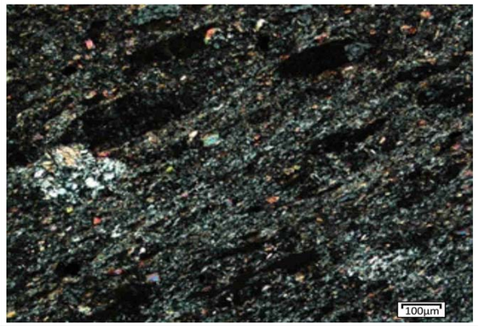	
FT_17	SDT	SFO/STS	Thin section including a diamictite with a large clast of mafic igneous rock. This large clast is composed of chlorite, muscovite, biotite, quartz and carbonate. Other clasts in the diamictite are composed of quartz, micas, chlorite, carbonate and their sizes vary from 100 µm – 0.5 cm. The matrix is fine-grained and composed of chlorite, quartz, muscovite and biotite. Continuous schistosity defined by the alignment of minerals in the matrix and the alignment and elongation of clasts. Chlorite and carbonate form strain shadows/fringes to euhedral pyrite. Pyrite occurs as fine- and coarse-grained disseminations.		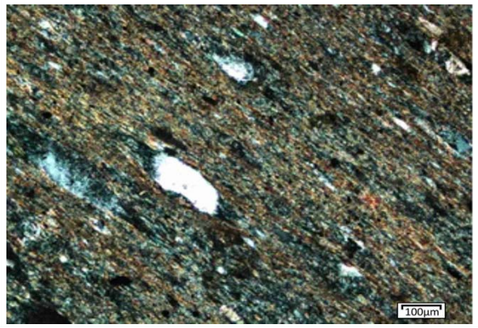	
FT_18	SDT	SFO/STS	Thin section composed of a diamictite showing a strong foliation. The thin section is constituted of about 75% of clasts and 25% of matrix. Clasts are composed of quartz, carbonates, biotite, plagioclase and chlorite, their size varies from 5 µm to 5 mm. The matrix is fine-grained and comprises quartz, chlorite and biotite. Continuous schistosity defined by the elongation/alignment of clasts and by the alignment of minerals in the matrix. Chlorite and quartz are in strain fringes to clasts. Pyrite occurs as fine-grained disseminations in the matrix.		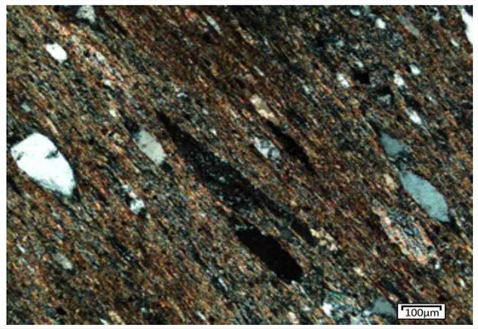	
FT_19	SDT	SFO/STS	Thin section including a diamictite showing a strong foliation. The rock comprises clasts which are composed of quartz, plagioclases, carbonates with minor biotite. The size of clasts varies between 5 µm to 3 mm. Possible boudinage defined by chlorite around the coarse-grained pyrite. The matrix is fine-grained and slightly aligned. Continuous foliation defined by the alignment of clasts and pyrite. Chlorite in strain fringes to pyrite. The mineralisation consists of 15% framboidal pyrite associated with about 2% euhedral pyrite.	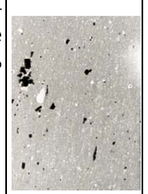	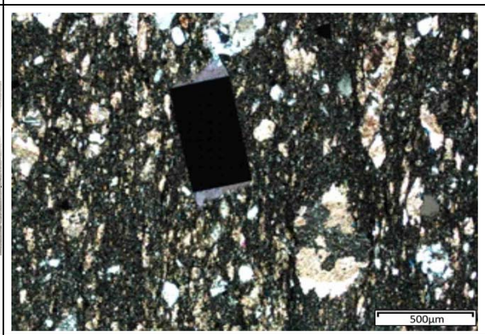	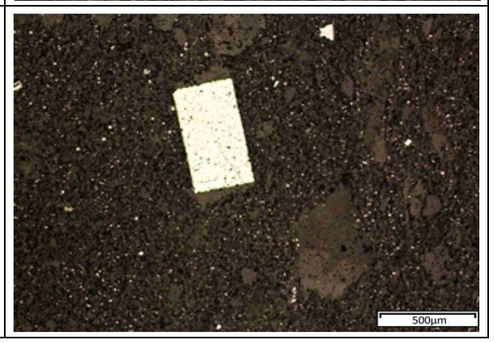

Sample ID	Lithology	Feature	Description	Scanned TS	Transmitted light_Photomicrograph (XPL and PPL)	Reflected light_Photomicrograph
FT_20A	SSL	FLD	Thin section displaying mesoscopic folds. The rock consists of fine- to medium-grained grains; it is composed of biotite, quartz, carbonates with minor muscovite. Quartz, carbonates, micas and minor K-feldspar constitute clasts. Mesoscopic folds do not display foliation, therefore interpreted as soft sedimentary deformation origin. S0 bedding is identified. 20 – 40% of framboidal pyrite disseminated in the layers. Occasional euhedral pyrite occurs in the matrix.	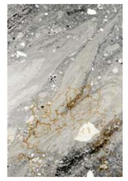	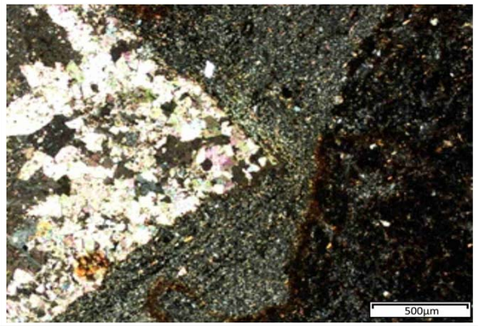	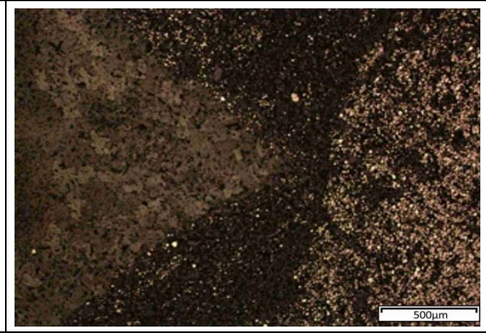
FT_20B	SSL	FLD	Thin section including mesoscopic folds. The rock is composed of mudstone and siltstone which consit mainly with biotite, quartz, carbonates with rare muscovite. Sedimentary rocks are slightly aligned. The mineralisation consists of 40 – 60% of framboidal pyrite. About 1.5% of euhedral pyrite in the occasional dropstone.		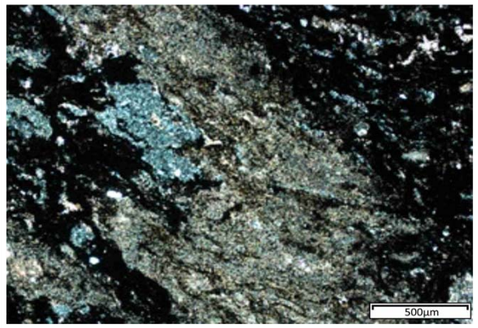	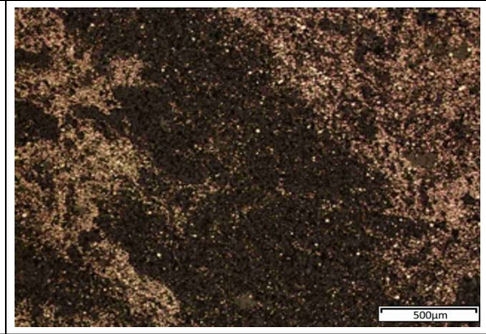
FT_21A	SSL	FLD	Thin section including a fold in a laminated mudstone/siltstone. The rock is composed of biotite, quartz and muscovite. S0 lamination spaced with less than 0.5 mm. 30 – 40% of the thin section comprises framboidal pyrite. Occasional clasts contain chalcopyrite and some bornite.		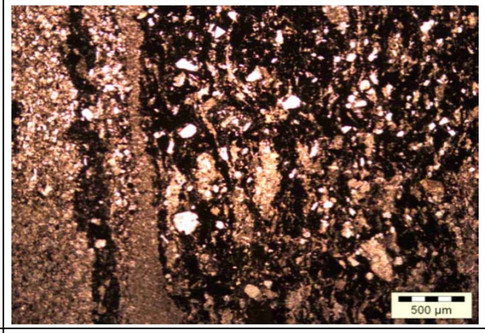	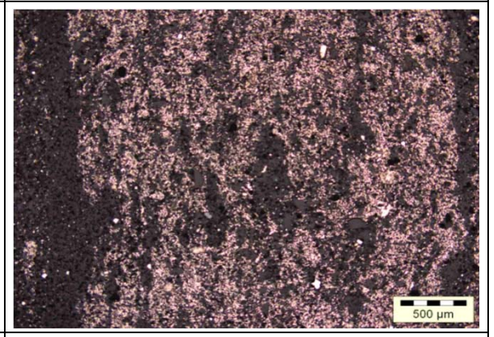
FT_21B	SSL	FLD	Thin section including a mesoscopic fold in siltstone. The rock is composed of fine-grained material and consists of quartz, micas, muscovite and carbonates. Small clasts (1.5mm) are observed, they are composed of quartz, micas and carbonates. The mesoscopic fold contains about 30 – 40% of framboidal pyrite. Occasional euhedral pyrite is observed (0.1 – 0.5%) .		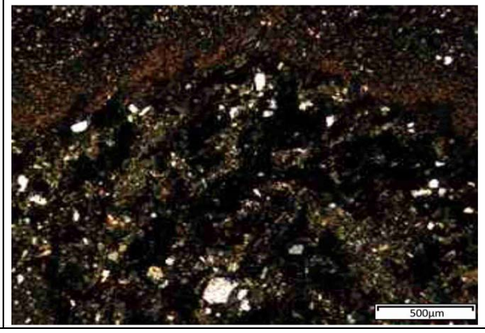	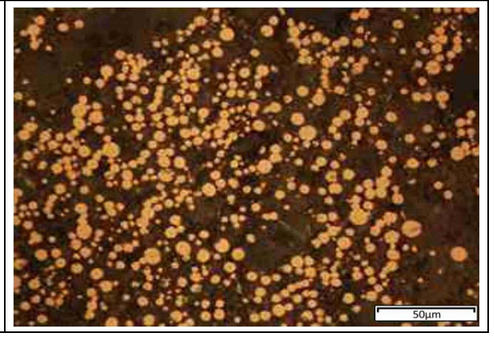

Sample ID	Lithology	Feature	Description	Scanned TS	Transmitted light_Photomicrograph (XPL and PPL)	Reflected light_Photomicrograph
FT_22	SSL/SST	BD	Thin section showing cross bedding in siltstone/sandstone. The rock is composed of carbonates, quartz and minor biotite. Bedding S0 is observed, it is associated with soft sediment deformation. Beds are spaced with less than 1 mm. About 4% pyrite occurs as framboidal, fine- and coarse-grained(euhedral) along bedding and in dissemination. Traces of chalcopyrite are observed in coarse-grained.		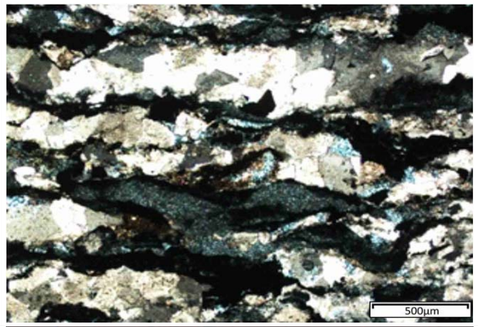	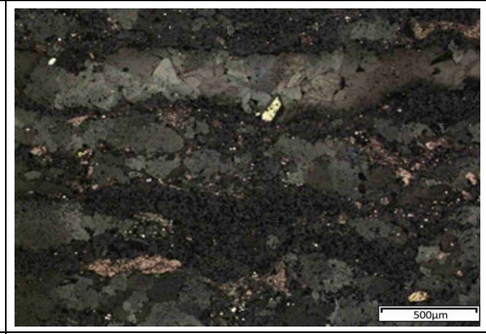
FT_23	SDT	STS	Thin section including a diamictite with two large clasts (1 cm). The matrix is fine-grained, it is composed of quartz, biotite and muscovite. Clasts are composed of quartz, K-feldspar, carbonate, micas, chlorite and minor muscovite. Chalcopyrite, chlorite, quartz, bornite and carbonates form strain shadows to clasts. 0.5 – 0.8% chalcopyrite associated with bornite (0.2%) in the replacement of clasts and in strain shadows/fringes. Some framboidal pyrites are observed in dissemination within the matrix.	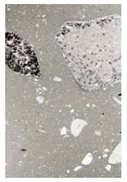	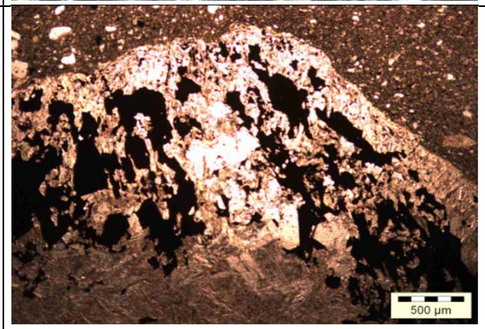	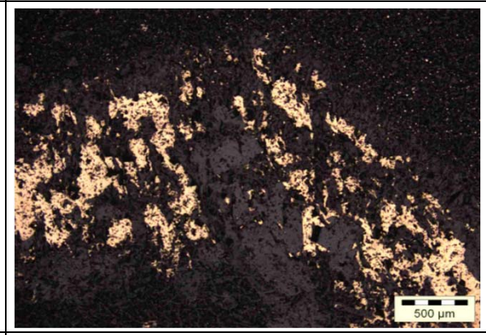
FT_24	SDT	STS/VWFO	Clast-rich diamictite in a fine-grained matrix. Quartz, biotite, chlorite with minor muscovite and carbonates constitute the minerals in the matrix. Clasts are composed of quartz, carbonates, chlorite, K-feldspar and plagioclase. Chlorite, carbonates and chalcopyrite in strain shadows to clasts. Very weak foliation defined by the alignment of chalcopyrite. 0.5 - 1.5% coarse-grained chalcopyrite associated with traces of bornite (0.5).		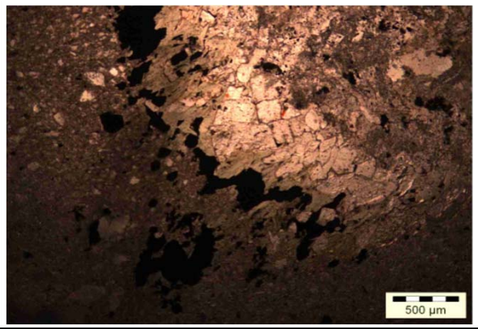	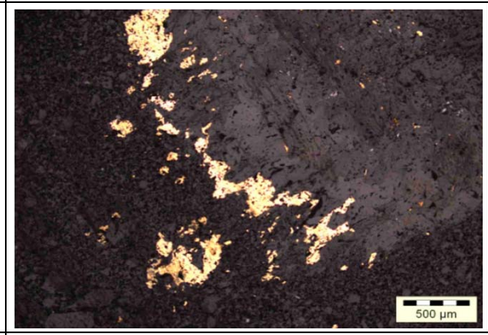
FT_25	SSL	SFO/STS	Thin section including a siltstone showing a strong foliation defined by the alignment of pyrite. The rock is composed mainly of quartz and micas. The mineralisation consists of coarse-grained euhedral pyrite (40%) associated with framboidal pyrite (30 – 40%). Some coarse-grained sphalerite are observed in association with pyrite. Minerals within the matrix are aligned and define a strong foliation. Quartz and micas form strain shadow to pyrite and sphalerite grains. Euhedral pyrite forms slaty or continuous foliation while framboidal pyrite are undeformed.		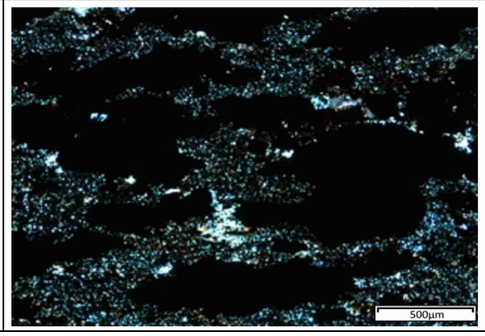	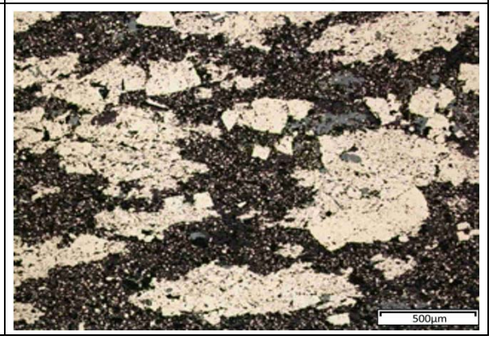

Sample ID	Lithology	Feature	Description	Scanned TS	Transmitted light_Photomicrograph (XPL and PPL)	Reflected light_Photomicrograph
FT_25H	SSL	SFO	Thin section perpendicular to FT_25. Strong foliation defined by the alignment of sulphides and minerals within the matrix. The intensity of foliation and the composition of the rock is similar to that of FT_25.		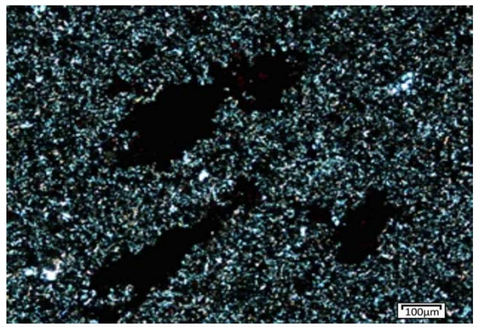	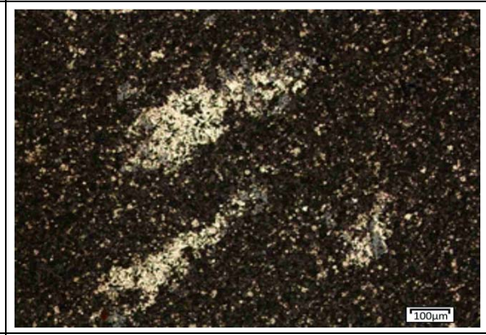
FT_26	SSL	SFO	Thin section including a strong foliation defined by the alignment of pyrite and minerals within the siltstone. The rock is composed mainly with quartz and biotite. Pyrite occurs in abundance as euhedral coarse-grained and as framboidal pyrite. Quartz and micas in strain shadows to euhedral pyrite. Coarse-grained pyrites define a slaty or continuous foliation while framboidal pyrites are completely undeformed .		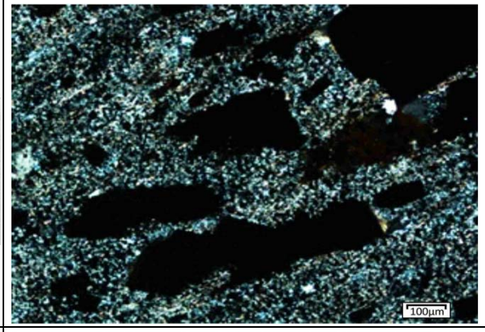	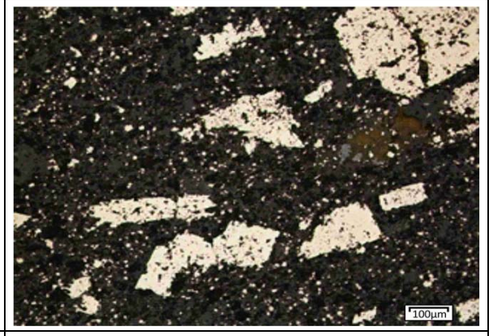
FT_26H	SSL	WFO	Thin section perpendicular to FT_26. Weak foliation defined by the alignment of minerals within the matrix. The composition of the rock is similar to that of FT_26, however the intensity of foliation decreases.		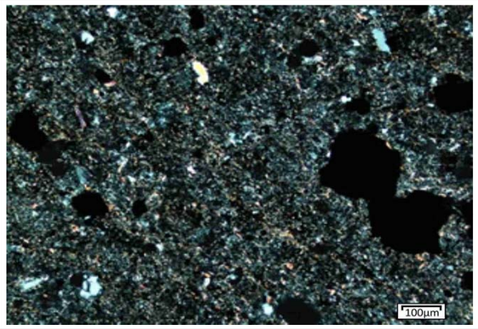	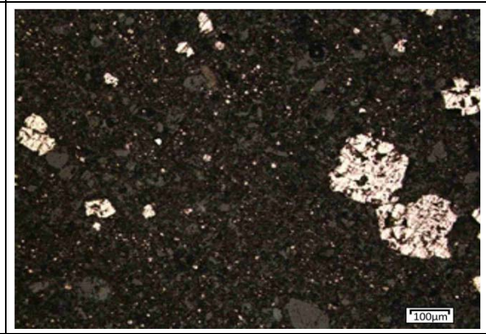
FT_27	SSL	WFO	Diamictite in a fine-grained matrix composed of quartz, biotite, carbonates and muscovite. Clasts range from 0.5 – 1 cm, they are composed of quartz, chlorite, carbonates, plagioclases and minor muscovite. Chlorite, quartz and carbonate are in strain shadows/fringes to pyrite. The mineralisation consists of framboidal (2.5%) and coarse-grained euhedral pyrite (1%). Within clasts, coarse-grained pyrite is associated with some chalcopyrite and occasional sphalerite.	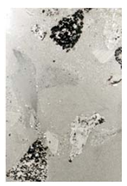	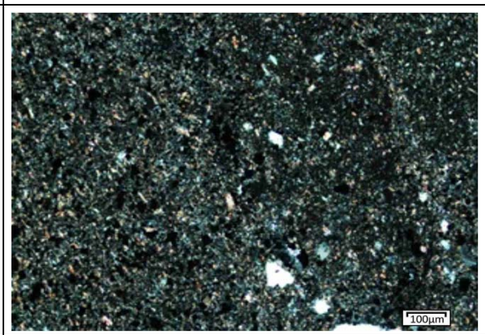	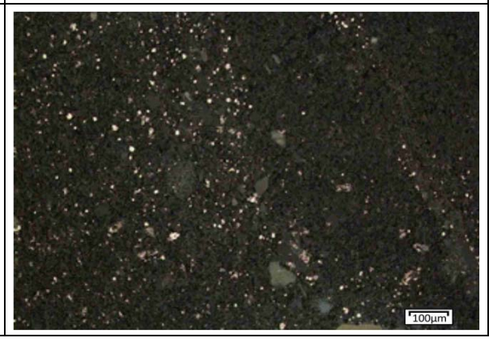

Sample ID	Lithology	Feature	Description	Scanned TS	Transmitted light_Photomicrograph (XPL and PPL)	Reflected light_Photomicrograph
FT_28	SSL	MFA	Thin section illustrating mesoscopic faults defined by the offset of siltstones beds. The rock is mainly composed of quartz and biotite. The mineralisation consists of abundant framboidal pyrite finely disseminated int the rock. Beds are spaced with less than 1 mm. Mesoscopic folds are observed. Occasional dropstones composed of quartz and micas are also observed. Framboidal pyrite fills the fault plane, suggesting a growth fault.	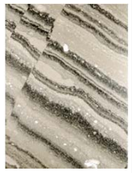	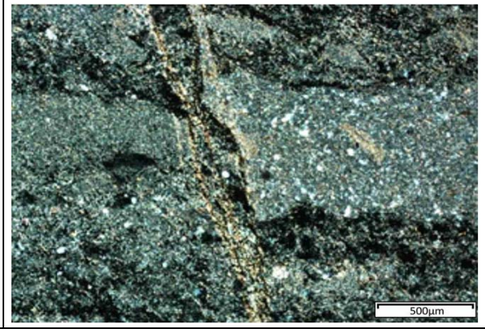	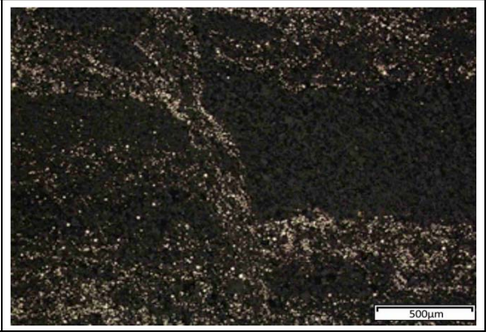

Sample ID	Lithology	Feature	Description	Scanned TS	Transmitted light photomicrographs (XPL and PPL)	Reflected light Photomicrographs
FT_29	SDT	STS/MFO	Thin section including a large clast with bornite in strain fringe. Clasts are composed of quartz, plagioclase, biotite with minor carbonates. The composition of the large clast is similar to that of other clasts on the thin section. The matrix is fine-grained and aligned, it is composed of biotite and quartz. Fibres in the strain fringe are straight, lack undulose extinction and grain boundary structure. They are composed of quartz, chlorite, muscovite and carbonates. Moderate foliation defined by the alignment of coarse-grained bornite is parallel to the orientation of the strain fringe. The contact between the strain fringe and the matrix is sharp. 4 – 6% of bornite in coarse-grained, strain fringe, fine-grained and in replacement of clasts. Traces of fine-grained chalcocite are observed. Disseminated iron oxides are present in the matrix.	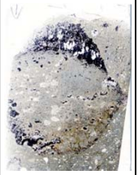	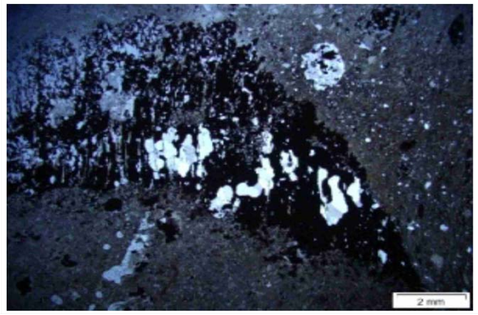	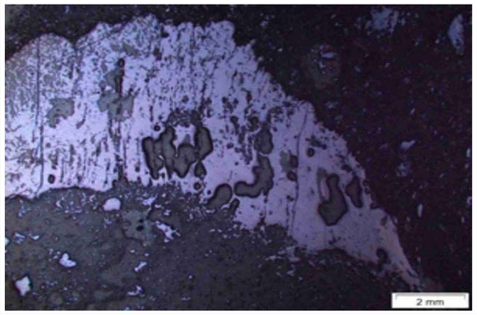
FT_30	SDT	STS/VWFO	Thin section showing a clast-moderate diamictite, it is constitutes of about 70% of matrix and 30% of clasts. The matrix is composed of biotite, chlorite, quartz with minor muscovite. Clasts are composed of quartz, chlorite, carbonates and muscovite. Carbonates, quartz, chlorite, chalcopyrite and chalcocite form strain fringes to clasts. A very weak foliation is defined by the alignment of chalcopyrite and chalcocite. 0.5 – 1.5% chalcopyrite is observed in the replacement of clasts associated with traces chalcocite. Iron oxides fill thin veins.		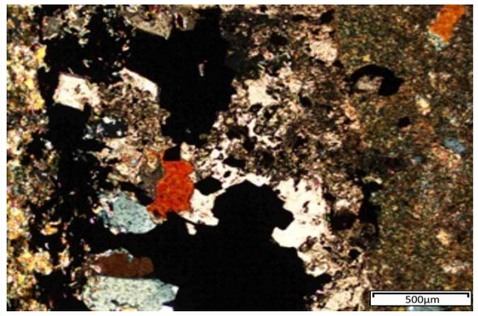	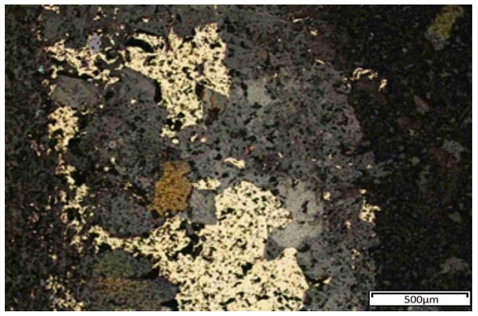
FT_31	SDT	STS/MFO	Thin section including a diamictite with a large clast and abundant chalcopyrite. The rock is intercalated with siltstone and mudstone composed of biotite and quartz. The large clast is composed of plagioclase, biotite, carbonates and chlorite. 3 – 5% chalcopyrite is observed in the replacement of clasts, 1 – 2% occurs as fine- to coarse-grained dissemination. The large clast seems to fold the beds suggesting that it may happen during the deposition. S0 bedding is spaced with less than 1mm. S1 foliation is defined by the alignment of chalcopyrite which is parallel to the strain fringe defined by carbonates, albite, plagioclase, quartz and chlorite. The minerals within the fringes are straight. S1 foliation is perpendicular to S0.		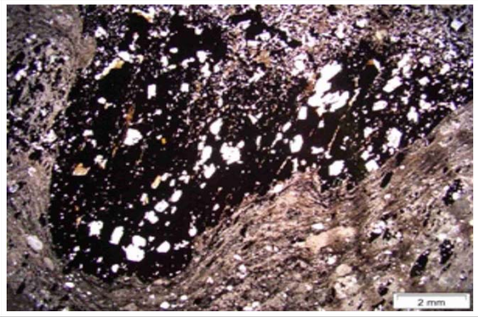	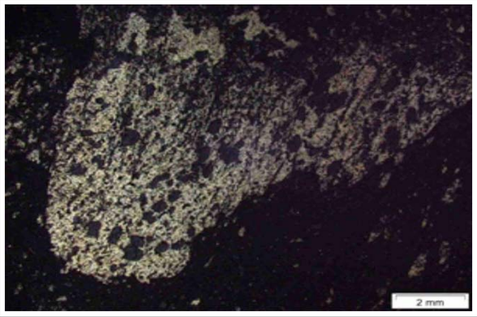
FT_32	SDT	STF/WFO	Thin section consists of a large quartzite clast (60%) with bornite/chalcopyrite strain fringe in a fine-grained matrix (20-30%). The fine-grained matrix is composed of micas and sub-angular quartz fragments. The large clast is composed of: 70% of quartz, 20% of micas and 10% of sericitised feldspar. On the thin section two categories of clasts are observed: the granite (80%) and the schist clasts (20%). Bornite occurs as fine- and coarse-grained material and define a weak foliation. Bornite, chalcopyrite, micas and possible carbonate form strain fringe to the large clast. Bornite is replacing chalcopyrite. Possible covellite replacing bornite. The strain fringe is parallel to the foliation. The fringe structure slightly bends.	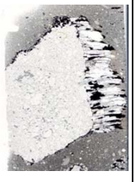	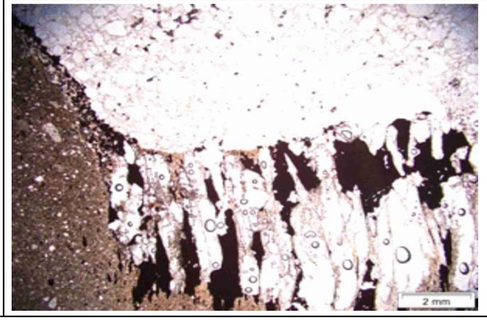	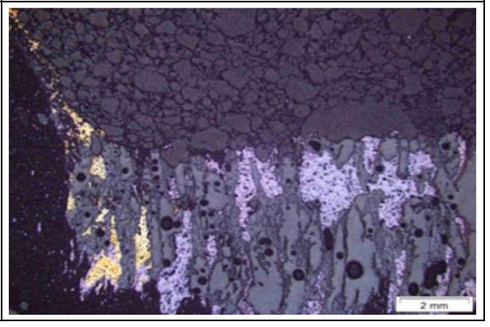

Sample ID	Lithology	Feature	Description	Scanned TS	Transmitted light photomicrographs (XPL and PPL)	Reflected light Photomicrographs
FT_32A	SDT	STS/MFO	Thin section including 75% of matrix and 20% of clasts (occasional large clasts size up to 1 cm). The matrix is composed of quartz, biotite and minor muscovite. Clasts are made of quartz, micas, carbonates and chlorite. Moderate foliation is defined by the alignment of fine- and coasre-grained bornite/chalcopyrite and by the alignment of minerals in the matrix. Bornite, chalcopyrite, chlorite and muscovite form strain fringes to clasts. The orientation of strain fringes is parallel to that of the S1 foliation. Within clasts, chalcopyrite seems to be replaced by bornite. The mineralisation consists of 5 – 7% of fine-grained bornite; 0.5 – 1.5% of coarse- and fine-grained chalcopyrite. Occasionsl thin veins comprise chalcopyrite and bornite.		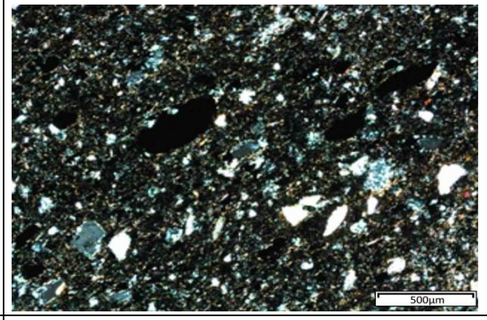	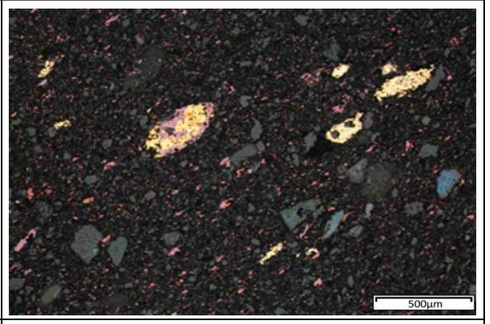
FT_33	SDT	STS/WFO	Diamictite showing a secondary foliation defined by the alignment of fine- and coarse-grained chalcopyrite. Thin section composed of 75% matrix and 20% of clasts. The matrix is fine-grained and consists of quartz, biotite, micas and minor chlorite. Clasts ranges from 0.5 mm to 2 cm, they are composed of carbonates, quartz, and chlorite. The composition of minerals within the fringes is similar to that in the matrix. Chalcopyrite represents 1.5 – 2% of the thin section, it is associated with trace of chalcocite in the replacement of clasts.		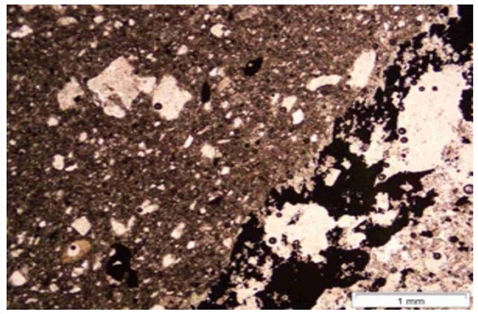	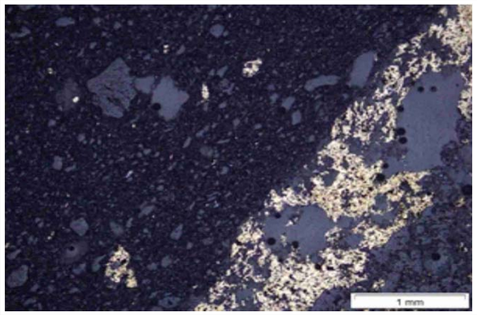
FT_34	SDT	STS/MFO	Thin section including a diamictite showing a moderate foliation defined by the alignment of chalcopyrite. The sample is composed of 75% of matrix, 12% clasts and about 13% of copper sulphides. The matrix is composed of quartz, muscovite, biotite and chlorite. Clasts are composed of quartz, chlorite and minor carbonates. Chalcopyrite with minor bornite/chalcocite, Chlorite, muscovite and quartz form strain shadows/fringes to the clasts. Trace pyrites seem to be replaced by chalcopyrite. Continuous foliation defined by the alignment of chalcopyrite, bornite and chalcocite. Clasts define a weak foliation. The most abundant copper sulphide is chalcopyrite that occurs as fine-(7 - 10%) and coarse-grained (5 – 7%). Traces bornite/chalcocite is associated with chalcopyrite in dissemination and in the replacement of clasts.			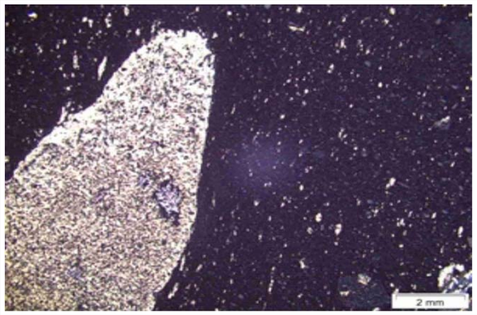
FT_34H	SDT	WFO	This thin section was cut perpendicular to FT_34. It contains a weak foliation. The composition of the rock is similar to that of the FT_034, howerver the intensity of foliation decreases.		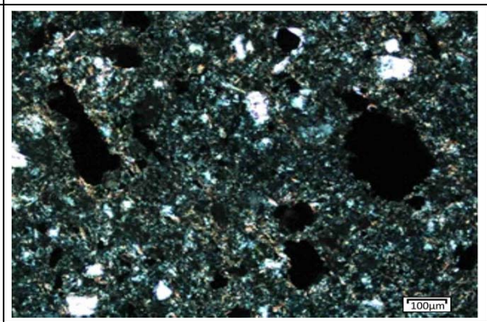	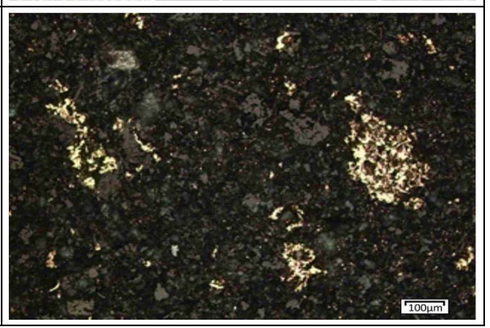

Sample ID	Lithology	Feature	Description	Scanned TS	Transmitted light photomicrographs (XPL and PPL)	Reflected light Photomicrographs
FT_35	SDT	STS/WFO	Thin section including a large strain shadow. The sample is composed of about 60% of clasts, 35 % of matrix and 5% of copper sulphides. The matrix is fine-grained and composed of quartz, biotite and rare muscovite. Clasts range from 0.5 – 1 mm with a large clast that sized 30 mm. Clasts are composed mainly of quartz with minor muscovite, carbonates, chlorite and plagioclases. Chalcopyrite, chlorite, muscovite and carbonates form strain shadow to the large clast. Continuous foliation defined by the alignment of fine- and coarse-grained chalcopyrite, and by the weak alignment of minerals in the matrix. Chalcopyrite occurs as coarse-grained in the replacement of clasts and as fine-grained in dissemination. Some chalcocite and bornite are observed, they appear to replace chalcopyrite.			
FT_36	SDT	STS/MFO	Thin section consists of a fine-grained matrix (50-60%), a large clast of quartz-areneite (25%) and coarse-grained aligned chalcopyrite (15-20%). The matrix is composed of micas and sub-angular quartz fragments. Within the matrix two types of clasts are observed: granitic (80%) and schistose clasts (20%). The large clast is composed of: 60% of quartz, 20% of micas and 20% of sericitised feldspar. Chalcopyrite occurs as elongate grains up to 5mm in length and also as a rim to clasts or fragments, and in addition as fine-grained material within the matrix. A secondary foliation is defined by a combination of elongate and aligned chalcopyrite grains, quartz clasts, composite clasts and micas within the matrix. Trace bornite is associated with chalcopyrite in the strain shadow. Weak crenulation is defined by chalcopyrite.		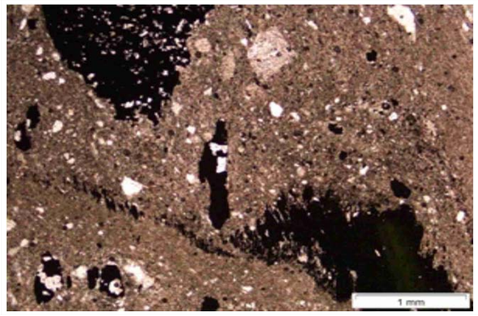	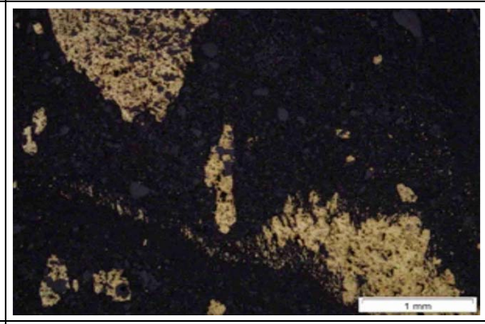
FT_36H	SDT	VWFO	This thin section is perpendicular to FT_36. It shows a very weak foliation defined by the alignment of minerals within the matrix and by the alignment of chalcopyrite.		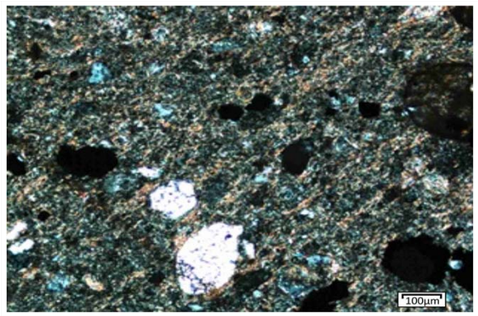	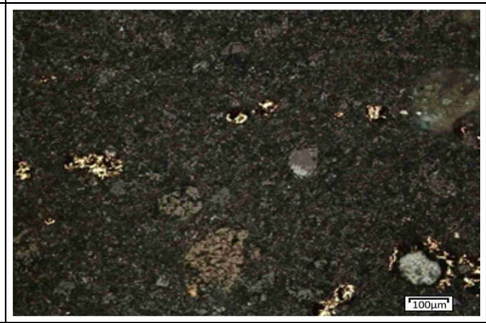
FT_37	SDT	WFO	Thin section including a diamictite with about 15% of clasts and 85% of matrix. The matrix is fine-grained and composed of quartz, muscovite, biotite and chlorite. Clasts are small (<1cm) and their composition is similar to that of the matrix, however plagioclases, carbonates and microclines occur. Incipient foliation defined by muscovite. Chlorite, carbonates and muscovite form strain fringes to clasts. The mineralisation is fine- and coarse-grained, it consists of bornite(1.5%)> chalcocite(0.5%)> chalcopyrite (0.3%). Weak foliation defined by the alignment of chalcopyrite, chalcocite, bornite and minerals in the matrix (mostly micas). Some clasts define also a weak foliation. A soft sediment deformation texture is observed.	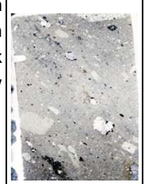	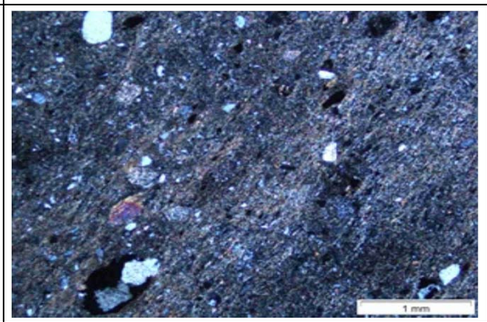	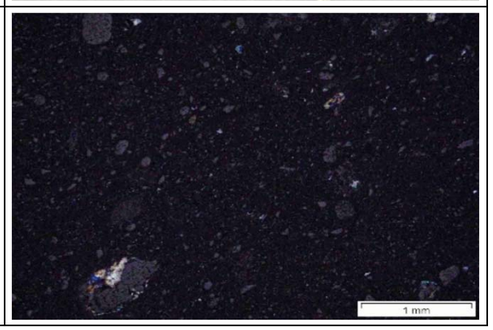

Sample ID	Lithology	Feature	Description	Scanned TS	Transmitted light photomicrographs (XPL and PPL)	Reflected light Photomicrographs
FT_38A	SDT	STS/WFO	Diamictite including a large mafic igneous rock (80%). This large clast is composed of chlorite, carbonate, quartz and biotite. The matrix in the diamictite is fine-grained, it includes quartz, biotite and muscovite. Clasts in the diamictite are small (< 1cm), they are composed of quartz, chlorite, carbonates, plagioclases and muscovite. Rare incipient foliation is defined by muscovite. Coarse-grained chalcopyrite is associated with trace bornite define S1 spaced foliation. Chalcopyrite, chlorite and carbonates are in strain shadows of the large mafic clast. Strain shadow is parallel to alignment of clasts. Chalcopyrite occurs as fine- and coarse-grained dissemination in the matrix (1%) and in the replacement of the large clast. Chalcopyrite in the strain shadow represents about 2.5%. Traces bornite is finelly disseminated in the matrix.	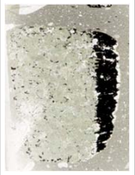	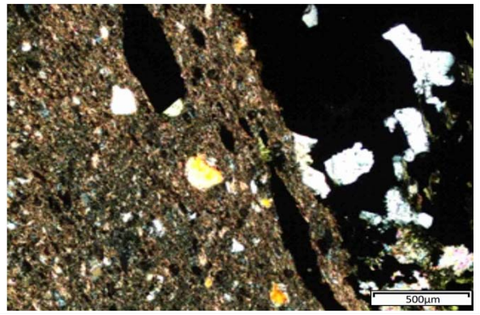	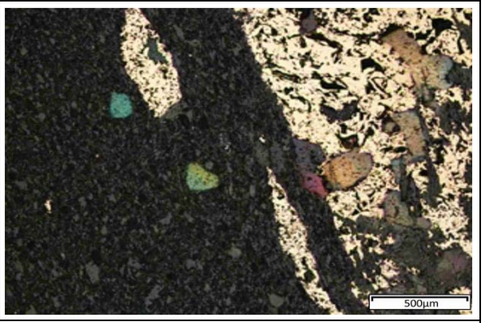
FT_38B	SDT	STS/WFO	Diamictite including a large mafic igneous rock (80%). This large clast is composed of chlorite, carbonate, quartz and biotite. The matrix in the diamictite is fine-grained, it includes quartz, biotite and muscovite. Clasts in the diamictite are small (< 1cm), they are composed of quartz, chlorite, carbonates, plagioclases and muscovite. Rare incipient foliation is defined by muscovite. Coarse-grained chalcopyrite is associated with trace bornite define S1 spaced foliation. Chalcopyrite, chlorite and carbonates are in strain shadows of the large mafic clast. Strain shadow is parallel to alignment of clasts. Chalcopyrite occurs as fine- and coarse-grained dissemination in the matrix (1%) and in the replacement of the large clast. Chalcopyrite in the strain shadow represents about 2.5%. Traces bornite is finelly disseminated in the matrix.		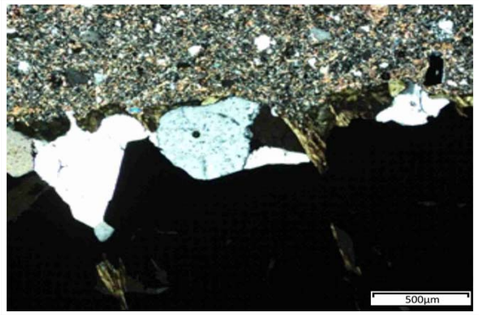	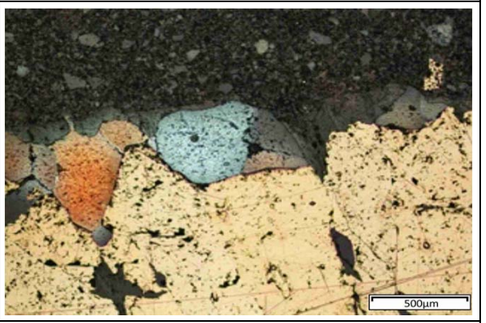
FT_38C	SDT	STS/MFO	Diamictite including a large mafic igneous rock (80%). This large clast is composed of chlorite, carbonate, quartz and biotite. The matrix in the diamictite is fine-grained, it includes quartz, biotite and muscovite. Clasts in the diamictite are small (< 1cm), they are composed of quartz, chlorite, carbonates, plagioclases and muscovite. Rare incipient foliation is defined by muscovite. Coarse-grained chalcopyrite is associated with trace bornite define S1 spaced foliation. Chalcopyrite, chlorite and carbonates are in strain shadows of the large mafic clast. Strain shadow is parallel to alignment of clasts. Chalcopyrite occurs as fine- and coarse-grained dissemination in the matrix (1%) and in the replacement of the large clast. Chalcopyrite in the strain shadow represents about 2.5%. Traces bornite is finelly disseminated in the matrix.		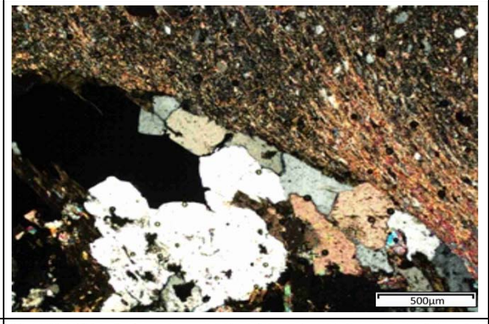	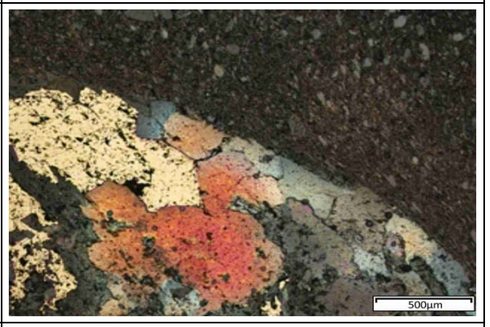
FT_39	SDT	STS/MFO	Diamictite including two large clasts with strain shadows. The matrix is fine-grained and composed of quartz, biotite and muscovite. The large clasts constitute 50% of the thin section, their size range from 1 to 2 cm. Clasts are composed mainly with quartz, micas and chlorite. Minerals(micas) within the matrix, chalcopyrite, bornite and chalcocite define a continuous foliation. Chlorite, quartz and chalcopyrite form strain shadows to quartz clasts. Structural features are parallel (strain shadows, S1 by alignment of clasts, alignment of minerals in the matrix and alignment of sulphides). The mineralisation is mainly composed of fine- (4 – 6%) and coarse-grained chalcopyrite (2 – 3%) associated with about 2.5% of fine-(1 - 1.5%) and coarse-grained(1%) bornite.		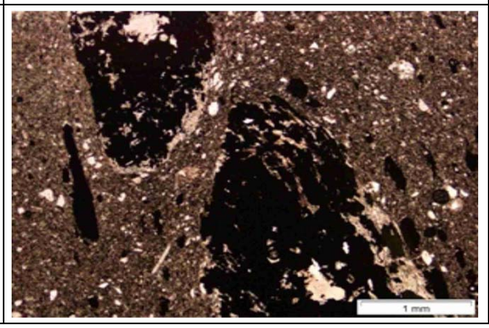	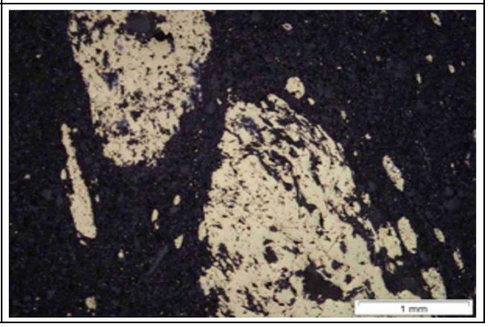

Sample ID	Lithology	Feature	Description	Scanned TS	Transmitted light photomicrographs (XPL and PPL)	Reflected light Photomicrographs
FT_40	SSL	FLD	Thin section including a fold in siltstone. The rock is fine-grained and composed of biotite and quartz with minor muscovite. Large fragments of quartz and minor biotite are observed, they range from 0.3 mm to 50 mm. There is not S1 foliation observed in the fold, therefore this fold is interpreted as a syn-sedimentary structure. About 10 – 15% of framboidal pyrite is disseminated in the fold. 1- 3% of euhedral coarse-grained pyrites are also observed.		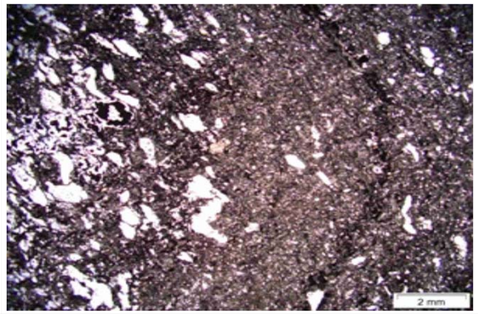	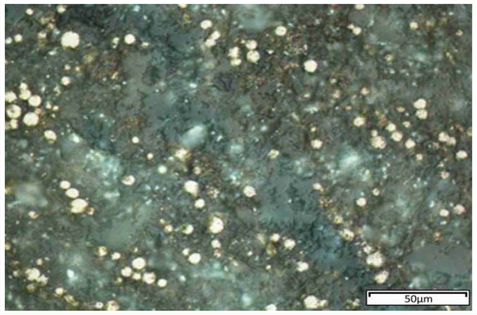
FT_41	SSL	FLD	Thin section including a fold with abundant pyrite in siltstone. This thin section consists of intercalation of siltstones and mudstones. The rock is composed of quartz and biotite with minor muscovite. Dark layers have not been identified. There is not foliation observed in the fold, therefore the fold is interpreted as a syn-sedimentary fold. 25 – 40% framboidal pyrite is observed in the fold.		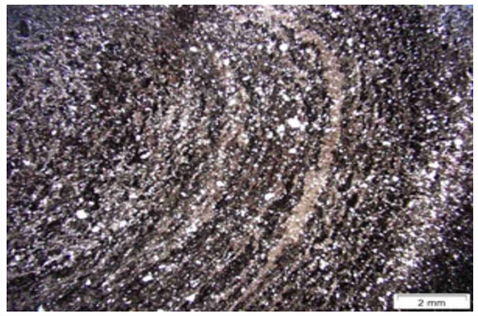	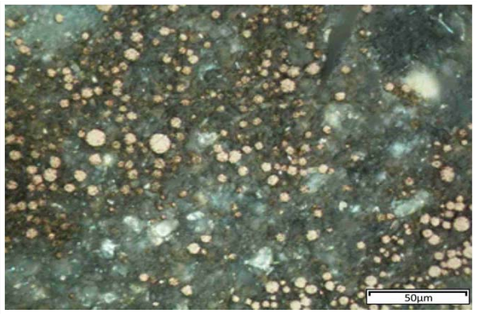
FT_42	SDT	STS/WFO	Thin section including strain shadows and weak foliation in the diamictite. The rock is composed of a fine-grained matrix which comprises quartz, biotite, muscovite and minor chlorite. Clasts are composed of quartz, carbonates and chlorite. Presence of incipient foliation defined by minerals in the matrix. Clasts are not aligned. There is a possible crenulation defined by muscovite. Fine-and coarse grained sulphides are aligned. Chalcopyrite in strain shadows to large clasts. The mineralisation consists of 3 – 5% chalcopyrite that occurs in the replacement of clasts and in strain shadows associated with trace bornite (0.2%). Presence of thin iron oxides veins.		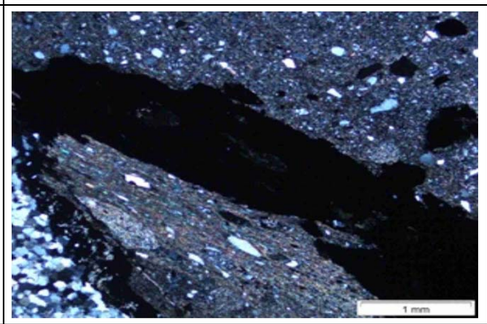	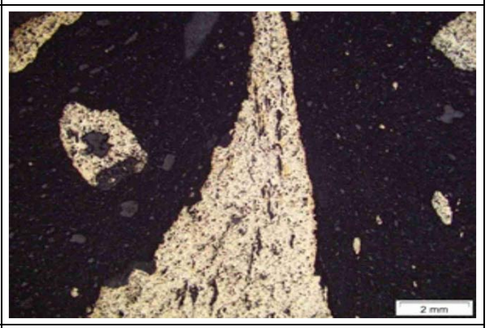
FT_43	SST/SSL	FLD	Thin section including a syn-sedimentary fold. The rock contains intercalations of siltstone and sandstone layers. Fine, medium to coarse-grained quartz, muscovite, chlorite and biotite constitute the mineralogy of the rock. A soft-sediment deformation texture is observed. The mineralisation is composed of 8 – 12% of framboidal pyrite finely disseminated in the rock. 1 – 2% euhedral pyrite is also observed in the rock.		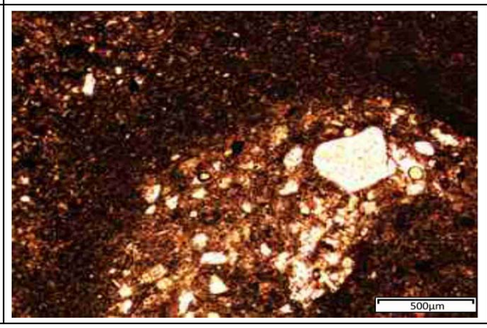	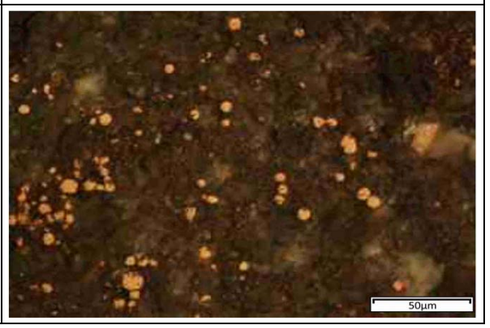

Sample ID	Lithology	Feature	Description	Scanned TS	Transmitted light photomicrographs (XPL and PPL)	Reflected light Photomicrographs
FT_44	SDT	STS/WFO	Thin section including a large clast with fringes. The matrix is fine-grained and composed of quartz, muscovite, chlorite and biotite. The composition of clasts includes carbonates, chlorite, quartz, muscovite and rare plagioclase. Fringes are composed of carbonates, quartz, chlorite, chalcopyrite associated with bornite. S1 foliation is defined by the alignment and elongation of fine- and coarse-grained chalcopyrite and by the alignment of minerals in the matrix (incipient domains). Structural features are parallels (S1 and strain shadows). The mineralisation consists of: 1 – 3.5% chalcopyrite in strain fringes associated with rare bornite (0.5%); 1 – 2.5% coarse-grained chalcopyrite associated with trace bornite and 1 – 3% fine-grained chalcopyrite disseminated in the matrix. Presence of thin veins filled with iron oxides.	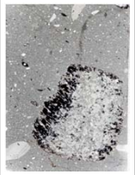	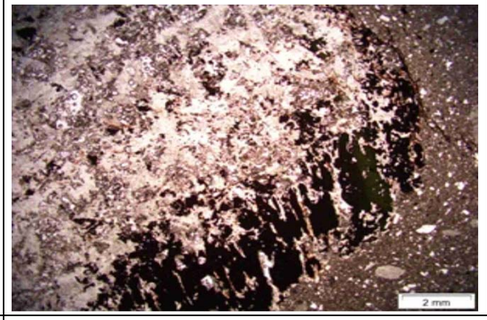	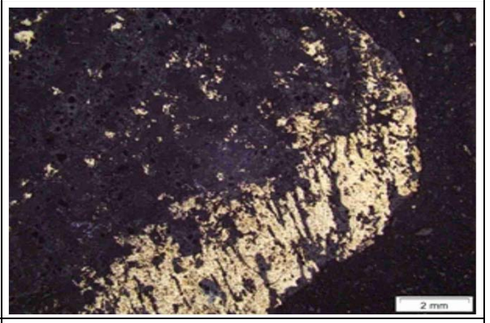
FT_45	SSL	FLD/STS	Thin section illustrating a fold with euhedral pyrite. The rock consists of siltstone and mudstone that is composed of quartz, biotite, chlorite, muscovite and iron oxides. There is not foliation observed in the thin section, therefore the fold is interpreted as a syn-sedimentary structure formed during the deposition. Chlorite, quartz and carbonates form strain shadows to pyrite. Presence of beddings spaced with less than 1 mm. Coarse-euhedral pyrites are aligned and define an S1 foliation. The mineralisation consists of 20 – 30% of coarse-grained euhedral pyrite, 25 – 35% of framboidal pyrite. Abundant iron oxides are observed in the rock.		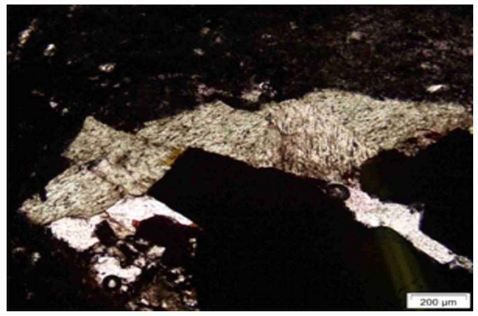	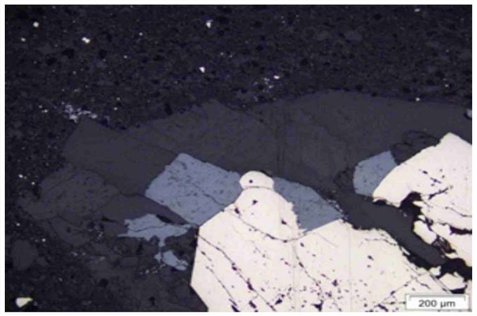
FT_46	SSL	FLD/STS	Thin section including intercalations of mudstone and siltstone. The mineralogy consists of quartz, biotite, chlorite and muscovite. Occasional clasts are composed of quartz and plagioclases (0.1 – 0.3 mm). The lack of foliation suggests that the fold is from a sedimentary origin. Euhedral pyrites overgrow the fold. Strain shadows are observed around euhedral pyrites, they are composed predominantly of chlorite, quartz and muscovite. 8-12% coarse-grained euhedral pyrite; 10 – 13% framboidal pyrite disseminated in the rock.		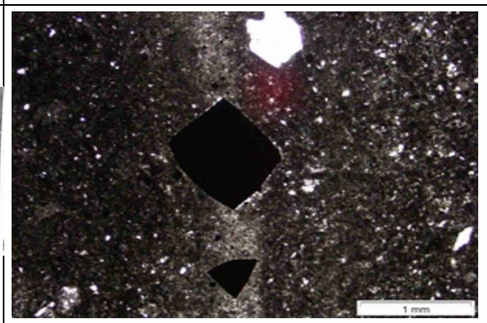	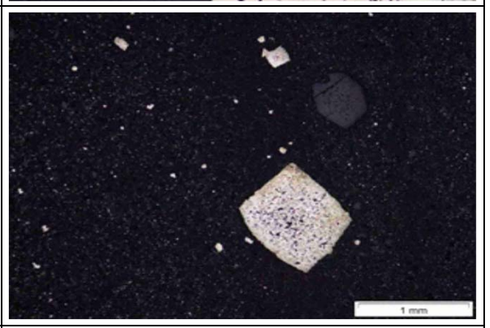
FT_47	SSL	FLD/STS	Thin section including a syn-sedimentary fold in siltstone. The rock is composed of quartz, biotite, muscovite and chlorite. A soft sediment deformation texture is observed. Chlorite, quartz and iron oxides form strain fringes/shadows to euhedral coarse-grained pyrite. Weak foliation defined by the alignment pyrite in one of the corner of the thin section. The mineralisation consists of 15 – 25% of coarse-grained pyrite with about 20 – 30% of framboidal pyrite disseminated in the rock. Possible coarse-grained sphalerite associated with euhedral pyrite. Iron oxides are disseminated in the thin layer of fold.		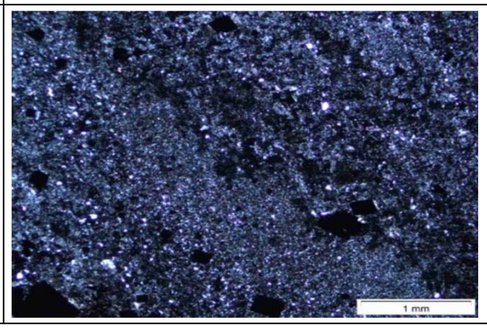	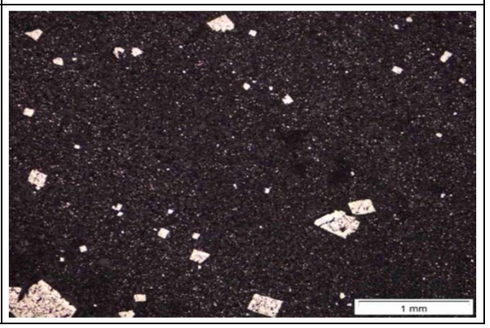

Sample ID	Lithology	Feature	Description	Scanned TS	Transmitted light photomicrographs (XPL and PPL)	Reflected light Photomicrographs
FT_48	SSL	FLD	This thin section includes a tight fold shown by folding of the S0 sedimentary layering. This layering is shown by grain size variation and alternating dark- and light-colored layers in PPL. These also correspond to a variation in grain size with the darker layers being more fine-grained and possibly containing more sheet silicates. The grain size is overall sub-5 µm with frequent slightly larger (up to 10µm) angular quartz fragments within the lighter layers. Within the darker layers disseminated rounded framboidal pyrite grains are common. There are also uncommon euhedral isolated pyrite grains with square cross-sections. There is a weak axial planar foliation to the fold shown by disruption of the light pyrite-free layers. 20 – 30% of framboidal pyrite is disseminated in the mudstone and siltstone layers.		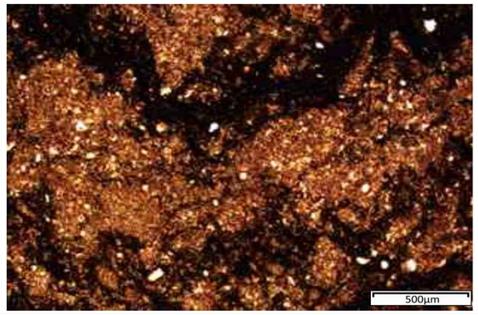	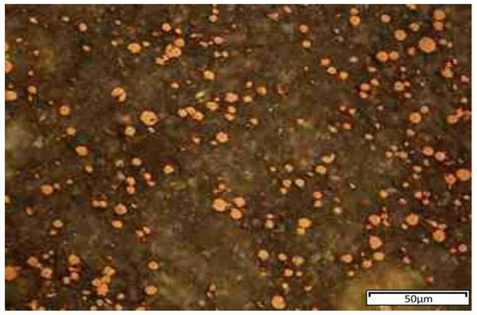
FT_49	SSL	FLD	This thin section includes a tight fold shown by folding of the S0 sedimentary layering. This layering is shown by grain size variation and alternating dark- and light-coloured layers in PPL. These also correspond to a variation in grain size with the darker layers being more fine-grained and possibly containing more sheet silicates. The grain size is overall sub-5 µm with frequent slightly larger (up to 10µm) angular quartz fragments within the lighter layers. Within the darker layers disseminated rounded framboidal pyrite grains are common. There are also uncommon euhedral isolated pyrite grains with square cross-sections. There is a weak axial planar foliation to the fold shown by disruption of the light pyrite-free layers. 25– 35% of framboidal pyrite disseminated in the mudstone and siltstone layers.		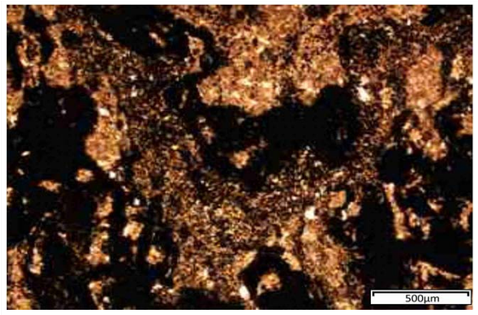	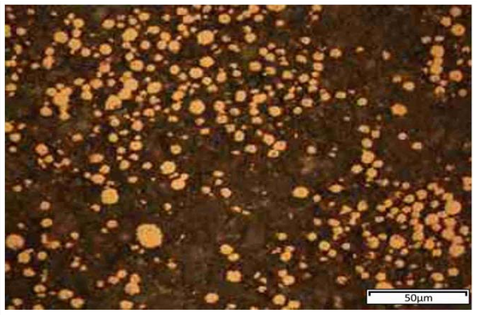
FT_50	SDT	STS/WFO	Thin section including a diamictite with an impressive strain shadow. The matrix is fine-grained, it is composed of quartz, carbonate, muscovite, biotite and chlorite. Clasts are composed of quartz, carbonates, chlorite, plagioclase, biotite and rare microclines. S1 foliation is defined by the alignment of coarse-grained chalcopyrite/bornite, alignment of minerals in the matrix, alignment of some clasts. S1 foliation is parallel to strain shadows. . Chlorite, muscovite and carbonate are located at the edge of the strain shadow that is composed mostly of chalcopyrite. The mineralisation consists mainly of fine- (1 - 2%) and coarse-grained (1 – 1.5%) chalcopyrite dissemination. Also 1 – 2.5% chalcopyrite is present in the replacement of clasts and in strain shadow/fringes. Some bornites (<1%) are observed as fine- and coarse-grained dissemination.		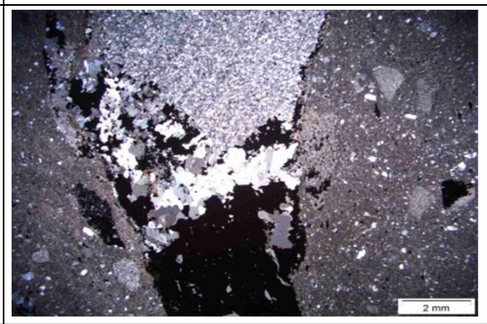	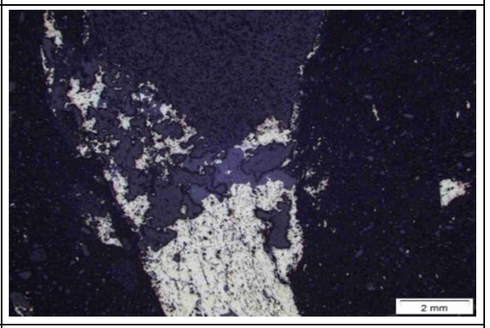
FT_50H	SDT	VWFO	Thin section including a very weak foliation defined by the alignment of chalcopyrite. This sample is perpendicular to FT_50H, it shows that the intensity of the foliation is not similar in the two the directions (X,Y).		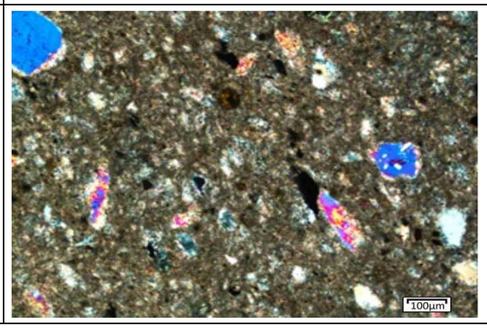	

Sample ID	Lithology	Feature	Description	Scanned TS	Transmitted light photomicrographs (XPL and PPL)	Reflected light Photomicrographs
FT_51(1)	SDT	STS	Thin section composed of a large quartz clast containing a fringe. The matrix is fine-grained and composed of quartz, carbonate, muscovite, chlorite and biotite. The large clast is composed mainly of quartz with minor carbonates, chlorite, biotite, muscovite and quartz. In the diamictite, the composition of other clasts is similar to that of the large clast. Fine- and coarse-grained chalcopyrite/bornite are aligned and define a weak foliation. Presence of a large fringe to the large quartz clast. This fringe is composed of chalcopyrite, chlorite, carbonates, quartz and some muscovite. S1 is parallel to the strain fringe. The fringe contains 2 – 3.5% chalcopyrite associated with trace bornite. 0.5 – 0.8% of coarse-grained chalcopyrite occurs in the replacement of clasts. Fine-grained chalcopyrite (0.5 - 0.7%) and fine-grained bornite(0.6 - 1%) occur in dissemination in the matrix.		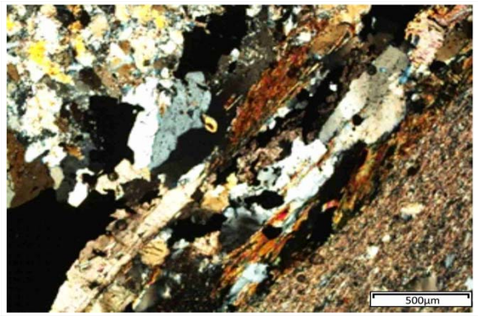	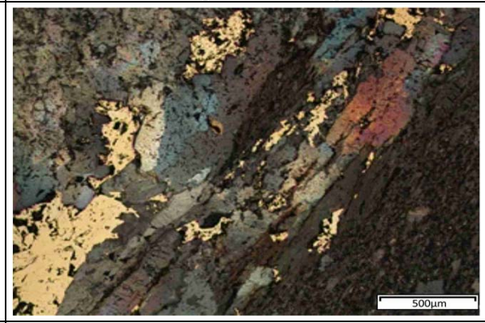
FT_51(2)	SDT	STS	Thin section composed of a large quartz clast containing a fringe. The matrix is fine-grained and composed of quartz, carbonate, muscovite, chlorite and biotite. The large clast is composed mainly of quartz with minor carbonates, chlorite, biotite, muscovite and quartz. In the diamictite, the composition of other clasts is similar to that of the large clast. Minerals within the matrix (micas) associated with fine- and coarse-grained chalcopyrite/bornite define a weak foliation. Presence of a large fringe that developed adjacent to the large quartz clast. This fringe is composed of chalcopyrite, chlorite, carbonate, quartz and rare micas. S1 is parallel to the strain fringe. The fringe contains 1 – 2% chalcopyrite associated with trace bornite. 0.5 – 1% of coarse-grained chalcopyrite occurs in the replacement of clasts. Fine-grained chalcopyrite (0.5 - 0.7%) and fine-grained bornite (0.7 – 1.2%) occur in dissemination in the matrix.	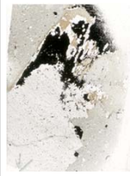	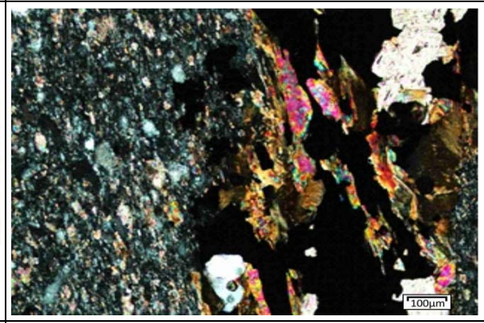	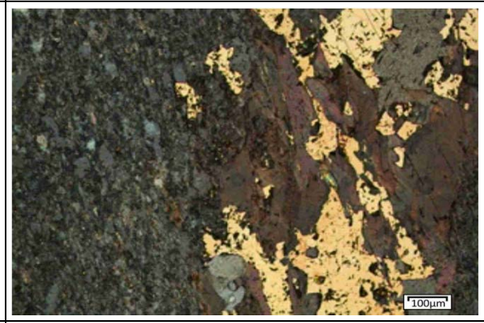
FT_52	SDT	STS/WFO	Thin section including a diamictite with chalcopyrite in strain shadows. The matrix within the diamictite consists of fine-grained material composed of quartz, muscovite, carbonate and biotite. Clasts are composed mainly of quartz, chlorite, muscovite, carbonates, plagioclases and K-feldspar. An incipient foliation is defined by the alignment of muscovite. A weak foliation is defined by the alignment of coarse-grained sulphides. Pyrite, bornite, quartz, carbonates and chlorite form strain shadows to the clasts. 0.3 – 0.8% of replacement chalcopyrite is associated with trace bornite (0.3%). Fine-grained chalcopyrite (0.3%) and fine-grained bornite (0.2%) occur in dissemination within the matrix. Coarse-grained euhedral pyrite is present in the clasts (0.6%) and in the matrix (0.2). Fine-grained and framboidal pyrite is disseminated in the matrix (up to 2%). Presence of thin veins filled with iron oxides.	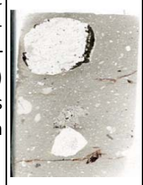	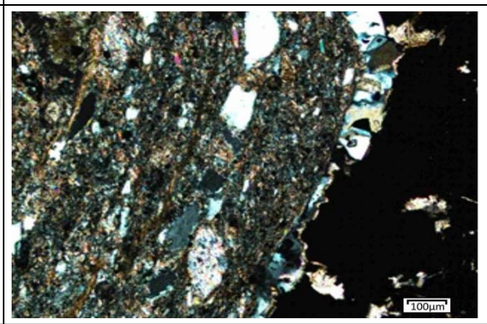	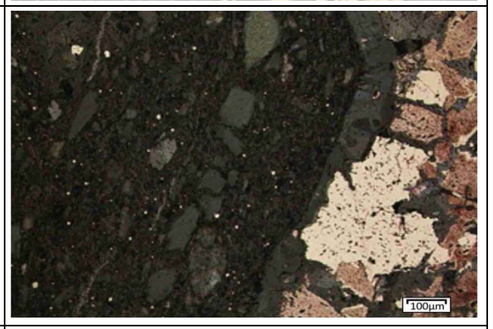
FT_53	SDT	STS/WFO	Thin section including a diamictite with a large quartz clast. The matrix is fine-grained and composed of quartz, iron oxides, muscovite and biotite. Clasts are composed of quartz, biotite, muscovite and carbonates. Thin iron oxides veins. S1 is defined by the alignment of coarse-grained chalcocite, it is parallel to the large quartz clast. Chalcocite forms strain shadow to the large clast. The mineralisation consists of 0.5 – 0.7% fine- and coarse-grained chalcocite in dissemination and in the replacement of clasts. Also fine-grained bornite is observed in dissemination, it represents about 5%.		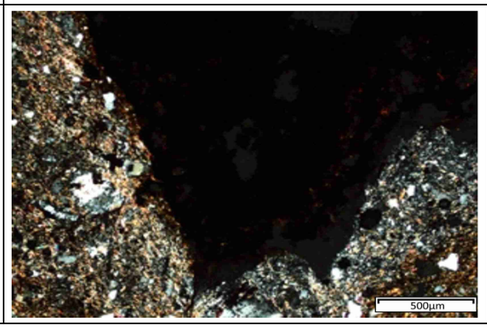	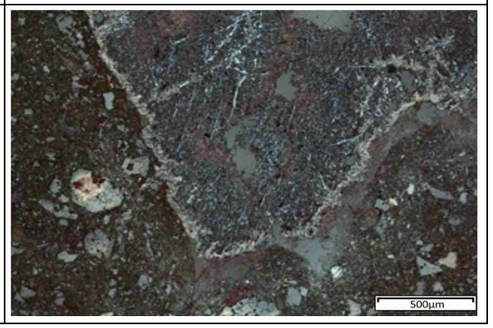

Sample ID	Lithology	Feature	Description	Scanned TS	Transmitted light photomicrographs (XPL and PPL)	Reflected light Photomicrographs
FT_54	SSL	STS/WFO	Thin section showing a large dropstone in siltstone/mudstone. The rock is composed of fine-grained material which comprises quartz, biotite, muscovite and dark layers. Quartz fragments occur in the mudstone layers(upto 1 mm). Laminations arespaced withless than0.5 mm. The large dropstone clast is mainly composed of quartz, it sized upto20 mm.This clastbends thesiltstone/mudstone layerssuggesting a formation during deposition. Pyrite is replacing the large clast. Euhedral pyrite overgrowth the primary foliation(S0). Quartzinstrainfringe to euhedral pyrite. The mineralisation consistsof pyritethat occursas coarse-grained euhedral dissemination (20– 25%) and as replacement of clasts (1%). About 0.5% of possible sphalerite is associated with euhedral pyrite. .		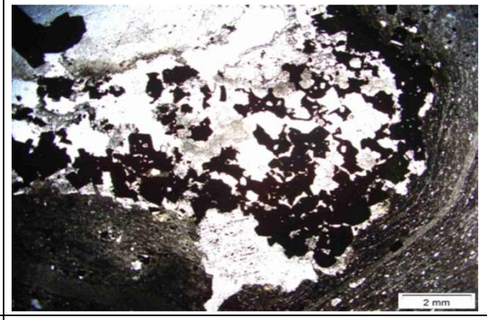	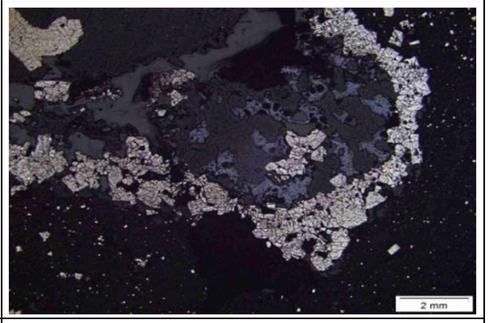
FT_55	SDT	STS/WFO	Thin section including a diamictite with abundant iron oxides. The matrix is fine-grained and composed of quartz, biotite, muscovite and chlorite. Clasts are small (≤ 10 mm), they are composed of quartz, muscovite, chlorite and carbonates. A weak foliation is defined by the alignment of coarse-grained sulphides. Quartz and chlorite form strain shadows to euhedral pyrite. A 1 mm vein is composed of euhedral pyrite. Crenulation observed in the clasts. The rock contains of coarse-grained euhedral pyrite (1 – 2.5%) associated with some sphalerite (0.5%). Also 1 -2% of fine-grained pyrite is disseminated in the matrix.	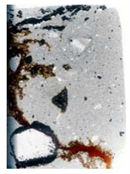	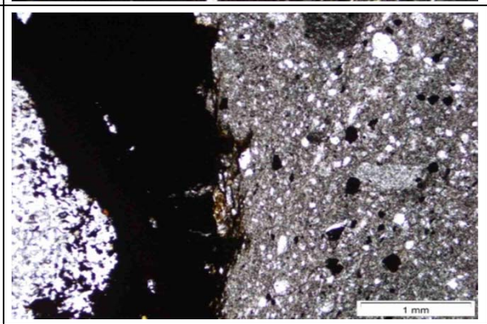	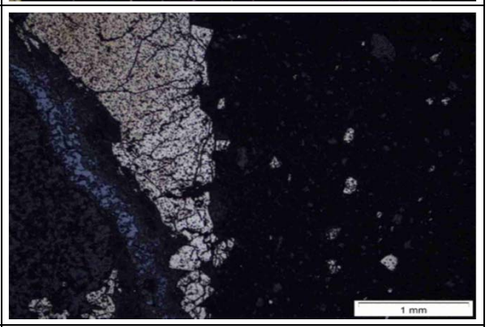
FT_56	SSL	LM/STS	Thin section illustrating a primary foliation S0 in siltstone/mudstone. The rock is composed of quartz, muscovite and biotite with minor chlorite. Some small fragments of quartz are presents within the rock. There are black layers that can't be seen at the microscope magnificence. The rock is finely laminated and layers are spaced with less than 0.5 mm. Pyrite overgrowth the laminations and contains strain shadows composed of quartz, chlorite and muscovite. The alignment of pyrite grains is parallel to S0. The mineralisation consists of 15 – 20% of coarse-grained euhedral pyrite and 10 – 15% of framboidal pyrite. Iron oxides are also obseved, they represent about 0.5 of the thin section.		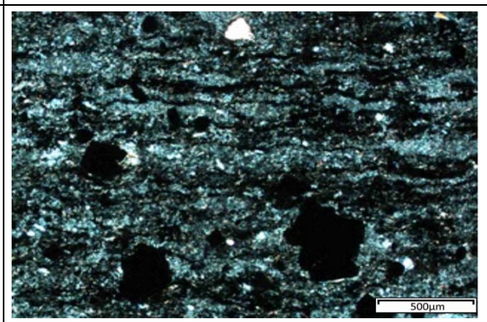	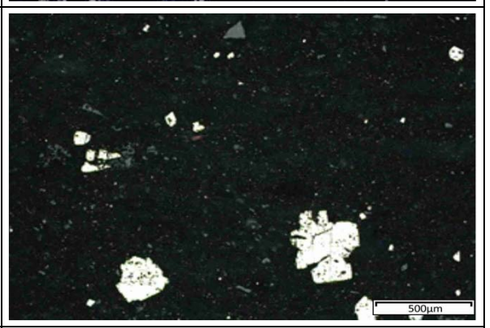
FT_57	SSL	LM	Thin section including a massive siltstone with pyrite dissemination. The rock is mainly composed of quartz, biotite and minor muscovite. A very weak foliation (S1) is defined by the alignment of coarse-grained pyrite and by a very weak alignment of minerals in the matrix. The mineralisation consists of 7 – 12% of euhedral pyrite and 5 – 9% of framboidal pyrite disseminated in the matrix.		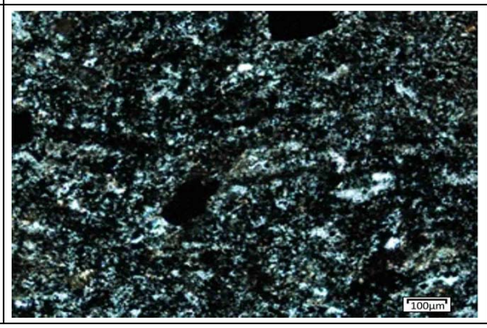	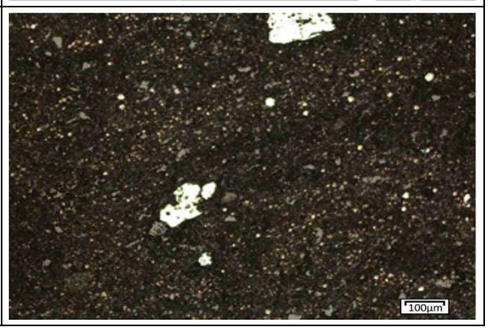

Sample ID	Lithology	Feature	Description	Scanned TS	Transmitted light photomicrographs (XPL and PPL)	Reflected light Photomicrographs
FT_58	SSL	LM	Silststone with abundant pyrite. The rock is composed of very fine-grained material which comprises mainly quartz, muscovite and biotite. There is not S1 foliation observed on this thin section. Bedding are weakly observed, they are spaced with 5 microns. The mineralisation consists of 20 – 25% of framboidal pyrite dissemination and 3 - 5% coarse-grained pyrite.		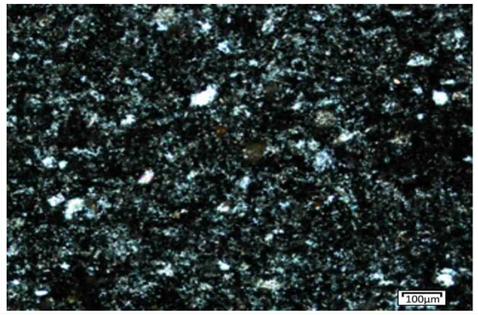	
FT_59	SST/SSL	LM	Thin section including a laminated sandstone/siltstone. The rock is composed of medium-grained material which comprises quartz, muscovite and biotite. Intercalations of white and black layers are observed. The rock is finely laminated and laminations range from 20 µm to 50 mm. The mineralisation consists of 20 to 30% of fine-grained dissemination pyrite with 4 to 6% of framboidal pyrite. Trace coarse-grained pyrite is present.		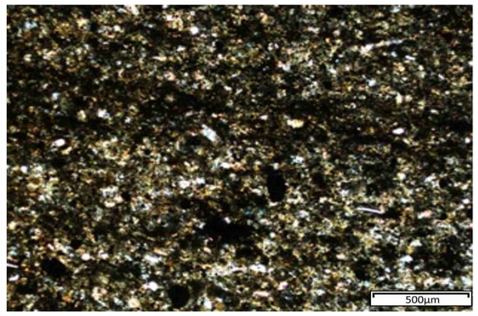	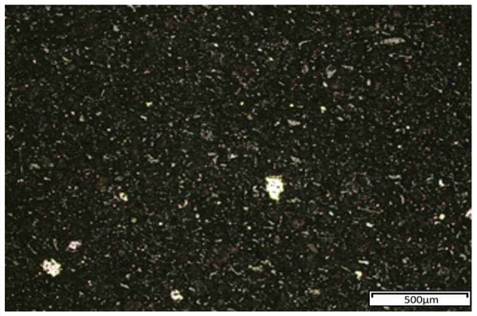
FT_60	SDT	STS/WFO	Clast-rich diamictite showing a weak foliation defined by the alignment of clasts. The matrix is fine-grained and composed of muscovite, quartz and chlorite. Clasts are composed of quartz, muscovite and carbonates with minor chlorite. The matrix is aligned and forms a weak foliation defined mainly by muscovite. Chlorite and biotite form strain fringe to pyrite. Coarse-grained pyrite defines also an S1 foliation. Structural features are parallels. Thin veins of iron oxides are commonly seen on the thin section (probably limonite). 0.5 – 1.5% of coarse-grained pyrite is observed in the replacement of clasts. Possible trace sphalerite associated with pyrite. 0.5 -1% of fine-grained pyrite disseminated in the matrix. Presence of iron oxides in the replacement of clasts and in their rims (about 1%).		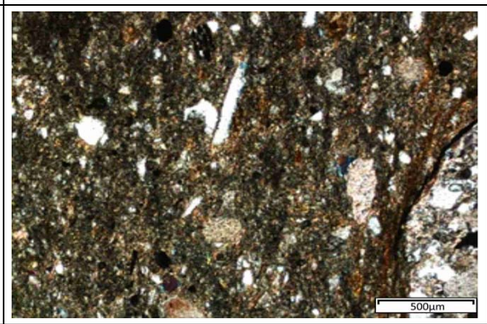	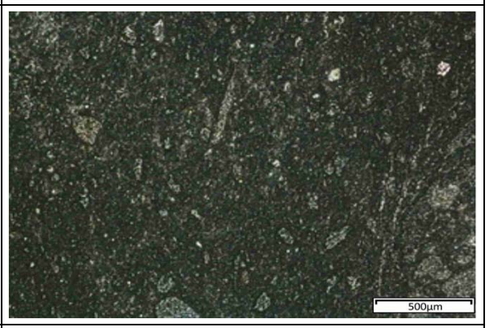
FT_61	SDT	STS	Thin section including a clast-rich diamictite. The matrix is very fine-grained and composed of quartz, biotite, muscovite and minor chlorite. Clasts are small (less than a 1 cm) and composed of quartz, muscovite, biotite, plagioclase, carbonates and chlorite. No alignment of clasts or matrix is observed. Plagioclases, quartz and muscovite in strain shadows to a 1 cm clast. Thin veins of irons oxides are presents on the thin section, they are located preferentially at the edge of the clasts. About 0.5% of coarse-grained chalcocite occurs in the replacement of clasts. Trace of fine-grained chalcocite is disseminated in the matrix.		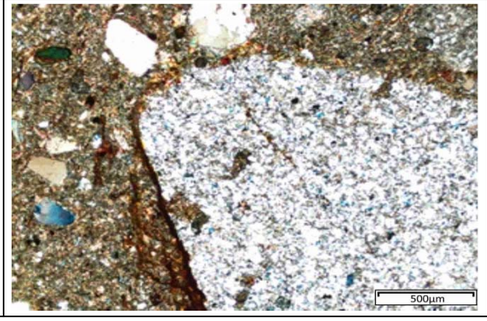	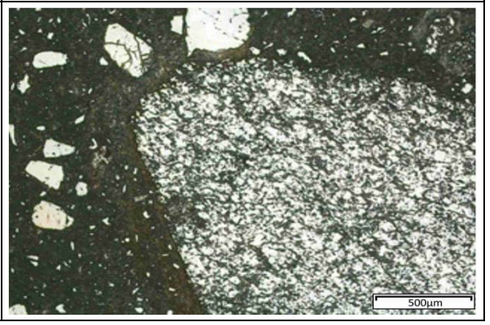

Sample ID	Lithology	Feature	Description	Scanned TS	Transmitted light photomicrographs (XPL and PPL)	Reflected light Photomicrographs
FT_64	SDT	STS/MFO	Diamictite showing a moderate S1 foliation defined by the aligned and elongate coarse-grained chalcopyrite in a clast-poor diamictite. The matrix is fine-grained, weakly aligned and composed of quartz, micas and muscovite. Clasts within the matrix are small (less than a 1 cm), they are composed of quartz, muscovite, biotite, carbonates, chlorite with minor plagioclases and K-feldspar. Fine- and coarse-grained chalcopyrites are aligned and elongate, they define an S1 foliation. The mineralisation consists of 6 – 7.5% of fine-grained chalcopyrite dissemination and 3.5 to 5% of coarse-grained chalcopyrite. There is 1 – 1.3% of chalcopyrite in the replacement and rims of clasts (including strain shadows). The replacement relationship is observed: chalcopyrite tends to replace euhedral pyrite in the clasts. Possible sphalerite associated with pyrite.	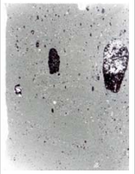	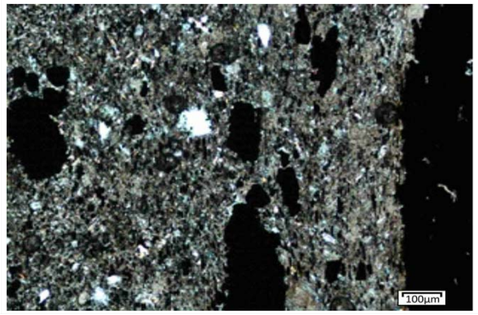	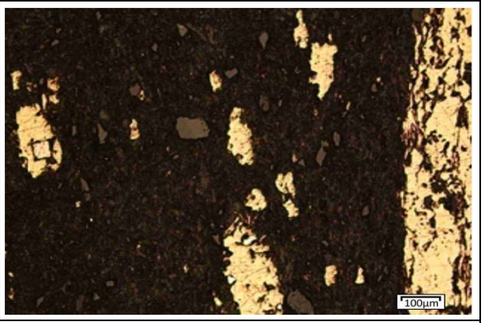
FT_64H	SDT	WFO	Thin section illustrating a weak foliation defined by the alignment of chalcopyrite. The intensity of foliation decreases compared to FT_64 cut perpendicular to this thin section.		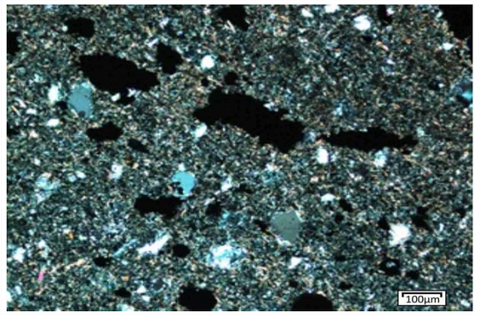	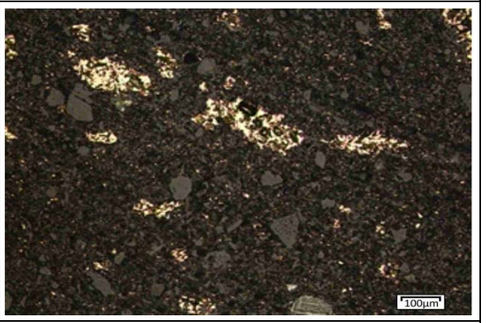
FT-66	SDT	STS/WFO	Thin section including a diamictite with a large clast that contains a strain shadow. The matrix is fine-grained and composed of quartz, biotite, muscovite and chlorite. Most of the clasts are small (less than 5mm), they are composed mainly of quartz, carbonates and chlorite. The large clast is composed mainly with quartz and carbonates. Fine- and coarse-grained chalcopyrite occur as elongate and aligned grains defining a weak to moderate foliation. Carbonate, biotite, chlorite and chalcopyrite form strain shadow to the large quartz clast. S1 is parallel to the strain shadow. The mineralisation consists of 8 to 10% of fine-grained disseminated chalcopyrite and 5 to 7% of coarse-grained, aligned and elongate chalcopyrite. Chalcopyrite occurs also in the replacement of clasts (1.5 – 2.5%). Trace pyrite is observed in association with chalcopyrite.		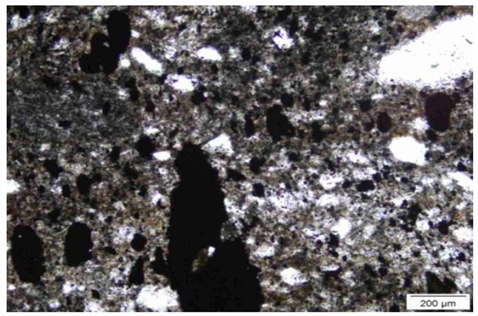	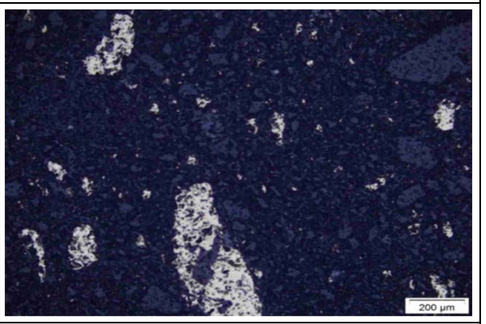
FT_66H	SDT	WFO	This thin section is perpendicular to FT_66. It shows a weak foliation defined by the alignment of chalcopyrite.		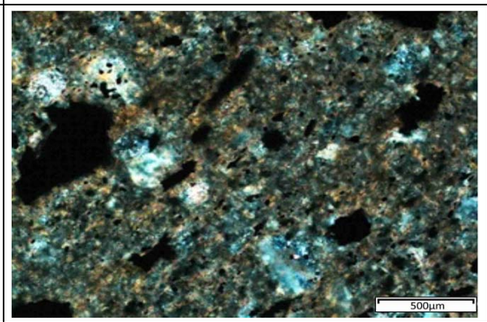	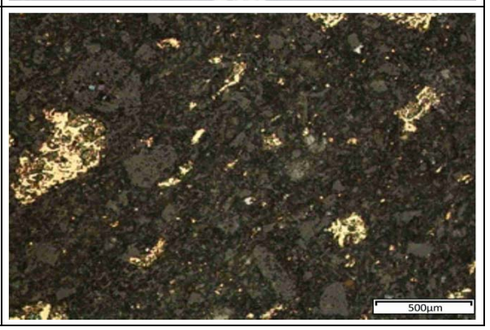

Sample ID	Lithology	Feature	Description	Scanned TS	Transmitted light_Photomicrograph (XPL and PPL)	Reflected light_Photomicrograph
FT_67	SDT	STS/WFO	Thin section including two large clasts with strain shadows. The matrix is fine-grained, it is composed of quartz, biotite, muscovite and minor chlorite. Small clasts range from 2 to 5 mm; large clasts vary from 1.5 to 2 cm. Clasts are composed of quartz, carbonates, muscovite, plagioclases, microclines and chlorite. The matrix is slightly aligned and constitutes incipient foliation domains defined by quartz and micas. S1 foliation is defined by the alignment of fine- and coarse-grained chalcocite. Also, chalcocite forms strain shadows to clasts. S1 is parrallel to strain shadows. The mineralisation consists of 1 to 1.2% of fine-grained dissemination chalcocite; 1.8 to 2% of coarse-grained chalcocite associated with bornite. Presence of possible trace of native copper disseminated in the matrix.		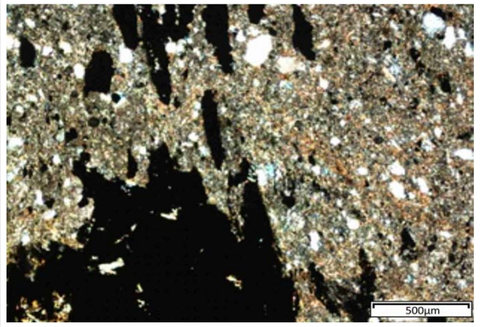	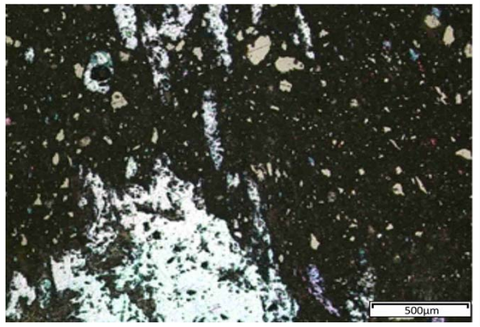
FT_68	SDT	STS	Thin section including a clast-poor diamictite with a large clast in the middle. The matrix is fine- grained, not aligned and composed of biotite, quartz, muscovite and chlorite. Clasts are small (less than 1 cm) and composed of quartz, carbonates, chlorite, biotite, plagioclases and microclines. Very weak foliation defined by alignment of minerals. The large clasts comprise a strain fringe structure which is defined by carbonates around the clast. Clasts are not aligned. 0.5 – 0.8% fine-grained chalcocite associated with about 0.5% fine grained bornite. Traces chalcocite associated bornite is visible in the replacement of clasts. Iron oxides are also present in dissemination within the matrix.			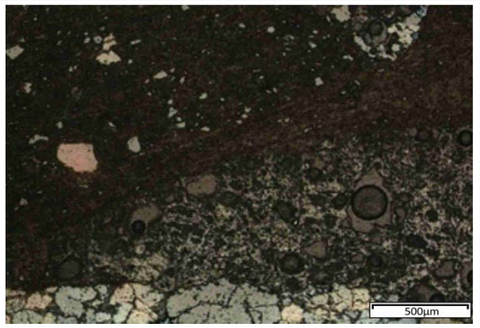
FT_69	SDT	STS	Thin section including a diamictite and a large clast (about 75 %) with strain shadow. The rock is composed of a fine-grained matrix that mainly comprises biotite, quartz and muscovite. Thin biotite veins are present in the matrix. Clasts are composed of quartz, K-feldspar and muscovite. The large clasts are mainly composed of quartz and contain biotite in the rims. Carbonates form a strain shadow structure to the large clast. Trace chalcocite/bornite occur in the strain shadow. Chalcocite occurs also in the replacement of clasts.		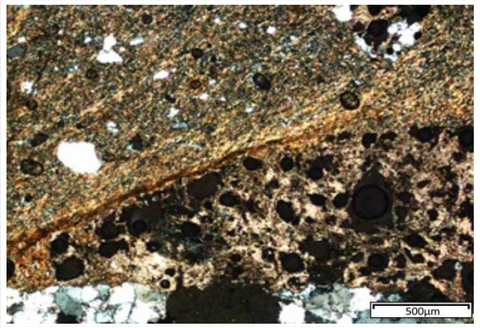	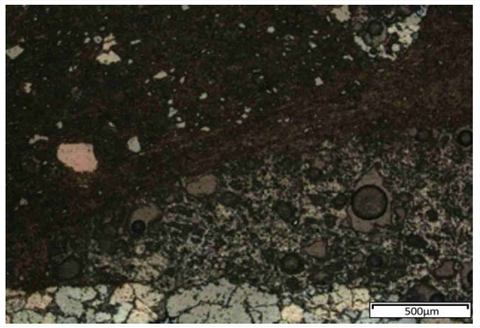
FT_70	SDT	STS/WFO	Clast-rich diamictite in a fine-grained matrix composed of quartz, biotite and muscovite (65%). Clasts are small, less than 0.5 centimetres (35%). They are composed of quartz, biotite, muscovite, carbonates, chlorite and plagioclases. Incipient foliation domains defined by the alignment of minerals. Occasional carbonates in strain shadows to quartz clasts. Biotite is commonly present in the rim of clasts. Occasional thin biotite veins are observed. The mineralisation consists of 0.5 to 0.8% of bornite in the replacement of clasts; 0.2 to 0.5% of chalcocite in fine-grained and in replacement of clasts.		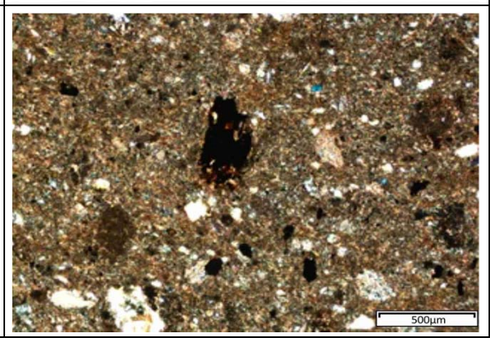	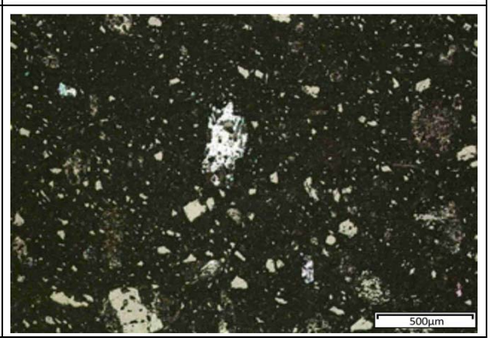

Sample ID	Lithology	Feature	Description	Scanned TS	Transmitted light_Photomicrograph (XPL and PPL)	Reflected light_Photomicrograph
FT_71	SDT	STS/WFO	Thin section displaying a clast-rich diamictite (about 20%) in a fine-grained matrix (80%). This matrix is composed mainly with biotite, muscovite and quartz. The size of clasts ranges from 0.2 to 1.5 cm, they are composed of quartz, chlorite, biotite and carbonates. Occasional carbonates in strain shadow to the chlorite clast. Trace fine-grained bornite and chalcocite is disseminated in the matrix and in the replacement of clasts.		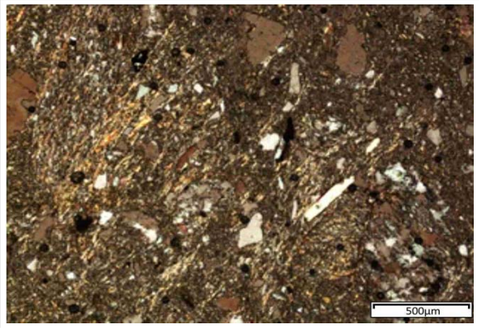	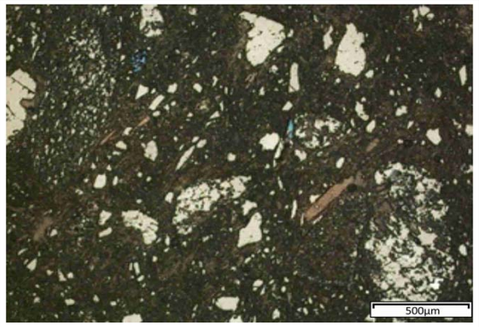
FT_72	SDT	STS	Thin section illustrating a diamictite with 25 to 35% clasts. The matrix is very fine-grained; it is composed of quartz, muscovite, biotite and chlorite. Clasts are composed of quartz muscovite, plagioclase, chlorite, carbonate and K-feldspar. Their size ranges from 0.2 to 5 mm, the large clast measures 1.5 cm. The composition of the large clast consists of quartz. Carbonate, quartz and micas form strain shadow to the large clast. Iron oxides are present in the rim of clasts and in dissemination within the matrix.		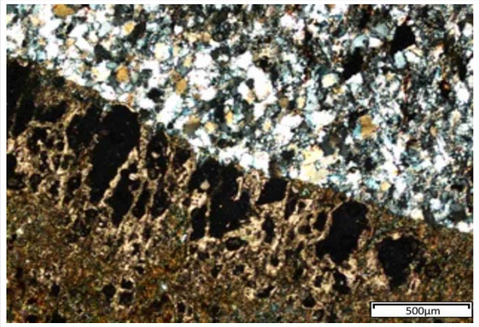	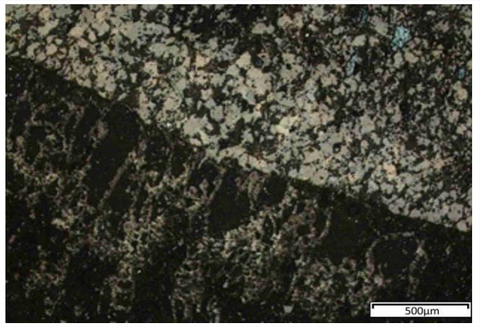
FT_73	SDT	WFO	Thin section including a diamictite with about 15 - 20% clasts. The matrix (85%) within the diamictite is very fine-grained, it is composed of quartz, muscovite, biotite and chlorite. Clasts are small (less than a cm), they are composed of quartz, muscovite and chlorite. Iron oxides occur as dissemination in the matrix and as thin veins. Some trace of chalcocite are observed in the replacement of clasts. Possible trace of native copper in the edge of clasts.		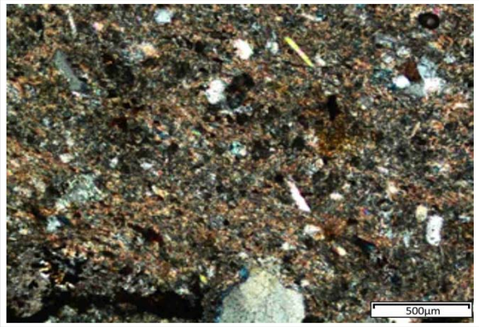	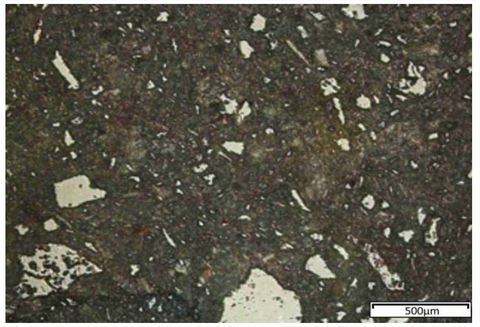
FT_74	SDT	WFO/STS	Thin section composed of a clast-rich diamictite (30%) in a fine-grained matrix (70%). The matrix is composed of quartz, muscovite, biotite and minor chlorite. Clasts range from 0.3 mm to 1 cm; they are composed of quartz, muscovite, biotite, carbonates, chlorite and plagioclases. Biotite occurs in the rim of clasts. Carbonates, chlorite and muscovite form strain shadows to clasts. Strain shadows are aligned and define a weak foliation. Minor pyrite is observed, it is associated with chalcopyrite in strain fringes of clasts. Possible sphalerite in association with pyrite. Iron oxides are present in the rim of clasts.		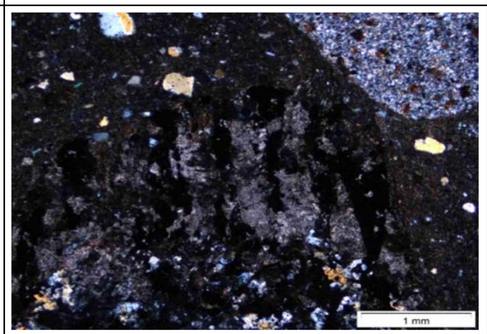	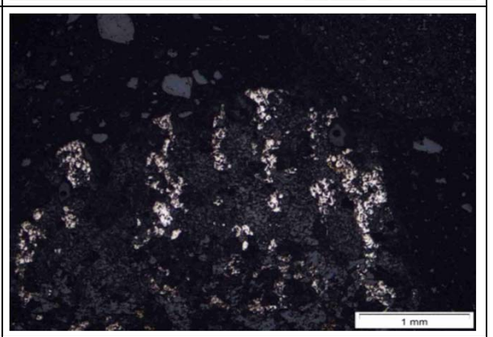

Sample ID	Lithology	Feature	Description	Scanned TS	Transmitted light_Photomicrograph (XPL and PPL)	Reflected light_Photomicrograph
FT_75	SST	WFO/STS	Thin section including a massive sandstone with abundant pyrite and iron oxides. The rock is composed mainly of quartz, muscovite and biotite. Chlorite and quartz form nice fringes/shadows around euhedral pyrites. Weak foliation defined by the alignment of coarse-grained pyrite. Strain shadows/fringes are parallel to the S1 foliation. The rock contains 10 to 12% of coarse-grained euhedral pyrite that is associated with about 3% sphalerite. Also 5 to 7% of fine-grained pyrite is disseminated in the matrix. Some framboidal pyrite (1%) are associated with fine-grained pyrite. Abundant iron oxides are disseminated in the rock.	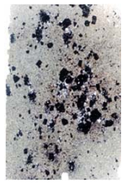	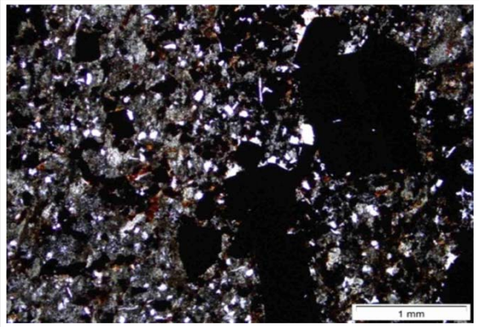	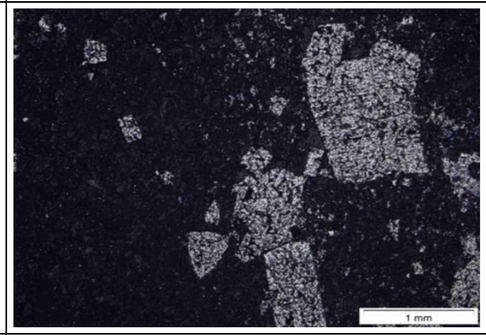
FT_76	SSL	MFO/STS	Thin section including a large clast in the diamictite. The matrix is very fine-grained, it is composed of quartz, muscovite and biotite (about 15%). The large clast (65%) is composed of plagioclases with some carbonates and quartz. Weak to moderate foliation defined by the alignment of coarse-grained chalcopyrite and the alignment of minerals in the matrix (micas). Chalcopyrite occurs in strain shadow to the large clast. Thin veins filled with chalcopyrite are also observed. Structural fearures are parallels. The rock contains chalcopyrite that occurs as fine-grained dissemination (1 – 1.2%), coarse-grained (5 – 7%) dissemination and as replacement (4 – 6%) of clasts. Trace pyrite and bornite are also observed in association with chalcopyrite.		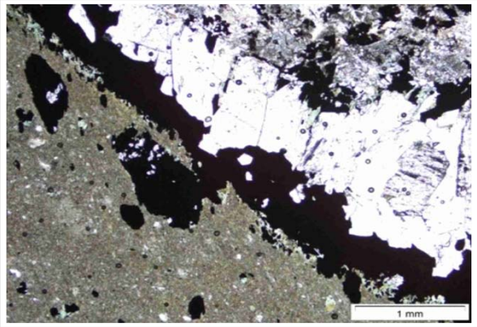	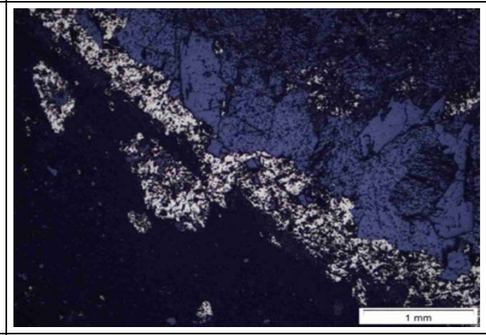
FT_77	SSL	FLD	Thin section including a fold in siltstone/mudstone. The rock is composed of fine- to medium-grained fragments mainly composed of quartz, muscovite, chlorite and minor biotite. The intercalation of white and dark layers defines the fold. There is not foliation observed in the fold, therefore the structure is interpreted as from a syn-sedimentary origin. The mineralisation consists of 7 to 10% of fine- and coarse-grained chalcopyrite disseminated in the rock.		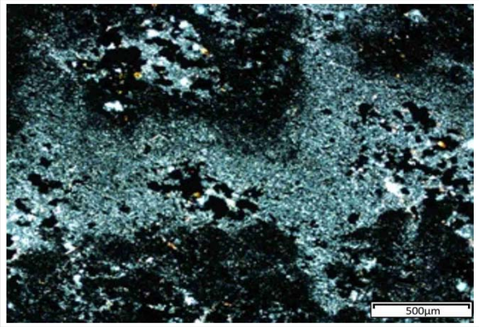	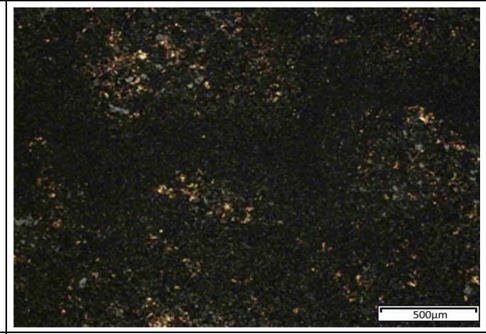
FT_78	SSL	SBD/SFO/STS	Thin section including a siltstone displaying a strong foliation. The host rock is composed of very fine-grained material which comprises mainly quartz, muscovite and minor micas. Occasional dropstones are observed, they range from 0.5 to 1 cm. Dropstones are composed of quartz, biotite and rare carbonates. S0 is observed (spaced with 0.1 to 1 cm). Continuous foliation defined by the alignment of minerals in the matrix, alignment and elongation of fine- and coarse-grained chalcopyrite. Fringes around dropstones are composed of chalcopyrite, chlorite, biotite, quartz and carbonates. Dropstones fold laminations suggesting a syn-depositional origin. The mineralisation consists of 40 to 50% of fine- and coarse-grained chalcopyrite.		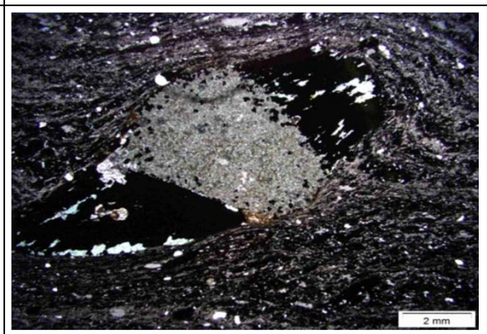	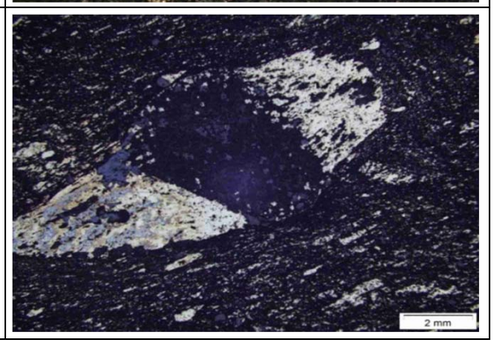

Sample ID	Lithology	Feature	Description	Scanned TS	Transmitted light_Photomicrograph (XPL and PPL)	Reflected light_Photomicrograph
FT_78H	SSL	MFO	Moderate foliation defined by the alignment of minerals in the matrix and the alignment of fine- and coarse-grained chalcopyrite. This thin section was cut perpendicular to FT_78, it shows that the intensity of foliation is not the same in all directions (X, Y).		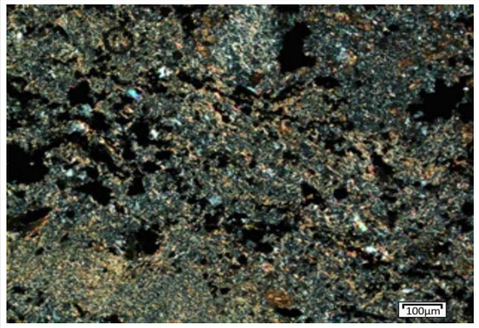	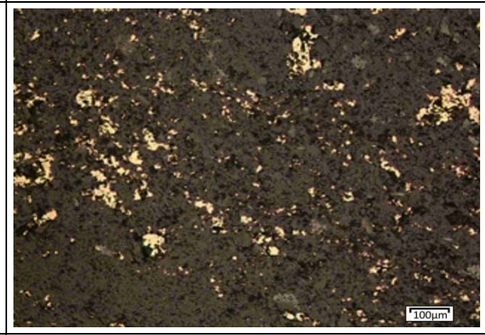
FT_79	SDT	WFO/STS	Thin section including a clast-rich diamictite. The matrix is fine-grained and composed of quartz, muscovite, biotite and chlorite (70%). Clasts are composed of quartz, biotite, chlorite, carbonates and plagioclases (25%). Clasts range from 0.2 – 0.5 cm, large clasts are up to 1 cm. A weak foliation is defined by the alignment of fine- and coarse-grained chalcopyrite nd by the alignment of muscovite in the matrix. The rock contains chalcopyrite as fine- (1 to 1.5%) and coarse-grained (1.5 to 2%). In addition 2 to 2.4% of chalcopyrite is observed in the rim clasts where it replaces partially to completely the mafic igneous clast.		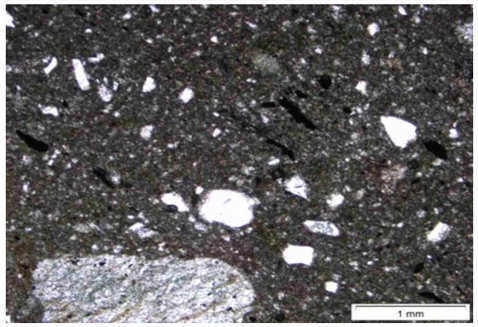	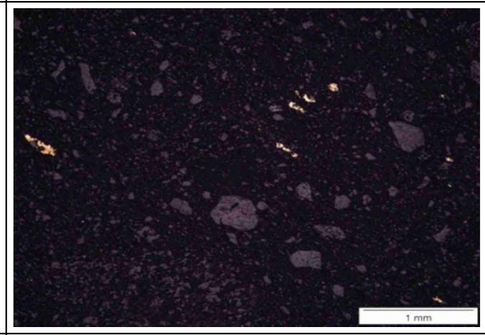
FT_79H	SDT	VWFO	Very weak foliation defined by the alignment of coarse-grained chalcopyrite. This thin section is perpendicular to FT_79, it shows that the intensity of foliation is not the same in all directions (X, Y).		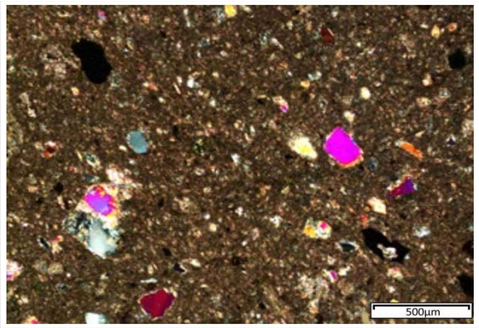	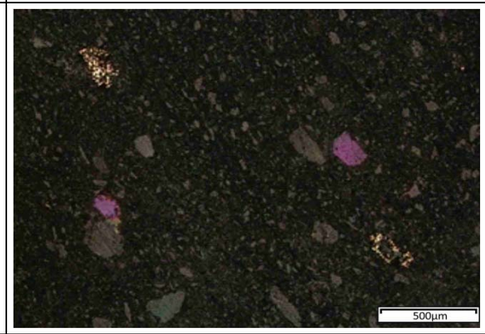
FT_80	SDT	WFO/STS	Thin section including a clast-rich diamictite that shows a weak foliation. The matrix (75%) is fine-grained and composed of quartz, muscovite, biotite and chlorite. Clasts are composed of quartz, biotite, chlorite, carbonates and plagioclases (25%). Their size ranges from 0.2 – 0.5 cm, locally up to 1.5 cm for the largest clast. The large clast is composed of siltstone and quartzite. Weak foliation defined by the alignment of coarse-grained chalcopyrite and alignment of muscovite in the matrix. Chalcopyrite is also present in the rim and in the replacement of clasts. The mineralisation consists of disseminated chalcopyrite that occurs as fine- (1 – 1.5%) and coarse-grained (3.5 – 4.5%).		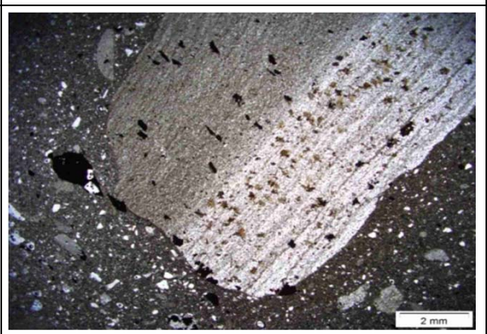	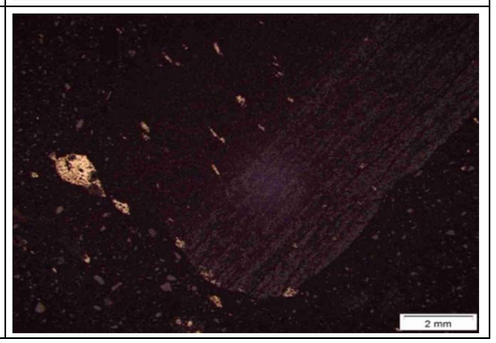

Sample ID	Lithology	Feature	Description	Scanned TS	Transmitted light_Photomicrograph (XPL and PPL)	Reflected light_Photomicrograph
FT_81	SSL	SBD	Sample including a siltstone with abundant bornite. The host rock is composed of fine-grained material that consists of quartz and muscovite. S0 is observed and the space between layers ranges from 0.5 to 1.5 cm. The matrix is aligned and defines a weak to moderate foliation which constitutes an angle of about 30˚ with S1. Fine- and coarse-grained bornite/chalcocite display also a weak to moderate foliation which is parallel to the alignment of the matrix. Some clasts are observed in the rock, they are composed of quartz and plagioclases. These clasts seem to be oriented parallel to S1. The mineralisation consists of 15 to 18% of fine- and coarse-grained bornite dissemination; 0.7 to 1% of fine- and coarse-grained chalcocite.		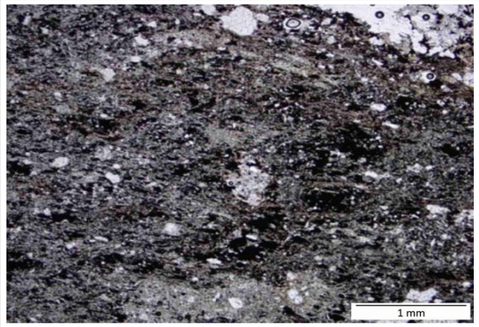	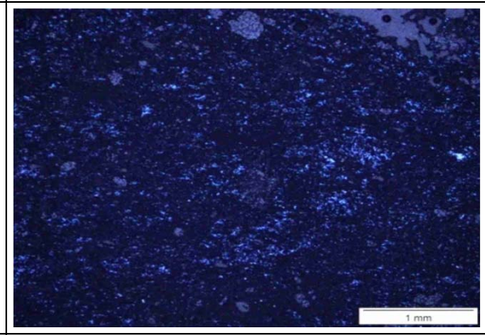
FT_82	SSL	SBD/MFA/ WFO	Thin section including a mesoscopic fault showing a normal sense of movement. The rock includes interclations of siltstone and mudstone. Quartz, muscovite, biotite and plagioclases (0.5 – 1mm) represent minerals in the rock. S0 is observed and the space between laminations ranges from 0.5 to 50 mm. Mesoscopic faults are defined by the offset of beds. Weak foliation defined by the alignment of fine- and coarse-grained copper sulphides (bornite and chalcocite). The angle between the beds and the foliation is about 30˚. The mineralisation consists of 15 to 18% of fine-grained bornite associated with 0.8 to 1.5% of fine-grained chalcocite.		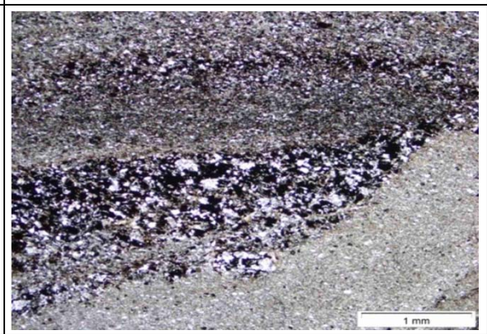	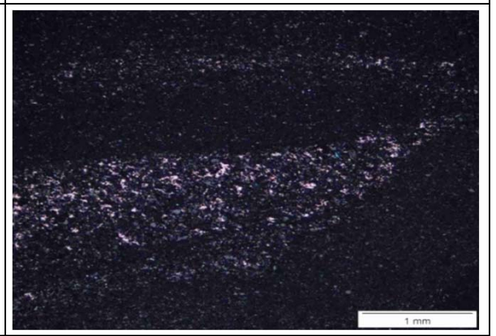
FT_85	SDT	FZ	Thin section illustrating a clast-rich diamictite with thin iron oxides veins. The matrix is very fine-grained, it is composed of quartz, muscovite and biotite. Clasts are composed mainly of quartz cemented by muscovite, chlorite and plagioclase matrix. The size of clasts ranges from 2 mm to 1 cm. Possible pressure solution suggested by the dissolution of clasts. Abundant thin iron oxides veins, especially in the edge of clasts. Trace chalcocite occurs in the replacement of clasts.	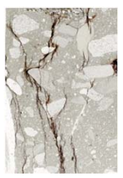	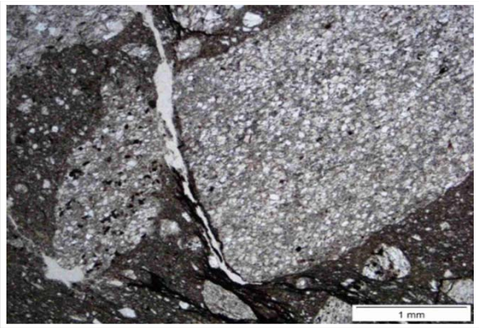	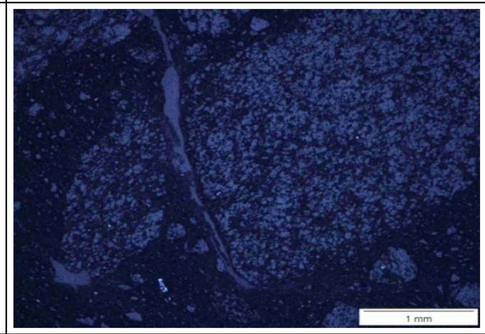
FT_87	SST	LM	Thin section illustrating cross bedding texture in sandstone layers. The rock is composed mainly of quartz, chlorite and muscovite. Presence of occasional small clasts composed of K-feldspar, quartz and carbonates. In the corner of the thin section, a greywacke is observed, it is composed of quartz, plagioclase, chlorite, muscovite, biotite and plagioclases. S0 (bedding) is present and ranges from 0.5 to 1 mm. The rock shows a soft sediment deformation texture. Chlorite forms fringes to chalcopyrite. The mineralisation consists of 13 to 15% of fine- and coarse-grained chalcopyrite; 8 – 10% of fine- and coarse-grained bornite disseminated in the rock.		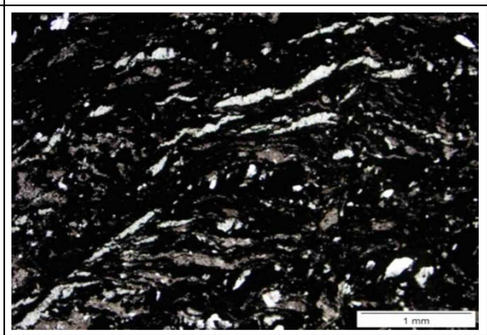	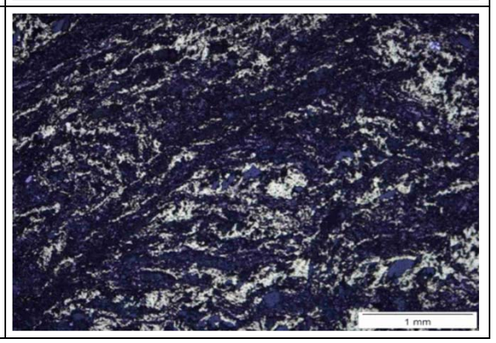

Sample ID	Lithology	Feature	Description	Scanned TS	Transmitted light_Photomicrograph (XPL and PPL)	Reflected light_Photomicrograph
FT_88	SSL	SBD	Thin section including an S0 and S1 foliation in siltstone/mudstone layers. The rock consists of intercalations of very fine-grained and fine grained material composed of quartz, biotite and minor chlorite. The rock is composed mainly of quartz and muscovite. S0 ranges from 1 to 5 mm. S1 is defined by the alignment of fine- and coarse-grained chalcopyrite. Chlorite forms the fringe to chalcopyrite. The mineralisation consists of 11 to 14% of fine-grained disseminated and elongate chalcopyrite. Trace euhedral pyrites are also observed.		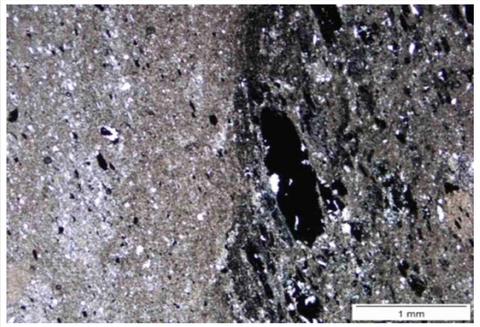	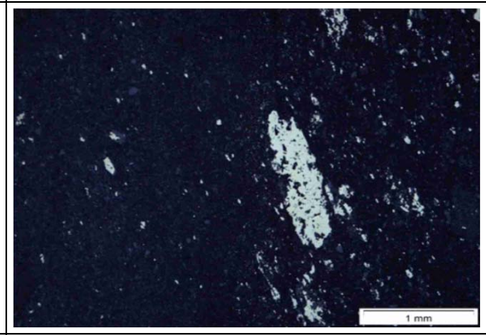
FT_89	SSL	LM/VN	Thin section including a bedded to laminated siltstone. The rock is fine-grained and composed of quartz, carbonates and minor micas. In the middle of the thin section, there is a 50 mm vein composed of quartz, carbonates, pyrite, chlorite and occasional muscovite. S0 is well observed on the thin section. Weak foliation defined by the alignment of coarse-grained pyrite. The mineralisation consists of 25 to 30% of coarse-grained and euhedral pyrite associated with 10 to 15% of fine-grained pyrite. Also 6 to 9% of framboidal pyrite is finely disseminated in the rock. Traces of sphalerite are observed in association with pyrite.		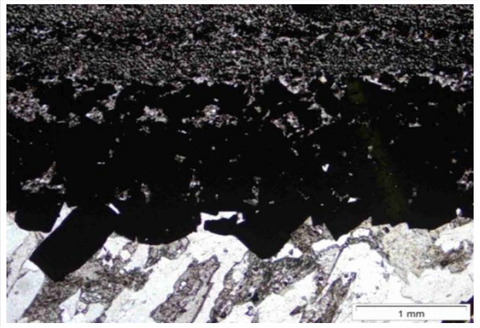	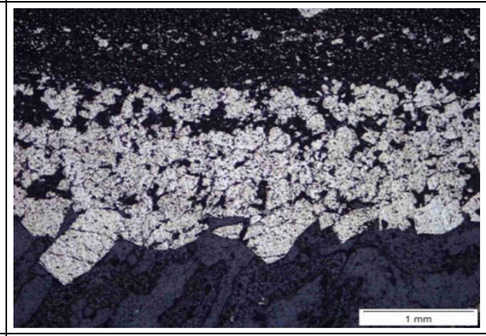
FT_90	SST	SFO/STS	Thin section including a sandstone. ilstrong to moderate foliation defined by the alignment of minerals. The rock is composed of quartz, carbonates and muscovite. Weak to moderate foliation defined by alignment of coarse-grained pyrrhotite. A soft sediment deformation texture is observed. The mineralisation consists of 3 to 5% of coarse-grained pyrrhotite. Trace chalcopyrite is associated pyrrhotite.	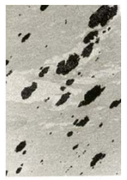	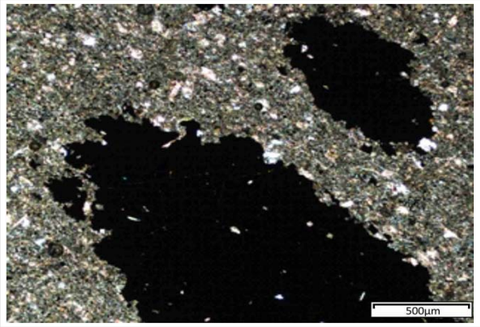	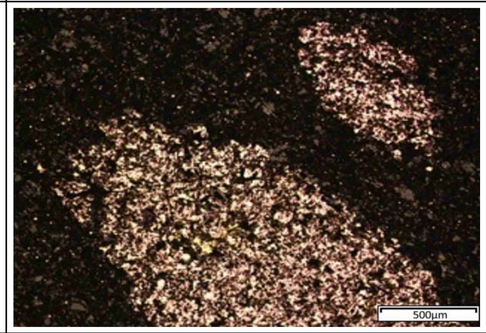
FT_91	SSL	LM	Thin section including siltstones and mudstones. The rock is fine- and medium-grained, it contains quartz, carbonates and biotite. Beddings and cross beddings are observed, they range from 0.5 mm to 1 cm. Quartz and chlorite with minor carbonates form the fringe to euhedral pyrite. Coarse-grained euhedral pyrites define a weak foliation. S1 and S0 form an angle of about 30 to 40˚. The mineralisation consists of 25 to 30% of coarse-grained euhedral pyrite and 15 to 20% of framboidal and fine- grained pyrite.		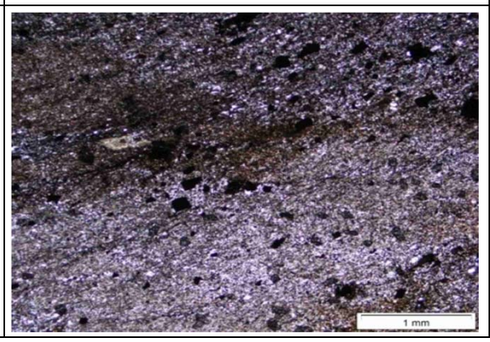	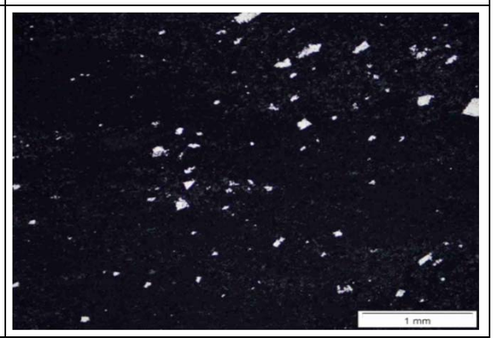

Sample ID	Lithology	Feature	Description	Scanned TS	Transmitted light_Photomicrograph (XPL and PPL)	Reflected light_Photomicrograph
FT_92	SDT	VWFO	Thin section including a clast-poor diamictite. The matrix is very fine and fine-grained, it is composed mainly of quartz, muscovite and chlorite. An incipient foliation is observed on the thin section. Clasts are small (≤5 mm), they are composed of quartz, carbonate, chlorite, muscovite and plagioclases. Trace bornite occurs in the replacement of clasts and in dissemination within the matrix. Occasional trace of fine- grained chalcopyrite are observed.		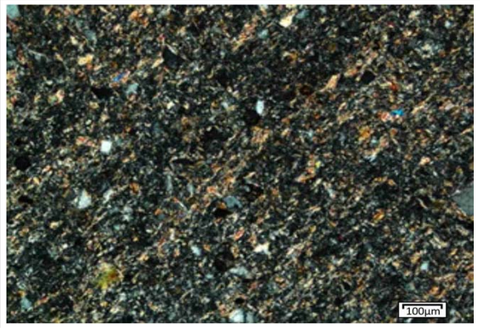	
FT_93	SSL	SSD/STS/MFO	Thin section composed of intercalations of siltstone and sandstone layers. The rock is fine-grained and composed of quartz, muscovite and biotite. Minerals in the matrix are aligned and define an S1 foliation. Mesoscopic faults are observed, they are defined by the offset of beds. Beddings are spaced with 0.1 to 1.5 cm. Moderate to strong foliation defined by the alignment of fine- and coarse-grained chalcopyrite. Quartz, biotite and chlorite form strain fringe to coarse-grained chalcopyrite. Trace coarse-grained pyrite and sphalerite are associated with chalcopyrite.	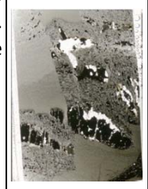	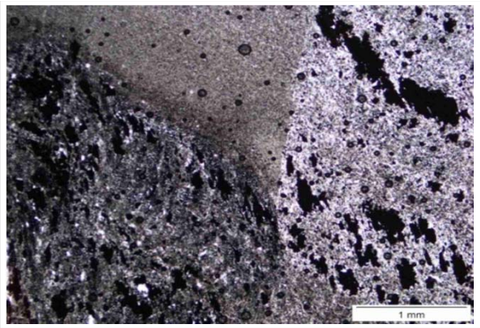	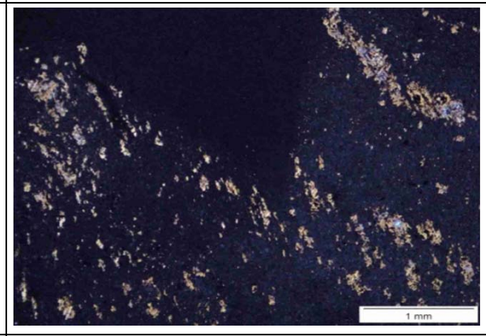
FT_94	SSL	SSD/STS/MFO	Thin section showing intercalations of silststone and mudstone layers. Mesoscopic faults defined by the offset of beds are observed. Quartz, muscovite and biotite are the main minerals that constitute the rock; they are aligned and define an S1 foliation. Beddings are observed on the thin section, they are associated with soft-sediment deformation texture and slump folds. Occasional clasts occur, they are composed of quartz and biotite. The alignment of fine- and coarse-grained chalcopyrite defines S1 foliation. The mineralisation consists mostly of chalcopyrite that occurs as coarse-grained (10 to 15%) and fine-grained (5 to 8%). Trace bornite in association with chalcopyrite.		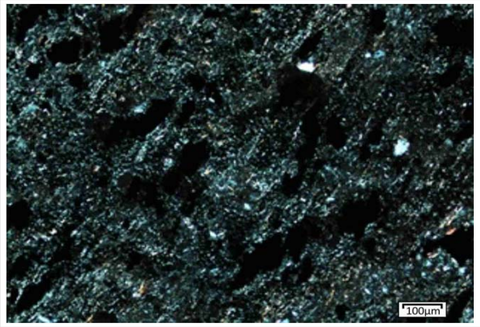	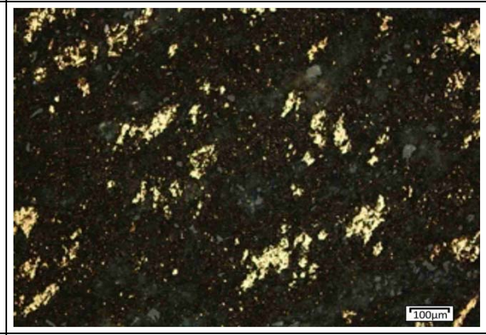
FT_95	SST	SSD/MFO	Sandstone showing a soft-sediment deformation texture. The rock contains mostly quartz, biotite and muscovite. Chalcopyrite seems to form clusters. Fine- and coarse-grained chalcopyrite are aligned and define a continuous foliation. The mineralisation consists ofmainly of chalcopyrite that occurs as coarse-grained (18 to 20% including chalcopyrite in the clusters) and as fine-grained disseminated (20 to 25%).	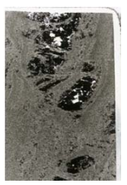	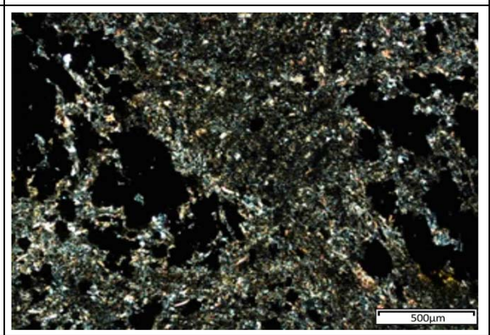	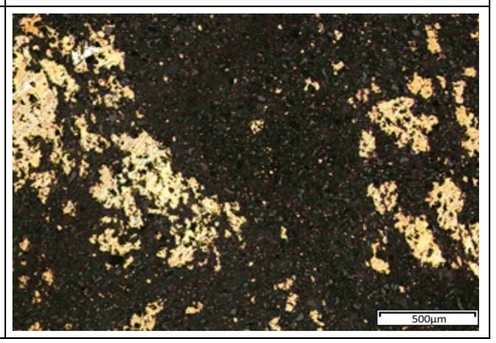

Sample ID	Lithology	Feature	Description	Scanned TS	Transmitted light_Photomicrograph (XPL and PPL)	Reflected light_Photomicrograph
FT_95H	SSL	VWFO	Very weak foliation defined by the alignment of coarse-grained chalcopyrite. This thin section is perpendicular to FT_95, it shows that the intensity of foliation is not the same in all directions (X, Y).		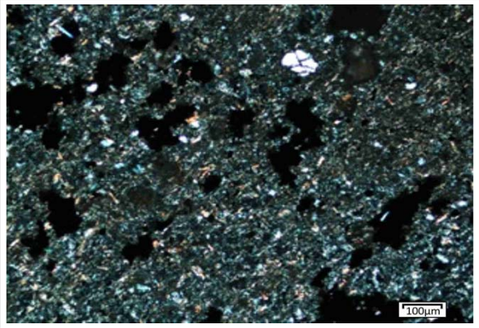	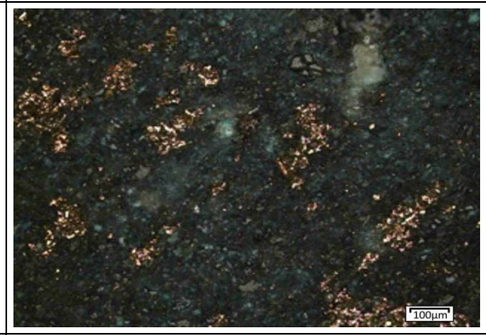
FT_96	SSL	SBD	Thin section including a mineralised vein in the siltstone. The host rock (siltstone) is fine-grained and contains quartz, biotite and muscovite. Minerals in the siltstone are aligned and defines an S1 foliation. The vein is composed of carbonate, quartz, biotite and chlorite. Minerals within the vein are aligned. The vein contains about 20 to 25% of bornite and ~ 1% chalcopyrite. Bornite seems to replace chalcopyrite. S1 foliation in the host rock is similar to that in the vein. The host-rock (siltstone) contains about 10 to 15% of fine-grained disseminated bornite.		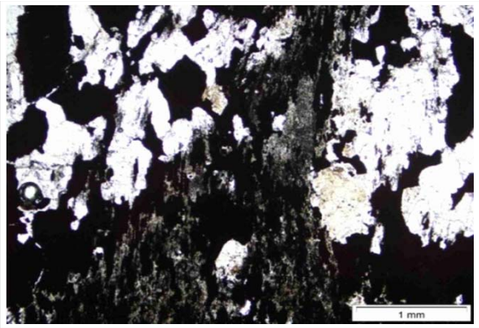	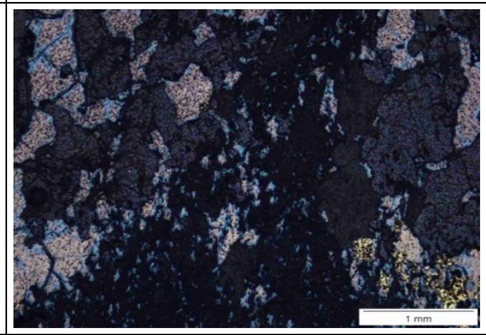
FT_97	SSL/SST	SBD	Thin section including intercalations of siltstones and sandstones. The rock is fine-grained and comprises mainly quartz and biotite. Minerals within the rock are aligned and define a weak foliation. Small clasts are observed (less than 0.5 cm), they are composed of quartz. The rock is laminated (laminations spaced with 1 mm to 1 cm) and contains mesoscopic faults defined by the displacement of beds. S1 foliation is defined by the alignment of sulphides. The mineralisation consists of bornite that occurs as fine-grained ranging from 20 to 25% and as coarse-grained ranging from 3 to 4%.		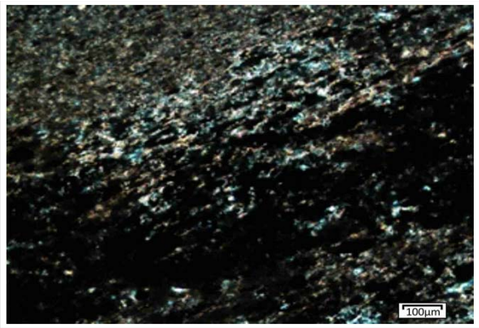	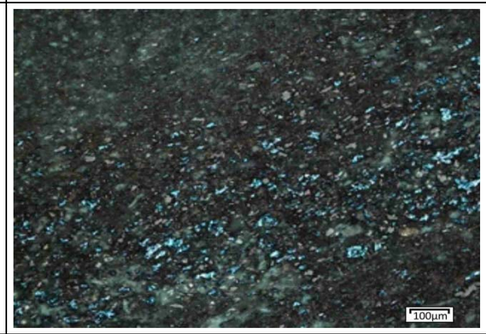
FT_98	SDT	MFO	Diamictite showing a moderate foliation defined by the alignment of chalcopyrite. The matrix is fine-grained and composed of quartz, muscovite and biotite. Clasts are small (less than a cm), they are composed of quartz, carbonate, muscovite, plagioclase and chlorite. S1 foliation is defined by the alignment of fine- and coarse-grained chalcopyrite. Also, the matrix shows a weak foliation defined by the alignment of muscovite. The mineralisation consists of 25 to 30% of coarse-grained chalcopyrite (including replacement) and 5 to 10% of fine-grained disseminated chalcopyrite.	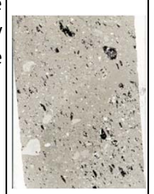	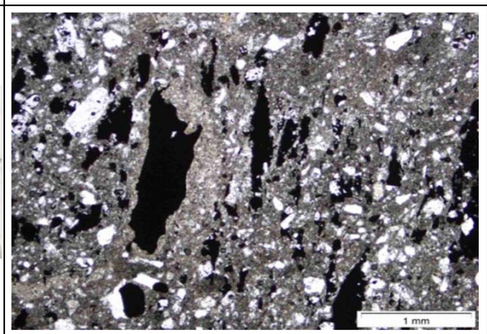	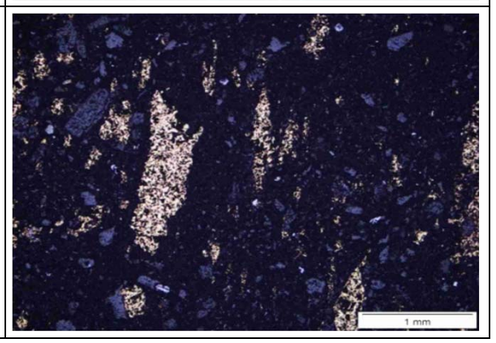

Sample ID	Lithology	Feature	Description	Scanned TS	Transmitted light_Photomicrograph (XPL and PPL)	Reflected light_Photomicrograph
FT_98H	SDT	WFO	Thin section perpendicular to FT_98. The rock shows weak foliation defined by the alignment of minerals in the matrix, and the alignment of coarse-grained chalcopyrite. The intensity of foliation decreases compared to FT_98, this demonstrating that the heterogeneity of foliation (X, Y).		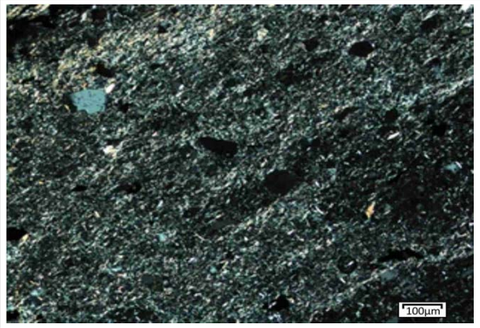	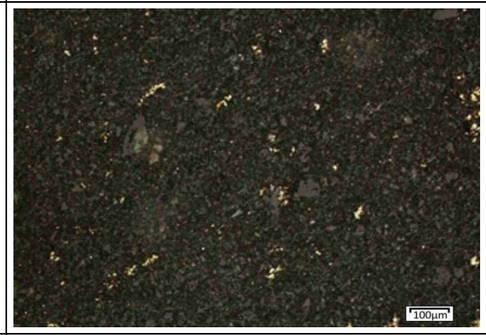
FT_99	SST		Thin section including an arkosic greywacke. The rock is composed of quartz, plagioclase and K-feldspar grains cemented in a micas matrix. Laminations are poorly developed. The mineralisation consists of fine-grained disseminated chalcopyrite ranging from 0.3 to 0.7%. Iron oxides are finely disseminated in the rock.		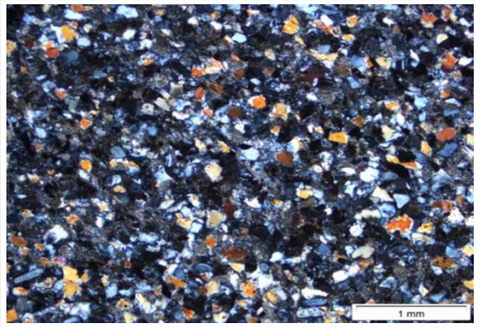	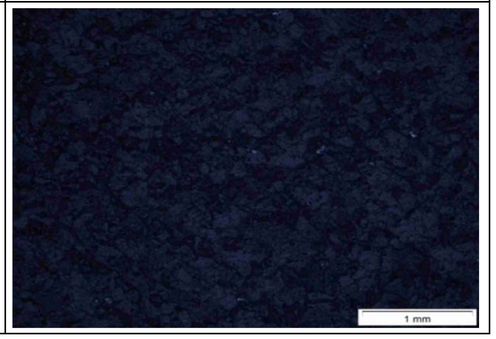

Borehole ID	Thin section ID	Stratigraphic units	Lithologic units	Feature	Description	Transmitted light_Photomicrograph (XPL and PPL)	Reflected light_Photomicrograph
DTJI_DD001	586.94	Ng111	SDT	SFO	Thin section including a clast-moderate diamictite showing a strong foliation defined by the alignment of clasts. The matrix is fine-grained and composed of quartz, micas and chlorite. Minerals in the matrix define also a strong foliation. Clasts are composed mainly of quartz, plagioclases and carbonates. Traces of pyrites (< 0.5%) are disseminated in the matrix. The rock shows a slaty cleavage.	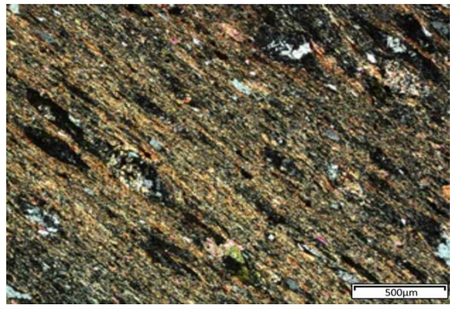	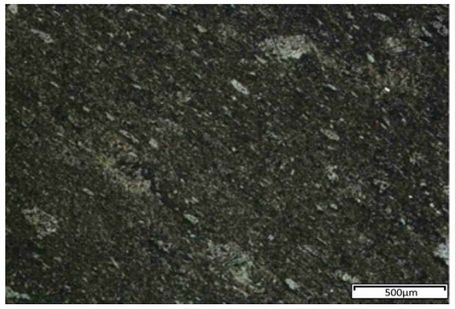
DTJI_DD001	615.58	R42	SST	SFO	Thin section including a sample from the Roan feldspathic sandstone. The rock is composed of quartz, plagioclases, feldspar, muscovite, chlorite and biotite. The minerals are aligned and elongated defining a strong foliation. It is possible that some fish structures are present. Trace fine-grained pyrites are observed. The rock shows a slaty cleavage and schistosity texture.	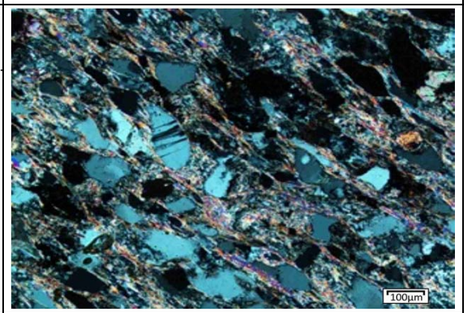	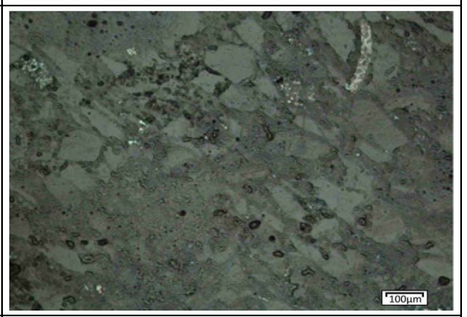
DTJI_DD001	611.92	R42	SST	SFO	Thin section including a Roan feldspathic sandstone. The rock is composed of plagioclases, quartz, feldspar, muscovite, biotite and chlorite. The minerals within the rock define a strong foliation, especially muscovite.	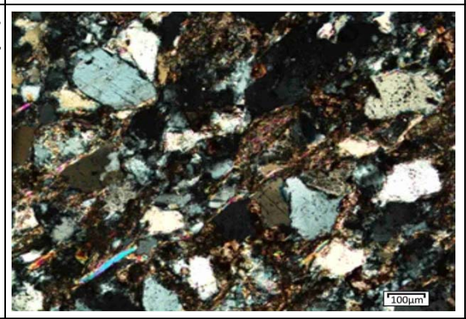	
DTJI_DD001	612.06	R42	SST	MFO	Roan feldspathic sandstone composed of quartz, plagioclases, muscovite, feldspar, biotite and occasional carbonates. A moderate foliation is defined by the alignment of muscovite and some quartz grains. 60% of the minerals in the rock are not aligned.	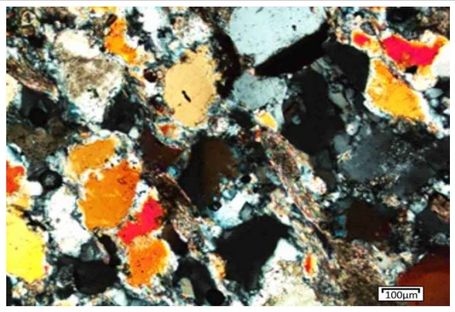	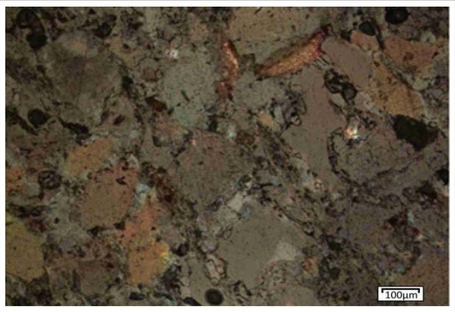

Borehole ID	Thin section ID	Stratigraphic units	Lithologic units	Feature	Description	Transmitted light_Photomicrograph (XPL and PPL)	Reflected light_Photomicrograph
DTJI_DD001	615.45	R42	SST	SFO	Thin section including a sample from the Roan feldspathic sandstone. The rock is composed of quartz, feldpar, muscovite, chlorite, carbonate and biotite. The minerals in the rock are aligned and define a strong foliation showing continous foliation texture.	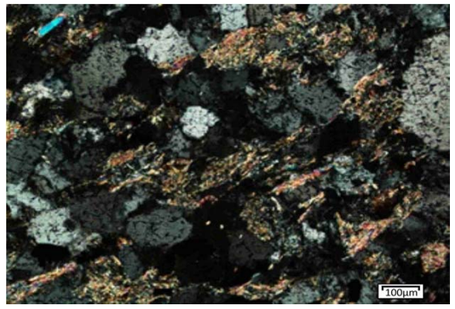	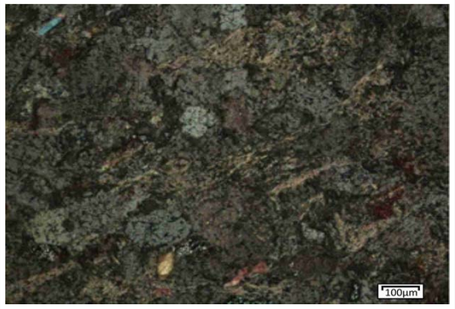

Thin section ID	Depth (m)	Lithologic units	Stratigraphic Units	Mineral association	CPY (%)	BN (%)	CCT (%)	Native CU (%)	PY (%)	Description	Transmitted light_Photomicrograph (XPL and PPL)	Reflected light_Photomicrograph
TS1	200.15	SSL	Ng 1.1.2	Py>>> Cpy	0.1				35	Very fine- to fine-grained mudstone/siltstone composed mainly of quartz and muscovite (5 - 30µm with occ. large grains are up to 150 µm). The rock contains framboidal pyrites, some of them have been replaced by euhedral pyrites and chalcopyrites. Continuous foliation defined by the alignment of coarse-grained chalcopyrite. Laminations are observed, they are perpendicular to S1 defined by chalcopyrite.	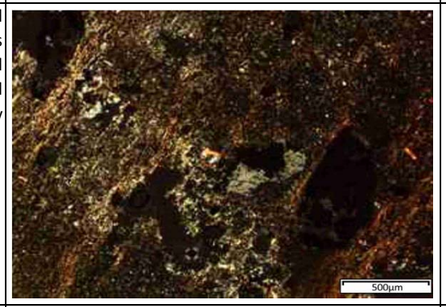	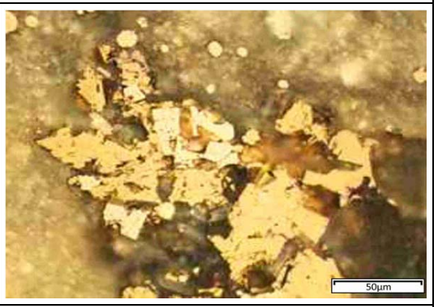
TS2	202.42	SDT	Ng 1.1.1.3	Py>>> Cpy	0.1				1.5	Clast-rich diamictite in a fine-grained matrix composed of quartz and micas. Clasts represent 30%; they are mainly composed of quartz, argillites and schists. Their size varies from 0.1 - 1 cm. Euhedral, fine- and coarse-grained pyrite are disseminated in the matrix. Some framboidal pyrites are visible. Trace chalcopyrites are observed in fine-grained. Continuous foliation defined by the alignment of clasts and minerals (micas) within the matrix. Coarse-grained pyrites define also a foliation.	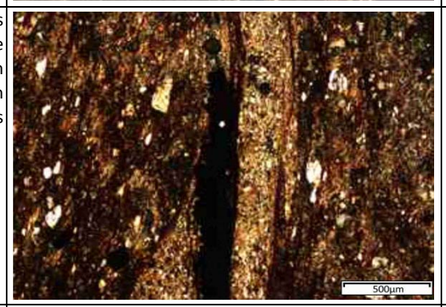	
TS3	205.13	SDT	Ng 1.1.1.3	Py>> Cpy	0.1				3	Diamictite in a fine-grained matrix (clasts ≤5%). The size of clasts varies from 0.1 to 0.5 cm; they are composed of quartz, micas and chlorite. The matrix within the rock is mainly composed of quartz and micas. Framboidal, euhedral, fine- and coarse-grained pyrites are disseminated in the matrix; they associated with sphalerite. Rare trace chalcopyrites are observed in dissemination. Chlorite forms fringe to coarse-grained and euhedral pyrite.	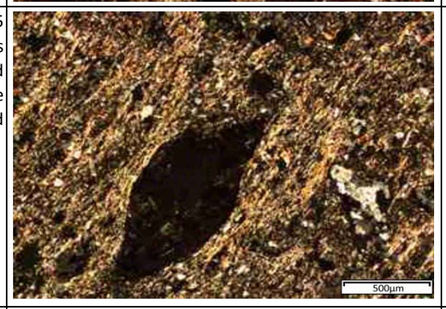	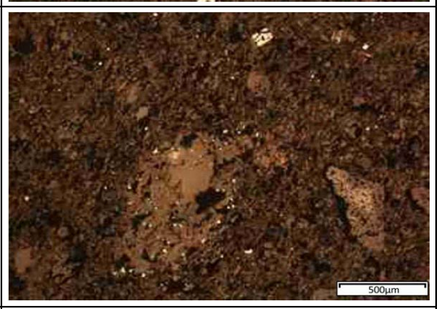
TS4	208.12	SDT	Ng 1.1.1.3	Py≥ Cpy	1.5				3	Clast-poor diamictite in a fine-grained matrix composed of micas and chlorite. The size of clasts is ≤ 1 cm; they are composed of quartz, micas and chlorite and K-feldspar. Euhedral and framboidal pyrites seem to be replaced by chalcopyrite. Continuous foliation defined by the alignment of minerals in the matrix, the alignment of elongate and coarse-grained chalcopyrite. Trace sphalerites are observed. Chlorite, quartz and chalcopyrite form strain shadows to the clasts.	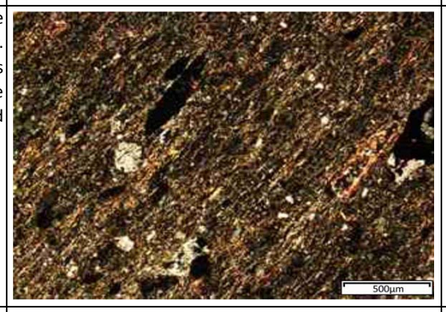	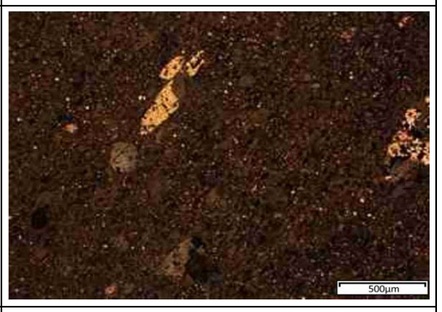
TS5	210.1	SDT	Ng 1.1.1.3	Cpy>>> Py	4.5				0.2	Diamictite, clast-poor small in a fine-grained matrix. Clasts are composed of quartz, muscovite, carbonate and chlorite; their size is < 0.5 cm. Chalcopyrite occurs in dissemination and in the replacement of clasts. Trace euhedral pyrite seems to be replaced by chalcopyrite. Pyrite is associated with trace sphalerite. Continuous foliation defined by the alignment of coarse-grained chalcopyrite, micas and quartz. Chalcopyrite, chlorite and muscovite form fringe to the quartz clast.	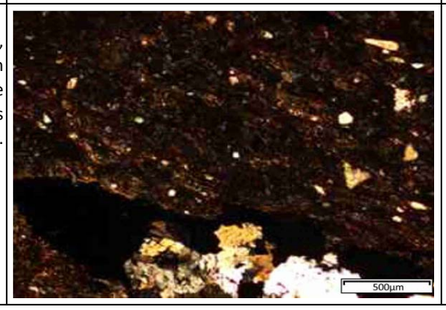	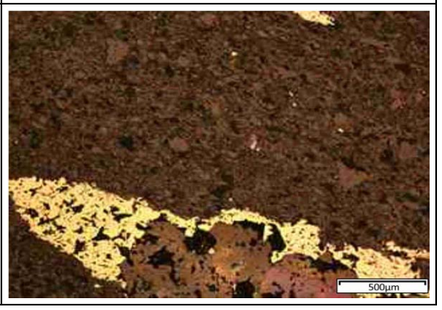

Thin section ID	Depth (m)	Lithologic units	Stratigraphic Units	Mineral association	CPY (%)	BN (%)	CCT (%)	Native CU (%)	PY (%)	Description	Transmitted light_Photomicrograph (XPL and PPL)	Reflected light_Photomicrograph
TS6	211.1	SDT	Ng 1.1.1.3	Cpy>>> Py	5.5				0.2	Diamictite, clast-poor, small clasts size in a fine-grained matrix. The rock is composed of quartz, micas, plagioclases and K-feldspar. Clasts have a similar composition compared to the matrix, their size is less than 0.5 cm. Coarse-grained chalcopyrite tends to replace the entire quartz clast. Chalcopyrite occurs in dissemination and in the replacement of clasts. Trace euhedral pyrite are replaced by chalcopyrite. Continuous foliation defined by the alignment of chalcopyrite, quartz and muscovite.	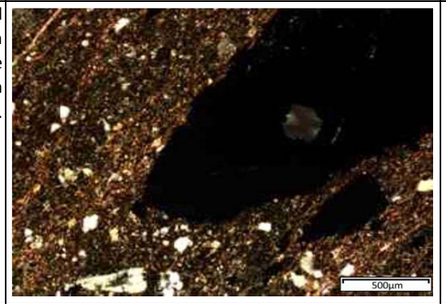	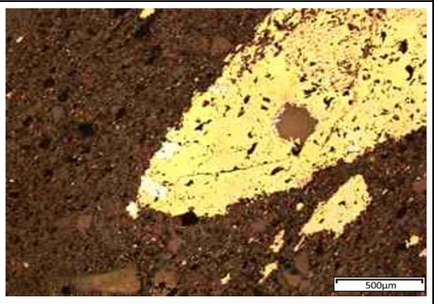
TS7	211.88	SDT	Ng 1.1.1.3	Cpy	5.5				0.1	Clast-poor diamictite, small size clasts in a fine-grained matrix. Clast are composed mainly of quartz, their size is < 0.5 cm. Chalcopyrite occurs as fine- and coarse-grained dissemination. Chalcopyrite increases while pyrite is rare. Trace fine-grained sphalerite are observed. Continuous foliation defined by the alignment of fine- and coarse-grained chalcopyrite. Quartz and chalcopyrite are present in fringes to quartz clasts.	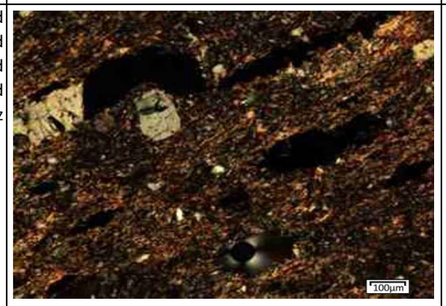	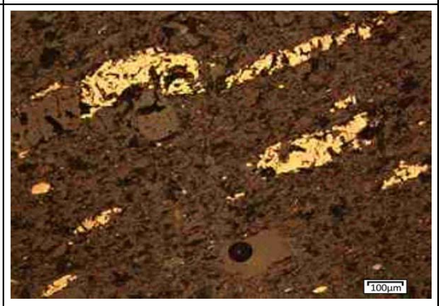
TS8	213.81	SDT	Ng 1.1.1.3	Cpy	6.5					Clast-poor diamictite in a fine-grained matrix. The rock consists mostly of quartz and muscovite. Clasts are small and do not exceed 0.3 mm. Chalcopyrite occurs mostly as fine-grained dissemination (5%), however some coarse-grained grains replacing clasts (2%) are also observed. Rare bornite occurs in dissemination in the matrix. Continuous foliation defined by the alignment of fine- and coarse-grained chalcopyrite.	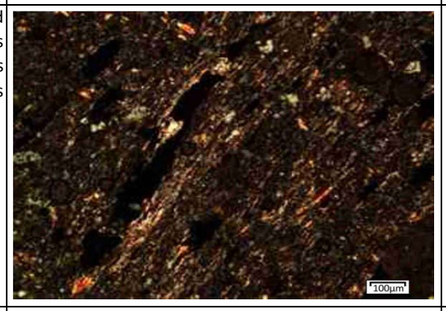	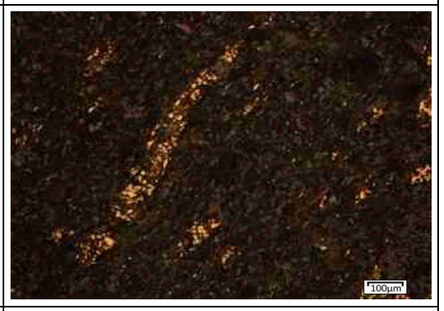
TS9	214.55	SDT	Ng 1.1.1.3	Cpy	7					Clast-poor diamictite in a fine-grained matrix. Clasts are small and do not exceed 0.3 mm. Chalcopyrite occurs in fine- and coarse-grained dissemination (7% fine-grained and 2% coarse-grained). Trace bornites are disseminated in the matrix. Continuous foliation defined by the alignment of fine- and coarse-grained chalcopyrite. Strain shadows are locally observed.	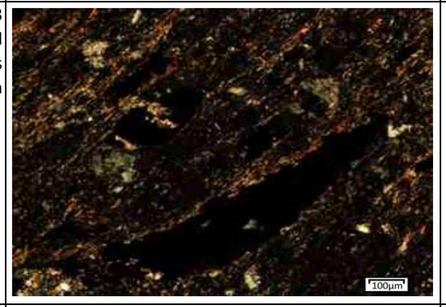	
TS10	216.17	SDT	Ng 1.1.1.3	Cpy≥ Bn	1.5	15	0.3			Clast-poor diamictite in a fine-grained matrix. The size of clasts is less than 0.5 cm. Abundant fine-grained bornites are disseminated in the matrix. Chalcopyrite occurs in the replacement of clasts and as fine-grained dissemination. Possible trace of chalcocite in dissemination in the matrix. Continuous foliation defines by the alignment of sulphides. Rare strain shadows are observed, they are composed mainly with copper sulphides.	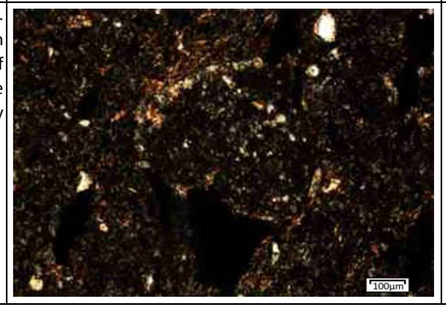	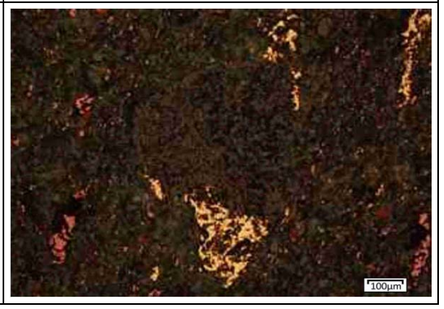

Thin section ID	Depth (m)	Lithologic units	Stratigraphic Units	Mineral association	CPY (%)	BN (%)	CCT (%)	Native CU (%)	PY (%)	Description	Transmitted light_Photomicrograph (XPL and PPL)	Reflected light_Photomicrograph
TS11	217.24	SST/SSL	Ng 1.1.1.3	Bn>> Cpy	7	20				Thin section composed of siltstone and sandstone. The rock is composed of quartz and micas. Chalcopyrite occurs as fine- and coarse-grained disseminations associated with bornite. Continuous foliation defined by the alignment and elongation of fine- and coarse-grained bornite/chalcopyrite. Minerals within the matrix are also defining a S1 foliation.	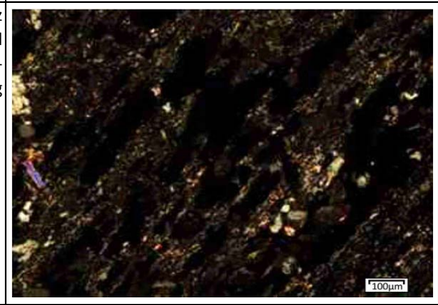	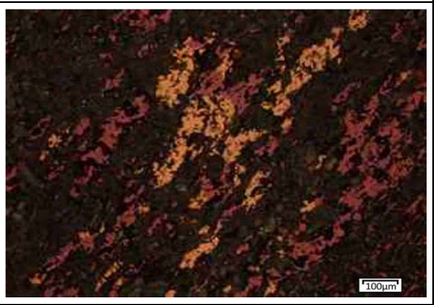
TS12	218.21	SST	Ng 1.1.1.3	Bn>> Cpy	0.2	10				Medium grained sandstone composed of quartz, plagioclases and micas. The mineralisation consists of fine-grained bornite disseminated in the rock. Bornite defines a continous foliation.	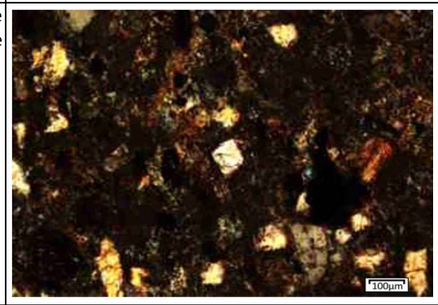	
TS13	218.71	SST/SSL	Ng 1.1.1.3	Bn>> Cct	0.2	25	4			Thin section including sandstone and siltstone. The rock is composed of quartz and micas with occasional large quartz grains. Bornite is finely disseminated and associated with some chalcocite. Continous foliation defined by the alignmnent and elongation of copper sulphides. The rock is slighlty folded (sedimentary feature).		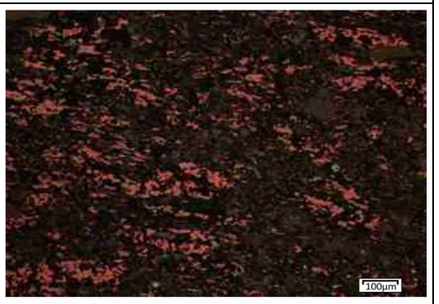
TS14	219.28	SST/SSL	Ng 1.1.1.3	Bn> Cpy >> Cct	6	18				Thin section including siltstone and sandstone. Rock composed of quartz and micas. Bornite is abundant compared to chalcopyrite. Slaty cleavage defined by the alignment of sulphides. A soft-sedmient deformation texture is observed.	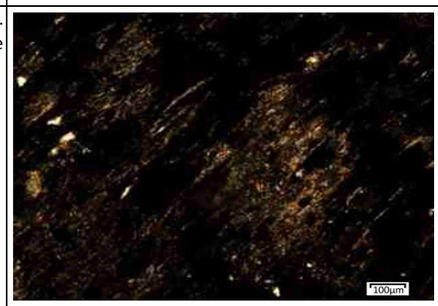	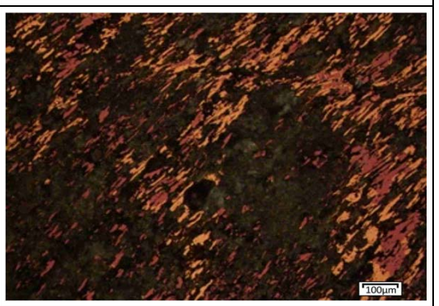
TS15	219.6	SST/SSL	Ng 1.1.1.3	Bn> Cpy > Cct	14	10	4			Thin section composed of siltstone and sandstone. The matrix consists of quartz and micas. Chalcopyrite, bornite and chalcocite are disseminated in the rock, they show a fine-grained, aligned and elongated textures that define a continuous foliation. Also a soft-sediment deformation texture is observed on the thin section.	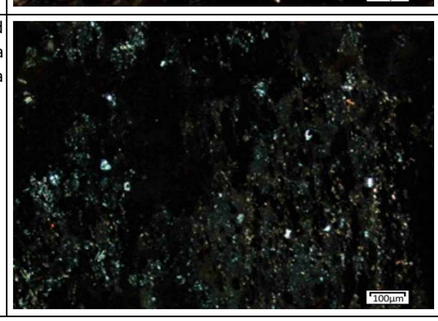	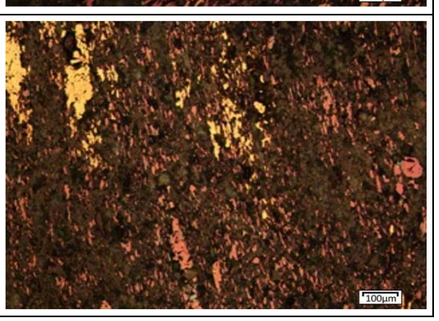

Thin section ID	Depth (m)	Lithologic units	Stratigraphic Units	Mineral association	CPY (%)	BN (%)	CCT (%)	Native CU (%)	PY (%)	Description	Transmitted light_Photomicrograph (XPL and PPL)	Reflected light_Photomicrograph
TS16	220.23	SST/SSL	Ng 1.1.1.3	Bn> Cct >>> Cpy	0.8	16	7			Rock composed of siltstone and sandstone. The matrix consists of quartz and micas. The minerals in the matrix are aligned and define an S1 foliation. Chalcopyrite, bornite and chalcocite occurs as fine-grained, aligned and elongate grains illustrating a slaty cleavage texture.	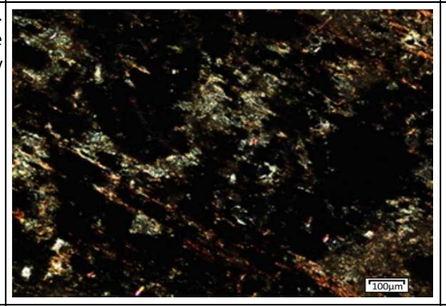	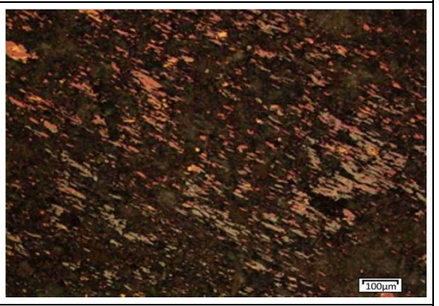
TS17	220.97	SDT	Ng 1.1.1.3	Bn> Cpy	1.5	3.3				Thin section including a clast-moderate diamictite (6 to 9%) in a fine-grained matrix. The size of clasts varies from 0.1 to 1cm. The matrix is composed of quartz, micas and chlorite. Clasts are composed of quartz, schists, chlorite, carbonates and micas. The mineralisation consists of fine-grained disseminated bornite that is associciated with chalcopyrite. Possible trace of covelite in association with bornite. Continuous foliation defined by the alignment of bornite.	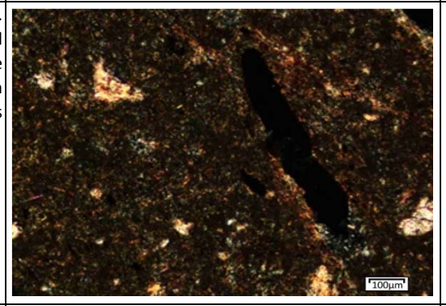	
TS18	221.71	SDT/SST	Ng 1.1.1.2	Bn> Cpy>> Cct	5.5	23	4			Thin section including a clast-poor diamictite (≤ 5%) in a fine-grained matrix composed of quartz, muscovite, biotite and chlorite. Clasts are composed mainly of quartz. The mineralisation is very fine- to fine-grained disseminated in the matrix. Bornite> chalcopyrite> chalcocite. Continous foliation and slaty cleavage defined by copper sulphides. Mesoscopic normal faults from syn-sedimentary origin are observed.	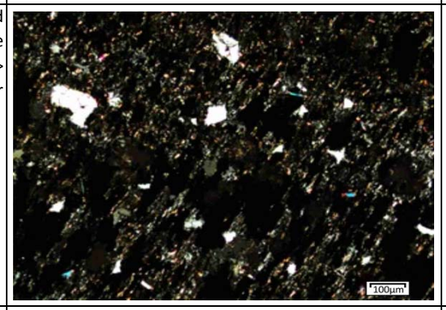	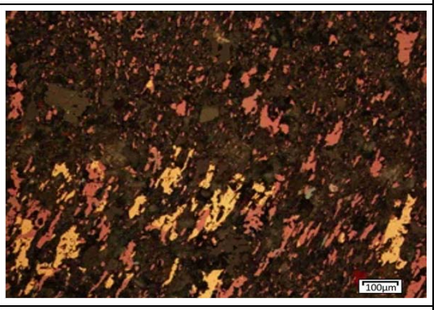
TS19	222.6	SSL	Ng 1.1.1.2	Bn> Cpy> Cct	14	21	0.5		0.1	Mudstone intercalated with very fine-grained siltstone. The gangue is composed of quartz, muscovite, biotite and chlorite. The mineralisation is very fine-grained and seems to replace the rock. Bornite> chalcopyrite>>> chalcocite. Slaty cleavage defined by the alignment and elongation of sulphides.	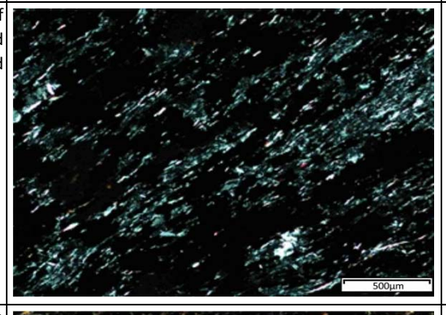	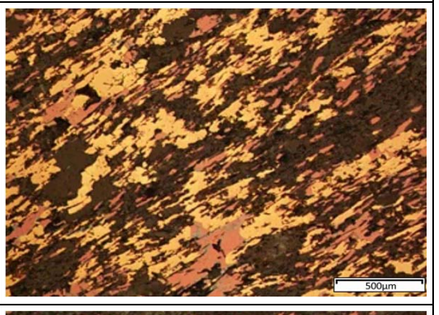
TS20	223.48	SDT	Ng 1.1.1.2	Bn> Cpy> Cct	1.5	18	0.2			Clast-poor diamictite in a fine-grained matrix composed of quartz, muscovite, chlorite and plagioclases. The composition of clasts is similar to that of the matrix. Copper sulphides are finely disseminated, they are composed of bornite> chalcopyrite> chalcocite. Slaty cleavage defines by the alignment of sulphides.	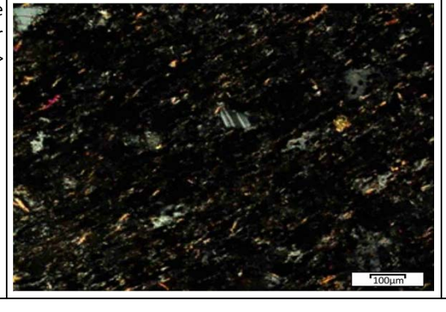	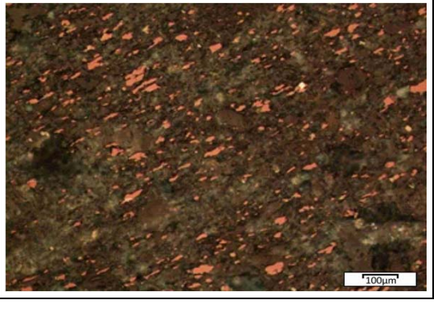

Thin section ID	Depth (m)	Lithologic units	Stratigraphic Units	Mineral association	CPY (%)	BN (%)	CCT (%)	Native CU (%)	PY (%)	Description	Transmitted light_Photomicrograph (XPL and PPL)	Reflected light_Photomicrograph
TS21	224.96	SSL	Ng 1.1.1.2	Bn> Cpy> Cct	1.5	8	0.1			Thin section including a finely laminated siltstone composed of quartz, muscovite and biotite and plagioclases. The space between lamiations ranges from 0.1 mm to 0.5 cm. The mineralisation is mostly disseminated and consists of fine-grained bornite associated with chalcopyrite. Coarse-grained bornite are also observed. The rock shows a continous foliation defined by the alignment of copper sulphides. S1 foliation is sub-perpendicular to S0 bedding.	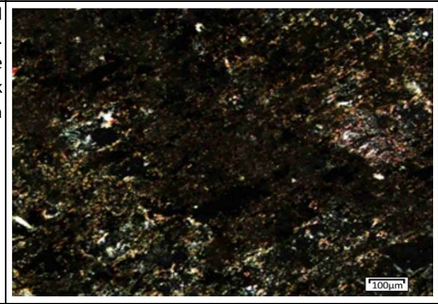	
TS22	225.35	SDT	Ng 1.1.1.2	Cct>> Bn>> Cpy		0.5	1.8			Clast-rich diamictite in a silty to sandy matrix composed of quartz, micas, carbonates and plagioclases. The composition of clasts is similar to that of the matrix; their size is less than a centimetre. Chalcocite is the most abundant copper sulphide, it is associated with trace bornite. Weak foiliation defined by the alignment of chalcocite.	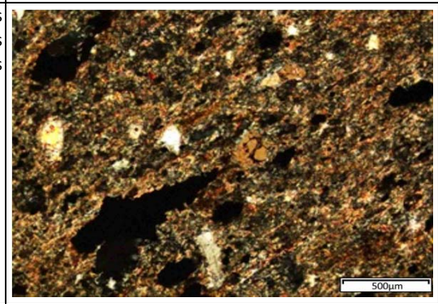	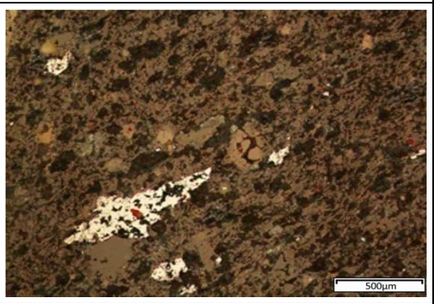
TS23	226.13	SDT	Ng 1.1.1.1	Bn> Cpy> Cct	0.3	1	0.1			Clast-rich diamictite (20 to 30% clasts) comprising a large quartz clast. Clasts are composed of quartz, carbonate, micas, chlorite and plagioclases. The matrix is silty to sandy, it is composed mainly of quartz and micas. Disseminated chalcocite is observed in the matrix. Carbonates, bornite, chalcopyrite constitute the strain shadow to the large quartz clast. A strain cape is observed around this large clast.	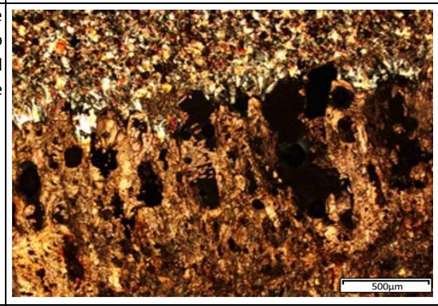	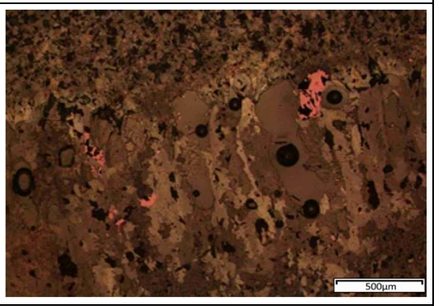
TS24	226.97	SDT	Ng 1.1.1.1	Bn> Cct	0.1	1.2	0.6			Thin section including a clast-rich diamictite (20 to 30%). Clasts are composed of schists, quartz, carbonates, plagioclases, muscovite and chlorite. The size of clasts varies from 0.1 to 0.5 cm. The matrix is fine-grained and his composition is similar to that of the clasts. The mineralisation consists of fine-grained bornite associated with some chalcocite. Bornite is locally observed in the replacement of clasts.	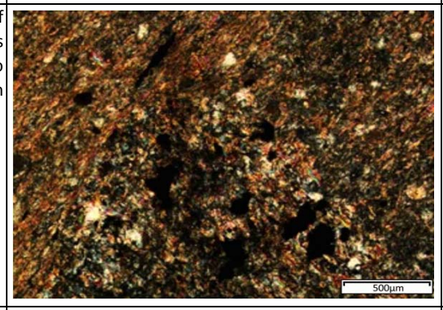	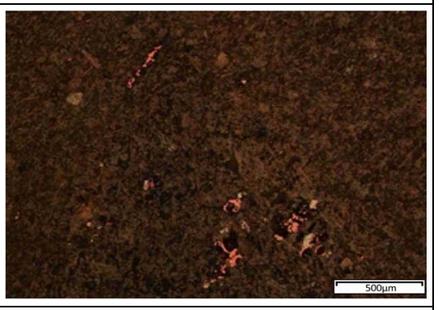
TS25	228.71	SDT	Ng 1.1.1.1	Bn> Cct	0.6	0.8	0.3			Clast-poor diamictite (5 to 10% clasts) in a fine-grained matrix that is composed of quartz, micas, carbonate and plagioclases. The size of clasts is less than a centimetre and the composition similar to that of the matrix. The mineralisation consists of chalcocite, bornite and trace chalcopyrite. Within copper sulhides, the replacement relationship is observed: chalcocite seems to replace bornite which seems to replace chalcopyrite. Weak foliation defined by the alignmnent of copper sulphides.	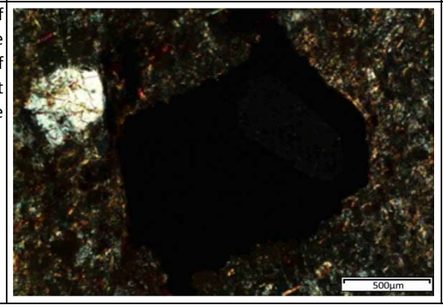	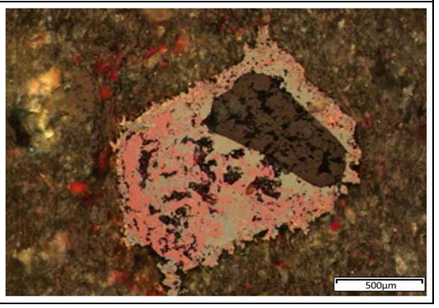

Thin section ID	Depth (m)	Lithologic units	Stratigraphic Units	Mineral association	CPY (%)	BN (%)	CCT (%)	Native CU (%)	PY (%)	Description	Transmitted light_Photomicrograph (XPL and PPL)	Reflected light_Photomicrograph
TS26	230.28	SDT	Ng 1.1.1.1	Cct	0.05	0.1	1.8			Thin section including a clast-poor diamictite (about 7% clasts) in a fine-grained matrix. Clasts size less than a centimetre. The matrix is silty to sandy, it is composed of quartz and micas. The copper mineralisation is mainly composed of chalcocite, however rare trace of bornite is associated with some chalcopyrite. Chalcocite grains are aligned and defines a weak foliation. Iron oxides are disseminated in the rock.	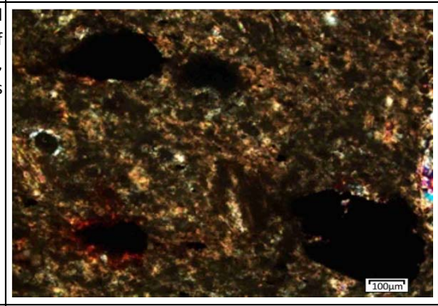	
TS27	231.77	SDT	Ng 1.1.1.1	Cct		0.1	1.5			Clast-rich diamictite (20 to 25% clasts) in a fine-grained matrix composed of quartz and micas with minor plagioclases and carbonates. Clasts are composed of schists, quartz, chlorite, carbonates and micas. The mineralisation consists of chalcocite associated with rare bornite. Weak foliation defined by the alignmnent of sulphides. Iron oxides are disseminated in the matrix.	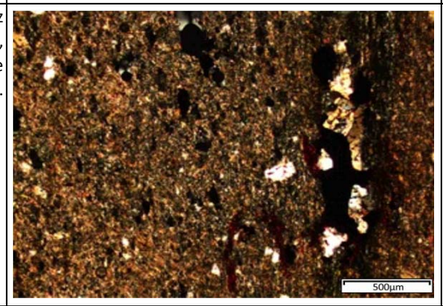	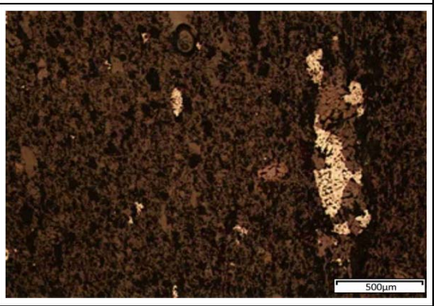
TS28	233.5	SDT	Ng 1.1.1.1	Cct>> Cu			1.2	0.2		Clast-moderate diamictite (10 to 15% clasts) in a fine-grained matrix. The matrix is mainly composed of quartz, micas and minor carbonates. The size of clasts is small, generally less than 0.5 cm. Chalcocite occurs as fine-grained dissemination in the matrix and as coarse-grained in the replacement of clasts. Trace native copper are disseminated in the fine-grained matrix. Some chalcocite/bornite occur in strain fringe to a quartz clast. Iron oxides are disseminated in the matrix.	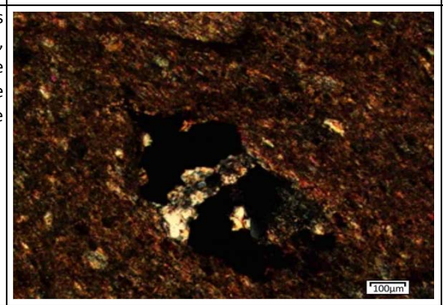	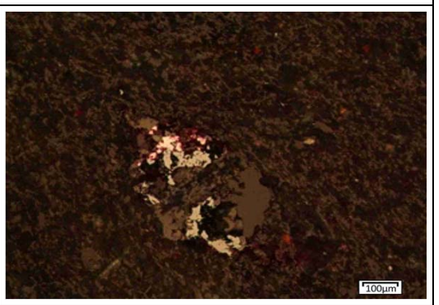
TS29	235.92	SDT	Ng 1.1.1.1	Cct>> Cu			1.5	0.2		Clast-rich diamictite (30 - 40% of clasts) in a fine-grained matrix. A large (3cm size) quartz clast is observed on the thin section. The matrix is fine-grained and composed of quartz, micas, chlorite and plagioclases. Clasts display a similar composition to that of the matrix; their size is generally less than 0.5 cm. Chalcocite occurs as fine-grained disseminations and as coarse-grained in the replacement of clasts where it is associated with trace of native copper. Weak foliation defined by the alignment of chalcocite. Iron oxides are disseminated in the matrix.	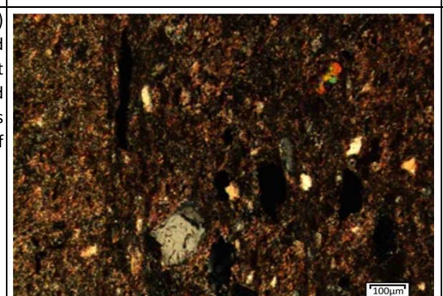	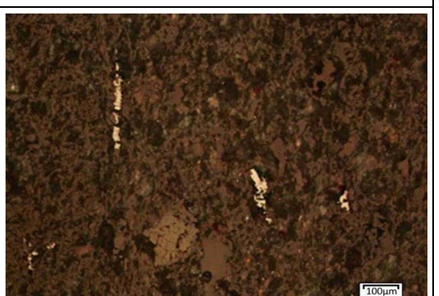
TS30	238.56	SDT	Ng 1.1.1.1	Cct>> Cu			1.2	0.2		Diamictite with about 15% clasts. The matrix is fine-grained and composed of quartz, micas, carbonate and chlorite. Clasts are small and composed of schists, chlorite, quartz and carbonates. Chalcocite occurs as fine-grained disseminations in the matrix and as coarse-grained in the replacement of clasts. Native copper is observed in dissemination and in the thin veins (1 mm). Iron oxides are disseminated in the rock. Weak foliation defined by the alignment of chalcocite.	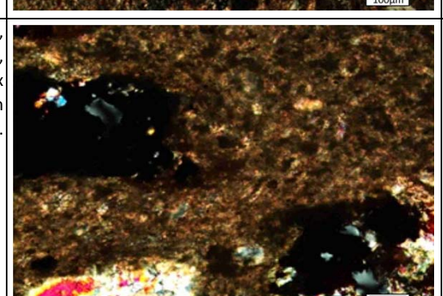	

Thin section ID	Depth (m)	Lithologic units	Stratigraphic Units	Mineral association	CPY (%)	BN (%)	CCT (%)	Native CU (%)	PY (%)	Description	Transmitted light_Photomicrograph (XPL and PPL)	Reflected light_Photomicrograph
TS31	241.96	SDT	Ng 1.1.1.1	Cct>> Cu	0.2		0.8	0.2		Clast-rich diamictite (25 to 35% of clasts) in a fine-grained matrix composed of quartz, micas and chlorite. Clasts are composed quartz, carbonates and schists, their size of varies from 0.1 to 1.5 cm. The mineralisation consists of disseminated fine-grained chalcocite associated with native copper. Iron oxides are disseminated in the rock. Very weak foliation defined by the alignment of fine-grained chalcocite. Thin iron oxides veins are parallel to the S1 foliation.	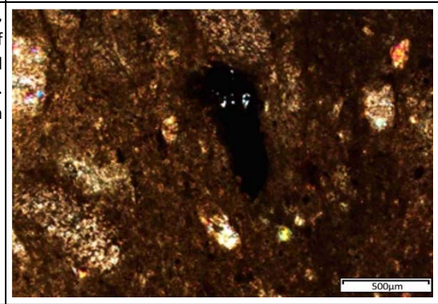	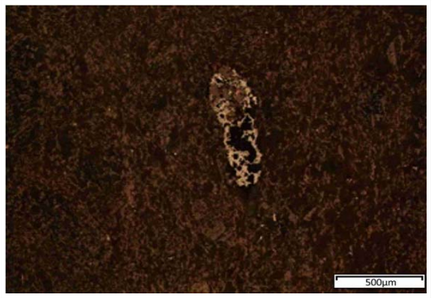
TS32	245.5	SDT	Ng 1.1.1.1	Cct			0.01			Clast-moderate diamictite (10 to 15% of clasts) in a silty to sandy matrix. This matrix is composed mainly of quartz and micas. The composition of clasts is similar to that of the matrix. Trace fine-grained chalcocite are disseminated in the matrix. Slaty cleavage defined by the alignment of quartz and micas.	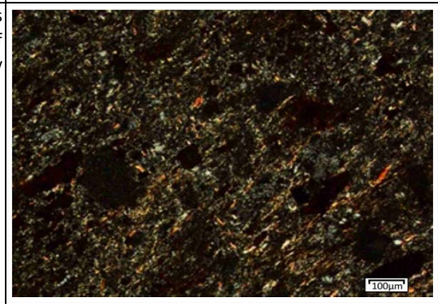	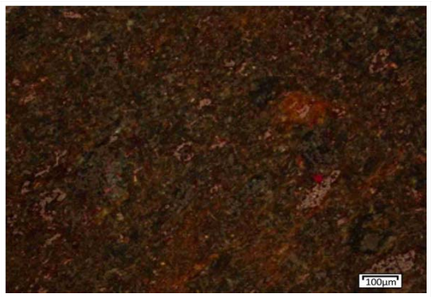
TS34	249.9	SST	R4.2	Hae						Poorly laminated, fine- to medium-grained Roan feldspathic sandtone. The rock is composed of quartz, feldspar, chlorite and biotite. The grain size varies from 3 - 500 µm. Abundant iron oxides disseminated in the rock.	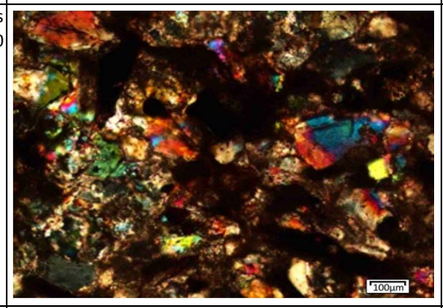	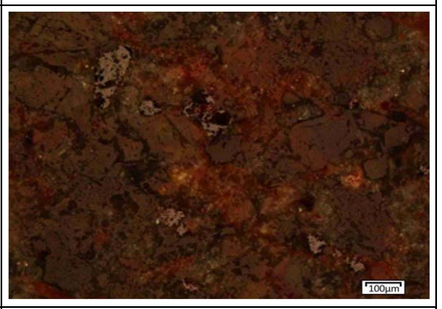
TS35	251.96	SST	R4.2	Hae						Roan feldspathic sandstone composed of quartz, feldspar and micas. The size of grains varies from 30 - 500 µm. Presence of thin veins composed of carbonates. Iron oxides are disseminated in the rock.	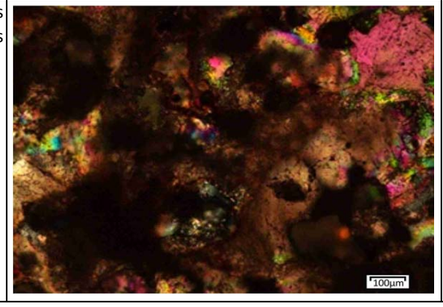	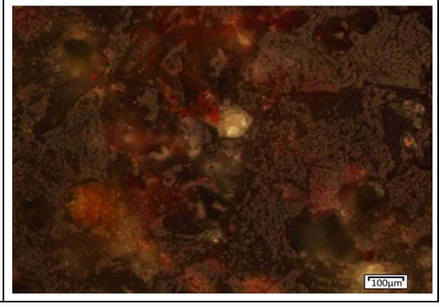

Borehole ID	Thin section ID	Stratigraphic units	Lithologic units	Description	Transmitted light_Photomicrograph (XPL and PPL)	Reflected light_Photomicrograph
DD904	115.22	Ng 1.1.6	SDT	Thin section consists of a clast-poor diamictite with small sized clasts. The matrix constitutes 95%, it is composed of quartz, biotite, feldspar, chlorite and muscovite (5 -25 µm). Clasts are dominantly composed of quartz, feldspar, micas and carbonate. Plagioclase is well observed in the cross-polarized. 0.1 to 1% of euhedral pyrite is disseminated in the matrix. Rare Trace coarse-grained chalcopyrite around the clasts.	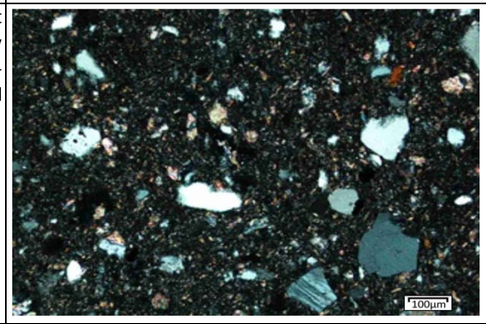	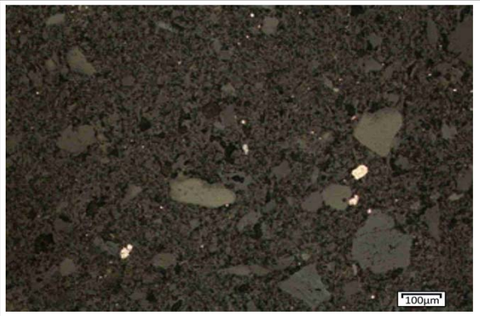
DD904	149.5	Ng 1.1.6	SST	Thin section including a laminated sandststone intercalated with siltstone. The matrix is mainly composed of quartz, feldpar, chlorite, carbonate and minor micas. The grain size is varying from 5 to 50 µm. The mineralisation consists mainly of pyrite that occurs as fine-grained (1 to 1.5%) and as coarse-grained dissemination (0.1 to 0.5%).	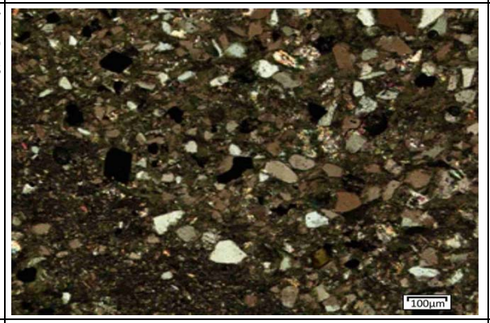	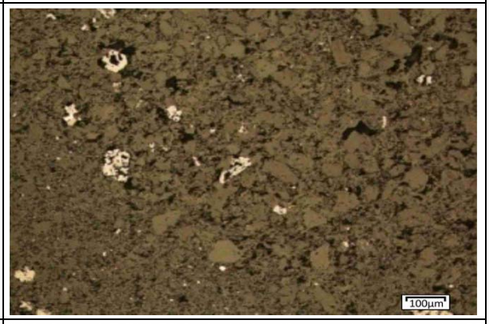
DD904	262.38	Ng 1.1.6	SST	Thin section composed of a laminated sandstone. The rock is composed of quartz, feldspar, micas, chlorite and some carbonates. The overall size of grains varies from 3 to 25 µm. Laminations and cross laminations are observed, they are spaced with about 10 µm. The mineralisation consists of 0.1 to 0.5% of euhedral and framboidal pyrites disseminated in the matrix (5 - 25 µm).	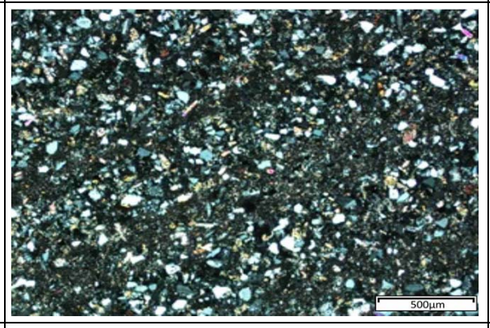	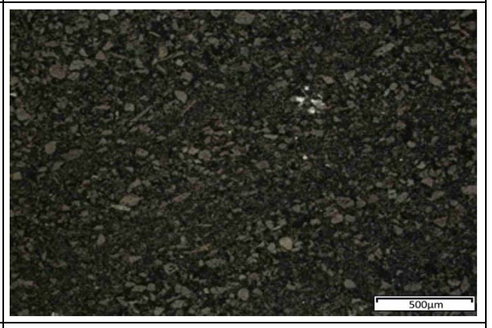
DD904	536.06	Ng 1.1.5	SDT	Thin section composed of clast-poor diamictite with small sized clasts (0.1 to 0.5cm). The matrix constitutes about 90% of the thin section and clasts represent about 8%. The matrix is very fine-grained and composed mainly with quartz, micas, chlorite, plagioclases and K-feldspar. The composition of clasts is similar to that of the matrix. The mineralisation consists of 0.1 to 0.8% of euhedral and framboidal pyrite disseminated in the matrix.	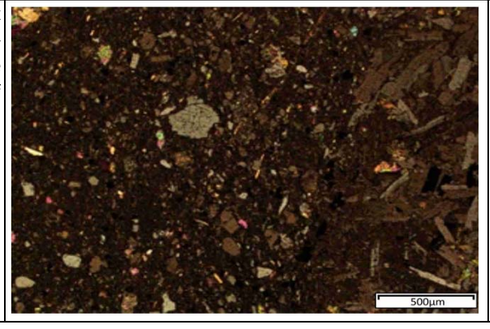	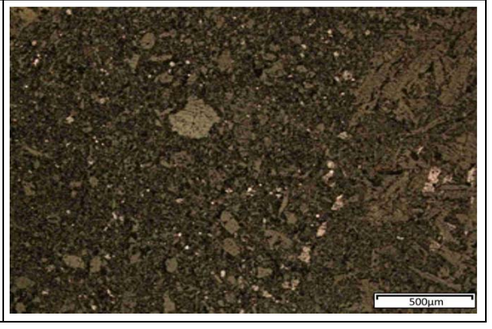

Borehole ID	Thin section ID	Stratigraphic units	Lithologic units	Description	Transmitted light_Photomicrograph (XPL and PPL)	Reflected light_Photomicrograph
DD904	568.9	Ng 1.1.5	SCG	Thin section including a conglomerate. The rock is composed of quartz, plagioclases, carbonates (possible calcite), K-feldspar, chlorite and micas. Grains range from 1 to 3 mm, they are cemented by a fine-grained matrix constitutes of quartz, chlorite and micas. The mineralisation is mainly composed of euhedral (0.5%) and fine-grained pyrite (0.3%) disseminated in the rock.	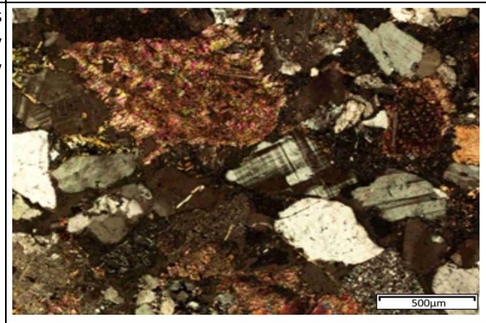	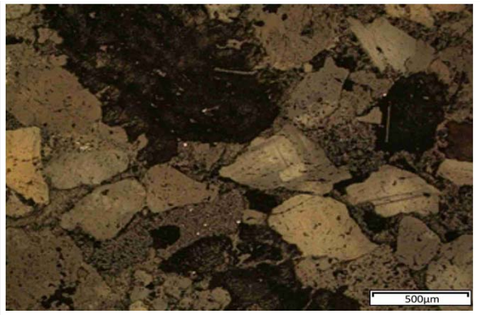
DD904	659.8	Ng 1.1.5	SSL	Thin section including a finely laminated pyritic siltstone. The gangue is fine-grained and composed of quartz, micas, chlorite and carbonates. The overall grain size varies from 2 to 40 µm with rare coarse-grained material which are up to 150 µm. Laminations are spaced with 0.1 to 1 cm. The mineralisation consists of 15 to 25 % of framboidal pyrite and rare coarse-grained pyrite (0.01 to 0.2 cm).		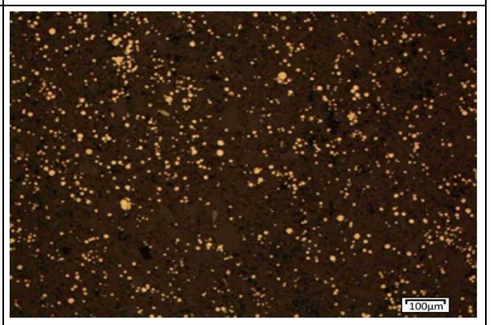
DD904	769.38	Ng 1.1.5	SDT	Thin section including a clast-moderate diamictite (15%). The matrix constitutes 80% of the thin section, it is fine-grained (5 - 25µm) and composed of quartz, micas, carbonates with minor chlorite. Clasts are composed mainly of quartz, plagioclases, feldspar, micas and carbonates. The mineralisation is constituted of 12 to 15% of framboidal pyrite associated with 3 - 5% of coarse-grained pyrite. Coarse-grained pyrite is locally replacing clasts.	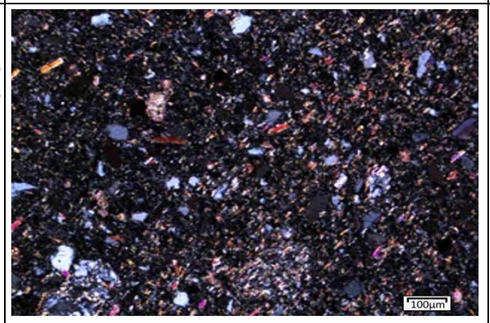	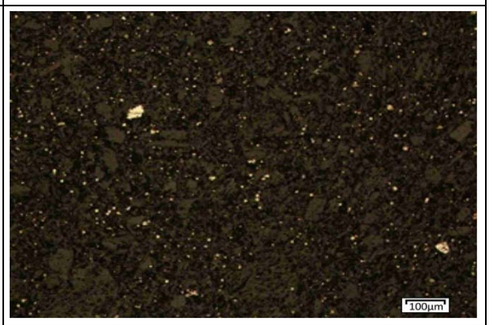
DD904	789.08	Ng 1.1.4	SSL	Thin section including a finely laminated pyritic siltstone. The gangue is very fine- and fine-grained (5 to 20 µm), it is composed of quartz, pyrite, chlorite, carbonate, biotite and muscovite. Presence of occasional dropstones composed mainly of quartz and plagioclases. Laminations are spaced with 10 to 50 µm. Euhedral pyrites with chlorite in strain shadow appear to overgrow the laminations. The mineralisation consists of 15 to 20% of euhedral and coarse-grained pyrite; and 20- 25% framboidal pyrite. Iron oxides are also present in the edge of pyrite grains.	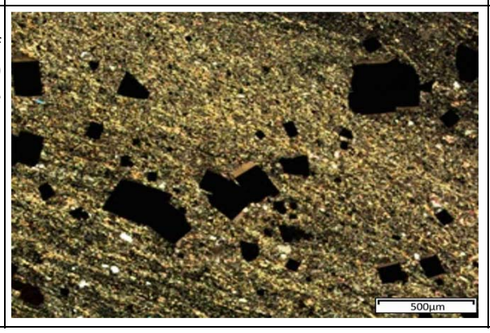	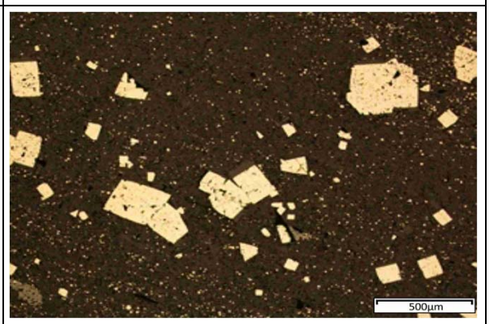

Borehole ID	Thin section ID	Stratigraphic units	Lithologic units	Description	Transmitted light_Photomicrograph (XPL and PPL)	Reflected light_Photomicrograph
DD904	823.66	Ng 1.1.3	SDT	Thin section including a clast-moderate diamictite (20% of clasts) in a fine-grained matrix (80%). The rock contains quartz, biotite, muscovite, potassium feldspar, chlorite and minor carbonate (grains varying from 3 – 40 µm). Clasts are sub-rounded and show a similar composition to that of the matrix. The overall size of clasts ranges from 1 mm to 1 cm. Pyrite is observed in fine- and coarse-grained dissemination and the mineral estimation ranges from 7 to 12%. Pyrite and chlorite occur in strain shadow to quartz clasts.	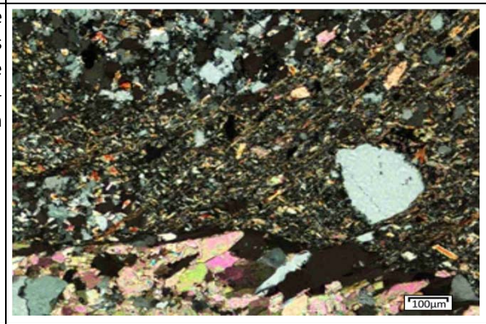	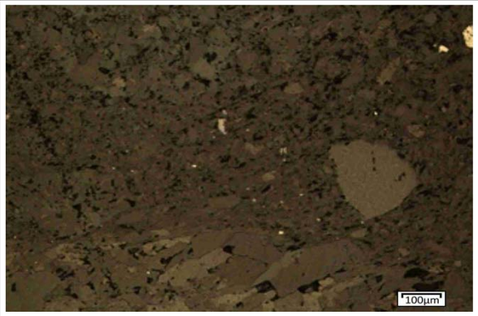
DD904	837.4	Ng 1.1.3	SDT	Thin section including a clast-moderate diamictite (85% matrix and about 10% clasts) in a fine-grained matrix composed of quartz, biotite, muscovite, chlorite and carbonate minerals. The matrix size ranging from 4 – 20 µm. Clasts are composed of quartz, carbonates (calcite), micas, chlorite, muscovite and potassium feldspar. The overall size of clasts is varying from 1 to 4 mm. The mineralisation consists of fine- (5 to 7%) and coarse-grained euhedral pyrite (1 to 1.5%) disseminated in the matrix and in the replacement of clasts.		
DD904	979.6	Ng 1.1.3	SDT	Thin section including a clast-moderate diamictite with a large argillite clast in the middle (15 % of clasts and 85% of matrix). The matrix is fine-grained and composed of quartz, biotite, muscovite, chlorite and carbonate. Clasts are sub-rounded and composed of quartz, potassium feldspar, biotite, muscovite, carbonate and chlorite. The size of clasts varies from 0.3 to 3 mm. The large clast in the middle is composed of quartz and unknown black minerals. Pyrite is the main sulphide mineralisation seen in the thin section. It occurs as fine- (5 to 7%) and coarse-grained dissemination (1 to 1.5%).	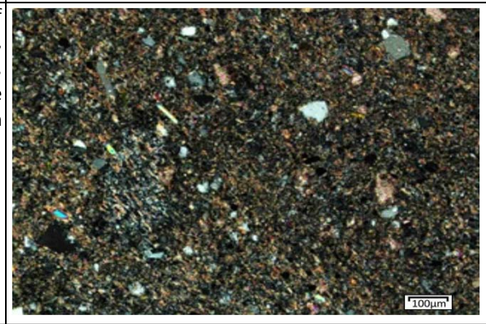	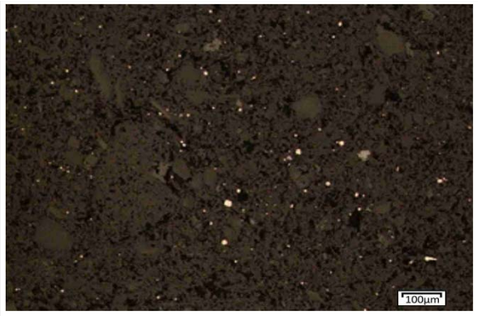
DD915	581.67	R 42	SST	Thin section consists of arkosic graywackes intercalated with thin layers of siltstone. The arkosic graywackes consists of quartz, micas (muscovite, biotite), plagioclases and microclines cemented with quartz, muscovite, chlorite. The difusely laminated siltstone is composed of quartz and specular haematite. The overall grain size ranges from 10 to 120 µm. The grains are not sorted or aligned. The space between laminations varies from 0.1 to 1 mm. Pyrite is the main mineralisation, it occurs as fine-grained dissemination (3 – 15 µm).	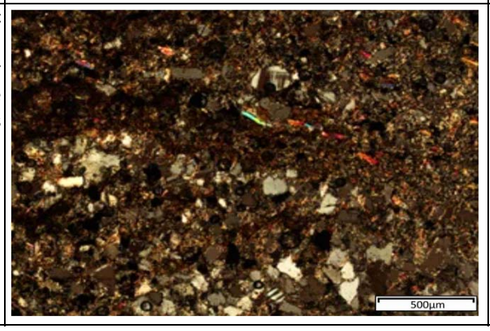	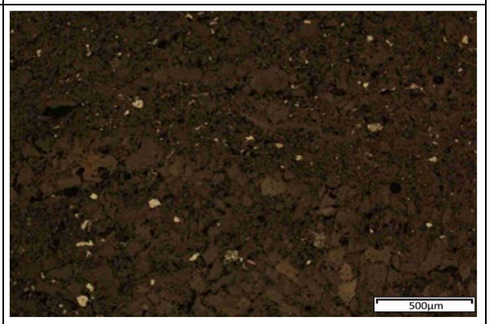

BHID	From	Sample #	Lithology	Stratigraphic unit	Feature code	Comments
DD440	158.12	FT_05	SSL	Ng1.1.2	Weak foliation	
DD888	265.72	FT_29	SDT	Ng1.1.1	Strain shadows and moderate foliation	Presented in chapter 4
DD014	522.46	FT_31	SDT	Ng1.1.1	Strain shadows and moderate foliation	Presented in chapter 4
DD895	580.46	FT_36	SDT	Ng1.1.1	Strain shadows and moderate foliation	Presented in chapter 4
DD856	137.28	FT_37	SDT	Ng1.1.1	Weak foliation	
DD381	240.16	FT_39	SDT	Ng1.1.1	Strain shadows and moderate foliation	Presented in chapter 4
DD033	234.79	FT_48	SSL	Ng1.1.2	Fold	Presented in chapter 4
DMAK_RD023	96.37	FT_49	SSL	Ng1.1.2	Fold	Presented in chapter 4
DD401	784.63	FT_51	SDT	Ng1.1.1	Strain shadows and weak foliation	Presented in chapter 4
DD944	227.31	FT_66	SDT	Ng1.1.1	Strain shadows and moderate foliation	Presented in chapter 4
DD944	227.31	FT_66H	SDT	Ng1.1.1	Moderate foliation	
DKMC_GD002	379.58	FT_78	SSL	Ng1.1.1	Sub-vertical bedding and strong foliation	Presented in chapter 4
DKMC_GD002	379.58	FT_78H	SSL	Ng1.1.1	Weak to moderate foliation	
DD453	1149.9	FT_79	SDT	Ng1.1.1	Weak foliation	
DD453	1149.9	FT_79H	SDT	Ng1.1.1	Weak to very weak foliation	
DMAK_RD030	641.86	FT_88	SSL	Ng1.1.1	Sub-vertical bedding and strong foliation	Presented in chapter 4
DD895	585.47	FT_98	SDT	Ng1.1.1	Moderate foliation	
DD895	585.47	FT_98H	SDT	Ng1.1.1	Weak foliation	

SEM images

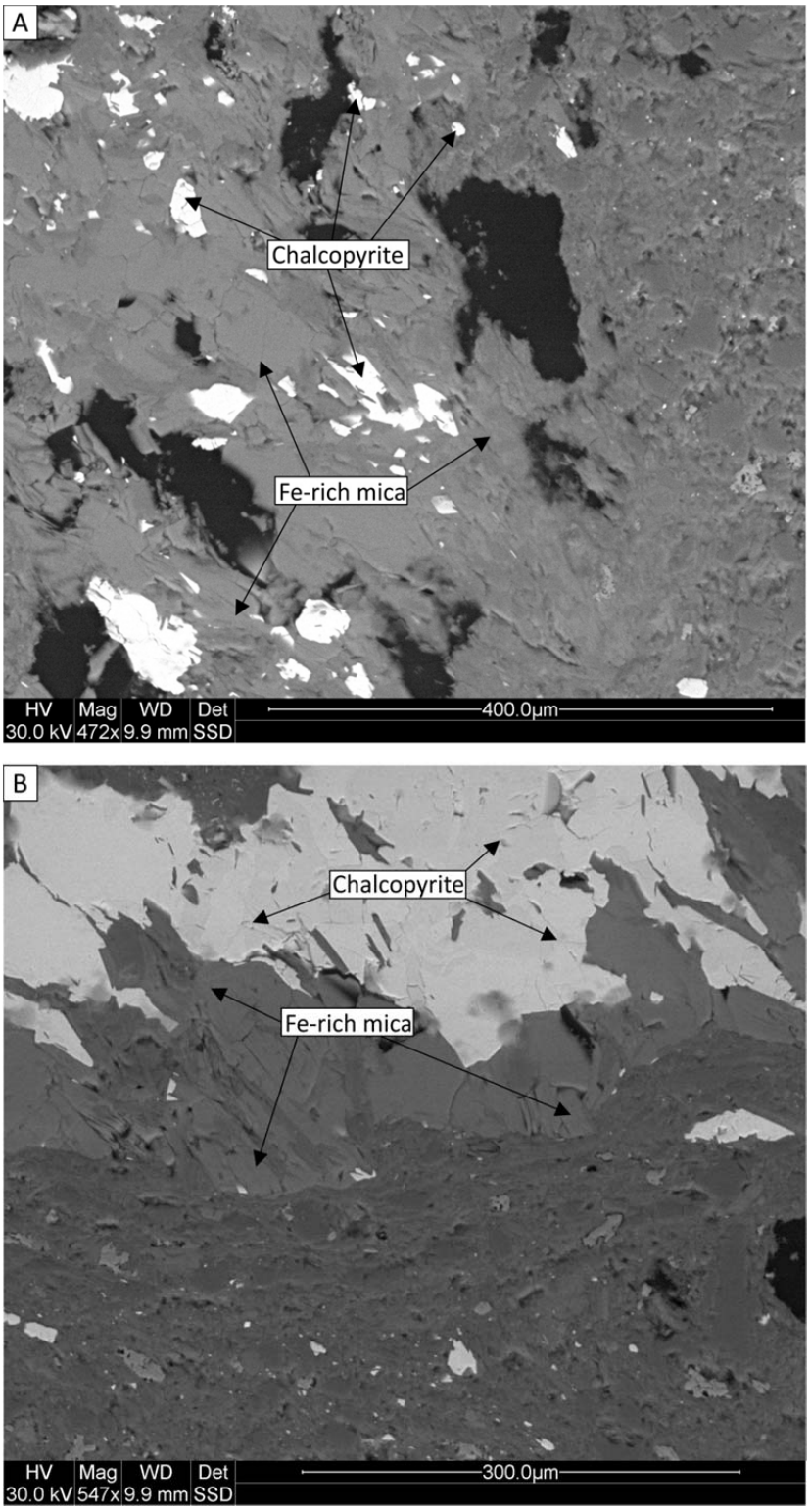

Fig. A.1: (A). Weak foliation defined by the alignment of chalcopyrite and iron-rich mica. (B). Strain shadow composed of chalcopyrite and iron rich mica. Sample FT_37.

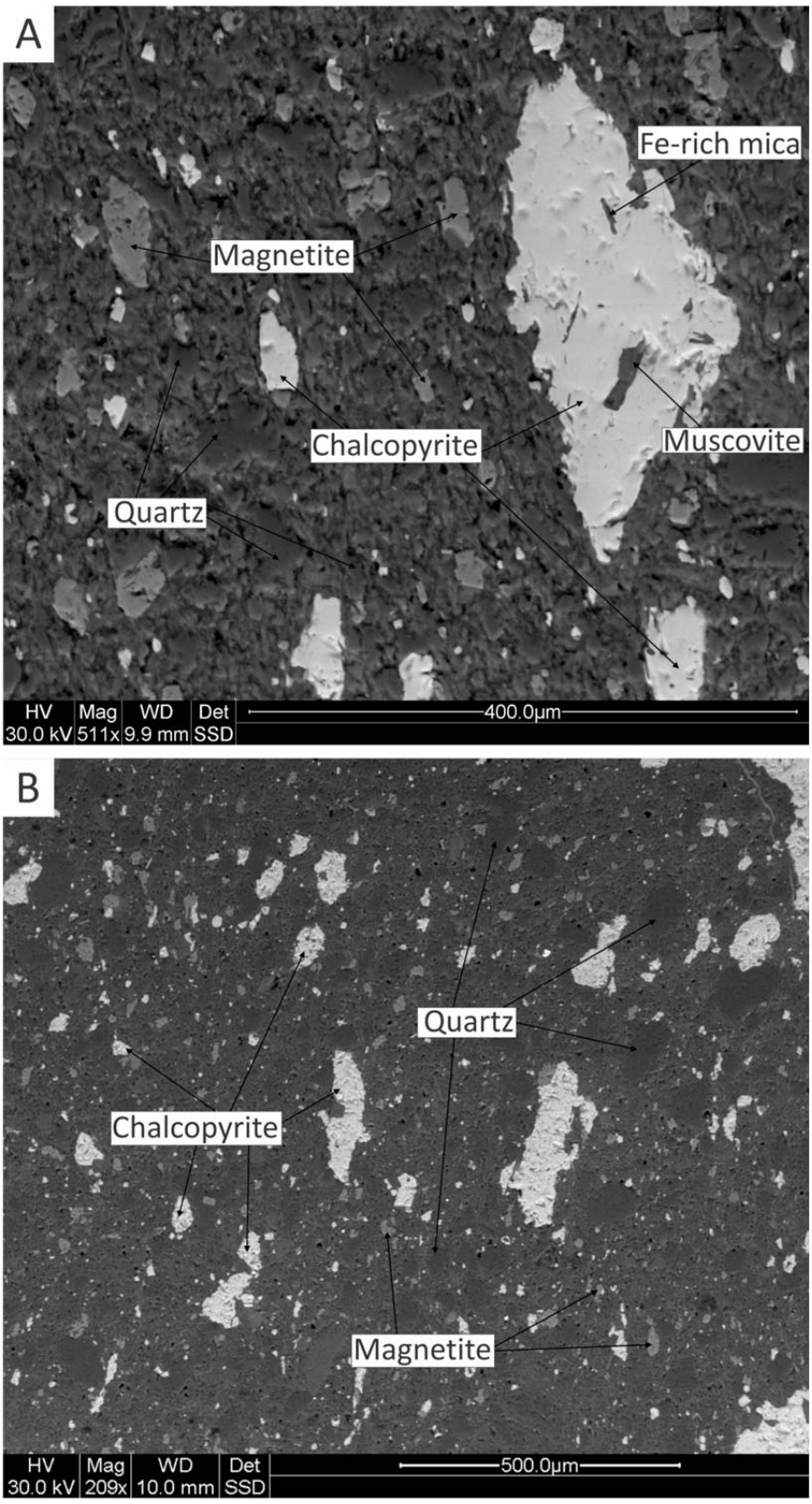

Fig. A.2: Moderate foliation defined by the alignment chalcopyrite, magnetite, quartz and iron-rich mica. (A). Sample FT_66. (B). Sample FT_66H.

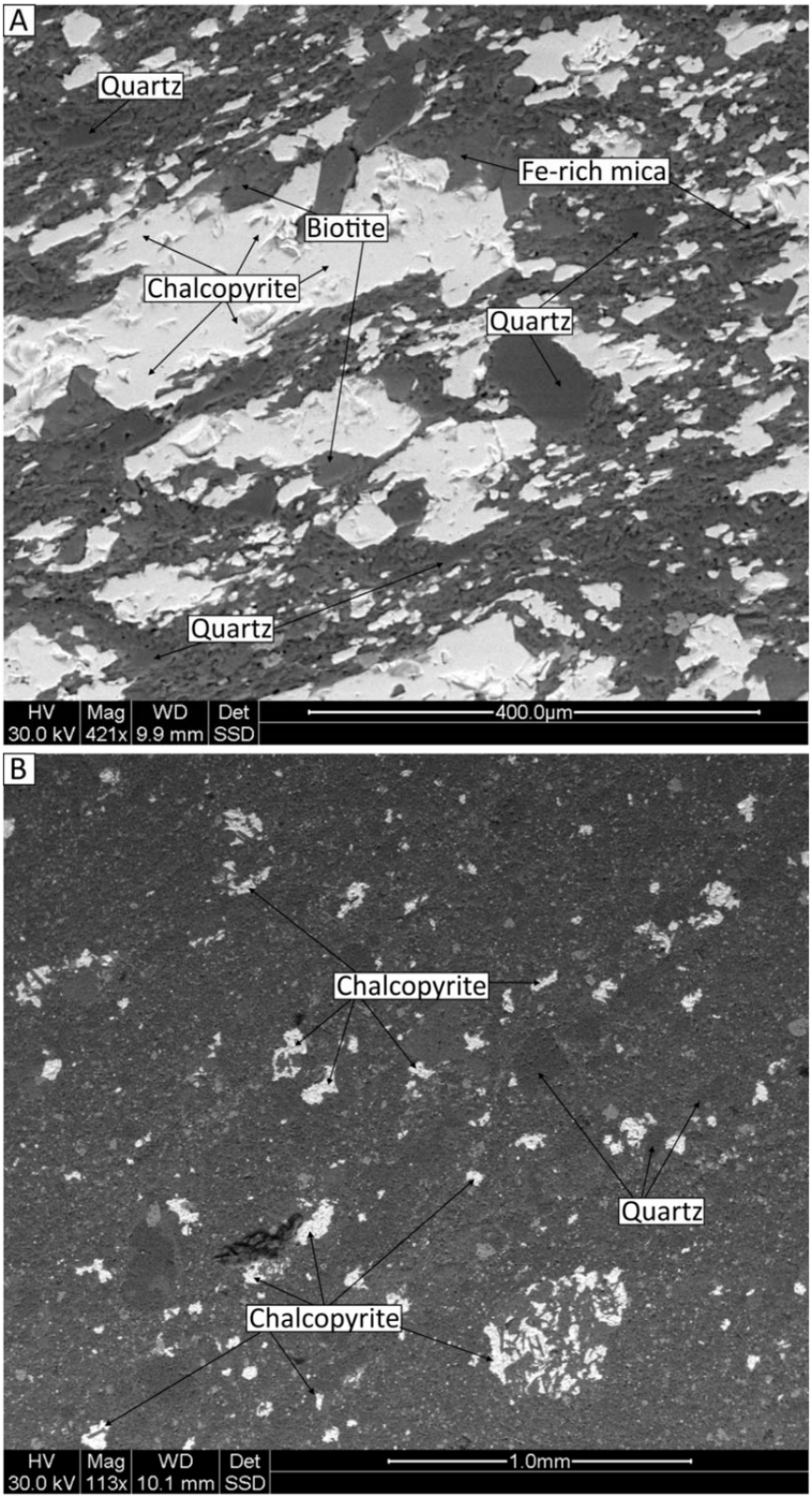

Fig. A.3: (A). Strong foliation defined by the alignment of chalcopyrite and minerals in the matrix. Sample FT_78. (B). Weak to moderate foliation defined by the alignment of chalcopyrite and quartz grains. Sample FT_78H.

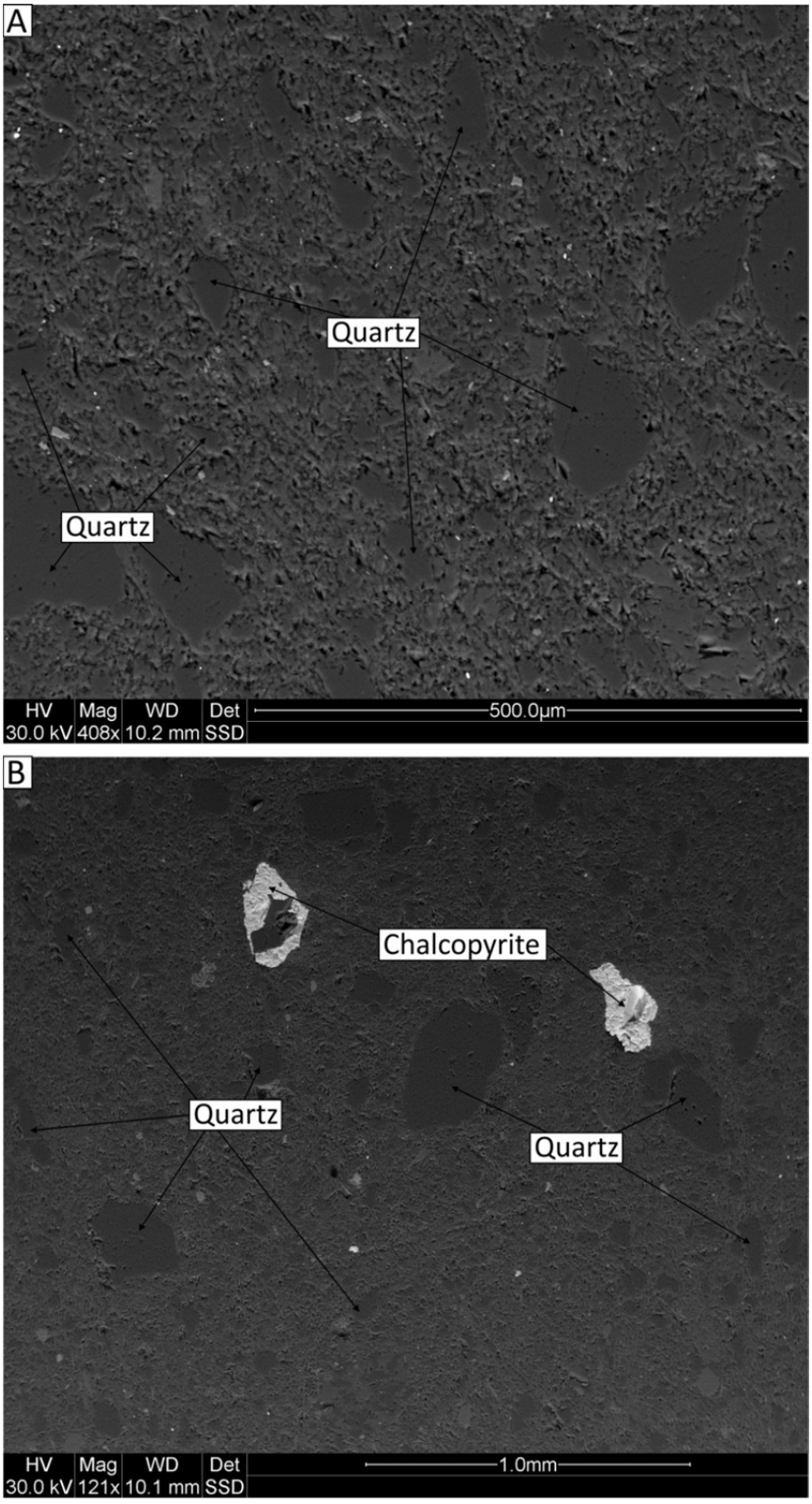

Fig. A.4: (A). Weak foliation defined by the alignment of quartz grains and minerals in the matrix. Sample FT_79. (B). Weak to very weak foliation defined by the alignment of quartz and minerals in the matrix. Sample FT_79H.

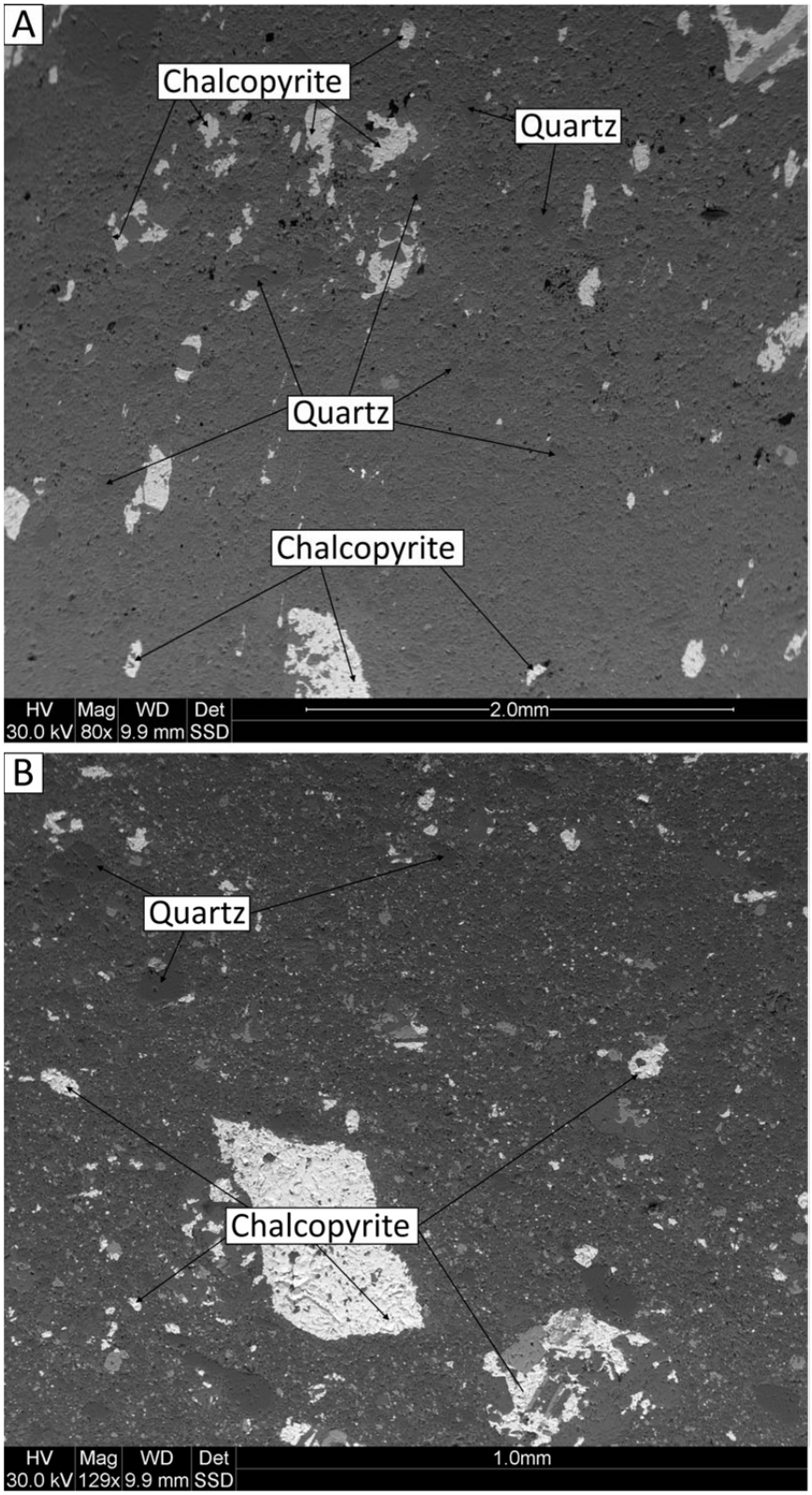

Fig. A.5: (A). Moderate foliation defined by the alignment of chalcopyrite. Quartz grains are slightly aligned. Sample FT_98. (B). Weak foliation defined by the alignment of chalcopyrite. Sample FT_98H.

Spectra of common minerals of the Kamoa deposit

Quartz. Sample FT_88.

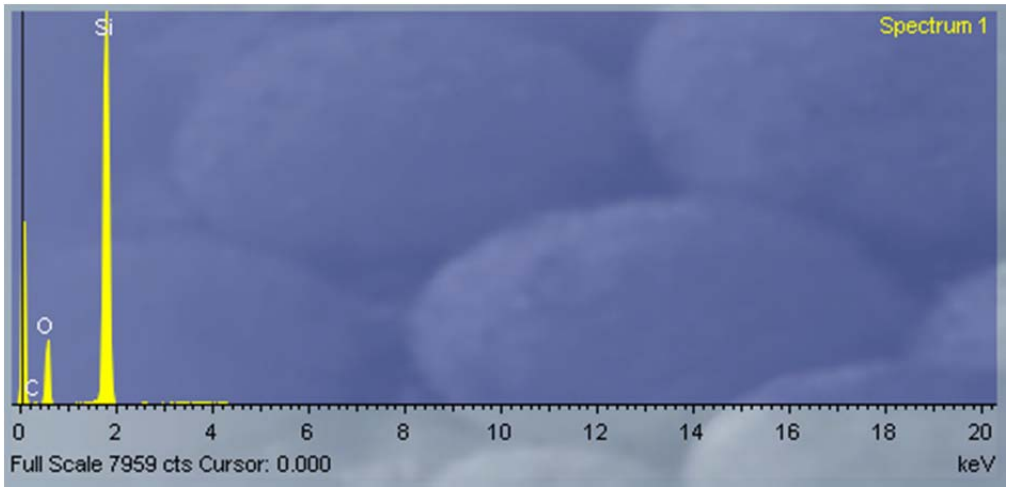

Biotite. Sample FT_78.

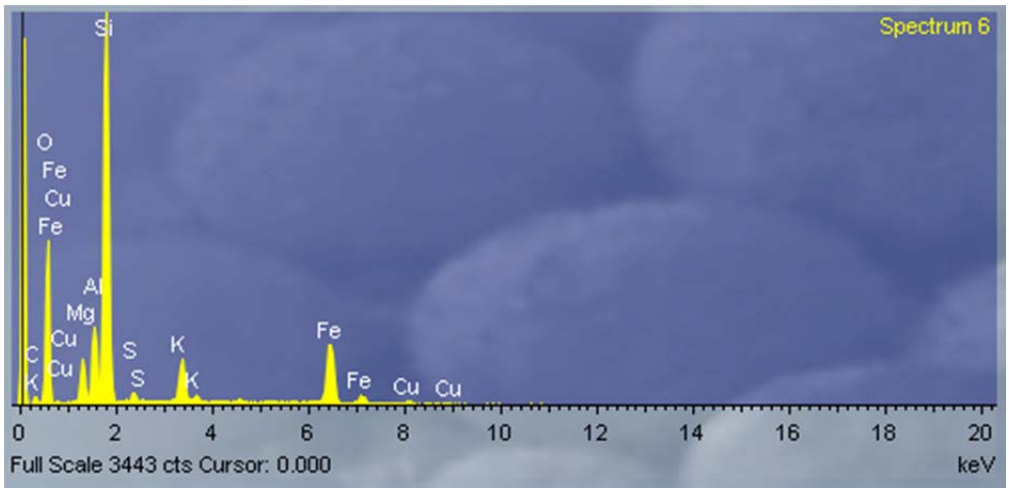

Iron-rich mica. Sample FT_88.

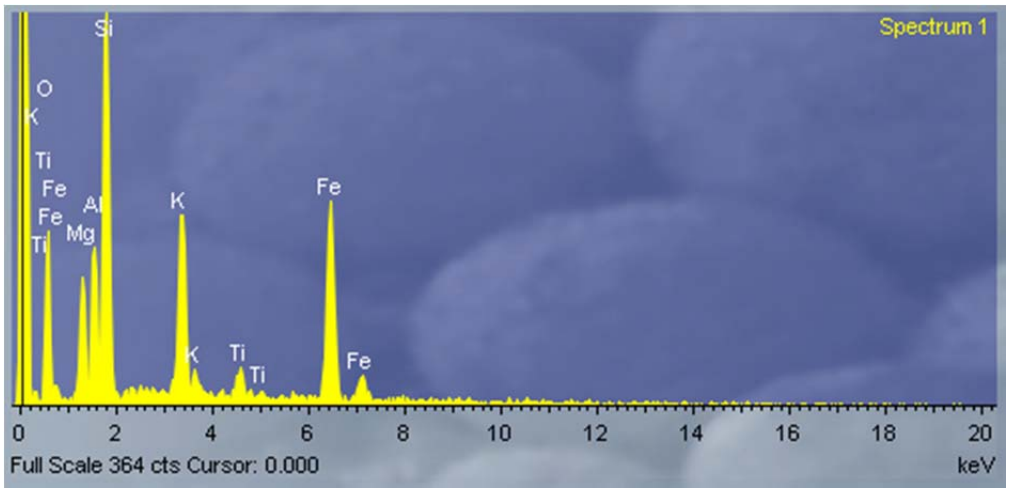

Muscovite Sample FT_37

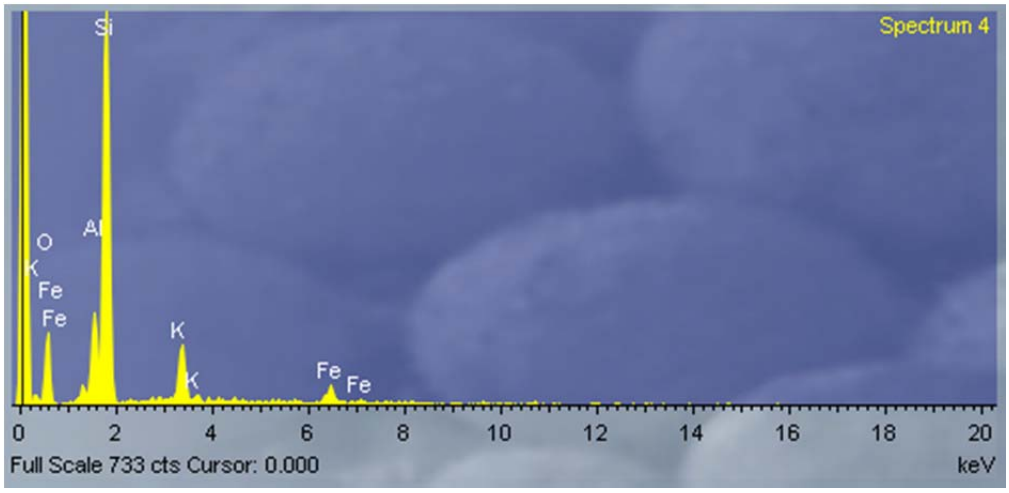

Feldspar. Sample FT_78

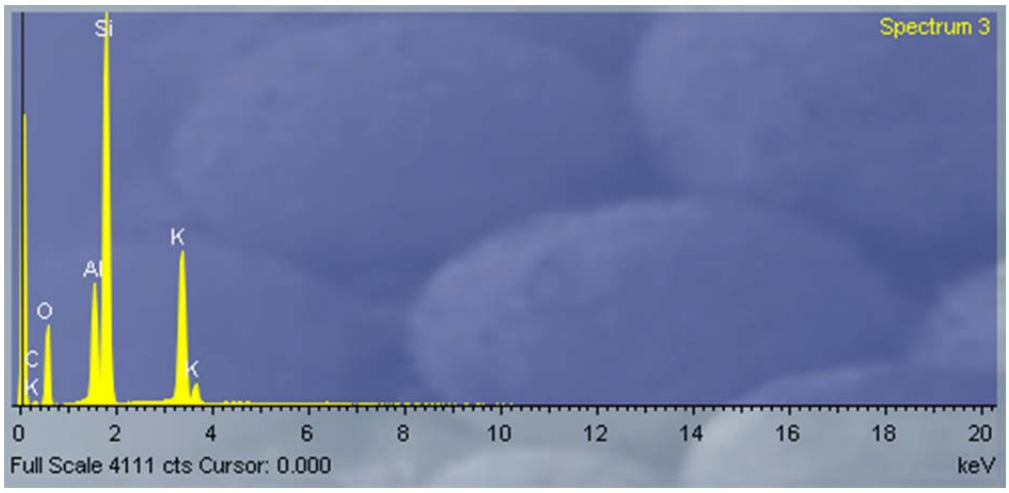

Albite. Sample FT_29

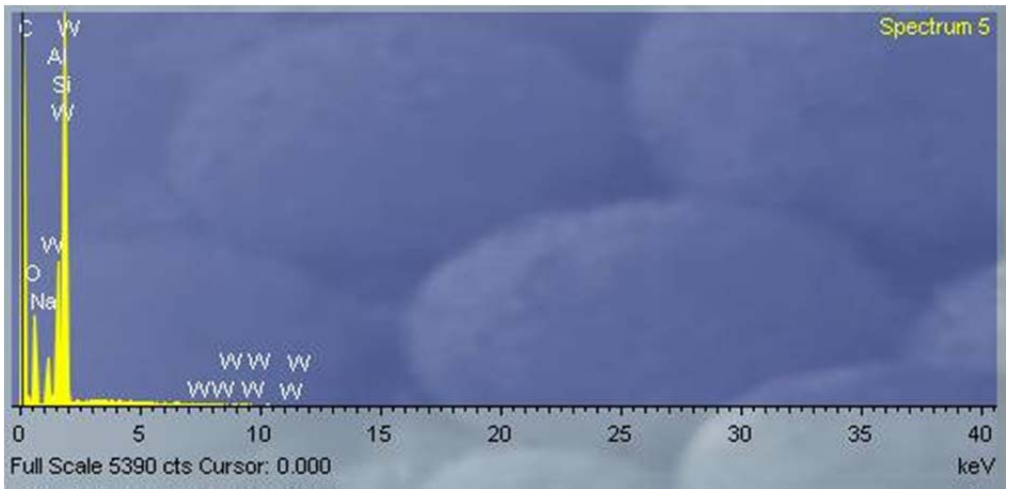

Rutile. Sample from FT_36.

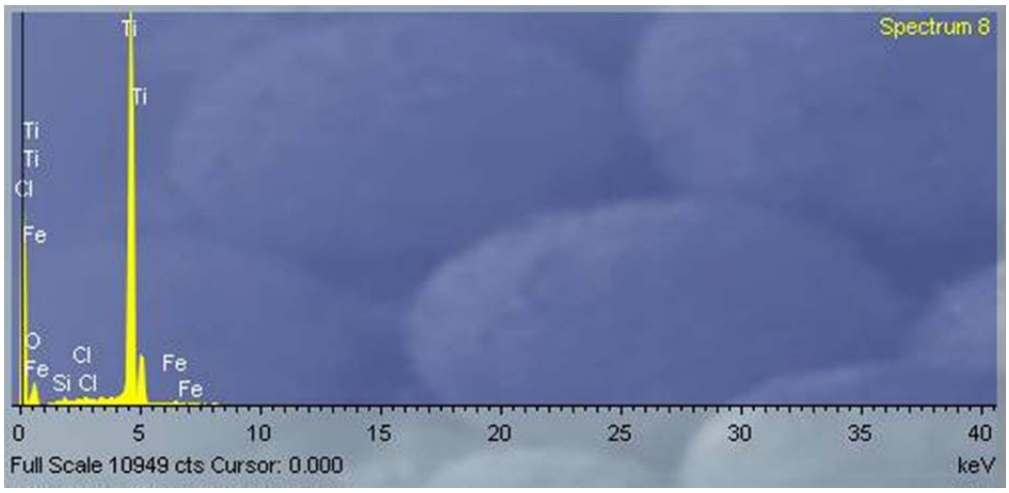

Chalcopyrite FT_78

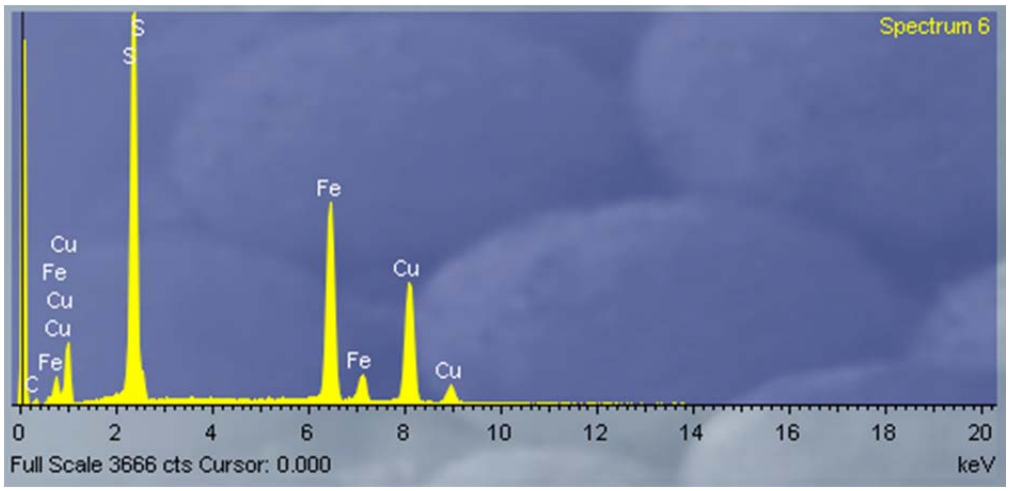

Magnetite. Sample FT_66

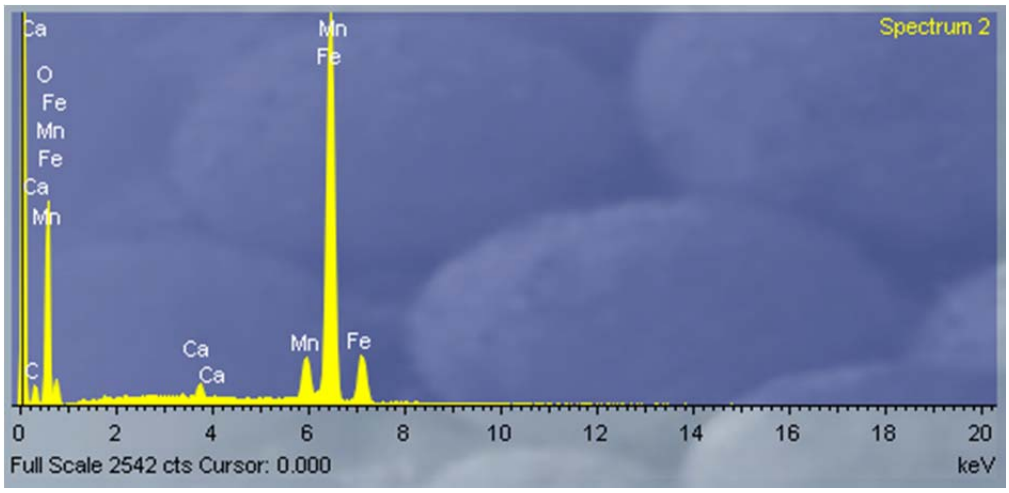

Bornite. Sample FT_29.

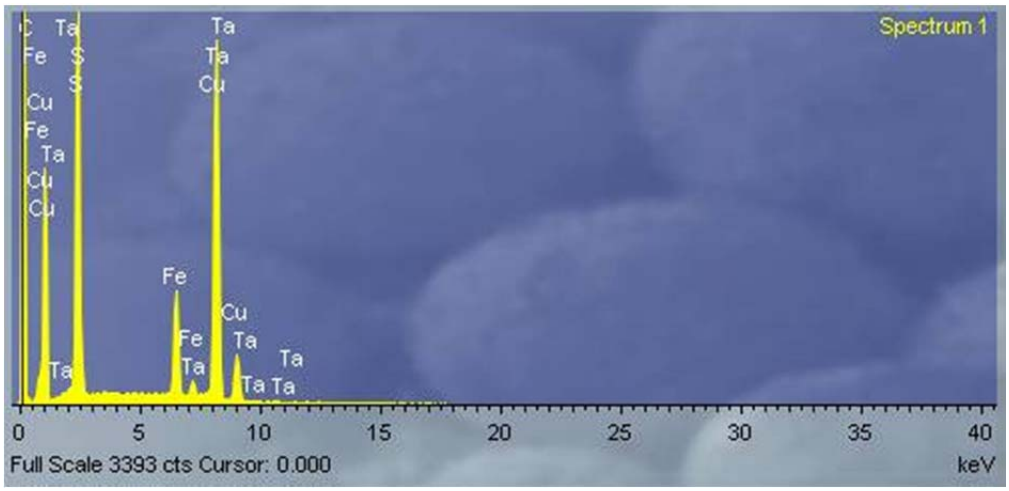

Pyrite. Sample FT39.

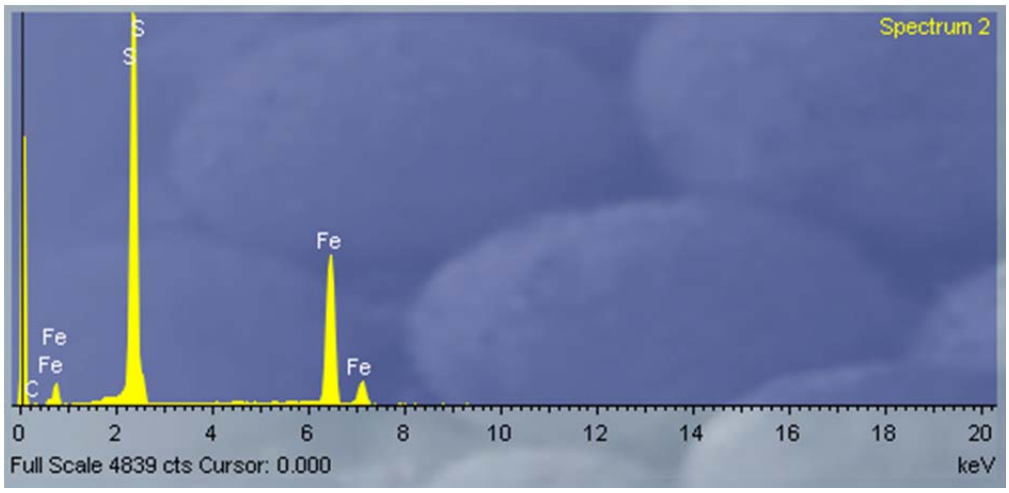

Ankerite. Sample FT_051.

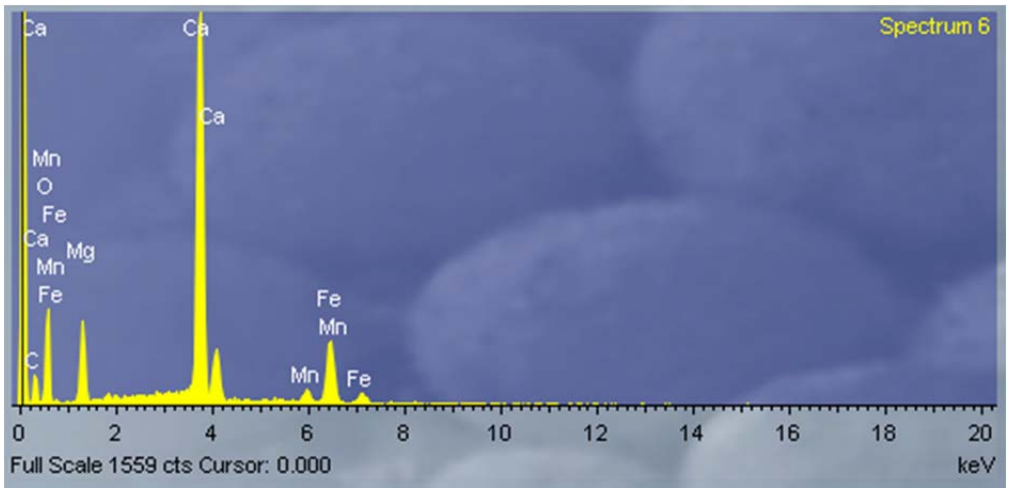

Appendix B

List of boreholes logged and samples collected

In the Kamoa project, boreholes commonly has the prefix “DKMC_DD”, in this study the prefix has been abbreviated as “DD” (i.e. DKMC_DD641 will be DD641). However the prefixes “DMAK_DD”, “DMAK_RD” and “DKMC_GD” are not abbreviated (i.e. DMAK_RD030 remains DMAK_RD030). The abbreviations used in this section are the same as in Appendix A.

Boreholes logged are presented in Figure B.1 and tabulated in Table B.1. The list of thin sections collected is also presented below.

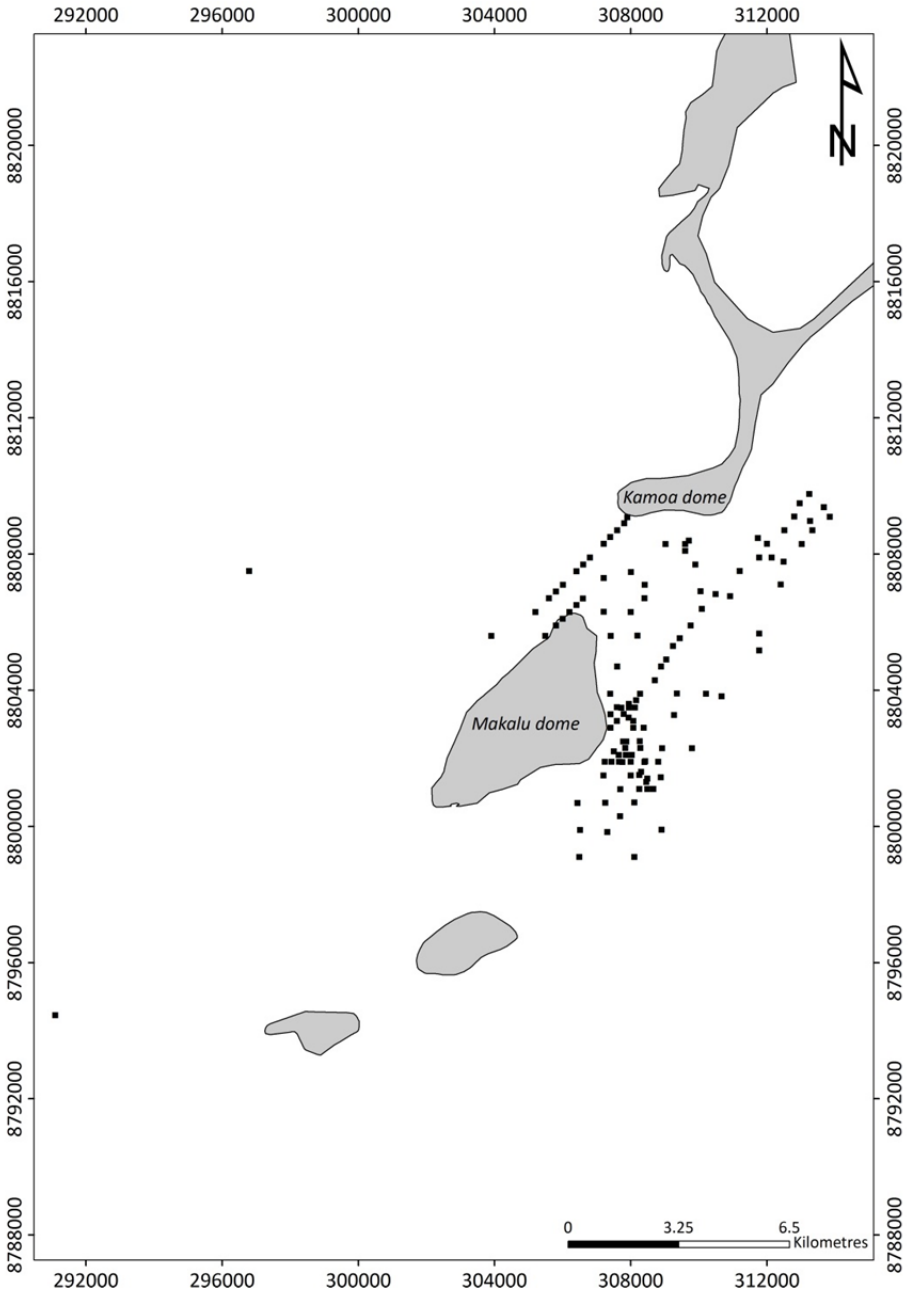

Fig. B.1: Boreholes logged in this study.

Borehole ID	UTM_E	UTM_N	Elevation	Grid UTM Zone	Azimuth	Dip
DD019	312800	8809103	1501	WGS84_35S	360	-90
DD022	307413	8805602	1454	WGS84_35S	360	-90
DD023	308199	8805604	1471	WGS84_35S	360	-90
DD025	305492	8805602	1447	WGS84_35S	360	-90
DD027	303907	8805596	1409	WGS84_35S	360	-90
DD037	296793	8807501	1288	WGS84_35S	360	-90
DD051	311197	8807505	1482	WGS84_35S	360	-90
DD052	312002	8808304	1488	WGS84_35S	360	-90
DD084	309600	8808300	1462	WGS84_35S	360	-90
DD104	306800	8807900	1444	WGS84_35S	360	-90
DD197	309602	8808099	1466	WGS84_35S	360	-60
DD199	308007	8807476	1455	WGS84_35S	360	-90
DD200	309704	8808393	1461	WGS84_35S	180	-60
DD202	309018	8808297	1457	WGS84_35S	90	-60
DD215	312511	8808702	1495	WGS84_35S	270	-80
DD224	309757	8805903	1473	WGS84_35S	270	-67
DD228	311731	8808471	1483	WGS84_35S	330	-75
DD240	307201	8808301	1458	WGS84_35S	360	-90
DD241	307598	8808700	1464	WGS84_35S	360	-90
DD248	307399	8808502	1460	WGS84_35S	360	-90
DD252	311772	8807903	1497	WGS84_35S	270	-75
DD309	308888	8804701	1475	WGS84_35S	270	-79
DD311	306008	8807098	1427	WGS84_35S	360	-90
DD314	306402	8807495	1409	WGS84_35S	360	-90
DD320	307604	8804699	1469	WGS84_35S	360	-90
DD322	312138	8807901	1500	WGS84_35S	270	-79
DD327	305600	8806700	1426	WGS84_35S	360	-90
DD330	309354	8803905	1476	WGS84_35S	270	-75
DD354	307804	8808905	1463	WGS84_35S	360	-90
DD365	313017	8808300	1503	WGS84_35S	270	-75
DD375	313842	8809101	1499	WGS84_35S	270	-75
DD377	307999	8806301	1462	WGS84_35S	360	-90
DD378	307205	8806304	1441	WGS84_35S	360	-90
DD381	308076	8803098	1470	WGS84_35S	270	-75
DD387	313329	8808700	1504	WGS84_35S	270	-79
DD401	310210	8803902	1470	WGS84_35S	270	-75
DD404	307593	8803096	1468	WGS84_35S	360	-90
DD405	308920	8802298	1445	WGS84_35S	270	-75
DD411	309795	8802300	1476	WGS84_35S	270	-75
DD414	312962	8809493	1502	WGS84_35S	270	-72
DD416	307597	8803500	1473	WGS84_35S	360	-90
DD421	307398	8803900	1474	WGS84_35S	360	-90
DD440	307657	8801902	1448	WGS84_35S	270	-74
DD441	307237	8801901	1450	WGS84_35S	270	-74
DD443	308802	8801901	1426	WGS84_35S	270	-70
DD448	307432	8801902	1450	WGS84_35S	270	-78

Borehole ID	UTM_E	UTM_N	Elevation	Grid UTM Zone	Azimuth	Dip
DD449	308403	8801898	1444	WGS84_35S	270	-70
DD453	311774	8805171	1512	WGS84_35S	270	-81
DD456	311769	8805669	1510	WGS84_35S	270	-81
DD465	306605	8807698	1433	WGS84_35S	360	-90
DD493	307203	8807299	1437	WGS84_35S	360	-90
DD506	306598	8806696	1442	WGS84_35S	360	-90
DD508	306401	8806503	1451	WGS84_35S	360	-90
DD516	305803	8806904	1418	WGS84_35S	360	-90
DD538	306002	8806100	1451	WGS84_35S	360	-90
DD547	310662	8803823	1483	WGS84_35S	270	-85
DD550	305202	8806302	1423	WGS84_35S	270	-90
DD561	306200	8806298	1454	WGS84_35S	270	-90
DD571	310918	8806766	1489	WGS84_35S	270	-85
DD583	305801	8805900	1447	WGS84_35S	270	-90
DD595	310084	8806393	1484	WGS84_35S	270	-78
DD598	312483	8807780	1503	WGS84_35S	270	-85
DD603	313668	8809376	1501	WGS84_35S	270	-85
DD619	308406	8807103	1460	WGS84_35S	270	-90
DD620	308403	8806701	1460	WGS84_35S	270	-90
DD627	310490	8806825	1489	WGS84_35S	270	-79
DD637	309267	8803274	1452	WGS84_35S	273	-85
DD642	310049	8806911	1485	WGS84_35S	270	-83
DD643	313265	8808977	1504	WGS84_35S	270	-85
DD645	313244	8809771	1502	WGS84_35S	270	-85
DD757	309042	8804904	1478	WGS84_35S	270	-85
DD793	309240	8805304	1482	WGS84_35S	270	-85
DD795	307902	8809084	1461	WGS84_35S	360	-90
DD802	309435	8805533	1484	WGS84_35S	270	-85
DD816	307401	8802903	1465	WGS84_35S	270	-90
DD821	308282	8802306	1458	WGS84_35S	270	-75
DD825	307837	8802307	1458	WGS84_35S	270	-75
DD844	307402	8803294	1469	WGS84_35S	270	-90
DD855	307774	8802500	1460	WGS84_35S	270	-70
DD856	307870	8802499	1461	WGS84_35S	270	-70
DD860	307790	8803303	1472	WGS84_35S	270	-90
DD862	308273	8803900	1477	WGS84_35S	270	-75
DD866	308072	8802904	1467	WGS84_35S	270	-75
DD869	308267	8802504	1461	WGS84_35S	270	-75
DD875	308705	8804298	1475	WGS84_35S	270	-75
DD887	308377	8802901	1465	WGS84_35S	270	-75
DD888	308025	8802099	1454	WGS84_35S	270	-85
DD895	308252	8801100	1436	WGS84_35S	270	-85
DD897	308426	8801918	1444	WGS84_35S	270	-85
DD901	308659	8801101	1441	WGS84_35S	270	-85
DD903	307648	8802100	1453	WGS84_35S	270	-75
DD904	312405	8807110	1507	WGS84_35S	360	-90

Borehole ID	UTM_E	UTM_N	Elevation	Grid UTM Zone	Azimuth	Dip
DD908	308248	8801509	1423	WGS84_35S	260	-85
DD909	308452	8801310	1430	WGS84_35S	270	-85
DD912	308485	8801403	1425	WGS84_35S	320	-80
DD915	307500	8802204	1455	WGS84_35S	270	-85
DD920	307853	8802102	1453	WGS84_35S	270	-75
DD922	308117	8803498	1475	WGS84_35S	270	-80
DD928	307726	8803490	1473	WGS84_35S	293	-80
DD929	307940	8803498	1474	WGS84_35S	270	-80
DD934	308161	8803705	1476	WGS84_35S	265	-75
DD944	307945	8803601	1474	WGS84_35S	270	-80
DD963	307938	8803201	1455	WGS84_35S	270	-80
DKMC_GD002	307755	8801896	1449	WGS84_35S	140	-50
DKMC_GD003	309897	8807697	1479	WGS84_35S	150	-55
DKMC_RD432	307998	8801900	1447	WGS84_35S	360	-90
DMAK_DD004	308300	8801602	1430	WGS84_35S	270	-70
DMAK_DD013	308880	8801445	1422	WGS84_35S	305	-80
DMAK_DD014	308106	8800703	1446	WGS84_35S	270	-78
DMAK_DD016	307254	8800701	1430	WGS84_35S	270	-80
DMAK_DD025	306437	8800689	1414	WGS84_35S	360	-90
DMAK_DD027	307681	8800304	1445	WGS84_35S	270	-80
DMAK_DD033	307695	8801090	1420	WGS84_35S	270	-75
DMAK_DD034	307999	8801500	1422	WGS84_35S	270	-79
DMAK_DD035	307197	8801500	1438	WGS84_35S	360	-90
DMAK_RD018	308907	8799902	1465	WGS84_35S	270	-78
DMAK_RD019	308101	8799104	1454	WGS84_35S	270	-78
DMAK_RD021	307309	8799835	1424	WGS84_35S	300	-76
DMAK_RD023	306515	8799901	1439	WGS84_35S	270	-72
DMAK_RD024	306491	8799102	1448	WGS84_35S	270	-74
DMAK_RD030	308483	8801100	1440	WGS84_35S	270	-80
DTJI_DD001	291101	8794452	1311	WGS84_35S	360	-90

Borehole ID	Depth	Sample #	Lithology	Strat Unit
DD448	152.50	FT_01	SDT	Ng1.1.1
DD448	134.50	FT_02	SDT	Ng1.1.1
DD448	130.05	FT_03	SDT	Ng1.1.1
DD440	131.43	FT_04	SSL	Ng1.1.2
DD440	158.12	FT_05	SSL	Ng1.1.2
DD440	190.12	FT_06	SDT	Ng1.1.1
DD440	196.54	FT_07	SDT	Ng1.1.1
DD440	196.54	FT_07H	SDT	Ng1.1.1
DD440	198.91	FT_08 A	SDT	Ng1.1.1
DD440	198.91	FT_08 A_H	SDT	Ng1.1.1
DD440	198.91	FT_08 B	SDT	Ng1.1.1
DD440	200.92	FT_09	SDT	Ng1.1.1
DD440	200.92	FT_09H	SDT	Ng1.1.1
DD440	228.70	FT_10	SSL	Ng1.1.1
DMAK_RD019	487.02	FT_11	SSL	Ng1.1
DTJI_DD001	92.24	FT_12 A	SDT	Ng1.1
DTJI_DD001	92.24	FT_12 B	SDT	Ng1.1
DTJI_DD001	92.24	FT_12 C	SDT	Ng1.1
DTJI_DD001	92.24	FT_12 CH	SDT	Ng1.1
DTJI_DD001	398.61	FT_13	SDT	Ng1.1
DTJI_DD001	400.16	FT_14	SDT	Ng1.1
DTJI_DD001	431.90	FT_15	SDT	Ng1.1
DTJI_DD001	431.90	FT_15H	SDT	Ng1.1
DTJI_DD001	567.00	FT_16	SDT	Ng1.1
DTJI_DD001	567.00	FT_16H	SDT	Ng1.1
DTJI_DD001	568.38	FT_17	SDT	Ng1.1
DTJI_DD001	569.88	FT_18	SDT	Ng1.1
DTJI_DD001	100.51	FT_19	SDT	Ng1.1
DKMC_GD003	513.74	FT_20 A	SSL	Ng1.1.2
DKMC_GD003	513.74	FT_20 B	SSL	Ng1.1.2
DKMC_ GD003	515.15	FT_21 A	SSL	Ng1.1.2
DKMC_GD003	515.32	FT_21 B	SSL	Ng1.1.2
DKMC_GD003	516.11	FT_22	SSL	Ng1.1.2
DKMC_GD003	520.38	FT_23	SDT	Ng1.1.1
DKMC_GD003	529.37	FT_24	SDT	Ng1.1.1
DKMC_GD002	245.00	FT_25	SSL	Ng1.1.2
DKMC_GD002	245.00	FT_25H	SSL	Ng1.1.2
DKMC_GD002	255.00	FT_26	SSL	Ng1.1.2
DKMC_GD002	255.00	FT_26H	SSL	Ng1.1.2
DKMC_GD002	280.60	FT_27	SSL	Ng1.1.2
DKMC_GD002	338.28	FT_28	SSL	Ng1.1.1
DD888	265.72	FT_29	SDT	Ng1.1.1
DD866	266.74	FT_30	SDT	Ng1.1.1
DMAK_DD014	522.46	FT_31	SDT	Ng1.1.1
DD944	227.89	FT_32	SDT	Ng1.1.1
DD944	227.89	FT_32A	SDT	Ng1.1.1

Borehole ID	Depth	Sample #	Lithology	Strat Unit
DD929	228.65	FT_33	SDT	Ng1.1.1
DD928	177.36	FT_34	SDT	Ng1.1.1
DD928	177.36	FT_34H	SDT	Ng1.1.1
DD922	283.66	FT_35	SDT	Ng1.1.1
DD895	580.46	FT_36	SDT	Ng1.1.1
DD895	580.46	FT_36H	SDT	Ng1.1.1
DD856	137.28	FT_37	SDT	Ng1.1.1
DD453	1148.94	FT_38A	SDT	Ng1.1.1
DD453	1148.94	FT_38B	SDT	Ng1.1.1
DD453	1148.94	FT_38C	SDT	Ng1.1.1
DD381	240.16	FT_39	SDT	Ng1.1.1
DD200	189.55	FT_40	SSL	Ng1.1.2
DD200	201.9	FT_41	SSL	Ng1.1.1
DD200	188.97	FT_42	SDT	Ng1.1.1
DD197	205.04	FT_43	SST	Ng1.1.2
DD197	211.85	FT_44	SDT	Ng1.1.1
DD202	165.75	FT_45	SSL	Ng1.1.2
DD027	77.65	FT_46	SSL	Ng1.1.5
DD084	149.85	FT_47	SSL	Ng1.1.2
DMAK_DD033	234.79	FT_48	SSL	Ng1.1.2
DMAK_RD023	96.37	FT_49	SSL	Ng1.1.2
DD401	783.29	FT_50	SDT	Ng1.1.1
DD401	783.29	FT_50H	SDT	Ng1.1.1
DD401	784.63	FT_51	SDT	Ng1.1.1
DD401	784.63	FT_51(2)	SDT	Ng1.1.1
DD897	448.25	FT_52	SDT	Ng1.1.1
DD022	71.27	FT_53	SDT	Ng1.1.1
DD443	537.63	FT_54	SSL	Ng1.1.2
DD944	184.08	FT_55	SDT	Ng1.1.2
DD944	188.68	FT_56	SSL	Ng1.1.2
DD944	191.64	FT_57	SSL	Ng1.1.2
DD944	196.98	FT_58	SSL	Ng1.1.2
DD944	203.2	FT_59	SST	Ng1.1.2
DD944	211.53	FT_60	SDT	Ng1.1.1
DD944	217.36	FT_61	SDT	Ng1.1.1
DD944	224.64	FT_64	SDT	Ng1.1.1
DD944	224.64	FT_64H	SDT	Ng1.1.1
DD944	227.31	FT_66	SDT	Ng1.1.1
DD944	227.31	FT_66H	SDT	Ng1.1.1
DD944	230.28	FT_67	SDT	Ng1.1.1
DD944	232.22	FT_68	SDT	Ng1.1.1
DD944	235.57	FT_69	SDT	Ng1.1.1
DD944	236.6	FT_70	SDT	Ng1.1.1
DD944	237.98	FT_71	SDT	Ng1.1.1
DD944	238.19	FT_72	SDT	Ng1.1.1
DD944	241.22	FT_73	SDT	Ng1.1.1

Borehole ID	Depth	Sample #	Lithology	Strat Unit
DD944	241.52	FT_74	SDT	Ng1.1.1
GD002	243	FT_75	SSL	Ng1.1.2
GD002	373.66	FT_76	SSL	Ng1.1.1
GD002	377.28	FT_77	SSL	Ng1.1.1
GD002	379.58	FT_78	SSL	Ng1.1.1
GD002	379.58	FT_78H	SSL	Ng1.1.1
DD453	1149.9	FT_79	SDT	Ng1.1.1
DD453	1149.9	FT_79H	SDT	Ng1.1.1
DD453	1149.95	FT_80	SDT	Ng1.1.1
RD432	330	FT_81	SSL	Ng1.1.1
RD432	333	FT_82	SSL	Ng1.1.1
DD084	170.8	FT_85	SDT	Ng1.1.1
DD793	404.37	FT_87	SST	Ng1.1.1
DMAK_RD030	641.86	FT_88	SSL	Ng1.1.1
DMAK_DD014	443.59	FT_89	SSL	Ng1.1.2
DMAK_DD014	449.07	FT_90	SSL	Ng1.1.2
DMAK_DD014	454.69	FT_91	SSL	Ng1.1.2
DMAK_DD014	559.47	FT_92	SDT	Ng1.1.1
DD860	165.86	FT_93	SSL	Ng1.1.1
DD860	165.86	FT_94	SSL	Ng1.1.1
DD860	165.9	FT_95	SSL	Ng1.1.1
DD860	165.9	FT_95H	SSL	Ng1.1.1
DD860	173.96	FT_96	SSL	Ng1.1.1
DD860	174.56	FT_97	SSL	Ng1.1.1
DD895	585.47	FT_98	SDT	Ng1.1.1
DD895	585.47	FT_98H	SDT	Ng1.1.1
DD895	627.5	FT_99	SST	R42
DD963	200.15	TS_1	SSL	Ng1.1.1
DD963	202.42	TS_2	SDT	Ng1.1.1
DD963	205.13	TS_3	SDT	Ng1.1.1
DD963	208.12	TS_4	SDT	Ng1.1.1
DD963	210.1	TS_5	SDT	Ng1.1.1
DD963	211.1	TS_6	SDT	Ng1.1.1
DD963	211.88	TS_7	SDT	Ng1.1.1
DD963	213.81	TS_8	SDT	Ng1.1.1
DD963	214.55	TS_9	SDT	Ng1.1.1
DD963	216.17	TS_10	SDT	Ng1.1.1
DD963	217.24	TS_11	SST	Ng1.1.1
DD963	218.21	TS_12	SST	Ng1.1.1
DD963	218.71	TS_13	SST	Ng1.1.1
DD963	219.28	TS_14	SST	Ng1.1.1
DD963	219.6	TS_15	SST	Ng1.1.1
DD963	220.23	TS_16	SST	Ng1.1.1
DD963	220.97	TS_17	SDT	Ng1.1.1
DD963	221.71	TS_18	SDT	Ng1.1.1
DD963	222.6	TS_19	SSL	Ng1.1.1

Borehole ID	Depth	Sample #	Lithology	Strat Unit
DD963	223.48	TS_20	SDT	Ng1.1.1
DD963	224.96	TS_21	SSL	Ng1.1.1
DD963	225.35	TS_22	SDT	Ng1.1.1
DD963	226.13	TS_23	SDT	Ng1.1.1
DD963	226.97	TS_24	SDT	Ng1.1.1
DD963	228.71	TS_25	SDT	Ng1.1.1
DD963	230.28	TS_26	SDT	Ng1.1.1
DD963	231.77	TS_27	SDT	Ng1.1.1
DD963	233.5	TS_28	SDT	Ng1.1.1
DD963	235.92	TS_29	SDT	Ng1.1.1
DD963	238.56	TS_30	SDT	Ng1.1.1
DD963	241.96	TS_31	SDT	Ng1.1.1
DD963	245.5	TS_32	SDT	Ng1.1.1
DD963	249.9	TS_34	SST	R 42
DD963	251.96	TS_35	SST	R 42
DD904	115.22	115.22	SDT	Ng1.1.6
DD904	149.5	149.5	SSL	Ng1.1.6
DD904	262.38	262.38	SST	Ng1.1.6
DD904	536.06	536.06	SDT	Ng1.1.5
DD904	568.9	568.9	SCG	Ng1.1.5
DD904	659.8	659.8	SSL	Ng1.1.5
DD904	769.38	769.38	SDT	Ng1.1.5
DD904	789.08	789.08	SSL	Ng1.1.4
DD904	823.66	823.66	SDT	Ng1.1.3
DD904	837.4	837.4	SDT	Ng1.1.3
DD904	979.6	979.6	SDT	Ng1.1.3
DD915	581.67	581.67	SST	R 42
DTJI_DD001	586.94	586.94	SDT	Ng1.1.1
DTJI_DD001	615.58	615.58	SST	R42
DTJI_DD001	611.92	611.92	SST	R42
DTJI_DD001	612.06	612.06	SST	R42
DTJI_DD001	615.45	615.45	SST	R42

Appendix C

Structural measurements and descriptions

This section presents the structural measurements and descriptions. The list of abbreviations is presented below (Table C.1). Some of the abbreviations are similar to that in Appendix A.

The methodology of measuring alpha and beta angles in borehole core is shown in Figure C.1 of this appendix and the data obtained from boreholes are presented in Tables C.2; C.3 and C4.

Table C.1: List of abbreviations.

CATEGORY	Code	Description
LITHOLOGY		
	SSL	Siltstone
	SST	Sandstone
	SDT	Diamictite
	SCG	Conglomerate
	BDR	Mafic boulder
	MI	Mafic intrusion
STRUCTURE		
	BD	Bedding
	FA1	Significant fault
	FA3	Improbable fault
	FB	Fabric
	FLD	Fold
	FLT	Fault undefined
	FSX	Fault by sedimentary breccia
	FW	Fault by weathering
	FZ	Fractured zone
	LM	Lamination
	MFA	Mesoscopic fault
	NFA	Normal mesoscopic fault
	RFA	Reverse mesoscopic fault
	SBD	Steep bedding
	SL	Slickensides
	SS	Strain shadows/fringes
	SSD	Soft sediment deformation
	VN	Vein
	VWFO	Very weak foliation
	WFO	Weak foliation
	MFO	Moderate foliation
	SFO	Strong foliation
	X	Cohesive breccia

CATEGORY	Code	Description
MORPHOLOGY OF STRAIN SHADOWS/FRINGES		
	CR	Clast with growth all the way around
	ASU	Asymmetric upwards strain shadows/fringes
	ASD	Asymmetric downwards strain shadows/fringes
	SYM	Symmetric strain shadows/fringes

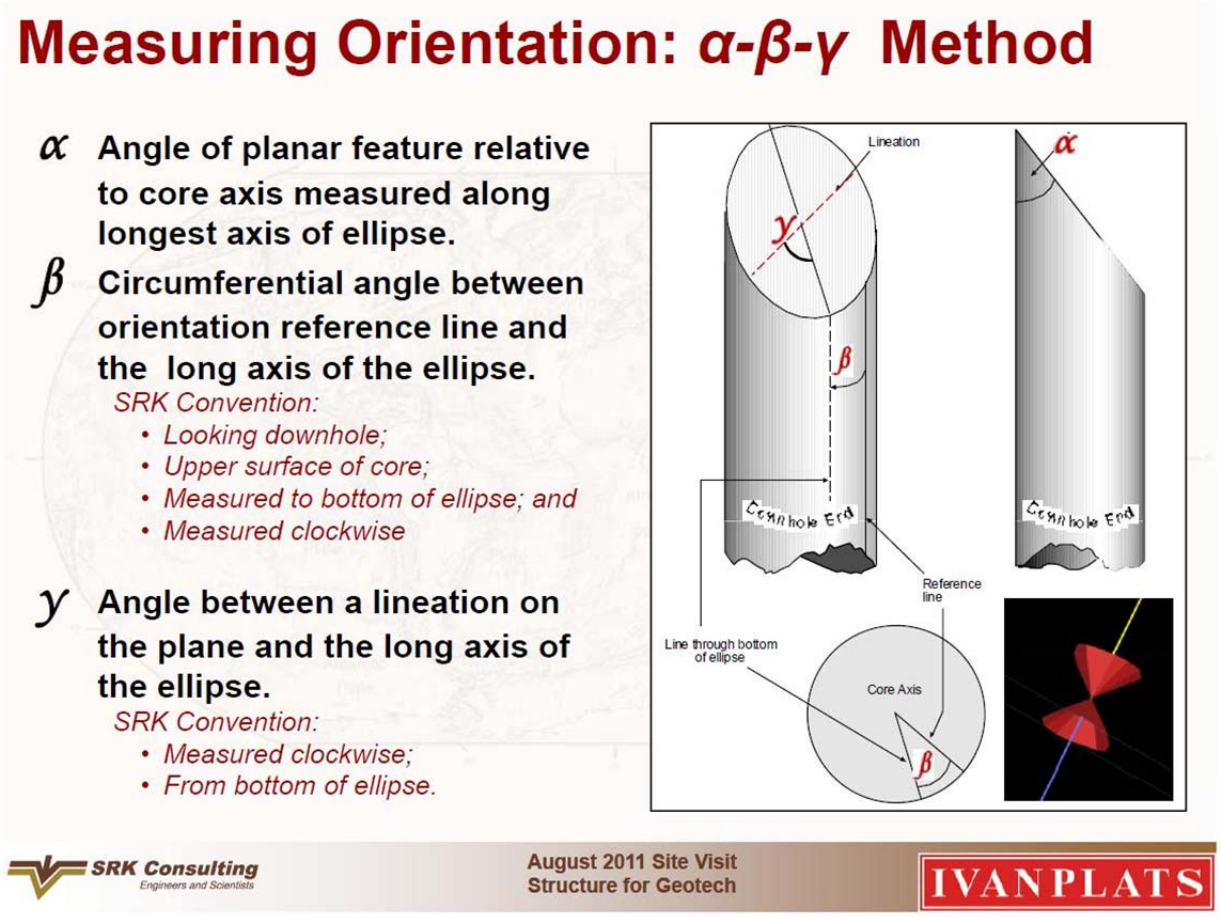

Fig. C.1: Methodology of measuring alpha and beta angles in borehole core.

BHID	Box #	From	To	Feature code	Feature	Lithology	Strat unit
DD019	133	630.5	637.58	SS	Upward strain shadow defined by chalcopyrite on top of the interval and chalcocite at the base.	SDT	Ng1.1.1
DD022	12	48.21	48.36	FSX	Fault by sedimentary breccia.	SSL	Ng1.1.2
DD022	13	51.13	51.14	RFA	Reverse fault based on displacement of beds.	SSL	Ng1.1.2
DD022	13	51.82	51.83	RFA	Reverse fault based on displacement of beds.	SSL	Ng1.1.2
DD022	15	56.29	56.3	RFA	Reverse fault based on displacement of beds.	SSL	Ng1.1.2
DD022	16	60.73	60.74	RFA	Reverse fault based on displacement of beds.	SSL	Ng1.1.2
DD022	16	61.31	61.61	RFA	Reverse fault based on displacement of beds.	SSL	Ng1.1.2
DD022	16	61.66	61.83	FLT	Fault breccia.	SSL	Ng1.1.2
DD022	17	63.58	63.62	X	Cohesive breccia.	SDT	Ng1.1.1
DD022	17	64.65	64.73	X	Cohesive breccia.	SDT	Ng1.1.1
DD022	17	66.6	66.67	X	Fault by cohesive breccia.	SDT	Ng1.1.1
DD022	18	68.34	71.24	FLT	Brecciated zone with micro fractures.	SDT	Ng1.1.1
DD022	18	71.24	71.36	SS	Strain shadow defined by FeOx. Up hole SS.	SDT	Ng1.1.1
DD022	19	74.09	74.86	X	Fault by cohesive breccia. Rubble to broken zone.	SDT	Ng1.1.1
DD022	20	77.38	77.52	X	Fault by cohesive breccia.	SDT	Ng1.1.1
DD022	21	82.1	82.11	RFA	Reverse fault based on the cut clast.	SDT	Ng1.1.1
DD022	23	90.1	93.44	FZ	Broken to rubble zone with Kaolinite infill.	SST	R4.2
DD027	23	68	69.8	VWFO	Very weak foliation defined by the alignment of iron oxides (leached zone) sub-parallel to the core axis.	SSL	Ng1.1.5
DD027	23	352	352.5	WFO	Weak foliation defined by alignment of iron oxides(leached Py siltstone) sub parallel to the core axis.	SSL	Ng1.1.4
DD027	26	77.6	77.64	FLD	Fold axial plane. Pyrite grains are also following the plane of the fold.	SSL	Ng1.1.5
DD027	25, 26	74.5	78.77	VWFO	Very weak foliation defined by alignment of pyrite. Sub parallel to the core axis.	SSL	Ng1.1.5
DD037	192	865.00	870.50	MFO	Moderate foliation defined by alignment of pyrite. Vuggy texture.	SSL	Ng1.1
DD037	195	886.47	887.49	FLD	Tight fold sub parallel to the bedding. Bedding alpha= 40.	SSL	Ng1.1
DD037	196	887.12	887.16	RFA	Bedding disrupt by reverse movement. Presence of microfracturing.	SSL	Ng1.1
DD037	197	899.40	899.50	FLD	Fold axial plane.	SSL	Ng1.1
DD037	198	899.50	904.00	MFO	Moderate foliation defined by the alignment of pyrite. Bedding alpha = 49.	SSL	Ng1.1
DD037	198	1050.00	1082.00	MFO	Moderate foliation defined by the alignment of clasts.	SDT	Ng1.1
DD037	228	1087.40	1091.00	VN	Dolomite vein.	VN	Ng1.1
DD037	230	1099.55	1105.00	VN	Dolomite and Quartz veins sub parallel to beds. Presence of Pyrite. Possible extensional veins. alpha= 47.	VN	Ng1.1
DD037	262	1298.73	1298.78	VN	Quartz vein parallel to the beddings. Presence of chlorite. Vein possible formed at the same time with deposit.	VN	Ng1.1
DD051	123	538.96	539.04	VN	Quartz vein with pyrite infill.	SSL	Ng1.1.1
DD051	123	539.13	539.16	VN	Quartz vein with pyrite in the seveldge. Undulated.	SSL	Ng1.1.1
DD051	123-125	541	550	VWFO	Very weak foliation defined by coarse-grained pyrite.	SSL	Ng1.1.1
DD051	125-127	553	561.02	SS	Very weak foliation defined by the alignment of small mafic clasts. Predominance of upwards strain shadows>>> upwards strain fringes. The quartzite clasts are not aligned. Predominance of fractures with FeOx and clay infill.	SDT	Ng1.1.1
DD051	127-128	563.5	572.5	FZ	Broken to rubble zone.	SST/SDT	Ng1.1.1
DD052	152	675.66	675.74	RFA	Reverse fault defined by offset of beds. Rare normal faults are observed.	SSL	Ng1.1.2
DD052	152, 153	676	683.5	FZ	Fractured and unusually weathered zone.	SDT	Ng1.1.1
DD052	155,156	687.25	690.65	FZ	Fractured zone with FeOx inside.	SDT	Ng1.1.1
DD084	32	142.46	142.48	MFA	Micro-fault showing both normal and reverse movement based on the offset of coarse-grained pyrite beds. Alpha=41; 35.	SSL	Ng1.1.2
DD084	33	143.05	143.06	MFA	Micro-fault defined by the displacement of beds. Possible normal sense of movement.	SSL	Ng1.1.2
DD084	33	146.13	146.58	BD	Bedded pyritic siltstone. No foliation observed.	SSL	Ng1.1.2
DD084	33	146	146.13	NFA	Micro fault showing normal sense of movement.	SSL	Ng1.1.2
DD084	34	149.82	149.86	FLD	Tight fold. The minerals are parallel to the axial plane fold.	SSL	Ng1.1.2
DD084	37,38	161.5	165.83	SS	Weak foliation defined by the alignment of minerals and upwards chalcopyrite strain shadows.	SDT	Ng1.1.1
DD084	38	165.83	166.63	SS	Weak foliation defined by symmetric strain shadow.	SDT	Ng1.1.1
DD084	38	166.33	167.96	SSD	Soft sediment deformation with abundant chlcocite.	SSL/SDT	Ng1.1.1
DD104	9	39.15	39.16	RFA	Reverse fault based on displacement of beds.	SSL	Ng1.1.2
DD104	10	43.19	43.47	X	Brecciated rock likely a crackle breccia with micro-faults (reverse and normal fault)	SSL	Ng1.1.2
DD104	11	48.77	49	X	Brecciated zone.	SDT	Ng1.1.1
DD104	12	52.28	52.38	X	Brecciated zone.	SDT	Ng1.1.1
DD104	13	53.56	53.8	X	Brecciated zone.	SDT	Ng1.1.1
DD104	13	56.16	56.53	VN	Quartz vein.	SDT	Ng1.1.1
DD104	13	57.64	57.69	X	Cohesive breccia filled the fracture. FeOx infill	SDT	Ng1.1.1

BHID	Box #	From	To	Feature code	Feature	Lithology	Strat unit
DD104	14	59	61.8	VWFO	Very weak foliation defined by the alignment of small mafic clasts.	SDT	Ng1.1.1
DD197	44,45	192.06	192.06	BD	Bedded siltstone with pyrite infill. No foliation.	SSL	Ng1.1.2
DD197	46	205.03	205.07	FLD	Fold axial plane.	SSL	Ng1.1.2
DD197	48	211.5	212.4	SS	Weak foliation defined by upwards strain shadows and by the alignment of minerals.	SDT	Ng1.1.1
DD197	50, 51	219	224.05	VWFO	Very weak foliation defined by the alignment of clasts (most argillites).	SDT	Ng1.1.1
DD199	55	246.61	247.00	SS	Symmetric strain shadows defining a foliation.	SDT	Ng1.1.3
DD199	57	254.00	254.50	WFO	Weak to moderate foliation defined by the alignment of iron oxides (leached pyritic siltstone)	SSL	Ng1.1.2
DD199	58	258.00	259.00	WFO	Weak foliation defined by the alignment of pyrite.	SSL	Ng1.1.2
DD199	62	278.86	278.98	VN	Quartz vein showing vuggy texture. Bedding = 54	SSL	Ng1.1.2
DD199	64	285.13	285.14	NFA	Micro fault showing normal fault.	SSL	Ng1.1.2
DD199	64	285.35	299.00	SS	Weak foliation defined by the alignment of clasts. Predominance of asymmetric upwards strain shadows.	SDT	Ng1.1.1
DD199	67, 68	299.00	304.00	VWFO	Very weak foliation defined by the alignment of clasts. Fractured rock.	SDT	Ng1.1.1
DD199	68	304.00	305.50	FZ	Fractured zone possible due to the significant fault below. Weak foliation defined by the alignment of clasts.	SDT	Ng1.1.1
DD199	68	305.5	305.65	FLT	Significant fault. Gouge. Mosaic breccia; abundant clay material.	SDT	Ng1.1.1
DD199	68	305.65	312.60	VWFO	Very weak foliation defined by the alignment of clasts. Fractured due to the significant fault above.	SDT	Ng1.1.1
DD200	38,39	174	174	BD	Bedding with pyrite inside. No foliation in the rock.	SSL	Ng1.1.2
DD200	40	178.51	178.53	NFA	Mesoscopic fault showing normal sense of movement.	SSL	Ng1.1.2
DD200	42	188.35	188.36	NFA	Mesoscopic fault showing normal sense of movement.	SST	Ng1.1.2
DD200	42	188.86	188.91	FLD	Tight fold axial plane.	SST	Ng1.1.2
DD200	42	189.5	189.58	FLD	Tight fold.	SST	Ng1.1.2
DD200	45,46	201.54	205	SS	Weak foliation defined by the alignment of chalcopyrite and strain shadows.	SDT	Ng1.1.1
DD202	32	146.45	146.46	RFA	Mesoscopic fault showing a reverse sense of movement based on displacement of coarse-grained laminated beds.	SSL	Ng1.1.2
DD202	34	147.00	147.00	LM	Lamination with pyrite inside.	SSL	Ng1.1.2
DD202	36	165.77	165.82	FLD	Fold axial plane.	SSL	Ng1.1.2
DD202	39	179.10	179.19	NFA	Soft sediment deformation with mesoscopic fault showing a normal sense of movement.	SSL	Ng1.1.1
DD202	40,41	183.38	188.69	VWFO	Very weak foliation defined by the alignment of clasts.	SSL	Ng1.1.1
DD202	41,42	188.69	192.03	WFO	Weak foliation defined by the alignment of clasts.	SDT	Ng1.1.1
DD202	42	192.03	195.63	WFO	Weak foliation defined by the alignment of clasts.	SDT	Ng1.1.1
DD202	43	195.63	197.51	WFO	Weak foliation defined by the alignment of clasts.	SDT	Ng1.1.1
DD215	124,125	575.41	578.51	WFO	Weak foliation defined by the alignment of pyrite.	SSL	Ng1.1.2
DD215	125	578.51	578.58	NFA	Zone with mesoscopic normal faults. Occasional reverse faults.	SSL	Ng1.1.2
DD215	125	578.58	579.11	WFO	Weak foliation defined by the alignment of pyrite.	SSL	Ng1.1.2
DD215	125	579.11	579.15	NFA	Normal fault based on displacement of siltstone beds.	SSL	Ng1.1.2
DD215	125	579.15	579.79	WFO	Weak foliation defined by the alignment of pyrite.	SSL	Ng1.1.2
DD215	125	579.79	579.8	NFA	Normal fault observed in the displacement of beds.	SSL	Ng1.1.2
DD215	125	580.1	580.68	WFO	Weak foliation defined by the alignment of pyrite(Fine- and coarse-grained).	SSL	Ng1.1.2
DD215	125	580.68	580.69	RFA	Reverse fault defined by the offset of pyrite beds.	SSL	Ng1.1.2
DD215	125	579.07	580.1	FLD	Fold. The foliation is oblique to the fold.	SSL	Ng1.1.2
DD215	125	580.69	582.96	WFO	Weak foliation defined by the alignment of fine- and coarse-grained pyrite.	SSL	Ng1.1.2
DD215	125	582.96	583.06	VN	Quartz vein.	SSL	Ng1.1.2
DD215	125	583.06	583.95	WFO	Weak foliation defined by the alignment FG+CG pyrite.	SSL	Ng1.1.2
DD215	129	596.53	599.39	SS	Foliation defined by the alignment of chalcopyrite associated with strain shadows/fringes composed of chalcopyrite. Oriented but quarter core.	SDT	Ng1.1.1
DD215	130	602.66	603.73	FZ	Fractured zone with FeOx inside.	SST	R4.2
DD224	91	382.62	382.81	NFA	Normal fault based on displacement of beds.	SSL	Ng1.1.2
DD224	94,95	398	402.28	SS	Weak foliation defined by the alignmnent of chalcopyrite and upwards strain shadows.	SDT	Ng1.1.1
DD224	96	402.87	409.05	VWFO	Very weak foliation defined by the alignment of clasts. The mafic clasts are aligned, the quartzite are not aligned. Quartzite>>Mafic clasts.	SDT	Ng1.1.1
DD240	8,9	25.96	26.6	FLT	Crackle breccia with FeOx in fractures. Presence of mesoscopic normal faults.	SSL	Ng1.1.2
DD240	11	26.6	34.71	FZ	Broken to rubble zone.	SSL	Ng1.1.2
DD240	11,12	34.71	35.71	FLT	Brecciated and rubbled zone.	SSL	Ng1.1.2
DD240	12	35.74	35.75	NFA	Mesoscopic faults showing normal sense of movement.	SSL	Ng1.1.2
DD240	12,13	36.31	39.44	FZ	Fractured zone with some breccias inside.	SSL	Ng1.1.2
DD240	13	39.47	39.48	NFA	Normal mesoscopic fault observed in the displacement of beds.	SSL	Ng1.1.2
DD240	13	39.57	39.58	RFA	Reverse fault like a thrust fault.	SSL	Ng1.1.2
DD240	13	39.58	41.14	FLT	Rubble and broken zone with cohesive breccia.	SSL	Ng1.1.2

BHID	Box #	From	To	Feature code	Feature	Lithology	Strat unit
DD240	14	42.21	42.26	RFA	Reverse fault based on displacement of clasts.	SDT	Ng1.1.1
DD240	14	43.28	43.33	X	Cohesive breccia.	SDT	Ng1.1.1
DD241	6	22.07	22.29	X	Brecciated zone.	SSL	Ng1.1.2
DD241	10	37.69	37.77	VN	Quartz vein.	SDT	Ng1.1.1
DD241	15	53.21	53.23	NFA	Mesoscopic normal fault defined by displacement of beds.	SST	R4.2
DD248	2,3,4	10.87	20.67	FZ	Broken to rubble zone, possible due to the weathered zone.	SSL	Ng1.1.2
DD248	4,5	22	23.1	FZ	Fractured zone with FeOx infill.	SSL	Ng1.1.2
DD248	5	23.11	23.11	NFA	Normal fault defined by displacement of beds.	SSL	Ng1.1.2
DD248	5	26.14	26.26	X	Brecciated zone like micro fracturing.	SSL	Ng1.1.2
DD248	6	26.26	30	FZ	Broken to rubble zone possible due to the weathered zone. Most of the fractures are sub parallel to the beds.	SSL	Ng1.1.2
DD248	7	32.04	32.05	NFA	Normal fault based on displacement of beds.	SSL	Ng1.1.2
DD248	7	33.38	33.39	NFA	Normal fault based on diplacement of beds.	SSL	Ng1.1.1
DD248	10,11	51.47	55.27	VWFO	Very weak foliation, subvertical, defined by small mafic clasts.	SDT	Ng1.1.1
DD248	11	55.82	57.33	FZ	Fractured zone. Broken to rubble with FeOx and MnOx in fractures.	SDT	Ng1.1.1
DD252	148	678.12	681.5	SS	Weak foliation defined by the alignment of upwards strain shadows and the alignment of coarse-grained chalcopyrite. Quarter core. Foliation defined also by the alignment of mafic clasts.	SDT	Ng1.1.1
DD252	148-150	681.5	687.5	SS	Weak foliation defined by the alignment of mafic clasts and the alignment of coarse-grained upwards strain shadows composed of bornite. Quartz clasts are not align.	SDT	Ng1.1.1
DD309	84	374.26	374.29	FLD	Fold axial plane. Presence of foliation defined by the alignment of coarse-grained chalcopyrite which is sub parallel to the fold axis.	SSL	Ng1.1.2
DD309	86,87	384.31	384.78	X	Brecciated zone with abundant clay inside.	SDT	Ng1.1.1
DD309	88	389.42	389.44	X	Thin gouge breccia filled the diamictite. Abundant clay inside.	SDT	Ng1.1.1
DD309	88	389.64	390.54	VWFO	Very weak foliation defined by the alignment of clasts (mafic clasts).	SDT	Ng1.1.1
DD309	88	390.54	390.86	FZ	Fractured zone. Broken to rubble. Abundant clayey materials.	SDT	Ng1.1.1
DD309	89	394.52	396	VWFO	Very weak foliation defined by the alignment of clasts (most mafic clasts). Quartz are not aligned.	SDT	Ng1.1.1
DD309	91,92	403	411.42	VWFO	Very weak foliation defined by the alignment of mafic clasts. Quartz clasts are not aligned. The small clasts are well aligned.	SDT	Ng1.1.1
DD311	13	63.27	63.29	NFA	Mesoscopic normal fault based on the displacement of pyrite beds. Syn sedimentary fault.	SSL	Ng1.1.2
DD311	13	64.21	64.21	NFA	Mesoscopic normal fault, strike slip.	SSL	Ng1.1.2
DD311	13	65.06	65.08	NFA	Soft sedimentary deformation with normal mesoscopic fault.	SSL	Ng1.1.2
DD311	17	84.11	84.2	FLT	Crackle breccia with mesoscopic normal faults.	SSL	Ng1.1.2
DD311	19	92.41	92.42	NFA	Syn-sedimentary normal faults based on beds.	SSL	Ng1.1.1
DD314	3	18.99	19	RFA	Reverse fault defined by the displacement of siltstone beds.	SSL	Ng1.1.2
DD314	4	24.31	24.32	NFA	Normal mesoscopic fault defined by the displacement of beds.	SSL	Ng1.1.2
DD314	6	37.37	37.39	FLD	Fold axial plane with moderate foliation subparallel to axial plane. Bedding: 82 degrees.	SSL	Ng1.1.2
DD314	9	46.98	47.09	WFO	Weak foliation defined by the alignment of coarse-grained chalcopyrite.	SSL	Ng1.1.2
DD314	9	47.7	49.6	SS	Upwards strain shadows associated with coarse-grained chalcopyrite.	SDT	Ng1.1.1
DD314	11	58.18	59.26	VWFO	Very weak foliation defined by the alignment of small mafic clasts.	SDT	Ng1.1.1
DD327	16	80.8	89	FZ	Broken to rubble zone; unusually weathered.	SSL	Ng1.1.2
DD327	17	90.15	90.18	NFA	Mesoscopic fault showing normal sense of movement.	SSL	Ng1.1.2
DD327	19	97.09	97.09	NFA	Normal fault based on the displacement of beds.	SSL	Ng1.1.2
DD327	19	98.53	98.54	NFA	Normal fault based on the displacement of beds.	SSL	Ng1.1.2
DD327	20	102.44	102.47	FSX	Fault by sedimentary breccia.	SSL	Ng1.1.2
DD327	20	106.95	107	FLT	Fault by cohesive breccia. Crackle breccia, clasts touch each others.	SSL	Ng1.1.1
DD327	21	108.08	108.13	RFA	Syn-sedimentary reverse fault.	SSL	Ng1.1.1
DD327	21	110.42	110.57	X	Fault breccia.	SSL	Ng1.1.1
DD327	22	112.25	112.26	NFA	Syn-sedimentary normal fault.	SSL	Ng1.1.1
DD327	22	112.36	112.37	FSX	Thin fault by sedimentary breccia.	SSL	Ng1.1.1
DD327	25	127.02	127.04	X	Brecciated zone.	SSL	Ng1.1.1
DD327	25	128.84	128.91	X	Brecciated zone like a cohesive breccia.	SSL	Ng1.1.1
DD327	26	134.19	134.23	X	Cohesive breccia with FeOx infill. Possible sedimentary feature.	SSL	Ng1.1.1
DD327	26	135.6	135.64	X	Cohesive breccia like a sedimentary breccia.	SSL	Ng1.1.1
DD354	3,4	21	23	FZ	Fractured zone with FeOx infill.	SDT	Ng1.1.1
DD354	4	26.79	26.88	X	Fault breccia.	SDT	Ng1.1.1
DD354	4	27.22	28.39	FZ	Fractured zone with mesoscopic fractures.	SST	Ng1.1.1

BHID	Box #	From	To	Feature code	Feature	Lithology	Strat unit
DD381	55,56	239.00	243.00	SS	Weak foliation defined by the alignment of clasts and minerals (replacement chalcopyrite). Presence of upwards strain shadows.	SDT	Ng1.1.1
DD381	56	243.00	246.30	SSD	Soft sediment deformation texture. High grade bornite, chalcopyrite.	SSL	Ng1.1.1
DD401	157	755	756	BD	Pyrite mineralisation is parallel to the bedding	SSL	Ng1.1.2
DD401	157	759.05	759.17	VN	Quartz vein with pyrite.	SSL	Ng1.1.2
DD401	157	757.86	757.90	VN	Quartz vein with pyrite.	SSL	Ng1.1.2
DD401	158	762.23	762.25	VN	Quartz vein with pyrite.	SSL	Ng1.1.2
DD401	158	762.74	762.76	VN	Quartz vein with pyrite inside.	SSL	Ng1.1.2
DD401	159	765.12	765.27	VN	Quartz vein with pyrite inside. Unconformable edge.	SSL	Ng1.1.2
DD401	159	766.63	766.68	VN	Quartz vein with pyrite in seveldge and inside the vein.	SSL	Ng1.1.2
DD401	159	768.30	768.32	VN	Quartz vein with pyrite inside.	SSL	Ng1.1.2
DD401	160-161	774.30	781.00	SS	Predominance of asymmetric upwards strain shadows. The mineralisation is align, sub parallel to the core axis.	SDT	Ng1.1.1
DD401	162	783.00	784.00	SS	Predominance of upwards strain shadows.	SDT	Ng1.1.1
DD401	162-163	784.00	788.00	SS	Predominance of downwards assymmetric strain shadows. The mineralisation is align, sub parallel to the core axis.	SDT	Ng1.1.1
DD401	165	795.82	795.83	VN	Quartz vein cutting the clasts.	SDT	Ng1.1.1
DD401	169	816.00	816.30	WFO	Weak foliation defined by the alignment of clasts (most mafics).	SDT	Ng1.1.1
DD401	169-170	819.00	827.62	FLT	Significant fault seen by badly broken to rubble zone. The lost core is > to 4 m.	SDT	Ng1.1.1
DD401	170	828.25	828.34	VN	Quartz vein.	SST	R4.2
DD404	15	53	54.5	WFO	Weak foliation defined by the alignment of FeOx grains.	SSL	Ng1.1.2
DD404	16	55	55.01	NFA	Mesoscopic normal fault defined by the offset of beds.	SSL	Ng1.1.2
DD404	16	57.18	57.2	FLD	Tight fold.	SSL	Ng1.1.2
DD404	17	58.06	59.4	VN	Quartz vein with FeOx inside.	SSL	Ng1.1.2
DD404	17	59.5	61.34	WFO	Weak foliation defined by the alignment of FeOx grains.	SSL/SST	Ng1.1.2
DD404	20	72.24	72.44	NFA	Mesoscopic faults showing normal sense of movement.	SST	Ng1.1.2
DD404	22-24	75.78	82.79	FW	Oxydised zone.	SSL	Ng1.1.2
DD404	26	91.27	91.34	RFA	Reverse fault mixed with normal fault. Reverse faults are dominant. Soft sediment deformation.	SSL	Ng1.1.1
DD404	28	95.5	95.74	X	Cohesive breccia.	SST	Ng1.1.1
DD404	30	106.01	106.21	X	Cohesive breccia.	SDT	Ng1.1.1
DD404	31	107.57	107.75	X	Brecciated zone.	SDT	Ng1.1.1
DD404	31	110	110.23	X	Cohesive breccia with FeOx infill.	SDT	Ng1.1.1
DD404	29	100.6	100.71	SBD	Subvertical beds with high grade chalcocite.	SSL	Ng1.1.1
DD404	29	100.60	100.71	SBD	Subvertical beds with high grade chalcocite.	SSL	Ng1.1.1
DD405	107	490.00	498.73	MFO	Moderate foliation defined by the alignment of pyrite.	SSL/SST	Ng1.1.2
DD405	108	498.73	498.76	RFA	Reverse mesoscopic fault. The minerals overgrow in the fault (pyrite).	SSL	Ng1.1.2
DD405	108	498.94	498.98	NFA	Normal mesoscopic fault.	SSL	Ng1.1.2
DD405	108	499.00	499.04	VN	Quartz vein.	SSL	Ng1.1.2
DD405	108,109	499.04	503.00	WFO	Weak to moderate foliation defined by the alignement of minerals.	SSL/SST	Ng1.1.2
DD405	114,115	529.00	532.88	VWFO	Very weak foliation defined by the alignement of clasts. The mafic clasts are align. The Quartz clasts are not align.	SDT	Ng1.1.1
DD411	158	772.34	772.66	NFA	Mesoscopic fault showing a normal sense of movement. Soft sediment deformation.	SSL	Ng1.1.2
DD411	159-160	776.00	785.29	WFO	The alignment of pyrite defines the S1 foliation.	SSL	Ng1.1.2
DD411	160	785.29	785.35	VN	Quartz vein with pyrite and sphalerite.	SSL	Ng1.1.2
DD411	160-161	785.35	794.00	WFO	The alignment of pyrite defines the S1 foliation.	SSL	Ng1.1.2
DD411	166	812.48	812.83	MFA	Mesoscopic fault. Possible reverse sense of movement based on beds.	SSL	Ng1.1.2
DD411	167	816.77	816.84	VN	Possible pyrite tensional veins.	SSL	Ng1.1.2
DD411	167	817.31	817.32	VN	Quartz vein with Py in the edge.	SSL	Ng1.1.2
DD416	33	145.33	145.68	SBD	Subvertical beddings with alot of mesoscopic normal faults. High grade chalcocite, chalcopyrite. Very weak foliation defined by the alignment of minerals sub perpendicular to the beds.	SST	Ng1.1.1
DD440	33	126.77	126.86	SSD	Soft sediment deformation	SSL	Ng1.1.2
DD440	36	148.00	148.10	WFO	Weak S_1 defines by pyrite. Broken rock.	SSL	Ng1.1.2
DD440	40	169.19	169.37	SSD	Soft sediment deformation	SSL/SST	Ng1.1.2
DD440	40	171.50	171.64	SSD	Soft sediment deformation	SSL	Ng1.1.2
DD440	40	172.08	172.21	SSD	Soft sediment deformation	SSL	Ng1.1.2
DD440	34	131.43	131.50	FLD	Fold axial plane	SSL	Ng1.1.2
DD440	45	196.74	196.88	SS	Weak S1 defines by sulphides.	SDT	Ng1.1.1
DD440	46	198.60	198.77	WFO	Weak S1 defines by sulphides.	SDT	Ng1.1.1
DD440	38	158.12	158.19	SSD	Soft sediment deformation	SSL	Ng1.1.2

BHID	Box #	From	To	Feature code	Feature	Lithology	Strat unit
DD440	44	190.12	190.20	VN	Mafic clast cut by quartz and pyrite	SDT	Ng1.1.1
DD440	47	203.50	203.59	RFA	Reverse fault based on the offset of beds.	SSL/SST	Ng1.1.1
DD440	47	204.30	204.39	NFA	Normal fault based on the offset of beds.	SSL/SST	Ng1.1.1
DD440	52	228.24	228.42	NFA	Soft sedimnt deformation showing normal fault	SSL	Ng1.1.1
DD440	45	196.54	196.67	SS	Strain shadows define by chalcopyrite. Upwards and downwards strain shadows	SDT	Ng1.1.1
DD440	55	242.35	242.50	WFO	Weak foliation with strain shadows	SDT	Ng1.1.1
DD440	46	198.91	199.19	SS	Weak S1 defines by sulphides.	SDT	Ng1.1.1
DD440	46	198.91	199.19	SS	Weak S1 defines by sulphides.	SDT	Ng1.1.1
DD440	46	200.92	201.27	SS	Weak S1 defines by sulphides perpendicular to the bedding	SDT	Ng1.1.1
DD440	52	228.70	228.74	X	Crackle breccia	SSL	Ng1.1.1
DD440	33	124.40	124.55	SSD	Soft sediment deformation	SSL	Ng1.1.2
DD441	2	11.50	11.70	SSD	Dewatering structure like soft sediment deformation.	SSL	Ng1.1.2
DD441	6	26.43	26.48	SSD	Soft sediment deformation including normal and reverse faults.	SSL	Ng1.1.2
DD441	17	62.49	62.67	SSD	Soft sediment deformation like a fold.	SSL	Ng1.1.2
DD441	18	66.46	66.50	X	Breccia; normal fault based on beds.	SSL	Ng1.1.2
DD441	21	79.90	80.10	VN	Undulated vein in the siltstone.	SSL	Ng1.1.2
DD441	24	94.28	94.38	X	Crackle breccia with reverse fault.	SSL	Ng1.1.2
DD441	25	96.40	96.66	WFO	Very weak foliation observed based on the alignment of clasts	SSL	Ng1.1.1
DD441	26	100.36	100.44	SS	Zone with occasional strain shadows composed of malachite.	SDT	Ng1.1.1
DD441	28	113.81	113.84	RFA	Micro-fracturing in the siltstone showing a reverse sense of movement.	SDT	Ng1.1.1
DD443	112	525.10	525.15	NFA	Soft sediment deformation showing a fault with normal sense of movement.	SSL	Ng1.1.2
DD443	113	532.67	532.74	SSD	Soft sediment deformation in siltstone and sandstone.	SSL	Ng1.1.2
DD443	114	537.62	537.70	SS	Upward strain shadows.	SSL	Ng1.1.2
DD443	116	546.74	546.84	SSD	Soft sediment deformation with mesoscopic faults showing a reverse sense of movement.	SSL	Ng1.1.2
DD443	118	558.10	561.37	WFO	Weak foliation defined by the alignment of clasts. The foliation is sub parallel to the core axis.	SDT	Ng1.1.1
DD443	119	565.54	567.00	MFO	Moderate foliation sub parallel to the strain shadows sub-parallel to the core axis.	SDT	Ng1.1.1
DD443	120	569.26	575.00	WFO	Weak foliation defines by the alignment of clasts.	SDT	Ng1.1.1
DD448	36	152.50	153.00	WFO	Weak sub-vertical S1 foliation	SDT	Ng1.1.1
DD448	33	134.50	134.74	WFO	Weak sub-vertical S1 foliation	SDT	Ng1.1.1
DD448	32	130.05	130.32	X	Alteration pathway breccia	SDT	Ng1.1.1
DD448	21	73.18	73.28	NFA	Mesoscopic normal fault shown by the offset of beds. Minor breccia, fluid pathway.	SSL	Ng1.1.2
DD448	16	54.50	54.60	SSD	Soft sediment deformation associated with mesoscopic faults.	SSL	Ng1.1.2
DD448	15	48.50	48.70	NFA	Normal mesoscopic fault.	SSL	Ng1.1.2
DD448	14	46.25	46.35	NFA	Normal mesoscopic fault.	SSL	Ng1.1.2
DD448	13	42.04	42.12	NFA	Normal mesoscopic fault.	SSL	Ng1.1.2
DD449	87	386.37	386.58	WFO	Weak foliation defines by the alignment of pyrite	SSL	Ng1.1.2
DD449	90	401.38	401.47	FLD	Fold. Possible syn-sedimentary origin.	SSL	Ng1.1.2
DD449	93	420.00	420.11	SSD	Soft sediment deformation associated with mesoscopic faults showing a reverse sense of movement.	SSL	Ng1.1.2
DD449	95	431.00	431.25	NFA	Normal mesoscopic fault defined by the offset of beds.	SSL	Ng1.1.2
DD449	97	441.85	442.00	SSD	Soft sediment deformation texture.	SSL	Ng1.1.1
DD449	98	443.00	447.00	SS	Strain shadow parallel to the S1 sub parallel to the core axis.	SDT	Ng1.1.1
DD453	222,223	1147.61	1150.29	SS	Strain shadows and moderate foliation defined by the alignment of clasts and upwards asymmetric strain shadows.	SDT	Ng1.1.1
DD453	223,224	1150.89	1155.66	SS	Weak foliation defined by the alignment of coarse-grained chalcopyrite, coarse-grained bornite; alignment of symmetric and assymmetric shadows. Predominance of upwards strain shadows.	SDT	Ng1.1.1
DD453	222,223	1147.61	1150.29	SS	Weak to moderate foliation defined by the alignment of clasts and upwards strain shadows.	SDT	Ng1.1.1
DD465	9	34.5	34.57	FLD	Fold. The foliation seems parallel to the fold axial plane.	SSL	Ng1.1.2
DD465	15	52.15	52.25	MFO	Moderate foliation around the 8 cm quartz clasts. This foliation is possibly related to the clast.	SDT	Ng1.1.1
DD465	15,16	52.6	56	SS	Strain shadows composed ofchalcocite and FeOx.	SDT	Ng1.1.1
DD493	21	73.12	73.32	X	Brecciated zone.	SSL/SST	Ng1.1.2
DD493	22	77.08	77.81	X	Brecciated zone. Presence of mesoscopic faults with normal sense of movement.	SSL	Ng1.1.2
DD493	22	78.52	78.61	RFA	Bedding disrupt by mesoscopic faults showing a reverse sense of movement.	SSL	Ng1.1.2
DD493	22	78.9	78.95	NFA	Mesoscopic fault seen by the offset of beds. Normal sense of movement.	SSL	Ng1.1.2
DD493	23	79.49	79.53	MFA	Mesoscopic fault disrupting the beds. No clear movement. Iron oxides in the fault.	SSL	Ng1.1.2
DD506	6	22.81	22.83	X	Thin breccia in the siltstone. Cohesive.	SSL	Ng1.1.2
DD506	8	31.33	31.37		Dewatering structure.	SDT	Ng1.1.1
DD506	8	30.9	31	NFA	Mesoscopic fault showing a normal sense of movement.	SSL	Ng1.1.2

BHID	Box #	From	To	Feature code	Feature	Lithology	Strat unit
DD508	6	22.1	22.14	NFA	Mesoscopic fault showing a normal sense of movement. Soft sediment deformation texture.	SSL	Ng1.1.1
DD508	6	23.23	23.96	SS	Very weak foliation defined by the alignment of strain shadows composed of chalcocite (Predominance of upwards strain shadows). Sub -arallel to the core axis, no clear the alignment.	SDT	Ng1.1.1
DD516	16-19	59	67	FW	Abundant dewatering structures. Fractures possibly due to the weathering zone.	SSL	Ng1.1.2
DD516	19	69.21	69.23	FLD	Tight fold. The alpha angle is parallel to the bedding, possible soft sediment deformation.	SSL	Ng1.1.2
DD516		71	79.14	FA3	Badly broken to rubbly; brecciated and gougy core zone with haematite and limonite in fractures.	SSL	Ng1.1.2
DD516	21	76.88	76.89	RFA	Reverse fault based on the offset of beds.	SSL	Ng1.1.2
DD516		80.24	81.5	FZ	Broken to rubbled core with haematite in fractures.	SSL	Ng1.1.2
DD516		83.57	83.63	FA3	Clast supported breccia with gouge	SDT	Ng1.1.2
DD516		99	101.9	FZ	Broken to rubbled zone with haematite in fractures.	SDT/SSL	Ng1.1.1
DD516		101.9	104	FA1	Unusually weathered; badly rubbled clast supported breccia with gouge.	SDT	Ng1.1.1
DD516		104	107.1	FZ	Fractured zone below the fault.	SSL	Ng1.1.1
DD516	30	112.27	112.29	RFA	Reverse fault based on the offset of sandstone beds.	SST/SSL	R4.2
DD538	2	10.91	10.94	FLD	Fold axial plane sub-parallel to beddings.	SSL	Ng1.1.2
DD538	3	15.54	15.54	LM	Planar lamination in SSL.	SSL	Ng1.1.2
DD538	7	41.66	41.71	X	Brecciated zone.	SDT	Ng1.1.1
DD538	7	43.36	43.38	NFA	Mesoscopic fault showing a normal sense of movement. Soft sediment deformation texture.	SSL	Ng1.1.1
DD550	28	141.24	141.25	RFA	Reverse fault defined by the offset of beds.	SSL	Ng1.1.2
DD550		141.6	146.12	FLT	Broken to rubble zone with many crackle breccia. Unusually weathered zone. Mesoscopic fault inside.	SSL	Ng1.1.2
DD550	29	146.12	146.18	MFA	Normal mesoscopic fault associated with reverse faults.	SSL	Ng1.1.2
DD550		146.18	147	FLT	Hard healed, mesoscopic-fault offset with crackle breccia and rubble zone. Faulted contact between two lithologies. Presence of gougy. Also lost core texture.	SDT	Ng1.1.2
DD550		147	164.2	FLT	Broken to rubble zone with many breccias. Unusually weathered zone.	SDT	Ng1.1.1
DD550		173.85	186	FZ	Fractured zone.	SSL	Ng1.1.1
DD550		186	186.3	FLT	Crackle breccia with strike slip slickensides.	SSL	Ng1.1.1
DD550		186.3	195.5	FZ	Broken to rubble zone.	SSL	Ng1.1.1
DD550	39,40	195.5	199.2	VWFO	Very weak foliation defined by the alignment of small mafic clasts. Sub vertical. Fractured zone.	SDT	Ng1.1.1
DD550		199.1	205.5	FZ	Fractured zone.	SST	Ng1.1.1
DD561	1	5.21	5.31	X	Cohesive breccia.	SSL	Ng1.1.2
DD561	3	18.22	18.32	NFA	Soft sediment deformation with mesoscopic normal faults.	SSL	Ng1.1.1
DD561	4	20.60	20.65	NFA	Mesoscopic fault showing a normal sense of movement.	SSL	Ng1.1.1
DD561	4	21.19	21.21	X	Cohesive breccia in the siltstone.	SSL	Ng1.1.1
DD583	2, 3	19.00	23.00	VWFO	Very weak foliation defined by the alignment of clasts	SDT	Ng1.1.1
DD583	4	26.65	26.65	LM	Planar lamination in the siltstone.	SSL	Ng1.1.1
DD583	5	32.16	32.25	X	Crackle breccia.	SSL	Ng1.1.1
DD595	87	411.52	411.54	NFA	Mesoscopic fault with normal sense of movement.	SSL	Ng1.1.2
DD595	88	411.45	411.51	FLD	Possible fold looks like soft sediment deformation. Coarse-grained pyrite defined the fold.	SSL	Ng1.1.2
DD595	90-91	427.32	431.79	SS	Upwards strain shaddows>>>upwards strain fringes.	SDT	Ng1.1.1
DD595	92-94	434	445.19	VWFO	Very weak foliation defined by only the alignment of small mafic clasts. The quartzite are not aligned.	SDT	Ng1.1.1
DD619	47,48	237.4	243.8	FZ	Fractured zone with haematite and clay infill. Unusually weathered zone. Fractures are parallel to the beds.	SSL	Ng1.1.2
DD619	49	247.05	247.08	FSX	Fault by sedimentary breccia.	SSL	Ng1.1.2
DD619	49	249.13	249.22	FW	Broken and unusually weathered zone.	SSL	Ng1.1.2
DD619	49	249.4	249.45	FLD	Fold.	SSL	Ng1.1.2
DD619	49	250.9	250.91	NFA	Normal mesoscopic fault based on displacement of beds.	SSL	Ng1.1.2
DD619	51	256.56	256.65	FSX	Fault by sedimentary breccia.	SSL	Ng1.1.2
DD619	51	257.35	257.36	RFA	Reverse fault based on the cut clasts and displacement of beds.	SSL	Ng1.1.1
DD619	52	261.42	261.88	FZ	Fractured and unusually weathered zone.	SDT	Ng1.1.1
DD619	54	273.47	223.49	X	Fault by cohesive breccia.	SDT	Ng1.1.1
DD619	54	273.88	274.91	FZ	Broken to rubble; unusually weathered zone.	SST	R4.2
DD619	54	274.91	274.95	X	Fault by cohesive breccia with FeOx and clay in fractures.	SST	R4.2
DD619	54	274.95	275.62	FZ	Broken to rubble zone. FeOx infill.	SST	R4.2
DD620	34	187.48	187.66	FW	Fault by weathered associated with mesoscopic fracturing. Clay and FeOx infill.	SSL	Ng.1.1.2
DD620	35	188.43	188.64	FW	Fault by weathered with clay and FeOx infill.	SSL	Ng.1.1.2
DD620	35	189.04	189.05	NFA	Normal fault based on the displacement of beds.	SSL	Ng.1.1.2
DD620	35	189.19	189.23	NFA	Normal fault based on displacement of beds.	SSL	Ng.1.1.2
DD620	35	190.8	191.1	FW	Unusually weathered zone with clay inside.	SSL	Ng.1.1.2

BHID	Box #	From	To	Feature code	Feature	Lithology	Strat unit
DD620	35	192.8	192.84	FLD	Fold.	SSL	Ng.1.1.2
DD620	36	186.94	187	X	Fault by cohesive breccia.	SSL	Ng.1.1.2
DD620	38	209.13	209.14	NFA	Normal mesoscopic fault based on displacement of beds.	SSL	Ng.1.1.1
DD620	42	224.88	224.89	VN	Quartz vein.	SDT	Ng.1.1.1
DD620	42	226.64	230.86	FZ	Fractured zone with FeOx and MnOx infill. Also goetite infill.	SDT	Ng.1.1.1
DD627	102	476.9	476.93	FLD	Fold with pyrite inside.	SSL	Ng.1.1.2
DD627	105,106	489	497.18	SS	Very weak foliation defined by the alignment of coarse grained chalcopyrite and strain shadows(asymmetric upwards and symmetric strain shadows; predominantly upwards strain shadows).	SDT	Ng.1.1.1
DD627	106-107	497.18	502.29	WFO	Weak foliation defined by the alignment of mafic clasts. Quartz clasts are not aligned. Most of the mafic clasts aligned are small.	SDT	Ng.1.1.1
DD637	116	576.48	576.49	NFA	Mesoscopic-normal fault defined by the offset of beds. Soft sediment deformation texture.	SSL	Ng1.1.2
DD637	117	579.15	579.25	NFA	Mesoscopic normal fault defined by the offset of beds.	SSL	Ng1.1.2
DD637	122	606.13	606.17	NFA	Mesoscopic-normal fault defined by offset of beds.	SSL	Ng1.1.1
DD637	123,124	609.82	618.6	VWFO	Very weak foliation defined by the alignment of clasts is sub parallel to the core axis (mafic clasts). Malachite in replacement of clasts is also align.	SDT	Ng1.1.1
DD642	80	389.14	394.00	SS	Weak foliation defined by upwards chalcopyrite strain shadows.	SDT	Ng1.1.1
DD645	91	460.82	460.84	VN	Calcite vein in the mafic.	MI	Ng1.1.3
DD645	91	460.29	460.3	VN	Calcite vein in the mafic.	MI	Ng1.1.3
DD645	91	462.33	462.34	VN	Calcite vein in the mafic.	MI	Ng1.1.3
DD645	91	462.65	462.66	VN	Calcite vein in the mafic.	MI	Ng1.1.3
DD645	91	462.93	462.95	VN	Calcite vein in the mafic.	MI	Ng1.1.3
DD645	91	463.92	463.95	VN	Calcite vein in the mafic.	MI	Ng1.1.3
DD645	91	464.06	464.08	VN	Quartz vein in the mafic.	MI	Ng1.1.3
DD645	91	464.58	464.61	VN	Quartz and calcite vein in the mafic.	MI	Ng1.1.3
DD645	92	467.42	467.43	VN	Quartz vein.	MI	Ng1.1.3
DD645	93	471.26	471.27	VN	Quartz vein.	MI	Ng1.1.3
DD645	94	477.22		FZ	Fractured zone.	MI	Ng1.1.3
DD645	94	480	483	FZ	Fractured zone.	MI	Ng1.1.3
DD645	95-98	485.06	495	FZ	Broken to rubble zone with haematite and clay in fractures.	MI/SDT	Ng1.1.3
DD645	99,100	505.44	506.41	WFO	Weak foliation defined by the alignment of clasts (mafics).	SDT	Ng1.1.3
DD645	101,100	506.46	511.56	FZ	Broken to rubble zone with some quartz veins.	SST	R4.2
DD645	101	514.18	514.39	FLT	Fault gouge with abundant clay.	SST	R4.2
DD645	102	514.39	516.54	FZ	Broken to rubble; unusually weathered zone possibly due to the fault around.	SST	R4.2
DD645	102	516.54	516.56	FLT	Fault gouge with oblique slickensides.	SST	R4.2
DD645	102	516.56	516.88	FZ	Fractured zone with clay and haematite inside.	SST	R4.2
DD645	102	516.88	516.91	FLT	Mosaic to chaotic breccia. Abundant clay and FeOx inside. The clasts are highly deformed. No rotation or dilation are observe.	SST	R4.2
DD645	102	516.91	519	FZ	Broken to rubble zone.	SST	R4.2
DD757	85	393.98	393.99	NFA	Mesoscopic-normal fault defined by displacement of SSL beds.	SSL	Ng1.1.2
DD757	89	416.77	417.92	SS	Strain shadows and strain fringes. Weak foliation defined by the alignment of coarse-grained chalcopyrite and the alignment of strain shadows>>strain fringes composed mainly of chalcopyrite. Upwards strain shadows> symmetric strain shadows> downwards strain shadows.	SDT	Ng1.1.1
DD757	90	419.95	419.96	VN	Thin chalcopyrite vein looking like a tensional vein.	SSL	Ng1.1.1
DD757	90	421.4	422.68	WFO	Weak foliation defined by coarse-grained chalcopyrite. Pyrite beds are aligned.	SSL	Ng1.1.1
DD757	91,92	427.63	430.95	VWFO	Very weak foliation defined by the alignment of small mafic clasts. Quartzite are not aligned. Mafic>quartzite. There is no clear plane to measure foliation.	SDT	Ng1.1.1
DD793	79	375.98	376.02	NFA	Mesoscopic-fault showing a normal sense of movement. The displacement is observed in beds.	SSL	Ng1.1.2
DD793	79	379.24	379.41	RFA	Reverse fault defined by the displacement of beds.	SSL	Ng1.1.2
DD793	83	397.96	400.9	WFO	Weak foliation defined by the alignment of coarse-grained sulphides and strain shadows (predominance of upwards strain shadows).	SDT	Ng1.1.1
DD793	84	404.73	405.49	FZ	Micro-fracturing in the siltstone. Presence of tensional veins.	SDT	Ng1.1.1
DD793	85,86	408.67	414.72	VWFO	Very weak foliation defined by the alignment of mafic clasts. Quartzite are not aligned.	SDT	Ng1.1.1
DD795	2	9.25	9.26	RFA	Reverse fault based on the cut clast	SDT	Ng1.1.1
DD795	2,3	11.53	18.1	FZ	Fractured zone; broken to rubble possibly due to the weathered zone.	SDT/SST	Ng1.1.1 and R42
DD795	3	18.1	18.19	X	Cohesive breccia. FeOx infill.	SST	R4.2

BHID	Box #	From	To	Feature code	Feature	Lithology	Strat unit
DD802	75	398.13	399.12	VWFO	Very weak foliation defined by the alignment of coarse-grained pyrite.	SSL	Ng1.1.2
DD802	77	411.11	414	SS	Weak foliation defined by the alignment of coarse-grained chalcopyrite and strain shadows.	SDT	Ng1.1.1
DD802	78	415.93	416.08	VN	Quartz vein.	SDT	Ng1.1.1
DD802	78,79	416.82	421.64	FZ	Fractured zone with malachite and Haematite inside.	SDT	Ng1.1.1
DD802	79,80	421.72	425	VWFO	Very weak foliation defined by the alignment of mafic clasts. Quartzites are not aligned.	SDT	Ng1.1.1
DD816	10	44	44.69	X	Brecciated zone likely a monolotic breccia.	SST	R4.2
DD821	43-46	205.68	224.67	WFO	Weak foliation defined by the alignment of minerals (pyrite). Bedding = 78.	SSL	Ng1.1.2
DD821	48	234.00	234.50	NFA	Mesoscopic-normal fault defined by the offset of beds.	SSL	Ng1.1.1
DD821	50	243.02	243.14	WFO	Weak foliation defined by the alignment of chalcopyrite is sub parallel to the core axis.	SSL	Ng1.1.1
DD821	50,51	243.50	247.40	WFO	Weak foliation defined by the alignment of clasts is sub parallel to core axis.	SDT	Ng1.1.1
DD825	34	163.50	169.00	MFO	Moderate foliation defined by the alignment of clasts. Clasts are also deformed.	SSL/SDT	Ng1.1.1
DD844W1		981.40	999.00	VWFO	Very weak foliation defined by the alignment of clasts and minerals (pyrite, pyrrhotite).	SDT	Ng1.1.3
DD855	22	112.85	116.85	SS	Weak foliation defined by the alignment of clasts and minerals (bornite). Presence of symmetric and upwards strain shadows.	SDT	Ng1.1.1
DD856	28	135.77	140.00	VWFO	Very weak foliation defined by the alignment of minerals (bornite) and clasts.	SDT	Ng1.1.1
DD860	34	122.02	125	MFO	Moderate foliation defined by the alignment of pyrite.	SSL	Ng1.1.2
DD860	34	125	126	MFO	Moderate foliation defined by the alignment of pyrite. Presence of normal syn-sedimentary fault defined by offset of pyrite beds.	SSL	Ng1.1.2
DD860	35,36	126	130	WFO	Weak foliation defined by the alignment of pyrite.	SSL	Ng1.1.2
DD860	36	130	130.04	VN	Quartz vein with pyrite and FeOx inside. The vuggy and brecciated textures are observed.	SSL	Ng1.1.2
DD860	36,37	130.42	134.76	SFO	Strong foliation defined by the alignment of fine- to coarse-grained pyrite.	SSL	Ng1.1.2
DD860	38,39	136.5	141.09	MFO	Moderate foliation defined by the alignmnent of FeOx. Fractured and unusually weathered.	SSL	Ng1.1.2
DD860	39	141.09	141.41	X	Brecciated zone with moderate foliation. Alpha FO=12.	SSL	Ng1.1.2
DD860	39	141.95	142.02	X	Brecciated zone.	SSL	Ng1.1.2
DD860	40	142.18	144.49	MFO	Moderate foliation defined by the alignment of minerals: pyrite and FeOx.	SSL	Ng1.1.2
DD860	40,41	145.5	146.45	MFO	Moderate foliation defined by alignmnent of coarse-grained pyrite .	SCG	Ng1.1.2
DD860	42,43	152.23	153.5	WFO	Weak foliation defined by the alignment of pyrite and occasional bornite.	SSL	Ng1.1.2
DD860	43	154.2	156	WFO	Weak foliation defined by the alignment of bornite and pyrite.	SSL	Ng1.1.2
DD860	43	156	156.11	NFA	Mesoscopic fault defined by the offset of beds of varves.	SSL	Ng1.1.2
DD860	43,44	156.1	161	VWFO	Very weak foliation defined the alignment of clasts (talc, argillites and quartz).	SDT	Ng1.1.1
DD860	45,46	161.51	168.31	WFO	Weak foliation defined by the alignment of chalcopyrite. Presence of thin tensional veins of chalcopyrite. Soft sediment deformation.	SSL	Ng1.1.1
DD860	48	173.2	175.16	SBD	Sub-vertical bedding associated with high grade bornite and trace chalcopyrite. Presence of mesoscopic faults showing a normal sense of movement.	SSL	Ng1.1.1
DD860	48,49	175.16	176	SSD	Soft sediment deformation textures	SSL	Ng1.1.1
DD860	49-52	178.31	189.69	WFO	Weak foliation defined by the alignment of clasts (quartz, siltstone and mafic)	SDT	Ng1.1.1
DD860	53	191.82	191.98	NFA	Mesoscopic fault showing a normal sense of movement. Soft sediment deformation texture.	SDT	Ng1.1.1
DD860	54	195.37	195.88	WFO	Weak foliation defined by the alignment of clasts (mafic).	SDT	Ng1.1.1
DD860	56	200.8	207	FZ	Badly fractured zone with rubble material on top.	SDT	Ng1.1.1
DD862	55	246.39	247.5	MFO	Moderate foliation defined by the alignment of fine- and coarse-grained pyrite.	SSL	Ng1.1.2
DD862	56	249.5	250.77	WFO	Weak foliation defined by the alignment of coarse-grained pyrite.	SSL	Ng1.1.2
DD862	56,57	255	257.67	WFO	Weak foliation defined by the alignment of coarse-grained pyrite.	SSL	Ng1.1.2
DD862	57	258.56	258.6	NFA	Mesoscopic-normal fault defined by the displacement of pyrite beds.	SSL	Ng1.1.2
DD862	58	262.07	262.12	FLD	Fold with pyrite and FeOx infill.	SSL	Ng1.1.2
DD862	59	267.62	267.64	FLD	Tight fold. The foliation is sub parallel to the fold axial plane.	SSL	Ng1.1.2
DD862	60	273.23	276.1	SS	Weak foliation defined by the alignment of strain shadows (most upwards). Strain shadows>strain fringes; they are composed of chalcopyrite.	SDT	Ng1.1.1
DD862	60	276.37	276.38	VN	Quartz vein with abundant chalcopyrite in the seveldge. Undulated shape.	SDT	Ng1.1.1
DD862	60,61	276.96	278.23	SS	Very weak foliation defined by the alignment of coarse-grained and strain shadows composed of chalcopyrite.	SDT	Ng1.1.1
DD862	61,64	283	299.83	VWFO	Very weak foliation defined by the alignment of very small mafic clasts. No clear plan for beta measurement.	SDT	Ng1.1.1
DD866	51	261.45	265.36	MFO	Weak to moderate foliation defined by the alignment of clasts and minerals(Bn).	SDT	Ng1.1.1
DD869	13	206.28	223	WFO	Weak foliation defined by the alignment of pyrite.	SSL	Ng1.1.2
DD869	41	208.5	208.57	RFA	Mesoscopic fault showing possible reverse sense of movement based on offset of beds.	SSL	Ng1.1.2
DD869	41	209.5	216	WFO	Weak foliation defined by the alignment of pyrite.	SSL	Ng1.1.2
DD869	43	219.21	219.3	SSD	Soft sediment deformation texture.	SSL	Ng1.1.2
DD869	43	220.14	220.22	SSD	Soft sediment deformation texture.	SSL	Ng1.1.2

BHID	Box #	From	To	Feature code	Feature	Lithology	Strat unit
DD869	47,48	246	251	VWFO	Very weak foliation defined by the alignment of clasts; it is sub parallel to the core axis.	SDT/SSL	Ng1.1.1
DD875	75	369.34	369.39	FLD	Fold. Pyrite grains defines the fold.	SSL	Ng1.1.2
DD875	78	387.09	387.1	NFA	Mesoscopic-normal fault defined based on the displacement of beds. Presence of pyrite in the mesoscopic fault.	SSL	Ng1.1.2
DD875	79	390.32	393	SS	Strain shadows>>>strain fringes; very weak foliation defined by the alignment of small mafic clasts.	SDT	Ng1.1.1
DD887	65	312.67	316.20	SS	Weak foliation defined by the alignment of coarse-grained chalcopyrite and upwards strain shadows.	SDT	Ng1.1.1
DD888	56	265.00	271.51	SS	Moderate foliation defined by the alignment of bornite coarse-grained, clasts and upwards bornite strain shadows. Soft sediment deformation with undulated and disrupted beds. Foliation is sub-perpendicular to the beds. Presence of mesoscopic faults; most of them show a normal sense of movement. Rare reverse mesoscopic faults are also observed. Bedding: ori 3 alpha= 28; beta= 42.	SDT	Ng1.1.1
DD888	43,46	196.18	216.70	WFO	Weak foliation defined by the alignment of pyrite; it is sub-parallel core axis.	SSL	Ng1.1.2
DD888	47	220.09	220.50	WFO	Weak foliation defines by the alignment of pyrite.	SSL	Ng1.1.2
DD888	50	233.72	233.76	X	Brecciated zone.	SDT	Ng1.1.1
DD888	53,54	252.70	259.00	VWFO	Very to weak foliation defined by the alignment of clasts. Mafic clasts are aligned while quartzites are not.	SDT	Ng1.1.1
DD888	55	259.00	265.00	SS	Weak foliation defined by the alignment of minerals and clasts (sulphide such as chalcopyrite, bornite). Upwards strain shadows>symmetric strain shadows.	SDT	Ng1.1.1
DD888	58	274.66	279.00	WFO	Weak foliation defined by the alignment of clasts (mostly mafic).	SDT	Ng1.1.1
DD895	119,120	579.89	584.60	SS	Weak foliation defined by symmetric and assymmetric upwards chalcopyrite strain shadows.	SDT	Ng1.1.1
DD895	120	584.70	585.15	SBD	Subvertical bedding with high grade chalcopyrite and bornite mineralisation. Presence of weak foliation defined by the alignment of minerals; sub-perpendicular to the bed.	SSL/SDT	Ng1.1.1
DD895	120	585.15	586.85	WFO	Weak foliation defined by the alignment chalcopyrite. Presence of subvertical beds.	SDT/SSL	Ng1.1.1
DD897	85	417.35	419.00	SFO	Strong S1 defines by pyrite is sub-parallel to core axis. Vuggy rock.	SSL	Ng1.1.2
DD897	86	423.14	423.16	RFA	Mesoscopic-fault showing a reverse sense of movement.	SSL	Ng1.1.2
DD897	87	426.00	426.16	VN	Quartz vein parallel to the beddings. Presence of FeOx.	SSL	Ng1.1.2
DD897	89	438.00	438.20	SSD	Soft sediment deformation with some folds.	SSL	Ng1.1.2
DD897	91	448.23	450.15	SS	Pyrite in strain shadows.	SDT	Ng1.1.1
DD897	92	452.73	453.19	SSD	Soft sediment deformation with mesoscopic faults showing a normal sense of movement.	SDT	Ng1.1.1
DD897	95	468.64	469.66	SS	Strain shadows composed of chalcopyrite. Weak foliation defined by chalcopyrite is also observed.	SDT	Ng1.1.1
DD901	122	595.07	597	MFO	Moderate foliation defined by the alignment of pyrite and pyrrhotite. Slighty vuggy.	SSL	Ng1.1.2
DD901	122-123	597.00	604.08	MFO	Moderate foliation defined by the alignment of pyrite.	SSL	Ng1.1.2
DD901	124	604.08	604.37	RFA	Possible reverse fault observed in rock showing soft sediment deformation texture.	SSL	Ng1.1.2
DD901	124	604.47	604.49	VN	Thin veins in bedding.	SSL	Ng1.1.2
DD901	124	608.82	608.84	NFA	Mesoscopic-normal fault. The fault cut the minerals.	SSL	Ng1.1.2
DD901	124	608.84	611.00	MFO	Moderate foliation defined by the alignment of minerals (mostly pyrite).	SSL	Ng1.1.2
DD901	125	611.00	611.12	VN	Quartz vein with pyrite inside.	SSL	Ng1.1.2
DD901	125-126	611.12	616.71	MFO	Moderate foliation defined by the alignment of pyrite.	SSL	Ng1.1.2
DD901	126	616.71	616.85	VN	Quartz vein, vuggy.	SSL	Ng1.1.2
DD901	126-128	616.71	616.85	MFO	Moderate foliation defined by the alignment of pyrite. Soft sediment deformation texture.	SSL	Ng1.1.2
DD901	135-136	665.65	670.46	SS	Weak foliation defined by the alignment of clasts and sulphides (chalcopyrite, bornite). Strain shadows and strain fringes are present. Parted rock.	SDT	Ng1.1.1
DD901	137-138	673.82	681.74	WFO	Weak foliation defined by the alignment of clasts. The minerals are also align. The rock is parted.	SDT	Ng1.1.1
DD903	26	108.92	111.17	X	Brecciated zone.	SSL	Ng1.1.2
DD903	26-28	112	124.60	WFO	Weak foliation defined by the alignment of iron oxides. Leached zone.	SSL	Ng1.1.2
DD903	30	130.00	133.70	WFO	Weak foliation defined by the alignment of minerals(Py in Rp and CG).	SST	Ng1.1.2
DD903	36	164.00	164.36	NFA	Abundant mesoscopic-normal faults defined by the offset of beds.	SSL	Ng1.1.1
DD903	37	169.10	170.61	WFO	Weak foliation defined by the alignment of clasts.	SDT	Ng1.1.1
DD903	37	170.73	171.24	X	Brecciated siltstone.	SSL	Ng1.1.1
DD903	38	171.61	179.64	VWFO	Very weak foliation defined by the alignment of clasts.	SDT	Ng1.1.1
DD903	40-41	184.56	187.80	SS	Weak foliation defined by the alignment of minerals. Presence of up hole strain shadows.	SDT	Ng1.1.1
DD903	41	191.15	191.60	BD	Beddings	SSL	Ng1.1.1
DD903	42	195.13	195.15	NFA	Mesoscopic-normal fault defines by the offset of beds.	SSL	Ng1.1.1
DD903	43	199.21	200.00	WFO	Weak foliation defined by the alignment of clasts (mafic clasts).	SDT	Ng1.1.1
DD903	46-48	215.60	225.20	WFO	Weak foliation defined by the alignment of clasts. The aligned clasts are mafic, quartzite are not aligned. The rock is slighty parted.	SDT	Ng1.1.1
DD908	72-73	337.87	340.71	MFO	Moderate foliation defined by the alignment of sulphides(pyrite, pyrrhotite). The iron oxides are also parallel to the foliation. The rock is slighty vuggy.	SSL	Ng1.1.2
DD908	73	340.81	347.68	MFO	Moderate foliation defined by the alignment of minerals.	SSL	Ng1.1.2

BHID	Box #	From	To	Feature code	Feature	Lithology	Strat unit
DD908	73	345.23	345.25	RFA	Mesoscopic-reverse fault based on displacement of beds.	SSL	Ng1.1.2
DD908	74-75	350.50	353.00	WFO	Weak foliation defined by the alignment of minerals (pyrite). No orientation.	SSL	Ng1.1.2
DD908	76	358.20	358.80	WFO	Weak foliation defined by pyrite.	SSL	Ng1.1.2
DD908	82-83	393.00	398.90	SS	Weak foliation defined by the alignment of minerals (chalcopyrite, bornite). Upwards strain shadows associated with symmetric strain shadow.	SDT	Ng1.1.1
DD908	85	403.90	407.58	WFO	Weak foliation defined by the alignment of clasts. The rock is slighty parted.	SDT	Ng1.1.1
DD908	87	415.46	416.00	WFO	Weak foliation defined by the alignment of clasts.	SDT	Ng1.1.1
DD909	99	483.52	487.52	MFO	Moderate foliation defined by the alignment of pyrite and pyrrhotite.	SSL	Ng1.1.2
DD909	100-103	487.52	505.46	WFO	Weak to moderate foliation defined by the alignment of pyrite.	SSL	Ng1.1.2
DD909	112-113	552.40	558.09	SS	Moderate foliation defined by the alignment of chalcopyrite. Presence of upwards strain shadows.	SDT	Ng1.1.1
DD909	114-115	561.43	567.40	WFO	Weak foliation defined by the alignment of clasts. Sulphides are also align. The rock is slighty parted.	SDT	Ng1.1.1
DD909	117	578.00	578.50	VN	Quartz vein, fractured.	SDT	Ng1.1.1
DD909	117	578.86	579.24	VWFO	Very weak foliation defined by the alignment of clasts.	SDT	Ng1.1.1
DD912	91	438.63	440.9	MFO	Moderate foliation defined by the alignment of sulphides.	SSL	Ng1.1.2
DD912	94	440.90	458.54	MFO	Moderate foliation defined by the alignment of pyrite. Slighty vuggy rock.	SSL	Ng1.1.2
DD912	95-96	462.19	468.78	WFO	Weak foliation defined by the alignment of pyrite.	SSL	Ng1.1.2
DD912	98	478.79	478.82	NFA	Mesoscopic-normal fault in soft sediment deformation.	SSL	Ng1.1.1
DD912	101	494.14	494.19	VN	Quartz vein with chalcopyrite.	SSL	Ng1.1.1
DD912	102	496.00	500.18	SS	Weak foliation defined by the alignment of clasts. The strain shadow is also align.	SDT	Ng1.1.1
DD912	103	503.30	507.00	WFO	Weak foliation defined by the alignment of clasts.	SDT	Ng1.1.1
DD915	105	506.4	507.75	WFO	Weak foliation defined by the alignment of pyrrhotite and pyrite.	SSL	Ng1.1.2
DD915	105-107	507.75	517.00	WFO	Weak foliation defined by the alignment of minerals. Presence of soft sediment deformation texture.	SSL	Ng1.1.2
DD915	107	517.00	517.09	NFA	Mesoscopic-normal fault defined by the offset of beds. The fault cut the mineralised Py beds. Py overgrow in the fault.	SSL	Ng1.1.2
DD915	109	527.75	527.78	FLD	Fold axial plane subparallel to the bedding. Bedding: 74.	SSL	Ng1.1.2
DD915	107-109	517.09	527.00	MFO	Moderate foliation defined by the alignment of pyrite. Soft sediment deformation	SSL	Ng1.1.2
DD915	109-111	527.78	535.07	MFO	Moderate foliation defined by the alignment of pyrite. Presence of euhedral Pyrite. Soft sediment deformation like slumps.	SSL	Ng1.1.2
DD915	112	543.82	543.94	VN	Quartz vein.	SDT	Ng1.1.1
DD915	113	545.19	545.22	VN	Quartz vein with chlorite and black minerals.	SDT	Ng1.1.1
DD915	116	563.00	569.00	SS	Weak foliation defined by the alignment of chalcopyrite and the alignment of clasts.	SDT	Ng1.1.1
DD915	117	570.12	572.85	WFO	Weak foliation defined by the alignment of clasts. The foliation is most defined by the mafic clasts.	SDT	Ng1.1.1
DD920	34	147.42	147.50	MFO	Moderate foliation defined by the alignment of pyrite. Coarse-grained pyrite is also align.	SSL	Ng1.1.2
DD920	38	170.33	171.50	MFO	Moderate foliation defined by the alignment of pyrite.	SSL	Ng1.1.2
DD920	38	172.00	172.55	MFO	Moderate foliation defined by the alignment of pyrite.	SSL	Ng1.1.2
DD920	46	215.30	216.11	SS	Moderate foliation defined by the alignment of minerals and strain shadow both sub parallel to the core axis. Upwards strain shadows>>symmetric strain shadows.	SDT	Ng1.1.1
DD920	47	216.11	220.00	SS	Moderate foliation defined by the alignment of clasts and minerals. Strain shadows are also align.	SDT	Ng1.1.1
DD920	49,50	230.00	233.00	WFO	Weak foliation defined by the alignment of clasts.	SDT	Ng1.1.1
DD922	58,59	280.00	290.00	SS	Weak foliation defined by upwards strain shadows. The composition of strain shadows is chalcopyrite on top, bornite at the base.	SDT	Ng1.1.1
DD928	36,37,38	173.24	182.00	SS	Weak foliation defined by the alignment of chalcopyrite and symmetric/upwards assymmetric strain shadows (composed of chalcopyrite).	SDT	Ng1.1.1
DD928	40,41,42	187.00	200.00	MFO	Moderate to weak foliation defined by the alignment of clasts.	SDT	Ng1.1.1
DD929	47,48	235.50	240.00	SS	Weak foliation defined by the alignment of clasts.	SDT	Ng1.1.1
DD929	48,49	240.00	248.70	WFO	Weak foliation defined by the alignment of clasts.	SDT	Ng1.1.1
DD929	45,46	224.00	233.00	WFO	Weak foliation defined by upwards strain shadows and coarse- grained chalcopyrite	SDT	Ng1.1.1
DD929	38	190.27	206	MFO	Moderate foliation defined by the alignment of pyrite	SSL	Ng1.1.2
DD929	45,46	225.5	230	SS	Weak foliation defined by the alignment of chalcopyrite and upwards strain shadows.	SDT	Ng1.1.2
DD929	46	230	233	SS	Weak foliation defined by the alignment of strain shadows, mostly symmetric.	SDT	Ng1.1.1
DD929	49	245	249	WFO	Weak foliation defined by the alignment of clasts.	SDT	Ng1.1.1
DD934	45	216.00	218.16	WFO	Weak foliation defined by the alignment of pyrite and iron oxides. Weathered rock.	SSL	Ng1.1.2
DD934	46, 47	220.00	223.00	WFO	Weak foliation defined by the alignment of pyrite.	SSL	Ng1.1.2
DD934	47	222.50	225.50	MFA	Syn-sedimentary fault disrupting the coarse-grained pyrite beds.	SSL	Ng1.1.2
DD934	48	229.50	231.50	WFO	Weak foliation defined by the alignment of CG pyrite.	SSL	Ng1.1.2
DD934	50	243.15	243.50	SS	Weak foliation defined by the alignment of chalcopyrite.	SSL	Ng1.1.2

BHID	Box #	From	To	Feature code	Feature	Lithology	Strat unit
DD934	58	282.00	283.78	X	Brecciated zone with some natif copper infill.	SDT	Ng1.1.1
DD934	57	277.00	279.00	VWFO	Very weak foliation defined by the alignment of mafic clasts.	SDT	Ng1.1.1
DD944		220.26	228.57	SS	Weak foliation defined by the alignment of minerals and upwards chalcopyrite strain shadows.	SDT	Ng1.1.1
DKMC_GD002	73	242.18	244.21	SFO	Strong foliation defines by the alignment of pyrite. S1 is subparallel to the core axis. Presence of vugs.	SSL	Ng1.1.2
DKMC_GD002	76	252.60	252.77	NFA	Mesoscopic-fault showing normal sense of movement based on beds.	SSL	Ng1.1.2
DKMC_GD002	77	253.68	253.78	NFA	Moderate foliation defined by the alignment of pyrite.	SSL	Ng1.1.2
DKMC_GD002	79;80	260.00	264.00	MFO	Moderate foliation defined by the alignment of pyrite.	SSL	Ng1.1.2
DKMC_GD002	83	271.41	275.24	MFO	Moderate foliation defined by the alignment of pyrite.	SSL	Ng1.1.2
DKMC_GD002	85	278.43	279.15	SSD	Soft-sediment deformation texture associated with strain shadows composed of pyrite.	SSL	Ng1.1.2
DKMC_GD002	89	290.42	290.62	MFO	Moderate foliation defines by pyrite subparallel to the core axis.	SSL	Ng1.1.2
DKMC_GD002	102	333.50	333.73	SSD	Soft sediment deformation; siltstone intercalated by sandstone.	SST	Ng1.1.1
DKMC_GD002	105	342.15	342.20	NFA	Normal mesoscopic fault sub-parallel to the core axis.	SSL/SST	Ng1.1.1
DKMC_GD002	105	345.34	345.39	SSD	Soft sediment deformation showing normal sense of movement based on offset of beds.	SSL	Ng1.1.1
DKMC_GD002	107	349.65	349.79	WFO	Weak foliation define by elongation of clasts.	SDT	Ng1.1.1
DKMC_GD002	110	357.50	359.15	WFO	Weak foliation defines by the alignment of clasts. The diamictite is showing stylolite texture.	SDT	Ng1.1.1
DKMC_GD002	112;113;114	365.00	372.50	SS	Chalcopyrite strain shadows associated with occasional symmetric strain shadows.	SDT	Ng1.1.1
DKMC_GD002	114	372.50	374.70	SS	Moderate foliation defines by chalcopyrite. Strain shadow parallel to the foliation.	SDT	Ng1.1.1
DKMC_GD002	115;116	374.70	380.00	SBD	Soft sediment deformation associated with sub-vertical foliation defined by chalcopyrite. Strain shadow composed of clasts and chalcopyrite pyparallel to the foliation defined by sulphide. Bornite replacing chalcopyrite in strain shadow.	SSL	Ng1.1.1
DKMC_GD002	117;118;119	380.00	391.27	SS	Weak foliation defined by chalcopyrite and clasts. Chalcopyrite with bornite in strain shadow. Quatrzite+mafics<3cm. Presence of soft sediment deformation texture in the middle.	SDT	Ng1.1.1
DKMC_GD002	74;75	245.00	248.00	MFO	Moderate foliation defines by pyrite. BD=38	SSL	Ng1.1.2
DKMC_GD002	77	255.00	259.30	MFO	Moderate foliation defines by sulphide subparallel to the core axis.	SSL	Ng1.1.2
DKMC_GD002	86	280.60	281.23	MFO	Strain shadow with pyrite associated with moderate foliation defined by pyrite.	SSL	Ng1.1.2
DKMC_GD002	103; 104	338.28	339.00	NFA	Mesoscopic-fault showing a normal sense of movement.	SSL	Ng1.1.1
DKMC_GD003	150	499.41	499.47	NFA	Mesoscopic-fault. No clear sense of movement.	SSL	Ng1.1.2
DKMC_GD003	152	505.38	505.45	MFO	Mesoscopic-fault showing a normal sense of movement. The fault plane is sub-perpendicular to the core axis.	SSL	Ng1.1.2
DKMC_GD003	158	525.60	525.69	SS	Strain shadows.	SDT	Ng1.1.1
DKMC_GD003	158	527.23	527.29	SS	Strain shadows with very weak foliation.	SDT	Ng1.1.1
DKMC_GD003	159	528.38	528.43	SS	Strain shadow with weak foliation defined by sulphides. Soft-sediment deformation texture.	SDT	Ng1.1.1
DKMC_GD003	163	544.31	544.31	SL	Strike slip slickensides.	SST	R4.2
DKMC_GD003	154	513.74	513.83	FLD	Fold. The fold axial plane is similar/sub-parallel to the bedding.	SSL	Ng1.1.2
DKMC_GD003	154	513.74	513.83	FLD	Fold. The fold axial plane is similar/sub-parallel to the bedding.	SSL	Ng1.1.2
DKMC_GD003	155	515.15	515.25	FLD	Fold. The fold axial plane is similar/sub-parallel to the bedding.	SSL	Ng1.1.2
DKMC_GD003	155	515.32	515.41	FLD	Fold. The fold axial plane is similar/sub-parallel to the bedding.	SSL	Ng1.1.2
DKMC_GD003	155	516.11	516.20	SSD	Soft sediment deformation with quartz and chalcopyrite.	SSL	Ng1.1.2
DKMC_GD003	156	520.38	520.46	SS	Strain shadows.	SDT	Ng1.1.1
DKMC_GD003	159	529.37	529.46	SS	Strain shadows defined by chalcopyrite.	SDT	Ng1.1.1
DKMC_RD432	25	229.04	229.06	SSD	Soft sediment deformation with mesoscopic faults showing a normal sense of movement.	SSL	Ng1.1.2
DKMC_RD432	27	240.00	240.10	VN	Quartz vein associated withpyrite. Brecciated texture.	SSL	Ng1.1.2
DKMC_RD432	30	255.60	255.70	WFO	Aligned pyrite perpendicular to the bedding. Possible S1 foliation.	SSL	Ng1.1.2
DKMC_RD432	31	259.38	259.59	VN		SSL	Ng1.1.2
DKMC_RD432	31	260.54	260.56	SSD	Soft sediment deformation with mesoscopic faults showing normal sense of movement.	SSL	Ng1.1.2
DKMC_RD432	33	271.70	272.30	SSD	Zone with soft sediment deformation.	SSL	Ng1.1.2
DKMC_RD432	37	295.70	297.82	SS	Weak foliation parallel to strain shadows. Upwards and downwards asymmetric strain shadows composed of chalcopyrite.	SDT	Ng1.1.1
DKMC_RD432	38	297.82	300.10	SS	Weak foliation parallel to strain shadows subparallel to the core axis. Bornite is present in the strain shadow. Presence of soft sediment deformation.	SDT	Ng1.1.1
DKMC_RD432	38	300.14	300.54	SBD	Steep bedding with mesoscopic-normal faults. Very high grade interval.	SDT	Ng1.1.1
DKMC_RD432	38	302.00	302.10	SSD	Zone with soft sediment deformation.	SDT	Ng1.1.1
DKMC_RD432	39	303.00	306.54	SS	Very weak foliation with asymmetric downwards strain shadows composed of bornite. Structures are subparallel to the core axis.	SDT	Ng1.1.1
DKMC_RD432	49	310.92	313.00	WFO	Very weak foliation defined by the alignment of clasts. Presence of possible stylolyte.	SDT	Ng1.1.1
DMAK_DD004	93	388.94	388.96	NFA	Mesoscopic-normal fault based on the offset of beds.	SSL	Ng1.1.1
DMAK_DD004	96	398.64	398.68	RFA	Possible reverse fault based on the offset of beds. Chalcopyrite is present along the fault.	SDT	Ng1.1.1

BHID	Box #	From	To	Feature code	Feature	Lithology	Strat unit
DMAK_DD004	96-97	399.00	403.00	SS	Weak foliation defined by the alignment of clasts and minerals.	SDT	Ng1.1.1
DMAK_DD004	97	403.00	406.00	SSD	Zone with soft sediment deformation.	SDT/SSL	Ng1.1.1
DMAK_DD013	123	575.25	576.71	MFO	Moderate foliation defined by pyrite and pyrrhotite.	SSL	Ng1.1.2
DMAK_DD013	124-125	576.71	586.00	WFO	Weak foliation defined by the aligment of minerals.	SSL	Ng1.1.2
DMAK_DD013	126-127	589	595.24	MFO	Moderate foliation defined by the alignment of pyrite.	SSL	Ng1.1.2
DMAK_DD013	132	617.50	622.00	VWFO	Very weak foliation defined by the alignment of clasts.	SDT/SSL	Ng1.1.2
DMAK_DD013	133	622.00	624.30	VWFO	Very weak foliation defined by the alignement of minerals and clasts.	SDT/SSL	Ng1.1.2
DMAK_DD013	133-135	626.00	635.30	SS	Very weak foliation defined by the alignment of clasts and strain shadows when present. Parted rock with possible stylolite texture.	SDT/SSL	Ng1.1.2
DMAK_DD014	92	442.85	444.16	MFO	Moderate foliation defined by pyrite and pyrrhotite.	SSL	Ng1.1.2
DMAK_DD014	92-93	444.00	458.00	WFO	Weak foliation defined by the alignment of pyrite and pyrrhotite. Structures sub-parallel to the core axis.	SSL	Ng1.1.2
DMAK_DD014	96	461.61	461.69	FLD	Possible fold.	SSL	Ng1.1.2
DMAK_DD014	96-98	464.00	475.25	WFO	Weak foliation defined by the alignment of clasts, pyrite and pyrrhotite.	SSL	Ng1.1.2
DMAK_DD014	100	481.86	481.97	NFA	Soft sediment deformation with mesoscopic fault showing a normal sense of movement.	SDT	Ng1.1.1
DMAK_DD014	100-105	486.00	502.00	VWFO	Weak foliation defined by the alignment of clasts and minerals.	SDT	Ng1.1.1
DMAK_DD014	106	509.59	512.30	WFO	Weak foliation defined by the alignment of clasts and chalcopyrite.	SDT	Ng1.1.1
DMAK_DD014	107-108	516.00	522.69	SS	Weak foliation defined by the alignment of minerals and clasts. Presence of asymmetric upwards strain shadows.	SDT/SSL	Ng1.1.1
DMAK_DD014	109-112	528.48	540.77	SS	Weak to moderate foliation defined by the alignment of clasts and minerals. Presence of downward strain shadows.	SDT	Ng1.1.1
DMAK_DD014	113	544.12	544.13	VN	Quartz vein with chalcopyrite in the seveldge.	SSL	Ng1.1.1
DMAK_DD014	113	546.00	547.50	SSD	Zone with soft sediment deformation. Mesoscopic-reverse faults are observed.	SSL	Ng1.1.1
DMAK_DD014	115-116	555.40	561.50	WFO	Weak foliation defined by the alignment of clasts and minerals.	SDT	Ng1.1.1
DMAK_DD014	116	560.20	560.21	VN	Quartz vein with chalcopyrite and bornite infill. This vein is sub parallel to the S1 foliation	SDT	Ng1.1.1
DMAK_DD014	116	560.21	562.32	WFO	Weakly foliation defined by the alignment of clasts and minerals.	SDT	Ng1.1.1
DMAK_DD014	117-118	568.00	571.50	SSD	Zone with soft sediment deformation. Mesoscopic-reverse faults are observed.	SSL	Ng1.1.1
DMAK_DD014	118	571.50	572.03	WFO	Weak foliation defined by the alignment of clasts.	SDT	Ng1.1.1
DMAK_DD016	36	142.63	144.31	MFO	Moderate foliation defined by the alignment of pyrite. The rock is vuggy.	SSL	Ng1.1.2
DMAK_DD016	37	145.19	145.23	NFA	Normal mesoscopic fault shown by the offset of beds.	SSL	Ng1.1.2
DMAK_DD016	38	150.13	150.28	RFA	Zone with mesoscopic-reverse fault associated with some normal faults. The movement sense is defined by the offset of beds.	SSL	Ng1.1.2
DMAK_DD016	38	151.64	153.00	WFO	Weak foliation defined by the alignment of pyrite.	SSL	Ng1.1.2
DMAK_DD016	38,39	154.00	155.57	WFO	Weak foliation defined by the alignment of pyrite.	SSL	Ng1.1.2
DMAK_DD016	40	162.36	162.39	X	Brecciated rock with quartz vein inside.	SSL	Ng1.1.2
DMAK_DD016	41	163.92	164.00	SSD	Soft sediment deformation likely a fold. No really which structure it is.	SSL	Ng1.1.2
DMAK_DD016	42	171.61	171.88	RFA	Mesoscopic reverse fault based on beds. Brecciated zone.	SSL	Ng1.1.2
DMAK_DD016	45	185.19	186.35	SSD	Zone with soft sediment deformation and thin cohesive breccia.	SSL	Ng1.1.2
DMAK_DD016	45	187.15	187.19	X	Brecciated zone.	SDT	Ng1.1.1
DMAK_DD016	51	215.50	215.60	X	Brecciated zone.	SDT	Ng1.1.1
DMAK_DD016	54,55	232.00	242.00	WFO	Weak foliation defined by the alignment of clasts (mafics). Mafic clasts are oriented and sub-parallel to the core axis.	SDT	Ng1.1.1
DMAK_DD016	58	249.15	249.34	WFO	Weak foliation defined by the alignment of clasts (mafics). Mafic clasts are oriented sub-parallel to the core axis.	SDT	Ng1.1.1
DMAK_DD016	61	262.40	262.45	X	Brecciated rock; fractured.	SDT	Ng1.1.1
DMAK_DD016	62,63	269.00	273.00	WFO	Very weak foliation defined by the alignment of clasts sub-parallel to the core axis.	SDT/SSL	Ng1.1.1
DMAK_DD016	66	290.46	290.86	VWFO	Very weak foliation defined by the alignment of clasts sub-parallel to the core axis.	SDT/SSL	Ng1.1.1
DMAK_DD025	6	26.00	28.00	MFO	Moderate foliation defined by the alignment of pyrite. The rock is vuggy.	SSL	Ng1.1.2
DMAK_DD025	7	31.15	31.22	NFA	Mesoscopic-normal fault defined by the offset of beds. The fault cuts the mineralised beds.	SSL	Ng1.1.2
DMAK_DD025	8	37.14	37.17	FLD	Fold. The axial plan is sub-parallel to the bedding.	SSL	Ng1.1.2
DMAK_DD025	13	61.43	61.51	X	Brecciated zone likely a crackle breccia.	SSL	Ng1.1.2
DMAK_DD025	13	63.08	63.11	FLD	Fold sub-parallel to bedding. Alpha bedding= 52.	SSL	Ng1.1.2
DMAK_DD025	13	65.28	65.58	FLD	Fold in a zone showing a soft sediment deformation.	SSL	Ng1.1.2
DMAK_DD025	13	65.71	65.76	FLD	Fold. Bedding alpha=87.	SSL	Ng1.1.2
DMAK_DD025	13	66.68	66.79	FLD	Fold axial plane parallel to the bedding. Bedding=80.	SSL	Ng1.1.2
DMAK_DD025	22,23	110.64	113.32	WFO	Weak foliation defined by the alignment of clasts. Foliation sub-parallel to the core axis.	SDT	Ng1.1.1
DMAK_DD025	24,25	117.34	124.00	WFO	Weak foliation defined by the alignment of clasts. Foliation sub-parallel to the core axis.	SDT	Ng1.1.1
DMAK_DD025	29,30	141.31	149.00	WFO	Weak foliation defined by the alignment of clasts. Foliation sub-parallel to the core axis.	SDT	Ng1.1.1

BHID	Box #	From	To	Feature code	Feature	Lithology	Strat unit
DMAK_DD025	35	168.66	172.12	VWFO	Very weak foliation defined by the alignment of clasts. Foliation sub-parallel to the core axis. Chalcocite in replacement of clasts is also align.	SDT	Ng1.1.1
DMAK_DD027	71	343.35	345.32	MFO	Moderate foliation defined by pyrite and pyrrhotite.	SSL	Ng1.1.2
DMAK_DD027	72	349.69	349.72	NFA	Mesoscopic-faults showing a normal sense of movement.	SSL	Ng1.1.2
DMAK_DD027	73	353	353.29	VN	Quartz vein slighty brecciated.	SSL	Ng1.1.2
DMAK_DD027	75	361.00	361.50	MFO	Moderate foliation defined by the alignment of pyrite; subparallel to the core axis.	SSL	Ng1.1.2
DMAK_DD027	75	363.48	363.60	MFO	Moderate foliation defined by the alignment of pyrite. The pressure shadow is also aligned.	SSL	Ng1.1.2
DMAK_DD027	75-76	364.90	367.00	WFO	Weak foliation defined by the alignment of sulphide. Foliation is sub-parallel to the core axis.	SSL	Ng1.1.2
DMAK_DD027	76	367.40	368.67	SS	Moderate foliation defined by the alignment of pyrite and strain shadows.	SDT	Ng1.1.2
DMAK_DD027	76-77	368.67	373.65	MFO	Moderate foliation defined by the alignment of pyrite and pyrrhotite.	SSL	Ng1.1.2
DMAK_DD027	78	375.50	375.70	X	Crackle breccia with some reverse faults.	SSL	Ng1.1.2
DMAK_DD027	80	384.25	384.30	RFA	mesoscopic-fault showing reverse fault based on clasts.	SDT	Ng1.1.1
DMAK_DD027	81	388.72	393.40	VWFO	Very weak foliation defined by the alignment of clasts.	SDT	Ng1.1.1
DMAK_DD027	82-84	394.89	406.50	VWFO	Very weak foliation defined by the alignment of clasts. Presence of rare strain shadows aligned defining a very weak foliation. S1 is parallel to the core axis	SDT	Ng1.1.1
DMAK_DD027	85	407.64	409.00	X	Brecciated zone.	SDT	Ng1.1.1
DMAK_DD027	85-87	409.00	420.00	WFO	Weak foliation defined by the alignment of clasts and minerals.	SDT	Ng1.1.1
DMAK_DD027	87-88	420.00	424.00	MFO	Moderate foliation defined by the alignment of clasts.	SDT	Ng1.1.1
DMAK_DD027	88-89	425.69	427.65	MFO	Moderate foliation defined by the alignment of clasts. S1 is sub-parallel to the core axis.	SDT	Ng1.1.1
DMAK_DD027	90-91	427.65	436.50	SS	Moderate foliation defined by the alignment of minerals. Symmetric strain shadows>> asymmetric upwards strain shadows.	SDT	Ng1.1.1
DMAK_DD027	91-92	436.50	444.68	MFO	Moderate foliation defined by the alignment of clasts. Sulphide such as chalcopyrite and chalcocite are aligned.	SDT	Ng1.1.1
DMAK_DD027	93	445.20	445.44	X	Crackle breccia with mesoscopic-fault showing reverse sense of movement.	SDT	Ng1.1.1
DMAK_DD027	93-94	453.37	454.07	MFO	Moderate to strongly foliation defined by the the alignment of clasts.	SDT	Ng1.1.1
DMAK_DD027	94	454.42	454.58	X	Crackle breccia.	SSL	Ng1.1.1
DMAK_DD027	95	455.28	467.00	SFO	Moderate to strongly foliation defined by the the alignment of clasts.	SDT/SSL	Ng1.1.1
DMAK_DD027	99	474.60	475.70	X	Crackle breccia.	SSL	Ng1.1.1
DMAK_DD027	99	475.70	483.00	MFO	Moderate foliation defined by the alignment of clasts and sulphides.	SSL	Ng1.1.1
DMAK_DD027	100-102	483.00	492.02	SFO	Strong foliation defined by the alignment of clasts.	SDT	Ng1.1.1
DMAK_DD027	105	505.03	506.13	VN	Quartz vein with some chalcocite.	SSL	Ng1.1.1
DMAK_DD027	105	506.83	508.11	WFO	Very weak foliation defined by the alignment of clasts.	SDT	Ng1.1.1
DMAK_DD027	105	508.11	508.61	VN	Brecciated quartz vein associated with crackle breccia.	SDT	Ng1.1.1
DMAK_DD027	106	509.05	509.90	VN	Brecciated vein associated with quartz.	SST	R4.2
DMAK_DD033	51,52	203.46	218.90	MFO	Weak to moderate foliation defined by the alignment of minerals. Bedding= 68.	SSL	Ng1.1.2
DMAK_DD033	52,53	224.00	232.00	MFO	Weak to moderate foliation defined by the alignment of minerals.	SSL	Ng1.1.2
DMAK_DD033	56	234.75	234.84	FLD	Fold sub-parallel to the bedding. Bedding=71.	SSL	Ng1.1.2
DMAK_DD033	61-63	256.00	268.00	WFO	Weak foliation defined by the alignment of clasts (mostly mafic).	SDT	Ng1.1.1
DMAK_DD033	66	281.00	283.63	WFO	Weak to moderate foliation defined by the alignment of clasts. Pyrite in the replacement of clasts is also align and deines an S1 foliation.	SDT	Ng1.1.1
DMAK_DD033	67	285.47	285.64	VN	Brecciated quartz vein, vuggy.	SSL	Ng1.1.1
DMAK_DD033	67	287.15	287.20	X	Brecciated quartz vein.	SSL	Ng1.1.1
DMAK_DD033	67	288.40	288.53	VN	Quartz vein, vuggy.	SSL	Ng1.1.1
DMAK_DD033	68	292.61	292.62	X	Brecciated quartz vein.	SDT	Ng1.1.1
DMAK_DD033	68	293.20	295.00	X	Brecciated zone with lost core of 1m.	SDT	Ng1.1.1
DMAK_DD033	68,69,70	295.50	305.50	WFO	Weak foliation defined by the alignment of clasts.	SDT	Ng1.1.1
DMAK_DD033	71	307.50	313.89	WFO	Weak foliation defined by the alignment of clasts.	SDT	Ng1.1.1
DMAK_DD033	74	325.00	325.29	VN	Quartz vein, vuggy.	SSL	Ng1.1.1
DMAK_DD033	75	326.29	326.35	VN	Quartz vein, vuggy.	SSL	Ng1.1.1
DMAK_DD033	75	328.50	328.56	X	Crackle breccia in the contact with quartz vein.	SSL	Ng1.1.1
DMAK_DD033	75	328.56	329.00	VN	Quartz and specular haematite vein showing a vuggy texture.	SSL	Ng1.1.1
DMAK_DD033	75	329.77	331.00	WFO	Weak foliation defined by the alignment of clasts.	SDT	Ng1.1.1
DMAK_DD033	75	331.50	331.68	VN	Vuggy quartz vein.	SDT	Ng1.1.1
DMAK_DD033	76	334.63	334.79	VN	Vuggy quartz vein.	SDT	Ng1.1.1
DMAK_DD033	76	334.79	338.00	WFO	Weak foliation defined by the alignment of clasts.	SDT	Ng1.1.1
DMAK_DD033	77	339.16	339.19	X	Thin crackle breccia.	SDT	Ng1.1.1
DMAK_DD033	78	343.39	343.92	X	Brecciated zone like a crackle breccia.	SSL	Ng1.1.1

BHID	Box #	From	To	Feature code	Feature	Lithology	Strat unit
DMAK_DD033	79	349.88	350.68	NFA	Abundant mesoscopic-normal faults.	SSL	Ng1.1.1
DMAK_DD033	80	354.27	355.36	WFO	Weak foliation defined by the alignment of clasts. Malachite in replacement is also aligned.	SDT	Ng1.1.1
DMAK_DD034		307.14	307.35	SBD	Subvertical bedding with sub-perpendicular weak foliation defined by the alignment of minerals. Chalcopyrite is associated with trace bornite. Mesoscopic faults.	SSL	Ng1.1.1
DMAK_DD034		307.35	311.60	SS	Moderate foliation defined by the alignment of clasts and minerals. Abundant upward asymmetric strain shadows. Presence of bedding parallel to the soft sediment deformation. Bedding alpha= 54; beta = 43.	SDT/SSL	Ng1.1.1
DMAK_DD034		311.60	312.35	SBD	Subvertical beds likely soft sediment deformation with abundant bornite and chalcopyrite. Foliation sub-parallel to beds. Moderate foliation defined by the alignment of clasts and minerals. No mesoscopic faults. Foliation Ori=1; alpha= 26; beta= 28.	SDT/SSL	Ng1.1.1
DMAK_DD035	3	11.37	11.40	FLD	Fold. The axial plane is sub-parallel to the bedding. Bedding alpha=72	SSL	Ng1.1.2
DMAK_DD035	3	11.92	11.95	FLD	Fold. The axial plane is sub-parallel to the bedding. Bedding alpha=69	SSL	Ng1.1.2
DMAK_DD035	7	24.80	25.00	X	mesoscopic-fracturing zone showing a brecciated texture.	SSL	Ng1.1.2
DMAK_DD035	7	25.43	25.60	WFO	Weakly foliation defined by the alignment of FeOx grains.	SSL/SDT	Ng1.1.2
DMAK_DD035	13	42.29	42.38	SSD	Soft sediment deformation associated with mesoscopic-normal and reverse faults.	SSL	Ng1.1.2
DMAK_DD035	18	61.11	61.25	X	Gouge zone, brecciated with abundant clay.	SDT	Ng1.1.1
DMAK_DD035	20	72.88	72.92	RFA	Mesoscopic-reverse faults defined by the offset of beds.	SSL	Ng1.1.1
DMAK_DD035	21	76.38	76.53	NFA	Mesoscopic-normal faults with natif copper growing in the fault.	SSL/SST	Ng1.1.1
DMAK_DD035	22,23	81.00	87.00	VWFO	Very weak foliation defined by the alignment of clasts and minerals. S1 is parallel to the core axis.	SDT	Ng1.1.1
DMAK_DD035	24	91.00	94.00	WFO	Weak foliation defined by the alignment of clasts. Sub-parallel to the core axis.	SDT	Ng1.1.1
DMAK_DD035	27	108.97	108.99	X	Brecciated zone likely a crackle breccia. Possible sedimentary breccia.	SSL/SST	Ng1.1.1
DMAK_DD035	27,28	108.99	111.00	WFO	Weak foliation defined by the alignment of clasts. S1 sub-parallel to the core axis.	SDT	Ng1.1.1
DMAK_DD035	28,29	112.00	117.71	WFO	Weak foliation defined by the alignment of clasts. S1 sub-parallel to the core axis.	SDT	Ng1.1.1
DMAK_DD035	32	132.04	134.80	MFO	Moderate foliation defined by the alignment of clasts and minerals (most malachite).	SDT	Ng1.1.1
DMAK_DD035	20	72.66	72.88	WFO	Weak foliation defined by the alignment of chalcopyrite.	SDT	Ng1.1.1
DMAK_RD018	171	957.38	959.95	MFO	Moderate foliation defined by the alignment of clasts.	SDT	Ng1.1.1
DMAK_RD019	81	487.02	487.27	FB	Fabric, possible S1	SSL	Ng1.1
DMAK_RD021	11	104.00	105.33	WFO	Weakly foliation defined by the the alignment of sulphide. The rock shows a vuggy texture.	SSL	Ng1.1.2
DMAK_RD021	12	102.33	105.58	X	Crackle breccia and foliation	SDT/SSL	Ng1.1.2
DMAK_RD021	12	105.58	107.58	MFO	Moderate foliation defined by the alignment of pyrte.	SDT	Ng1.1.2
DMAK_RD021	13	110.00	115.00	X	Badly fractured zone with breccias. Significant fault.	SSL	Ng1.1.2
DMAK_RD021	14	116.00	116.15	X	Crackle breccia possible related to the significant fault above.	SSL	Ng1.1.2
DMAK_RD021	14	116.94	116.99	X	Crackle breccia	SSL	Ng1.1.2
DMAK_RD021	14	117.67	117.73	MFA	Mesoscopic fault showing a reverse sense of movement.	SSL	Ng1.1.2
DMAK_RD021	15	120.65	120.93	NFA	Mesoscopic-fault showing a normal sense of movement based on beds.	SSL	Ng1.1.2
DMAK_RD021	15	121.85	121.91	NFA	Mesoscopic-fault showing a normal sense of movement. Faults cutting sulphides.	SSL	Ng1.1.2
DMAK_RD021	16	124.68	125.32	VN	Brecciated quartz vein with py and iron oxides.	SSL	Ng1.1.2
DMAK_RD021	16	126.16	126.26	NFA	Mesoscopic-fault showing a normal sense of movement. Pyrite in the fracture.	SSL	Ng1.1.2
DMAK_RD021	16	126.99	127.04	RFA	Mesoscopic-reverse fault based on the offset of beds.	SSL	Ng1.1.2
DMAK_RD021	17	131.38	131.81	SSD	Zone with soft sediment deformation associated with cross beds.	SSL	Ng1.1.2
DMAK_RD021	18	135.18	135.24	SSD	Interval with soft sediment deformation and possible fold.	SSL	Ng1.1.2
DMAK_RD021	18	136.42	136.49	X	Cohesive breccia likely a crackle breccia.	SSL	Ng1.1.2
DMAK_RD021	19	141.37	141.42	RFA	Reverse fault based on the offset of beds. Brecciated texture is observed.	SSL	Ng1.1.2
DMAK_RD021	21	148.46	148.48	FLD	Sub-horizontal fold.	SSL	Ng1.1.2
DMAK_RD021	21	149.73	149.75	FLD	Sub-horizontal fold parallel to the beddings.	SSL	Ng1.1.2
DMAK_RD021	21	150.65	150.67	FLD	Fold. The axial plane is parallel to the beddind.	SSL	Ng1.1.2
DMAK_RD021	21	150.87	150.91	X	Crackle breccia.	SSL	Ng1.1.2
DMAK_RD021	22	154.13	154.17	RFA	Mesoscopic-fault showing a reverse sense of movement.	SSL	Ng1.1.1
DMAK_RD021	23	158.03	158.05	X	Crackle breccia	SDT	Ng1.1.1
DMAK_RD021	24	164.21	164.27	VWFO	Very weak foliation defined by the alignment of clasts.	SDT	Ng1.1.1
DMAK_RD021	25	168.23	168.29	X	Crackle breccia with iron oxides and clay.	SDT	Ng1.1.1
DMAK_RD021	25	169.19	169.84	X	Crackle breccia. Cohesive.	SDT	Ng1.1.1
DMAK_RD021	26	173.72	174.80	X	Crackle breccia	SDT	Ng1.1.1
DMAK_RD021	27	176.83	176.89	VWFO	Very weak foliation.	SDT	Ng1.1.1
DMAK_RD021	30	192.50	192.60	NFA	Normal mesoscopic fault in a rock showing a soft sedimentary deformation texture.	SSL	Ng1.1.1
DMAK_RD021	31	199.00	199.16	X	Crackle breccia intercalated by quartz.	SSL	Ng1.1.1
DMAK_RD021	31	201.12	201.20	X	Crackle breccia with quartz in fractures.	SSL	Ng1.1.1

BHID	Box #	From	To	Feature code	Feature	Lithology	Strat unit
DMAK_RD021	32	201.60	201.64	X	Crackle breccia with quarz inside.	SSL	Ng1.1.1
DMAK_RD021	32	205.39	205.44	X	Crackle breccia with quartz.	SDT	Ng1.1.1
DMAK_RD021	33	209.33	209.34	NFA	Mesoscopic-fault showing a normal sense of movement based on the displacement of beds.	SSL	Ng1.1.1
DMAK_RD021	33	210.90	211.00	X	Crackle to mosaic breccia.	SSL	Ng1.1.1
DMAK_RD021	34	216.31	216.35	X	Crackle to mosaic breccia.	SSL	Ng1.1.1
DMAK_RD021	37-38	231.00	233.50	VWFO	Very weak foliation defined by the alignment of clasts.	SDT	Ng1.1.1
DMAK_RD021	38	234.18	234.23	X	Brecciated rock with calcite, malachite and chrysocolla along fractures.	SDT	Ng1.1.1
DMAK_RD021	38	236.45	236.53	X	Brecciated rock like a crackle breccia.	SSL/SDT	Ng1.1.1
DMAK_RD021	39	237.56	237.62	X	Crackle breccia.	SSL	Ng1.1.1
DMAK_RD021	39	240.14	240.77	X	Crackle breccia.	SSL	Ng1.1.1
DMAK_RD021	40	244.29	244.35	X	Crackle breccia.	SSL	Ng1.1.1
DMAK_RD021	41	248.22	248.49	X	Brecciated rock with quartz and cuprite inside.	SSL	Ng1.1.1
DMAK_RD021	42	251.79	252.00	X	Crackle to mosaic breccia with quartz inside.	SSL	Ng1.1.1
DMAK_RD021	42	256.10	256.45	SSD	Zone showing a soft sediment deformation texture.	SDT	Ng1.1.1
DMAK_RD021	44	263.50	263.60	X	Breccia with quartz inside.	SST	R4.2
DMAK_RD023	5	92.00	92.05	NFA	Mesoscopic-normal fault characterised based on beds.	SSL	Ng1.1.2
DMAK_RD023	6	96.32	96.36	FLD	Fold. The axial plane is parallel to bedding. Alpha bedding=81.	SSL	Ng1.1.2
DMAK_RD023	6	98.69	98.74	FLD	Fold. Alpha= 79.	SSL	Ng1.1.2
DMAK_RD023	7	103.33	103.45	X	Crackle breccia.	SDT	Ng1.1.1
DMAK_RD023	8	108.8	109.00	NFA	Mesoscopic-normal fault shown based on the displacement of beds.	SSL	Ng1.1.1
DMAK_RD023	10	116.82	116.85	X	Brecciated rock.	SDT	Ng1.1.1
DMAK_RD023	13,14	134.10	136.10	VWFO	Very weak foliation defined by the alignment of clasts (mafic).	SDT	Ng1.1.1
DMAK_RD023	15	139.65	143.50	VWFO	Very weak foliation defined by the alignment of clasts.	SDT	Ng1.1.1
DMAK_RD023	19	160.00	160.18	NFA	Mesoscopic-normal fault based on beds.	SS/SST	Ng1.1.1
DMAK_RD023	22,24	175.58	184.07	WFO	Weak foliation defined by the alignment of clasts (mafic). Parted rock like stylolites.	SDT	Ng1.1.1
DMAK_RD023	26	197.00	197.50	X	Brecciated rock.	SSL	Ng1.1.1
DMAK_RD023	28	204.30	207.50	VWFO	Very weak foliation defined by the alignment of clasts. Chalcocite is also aligned and defines S1.	SDT	Ng1.1.1
DMAK_RD024	1	56.31	56.40	X	Crackle breccia	SSL	Ng1.1.2
DMAK_RD024	2	61.00	61.08	FLD	Fold.	SSL	Ng1.1.2
DMAK_RD024	3	75.54	75.62	FLD	Fold.	SSL	Ng1.1.2
DMAK_RD024	4	76.20	76.30	X	Crackle breccia	SSL	Ng1.1.2
DMAK_RD024	8	89.42	89.45	VN	Quartz vein	SDT	Ng1.1.1
DMAK_RD024	13	116.77	116.84	NFA	Zone with soft sediment deformation and normal mesoscopic faults >reverse faults.	SSL	Ng1.1.1
DMAK_RD024	18	117.19	117.24	NFA	Mesoscopic fault showing a normal sense of movement based on displacement of beds.	SSL	Ng1.1.1
DMAK_RD024	18	140.43	140.50	RFA	Mesoscopic fault showing a reverse sense of movement based on displacement of beds.	SSL	Ng1.1.1
DMAK_RD024	18	142.24	142.28	RFA	Mesoscopic fault showing a reverse sense of movement based on displacement of beds.	SSL	Ng1.1.1
DMAK_RD024	23	167.29	167.39	RFA	Mesoscopic fault showing a reverse sense of movement based on displacement of beds.	SSL	Ng1.1.1
DMAK_RD024	24	168.00	168.10	X	Crackle breccia with malachite inside.	SSL	Ng1.1.1
DMAK_RD024	24	168.31	168.35	NFA	Mesoscopic fault showing a normal sense of movement based on displacement of beds.	SSL	Ng1.1.1
DMAK_RD024	24	168.81	168.86	RFA	Mesoscopic fault showing a reverse sense of movement based on displacement of beds.	SSL	Ng1.1.1
DMAK_RD030	89	557.38	557.84	WFO	Weak foliation defined by the alignment of pyrite.	SSL	Ng1.1.2
DMAK_RD030	89	559.34	559.44	NFA	Mesoscopic fault showing a normal sense of movement based on displacement of beds.	SSL	Ng1.1.2
DMAK_RD030	89-90	559.44	563.08	WFO	Weak foliation defined by the alignment of pyrite.	SSL	Ng1.1.2
DMAK_RD030	90	563.08	563.19	SSD	Soft sediment deformation likely a fold. pyrite is slighty aligned.	SSL	Ng1.1.2
DMAK_RD030	90-91	563.19	575.75	WFO	Weak foliation defined by the alignment of pyrite.	SSL	Ng1.1.2
DMAK_RD030	92-94	579.09	590.72	WFO	Weak foliation defined by the alignment of pyrite.	SSL	Ng1.1.2
DMAK_RD030	97	599.00	601.11	SSD	Soft sediment deformation. Mesoscopic fault showing normal sense of movement based on displacement of beds.	SST	Ng1.1.1
DMAK_RD030	98	602.46	602.48	VN	Quartz vein.	SST	Ng1.1.1
DMAK_RD030	98	603.05	607.00	SSD	Soft sediment deformation with normal mesoscopic faults.	SST/SSL	Ng1.1.1
DMAK_RD030	98	607.09	607.18	FLD	Fold.	SSL	Ng1.1.1
DMAK_RD030	103	630.11	630.23	WFO	Weak foliation defined by the alignment of clasts.	SDT	Ng1.1.1
DMAK_RD030	105	636.63	639.00	SSD	Zone with soft sediment deformation texture.	SDT	Ng1.1.1
DMAK_RD030	105	639.00	640.66	SS	Weak foliation defined by sulphide. Presence of symmetric strain shadows composed of chalcopyrite.	SDT	Ng1.1.1
DMAK_RD030	105; 106	640.66	641.80	SSD	Soft sediment deformation. Presence of normal mesoscopic faults. Weak foliation defined by the alignment of chalcopyrite. Presence of thin veins like tensional veins.	SDT	Ng1.1.1

BHID	Box #	From	To	Feature code	Feature	Lithology	Strat unit
DMAK_RD030	106	641.80	642.03	SBD	Steep bedding. S1 foliation defined by the alignment of chalcopyrite. The mineralisation is sub-parallel to the steep bedding.	SDT	Ng1.1.1
DMAK_RD030	106	642.03	643.69	SS	Weak foliation defined by the alignment of sulphides and clasts. Presence of asymmetric strain shadows.	SDT	Ng1.1.1
DMAK_RD030	107-110	648.22	659.24	WFO	Weak foliation defined by the alignment of clasts. Quartzite clasts are not well aligned; possible due to their strenght.	SDT	Ng1.1.1
DMAK_RD030	110	660.86	660.94	NFA	Normal mesoscopic fault like a grabben.	SDT/SSL	Ng1.1.1
DMAK_RD030	112-113	674.30	679.29	NFA	Abundant normal mesoscopic faults (each 5cm).	SSL	Ng1.1.1
DMAK_RD030	114	679.44	680.64	VWFO	Very weak foliation defined by the alignment of clasts. S1 foliation is sub-parallel to the core axis.	SDT	Ng1.1.1
DTJI_DD001	20	92.24	93.11	MFO	Moderate S1 define by pyrite and pyrrhotite	SDT	Ng1.1
DTJI_DD001	20	92.24	93.11	MFO	Moderate S1 define by pyrite and pyrrhotite	SDT	Ng1.1
DTJI_DD001	20	92.24	93.11	MFO	Moderate S1 define by pyrite and pyrrhotite	SDT	Ng1.1
DTJI_DD001	91	398.61	398.82	SFO	Strong S1 defines by the alignment of clasts	SDT	Ng1.1
DTJI_DD001	91	400.16	400.78	SFO	Strong S1 defines by the alignment of clasts	SDT	Ng1.1
DTJI_DD001	98	431.90	432.10	SFO	Strong S1 defines by the alignment of clasts	SDT	Ng1.1
DTJI_DD001	126	567.00	567.50	SFO	Strong S1 defines by the alignment of clasts	SDT	Ng1.1
DTJI_DD001	126	568.38	569.10	SFO	Strong S1 defines by the alignment of clasts	SDT	Ng1.1
DTJI_DD001	126	569.88	570.11	SFO	Strong S1 defines by the alignment of clasts	SDT	Ng1.1
DTJI_DD001	22	100.51	100.74	SFO	S1 defined by the alignment of clasts and sulphides such as pyrite and pyrrhotite.	SDT	Ng1.1
DTJI_DD001	20	93.50	93.90	SFO	S1 defined by pyrite and pyrrhotite	SDT	Ng1.1
DTJI_DD001	20	100.32	100.69	SFO	Weak to moderate foliation defined by clasts. S1 defined by the alignment of pyrite and pyrrhotite	SDT	Ng1.1
DTJI_DD001	91	401.00	401.23	SFO	Strong S1 defined by the alignment and elongation of clasts	SDT	Ng1.1
DTJI_DD001	98	429.00	429.74	SFO	Strong S1 defined by the alignment and elongation of clasts	SDT	Ng1.1
DTJI_DD001	108	471.84	411.41	MFO	Moderate foliation defined by the alignment and elongation of clasts.	SDT	Ng1.1
DTJI_DD001	108	471.50	471.94	SFO	Strong S1 defined by the alignment and elongation of clasts	SDT	Ng1.1

Borehole ID	Depth From (m)	Depth To (m)	Lithology 1	Strat Major	Strat Minor	CR	ASU	ASD	SYM	Predominant mineral in strain shadow/fringes	Clast-composition_1	Clast-composition_2	Comments
DD793	394.46	395	SDT	Ng 1.1.1	Ng 1.1.1.3	7				chalcopyrite	Mafic		
DD793	395	395.5	SDT	Ng 1.1.1	Ng 1.1.1.3	16				chalcopyrite	Mafic		
DD793	395.5	396	SDT	Ng 1.1.1	Ng 1.1.1.3	16		1	1	chalcopyrite	Mafic		
DD793	396	396.5	SDT	Ng 1.1.1	Ng 1.1.1.3	28				chalcopyrite	Mafic	Quartzite	
DD793	396.5	397	SDT	Ng 1.1.1	Ng 1.1.1.3	44	1	2	1	chalcopyrite	Quartzite	Mafic	
DD793	397	397.5	SDT	Ng 1.1.1	Ng 1.1.1.3	39	2			chalcopyrite	Quartzite	Mafic	
DD793	397.5	398	SDT	Ng 1.1.1	Ng 1.1.1.3	44	2			chalcopyrite	Quartzite	Mafic	
DD793	398	398.5	SDT	Ng 1.1.1	Ng 1.1.1.3	12	6	2		chalcopyrite	Quartzite	Mafic	
DD793	398.5	399	SDT	Ng 1.1.1	Ng 1.1.1.3	25	11	3		chalcopyrite	Quartzite	Mafic	
DD793	399	399.5	SDT	Ng 1.1.1	Ng 1.1.1.3	37	32	2	2	chalcopyrite	Quartzite	Mafic	
DD793	399.5	400	SDT	Ng 1.1.1	Ng 1.1.1.3	51	12		4	chalcopyrite	Quartzite	Mafic	
DD793	400	400.45	SDT	Ng 1.1.1	Ng 1.1.1.3	28	10	2	15	chalcopyrite>>>bornite	Quartzite	Mafic	
DD793	400.45	400.65	SDT	Ng 1.1.1	Ng 1.1.1.3								
DD793	400.65	400.9	SDT	Ng 1.1.1	Ng 1.1.1.3	4	1		9	chalcopyrite	Quartite	Mafic	
DD595	423.5	424	SSL	Ng 1.1.1	Ng 1.1.1.3	10	1			chalcopyrite	Mafic	Quartzite	Laminated; fine- to medium-grained silstone. Dropstones in the siltstone. 90% of clasts are < 1cm.
DD595	424	424.7	SSL	Ng 1.1.1	Ng 1.1.1.3	13				chalcopyrite	Mafic	Quartzite	Laminated; fine- to medium-grained silstone. Dropstones in the siltstone. 90% of clasts are < 1cm.
DD595	424.7	425	SDT	Ng 1.1.1	Ng 1.1.1.3	44				chalcopyrite	Mafic	Quartzite	90% of clasts are < 1cm.
DD595	425	425.5	SDT/SSL	Ng 1.1.1	Ng 1.1.1.3	31				chalcopyrite	Mafic	Quartzite	90% of clasts are < 1cm.
DD595	425.5	426	SDT	Ng 1.1.1	Ng 1.1.1.3	32				chalcopyrite	Mafic	Quartzite	90% of clasts are < 1cm.
DD595	426	426.5	SDT	Ng 1.1.1	Ng 1.1.1.3	23				chalcopyrite	Mafic	Quartzite	90% of clasts are < 1cm.
DD595	426.5	427	SDT	Ng 1.1.1	Ng 1.1.1.3	28				chalcopyrite	Mafic	Quartzite	90% of clasts are < 1cm.
DD595	427	427.5	SDT	Ng 1.1.1	Ng 1.1.1.3	32	3	1		chalcopyrite	Mafic	Quartzite	90% of CR clasts are < 1cm
DD595	427.5	428	SDT	Ng 1.1.1	Ng 1.1.1.3	56	9	2		chalcopyrite	Mafic	Quartzite	90% of CR clasts are < 1cm.
DD595	428	428.5	SDT	Ng 1.1.1	Ng 1.1.1.3	54	4			chalcopyrite	Mafic	Quartzite	90% of CR clasts are < 1cm.
DD595	428.5	429	SDT	Ng 1.1.1	Ng 1.1.1.3	58	8	2		chalcopyrite	Mafic	Quartzite	90% of CR clasts are < 1cm.
DD595	429	429.5	SDT	Ng 1.1.1	Ng 1.1.1.3	19	2	1	3	chalcopyrite	Mafic	Quartzite	90% of CR clasts are < 1cm.
DD595	429.5	430	SDT	Ng 1.1.1	Ng 1.1.1.3	31	6		5	chalcopyrite	Mafic	Quartzite	90% of CR clasts are < 1cm.
DD595	430	430.5	SDT	Ng 1.1.1	Ng 1.1.1.3	49	5		5	chalcopyrite	Mafic	Quartzite	90% of CR clasts are < 1cm.
DD595	430.5	431	SDT	Ng 1.1.1	Ng 1.1.1.3	55	2	1	2	chalcopyrite	Mafic	Quartzite	90% of CR clasts are < 1cm.
DD595	431	431.5	SDT	Ng 1.1.1	Ng 1.1.1.3	72	4		3	chalcopyrite	Mafic	Quartzite	90% of CR clasts are < 1cm.
DD595	431.5	432	SDT	Ng 1.1.1	Ng 1.1.1.3	19	6			chalcopyrite	Mafic	Quartzite	90% of CR clasts are < 1cm.
DD595	432	432.5	SDT	Ng 1.1.1	Ng 1.1.1.3	42	5	1		chalcopyrite	Mafic	Quartzite	90% of CR clasts are < 1cm.
DD595	432.5	433	SDT	Ng 1.1.1	Ng 1.1.1.3	26				chalcopyrite	Mafic	Quartzite	90% of CR clasts are < 1cm.
DD595	433	433.5	SDT	Ng 1.1.1	Ng 1.1.1.1	24		2		chalcopyrite	Mafic	Quartzite	90% of CR clasts are < 1cm.
DD595	433.5	434	SDT	Ng 1.1.1	Ng 1.1.1.1	2	1			chalcopyrite	Mafic		Mafic > 5cm.
DD595	434	434.5	SDT	Ng 1.1.1	Ng 1.1.1.1	5				chalcopyrite	Mafic		
DD595	434.5	435	SDT	Ng 1.1.1	Ng 1.1.1.1	17	1			chalcopyrite	Mafic		CR < 1cm; ASU = 7cm.
DD595	435	435.5	SDT	Ng 1.1.1	Ng 1.1.1.1	7	3			chalcopyrite	Mafic		CR< 1.5cm; ASU < 1.5cm.
DD595	435.5	436	SDT	Ng 1.1.1	Ng 1.1.1.1	10	1			chalcopyrite	Mafic		CR < 1cm; ASU< 1cm.
DD595	436	436.5	SDT	Ng 1.1.1	Ng 1.1.1.1	32				chalcopyrite	Mafic		CR < 1cm.
DD595	436.5	437	SDT	Ng 1.1.1	Ng 1.1.1.1	11	1			chalcopyrite	Mafic		CR < 1cm; T2 ASU = 1cm.
DD595	437	437.5	SDT	Ng 1.1.1	Ng 1.1.1.1	4				chalcopyrite	Mafic		
DD595	437.5	438	SDT	Ng 1.1.1	Ng 1.1.1.1	13				chalcopyrite	Mafic		
DD595	438	438.5	SDT	Ng 1.1.1	Ng 1.1.1.1	6				chalcopyrite	Mafic		CR < 1 cm.
DD595	438.5	439	SDT	Ng 1.1.1	Ng 1.1.1.1	9				chalcopyrite	Mafic		CR < 1 cm.
DD595	439	439.5	SDT	Ng 1.1.1	Ng 1.1.1.1	16				chalcopyrite	Mafic		CR < 1 cm.
DD595	439.5	440	SDT	Ng 1.1.1	Ng 1.1.1.1	4				chalcopyrite	Mafic		CR < 1 cm.

Borehole ID	Depth From (m)	Depth To (m)	Lithology 1	Strat Major	Strat Minor	CR	ASU	ASD	SYM	Predominant mineral in strain shadow/fringes	Clast-composition_1	Clast-composition_2	Comments
DD595	440	440.5	SDT	Ng 1.1.1	Ng 1.1.1.1	2				chalcopyrite	Mafic		CR < 1 cm.
DD595	440.5	441	SDT	Ng 1.1.1	Ng 1.1.1.1	2		1		chalcopyrite	Mafic		T2 ASD 6 cm.
DD595	441	441.5	SDT	Ng 1.1.1	Ng 1.1.1.1	3	1			chalcopyrite	Mafic		CR and T2 ASU < 1cm.
DD595	441.5	442	SDT	Ng 1.1.1	Ng 1.1.1.1	3				chalcopyrite	Mafic		CR < 1 cm.
DD595	442	442.5	SDT	Ng 1.1.1	Ng 1.1.1.1	1				chalcopyrite	Mafic		CR < 1 cm.
DD595	442.5	443	SDT	Ng 1.1.1	Ng 1.1.1.1	2				chalcopyrite	Mafic		CR < 1 cm.
DD595	443	443.5	SDT	Ng 1.1.1	Ng 1.1.1.1	1				chalcocite	Quartzite		CR < 1 cm.
DD084	159.5	160	SDT	Ng 1.1.1	Ng 1.1.1.3	28	3			chalcopyrite>>>chalcocite	Mafic	Quartzite	Mafic+Quartzite < 1cm.
DD084	160	160.5	SDT	Ng 1.1.1	Ng 1.1.1.3	20	2			chalcopyrite	Mafic	Quartzite	CR < 1cm.
DD084	160.5	161	SDT	Ng 1.1.1	Ng 1.1.1.3	4	1	1		chalcopyrite	Mafic	Quartzite	CR < 1cm.
DD084	161	161.5	SDT	Ng 1.1.1	Ng 1.1.1.3	13	1			chalcopyrite	Mafic	Quartzite	CR < 1cm.
DD084	161.5	162	SDT	Ng 1.1.1	Ng 1.1.1.3	20	1		1	chalcopyrite	Mafic	Quartzite	CR < 1cm.
DD084	162	162.5	SDT	Ng 1.1.1	Ng 1.1.1.3	60	5		4	chalcopyrite	Mafic	Quartzite	CR < 1cm.
DD084	162.5	163	SDT	Ng 1.1.1	Ng 1.1.1.3	14	2	2	3	chalcopyrite	Mafic	Quartzite	CR < 1cm.
DD084	163	163.5	SDT	Ng 1.1.1	Ng 1.1.1.3	68	2		3	chalcopyrite	Mafic	Quartzite	CR < 0.7cm; SYM < 1cm; ASU >1 cm.
DD084	163.5	164	SDT	Ng 1.1.1	Ng 1.1.1.3	77	5	2	3	chalcopyrite	Mafic	Quartzite	
DD084	164	164.5	SDT	Ng 1.1.1	Ng 1.1.1.3	131	3		5	chalcopyrite	Mafic	Quartzite	CR < 1cm; ASU> 1 cm; SYM < 1cm.
DD084	164.5	165	SDT	Ng 1.1.1	Ng 1.1.1.3	97	4		3	chalcopyrite	Mafic	Quartzite	CR< 1cm; ASU 1-4cm; SYM < 1cm; ASU < 1cm.
DD084	165	165.5	SDT	Ng 1.1.1	Ng 1.1.1.3	39	5	2		chalcopyrite	Mafic	Quartzite	
DD084	165.5	166	SDT	Ng 1.1.1	Ng 1.1.1.3	45	4		3	chalcopyrite	Mafic	Quartzite	CR < 0.5cm; ASU< 1cm; SYM < 0.5cm.
DD084	166	166.5	SDT	Ng 1.1.1	Ng 1.1.1.3	27	2		7	chalcopyrite	Mafic	Quartzite	CR< 0.5cm; ASU < 0.5cm; SYM= 0.2-3cm.
DD084	166.5	166.63	SDT	Ng 1.1.1	Ng 1.1.1.3	32	3		2	chalcopyrite	Mafic	Quartzite	CR < 0.4cm; ASU < 1cm; SYM < 0.2cm.
DD084	166.63	167	SSL/SDT	Ng 1.1.1	Ng 1.1.1.3	6	3			chalcopyrite	Mafic	Quartzite	CR < 0.4cm; ASU Cpy>>>Cct <1cm.
DD084	167	167.5	SSL/SDT	Ng 1.1.1	Ng 1.1.1.3	7	2		1	chalcocite	Mafic	Quartzite	CR < 0.5cm; ASU < 0.3cm; SYM < 2 cm.
DD944	208	209	SSL	Ng 1.1.2			1			pyrite	mafic	Quartz	siltstone with dropstones.
DD944	209	209.5	SSL	Ng 1.1.2									
DD944	209.5	211	SDT	Ng 1.1.1	Ng 1.1.1.3				2	chalcopyrite	mafic	Quartz	<1cm.
DD944	211	212	SDT	Ng 1.1.1	Ng 1.1.1.3	6		1	8	pyrite>>>chalcopyrite	mafic	Quartz	CR<0.8cm; SYM 0.5-2cm.
DD944	212	213	SDT	Ng 1.1.1	Ng 1.1.1.3			1		pyrite	mafic	Quartz	
DD944	213	214.36	SDT	Ng 1.1.1	Ng 1.1.1.3				1	pyrite	mafic	Quartz	ASU; SYM<1cm.
DD944	214.36	215	BDR	Ng 1.1.1	Ng 1.1.1.3		4			chalcopyrite	mafic	Quartz	<1cm.
DD944	215	216	SDT	Ng 1.1.1	Ng 1.1.1.3				2	pyrite	mafic	Quartz	Clasts with rims < 1cm.
DD944	216	217	SDT	Ng 1.1.1	Ng 1.1.1.3	24			2	chalcopyrite>>pyrite	mafic	Quartz	Clasts with rims < 1cm.
DD944	217	218	SDT	Ng 1.1.1	Ng 1.1.1.3	16	1	1		chalcopyrite	mafic	Quartz	Clasts with rims < 1cm.
DD944	218	219	SDT	Ng 1.1.1	Ng 1.1.1.3				3	chalcopyrite	mafic	Quartz	Clasts with rims < 1cm.
DD944	219	220	SDT	Ng 1.1.1	Ng 1.1.1.3	5	2			chalcopyrite	mafic	Quartz	
DD944	220	221	SDT	Ng 1.1.1	Ng 1.1.1.3	14	1		4	chalcopyrite	mafic	Quartz	
DD944	221	222	SDT	Ng 1.1.1	Ng 1.1.1.3	4	2		7	chalcopyrite	mafic	Quartz	CR< 0.8cm; ASU<0.8cm; SYM< 1cm.
DD944	222	223	SDT	Ng 1.1.1	Ng 1.1.1.3	21			4	chalcopyrite	mafic	Quartz	CR, SYM<1cm.
DD944	223	224	SDT	Ng 1.1.1	Ng 1.1.1.3	21	4		4	chalcopyrite	mafic	Quartz	CR, ASU, SYM<1cm.
DD944	224	225	SDT	Ng 1.1.1	Ng 1.1.1.3	36	18		5	chalcopyrite	mafic	Quartz	CR<1; ASU 1-2.5cm; SYM<1cm.
DD944	225	225.76	SDT	Ng 1.1.1	Ng 1.1.1.3	25	8		4	chalcopyrite	mafic	Quartz	CR<1; ASU 1-2cm; SYM<1cm.
DD944	225.76	226.3	SDT	Ng 1.1.1	Ng 1.1.1.3	7	4		3	chalcopyrite	mafic	Quartz	CR<1; ASU 1-2cm; SYM<1cm.
DD944	226.3	227	SDT	Ng 1.1.1	Ng 1.1.1.3	11	7		5	chalcopyrite	mafic	Quartz	CR<1; ASU 1-2.5cm; SYM<1cm.
DD944	227	227.5	SDT	Ng 1.1.1	Ng 1.1.1.3	12	5		3	chalcopyrite	mafic	Quartz	CR<1; ASU 1-2.5cm; SYM<1cm.
DD944	227.5	228	SDT	Ng 1.1.1	Ng 1.1.1.3	13			6	chalcopyrite	mafic	Quartz	CR<1; ASD 1-2.5cm; SYM<1cm.
DD944	228	228.5	SDT	Ng 1.1.1	Ng 1.1.1.3	13		2	2	chalcopyrite>>bornite	mafic	Quartz	All types are < 1cm.
DD944	228.5	229.2	SDT	Ng 1.1.1	Ng 1.1.1.3	12	8		3	bornite>chalcopyrite	mafic	Quartz	
DD944	229.2	229.9	SDT	Ng 1.1.1	Ng 1.1.1.1	10	7		1	bornite>chalcocite	mafic	Quartz	
DD944	229.9	230.4	SDT	Ng 1.1.1	Ng 1.1.1.1	2	6		1	bornite	mafic	Quartz	
DD944	230.4	230.9	SDT	Ng 1.1.1	Ng 1.1.1.1	4	10		2	bornite	mafic	Quartz	

Borehole ID	Depth From (m)	Depth To (m)	Lithology 1	Strat Major	Strat Minor	CR	ASU	ASD	SYM	Predominant mineral in strain shadow/fringes	Clast-composition_1	Clast-composition_2	Comments
DD944	230.9	231.83	SDT	Ng 1.1.1	Ng 1.1.1.1	3	5		6	bornite>>>chalcocite	mafic	Quartz	
DD944	231.83	232.5	SDT	Ng 1.1.1	Ng 1.1.1.1	5	4		1	bornite, chlorite	mafic	Quartz	
DD944	232.5	233	SDT	Ng 1.1.1	Ng 1.1.1.1	1			1	bornite	mafic	Quartz	
DD944	233	234	SDT	Ng 1.1.1	Ng 1.1.1.1	15		1	2	bornite>>chlorite	mafic	Quartz	CR,ASU< 0.5cm.
DD944	234	235	SDT	Ng 1.1.1	Ng 1.1.1.1	5			3	bornite	mafic	Quartz	CR<0.3cm; ASD>1cm.
DD944	235	236	SDT	Ng 1.1.1	Ng 1.1.1.1			2		carbonates,bornite	mafic	Quartz	CR, ASD< 0.5cm.
DD944	236	237	SDT	Ng 1.1.1	Ng 1.1.1.1				1	carbonates	mafic	Quartz	SYM 1.5-5cm.
DD944	237	238	SDT	Ng 1.1.1	Ng 1.1.1.1		1			carbonates,chlorite	mafic	Quartz	ASU =3cm.
DD944	238	239	SDT	Ng 1.1.1	Ng 1.1.1.1		1		1	carbonates,chlorite	mafic	Quartz	
DD944	239	240	SDT	Ng 1.1.1	Ng 1.1.1.1						mafic	Quartz	
DD944	240	241	SDT	Ng 1.1.1	Ng 1.1.1.1						mafic	Quartz	
DD944	241	242	SDT	Ng 1.1.1	Ng 1.1.1.1						mafic	Quartz	
DD944	242	243	SDT	Ng 1.1.1	Ng 1.1.1.1						mafic	Quartz	
DD944	243	243.5	SDT	Ng 1.1.1	Ng 1.1.1.1						mafic	Quartz	
DD944	243.5	244	SDT	Ng 1.1.1	Ng 1.1.1.1						mafic	Quartz	
DD895	539.53	539.7	SSL	Ng 1.1.2		2				haematite			
DD895	539.7	540.4	SDT	Ng 1.1.1	Ng 1.1.1.3	2	1			haematite			
DD895	540.4	540.88	SDT	Ng 1.1.1	Ng 1.1.1.3		1			haematite			
DD895	540.88	541.85	MF	Ng 1.1.1	Ng 1.1.1.3								
DD895	541.85	542	SDT	Ng 1.1.1	Ng 1.1.1.3								
DD895	542	543	SDT	Ng 1.1.1	Ng 1.1.1.3								
DD895	543	544	SDT	Ng 1.1.1	Ng 1.1.1.3								
DD895	544	545	SDT	Ng 1.1.1	Ng 1.1.1.3								
DD895	545	546	SDT	Ng 1.1.1	Ng 1.1.1.3	2	2	1	2	pyrite			
DD895	546	547	SDT	Ng 1.1.1	Ng 1.1.1.3	8			2	pyrite			
DD895	547	548	SDT	Ng 1.1.1	Ng 1.1.1.3				2	pyrite			
DD895	548	549	SDT	Ng 1.1.1	Ng 1.1.1.3	6	1			pyrite, iron oxides			
DD895	549	550	SDT	Ng 1.1.1	Ng 1.1.1.3	1		2	4	pyrite, iron oxides			
DD895	550	550.52	SDT	Ng 1.1.1	Ng 1.1.1.3	4				iron oxides			
DD895	550.52	552	SSL/SST	Ng 1.1.1	Ng 1.1.1.3								
DD895	552	570.23	SSL	Ng 1.1.1	Ng 1.1.1.3								
DD895	570.23	573.3	SDT	Ng 1.1.1	Ng 1.1.1.3								
DD895	573.3	574.42	SDT	Ng 1.1.1	Ng 1.1.1.3	5	3			chalcopyrite			
DD895	574.42	575	SDT	Ng 1.1.1	Ng 1.1.1.3	1	1			chalcopyrite			
DD895	575	575.4	SDT/SSL	Ng 1.1.1	Ng 1.1.1.3	5				chalcopyrite,pyrite			
DD895	575.4	575.71	SSL	Ng 1.1.1	Ng 1.1.1.3	3				pyrite			
DD895	575.71	576.5	SDT	Ng 1.1.1	Ng 1.1.1.3	7				pyrite,chalcopyrite			
DD895	576.5	577	SDT	Ng 1.1.1	Ng 1.1.1.3	5				chalcopyrite,pyrite			
DD895	577	577.5	SDT	Ng 1.1.1	Ng 1.1.1.3	17				chalcopyrite			
DD895	577.5	578.23	SDT	Ng 1.1.1	Ng 1.1.1.3	11				chalcopyrite			
DD895	578.23	578.77	SSL	Ng 1.1.1	Ng 1.1.1.3	2				chalcopyrite			
DD895	578.77	579.47	SSL	Ng 1.1.1	Ng 1.1.1.3	6				chalcopyrite>>>bornite			CR< 1cm.
DD895	579.47	580	SDT	Ng 1.1.1	Ng 1.1.1.3	11				chalcopyrite			
DD895	580	581	SDT	Ng 1.1.1	Ng 1.1.1.3	26	21	3	33	chalcopyrite			
DD895	581	582	SDT	Ng 1.1.1	Ng 1.1.1.3	63	17		8	chalcopyrite			ASU>1cm-10cm; SYM 0.5-1.5cm.
DD895	582	583	SDT	Ng 1.1.1	Ng 1.1.1.3	72	12	1	24	chalcopyrite			ASU>1cm-10cm; SYM 0.5-1.5cm.
DD895	583	584	SDT	Ng 1.1.1	Ng 1.1.1.3	87	16		28	chalcopyrite			ASU>1cm-10cm; SYM 0.5-1.5cm.
DD895	584	584.6	SDT	Ng 1.1.1	Ng 1.1.1.3	58	17		7	chalcopyrite			ASU>1cm-10cm; SYM 0.5-1.5cm. CR , 1cm.
DD895	584.6	585	SSL	Ng 1.1.1	Ng 1.1.1.2								
DD895	585	585.55	SDT	Ng 1.1.1	Ng 1.1.1.2	36	8		18	chalcopyrite			
DD895	585.55	586	SDT/SSL	Ng 1.1.1	Ng 1.1.1.2	21			12	chalcopyrite			

Borehole ID	Depth From (m)	Depth To (m)	Lithology 1	Strat Major	Strat Minor	CR	ASU	ASD	SYM	Predominant mineral in strain shadow/fringes	Clast-composition_1	Clast-composition_2	Comments
DD895	586	586.85	SDT/SSL	Ng 1.1.1	Ng 1.1.1.2	37	3		3	chalcopyrite			
DD895	586.85	587.73	SSL	Ng 1.1.1	Ng 1.1.1.2		1			chalcopyrite			Dropstones in siltstone.
DD895	587.73	588.5	SSL	Ng 1.1.1	Ng 1.1.1.2								
DD895	588.5	589	SSL	Ng 1.1.1	Ng 1.1.1.2		1			chalcopyrite			
DD895	589	590	SSL	Ng 1.1.1	Ng 1.1.1.2								
DD895	590	590.5	SSL	Ng 1.1.1	Ng 1.1.1.2								
DD895	590.5	591.18	SSL	Ng 1.1.1	Ng 1.1.1.2								
DD895	591.18	592	SDT	Ng 1.1.1	Ng 1.1.1.1	7	6			chalcopyrite			CR< 1cm; ASU> 1cm.
DD895	592	592.93	SDT	Ng 1.1.1	Ng 1.1.1.1	17				chalcopyrite			
DD895	592.93	593.5	SDT	Ng 1.1.1	Ng 1.1.1.1	8			2	chalcopyrite			
DD895	593.5	594	SDT	Ng 1.1.1	Ng 1.1.1.1	15				chalcopyrite			
DD895	594	595	SDT	Ng 1.1.1	Ng 1.1.1.1	2			2	chalcopyrite			
DD895	595	596	SDT	Ng 1.1.1	Ng 1.1.1.1	24				chalcopyrite			
DD895	596	597	SDT	Ng 1.1.1	Ng 1.1.1.1	10	2	1		chalcopyrite			
DD895	597	597.45	SDT	Ng 1.1.1	Ng 1.1.1.1								
DD895	597.45	598	SDT	Ng 1.1.1	Ng 1.1.1.1		2			chalcopyrite			
DD895	598	599	SDT	Ng 1.1.1	Ng 1.1.1.1	12				chalcopyrite			
DD895	599	600	SDT	Ng 1.1.1	Ng 1.1.1.1	3	1	2		chalcopyrite			
DD895	600	600.4	SDT	Ng 1.1.1	Ng 1.1.1.1								
DD895	600.4	600.86	SSL/SST	Ng 1.1.1	Ng 1.1.1.1								
DD895	600.86	601.65	SDT	Ng 1.1.1	Ng 1.1.1.1	1			2	chalcopyrite			
DD895	601.65	602.5	SDT	Ng 1.1.1	Ng 1.1.1.1			1	7	chalcopyrite			ASD, SYM<0.5cm.
DD895	602.5	603	SDT	Ng 1.1.1	Ng 1.1.1.1		3		4	chalcopyrite			
DD895	603	604	SDT	Ng 1.1.1	Ng 1.1.1.1			1	1	chalcopyrite			
DD895	604	605	SDT	Ng 1.1.1	Ng 1.1.1.1								
DD895	605	606	SDT	Ng 1.1.1	Ng 1.1.1.1								
DD895	606	607	SDT	Ng 1.1.1	Ng 1.1.1.1								
DD895	607	608	SDT	Ng 1.1.1	Ng 1.1.1.1								
DD895	608	609	SDT	Ng 1.1.1	Ng 1.1.1.1	2				chalcopyrite			

BHID	From	To	Feature code	Comments	Material	Lithology	Strat Unit	Orientation	Alpha	Beta	Dip	Dip/Direction
DD197	211.5	212.4	WFO	Weak foliation defined by upwards strain shadows and the alignment of minerals.	chalcopyrite	SDT	Ng1.1.1	1	28	11	84	19
DD197	219	224.05	WWFO	Very weak foliation defined by the alignment of clasts(most argillites).	Clasts	SDT	Ng1.1.1	1	36	59	75	235
DD200	201.54	205	WFO	Weak foliation defined by the alignment of chalcopyrite and strain shadows.	chalcopyrite	SDT	Ng1.1.1	1	42	359	81	359
DD202	183.38	188.69	VWFO	Very weak foliation defined by the alignment of clasts.	Clasts	SSL	Ng1.1.1	1	38	36	77	303
DD202	188.69	192.03	WFO	Weak foliation defined by the alignment of clasts.	Clasts	SDT	Ng1.1.1	1	36	71	68	330
DD202	192.03	195.63	WFO	Weak foliation defined by the alignment of clasts.	Clasts	SDT	Ng1.1.1	1	36	61	71	323
DD202	195.63	197.51	WFO	Weak foliation defined by the alignment of clasts.	Clasts	SDT	Ng1.1.1	1	34	84	64	342
DD224	398.00	402.28	WFO	Strain shadows, weak foliation defined by the alignmnent of coarse-grained chalcopyrite. Upwards strain shadows>>symmetric shadows.	chalcopyrite	SDT	Ng1.1.1	2	21	68	79	165
DD224	402.87	409.05	VWFO	Very weak foliation defined by the alignment of clasts. The mafic clasts are aligned, the Quartzite are not aligned. Quartzite>>Mafic clasts.	Clasts	SDT	Ng1.1.1	1	31	90	62	180
DD309	394.52	396	VWFO	Very weak foliation defined by the alignment of clasts (most mafic clasts). Quartz are not aligned.	Clasts	SDT	Ng1.1.1	1	21	334	80	72
DD309	403	411.42	VWFO	Very weak foliation defined by the alignment of mafic clasts. Quartz clasts are not aligned. The small clasts are well aligned.	Clasts	SDT	Ng1.1.1	1	13	303	84	43
DD330	591.51	594.00	VWFO	Very weak foliation defined by the alignment of small mafic clasts	Clasts	SDT	Ng1.1.1	1	24	53	79	153
DD453	1147.61	1150.29	MFO	Strain shadows and foliation defined by the alignment of clasts and upwards strain shadows.	chalcopyrite	SDT	Ng1.1.1	1	36	38	89	347
DD453	1150.89	1155.66	WFO	Weak foliation defined by the alignment of coarse-grained chalcopyrite, coarse-grained bornite; alignment of symmetric and asymmetric strain shadows.Predominance of upwards strain shadows.	chalcopyrite	SDT	Ng1.1.1	1	46	32	83	159
DD453	1147.61	1150.29	WFO	Weak to moderate foliation defined by the alignment of clasts and upwards strain shadows.	chalcopyrite	SDT	Ng1.1.1	1	36	38	89	347
DD757	416.77	417.92	WFO	Strain shadows and strain fringes. Weak foliation defined by the alignment of coarse-grained chalcopyrite and the alignment strain shadows. Strain shadow>>strain fringes. Upwards> symmetric> downwards strain shadows.	chalcopyrite	SDT	Ng1.1.1	1	22	212	63	309
DD757	421.4	422.68	WFO	Weak foliation defined by the alignment of coarse-grained chalcopyrite. Pyrite occurs along the beds, it is aligned and defines a foliation.	chalcopyrite	SSL	Ng1.1.1	1	24	12	71	107
DD793	397.96	400.9	WFO	Weak foliation defined by the alignment of coarse-grained chalcopyrite and upwards strain shadows (predominance of upwards strain shadows).	chalcopyrite	SDT	Ng1.1.1	1	24	217	58	335
DD793	408.67	414.72	VWFO	Very weak foliation defined by the alignment of mafic clasts; quartzite are not aligned.	Clasts	SDT	Ng1.1.1	1	20	66	74	180
DD802	411.11	414.00	WFO	Weak foliation defined by the alignment of coarse-grained chalcopyrite and strain shadows.	chalcopyrite	SDT	Ng1.1.1	1	18	332	78	103
DD802	421.72	425.00	VWFO	Very weak foliation defined by the alignment of mafic clasts; quartzite are not aligned.	Clasts	SDT	Ng1.1.1	2	22	317	73	89
DD215	575.41	578.51	WFO	Weak foliation defined by the alignment of pyrite.	pyrite	SSL	Ng1.1.2	1	18	77	74	181
DD215	578.58	579.11	WFO	Weak foliation defined by the alignment of pyrite.	pyrite	SSL	Ng1.1.2	1	2	343	85	269

BHID	From	To	Feature code	Comments	Material	Lithology	Strat Unit	Orientation	Alpha	Beta	Dip	Dip/Direction
DD215	579.15	579.79	WFO	Weak foliation defined by the alignment of pyrite.	pyrite	SSL	Ng1.1.2	1	20	92	70	196
DD215	580.1	580.68	WFO	Weak foliation defined by the alignment of fine- and coarse-grained pyrite.	pyrite	SSL	Ng1.1.2	1	22	77	70	180
DD215	580.69	582.96	WFO	Weak foliation defined by the alignment of fine- and coarse-grained pyrite.	pyrite	SSL	Ng1.1.2	1	29	89	61	191
DD215	583.06	583.95	WFO	Weak foliation defined by the alignment of fine- and coarse-grained pyrite.	pyrite	SSL	Ng1.1.2	1	28	103	61	205
DD322	797	801	WFO	Upwards strain shadows < symmetric strain shadows. Downwards strain shadows. The mineralisation is principally chalcopyrite>>> chalcocite. Fractured at the base. The fracturation caused the supergene mineralisation.	chalcopyrite	SDT	Ng1.1.1	1	28	36	71	168
DD322	803.69	804.5	VWFO	Very weak foliation defined by the alignment of small mafics clasts and some upwards strain shadows.	chalcopyrite	SDT	Ng1.1.1	1	27	30	73	162
DD365	966.58	971	WFO	Chalcopyrite upwards strain shadows>>strain fringes. Symmetric strain shadows at the base. Rare downward strain shadows. Ori 1 alpha 34; beta 34. Ori 1 alpha 27; beta 24.	chalcopyrite	SDT	Ng1.1.1	1	34	20	85	118
DD365	972.16	973.12	VWFO	Very weak foliation defined by the alignment of clasts. Mostly mafics.	Clasts	SDT	Ng1.1.1	1	17	62	89	159
DD375	901.63	904.83	MFO	Moderate foliation defined by the alignment of coarse-grained pyrite.	pyrite	SDT	Ng1.1.2	1	34	78	63	160
DD375	904.83	906.11	MFO	Moderate foliation defined by the alignment of coarse-grained pyrite.	pyrite	SDT	Ng1.1.2	1	36	106	51	184
DD375	909	911.26	WFO	Upwards strain shadows. Strain shadows>strain fringes.	chalcopyrite	SDT	Ng1.1.1	1	44	95	48	169
DD387	819.42	820	WFO	Weak foliation defined by the alignment of coarse-grained pyrite.	pyrite	SSL	Ng1.1.2	1	48	53	57	152
DD387	831.54	833.63	WFO	Upwards strain shadows.	chalcopyrite	SDT	Ng1.1.1	1	28	18	82	128
DD387	833.63	837	WFO	Upwards strain shadows> upwards strain strain fringes. Symmetric strain shadows/fringes at the base. Foliation defined by coarse grained bornite. Ori 1 alpha=29 beta=32; Ori 1 alpha=31 beta=35.	chalcopyrite	SDT	Ng1.1.1	1	36	15	74	125
DD387	835.5		WFO	Weak foliation defined by the alignment of sulphides (chalcopyrite and bornite).	chalcopyrite	SDT		1	29	32	79	141
DD387	836.5		WFO	Weak foliation defined by the alignment of sulphides (chalcopyrite and bornite).	chalcopyrite/ bornite	SDT		1	31	35	77	143
DD414	500.3	506	MFO	Moderate foliation associated with strain shadows defined by coarse-grained pyrite. Ori1 alpha=11; beta=244; Ori2 alpha=22; beta=222.	pyrite	SSL	Ng1.1.2	1	39	150	30	219
DD414	507.73	508.29	MFO	Moderate foliation defined by the alignment of coarse-grained pyrite.	pyrite	SSL	Ng1.1.2	1	27	192	37	287
DD414	511.37	512.32	MFO	Moderate folition defined by the alignment of coarse-grained pyrite.	pyrite	SSL	Ng1.1.2	1	37	216	34	326
DD571	545.26	547.8	WFO	Upwards strain shadows>> strain fringes. Chalcopyrite >> bornite at the base. Ori 1 alpha 24 beta 42.	chalcopyrite	SDT	Ng1.1.1	1	29	35	78	142
DD571	546		WFO	Upwards strain shadows>> strain fringes. Chalcopyrite >> bornite at the base.		SDT		1	24	42	81	149
DD598	905.98	906.55	WFO	Weak foliation defined by the alignment of coarse-grained pyrite.	pyrite	SSL	Ng1.1.2	1	42	33	56	102

BHID	From	To	Feature code	Comments	Material	Lithology	Strat Unit	Orientation	Alpha	Beta	Dip	Dip/Direction
DD598	930.19	936	WFO	Strain shadows> strain fringes. A good zonation observed from chalcopyrite on top and bornite at the base. Upwards strain shadows on top, downwards strain shadows at the base.	chalcopyrite	SDT	Ng1.1.1	1	27	335	72	49
DD598	933.8		WFO	Weak foliation defined by the alignment of chalcopyrite.				1	20	36	78	107
DD643	751.63	752.45	WFO	Weak foliation defined by the alignment of coarse-grained pyrite.	pyrite	SSL/SDT	Ng1.1.2	1	44	42	53	108
DD895	504.60	507.30	MFO	Moderate foliation defined by the alignment of coarse-grained pyrite.	pyrite	SSL	Ng1.1.2	1	37	53	59	153
DD895	507.85	515.00	WFO	Weak foliation defined by the alignment of coarse-grained pyrite.	pyrite	SSL	Ng1.1.2	1	33	29	65	135
DD895	579.89	584.60	WFO	Weak foliation defined by symmetric and asymmetric upwards chalcopyrite strain shadows.	chalcopyrite	SDT	Ng1.1.1	3	30	47	64	159
DD901	595.07	597	MFO	Moderate foliation defined by the alignment of pyrite and pyrrhotite. Slighty vuggy.	pyrrhotite	SSL	Ng1.1.2	1	25	353	73	118
DD901	611.12	616.71	MFO	Moderate foliation defined by the alignment of pyrite.	pyrite	SSL	Ng1.1.2	3	29	333	69	99
DD901	665.65	670.46	WFO	Weak foliation defined by the alignment of clasts and minerals (chalcopyrite, bornite). Parted rock.	chalcopyrite	SDT	Ng1.1.1	3	31	323	66	94
DD901	673.82	681.74	WFO	Weak foliation defined by the alignment of clasts. The minerals are also aligned. The rock is parted.	Clasts	SDT	Ng1.1.1	3	28	58	67	183
DD908	337.87	340.71	MFO	Moderate foliation defined by the alignment of sulphides(pyrite and pyrrhotite). The iron oxides are also parallel to the foliation. The rock is slighty vuggy.	pyrrhotite	SSL	Ng1.1.2	1	39	86	52	148
DD908	340.81	347.68	MFO	Moderate foliation defined by the alignment of pyrite.	pyrite	SSL	Ng1.1.2	1	43	58	51	121
DD908	393.00	398.90	WFO	Weak foliation defined by the alignment of minerals (chalcopyrite, bornite). Upwards strain shadows associated with symmetric strain shadows.	chalcopyrite	SDT	Ng1.1.1	1	40	42	56	110
DD908	403.90	407.58	WFO	Weak foliation defined by the alignment of clasts. The rock is slighty parted.	Clasts	SDT	Ng1.1.1	2	31	135	54	207
DD908	415.46	416.00	WFO	Weak foliation defined by the alignment of clasts.	Clasts	SDT	Ng1.1.1	2	41	71	52	143
DD909	483.52	487.52	MFO	Moderate foliation defined by the alignment of sulphides such as pyrite and pyrrhotite.	pyrrhotite	SSL	Ng1.1.2	3	39	62	55	162
DD909	487.52	505.46	MFO	Weak to moderate foliation defined by the alignment of pyrite.	pyrite	SSL	Ng1.1.2	3	37	52	58	154
DD909	552.40	558.09	MFO	Moderate foliation defined by the alignment of chalcopyrite. Presence of upwards strain shadows.	chalcopyrite	SDT	Ng1.1.1	1	23	50	73	161
DD909	561.43	567.40	WFO	Weak foliation defined by the alignment of clasts. Sulphides are also aligned. The rock is slighty parted.	Clasts	SDT	Ng1.1.1	1	10	41	87	155
DD912	438.63	440.9	MFO	Moderate foliation defined by the alignment of sulphides.	pyrrhotite	SSL	Ng1.1.2	1	42	32	60	139
DD912	440.90	458.54	MFO	Moderate foliation defined by the alignment of pyrite. Slighty vuggy.	pyrite	SSL	Ng1.1.2	1	68	48	33	144
DD912	462.19	468.78	WFO	Weak foliation defined by the alignment of pyrite.	pyrite	SSL	Ng1.1.2	3	54	51	46	152
DD912	496.00	500.18	WFO	Weak foliation defined by the alignment of clasts. Strain shadows are also aligned.	chalcopyrite	SDT	Ng1.1.1	1	28	52	71	160
DD912	503.30	507.00	WFO	Weak foliation defined by the alignment of clasts.	Clasts	SDT	Ng1.1.1	3	29	84	63	189
DMAK_DD013	575.25	576.71	MFO	Moderate foliation defined by pyrrhotite and pyrite.	pyrrhotite	SSL	Ng1.1.2.	1	41	76	55	190
DMAK_DD013	589	595.24	MFO	Moderate foliation defined by the alignment of pyrite.	pyrite	SSL	Ng1.1.2.	1	61	65	39	170
DMAK_DD014	486.00	502.00	WFO	Weak foliation defined by the alignment of clasts and minerals.	Clasts	SDT	Ng1.1.1	1	24	38	77	137
DMAK_DD014	516.00	522.69	WFO	Weak foliation defined by the alignment of minerals and clasts. Presence of asymmetric upwards strain shadows.	chalcopyrite	SDT/SSL	Ng1.1.1	1	34	70	62	165

BHID	From	To	Feature code	Comments	Material	Lithology	Strat Unit	Orientation	Alpha	Beta	Dip	Dip/Direction
DMAK_DD014	560.21	562.32	WFO	Weak foliation defined by the alignment of clasts and minerals.	Clasts	SDT	Ng1.1.1	1	19	68	77	170
DMAK_DD034	307.35	311.60	MFO	Moderate foliation defined by the alignment of clasts and chalcopyrite. Abundance of upwards strain shadows. Presence of bedding. A soft sediment deformation texture is observed. Bedding alpha= 54; beta = 43.	chalcopyrite	SDT/SSL	Ng1.1.1	1	36	62	61	172
DMAK_RD018	957.38	959.95	MFO	Moderate foliation defined by the alignment of clasts.	Clasts	SDT	Ng1.1.1	1	37	66	68	194
DMAK_RD019	766.50	782.00	WFO	Weak foliation defined by the alignment of coarse-graind pyrite.	pyrite	SSL	Ng1.1.2	1	48	54	64	170
DMAK_RD019	782.00	783.50	WFO	Weak foliation defined by al of CG py.	pyrite	SSL	Ng1.1.2	1	34	60	75	181
DMAK_RD019	812.00	830.89	MFO	Weak foliation defined by the alignment of clasts.	Clasts	SDT	Ng1.1.1	1	28	51	82	176
DMAK_RD019	876.00	879.77	MFO	Weak foliation defined by the alignment of clasts.		SDT	Ng1.1.1	1	39	34	78	159
DMAK_RD019	893.00	899.45	WFO	WFO to MFO defined by elongation of clasts.	Clasts	SDT	Ng1.1.1	1	23	67	81	192
DD381	239.00	243.00	WFO	Weak foliation defined by the alignment of clasts and minerals (Chalcopyrite). Presence of upwards strain shadows.	chalcopyrite	SDT	Ng1.1.1	1	19	273	72	3
DD405	529.00	532.88	VWFO	Very weak foliation defined by the alignement of clasts. The mafic clasts are aligned. Quartz clasts are not aligned.	Clasts	SDT	Ng1.1.1.	1	29	52	73	144
DD449	386.37	386.58	WFO	Weakly foliation define by the alignment of pyrite	pyrite	Siltstone	Ng1.1.2	1	51	82	49	146
DD825	163.50	169.00	MFO	Moderate foliation defined by the alignment of clasts. Clasts are also deformed.	Clasts	SSL/SDT	Ng1.1.1	1	37	352	68	81
DD844W1	981.40	999.00	VWFO	Very weak foliation defined by the alignment of clasts and minerals (pyrite, pyrrhotite).	pyrite	SDT	Ng1.1.3	1	34	12	56	280
DD855	112.85	116.85	WFO	Weak foliation defined by the alignment of clasts and minerals (Bornite). Presence of symmetric and upwards strain shadows.	Bornite	SDT	Ng1.1.1	1	36	62	65	143
DD856	135.77	140.00	VWFO	Very weak foliation defined by the alignment of minerals (bornite) and clasts.	Bornite	SDT	Ng1.1.1	1	52	44	54	118
DD862	246.39	247.5	MFO	Moderate foliation defined by the alignment of fine- and coarse-grained pyrite.	pyrite	SSL	Ng1.1.2	1	24	342	82	78
DD862	255	257.67	WFO	Weak foliation defined by the alignment of coarse-grained pyrite.	pyrite	SSL	Ng1.1.2	2	33	45	69	137
DD862	273.23	276.1	WFO	Weak foliation defined by the alignment of strain shadows (most upwards). Strain shadows>strain fringes. The predominant mineral in the strain shadows is chalcopyrite.	chalcopyrite	SDT	Ng1.1.1	1	23	52	78	146
DD862	276.96	278.23	VWFO	Very weak foliation defined by the alignment of coarse-grained chalcopyrite and strain shadows.	chalcopyrite	SDT	Ng1.1.1	1	24	57	76	150
DD866	261.45	265.36	MFO	Weak to moderate foliation defined by the alignment of clasts and minerals (bornite).	Bornite	SDT	Ng1.1.1	1	9	291	86	22
DD869	206.28	223	WFO	Weak foliation defined by the alignment of pyrite.	pyrite	SSL	Ng1.1.2.	1	48	218	31	326
DD869	209.5	216	WFO	Weak foliation defined by the alignment of pyrite.	pyrite	SSL	Ng1.1.2.	1	24	59	74	148
DD887	312.67	316.20	WFO	Weak foliation defined by the alignment of chalcopyrite. Upwards asymmetric strain shadows.	chalcopyrite	SDT	Ng1.1.1	1	27	56	72	135
DD888	265.00	271.51	MFO	Moderate foliation defined by the alignment of bornite coarse-grained, clasts and upwards asymmetric strain shadows. Soft sediment deformation with undulated and disrupted beds. Foliation sub-parallel to the beds. Presence of mesoscopic faults; most normal and rare reverse sense of movement. Bedding: ori3 alpha= 28; beta= 42.	Bornite	SDT	Ng1.1.1	3	37	56	56	137
DD903	169.10	170.61	WFO	Weak foliation defined by the alignment of clasts.	Clasts	SDT	Ng1.1.1	1	23	71	73	159
DD903	184.56	187.80	WFO	Weak foliation defined by the alignment of chalcopyrite.	chalcopyrite	SDT	Ng1.1.1	1	29	54	71	142

BHID	From	To	Feature code	Comments	Material	Lithology	Strat Unit	Orientation	Alpha	Beta	Dip	Dip/Direction
DD903	215.60	225.20	WFO	Weak foliation defined by the alignment of clasts. The aligned clasts are mafic, quartzite clasts are not aligned. The rock is slighty parted.	Clasts	SDT	Ng1.1.1	2	19	49	82	140
DD915	506.4	507.75	WFO	Weak foliation defined by the alignment of pyrite and pyrrhotite.	pyrrhotite	SSL	Ng1.1.2	1	29	64	64	179
DD915	507.75	517.00	WFO	Weak foliation defined by the alignment of pyrite. The rock shows a soft sediment deformation texture.	pyrite	SSL	Ng1.1.2	1	47	36	48	150
DD915	517.09	527.00	MFO	Moderate foliation defined by the alignment of pyrite. Pyrite tends to replace clasts that are also aligned. Soft sed deformation	pyrite	SSL	Ng1.1.2	3	42	68	51	181
DD915	527.78	535.07	MFO	Moderate foliation defined by the alignment of pyrite. Presence of euhedral pyrite. The soft sediment deformation texture is also observed.	pyrite	SSL	Ng1.1.2	1	26	82	65	196
DD915	563.00	569.00	WFO	Weak foliation defined by the alignment of sulphide minerals (chalcopyrite fine- and coarse-grained) and clasts.	chalcopyrite	SDT	Ng1.1.1	1	28	61	65	178
DD915	570.12	572.85	WFO	Weak foliation defined by the alignment of clasts. The foliation is most observed in the mafic clasts.	Clasts	SDT	Ng1.1.1	1	24	62	69	180
DD920	147.42	147.50	MFO	Moderate foliation defined by the alignment of pyrite. Pyrite coarse-grained in the clasts is also aligned.	pyrite	SSL	Ng1.1.2	1	49	74	48	152
DD920	170.33	171.50	MFO	Moderate foliation defined by the alignment of pyrite.	pyrite	SSL	Ng1.1.2	2	26	17	80	111
DD920	172.00	172.55	MFO	Moderate foliation defined by the alignment of pyrite.	pyrite	SSL	Ng1.1.2	2	26	27	79	120
DD920	215.30	216.11	MFO	Moderate foliation defined by the alignment of minerals and strain shadows both sub-parallel to the core axis. Upwards strain shadows>>symmetric stain shadows. Chalcopyrite is the predominant mineral in the strain shadows.	chalcopyrite	SDT	Ng1.1.1	1	23	18	83	112
DD920	216.11	220.00	MFO	Moderate foliation defined by the alignment of clasts and minerals. Strain shadows are also align.	Clasts	SDT	Ng1.1.1	1	24	13	82	107
DD920	230.00	233.00	WFO	Weak foliation defined by the alignment of clasts.	Clasts	SDT	Ng1.1.1	1	18	13	88	108
DD922	280.00	287.00	WFO	Weak foliation defined by the alignement of upwards strain shadows. Chalcopyrite is the predominant mineral in the strain shadows.	chalcopyrite	SDT	Ng1.1.1	1	18	264	71	4
DD922	287.00	290.00	WFO	Weak foliation defined by upwards strain shadows composed of chalcopyrite on top of the interval and bornite at the base.	Bornite	SDT	Ng1.1.1	1	18	264	71	4
DD928	173.24	182.00	WFO	Weak foliation defined by the alignment of chalcopyrite. The alignment of symmetric and upwards strain shadows defines also a weak foliation.	chalcopyrite	SDT	Ng1.1.1	1	14	62	81	172
DD928	187.00	200.00	MFO	Moderate to weak foliation defined by the alignment of clasts.	Clasts	SDT	Ng1.1.1	1	24	62	71	171
DD929	190.27	206	MFO	Moderate foliation defined by the alignment of coarse-grained pyrite.	pyrite	SSL	Ng1.1.2	2	29	83	63	170
DD929	245	249	WFO	Weak foliation defined by the alignment of clasts.	Clasts	SDT	Ng1.1.1	2	35	272	56	10
DD929	235.50	240.00	WFO	Weak foliation defined by the alignment of clasts.	Clasts	SDT	Ng1.1.1	2	31	56	65	144
DD929	240.00	248.70	WFO	Weak foliation defined by the alignment of clasts.	Clasts	SDT	Ng1.1.1	2	17	307	79	41
DD929	224.00	233.00	WFO	Weak foliation defined by upwards strain shadows and coarse-grained chalcopyrite	chalcopyrite	SDT	Ng1.1.1	3	22	282	70	18
DD934	220.00	223.00	WFO	Weak foliation defined by the alignment of pyrite.	pyrite	SSL	Ng1.1.2	2	23	32	79	123
DD934	229.50	231.50	WFO	Weak foliation defined by the alignment of coarse-grained pyrite.	pyrite	SSL	Ng1.1.2	2	28	112	58	198
DD934	243.15	243.50	WFO	Weak foliation defined by the alignment of chalcopyrite.	chalcopyrite	SSL	Ng1.1.1	3	12	22	89	295

BHID	From	To	Feature code	Comments	Material	Lithology	Strat Unit	Orientation	Alpha	Beta	Dip	Dip/Direction
DD934	277.00	279.00	VWFO	Very weak foliation defined by the alignment of mafic clasts.	Clasts	SDT	Ng1.1.1	1	9	337	86	252
DD944	220.26	228.57	WFO	Weak foliation defined by the alignment of minerals and upwards asymmetric strain shadows.	chalcopyrite	SDT	Ng1.1.1	1	22	76	71	167